

**QUANTIFYING MARINE REDOX ACROSS
THE TRIASSIC–JURASSIC MASS
EXTINCTION**

Andrew D. Bond

Department of Earth Sciences
Royal Holloway University of London

September 2022



*A thesis submitted in fulfilment of the requirements for
the degree of Doctor of Philosophy*

*This thesis is dedicated to my late mother, Dawn Bond, to my wife,
Catherine Bond, and to fellow geologist Mr D. G. Binns*

DECLARATION OF AUTHORSHIP

I, Andrew Derek Bond, hereby declare that this thesis and the work presented in it is entirely my own unless stated otherwise. Where I have consulted the work of others, this is always clearly stated.

Signed:

A handwritten signature in black ink, appearing to read 'A. Bond', written in a cursive style.

Date: 22/09/22

ABSTRACT

As anthropogenic carbon emissions continue to alter global temperatures and weathering rates, studies of environmental analogues attempt to predict the pattern of subsequent marine redox changes as well as the vulnerability of marine ecosystems. One such analogue may take the form of the Triassic–Jurassic boundary interval (~201 Ma) which has been closely associated with widespread marine de-oxygenation and marine mass extinction. However, relatively little is understood about the initiation and spatio-temporal progression of marine redox change during this interval, as well as the vulnerability of different sub-environments and/or biota to redox changes. This thesis has used the elemental and isotopic compositions of marine sediments to reconstruct marine redox change on the Tethyan shelf, during the Triassic–Jurassic boundary interval, in a bid to further understand the complex nature of marine de-oxygenation during an interval of global environmental change. The work undertaken within this thesis demonstrates that Triassic–Jurassic marine de-oxygenation on the Tethyan shelf, and in the open ocean, coincided with intervals of marine extinction, particularly amongst benthic organisms, potentially suggesting causality. This thesis reveals that marine redox change on the Tethyan shelf was pulsed in nature and was largely preceded by open ocean de-oxygenation, meaning that marine redox change may have progressed from the open ocean to marginal marine environments. Mo isotope data presented here reveals that sulfidic conditions covered no more than 0.05–0.1% of the Late Triassic seafloor and were likely geographically restricted to marginal marine environments. However, on the marginal marine Tethyan shelf sulfidic conditions were limited spatially in comparison to sedimentary porewater and bottom water de-oxygenation, which was more widespread. Late Triassic marine redox change is poorly correlated to changes in detrital input, weathering, grain size and hydrography on the Tethyan shelf potentially suggesting marine redox change being driven by regional nutrient changes, stratification, ocean warming or changes to ocean circulation. The work undertaken within this thesis therefore advances understanding of redox evolution during the Triassic–Jurassic boundary interval as well as its potential role in marine extinctions during the ETME.

ACKNOWLEDGEMENTS

The past four years have been a very surreal experience. For example, I could have never predicted that my doctoral research would coincide with a global pandemic, the United Kingdom's exit from the European Union, the deaths of Queen Elizabeth II and Prince Philip, Duke of Edinburgh, and the beginnings of a European war. My co-supervisor Micha Ruhl quoted in his doctoral thesis the R.E.M. lyrics 'it's the end of the world as we know it'... yet at certain points within my PhD this was quite literally the case. There were definitely times throughout my PhD where I questioned whether this thesis, or the data within it, would ever reach the light of day. It's almost exclusively through the support of my family, friends, and the supervision I have received that this thesis has become a reality.

Firstly, thank you to my supervisors Alex Dickson and Micha Ruhl. Thank you for dedicating your time, your support and for allowing me to research an exciting and ground-breaking field. I'm not sure this thesis would be half as interesting as it is without your invaluable expertise and inciteful input. Particularly thank you to Alex Dickson, I know you probably questioned at times whether taking me on as a postgraduate research student would be your undoing. But we managed it in the end! Thank you for always making time to discuss theories and data, for being patient and supportive regardless of how work was proceeding, and for championing me to always get the most out of my research.

Thank you to my co-authors: Alex Dickson, Micha Ruhl, Robert Raine, Bas van de Schootbrugge, Remco Bos, József Pálffy, Emma Blanka Kovács and Christian Bjerrum. It has been a privilege to publish research and/or collaborate with you all.

Thank you to all those who have provided me with or have given me permission to analyse Triassic–Jurassic core and outcrop samples, particularly Jonathan Larwood, Micha Ruhl, Christian Bjerrum, Martin Blumenberg, Remco Bos and Emma Blanka Kovács.

Most of all I am thankful for my loving and supportive family.

“For I know the plans I have for you” declares the LORD “plans to prosper you and not to harm you, plans to give you hope and a future” – Jeremiah 29:11

Contents

2.3.5.5 The collapse of late Triassic reef environments.....	52
2.3.5.6 Other extinctions of late Triassic marine organisms.....	56
2.3.5.7 Section summary.....	65
2.3.6 <i>Potential causes of the Triassic–Jurassic mass extinction event</i>	67
2.3.6.1 Extraterrestrial impact	
2.3.6.2 Central Atlantic Magmatic Province (CAMP).....	71
2.3.6.3 Section summary.....	76
2.4 CHAPTER SUMMARY	
3 GEOCHEMICAL ENVIRONMENTAL PROXIES.....	78
3.1 INTRODUCTION	
3.2 PALAEO REDOX PROXIES	
3.3 PALAEO WEATHERING/DETRITAL INPUT PROXIES.....	84
3.4 PALAEO HYDROGRAPHIC PROXIES.....	85
3.5 CHAPTER SUMMARY.....	87
4 UPPER TRIASSIC AND LOWER JURASSIC CORE.....	88
AND OUTCROP SAMPLES	
4.1 INTRODUCTION	
4.2 CARNDUFF-2 CORE, LARNE BASIN, N. IRELAND.....	89
4.3 SOMERSET-1 & SOMERSET-2 CORES, ST. AUDRIE’S BAY,	91
BRISTOL CHANNEL BASIN, ENGLAND	
4.4 PREES 2C CORE, CHESHIRE BASIN, ENGLAND.....	93
4.5 CORE AND OUTCROP SAMPLES FROM THE CENTRAL.....	95
EUROPEAN BASIN	
4.5.1 <i>Hebelermeer-2 core, Germany</i>	96
4.5.2 <i>Schandelah-1 core, Germany</i>	97

Contents

4.5.3 Csővár Vár-hegy section, Hungary.....	99
4.6 CHAPTER SUMMARY.....	101
5 THE GEOCHEMICAL PROCESSING OF CORE.....	102
AND OUTCROP SAMPLES	
5.1 INTRODUCTION	
5.2 SAMPLE POWDERING	
5.3 LABWEAR CLEANING.....	103
5.4 INORGANIC ELEMENTAL ANALYSES	
5.4.1 Sample digestion (non-carbonate samples)	
5.4.2 Sample leaching (carbonate samples).....	104
5.4.3 Sample measurement	
5.5 ORGANIC ELEMENTAL ANALYSES.....	105
5.5.1 Sample processing	
5.5.2 C, N, S measurements	
5.6 ISOTOPIC ANALYSES	
5.6.1 Sample digestion (non-carbonate samples)	
5.6.2 Sample leaching (carbonate samples).....	106
5.6.3 Anion Exchanges Columns	
5.6.4 Measurement of isotopic composition(s)	
5.6.5 Processing of isotopic data.....	108
6 MARINE REDOX CHANGE AND EXTINCTION IN.....	109
TRIASSIC–JURASSIC BOUNDARY STRATA FROM	
THE LARNE BASIN, NORTHERN IRELAND <i>Published in</i>	
<i>Palaeogeography, Palaeoecology, Palaeoclimatology</i> , 598,	
111018 (2022).	

Contents

7 AN OXYGENATED GLOBAL OCEAN DURING THE.....110
END-TRIASSIC MASS EXTINCTION EVENT *in review*
Nature Geoscience.

8 GLOBAL OCEAN DE-OXYGEANATION PRECEDED....111
END TRIASSIC MASS EXTINCTION EVENT *submitted*
Geology

9 WIDESPREAD PULSES OF BENTHIC.....112
DE-OXYGENATION ON THE TETHYAN SHELF
DURING THE END-TRIASSIC MASS EXTINCTION *in prep*
Earth and Planetary Science Letters

10 DISCUSSION, CRITICAL EVALUATION, AND.....113
FUTURE WORK

10.1 DE-OXYGENATION OF THE TETHYAN SHELF DURING
THE END TRIASSIC MASS EXTINCTION

10.1.1 Initiation of marine redox change during the ETME

10.1.2 Spatio-temporal redox progression during the ETME.....115

10.1.3 The prevalence of de-oxygenation in the deep ocean.....116
during the ETME

10.1.4 The drivers of marine redox change during the ETME.....117

10.1.5 Marine redox change as a driver of extinction during
the ETME

10.2 UNCERTAINTY REGARDING LATE TRIASSIC.....118
STRATIGRAPHIC CORRELATION

10.3 SAMPLE ALTERATION, GEOCHEMICAL OVERPRINTING....119
AND PSEUDO EXTINCTIONS

10.3.1 Thermal and/or diagenetic alteration

10.3.2 Palaeozoic shale weathering, detrital input, and.....120
hydrographic changes

10.3.3 Organic matter input and near shore iron (Fe) remobilisation

10.3.4 Aragonite undersaturation.....121

Contents

10.3.5 <i>Facies changes and/or sea level change</i>	
10.4 SAMPLE CONTAMINATION, REPRESENTIVITY OF.....	122
SAMPLE MEASUREMENTS AND INSTRUMENTAL	
INTERFERENCE	
10.5 REPRESENTIVITY/SUITABILITY OF STUDY SECTIONS.....	123
AND PROXIES	
10.6 COVID LIMITATIONS AND FUTURE WORK.....	124
11 CONCLUSIONS.....	126
REFERENCES.....	127
GLOSSARY.....	172
APPENDICES.....	178

LIST OF FIGURES

CHAPTER 2:

Figure 1:- Leading figures in the debate of catastrophism vs gradualism – p. 19

Figure 2:- A revised severity ranking for the ‘Big Five’ Phanerozoic mass extinction events – p. 27

Figure 3:- Basal Hettangian GSSP candidate sites and sites from this thesis – p. 32

Figure 4:- Biostratigraphic characterisation of the basal Jurassic GSSP – p. 35

Figure 5:- Ammonite extinction and recovery during the Triassic–Jurassic boundary interval – p. 38

Figure 6:- Ammonoid generic diversity and its relationship to carbon cycle instability – p. 40

Figure 7:- Global, spatio-temporal changes in the generic biodiversity of Late Triassic bivalves – p. 43–44

Figure 8:- Variable extinction of organisms at the Triassic–Jurassic boundary according to skeletal physiology – p. 47

Contents

Figure 9:- Changes to bivalve ecology through the Triassic- Jurassic mass extinction –
p. 50

Figure 10:- The evolution of late Triassic reefal composition and architecture – *p. 53*

Figure 11:- Palaeogeographic distribution and composition of Triassic–Jurassic reef
ecosystems – *p. 55*

Figure 12:- Overview of diversity patterns, losses, and recovery during the ETME– *p.*
66

Figure 13:- Past and present extent of the CAMP – *p. 72*

CHAPTER 3:

Figure 14:- An overview of ‘the redox ladder’– *p. 82*

Figure 15:- A quantitative framework to interpret redox conditions – *p. 84*

CHAPTER 5:

Figure 16:- A comparison of standard values from literature and this thesis – *p. 108*

CHAPTER 6:

Figure 1:- The approximate location and extent of the Larne Basin – *p. 109*

Figure 2:- A high resolution geochemical dataset from the Larne Basin – *p. 109*

Figure 3:- C_{org}/P vs. C_{org}/N from the Triassic–Jurassic Larne Basin – *p. 109*

Figure 4:- Alternative controls on trace element enrichment – *p. 109*

Figure 5:- Marine redox vs. biodiversity from the Triassic–Jurassic Larne Basin – *p.*
109

Figure 6:- Palaeoenvironmental reconstruction of the Triassic–Jurassic Larne Basin – *p.*
109

Figure S1:- Larne Geochemical Data – *p. 109*

Figure S2:- Larne Palaeobiological Dataset – *p. 109*

Figure S3:- Faunal biostratigraphy of the Penarth and basal Lias of the Larne Basin – *p.*
109

Figure S4:- Bivalve biostratigraphy for the Penarth and basal Lias of the Larne Basin –
p. 109

Contents

Figure S5:- Invertebrate taxonomic range data from the Waterloo Bay Foreshore, Larne Basin – p. 109

Figure S6:- Sedimentary logs from the Larne Basin including ichnofaunal data – p. 109

Figure S7:- Miospore, dinocyst and algal diversity data from the Carnduff-1 core, Larne Basin – p. 109

Figure S8:- Foraminiferan, ostracod and conodont data from the Larne Basin – p. 109

Figure S9:- Dinocyst, prasinophycean and acritarch data from the Larne Basin – p. 109

Figure S10:- A correlation of Larne foreshore and core sections – p. 109

Figure S11:- Reconstructing changes in bivalve biodiversity from the Triassic–Jurassic Larne Basin – p.109

CHAPTER 7:

Figure 1:- Triassic–Jurassic palaeogeography of the Tethyan shelf – p. 110

Figure 2:- Overview of key stratigraphic and geochemical data for the Carnduff-2, Hebelermeer-2 and Carnduff-2 cores – p. 110

Figure 3:- Stepped evolution of marine de-oxygenation and extinction on the Triassic–Jurassic Tethyan shelf – p. 110

Figure 4:- Pulses of marine de-oxygenation and extinction on the Triassic–Jurassic Tethyan shelf – p. 110

Figure S1:- Chemostratigraphic correlation of Chapter 7 sections – p. 110

Figure S2:- Biostratigraphic correlation of Chapter 7 sections – p. 110

CHAPTER 8:

Figure 1:- Location of the Csővár section on the Tethyan shelf – p. 111

Figure 2:- X/Ca data from the Late Triassic Csővár section – p. 111

Figure 3:- A decline in carbonate X/Ca amongst unaltered Csővár samples – p. 111

Figure 4:- A comparison of local and global hydrogenic redox data from across the Triassic–Jurassic boundary interval – p. 111

Figure S1:- A comparison of different cleaning procedures on Csővár carbonate samples – p. 111

Figure S2:- X/Ca ratios plotted against Aluminium (ppb) – p. 111

Contents

Figure S3:- X/Ca ratios for redox sensitive elements amongst calcifying marine organisms – *p. 111*

Figure S4:- T-tests for X/Ca before and after NCIE-2 – *p. 111*

Figure S5:- X/Ca data for redox sensitive elements before and after NCIE-2 – *p. 111*

Figure S6:- Chemostratigraphic correlation of Chapter 8 sections – *p. 111*

Figure S7:- Revised chemostratigraphic correlation of Chapter 8 sections – *p. 111*

CHAPTER 9:

Figure 1:- Triassic–Jurassic palaeogeography of the Tethyan shelf showing key T-J sites – *p. 112*

Figure 2:- Elemental redox data from the Somerset-1 and Somerset-2 cores – *p. 112*

Figure 3:- Elemental redox data from the Prees-2c core – *p. 112*

Figure 4:- Elemental redox data from the Carnduff-2 core – *p. 112*

Figure 5:- Elemental redox data from the Schandelah-1 core – *p. 112*

Figure 6:- Elemental redox data from the Hebelermeer-2 core – *p. 112*

Figure 7:- The correlation between hydrography and marine redox data across the Bristol Channel, Cheshire, Germanic, Larne, and Lower Saxony Basins – *p. 112*

Figure 8:- The correlation between detrital input, grain size, weathering intensity and marine redox data across the Bristol Channel, Cheshire, Germanic, Larne, and Lower Saxony Basins – *p. 112*

Figure 9:- A regional correlation of elemental marine redox data – *p. 112*

Figure 10:- Coincident pulses of benthic de-oxygenation and extinction on the Tethyan shelf – *p. 112*

Figure S1:- T-tests for open marine and restricted sites vs. trace element enrichment >1 – *p. 112*

Figure S2:- Chemostratigraphic correlation of Chapter 9 sections (for figure 9) – *p. 112*

Figure S3:- Chemostratigraphic correlation of Chapter 9 sections (for figure 10) – *p. 112*

Figure S2:- Biostratigraphic correlation of Chapter 9 sections (for figure 9) – *p. 112*

CHAPTER 10:

Figure 17:- Redox compilation data from the Triassic Jurassic Tethyan shelf – *p. 114*

Figure 18:- Mo/U compilation from the sites studied within this thesis – *p. 124*

1 INTRODUCTION

1.1 RECONSTRUCTING MARINE REDOX CHANGE ACROSS THE END TRIASSIC MASS EXTINCTION EVENT

The vast majority of all marine mass extinction events that have occurred over the past 541Ma are thought to have been caused by marine anoxia [Grice *et al.*, 2005; Kasprak *et al.*, 2015; Bond & Grasby, 2017]. This marine anoxia is driven by variations in the global carbon cycle which are strongly linked to the extensive output of isotopically light carbon produced by large igneous provinces (LIPs) [Rampino & Stothers, 1988; Ruhl *et al.*, 2011; Saunders 2016, 2017; Stordal *et al.*, 2017; Ernst & Youbi 2017; Davies *et al.*, 2017; Percival *et al.*, 2017; Zaffani *et al.*, 2018; Clapham & Renne, 2019]. The current annual output of anthropogenic (human-induced) light carbon is akin to that released in the past by LIPs, which raises important questions regarding the effect of anthropogenic carbon output on future climate and subsequent marine de-oxygenation [Zeebe *et al.*, 2016].

Until recently, research on future climate reconstruction and prediction has largely been based on the Paleocene–Eocene Thermal Maximum (PETM), a hyperthermal event dated to ~56.0 Ma [Dickson *et al.*, 2014; Penman *et al.*, 2016; Carmichael *et al.*, 2017]. The intense study of the PETM is predominately due to the geography and ocean circulation being regarded as similar during both the Paleocene–Eocene boundary and the present day. However, research by Zeebe *et al.*, (2016) interprets that the current rate of anthropogenic carbon output is ‘unprecedented during the past 66 Ma’ and exceeds the rate of carbon output observed during the PETM. It is therefore pertinent to explore an additional, older analogue for future climate perturbation, particularly with regards to understanding ongoing changes to marine redox. Such an analogue may take the form of the Triassic–Jurassic boundary interval and mass extinction event.

Quantifying marine redox across the Triassic–Jurassic mass extinction

The Triassic–Jurassic boundary (~201.36 Ma, [Schoene *et al.*, 2010; Wotzlaw *et al.*, 2014]) and mass extinction event (~201.56 Ma, [Blackburn *et al.*, 2013]) coincided with the emplacement of the most aerially extensive LIP in Earth’s history, the Central Atlantic Magmatic Province (CAMP) [Marzoli *et al.*, 1999; Whiteside *et al.*, 2007; Whiteside *et al.*, 2010; Schoene *et al.*, 2010; Ruhl *et al.*, 2011; Percival *et al.*, 2017; Davies *et al.*, 2017]. CAMP volcanism is thought to have persisted for at least 610 Kyr, releasing large concentrations of isotopically light carbon into the atmosphere [Marzoli *et al.*, 2004; Whiteside *et al.*, 2007; Schaller *et al.*, 2012]. The presence of isotopically light volcanic emissions is supported through negative shifts in isotopic carbon (organic¹, compound specific and inorganic carbonate) of up to 8‰, within late Triassic sediments [Pálffy *et al.*, 2001; Hesselbo *et al.*, 2002; Ruhl *et al.*, 2009; Whiteside *et al.*, 2010; Ruhl *et al.*, 2010; Ruhl & Kürschner, 2011; Ruhl *et al.*, 2011; Zaffani *et al.*, 2018; Korte *et al.*, 2019; Ruhl *et al.*, 2020]. It is believed that subsequent environmental perturbation resulted in ocean acidification, marine de-oxygenation, and the eventual pulsed mass extinction of numerous marine animal groups during the Late Triassic and Early Jurassic [Raup & Sepkoski, 1982; Tanner *et al.*, 2004; Wignall & Bond, 2008; McRoberts *et al.*, 2012; Richoz *et al.*, 2012; Greene *et al.*, 2012; Kasprak *et al.*, 2015; Wignall & Atkinson, 2020].

1.2 AIMS AND RESEARCH QUESTIONS OF THIS THESIS

The aim of this research is to quantify spatio-temporal, marine de-oxygenation, as a result of environmental perturbation during the Triassic–Jurassic boundary interval and extinction event. In order to quantifying Triassic–Jurassic marine redox change this thesis will use elemental and isotopic geochemical data to answer the following research

¹ Recent work by Fox *et al.*, (2020, 2022a) alternatively attributes a negative shift in isotopic organic carbon from the Bristol Channel Basin to regional sea level change and subsequent microbial activity as well as reworking of organic deposits.

Chapter 1: Introduction

questions: Questions i) ‘When did marine redox change initiate during the ETME?’, ii) ‘How did marine redox progress spatio-temporally during the ETME?’, iii) ‘How prevalent was de-oxygenation in the deep ocean during the ETME?’ iv) ‘What were the drivers of marine redox change during the ETME?’, v) ‘To what extent was marine redox change a driver of extinction during the ETME?’

1.3 THESIS OUTLINE

To answer the research questions posed above, and fulfil the aim of this thesis:

Chapter 2 uses literature to evaluate the severity of the Triassic–Jurassic boundary mass extinction event, as well as the key marine organisms undergoing extinction. FAD and LAD of organisms which define the extinction horizon and the Triassic–Jurassic boundary at the GSSP are also discussed. Additional lines of evidence from literature are then analysed, alongside extinction selectivity, to list the potential causes of the mass extinction.

Chapter 3 uses literature to describe the key geochemical methods that have been used for palaeo-environmental reconstruction throughout this thesis (including palaeo-redox, palaeo-weathering and palaeo-hydrographic proxies).

Chapter 4 discusses the materials studied for this thesis. Including their origin, geological context, stratigraphy, collection, and nature.

Chapter 5 describes the geochemical methods used to digest, process and measure elemental concentrations and isotopic compositions of samples for this thesis.

Quantifying marine redox across the Triassic–Jurassic mass extinction

Chapter 6 studies fine-scale redox changes from the expanded GSSP candidate section at Larne, through detailed study of the Carnduff-2 core, and determines the relationship between small changes in basin oxygenation and marine biodiversity.

Chapter 7 analyses molybdenum isotope data from N. Ireland (Carnduff-2) and Germany (Schandelah-1, Hebelermeer-2) in order to determine global vs. local scale redox changes through the mass extinction interval.

Chapter 8 analyses element/calcium (X/Ca) data from Hungary (Csővár Vár-hegy) in order to reconstruct open ocean redox conditions through the Triassic–Jurassic boundary interval mass extinction event.

Chapter 9 analyses both minor and major elemental concentration data from sites throughout Europe, including: the Carnduff-2 core, Somerset-1 core, Somerset-2 core, Prees-2c core, Schandelah-1 core and Hebelermeer-2 core in order to identify regional controls on redox change and widespread redox pulses on the Tethyan shelf.

Chapter 10 will further discuss the data presented within this thesis as well as critically evaluating the interpretation of the data and discussing potential future studies.

Chapter 11 will conclude the key findings of this thesis.

Due to the multidisciplinary focus of this thesis (palaeontology, geochemistry, sedimentology, stratigraphy) a glossary has been included at the end of this thesis to clarify the definitions of subject specific terminologies and abbreviations.

2 THE END TRIASSIC MASS EXTINCTION EVENT

Scientists have been fascinated by the extinction of life, like that observed during the Late Triassic, for centuries [*Cuvier 1831; Lyell, 1830; Darwin, 1859; Simpson, 1944*]. Yet, despite mass extinction events being widely accepted as fact within the scientific community today, this wasn't the case merely 200 years ago.

2.1 EARLY THEORIES ON EXTINCTION

Theories about extinction were first proposed by Baron Georges Cuvier, during the early 19th century [*Cuvier 1800, 1818, 1827*] (*Fig. 1A*). Cuvier theorised that many now-extinct organisms had been wiped out by catastrophic events or “revolutions”; termed ‘catastrophism’ by Cuvier [*Cuvier, 1831; Newell, 1967; Rudwick, 1972*]. One such extinct group includes the mastodon (genus *Mammut*) which Cuvier had previously described in *Memoirs on living and extinct elephant species* in 1800 (*Fig. 1D–1F*). Cuvier's collective theories on extinction were detailed in his work *Essay on the Theory of the Earth*, which was published in 1813. However, Cuvier (1813)'s theories were strongly opposed, particularly by the church, due to the concept of extinction directly conflicting with the ‘sanctity of life’.

Certain researchers consequently favoured the notion that life had not abruptly disappeared but rather had failed to be preserved; That life, much like geological landforms, gradually changes through ‘steady-state’ processes over protracted periods of time [*Lyell, 1830*]. This was part of a geological principle known as gradualism or ‘uniformitarianism’, which was first theorised by James Hutton (1788) and popularised by Sir Charles Lyell (1830)

Quantifying marine redox across the Triassic–Jurassic mass extinction

(Fig. 1B). Uniformitarianism was seen as the answer to catastrophism by researchers of faith.

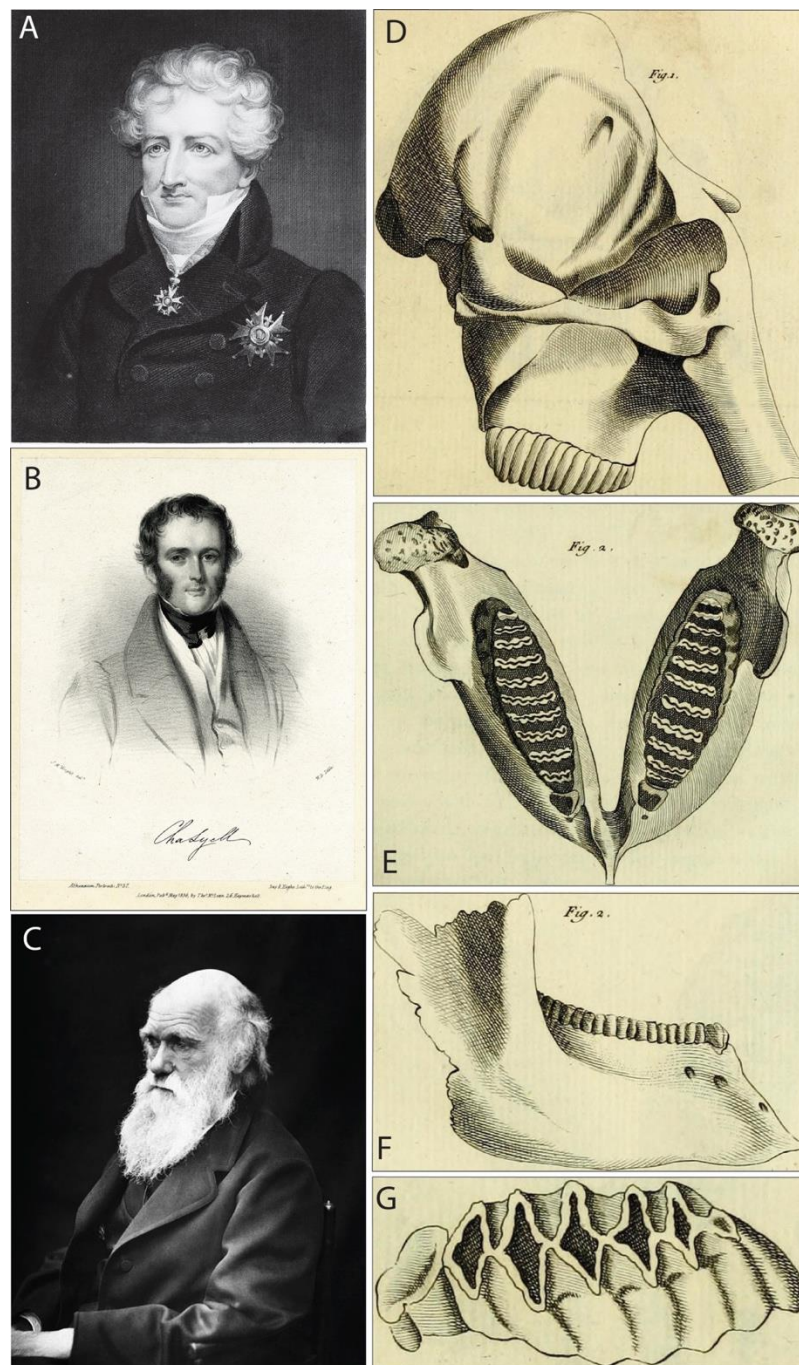


Figure 1:- Leading figures in the debate of catastrophism vs gradualism. A) A portrait drawing of Baron Georges Cuvier (see references); founding father of catastrophism [Cuvier 1800, 1813], B) A portrait drawing of Sir Charles Lyell (Smalley, 2020); author of ‘Principles of Geology’ and advocate of gradualism [Lyell, 1830], C) A portrait photograph of Sir Charles Darwin (see references); author of ‘On the Origin of Species’ and founding father of evolution [Darwin, 1859], D–G) Cuvier’s illustrations of mammoth teeth (all), jaw (E, F), and skull morphologies (D) from Cuvier (1800).

Chapter 2: The end-Triassic mass extinction event

It is through the influence of uniformitarianism that Charles Darwin postulated his work ‘On the Origin of Species’ in 1859 (*Fig. 1C*). Darwin, like Lyell, rejected Cuvier’s theory that life could disappear in large-scale, catastrophic events and also believed that the transition of life was gradual [*Darwin, 1859, p. 345*]. Uniformitarianism continued to gather widespread acceptance during the latter part of the 19th century and the early 20th century. This subsequently made the acceptance of catastrophism difficult, particularly given the insufficient evidence.

2.2 THE RISE OF CATASTROPHISM

However, in 1923, research by J Harlen Bretz described the occurrence of kilometre-sized channel structures from the U.S. state of Washington. Bretz, (1923) coined the term ‘scablands’ to describe the topography and interpreted that the structures were formed by cataclysmic flooding during the Last Glacial Maximum. Bretz (1923)’s revolutionary ideas directly contradicted uniformitarianism and were met with considerable resistance yet were finally accepted almost 40 years later.

As the evidence for mass extinctions and catastrophism continued to develop during the 20th century, research studies began to focus on the potential causes of extinction. This included research by Louis and Walter Alvarez who interpreted that a large meteor/bolide impact may have caused the extinction of non-avian dinosaurs [*Alvarez et al., 1980*].

Alvarez et al., (1980)’s monumental theory was rapidly followed by iconic extinction studies by David Raup and Jack Sepkoski during the 1980s, focussing on large palaeontological datasets of marine shelly fauna [*Raup & Sepkoski, 1982, 1986; Sepkoski & Raup, 1986; Sepkoski, 1989*]. Raup and Sepkoski, (1982) identified four major mass extinction events at the end of the Ordovician, Permian, Triassic, and Cretaceous periods, as well as a less well supported fifth mass extinction during the end-Devonian. Raup and

Quantifying marine redox across the Triassic–Jurassic mass extinction

Sepkoski (1982, 1986)'s datasets are still widely studied today, and the major Phanerozoic mass extinction events they identified 40 years ago have yet to be added to.

In 1988, Michael Rampino and Richard Stothers began to research the occurrence of Large Igneous Provinces (LIPs) over the past 250 million years [*Rampino and Stothers, 1988*].

Rampino and Stothers, (1988) discovered 11 distinct provinces, 9 of which directly correlated with marine mass extinction events. These included 2 of the major mass extinctions identified by Raup and Sepkoski, (1982); the end-Triassic and end-Cretaceous mass extinctions. Rampino and Stothers, (1988)'s discoveries initiated the theory that LIPs release large concentrations of greenhouse gases, resulting in global climate change, and the subsequent extinction of vulnerable organisms. LIPs remain the leading theory regarding the initiation of mass extinction events.

Raup & Sepkoski, (1982) and Rampino & Stothers, (1988)'s pioneering studies have contributed significantly to the currently accepted theory that uniformitarianism and catastrophism operate conjunctively.

The next section will clarify the currently accepted definition of a mass extinction event before focusing specifically on the Triassic–Jurassic boundary interval mass extinction event. The chapter will discuss the severity of the event, as well as its early study and the main groups of marine life which are known to have been affected, including those which define the extinction horizon at the GSSP. The chapter will then go on to discuss the potential causes of the mass extinction.

Chapter 2: The end-Triassic mass extinction event

2.3 THE END- TRIASSIC MARINE MASS EXTINCTION EVENT

2.3.1 A brief introduction to mass extinction events: An extinction event is defined by the widespread and rapid disappearance, or reduction, of a globally distributed group of organisms and is dated through their last appearances (LAD) [*Whiteside & Grice, 2016; Bond, 2018*]. If such organisms undergoing extinction are higher taxa, which typically include both marine and terrestrial species, then this is defined as a ‘mass extinction event’ [*Sepkoski, 1986; Whiteside & Grice, 2016*]. Multiple mass extinction events have punctuated Earth’s history, throughout the past 4.56 Ga, with five major mass extinctions known to have occurred throughout the Phanerozoic Eon (541Ma- Present) [*Raup & Sepkoski, 1982; Melott & Bambach, 2014; Bond & Grasby, 2017*]. One such extinction is the Triassic–Jurassic boundary interval extinction event. The Triassic–Jurassic boundary interval mass extinction event, also referred to in literature as the Rhaetian, Norian, Triassic–Jurassic and late/end Triassic mass extinction, occurred ~201.56 Ma [*Blackburn et al., 2013*] ~200 ka prior to the Triassic–Jurassic boundary (~201.36 Ma, [*Schoene et al., 2010; Wotzlaw et al., 2014*]) and only ~50 Ma after the largest known mass extinction event in Earth’s history (the end-Permian mass extinction event).

2.3.2 Nomenclature of Late Triassic marine extinctions within this thesis: As alluded to within the previous section (2.3.1) there are a range of terminologies associated with Late Triassic extinctions. This partly stems from the Triassic–Jurassic boundary interval mass extinction event consisting of multiple pulses of extinction during the Norian and Rhaetian stages [*Benton 1986; Wignall & Atkinson, 2020*]. However, in spite of this, there are also inconsistencies regarding the nomenclature of the overarching event. Whilst some publications have adopted the title of ‘Triassic–Jurassic mass-extinction event’ [*Olsen et al., 2003; Ward et al., 2004; Whiteside et al., 2007; Ritterbush et al., 2014; Allen et al.,*

Quantifying marine redox across the Triassic–Jurassic mass extinction

2018], others have used ‘Late Triassic mass-extinction’ [Benton 1986; Dunhill *et al.*, 2018], or ‘Late Triassic extinction event’ [Sephton *et al.*, 2002; Mander *et al.*, 2008; Onoue *et al.*, 2016]. Meanwhile several publications use a more informal style whilst acknowledging the presence of multiple pulses of extinction (e.g., ‘Late Triassic Extinction Events’ [Lucas & Tanner, 2004; Ward *et al.*, 2004] or ‘Late Triassic extinctions’ [Benton, 1993a; Fowell *et al.*, 1994; Tanner *et al.*, 2004; Onoue *et al.*, 2012]). Although some of these terminologies may refer to a specific resolution or focus during the Late Triassic, many are redundant and have not been used consistently within recent years.

Regardless of the various phrasings which have been used for this event over the years, many recent and leading publications have adopted the terminology ‘end-Triassic mass extinction’ [Schoene *et al.*, 2010; Ruhl *et al.*, 2011; Richoz *et al.*, 2012; Hautmann, 2012; Ritterbush *et al.*, 2015; Thibodeau *et al.*, 2016; Davies *et al.*, 2017; Percival *et al.*, 2017; Lindström *et al.*, 2019; Drukenmiller *et al.*, 2020; Ruhl *et al.*, 2020; Wignall & Atkinson, 2020; He *et al.*, 2020, 2022a; Beith *et al.*, 2021; Fox *et al.*, 2020, 2022b]. Despite not being in-keeping with the international stratigraphic framework this terminology has proven persistent over the past decade; ‘end-Triassic mass extinction’, here in referred to as the ETME, has therefore been adopted for the remainder of this thesis and is considered here to be synonymous with all previous terminologies. This phrasing is also endorsed here for use in future research of Late Triassic extinctions.

2.3.3 The identification of a suitable horizon to define the main phase of the end-Triassic mass extinction

As the ETME is defined by multiple phases of extinction across numerous sections that are not necessarily represented ubiquitously this thesis has instead focussed on a significant pulse of the event from a key section and has considered this pulse to represent the main

Chapter 2: The end-Triassic mass extinction event

phase of the ETME. This thesis uses the main phase of extinction at the basal Hettangian Global Stratotype Section and Point (GSSP), discussed in more detail within 2.3.5.1, as being equivalent to the main extinction interval. The main phase of the ETME at the GSSP may be correlated to other sections through the use of carbon isotope stratigraphy as it coincides with a prominent negative carbon isotope excursion. [Ruhl *et al.*, 2009, 2010] and is considered by some recent studies to also coincide with the significant disappearance of marine fauna from other Triassic–Jurassic marine sections, potentially representing a broadly ubiquitous main phase of the ETME [Wignall & Atkinson, 2020]. This interval will be referred to herein as ETME (Main interval) where possible in order to differentiate from the overarching event (ETME).

2.3.4 Severity of the end-Triassic mass extinction event: The end-Triassic mass extinction event, herein referred to as the ETME, witnessed the extinction of ~76% of all species and ~12% of all families [Raup & Sepkoski, 1982; Raup, 1992]. This comprised a 63% reduction in global diversity of marine invertebrates as well as the disappearance of ~45% of all continental tetrapod families [Olsen *et al.*, 1987; Alroy *et al.*, 2008]. The ETME has been interpreted by multiple studies as being similar in intensity to the End-Cretaceous mass extinction event (ECME) [Raup & Sepkoski, 1982, 1986; Sepkoski & Raup 1986; Benton, 1995; Sepkoski, 1989, 1996, 2002; Foote, 2003, 2007; McGhee *et al.*, 2004; Bond & Grasby, 2017] and is considered by some authors to be the second largest mass extinction event in Earth's history, behind the End-Permian event (EPME) [Foote, 2003, 2007; Peters, 2008; Alroy, 2010]. The ETME is ranked as the third most severe extinction, behind the EPME and ECME, by McGhee *et al.*, (2004, 2013) and Sepkoski (1996) in terms of ecological severity and percentage genus extinction, and the fourth most severe, behind the EPME, End Devonian (EDME) and End Ordovician (EOME) mass extinctions, by Benton, (1995) and Sepkoski, (1982) based on familial diversity loss. Bambach &

Quantifying marine redox across the Triassic–Jurassic mass extinction

Knoll, (2001) and Hallam & Wignall (1997) similarly rank the ETME as the fourth most severe mass extinction, behind the EPME, ECME and EOME, based on the extinction rate of marine genera and extinction intensity.

2.3.4.1 Low origination rates and the interpreted ‘absence of a major extinction’ during the Rhaetian (latest Triassic): Studies by Hallam, (2002) and Bambach et al., (2004) conclude that despite the ETME having thought to be of equal intensity to the ECME, diversity loss was maximised across the ETME by falling origination rates as opposed to increasing rates of extinction [McRoberts et al., 1995]. It is for this reason that Bambach et al., (2004) rank the ETME as only the fifth largest mass extinction event, based on the extinction rate of marine genera, and Hallam, (2002) evaluate there to be insufficient evidence for a major extinction at the Triassic–Jurassic boundary. Bambach et al., (2004) further state that the ETME should be removed as one of the ‘Big Five’ and are in favour of re-establishing the EPME, EOME and ECME as the ‘Big Three’ on the basis of being the only three mass extinction events with a diversity loss of >20% [Melott & Bambach, 2014]. Bambach et al., (2004)’s other main objection with the ETME is that ‘extinction rates are insufficient to explain the high diversity depletions at these times’ however they equally do not refute the possibility of a pulsed turnover.

In light of controversy regarding origination rates, studies by Michael Foote (2003, 2005, 2007) re-analysed Sepkoski’s (1996, 2002) data through an optimised extinction model. Foote’s (2003, 2005, 2007) optimised extinction model does not use LAD of organisms as proxies for extinction but instead takes into consideration incompleteness of sampling and origination through pulsed turnover. Rates of sampling, origination and extinction are simultaneously estimated from first (FAD) and last appearances (LAD) and are quantified to produce an optimised rate of extinction across geological intervals. Foote’s (2003, 2005,

Chapter 2: The end-Triassic mass extinction event

2007) studies conclude that rates of origination, when corrected for pulsed turnover and incomplete sampling, were increasing throughout the Triassic, matching rates during the Late Permian (EPME) and Late Cretaceous (ECME) by the Lower to Mid-Triassic. These results support Alroy et al., (2008)'s interpretation that biological recovery following the EPME was very rapid and conflict with interpretations by Bambach et al., (2004) and Hallam, (2002) regarding falling origination rates throughout the Triassic period.

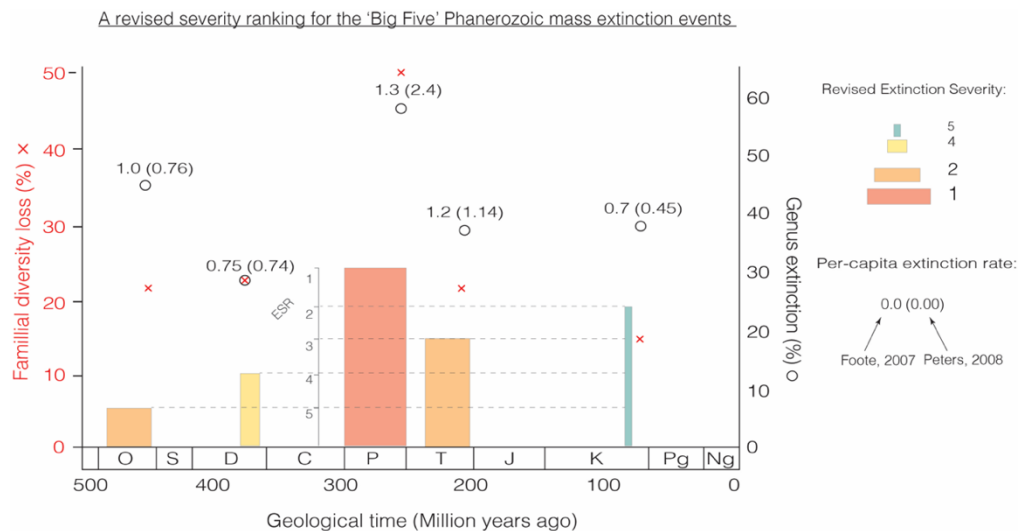
Research by Michael Foote (2003, 2005 2007) was furthered by John Alroy (2008) who plotted rates of both detrended origination and extinction throughout the Phanerozoic and concluded that the ETME represents one of the three largest mass extinction events in geological history. This was despite concerns expressed by Alroy (2008) regarding Foote (2007)'s use of turnover proportions in favour of continuous time rates. Alroy (2010) further developed his model through the use of three-timer extinction rates and through plotting log ratios between three-timer extinction rates and extinction rates from Foote (1999, 2000). Alroy (2010) came to the same conclusion as within his previous research [Alroy, 2008] affirming the status of the ETME as one of the three largest mass extinction events.

Subsequent work by Alroy (2014) questioned sampling methods used by Foote (2007) within his model. Particularly the use of boundary-crosser rate equations in favour of both gap-filler and part-timer rate equations. Alroy (2014) accordingly produced a newly revised model for Phanerozoic diversity changes which adopted both gap-filler and three-timer rate equations. Alroy (2014)'s revised model once again confirmed the position of the ETME within the Big Five, and as the second most severe mass extinction event within geological history.

Quantifying marine redox across the Triassic–Jurassic mass extinction

2.3.4.2 A revised severity ranking for the big five Phanerozoic mass

extinctions: In order to further account for the uncertainties and biases addressed by Hallam (2002), Bambach et al., (2004) and Alroy (2008, 2014) a multi-disciplinary dataset consisting of both qualitative and quantitative parameters, has been compiled for this thesis (*Appendix 1*). Data for extinction rate [Foote 2005, 2007; Peters, 2008], ecological severity [Bambach & Knoll, 2001; McGhee et al., 2004, 2013], familial diversity loss [Benton 1995, Sepkoski 1982], percentage genus extinction [Bambach et al., 2004; Sepkoski, 1996] as well as extinction intensity [Hallam & Wignall, 1997] and three-timer extinction probability [Alroy, 2010] have been collated and ranked for each of the ‘Big Five’ mass extinction events (*see Appendix 1*). Each of the ‘Big Five’ mass extinction events has then been given a score for each parameter depending on its relative ranking. The scores have been totalled and averaged to produce a final score which has then been ordered numerically relative to the other mass extinctions (*Fig. 2*). This multi-disciplinary method establishes the EPME as the most significant mass extinction followed jointly by the ETME and EOME, then the EDME and finally the ECME (*Fig. 2*). Furthermore, this approach establishes the ETME as not only firmly sitting within the big five, but also corroborates Alroy (2014) that the ETME is the (joint) second largest mass extinction event in geological history.



Chapter 2: The end-Triassic mass extinction event

Figure 2:- A revised severity ranking for the ‘Big Five’ Phanerozoic mass extinction events via a series of quantitative and qualitative characters. Familial diversity loss (%) (left-hand axis, red crosses) from Benton, 1995; Sepkoski, 1982, genus extinction (%) (right hand axis, unfilled circles) from Bambach et al., 2004; Sepkoski, 1996, ecological severity ranking (ESR) (smaller y-axis, indicated through height of coloured bars) from Bambach & Knoll, 2001; McGhee et al., 2004, 2013, per-capita extinction rate(s) (values above genus extinction (%) points, see key on figure) from Foote, 2007; Peters 2008, revised severity ranking indicated through width and colour of bars (see key on figure). Geological time windows on x-axis from Peters (2008). Where values are from more than one source then averaged (quantitative data) or modal values (qualitative data) are used. Refer to individual publications for degree of error on values. O = Ordovician, S = Silurian, D = Devonian, C = Carboniferous, P = Permian, T = Triassic, J = Jurassic, K = Cretaceous, Pg = Paleogene, Ng = Neogene.

2.3.5 Faunal turnover and marine extinction during the Late Triassic: Which studies first identified the presence of an extinction event around the Triassic–Jurassic boundary interval, herein referred to as the TJB, are not known. However, one potential candidate includes research by the ‘founding father’ of extinction events, Baron Georges Cuvier. Early nineteenth century biostratigraphic studies by Cuvier and Alexandre Brongniart of the Paris Basin were some of the first through the TJB [*Cuvier, 1831; Cuvier & Brongniart, 1808, 1811, 1822*].

Following a resistance from catastrophism after Cuvier’s death, subsequent studies of revolutions at the TJB were infrequent until the mid-twentieth century. Research by Edwin Colbert (1949, 1958) conceptualised a substantial extinction of terrestrial tetrapods near the TJB, with subsequent work by Norman Newell (1963) supporting Colbert (1958)’s interpretation. Newell (1963) believed that both reptile and amphibian groups were replaced by dinosaurs at the ETME. Newell (1963) also identified a major extinction

Quantifying marine redox across the Triassic–Jurassic mass extinction

within Late Triassic ammonites recording 24 out of 25 ammonoid families to have disappeared gradually throughout the Late Triassic. Newell (1963)'s studies on mass extinction events, including the ETME, lead to the interpretation that extinction events were not instantaneous, as described by Cuvier, but more gradual and persist over hundreds of thousands of years. However, the majority of Newell (1963)'s extinction figures lacked any explicit quantitative documentation [Tanner *et al.*, 2004].

A more detailed study of diversity change within marine invertebrates across the TJB was undertaken by Charles Pitrat, (1970). Pitrat (1970) estimated that 103 families of marine invertebrates underwent extinction throughout the Late Triassic and that a further 175 families persisted through to the Jurassic [Tanner *et al.*, 2004]. Pitrat (1970) interpreted that ~20% of 300 existing families underwent extinction throughout the ETME [Tanner *et al.*, 2004]. Pitrat (1970) supported Newell (1963) in that cephalopods were severely affected by environmental changes at the ETME (31 families extinct throughout the Late Triassic). However, Pitrat (1970) also identified disappearances amongst marine reptiles (7 families extinct), gastropods (6 families extinct), bivalves (6 families extinct) and articulated brachiopods (5 families extinct) throughout the Late Triassic.

Detailed studies, such as those undertaken by Pitrat (1970), will have contributed towards David Raup and Jack Sepkoski's renowned studies of Phanerozoic extinction (*see* 2.2). Raup & Sepkoski (1982) estimate that ~12% of all families underwent extinction across the ETME and later work by Raup (1992) quantifies species level extinction at ~76%. A further study by Sepkoski (1996) estimates that ~40% of marine, non-singleton genera underwent extinction during the ETME, this value was corrected to ~30% by Kiessling *et al.*, (2007) who also quantified a ~40% extinction of benthic taxa.

Chapter 2: The end-Triassic mass extinction event

Numerous groups were evidently affected by environmental changes occurring in the lead up to the TJB. The following section provides further detail on the key faunal turnovers that define both the ETME and TJB with a specific focus on the GSSP. The section also discusses the key groups of marine life undergoing extinction at the ETME, as well as to what extent marine organisms were affected by Late Triassic environmental perturbations. Extinction selectivity is also used to interpret causes of extinction, which are further discussed within the next sub-chapter (2.3.5).

2.3.5.1 Faunal turnover and the biostratigraphic definition of the latest

Triassic at the GSSP: Until relatively recently the TJB remained one of the last Period boundaries yet to have an allocated GSSP [*Ruhl 2010; Hillebrandt et al. 2013*]. Prior to the allocation of a GSSP for the base of the Jurassic Period, numerous sections had been proposed as GSSP candidate sections [*Hillebrandt et al. 2013*]. These included Kuhjoch (Austria) [*Hillebrandt et al. 2007; Hillebrandt et al. 2013*], Kunga Island (British Columbia, Canada) [*Carter & Tipper, 1999; Ward et al. 2001; Ward et al., 2004; Longridge et al. 2007a, 2007b*], New York Canyon (Nevada, USA) [*Taylor et al. 1983; Guex 1995; Guex et al. 1997; Guex et al., 2003; Guex et al. 2004; Ward et al. 2007; McRoberts et al. 2007; Lucas et al., 2007*], Waterloo Bay (Larne, Northern Ireland) [*Simms & Jeram, 2007*] and St. Audrie's Bay (Somerset, England) [*Warrington et al. 1994; Hesselbo et al. 2002; Hesselbo et al. 2004; Page, 2005*]. The GSSP was finally ratified by the International Commission on Stratigraphy (ICS) in 2010, as being located at the Kuhjoch Section in Austria [*Hillebrandt et al. 2013*] (*Fig. 3*). However, detailed biostratigraphic studies of the Rhaetian- Hettangian boundary had already begun at least 26 years previously [*Taylor et al., 1983*]. This prolonged length of time questions the cause for such a delay in defining the GSSP.

Quantifying marine redox across the Triassic–Jurassic mass extinction

The difficulties with correlating marine and terrestrial Triassic–Jurassic sections: Despite numerous research studies having recorded the ETME from both marine and terrestrial organisms (*see beginning of 2.3.4*), researchers had yet to correlate Late Triassic pulses of marine and terrestrial extinction [*Olsen et al. 1990; Fowell et al. 1994*]. This was partly due to difficulties of accurately correlating marine and continental sections, but also the absence of fine scale biostratigraphy for many marine sections [*Olsen et al. 1990*]. Early work correlating marine and continental boundary sections was undertaken by Hesselbo et al. (2002), through the use of carbon isotope stratigraphy, with later studies using magnetostratigraphy [*Krystyn et al., 2002; Gallet et al., 2003; Channell et al., 2003; Hounslow et al., 2004; Muttoni et al., 2004; Gallet et al., 2007*], and more recent research using both magnetostratigraphy and carbon isotope stratigraphy [*Muttoni et al., 2010; Whiteside et al. 2010; Lucas et al. 2011; Dal Corso et al., 2014*]. Although, it is only through the study of Upper Triassic palynostratigraphy and diagnostic marine fauna, in hand with carbon isotope stratigraphy, that marine and terrestrial extinctions have started to be correlated [*Kuerschner et al. 2007; Götz et al. 2009*]. It should be noted that these studies have only successfully correlated pulses of marine and terrestrial extinction at a regional scale. Global scale correlation of Late Triassic, marine and terrestrial extinction pulses has yet to be widely achieved. In spite of this, at least one study has successfully correlated the Late Triassic extinction of spores and pollen between marine and terrestrial sites on a global scale [*Whiteside et al. 2007*].

Chapter 2: The end-Triassic mass extinction event

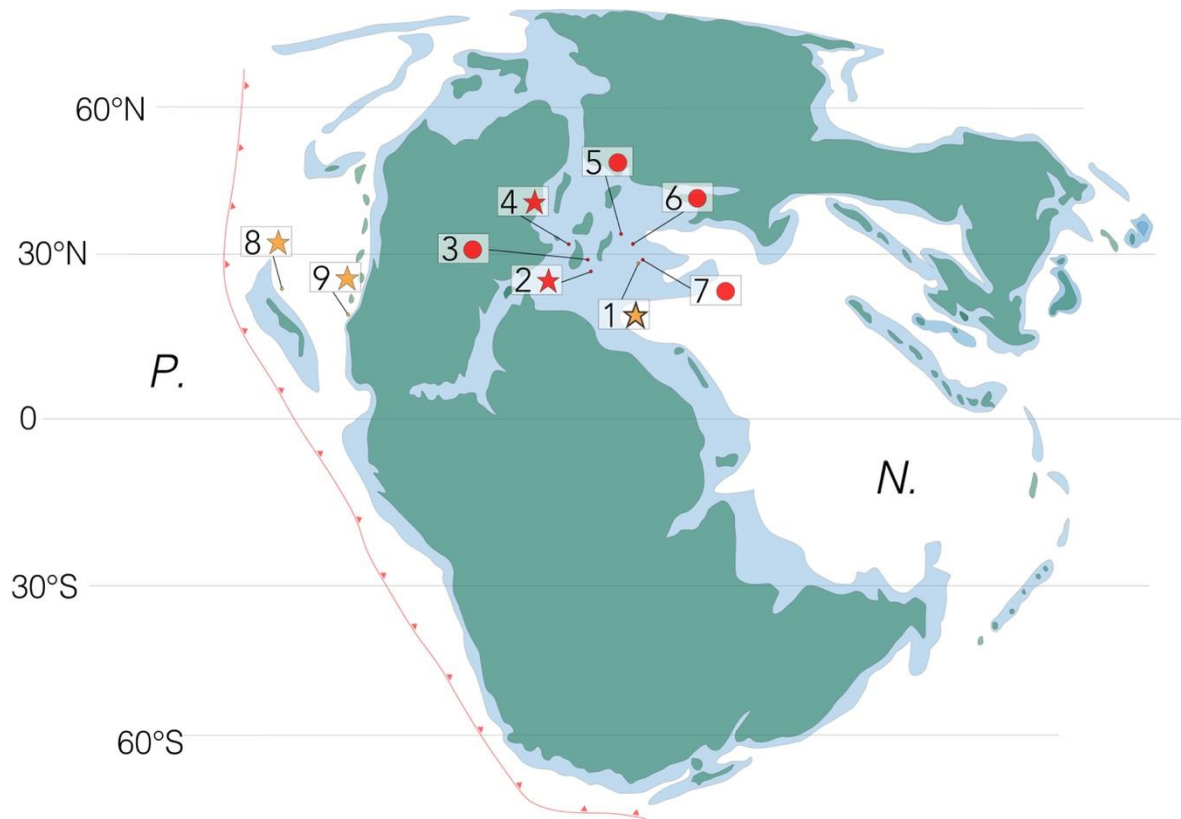


Figure 3:- Basal Hettangian GSSP candidate sites, and sites from this thesis, plotted against Triassic–Jurassic palaeogeography. 1) Kuhjoch Section, Tyrol, Austria, 2) St. Audrie’s Bay, Somerset, England 3) Cheshire Basin, England 4) Larne Basin, County Antrim, Northern Ireland, 5) Lower Saxony Basin, Germany, 6) Germanic Basin, Germany, 7) Csővár Basin, Hungary, 8) Kunga Island, Queen Charlotte Islands, British Columbia, Canada, 9)- New York Canyon, Nevada, USA. Stars represent Hettangian GSSP candidate sites. Circles represent non-GSSP candidate sites. Red symbols represent sites studied in this thesis. Yellow symbols represent sites not studied here. Darker outline = basal Hettangian GSSP. *N.*- Neotethys Ocean, *P.*- Panthalassa Ocean. Late Triassic palaeogeography from Al-Suwaidi et al., (2016) and Korte et al., (2019).

The difficulties with correlating different marine Triassic–Jurassic sections: There have also been problems with correlating different marine TJB sections. This is partly due to the catastrophic effects that the ETME had on traditional biostratigraphic fossil groups [Lindström et al. 2017], as well as the absence of ammonites within northwestern Europe during the latest Triassic [Bloos & Page, 2000; Hesselbo et al., 2002]. Detailed studies have therefore been undertaken to better understand the stratigraphy of marine Triassic–Jurassic boundary sections, as well as correlating marine TJB sections through a

Quantifying marine redox across the Triassic–Jurassic mass extinction

combination of palynology, carbon isotope stratigraphy, radiometric dating and ammonite biostratigraphy [Guex et al., 2004; Galli et al., 2005; Galli et al., 2007; Ruhl et al., 2009; Clemence et al., 2010; Bonis et al., 2010; Ruhl & Kürschner, 2011; Črne et al., 2011; Bachan et al., 2012; Lindström et al., 2012; Al-Suwaidi et al., 2016; Honig et al., 2016; Lindström et al. 2017; Yager et al., 2017; Todaro et al., 2018; Zaffani et al., 2018; Rigo et al., 2020; Ruhl et al., 2020].

Faunal turnover(s) and extinction at the GSSP: It is only upon the detailed stratigraphic study and correlation of numerous continental and marine TJB sites that a GSSP could finally be ratified in 2010 and inaugurated in 2011 [Morton, 2012; Hillebrandt et al. 2013]. This brief section of the thesis details the extinctions and turnovers which characterise the biostratigraphy of the GSSP and resulted in its selection as the basal Jurassic type locality.

Ammonites- The TJB at the GSSP is defined by the first appearance (FAD) of Lower Jurassic ammonite *Psiloceras spelae tirolicum* within the Kendlbach Formation [Hillebrandt & Krystyn, 2009] (Fig. 4). The appearance of *P. spelae tirolicum* is followed by the appearance of *P. ex. gr. P. tilmanni* (~9m) and *P. cf. pacificum* (~13m) and preceded by the disappearance (LAD) of Upper Triassic ammonite *Choristoceras marshi* (0m) within the Kössen Formation (Fig. 4) [Hillebrandt et al., 2007; Hillebrandt & Krystyn, 2009; Hillebrandt et al., 2013]. The LAD of *C. marshi* at the GSSP marks the lower boundary of the ETME (Fig. 4).

Conodonts- Conodonts occur commonly within the Kössen Formation with the last known conodont being the Triassic *Misikella ultima* [Hillebrandt et al., 2013]. Conodonts from the GSSP undergo extinction at the ETME and are therefore absent within the overlying Kendlbach Formation (Fig. 4) [Du et al., 2020].

Chapter 2: The end-Triassic mass extinction event

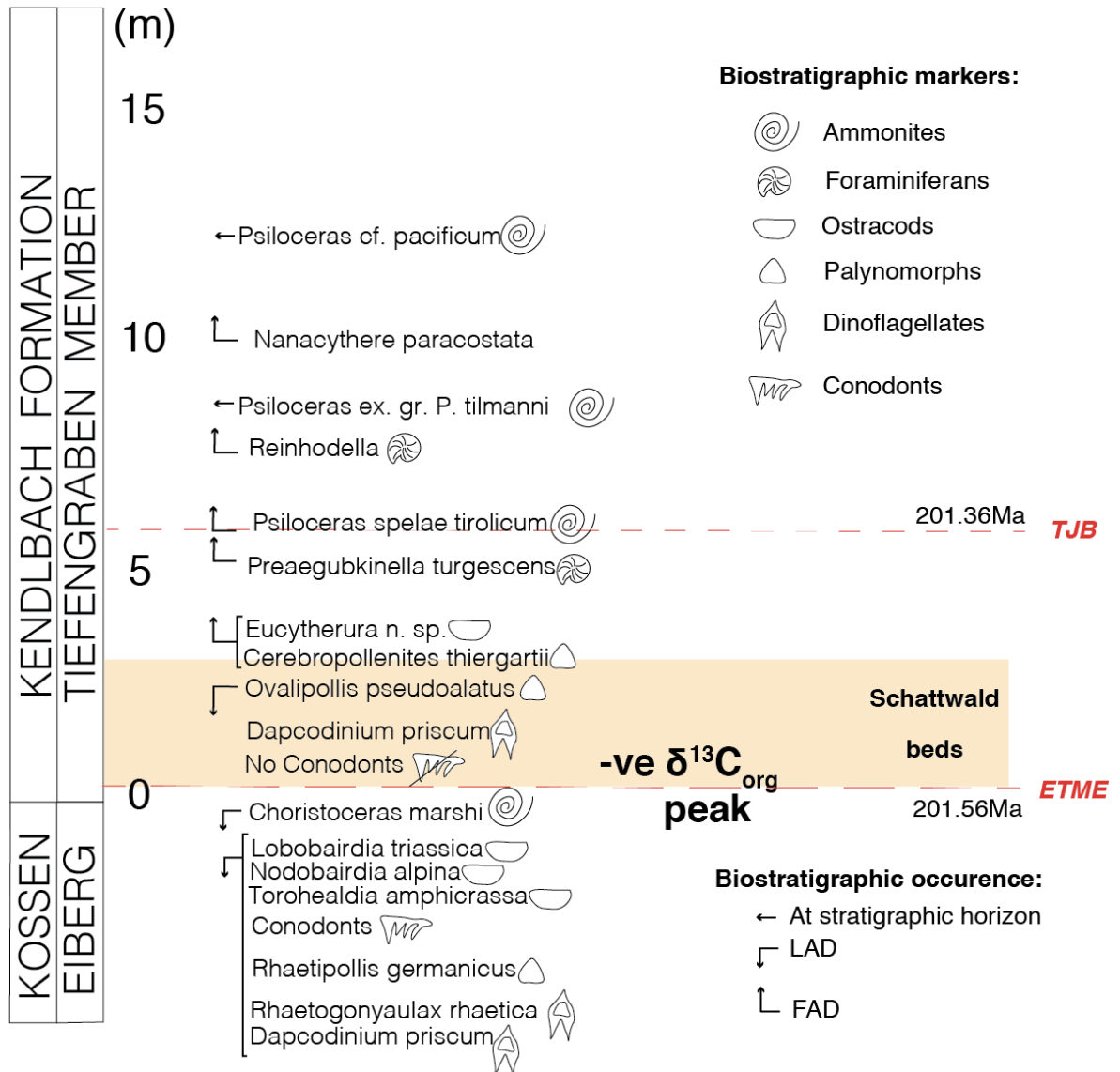
Ostracods- The Late Triassic ostracod species *Lobobairdia triassic*, *Nodobairdia alpina* and *Torohealdia amphiscrassa* last appear within the Kössen Formation, directly below the ETME interval (0m) (Fig. 4) [Hillebrandt et al. 2013]. The FAD of ostracod species *Eucytherua n. sp* within the lower Kendlbach Fm. (~4m), marks the latest Triassic, being found ~2 metres below the TJB (Fig. 4). The FAD of ostracod species *Nanacythere paracostata* subsequently marks the Jurassic Period, being found ~4 metres above the TJB (Fig. 4).

Foraminifera- The stratigraphic range of foraminiferan genus *Praegubkinella* is the next highest resolution biomarker for locating the boundary horizon after the FAD of *P. spelae tirolicum*. The FAD of *Praegubkinella turgescens* is ~0.5m below the TJB and its LAD is ~1.5 metres above the TJB. The FAD of the genus *Reinholdella* marks the Jurassic Period, ~2m above the TJB (Fig. 4) [Hillebrandt et al., 2013].

Palynomorphs- The lower boundary of the ETME at Kuhjoch is defined by the LAD of palynomorph *Rhaetipollis germanicus* [Hillebrandt et al., 2013] (Fig. 4). The FAD of palynomorph *Cerebropollenites thiergartii* is ~3m below the TJB at Kuhjoch [Hillebrandt et al., 2013] (Fig. 4).

Dinoflagellates- The Triassic dinoflagellate *Rhaetogonyaulax rhaetica* is present within the Kössen Fm. at Kuhjoch alongside *Dapcodinium priscum*. Dinoflagellate cysts become rare through the ETME interval and *Rhaetogonyaulax rhaetica* disappears entirely as is also observed at other TJB sections (Fig. 4) [Hesselbo et al., 2002; Hillebrandt et al., 2013; Boomer et al., 2021].

Figure 4 (below):- Biostratigraphic characterisation of the basal Jurassic GSSP, Kuhjoch Section, Tyrol, Austria. Stratigraphic data from Hillebrandt et al., 2013. Dates for the TJB and ETME from Blackburn et al., 2013 and Wotzlav et al., 2014. ETME- end-Triassic mass extinction, TJB- Triassic- Jurassic Boundary.



2.3.5.2 The definition of the Triassic–Jurassic boundary interval adopted

within this thesis: The definition of the Triassic–Jurassic boundary interval within this thesis partly follows that of *Hillebrandt et al.*, (2013) and considers the basal Jurassic to be primarily defined by the first appearance of ammonite *P. spelae* (Fig. 4). However, there exist some caveats with this method of stratigraphic definition which should be listed and resolved here. Firstly, the ammonite *P. spelae*, of the Tilmanni Zone, does not appear ubiquitously during the basal Jurassic and has only been identified from a select few, albeit geographically extensive, sections [*Guex et al.*, 2004; *Schoene et al.*, 2010; *Hillebrandt et al.*, 2013; *Lindström et al.*, 2017]. Within other Triassic–Jurassic boundary sections the

Chapter 2: The end-Triassic mass extinction event

first Jurassic ammonite appearance is marked by the appearance of *P. erugatum* (Somerset, UK; Larne, Northern Ireland) and *P. cf. tilmanni* (Rodby, Denmark) of the Tilmanni Zone [Lindström et al., 2017]. Where an erosional hiatus is thought to exist the first Jurassic ammonite is marked by the appearance of *Caloceras johnstoni* (Mingolsheim, Germany) and *Neophyllites imitans* (Schandelah, Germany) of the Planorbis Zone [Lindström et al., 2017]. Within this thesis *P. spelae* has been used to define the Triassic–Jurassic boundary interval at the GSSP. Given that *P. spelae* has not been recorded for any of the other Tethyan study sections, based on published records, here the Triassic–Jurassic boundary interval has been tenuously identified through the first common occurrence of palynomorph *Pinuspollenites minimus*. *P. minimus* has proven to be an effective biomarker for the basal Jurassic based on recent studies [Lindström et al., 2015; Lindström et al., 2017; Barth et al., 2018; Bos et al., 2023]. Where *P. minimus* and *P. spelae* have not been identified within a section (e.g., the Larne Basin), then the first occurrence of Jurassic palynomorph *Cerebropollenites thiergartii* has been used after Hillebrandt et al., (2013) and Jeram et al., (2021). Where identification of the boundary horizon is more uncertain then assignment has been based on the approximate position of the boundary given the available information with uncertainty being expressed through a greyed out section and/or a dashed boundary.

The remainder of this section will continue to discuss the key groups of marine life that underwent extinction, as well as discussing the extent to which marine organisms were affected by Late Triassic environmental changes. Marine organisms which are thought to have been more severely affected during the ETME will be discussed first (e.g., ammonites, bivalves, reefal organisms) before moving on to those that are only believed to have been moderately affected (e.g., radiolarians and foraminiferans). Extinction selectivity will also be used to interpret potential causes of extinction.

Quantifying marine redox across the Triassic–Jurassic mass extinction

2.3.5.3 Late Triassic ammonite extinctions: The ETME is considered to be the most ‘important’ extinction event within ammonite history based on the disappearance of ammonite Suborder Ceratitina and the persistence of only one ammonite lineage through to the Jurassic (Suborder Phylloceratina) [Tozer, 1981; House, 1989; Guex et al., 2004; Hillebrandt & Krystyn, 2009].

The stratigraphic distinction of the TJB and ETME on the basis of widespread ammonite extinction and gradual recovery emphasises how catastrophic the ETME was for ammonite species (see section 2.3.4.1). The ammonite turnover at the TJB is very well documented within the ammonite-rich, New York Canyon (NYC) section (Nevada) where certain Choristoceratid ammonites (*C. marshi*, *C. crickmayi*, *C. shoshonensis*) can be observed to gradually disappear during the latest Rhaetian followed by the first appearance of Psiloceratid ammonites (*P. spelae*, *P. tilmanni*) at the base of the Jurassic Period (Fig. 5) [Guex et al., 2004; Guex, 2016].

Choristoceratid ammonites represent one of the earliest examples of uncoiled Mesozoic ammonoids which ‘proliferated’ throughout the palaeo-environmentally unstable Rhaetian age, whilst most other non-heteromorph ammonoids disappeared [Whiteside & Ward, 2011; Guex, 2016]. The choristoceratid lineage narrowly persists through the TJB at NYC, as one of the only ammonoid survivors of the ETME, before disappearing entirely within the early Hettangian Planorbis beds (Fig. 5; *Choristoceras minutum*) [Guex et al., 2004; Shevyrev, 2005; Guex, 2016]. However, the survival of *C. minutum* through the TJB at NYC is not without its controversy as all ammonite workers agree that only one ammonite lineage (Psiloceratidae) survived through to the Jurassic [Lucas, 2018]. Aleksandr

Chapter 2: The end-Triassic mass extinction event

Shevyrev (2005) subsequently compares the NYC *C. minimum* to the biblical resurrection of Lazarus.

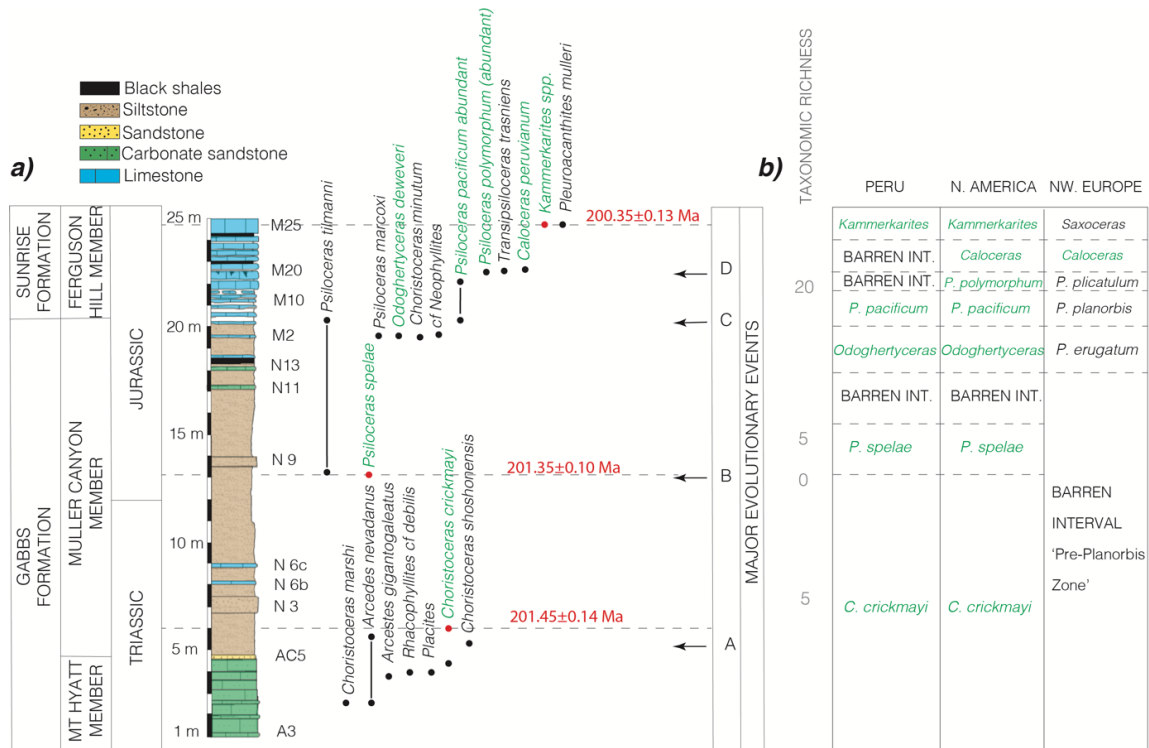


Figure 5:- a) The near-extinction and rapid recovery of the Subclass Ammonoidea as recorded from the Triassic–Jurassic New York Canyon (NYC) section, Nevada. $^{238}\text{U}/^{206}\text{Pb}$ dates (red) and corresponding red, circular markers signify dated first (FAD) and last (LAD) appearances of diagnostic Triassic (LAD) and Jurassic (FAD) ammonite taxa. **b)** Regional correlation of ammonite biozones and changes in Triassic–Jurassic ammonite taxonomic richness from the Pacific realm. Species and genus names in green signify ammonite species/genera observed within the NYC section (also seen within part **a**) of figure). Major evolutionary events: 'A' - Extinction of Triassic ammonites following the dominance of heteromorphic forms during the late Rhaetian, 'B' - First occurrence of *P. tilmanni* & *P. spelae* and disappearance of Choristoceratid ammonites, 'C' - First occurrence of highly abundant *Psiloceras*, 'D' - Main radiation and recovery of Jurassic ammonites. NYC stratigraphy, ammonite occurrences and major evolutionary events from Guex et al., (2004). $^{238}\text{U}/^{206}\text{Pb}$ dates, taxonomic richness and regional correlation of ammonite biostratigraphy from Guex et al., (2012).

Ammonite biodiversity changes during the Late Triassic: A compilation by Benton (1993b) reported that 8 ammonite families underwent extinction by the late Norian (middle Upper Triassic) with a further 17 ammonite families undergoing extinction by the late Rhaetian (late Upper Triassic). These figures would therefore support Newell (1963)'s study which believed 25 ammonite families to have disappeared throughout the ETME. However,

Quantifying marine redox across the Triassic–Jurassic mass extinction

contrary to the diversity changes reported by Benton (1993b), many of the known ammonite extinctions at the ETME are believed to have occurred during the late Norian with ammonite diversity remaining low throughout the Rhaetian [*Kummel, 1957; House, 1963; Newell, 1967; Tozer, 1981; Lucas, 2018*]. A large proportion of Triassic ammonite genera undergoing extinction by the late Norian is further supported by Whiteside & Ward, (2011). Whiteside & Ward, (2011) studied ammonite occurrences and generic diversity from the Triassic of the North Pacific (Frederick Island) and record 72 and 63 genera respectively from the Lower and Upper Norian (104 & 148 occurrences) with a significant decline to 10 ammonite genera by the early Rhaetian (15 occurrences) (*Fig. 6*).

Meanwhile, a broader study undertaken by Teichert (1988) records 150 ammonite genera and subgenera to have existed during the Carnian (early Upper Triassic), with this figure being reduced to 90 during the Norian and 6 or 7 by the early-mid Rhaetian. Similar figures are also quoted by Kennedy (1977) with there being ~150 Carnian genera, less than 100 Norian genera and less than 10 Rhaetian genera [*Kennedy, 1977; Lucas et al., 2018*]. Brayard et al., (2009) report 71–74 mid Norian genera, 31–33 late Norian genera and 18–19 Rhaetian genera based on data from the Goniat database, as well as chao2 and Jackknife 2 estimator data. Whilst compiled diversity numbers from Tozer (1981) record 25 Ladinian families, 22 Julian (lower Carnian) families, 15 families from the Lacinian (lower Norian) and 14 and 2 families from the Sevatian (upper Norian) and Rhaetian respectively [*Lucas, 2018*].

Therefore, the ETME is characterised by significant late Norian reductions in ammonite biodiversity, with ammonite biodiversity throughout the Rhaetian Age remaining low (*Fig. 6*). Late Norian extinctions may have occurred in pulses, with any surviving Rhaetian species undergoing extinction by the latest Rhaetian/ earliest Hettangian. This would

Chapter 2: The end-Triassic mass extinction event

support work by Taylor et al., (2000) which theorises two latest Triassic ammonite extinctions, one in the Norian and a second at the end of the Rhaetian.

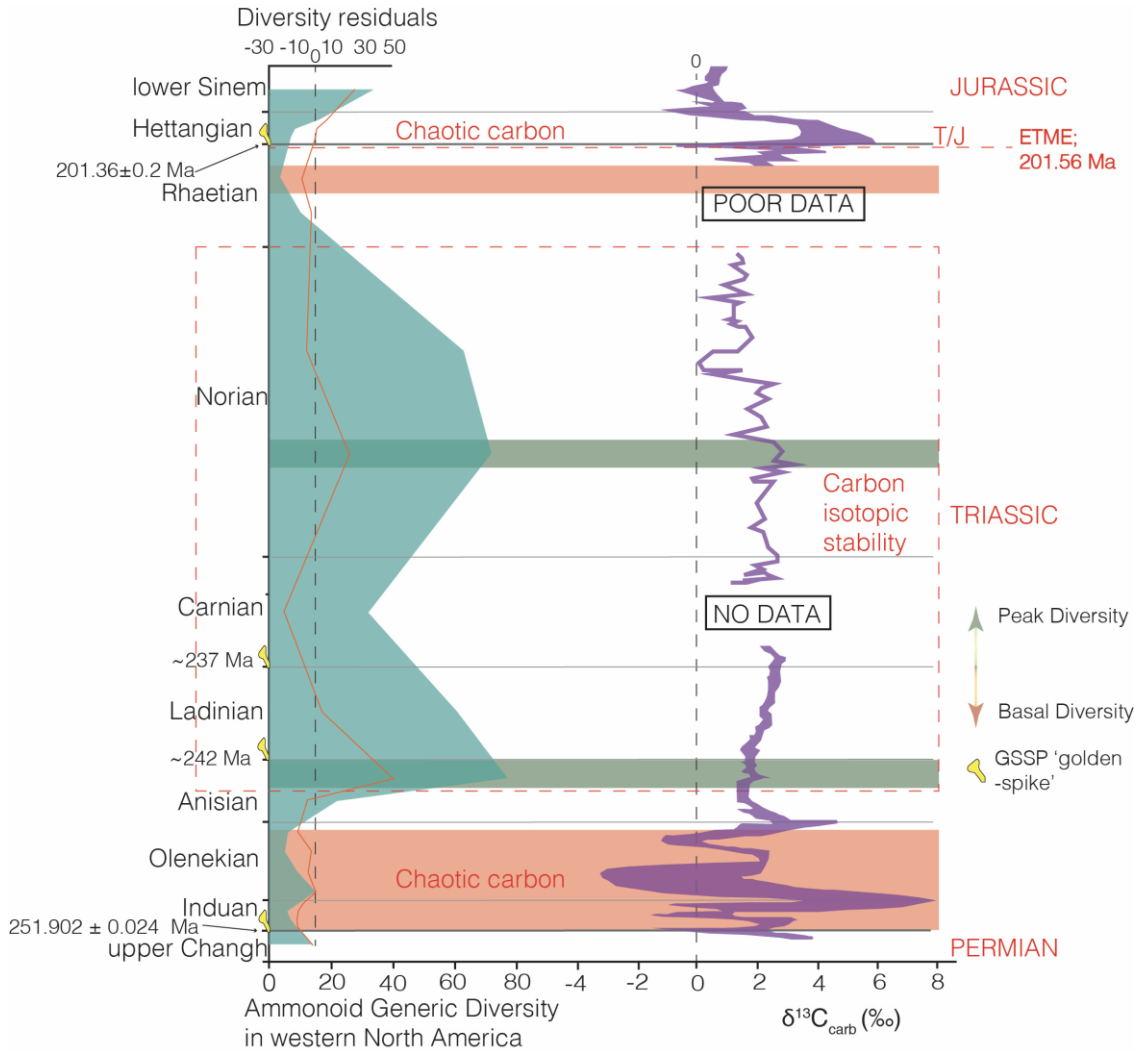


Figure 6:- Changing ammonoid generic diversity and its relationship to carbon cycle instability. Figure amended from Whiteside and Ward, (2011). Most recent date for Permian/Triassic boundary from the ICS International Chronostratigraphic Chart 2020. Dates for the Triassic–Jurassic boundary and End Triassic Mass Extinction from Blackburn et al., (2013) and Wotzlaw et al., (2014). Sinem- Sinemurian. Changh- Changhsingian. Position of GSSP ‘golden spikes’ from ICS Int. Chron. Ch. ’20. Ammonoid data are from Kennecott Point, Queen Charlotte Islands and therefore GSSP horizons have been correlated.

Quantifying marine redox across the Triassic–Jurassic mass extinction

Interpreted causes of Late Triassic ammonite extinctions: Rapid chemical pollution of the oceans during the ETME is interpreted to have contributed towards retardation in ammonite development [Hallam, 2002; Guex et al., 2004]. The appearance of atavistic (simplified) and asymmetric forms during the major crisis, as well as the disappearance of larger ammonite species (60cm) until the Sinemurian (early Jurassic), is thought to be the result of oceanic chemical changes by Guex et al., (2004).

Oceanic chemical changes associated with Triassic–Jurassic ammonite population changes may include ocean acidification, ocean anoxia and enhanced weathering resulting in the increased input of sediments to the oceans. Alternatively, Whiteside & Ward, (2011) interpret that the increased presence of primitive, passively floating ammonoid forms, *e. g.* heteromorph and serpenticone morphotypes, may be the result of functional redundancy and the collapse of the biological carbon pump during chaotic carbon cycles (*Fig. 6*). Recent computational modelling of serpenticone morphotypes by Hebdon et al., (2020) simulates increased shell drag compared to non-serpenticone forms, particularly at higher velocities. This further supports a more passively floating lifestyle for serpenticone ammonites and could add evidence to the theory of functional redundancy proposed by Whiteside and Ward, (2011). However, in order to further understand the roles of some of these factors on late Triassic ammonite extinctions, research must be undertaken to better understand late Triassic spatio-temporal redox changes which at present remains poorly understood. This thesis will therefore aim to make progress in understanding Late Triassic spatio-temporal redox change to aid understanding of changes to Late Triassic ammonite diversity.

Chapter 2: The end-Triassic mass extinction event

2.3.5.4 Late Triassic bivalve extinctions: It is believed that approximately half of the existing bivalve genera and almost all existing species underwent extinction at the ETME [Hallam, 1981; Ros et al., 2011; Hautmann, 2012]. Hallam, (1981) proposed that 92% of existing bivalve species, as well as 76 out of 135 genera, disappeared during the Late Triassic based on the compilation of a global bivalve dataset (Fig. 7). Hallam, (1981) also supported data by Pitrat (1970) that 6 out of 52 existing bivalve families became extinct. Yet, the disappearance of 6 bivalve families at the ETME conflicts with research by Skelton and Benton (1993) who record 5 out of 57 families to have undergone extinction, and also Benton (1993b) who only recorded the disappearance of 2 (out of 52) bivalve families during the ‘end-Triassic extinction’.

Spatio-temporal bivalve extinctions during the Late Triassic: The relatively low number of bivalve families quoted to have undergone extinction by Benton (1993b) may be due to the episodic and selective nature of bivalve extinctions throughout the Rhaetian Age. Research by McRoberts et al., (1995) records numerous episodic extinctions during the Rhaetian from Lombardia, Italy. Early Rhaetian Lombardian sections exhibit a 51% extinction of bivalve species whilst a 71% extinction of bivalve species is observed within Middle Rhaetian Lombardian sections [McRoberts et al., 1995]. Meanwhile, Wignall & Bond (2008), Mander et al., (2008) and Wignall & Atkinson (2020) have identified dramatic changes in palaeo-community structure and increased bivalve extinction rates to have occurred during the upper Westbury to Lilstock Formation (Penarth Group, Late Rhaetian) from the Southwest of England.

Figure 7 (below):- Global, spatio-temporal changes in the generic biodiversity of Late Triassic bivalves. Bivalve generic data, including extinction rates, origination rates, paleogeographic data and time bins from Hallam, (1981) [a & b]. Dates for the Landinian, Carnian, Norian and the Triassic–Jurassic boundary from the ICS International Chronostratigraphic Chart 2020 [a & b]. Green text and up arrows indicate increases in genus numbers and red text and down arrows indicate decreases in genus numbers [a & b]. Late Triassic palaeogeography from Al-Suwaidi et al., (2016) and Korte et al., (2019) [b]. A- Australia, EA- East Antarctica, E/B- Europe/ Baltica, G- Greenland, I- India, J- Japan, M- Madagascar, NA- North America, NAF- North Africa, SA- South America, SAF- South Africa, U- United Kingdom [b].

Quantifying marine redox across the Triassic–Jurassic mass extinction

a)

Triassic- Jurassic boundary: 201.3±0.2 Ma Origination rate: 29%↑ Extinction rate: 3%↓

Genera	Order	W. Tethys	E. Tethys	Japan	Arctic	Pacific N. America	Pacific S. America	New Zealand
3↓	NUCULOIDA	3↓	3↓	3-	2-	3-	2↓	2-
2↓	ARCOIDA	1-	2-	1-	1-	1-	0↓	1-
6↓	MYTILOIDA	4↓	3↓	2-	3-	5-	2-	1-
22↓	PTERIOIDA	19↓	15↓	12↓	14↓	10↓	7↓	4↓
1↓	UNIONOIDA	0↓	0↓	1↓	0↓	0↓	0-	0↓
1↓	TRIGONOIDA	1↓	1↓	1↓	1↓	0↓	0↓	0↓
4↓	VENEROIDA	4↓	1↓	1↓	2↓	2↓	2↓	1↓
0↓	HIPPURITOIDA	0↓	0↓	0-	0-	0↓	0↓	0↓
4↓	PHOLADOMYOIDA	3↓	2↓	1↓	2↓	2↓	0-	0-

Total genera: 43↓

Norian (including Rhaetian): ~227- 201.3±0.2 Ma Origination rate: 26%↓ Extinction rate: 42%↑

Genera	Order	W. Tethys	E. Tethys	Japan	Arctic	Pacific N. America	Pacific S. America	New Zealand
5-	NUCULOIDA	4↓	4↑	3-	2-	3-	3↑	2-
3-	ARCOIDA	1↓	2-	1-	1-	1-	1-	1-
7↓	MYTILOIDA	5↓	4-	2-	3-	5-	2-	1-
38↓	PTERIOIDA	30↓	29↑	19↑	19↓	17↑	9↑	9-
4↓	UNIONOIDA	3-	2-	3-	2-	1-	0-	2-
11-	TRIGONOIDA	6-	8-	6-	5-	5-	3↓	2↑
18↑	VENEROIDA	13↑	6↑	4↓	4-	6↑	8↑	3-
2↑	HIPPURITOIDA	2↑	1-	0-	0-	1-	1-	1-
9↑	PHOLADOMYOIDA	7↑	4↑	1-	2-	2-	0-	0-

Total genera: 97↓

Carnian: ~237- ~227 Ma Origination rate: 42% Extinction rate: 29%

Genera	Order	W. Tethys	E. Tethys	Japan	Arctic	Pacific N. America	Pacific S. America	New Zealand
5↑	NUCULOIDA	5↑	3-	3-	2-	3-	2-	2-
3-	ARCOIDA	3-	2-	1-	1-	1-	0-	1-
9↑	MYTILOIDA	8↑	4↓	2-	3↓	4-	2-	1-
46↑	PTERIOIDA	37↑	23↑	17↑	20↑	15↑	7↑	9↑
5↑	UNIONOIDA	4↑	2-	3↑	2↑	1-	0-	2-
11↑	TRIGONOIDA	6-	8↑	6↑	5↑	5↑	3↑	1↑
15↑	VENEROIDA	12↑	5↑	6↑	4↑	5↑	4↑	3↑
1-	HIPPURITOIDA	1-	1-	0-	0-	1-	1-	1-
4↑	PHOLADOMYOIDA	4↑	2↑	1-	2↑	2↑	0-	0-
1↑	?	1↑	0-	0-	0-	0-	0-	0-

Total genera: 100↑

Landinian: ~242- ~237 Ma

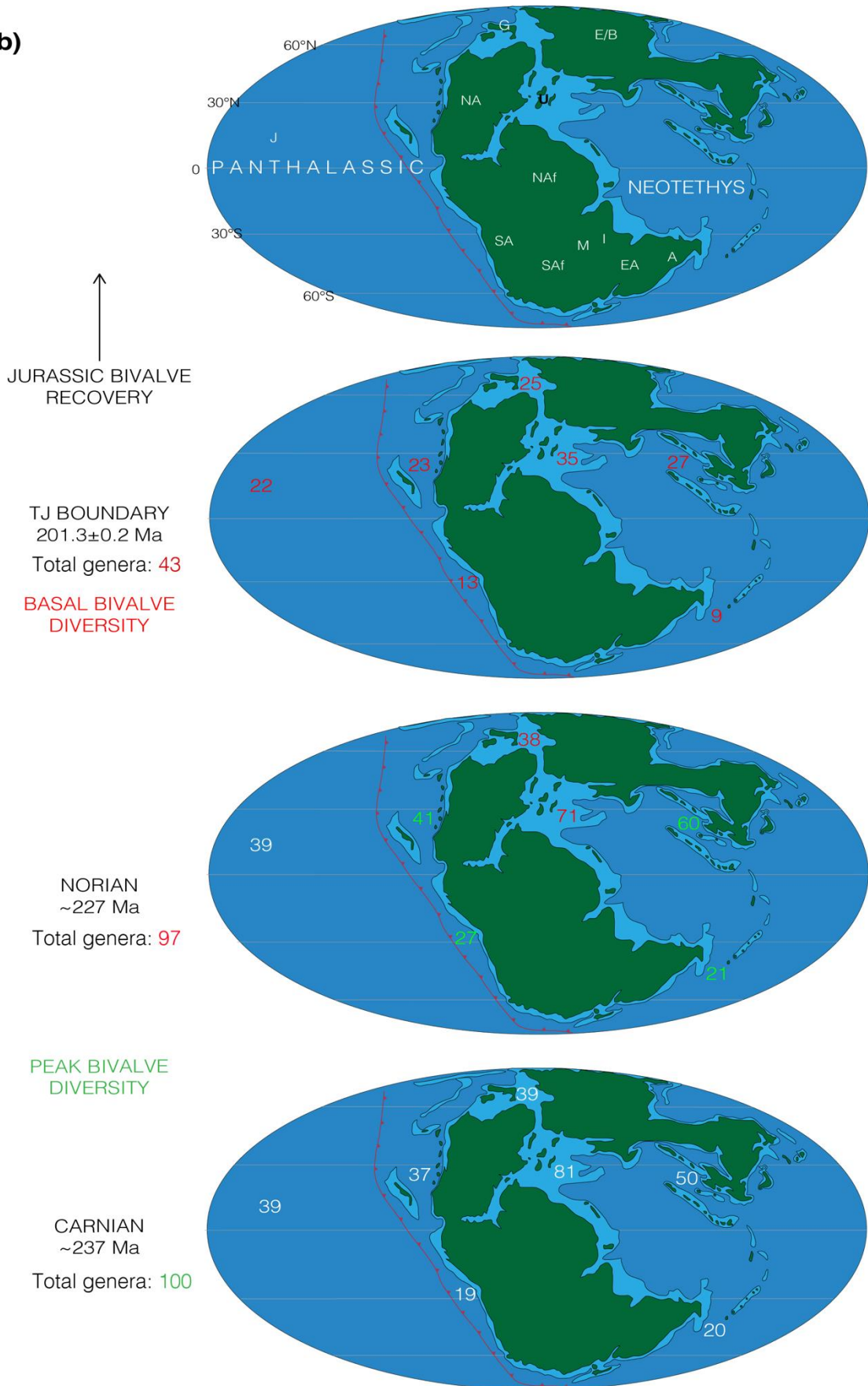
Genera	Order	W. Tethys	E. Tethys	Japan	Arctic	Pacific N. America	Pacific S. America	New Zealand
4	NUCULOIDA	4	3	3	2	3	2	2
3	ARCOIDA	3	2	1	1	1	0	1
7	MYTILOIDA	6	5	2	4	4	2	1
27	PTERIOIDA	27	19	13	16	10	5	5
3	UNIONOIDA	3	2	1	1	1	0	2
6	TRIGONOIDA	6	6	5	4	3	1	0
7	VENEROIDA	7	3	3	2	3	2	1
1	HIPPURITOIDA	1	1	0	0	1	1	1
2	PHOLADOMYOIDA	2	1	1	1	0	0	0

Total genera: 60

Regional extinction %							Order	Total late Triassic genera	# extinct by end Triassic
W.Tethys	E. Tethys	Jap.	Arc.	PNA	PSA	NZ			
1	12.3	-20	0	2.5	-10.8	-42.1	NUCULOIDA	6	3
2	50.7	55	43.5	34.2	43.9	51.8	ARCOIDA	5	3
							MYTILOIDA	10	4
							PTERIOIDA	60	33
							UNIONOIDA	5	4
							TRIGONOIDA	12	10
							VENEROIDA	26	16
							HIPPURITOIDA	2	2
							PHOLADOMYOIDA	9	1
(% genus extinction)									
1- Carnian to Norian									
2- Norian to Triassic/Jurassic Boundary									
							9 ORDERS	135	76

Chapter 2: The end-Triassic mass extinction event

b)



Quantifying marine redox across the Triassic–Jurassic mass extinction

In addition to work by these authors [McRoberts *et al.*, 1995, Wignall & Bond, 2008, Mander *et al.*, 2008 and Wignall & Atkinson, 2020], research by McRoberts & Newton (1995) records spatial selectivity of extinction throughout Western Europe. Despite Lombardian sections recording a 71% extinction of bivalve species [30/42 species], the Penarth Group of England and Wales records an 83.5% bivalve extinction [23/27 species] and an Austrian-German section from the Northern Calcareous Alps records a 90% bivalve extinction [45/50 species] [McRoberts & Newton, 1995]. Similar spatial variability was recorded by Hallam & Wignall (1997) within generic level bivalve studies; 4 bivalve genera out of 27 (~15%) are recorded to have undergone extinction from NW Europe compared to 9 out of 29 (31%) bivalve genera within the Northern Calcareous Alps.

Wignall & Bond (2008) interpret spatial selectivity of bivalve extinctions, on the Tethyan shelf, to reflect the more euryhaline tolerance of British bivalves as a result of inhabiting quasi-marine settings compared to the open marine settings within Southern Europe. However, this hypothesis is inconsistent with Late Triassic brackish conditions in Southern Europe reported by other authors [Bonis *et al.*, 2010; Blumenberg *et al.*, 2016; Barth *et al.*, 2018]. Therefore, extinction selectivity may be a function of spatio-temporal marine redox as suggested by McRoberts & Newton, (1995). The possibility that marine bivalves were potentially affected by marine redox conditions further emphasises the importance of Late Triassic redox studies in understanding changes to marine biodiversity.

Global scale extinction variability is also evident based on data from Hallam, (1981) (*Fig. 7*). Generic bivalve extinction rates range from 34.2% (Arctic) to 57.1% (New Zealand) during the Norian to end-Triassic with an average of 48% genus extinction (*Fig. 7*). There does not appear to be any clear correlation between sites exhibiting higher or lower percentages of genus extinction from the Norian through to the end-Triassic (*Fig. 7*).

Chapter 2: The end-Triassic mass extinction event

Tethyan sites (Arctic, Western Tethys & Eastern Tethys) exhibit an average of 46.6% genus extinction whilst Panthalassa sites (Japan, PSA, PNA, New Zealand) exhibit an average of 49% genus extinction (*Fig. 7*). However, during the latest Carnian–early Norian, higher percentages of extinction are clearly observed on the Tethyan shelf (*Fig. 7*). Meanwhile, Panthalassa sites remain highly productive.

As well as spatial variability, Late Triassic bivalve populations also exhibit temporal variability. This has already been alluded to through localised studies by McRoberts et al., (1995) and Mander et al., (2008). However, in order to understand global scale temporal extinction patterns, more extensive palaeobiological databases must be consulted. This once again brings us back to the global scale bivalve study by Anthony Hallam from 1981 [*Hallam, 1981*]. Research by Hallam, (1981) would suggest a large reduction in bivalve generic diversity during the ‘Norian’ (*Fig. 7*). However, due to Hallam, (1981) grouping the Norian and Rhaetian together, it is difficult to determine the exact timing and intensity of these diversity changes. Hallam, (1981) and Hallam (2002) have advocated a large disappearance of bivalves at the TJB. However, research by Morbey, (1975), Mostler et al., (1978), Allasinaz, (1992) and McRoberts & Newton, (1995) records numerous bivalve extinctions throughout the Rhaetian.

A more recent worldwide compilation of stage-level bivalve data by Ros et al., (2011) reports major reductions in generic diversity (GD) during the Rhaetian with GD increasing until the end Norian. Ros et al., (2011) also report mean standing diversity (MSD) to have decreased from the mid-Norian through to the mid-Hettangian with both proxies (GD & MSD) reporting bivalve recovery by the mid-Hettangian. Based on data from Ros et al., (2011) the most significant reductions in bivalve diversity occurred throughout the Rhaetian. These conclusions mirror those of Kiessling et al., (2007).

Quantifying marine redox across the Triassic–Jurassic mass extinction

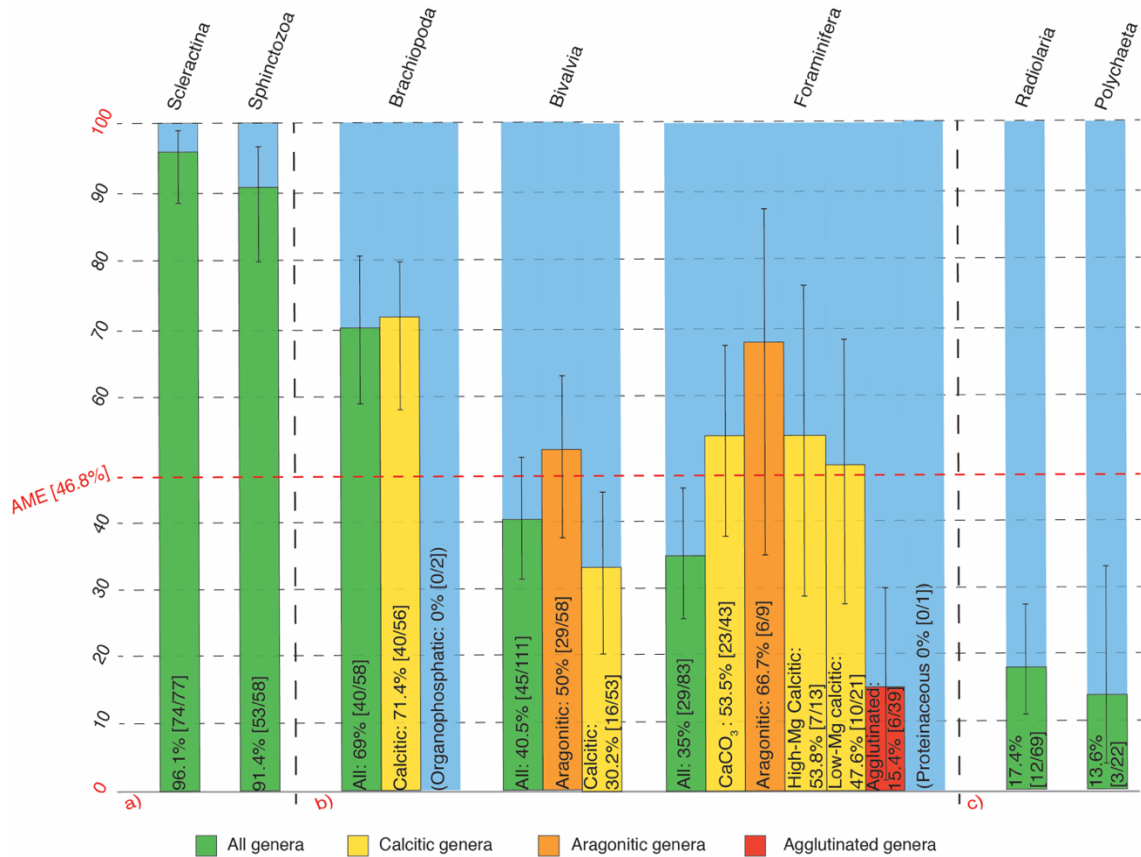


Figure 8:- Variable extinction of organisms at the Triassic–Jurassic boundary according to skeletal physiology— data from Hautmann, (2012). a) Hypercalcifying organisms with aragonitic and/or high-Mg calcite skeletal mineralogy, little physiological control of biomineralisation b) Variance in skeletal material, increased extinction risk from non-calcareous skeletons to low-Mg calcite, high-Mg calcite, and aragonite mineralogy c) non-calcareous skeletal physiology. AME- Average Marine Extinction.

Aragonite undersaturation and its effect on Upper Triassic, infaunal bivalve species:

Despite the large degree of variability concerning extinction within late Triassic bivalve populations, McRoberts et al., (1995) and McRoberts & Newton, (1995) consistently observed the near-complete disappearance of infaunal bivalve species within Northwest European (93% extinction) and both Northern and Southern Alpine (100% extinction) sections. McRoberts & Newton, (1995) interpreted this to be as a result of infaunal species being unable to compete for food resources during increased Late Triassic competition.

Chapter 2: The end-Triassic mass extinction event

However, Hautmann (2006, 2012) and Hautmann et al., (2008a) strongly correlated the disappearance of infaunal bivalve species to skeletal physiology (*Fig. 8*). Hautmann et al., (2008a) observed that bivalves underwent a 40% extinction of marine genera, consisting of a 50% loss of aragonitic species but only a 30% loss of calcitic species (*Fig. 8*). Infaunal bivalves are invariably aragonitic and epifaunal species predominantly calcitic (Hautmann et al., 2008). Hautmann et al., (2008a) therefore interpreted that the high percentage of infaunal bivalve species, as well as aragonite reliant organisms, undergoing extinction at the ETME was a function of shell composition (*Fig. 8*).

Hautmann (2004, 2006, 2012) further interprets that ocean acidification during the Late Triassic resulted in unfavourable conditions for aragonite biomineralisation and consequently the replacement of aragonite for calcite by biocalcifying benthic molluscs. This is referred to by some authors as the Triassic–Jurassic ‘biocalcification crisis’ [*Hautmann, 2004; Greene et al., 2012*]. Although, contrary to the title given to Late Triassic aragonite undersaturation, calcite undersaturation does not seem to have been equally affected [*Hautmann, 2004; Hautmann et al., 2008a; Greene et al., 2012; R. Twitchett 2019. pers. comm. 6 Sept*]. Furthermore, certain sites, e. g. Somerset show only 1 example of aragonitic bivalve disappearance [Pre-Planorbis Zone], whilst saturation of aragonite in equatorial sites is known to persist through both the ETME and TJB [*Mander & Twitchett, 2008; Al-Suwaidi et al., 2016*]. Therefore, aragonite undersaturation may be spatio-temporally variable.

Kiessling et al., (2007) similarly recorded an increased extinction risk of Late Triassic aragonitic bivalve species through compiling data from the Palaeobiology Database (PBDB). However, in addition to these repeat findings, Kiessling et al., (2007) also determined that the preferential extinction of aragonitic bivalve species holds for both the

Quantifying marine redox across the Triassic–Jurassic mass extinction

infauna and the epifauna. Yet, despite the preferential extinction of aragonitic species being well supported, the mineralogical composition of bivalve assemblages did not change substantially across the TJB [Hallam, 1981; Kiessling et al., 2007]. Other invariable factors included the proportion of infaunal to epifaunal bivalve occurrences, and changes to bivalve ecology outside of reef environments (Fig. 9) [Kiessling et al., 2007]. Furthermore, Kiessling et al., (2007) argue that the PBDB data do not support skeletal mineralogy as a significant factor in Late Triassic extinction(s) outside of the Bivalvia. Kiessling et al., (2007) were therefore reluctant to accept that skeletal mineralogy represented a dominant factor in Late Triassic extinction outside of Triassic reef environments, particularly given the isolated nature of bivalve shell excretion².

A subsequent study by Ros et al., (2011) agrees with Kiessling et al., (2007) that the ETME had little impact on bivalve ecological diversity and that aragonitic species were more severely affected regardless of ecology. Ros et al., (2011) also concluded that infaunal tiering was unaffected during the ETME and that that survivorship of infaunal species exceeded that of the epifaunal collective during the Lower Jurassic. Dunhill et al., (2018) alternatively propose that the ETME fits the ‘skeleton crew hypothesis’ proposed by Foster & Twitchett (2014); each ecological guild having survived, with the questionable exception of photosymbiotic megalodonts, but only occupied by a select few taxa.

In light of previous work on Late Triassic bivalve extinction selectivity [McRoberts et al., 1995; McRoberts & Newton, 1995; Hautmann 2006; Kiessling et al., 2007; Hautmann et al., 2008a], and potential uncertainty regarding aragonite undersaturation, Mander &

² Unlike other biomineralising organisms (e. g. corals) bivalves excrete their shells internally through a mantle. Therefore, bivalves are less prone to changes in water acidity [Harper et al., 1997; Harper, 2005; Kiessling et al., 2007].

Chapter 2: The end-Triassic mass extinction event

Twitchett, (2008) set out to determine the factors governing the completeness of the bivalve fossil record from the Northwest of Europe.

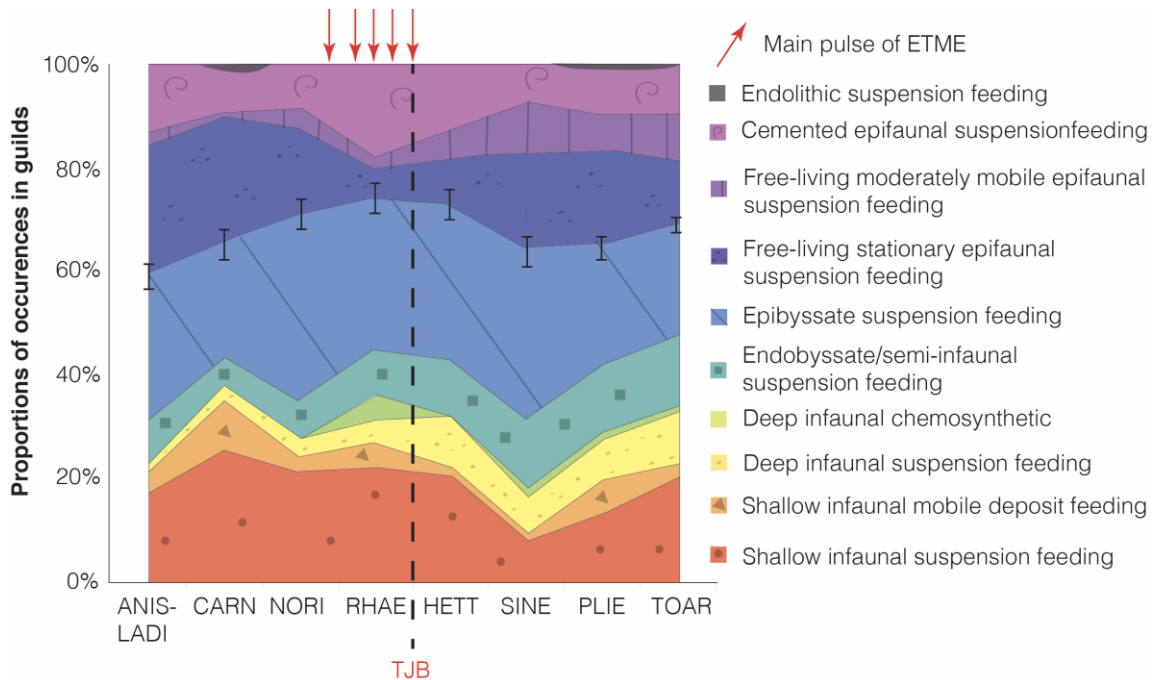


Figure 9:- Changes to bivalve ecology through the Triassic- Jurassic mass extinction. Figure amended from Kiessling et al., (2007). Main pulses of extinction specifically refer to known pulses of bivalve and ammonite extinction from the literature [Hallam, 1981; McRoberts et al., 1995; Mander et al., 2008; Whiteside & Ward, 2011]. ANIS-LADI: Anisian- Ladinian, CARN: Carnian, NORI: Norian, RHAE: Rhaetian, HETT: Hettangian, SINE: Sinemurian, PLIE- Pliensbachian, TOAR: Toarcian. TJB- Triassic- Jurassic Boundary.

Mander and Twitchett, (2008) found no evidence from the Lillstock Formation that the decline in bivalve diversity was a function of poor preservation, outcrop extent, sea level change, shell mineralogy or changes to lithofacies. This led Mander & Twitchett, (2008) to propose that bivalve extinction selectivity may be the result of an incomplete fossil record, particularly amongst semi-faunal and infaunal bivalves, a hypothesis mirrored by Wright et al., (2003) and partially supported by Hautmann et al., (2008b). Mander and Twitchett, (2008) further hypothesised that the absence of infaunal species may be due to benthic anoxia, and the presence of the redox boundary close to the sediment water

Quantifying marine redox across the Triassic–Jurassic mass extinction

interface. Benthic anoxia was further proposed to account for a reduction in the burrowing depth of soft-bodied benthos, and a decrease in the body-size of marine bivalves [*Barras and Twitchett 2007; Mander et al. 2008*].

Conversely, oxygen poor sediments may explain a reduction in bivalve diversity on a local scale, however generic diversity of infaunal bivalves exceeds that of epifaunal bivalves during the Norian, Rhaetian and Hettangian [*Ros et al., 2011*]. Furthermore, as stated previously for ammonite extinctions, spatio-temporal marine anoxia and its role in Late Triassic marine extinctions is only loosely understood. Marine redox studies from this thesis will therefore aid in the understanding of latest Triassic bivalve extinctions.

Particularly in answering whether the cause of infaunal bivalve disappearance was the result of benthic anoxia, but also in reconstructing spatio-temporal redox change and its potential correlation with Late Triassic bivalve extinctions.

Summary- Bivalves were severely affected by Late Triassic environmental change experiencing a species level extinction of up to 90% [*McRoberts & Newton, 1995*].

Bivalve extinction rate throughout the Rhaetian is known to have exhibited spatio-temporal variability with greater rates of extinction being observed during the middle Rhaetian and within Southern Europe [*McRoberts et al., 1995; McRoberts & Newton, 1995*]. Elevated levels of bivalve extinction have also been noted during the Rhaetian through a global compilation of generic data [*Ros et al., 2011*]. Spatio-temporal variability of bivalve extinctions may be the result of variable tolerances of bivalve populations to salinity changes [*Wignall & Bond, 2008*]. However, this has not been confirmed through subsequent studies and spatio-temporal bivalve extinctions may equally be a function of redox conditions. Despite aragonite undersaturation having been endorsed as the cause of infaunal bivalve disappearance, multiple studies find little correlation between shell

Chapter 2: The end-Triassic mass extinction event

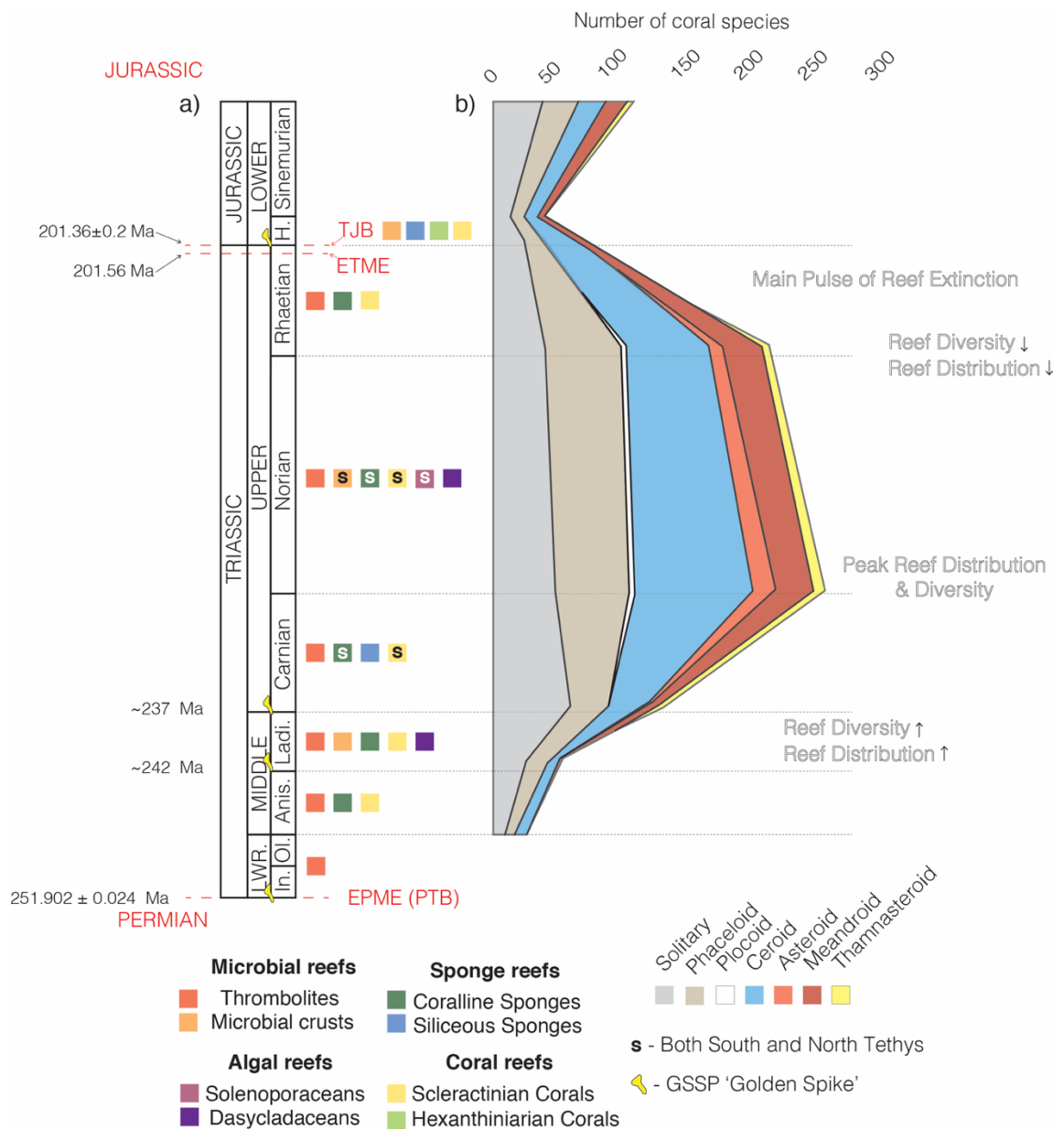
mineralogy and bivalve extinction rate [Kiessling *et al.*, 2007; Mander & Twitchett, 2008; Ros *et al.*, 2011; Hautmann, 2012]. It is therefore interpreted that benthic anoxia may have resulted in the localised absence of infaunal bivalve species [Mander & Twitchett, 2008]. However, the role of marine redox change as a driver of Late Triassic marine extinctions remains vaguely understood, and a more detailed understanding of spatio-temporal redox change from Late Triassic basins is essential to better understanding the controls on latest Triassic bivalve extinctions.

2.3.5.5 The collapse of Late Triassic reef environments: Much like other significant mass extinction events throughout geological history, the ETME was defined by the disappearance of reef building metazoans followed by a resurgence in microbial activity [Flügel, 1975; Jadoul & Galli, 2008; Baresel *et al.*, 2017; Zhang *et al.*, 2015; Lee & Riding 2018]. This event is termed the “Triassic–Jurassic reef gap” or “reef crisis” and is believed to be closely related to the ‘Triassic–Jurassic biocalcification crisis’ by some authors (*Fig. 8- Scleractina & Sphinctozoa*) [Flügel, 2002; Flügel & Kiessling, 2002; Črne *et al.*, 2011; McRoberts *et al.*, 2012].

Reefal biodiversity changes during the Late Triassic- Triassic reef environments underwent a drastic, 61% reduction in reef diversity between the Rhaetian and the Hettangian [Flügel & Kiessling, 2002]. The ETME is one of eight, first-order reef crises and one of two, alongside the EPME, which observed a decline in reefal carbonate production of almost 100% (>99.99%) [Flügel & Kiessling, 2002]. Despite Triassic reefs not being as widely distributed as those during other extinction events, the ETME eliminated the global reef component of marine ecosystems and is therefore interpreted as the most significant reef crisis across the entirety of the Phanerozoic (*Fig. 8*) [Flügel & Kiessling, 2002; McGhee *et al.*, 2004; Muscente *et al.*, 2018]. The ETME saw a 99%

Quantifying marine redox across the Triassic–Jurassic mass extinction

reduction in global reef volume (highest in Phanerozoic) and an 84% reduction in global reef numbers (2nd highest in Phanerozoic) [Flügel & Kiessling, 2002]. Triassic corals disappeared almost entirely at the TJB (Figs. 8 & 10) and reef environments did not recover for at least another 2 Ma with strong evidence of coral retrograde evolution (proteromorphosis) in the interim period, alongside the dominance of siliceous sponge communities [Kiessling *et al.*, 2007; Lucas & Tanner, 2008; Ritterbush *et al.*, 2015; Gretz *et al.*, 2015]. However, despite the large reduction in coral species during the ETME, the proportion of corals forming reef environments remained relatively consistent (Fig. 11).



Chapter 2: The end-Triassic mass extinction event

Figure 10 (above):- The evolution of late Triassic reefal composition and architecture. a) Triassic reef composition from the Tethys Ocean. Data from Bernecker, (2005). b) Global Triassic coral abundance and architecture. Data from Hodges & Stanley, (2015). Time bins from Hodges & Stanley, (2015) and the ICS International Chronostratigraphic Chart 2020. GSSP positions and dates from ICS Int. Chron. Ch. '20. Date of Triassic–Jurassic Mass extinction from Blackburn et al., (2013). Norian Panthalassic reefs exhibit similar composition based on Martindale et al., 2012. Early Hettangian reef composition based on Jadoul & Galli (2008), Kiessling et al., (2009), Ritterbush et al., (2015) and Gretz et al., (2015).

Unlike Late Triassic ammonoid and bivalve extinctions, which largely occurred during the Norian to Rhaetian, Late Triassic reef extinctions largely took place throughout the Rhaetian until the early Hettangian (*Fig. 10*) [Shepherd, 2013]. Therefore, as identified by Flügel & Kiessling, (2002), 'reef ecosystems are not necessarily the first ecosystems affected by crises'.

Spatial shifts in reef distribution during the Late Triassic- The ETME was associated with the northward shift of reef sites, and the absence of reef ecosystems from equatorial regions (*Figs. 10 & 11*) [Flügel & Kiessling, 2002; Hodges & Stanley, 2015]. Rhaetian reefs range latitudinally from 31°N to 31°S, whereas the reduced numbers of Hettangian reefs are restricted to higher latitudes (34°N to 41°N) [Flügel & Kiessling, 2002; Leinfedler et al., 2002]. On the other hand, Late Triassic reefs did not exhibit any change in longitudinal distribution [Flügel & Kiessling, 2002]. Latitudinal constriction of reef ecosystems in the absence of longitudinal restriction is also observed during the Cambrian Series 2- Miaolingian mass extinction event (~520 Ma), where marine redox change is interpreted to have played a prominent role [Flügel & Kiessling, 2002; Bond & Edgecombe, 2020].

The northward shift of reef environments during the latest Triassic and early Jurassic may also be a function of reefal architecture. Platform-margin reefs preferentially disappeared during the ETME, and such reefs were widespread in the Western and Southern Tethys prior to the TJB (*Fig. 11*) [Flügel & Kiessling, 2002].

Quantifying marine redox across the Triassic–Jurassic mass extinction

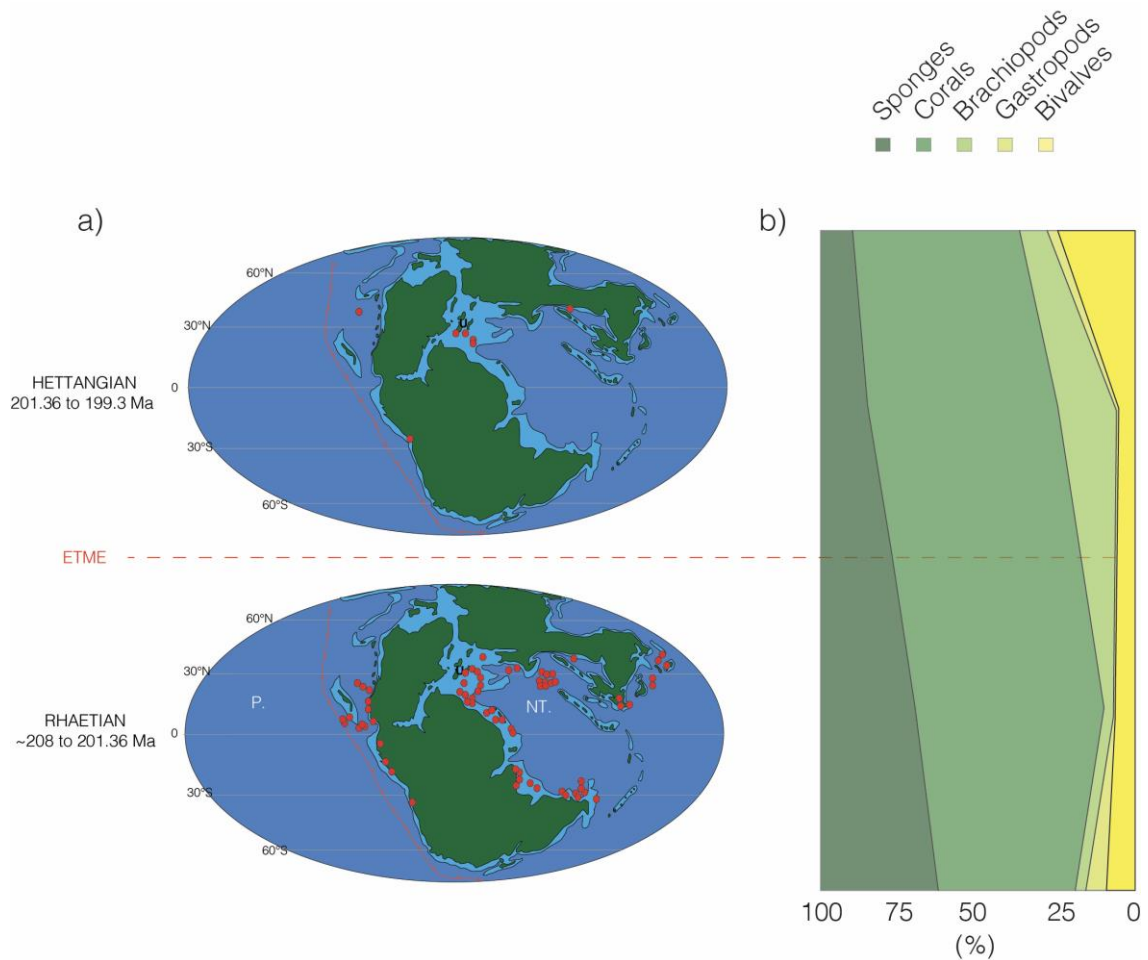


Figure 11:- Palaeogeographic distribution and invertebrate composition of late Rhaetian and early Hettangian reef ecosystems. a) Triassic- Jurassic reef distribution during the Rhaetian and Hettangian. Red dot denotes known location of a Triassic reef. Data from Hodges & Stanley, (2015). b) Invertebrate composition of Rhaetian and Hettangian reef ecosystems. Data from Kiessling et al., (2007). Dates for the Rhaetian and Hettangian ages from ICS International Chronostratigraphic Chart 2019. Late Triassic palaeogeography from Al-Suwaidi et al., (2016) and Korte et al., (2019). P.- Panthalassic Ocean, NT.- Neotethys Ocean.

Interpreted causes of Late Triassic reef extinctions- Clémence et al., 2010 interpret that the absence of calcified reef-building metazoans at the TJB is a function of changes in ocean chemistry as interpreted by Guex et al., (2004), with regards to ammonite development, and Hautmann, (2012), pertaining to changes in bivalve skeletal physiology (*Fig. 8*). This may be a function of increased siliciclastic input to the oceans as a result of enhanced weathering [*Hornung et al., 2007*]; Marine transgression and subsequent changes in marine

Chapter 2: The end-Triassic mass extinction event

oxygenation [Hallam & Goodfellow, 1990]; Ocean acidification and a subsequent increase in carbonate dissolution [Kiessling & Simpson, 2011; Kiessling & Danelian, 2011; Črne et al., 2011; Greene et al., 2012; Hodges & Stanley, 2015].

Yet, despite ocean acidification (OA) being strongly associated with the decline in reef building metazoans by multiple studies, there are several examples of reef collapse in the absence of OA [Kiessling & Simpson, 2011; Kiessling & Danelian, 2011; Črne et al., 2011; Green et al., 2012; Hautmann, 2012; Hodges & Stanley, 2015].

Therefore, as stated by Kiessling et al., (2000), the parameters governing reefal carbonate precipitation are very complex and sometimes difficult to predict. Late Triassic reefal collapse in the absence of OA may suggest multiple controls for extinction. These may include climate change and reduced salinity as suggested by McRoberts et al., (2012). But, more importantly, changing marine redox may have also played a very significant role in Late Triassic reef disappearances, as has been suggested for earlier extinctions [Bond & Edgecombe, 2020].

2.3.5.6 Other extinctions of Late Triassic marine organisms: As well as the major extinctions of ammonites, bivalves and reefal organisms, the ETME experienced the near disappearance of conodonts and the minor extinction of other marine organisms. A selection of these organisms will be discussed in the remainder of this section.

Conodonts- Conodonts went all but extinct at the ETME following a gradual decline in diversity throughout the Triassic Period [Hallam, 2002]. Four conodont families have been noted by Hallam, (2002) during the Early Triassic, reducing to two families during the Middle Triassic and just one family (Gondolellidae) during the Late Triassic. Figures from Mostler et al. (1978) from the Triassic of Austria also suggest a gradual decline in conodont diversity with no fewer than 10 genera within the early Kössen Formation, 5

Quantifying marine redox across the Triassic–Jurassic mass extinction

genera up to the marshi zone and just one genus (*Misikella*) surviving until the uppermost Triassic.

The single largest extinction of Triassic conodonts may have occurred during the Carnian, at the Julian–Tuvanian boundary, where the near complete disappearance of platform conodonts has been recorded [Kozur & Mock, 1991; Rigo et al., 2020]. Tanner et al., (2004) instead suggest maximum conodont extinction during the latest Norian based on higher extinction rates. More recent research advocates four main extinctions of conodonts throughout the Late Triassic [Rigo et al., 2018]. These include a weak extinction during the early Julian, a more significant extinction at the Julian–Tuvanian boundary, a faunal turnover at the Carnian–Norian boundary, and a fourth extinction at the Norian–Rhaetian boundary pronounced by a shift to simple cavitated species [Rigo et al., 2018, 2020]. Meanwhile, the final disappearance of conodonts has been correlated with the second pulse of extrusive CAMP volcanism by Deenen et al., (2010), and to the latest Triassic by Wignall & Atkinson (2020) during the second phase of a two-part Rhaetian extinction crisis.

Despite conodonts having been referred to as one of the most significant fauna to have undergone complete extinction at the ETME, Lucas & Tanner (2008) believe this to be misleading, and instead quote high rates of extinction and low rates of origination to be the cause of Late Triassic conodont disappearances [see data from Clark, 1980, 1981, 1983; Sweet, 1988; Kozur & Mock, 1991; Aldridge & Smith, 1993; De Renzi et al., 1996].

Accentuated extinctions of conodonts during the Late Triassic may have also be the result of sampling biases. Studies by Clark (1980, 1981) recorded the latest conodonts from the Norian, with later work by Orchard (1991) recording a single species from the Rhaetian of Canada (*Misikella posthernsteini*). At least thirteen more Rhaetian species have since been

Chapter 2: The end-Triassic mass extinction event

discovered including *Misikella ultima*, *M. buseri*, *M. kolarae* and *Neohindeodella detrei* [Kozur & Mock, 1991; Kolar-Jurkovšek, 2011; Karádi *et al.*, 2020].

N. detrei has subsequently been recorded from the Hettangian of Hungary which would extend the stratigraphic occurrence of conodonts through both the ETME and TJB and place their final extinction during the earliest Jurassic [Palfy *et al.*, 2007]. This may suggest that Late Triassic conodont extinctions were not as significant as previously thought, as alluded to by Hallam, (2002) and Lucas & Tanner (2008). Conversely, the final extinction of conodonts was globally asynchronous [Du *et al.*, 2020]. Whilst conodonts from Hungarian (Csővár) and Japanese sections (Katsuyama; Kurusu) survived into the Hettangian, conodonts from English (St. Audrie's Bay), Canadian (Kennecott Point) and Austrian sections (Kuhjoch) underwent extinction during an interval of Late Triassic carbon isotope perturbation termed the initial carbon isotope excursion (CIE), and conodonts from American (New York Canyon) and Italian sections (Lombardy; Muzzerone) underwent extinction below the initial CIE [Du *et al.*, 2020].

Summary- The gradual decline in conodont diversity throughout the Triassic Period will have resulted in low standing diversity which alongside low origination will have resulted in the inevitable disappearance of conodonts from marine environments. Despite low origination having been interpreted as the driving force behind the ETME by a select few studies [Hallam, 2002; Bambach *et al.*, 2004], conodonts provide the only proof of this so far, and notably from a class of organisms which had already been declining in diversity for millions of years. The phosphatic composition of conodont elements would suggest that acidification and carbonate undersaturation was not a significant factor in conodont extinction. This may suggest that other ecological changes were responsible (e. g. marine redox).

Quantifying marine redox across the Triassic–Jurassic mass extinction

Radiolarians- Radiolarians are considered by some authors as optimal for defining the TJB on the account their partial extinction during the latest Rhaetian [*Carter 1994; Ward et al 2001; Longridge et al., 2007b*]. However, other studies argue that the disappearance of radiolarians is nothing more than a local event [*Tanner et al. 2004; Hautmann, 2012*]. Kidder and Erwin (2001) found no evidence for a radiolarian extinction from variable bedded cherts, and Guex et al. (2002) associate the ‘extinction’ of radiolarians from the Queen Charlotte Islands with a stratigraphic gap. Furthermore, Hart and Williams (1993) argue that radiolarians show no decline across the TJB at the family level, and Kiessling and Danelian (2011) report that there is no evidence for a radiolarian mass extinction but rather a greater background extinction during the Triassic than the Jurassic. Meanwhile, Hautmann et al., (2008a) determine there to be no evidence of a radiolarian extinction through data from Sepkoski.

Other authors argue in favour of a radiolarian extinction at the TJB, however interpret that the extinction was gradual [*Hori, 1992*]. This includes research by Vishnevskaya (1997) who report the survival of 40% of Rhaetian radiolarian genera through to the Hettangian. This gradual extinction of Rhaetian radiolarians is still local in nature and has not been correlated globally. Although, it is possible that the correlation of Late Triassic radiolarian extinctions is complicated by Tethyan and North American sections differing markedly at the species level [*Blome, 1986*].

Conversely, there are an increasing number of studies that argue for a significant extinction of radiolarians during the Late Triassic [*Hori, 1992; Carter, 1994; Tekin 1999; Carter & Hori, 2005; Longridge et al., 2007b; Carter, 2007; O’Dogherty et al., 2010; Kocsis et al., 2014; Onoue et al., 2016; Wignall & Atkinson 2020*]. Tipper et al. (1994) report a diverse, evolved radiolarian assemblage from the Rhaetian of British Columbia overlain by a low

Chapter 2: The end-Triassic mass extinction event

diversity, primitive Hettangian assemblage consisting of just a few genera. The extinction of 45 radiolarian species is observed within the top 1.5m of the *Globolaxtorum tozeri* Zone (uppermost Rhaetian) from Kunga Island, with 5 families, 25 genera and most species of the *G. tozeri* Zone disappearing within just a few meters [Carter, 1994]. A similar study by Longridge et al., (2007b) from the same site reports the disappearance of 9 families, 27 genera and nearly all Rhaetian species over <1m. Although, as noted by Guex et al. (2002), this locality may exhibit a sedimentary hiatus. In spite of the proposed hiatus by Guex et al. (2002), comparable patterns have also been observed in the western Pacific [Hori, 1992] and the Tethys [Tekin, 1999]. Carter and Hori (2005) report the disappearance of 20 genera and 130 species across the TJB from Japan and a low diversity overlying Hettangian assemblage. Also, a global database summarised by Carter (2007) has correlated the disappearance of key radiolarian taxa from the late Triassic of British Columbia to sites in Mexico, the Philippines, China, Tibet, Russia, Italy, Turkey, and Hungary. It is for this reason that Carter (2007) argues for a major radiolarian turnover at the TJB.

Despite the reported absence of a radiolarian extinction based on Sepkoski's data by Hautmann et al. (2008a), a subsequent study by Kocsis et al. (2014) found a peak in extinction at the end-Rhaetian using a sample-standardised approach. Recent research from several late Triassic sites reports the disappearance of radiolarians as part of a two-phase extinction [Hori et al., 2007; Wignall & Atkinson, 2020]. This includes a major extinction of 20 radiolarian genera and 70 species at the top of the *G. tozeri* Zone (Haidi, Gwaii, British Columbia), followed by a minor radiolarian extinction during the latest Triassic [Wignall & Atkinson, 2020]. A two pulsed extinction of radiolarians was also reported by Onoue et al., (2016) with one pulse during the end-Rhaetian and another during the late-middle Norian, coincident with the Manicougan impact (*Fig. 12*). Substantial within-

Quantifying marine redox across the Triassic–Jurassic mass extinction

Rhaetian radiolarian extinctions are also evident based on data from Onoue et al. (2016) with more than 50% of radiolarian species present at the top of the *Proparvicingula moniliformis* Zone disappearing before the overlying *G. tozeri* Zone [Rigo et al., 2020]. However, data from Onoue et al., (2012) do not suggest a rapid extinction but rather a gradual, stepwise decline in diversity. Longridge et al., (2007b) similarly suggest that the extinction was not instantaneous due to the temporary persistence of some Rhaetian forms. Also, the abundance of opportunist taxa e.g., *Archaeocenosphaera laseekensis* suggests that any decline in marine productivity was short-lived [Longridge et al., 2007b]. Lucas and Tanner (2008) therefore evaluate the data from Longridge et al., (2007b), alongside other studies, to infer that radiolarians suffered a stepwise global turnover alongside a short-term reduction in marine productivity.

Alongside their global, multi-stage extinction, radiolarians also saw a shift to more simplified forms. This is similar to previous taxa discussed within this thesis (e.g., atavistic Ammonites, proteromorphosis within corals and cavitated conodonts) [Guex et al., 2004; Gretz et al., 2015; Rigo et al., 2020]. Radiolarians lost their architecturally complex forms e.g., spumellarians, nassellarians and enactiniids [Lucas & Tanner, 2008] as well as experiencing retrogradation of spine geometry across the TJB [Guex, 2016]. The twisted spines of radiolarian genera, e.g., *Tipperella* and *Bertaccium*, became simplified and straightened through the TJB [Guex, 2016].

Radiolarians exhibit a skeleton of amorphous silica and therefore, much like conodonts, carbonate undersaturation would not have been a determining factor in radiolarian extinctions. This once again suggests that other ecological changes may have played a role in radiolarian extinctions (e. g. marine redox).

Chapter 2: The end-Triassic mass extinction event

Brachiopods- Similar to radiolarians, brachiopods have been reported as exhibiting local disappearances with little evidence of a global brachiopod extinction across the TJB [Lucas & Tanner, 2008]. Major changes to brachiopod communities have been recorded by Tomasovych and Siblik (2007) from the Northern Calcareous Alps. However, no other local brachiopod disappearances were noted by Wignall & Atkinson (2020) from a range of Late Triassic sites. Furthermore, Lucas and Tanner (2008) propose that the localised extinction of brachiopod species recorded by Tomasovych and Siblik (2007) could be due to major palaeoecological changes in the Northern Calcareous Alps during the latest Triassic.

In spite of the apparent absence of widespread brachiopod extinctions reported by Wignall & Atkinson (2020), several other studies have recorded significant brachiopod disappearances across the TJB. Pearson (1977) note the disappearance of 8 out of 13 brachiopod genera through the TJB based on a European brachiopod compilation, whilst Benton (1993b) reports the disappearance of 5 brachiopod families out of 19 by the end-Rhaetian, all of which belonged to Order Spiriferida. A global compilation by Harper et al. (1993) records the disappearance of 17 families through a stepwise extinction. Meanwhile, compilation data from Hautmann et al., (2008a) records a 69% extinction of all brachiopod genera, and data from the Palaeobiology Database (PBDB) summarised by Kiessling et al., (2007) records a 55% per genus extinction rate.

Hautmann et al., (2008a) and Hautmann, (2012) also report a 71.4% (40/56) extinction of calcitic brachiopod species compared to a 0% (0/2) extinction amongst organophosphatic species. Hautmann (2012) subsequently interpret that shell mineralogy was a controlling factor in brachiopod extinctions, as has also been interpreted for bivalves. Unlike bivalves however, for which shell mineralogy seems questionable as a driving factor of extinction

Quantifying marine redox across the Triassic–Jurassic mass extinction

selectivity, brachiopod shell growth is less buffered by physiological mechanisms [Hautmann *et al.*, 2008a]. Although, Kiessling *et al.*, (2007) report higher rates of extinction in the more mineralogically stable low-Mg calcite brachiopods suggesting that brachiopod extinctions were not a function of shell mineralogy.

Similar to ammonites, brachiopods also experienced the disappearance of larger species during Late Triassic extinctions [Hallam, 2002]. Meanwhile, fixosessile suspension feeders, like brachiopods, were broadly affected by Late Triassic ecological changes [Dunhill *et al.*, 2018]. This resulted in a bottle neck of surficial, non-motile, attached, suspension feeders through the TJB and a reduction in generic richness of ~60% (220 to ~135) [Dunhill *et al.*, 2018]. What the driving factors were behind both this reduction and brachiopod extinctions remains uncertain, however much like other contemporaneous extinctions it may be partly the result of marine redox changes which remain poorly understood.

Dinoflagellates, Calcareous nannoplankton & Foraminiferans- As well as diversity depletions amongst radiolarians across the TJB, minor extinctions are also observed amongst phytoplankton (dinoflagellates, calcareous nannoplankton) and other zooplankton (foraminiferans),

Dinoflagellate extinctions are poorly understood from the latest Triassic on account of dinoflagellate diversity only being known from benthic resting cysts. In spite of this, 6 out of a recorded 8 dinoflagellate taxa disappear at the TJB [Riding *in* Hallam, 1995], and just 2 unequivocal cyst producing dinoflagellates were recorded from the basal Jurassic of St. Audrie's Bay by van de Schootbrugge *et al.*, (2007).

Calcareous nannoplankton were more severely affected, undergoing large disappearances during the latest Triassic [Lucas & Tanner, 2008]. This is particularly prominent within the

Chapter 2: The end-Triassic mass extinction event

Italcementi Quarry, Lombardian Alps, Italy where 5 out of 6 taxa of calcareous nannofossils disappear at the base of the Malanotte Formation [Bottini *et al.*, 2016; Wignall & Atkinson, 2020]. A 46% disappearance of calcareous algae (dasycladaleans) has also been reported from this locality [Barattolo & Romano, 2005]. Also, just one taxon of Late Triassic calcareous nannoplankton was recorded from the Early Jurassic of SW England by van de Schootbrugge *et al.*, (2007). As well as a decrease in diversity, latest Rhaetian nannoplankton taxa have been reported to decrease in size within the lower Lias e.g. *Schizosphaerella punctulata* [Wignall & Bond, 2008], and van de Schootbrugge *et al.*, (2007) report malformation of calcareous nannoplankton from St. Audrie's Bay. The reduction in the diversity, shape, and size of calcareous nannoplankton during the latest Triassic has been attributed to the 'biocalcification crisis' by Hautmann (2004) and van de Schootbrugge *et al.*, (2007). The reduction in diversity of calcareous nannoplankton has also been strongly correlated with blooms of organic walled disaster taxa in the form of prasinophytes and acritarchs [van de Schootbrugge *et al.*, 2007; Bonis *et al.*, 2009; Bonis *et al.*, 2010; Lindström *et al.*, 2012; Richoz *et al.*, 2012; van de Schootbrugge *et al.*, 2013; Ibarra *et al.*, 2016]. However, the organic composition of these plankton does not necessarily support carbonate undersaturation, as multiple studies interpret these blooms as being the result of marine de-oxygenation [Bonis *et al.*, 2010; Richoz *et al.*, 2012; Kasprak *et al.*, 2015].

Foraminiferans underwent minor extinctions during the latest Triassic, however their extinction was so insignificant that some studies believe there to be no evidence of an extinction at all [Tanner *et al.*, 2004]. Just 3 out of 17 families became extinct based on Hart & Williams (1993) (17%), and 3 out of 38 families underwent extinction based on Benton (1993b) (~8%). Meanwhile El Shaarawy (1981) and Loeblich and Tappan (1988) report extinction rates of 21% and 35% respectively. Clemence *et al.*, (2010) report a

Quantifying marine redox across the Triassic–Jurassic mass extinction

decrease in the diversity of calcareous taxa and the increased diversity of agglutinated taxa. Hautmann, (2012) similarly report higher extinction rates amongst aragonitic (66.7%) and high-Mg calcite (53.8%) taxa, with low extinction rates amongst agglutinated (15.4%) and proteinaceous forms (0%). This could possibly indicate the variable response of different foraminiferan taxa to carbonate undersaturation. However, there remains little definitive evidence of carbonate undersaturation from other organisms.

2.3.5.7 Section summary: The ETME witnessed the disappearance of numerous marine organisms at multiple trophic levels (*Fig. 12*). The Carnian saw multiple extinctions of an already depleted Conodonta, the Norian was marked by diversity depletions amongst radiolarians followed by major extinctions amongst ammonites, and the Rhaetian was defined by the widespread extinctions of corals, bivalves, and brachiopods as well as the turnover or final extinction of radiolarians, dinoflagellates, calcareous nannoplankton, conodonts, foraminiferans and ammonites near the Rhaetian-Hettangian boundary (*Fig. 12*). The late-stage turnover of ammonites defines the basal Hettangian, and the ETME, at the GSSP. Of the organisms which managed to survive the Late Triassic environmental changes, many were marred by simplified morphologies, malformation and/or size reduction. Multiple studies attribute these maladies to chemical oceanic changes including ocean acidification. However, despite extinction selectivity also indicating chemical changes within the oceans, the exact nature of chemical changes at the TJB are still difficult to interpret based on this information alone. Therefore, the next section further discusses the potential causes of the ETME through addition lines of evidence.

Chapter 2: The end-Triassic mass extinction event

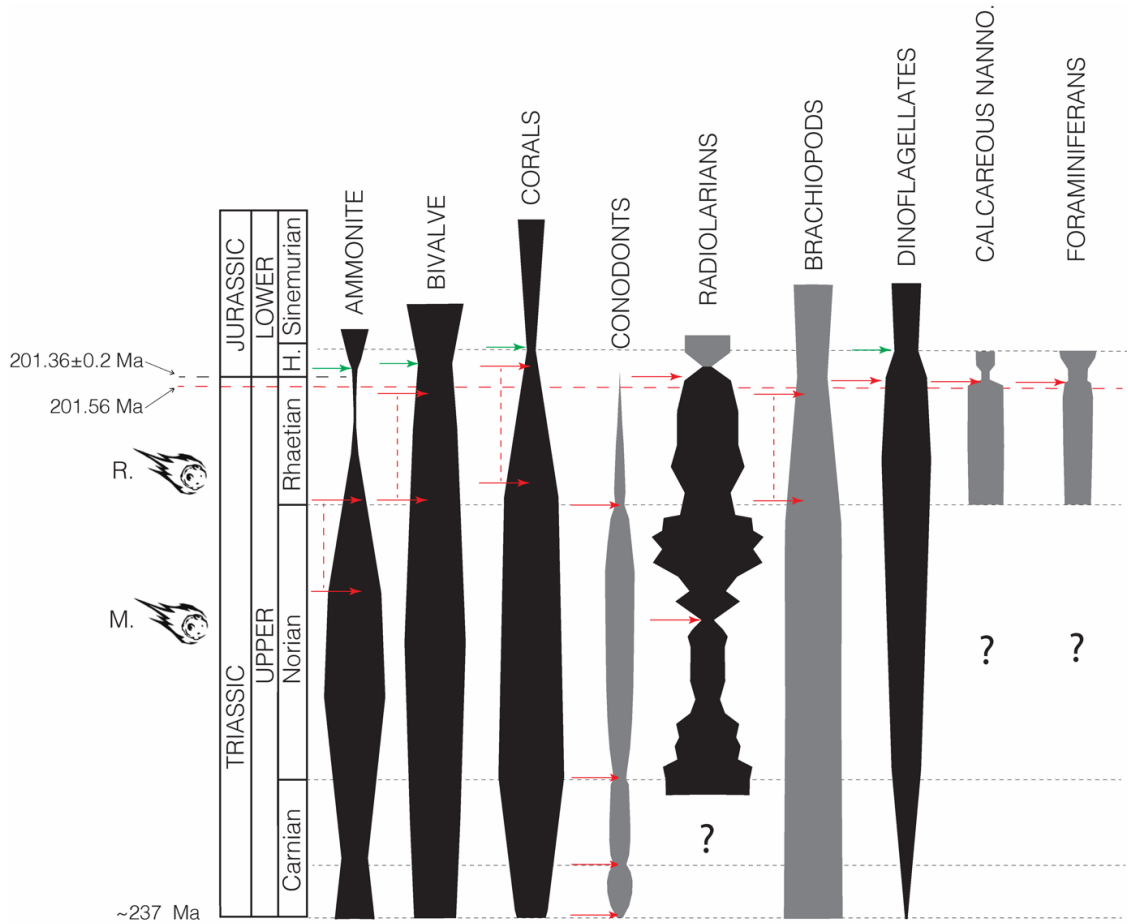


Figure 12:- Overview of diversity patterns, losses, and recovery during the ETME based on the organism extinctions discussed within this subchapter (2.3). Black fill based on numerical data, grey fill based on qualitative and/or empirical data. Red arrows mark periods of maximum extinction for each organism; single arrows denote relatively short-lived extinctions, red arrows with range bars mark prolonged periods of extinction. Green arrows denote initiation of recovery for selected organisms. Recovery horizons have only been marked here where numerical data is available. Ammonite data from Whiteside & Ward (2011), bivalve data from Ros et al., (2011), coral data from Hodges & Stanley, (2015), conodont diversity based on Lucas & Tanner, (2008); Rigo et al., (2018, 2020); Du et al., (2020), radiolarian data from Onoue et al., (2016), brachiopod diversity based on Kiessling et al., (2007); Dunhill et al., (2018), dinoflagellate data from Wiggan et al., (2017), calcareous nannoplankton diversity based on Bottini et al., (2016); van de Schootbrugge et al., (2007), foraminiferan diversity based on Tanner et al., (2004.) H.- Hettangian, NANNO.- nannoplankton, ?- diversity trend unknown. Time bins from Hodges & Stanley, (2015) and the ICS International Chronostratigraphic Chart 2020. GSSP positions and dates from ICS Int. Chron. Ch. '20. Date of Triassic- Jurassic Mass extinction from Blackburn et al., (2013). Short, dashed lines mark stage and substage boundaries, wider dashed line (black) marks T/J boundary, wider dashed line (red) marks ETME. R.- Rochechouart, M- Manicougan (impact events).

2.3.6 Potential causes of the end mass extinction event:

2.3.6.1 Extraterrestrial impact: Early research into possible causes of the ETME drew inspiration from Alvarez et al., (1980) and interpreted that much like the ECME, the ETME may have been triggered by a bolide/ meteorite impact [Olsen et al., 1987, 1990, 2002] (Fig. 12). Alvarez et al., (1980) identified the presence of elevated iridium concentrations from the Cretaceous–Palaeogene (K-Pg) boundary at Gubbio (Italy) and Stevns Klint (Denmark) reaching concentrations of up to 160x background levels (3ng/g) [Korte et al., 2019]. Iridium is known to be rare within the Earth’s crust (0.1ng/g) yet enriched within certain meteorites ($>1\mu\text{g/g}$) and Alvarez et al., (1980) therefore interpreted the increased concentrations of iridium at the ECME to be the result of a meteorite impact [Korte et al., 2019].

Iridium at the TJB: Elevated concentrations of iridium have been identified by numerous studies at the TJB from Kendelbach (Austria), St. Audries Bay (United Kingdom), the Jacksonwald Syncline (Newark Basin) and the Fundy Basin (Canada), [Orth, 1989; McLaren & Goodfellow, 1990; Olsen et al., 2002; Tanner & Kyte 2005]. Olsen et al., (2002) recorded iridium concentrations between 0.141 and 0.285 ng/g within a white clay layer from the Jacksonwald Syncline (Newark Basin). However, despite iridium being elevated relative to crustal concentrations the iridium anomaly observed at the TJB is much lower than that observed at the K–Pg boundary [Alvarez et al., 1980; Korte et al., 2019]. Even the slightly greater iridium concentrations measured by Tanner & Kyte, (2005) from the Fundy Basin (0.31ng/g) are one order of magnitude smaller than those observed at the boundary layer in Gubbio, Italy [Alvarez et al., 1980]. This has led certain studies to interpret increased concentrations of iridium at the TJB to be reflective of mantle volcanism [McCartney et al., 1990; Tanner et al., 2016].

Chapter 2: The end-Triassic mass extinction event

Planar Deformation Features: In addition to ‘modest iridium anomalies’ several other indicators have been reported to suggest an extraterrestrial impact at the TJB. One such proxy includes the reported presence of quartz with planar deformation features from both Kendelbach (Austria) and Calcare a Rhaetavicula (Italy) [Badjukov *et al.*, 1987; Bice *et al.*, 1992]. Planar deformation features, or PDFs, are fabrics which develop at high pressures (10-35 GPa) along specific crystallographic orientations and are attributed to shock (impact induced) metamorphism [Golbrant *et al.*, 1992; Chen *et al.*, 2011]. However, the planar deformed quartz from Kendelbach is not thought to be an impact fabric but rather a metamorphic fabric [Hallam & Wignall, 1997; Mossman *et al.*, 1998; Korte *et al.*, 2019]. Furthermore, Bice *et al.*, (1992) only identified 5–10% of quartz grains exhibiting one or more set of PDFs commonly associated with shock metamorphism. A re-investigation of the Calcare a Rhaetavicula by Fazzuoli & Orti, (2009) concluded that the PDFs described by Bice *et al.*, (1992) did not coincide with the TJB but were Rhaetian in age. However, the study by Fazzuoli & Orti, (2009) did not dismiss the possibility that these features were quartz PDFs. Meanwhile, Tanner *et al.*, (2004) and Hallam & Wignall, (1997) considered that both reports should be disregarded due to the evidence of shocked metamorphism being based solely on outdated petrographic techniques [French, 1998].

More recent studies of Late Triassic strata have similarly recorded quartz exhibiting PDFs, this time from the Bristol area (Wickwar), SW England [Walkden *et al.*, 2002; Kirkham, 2002, 2003]. Unlike the 5–10% of quartz grains with PDFs identified by Bice *et al.*, (1992), the same value from Bristol has been recorded as 50% [Walkden *et al.*, 2002]. Also, quartz PDFs have been found alongside glauconitic spherules closely allied to impact mechanisms through both their morphology (dumbbells, droplets, spheres, and shards) and mineralogy [Walkden *et al.*, 2002; Kirkham *et al.*, 2003]. It is therefore highly likely that these deposits were in part formed through an extraterrestrial impact [Glass *et al.*, 2003].

Quantifying marine redox across the Triassic–Jurassic mass extinction

However, no geochemistry has been undertaken to confirm an iridium anomaly, the ejecta layer exhibits evidence of turbulent reworking, and an Ar-Ar date from a coeval K-feldspar grain provides an age of 214 ± 2.5 Ma [Walkden *et al.*, 2002; Glass *et al.*, 2003]. These impact fabrics may therefore be affiliated with an older meteorite collision (e.g., Manicougan, Canada; Walkden *et al.*, 2002; *Fig. 12*).

Upper Triassic Seismites: Another line of evidence interpreted to indicate an extraterrestrial impact near the TJB is the presence of Upper Triassic seismites. Seismites and evidence of soft sediment deformation have been identified by Simms, (2003, 2007) within Upper Triassic strata of the Larne Basin (N. Ireland), Lavernock (S. Wales) and Manor Farm Quarry (SW England). Simms, (2003) interprets the wide distribution of the seismite deposits ($>250,000 \text{ km}^2$) as being too great for known terrestrial mechanisms and therefore believes the deposits to have been generated by a bolide impact. However, Simms, (2007) suggests that these sedimentary deposits may equally have been generated by several earthquakes or high magnitude seismic events. Subsequent studies, some of which identify seismite beds from Denmark, Sweden and Luxembourg, further support Simms, (2007) and interpret that seismites were generated by volcanically induced seismicity [Wignall & Bond, 2008; Lindström *et al.*, 2015; Lindström *et al.*, 2020; Laborde-Casadaban *et al.*, 2021]. This is partially based on the undisturbed sediment packages separating individual seismite deposits [Lindstrom *et al.*, 2015].

Research by Schmieder *et al.*, (2010) dated the 20 km diameter, Rochechouart impact structure (NW Massif Central, France) to between the Late Triassic and Early Jurassic ($^{40}\text{Ar}/^{39}\text{Ar}$ 201 ± 2 Ma) and corroborated Simms (2003) in that the Upper Triassic seismite deposits may be impact induced. Conversely, recalculation of Schmieder *et al.* (2010)'s data using a new decay constant resolves an age of 203 ± 2 Ma [Renne *et al.*, 2011; Cohen *et*

Chapter 2: The end-Triassic mass extinction event

al., 2017], whilst more recent research by Cohen et al., (2017) dates the impact structure to $206.92 \pm 0.2 \text{ Ma}$ ($^{40}\text{Ar}/^{39}\text{Ar}$) (Fig. 12).

The Absence of a Suitable Impact Structure: Regardless of whether the Rochechouart impact structure correlates with the Rhaetian seismite deposits, the Rochechouart crater (20km) is dwarfed by the Chixulub impact crater (200km) associated with the ECME [Alvarez et al., 1980; Hildebrand et al., 1991; Urrutia-Fucugauchi et al., 2011]. This raises important questions regarding whether larger meteorite impacts, than that which formed the Rochechouart crater, may have occurred during the Late Triassic which could have contributed towards significant marine extinctions.

Early work by Olsen et al., (1987) favoured the Manicougan impact structure (Quebec, Canada) as being a potential candidate. Ejecta layers associated with the Manicougan impact have been discovered from both Japan (Onoue et al., 2012) and SW England (Walkden et al., 2002). Studies of the Japanese ejecta layer by Sato et al., (2013) have also yielded a negative $^{188}\text{Os}/^{187}\text{Os}$ anomaly which has been interpreted to represent an extraterrestrial Os source. However, Hodych & Dunning, (1992) dated the Manicougan crater to $214 \pm 1 \text{ Ma}$ (U/Pb) and therefore refuted the possibility that the Manicougan impact contributed towards the ETME. More recent work dates the Manicougan crater to 215.5 Ma, however this also fails to coincide with a major pulse of the ETME [Ramezani et al., 2005]. The Manicougan impact has been closely associated with a local pulse of radiolarian extinction from Japan [Onoue et al., 2016] (Fig. 12). However, no widespread extinction(s) or shifts in diversity have been correlated with either the Rochechouart or Manicougan impact structures (Fig. 12). The insignificance role of extraterrestrial impacts in the ETME may also be interpreted from the relatively low crater formation rate during this time [Rampino & Caldera, 2017].

Quantifying marine redox across the Triassic–Jurassic mass extinction

Summary- Despite the low concentrations of iridium and seismites which may be volcanically induced, there are multiple lines of evidence (PDFs, ejecta layer, unradiogenic osmium, manicougan impact structure) to suggest extraterrestrial impacts during the Middle–Late Triassic (215.5Ma). Conversely, marine diversity changes as a result of these extraterrestrial impacts appear to have been minimal (*Fig. 12*). However, several lines of evidence initially interpreted as indicators of extraterrestrial impact have subsequently been argued to indicate sustained volcanism [*Simms, 2007; Tanner et al., 2016*]. The presence of ‘modest’ iridium anomalies, seismically induced sedimentary deposits, and late Rhaetian clay spherules (not discussed here) are all argued to have been generated through provincial volcanism in the form of the Central Atlantic Magmatic Province [*Simms, 2007; Zajzon et al., 2012; Tanner et al., 2016*].

2.3.6.2 Central Atlantic Magmatic Province (CAMP): The Central Atlantic Magmatic Province, herein referred to as CAMP, was a Large Igneous Province (LIP) which marked the break-up of the supercontinent of Pangaea during the Late Triassic (Rhaetian) [*Marzoli et al., 1999; Percival et al., 2017; Korte et al., 2019*]. The presence of a large igneous province (CAMP) which initiated during the Late Triassic, and persisted through to the Jurassic, is strongly supported as a fundamental driving mechanism of the ETME by multiple studies [*Hesselbo et al., 2002; Marzoli et al., 2004; Whiteside et al., 2007; Schoene et al., 2010; Cirilli et al., 2009; Deenen et al., 2010; Blackburn et al., 2013; Davies et al., 2017*].

The Late Triassic initiation of CAMP volcanism, and therefore the close association between LIP volcanic activity and the ETME, is partially supported through Upper Triassic CAMP deposits (*Fig. 13*). CAMP volcanic deposits in the form of extrusive tholeiitic (Mid Ocean Ridge) basalts have been recorded from Africa (Morocco), North America (Newark

Chapter 2: The end-Triassic mass extinction event

Basin; Hartford Basin; Deerfield Basin; Fundy Basin), South America (Brazil) and southwest Europe (Spain) (Fig. 13) [Marzoli et al., 1999; McHone, 2003; Marzoli et al., 2004; Whiteside et al., 2007; Whiteside et al., 2010; Merle et al., 2014]. CAMP deposits have been correlated through U-Pb dating, $^{40}\text{Ar}/^{39}\text{Ar}$ dating and biostratigraphy to both the Upper Triassic and the ETME [Marzoli et al., 2004; Whiteside et al., 2007; Cirilli et al., 2009; Jourdan et al., 2009; Schoene et al., 2010; Marzoli et al., 2011; Blackburn et al., 2013; Panfili et al., 2019]. Upper Triassic ash beds (201.3-201.5 Ma U/Pb), which correlate with early CAMP activity and the ETME, have also been recorded from both South and North America (Peru & Nevada) [Lindstrom et al., 2017].

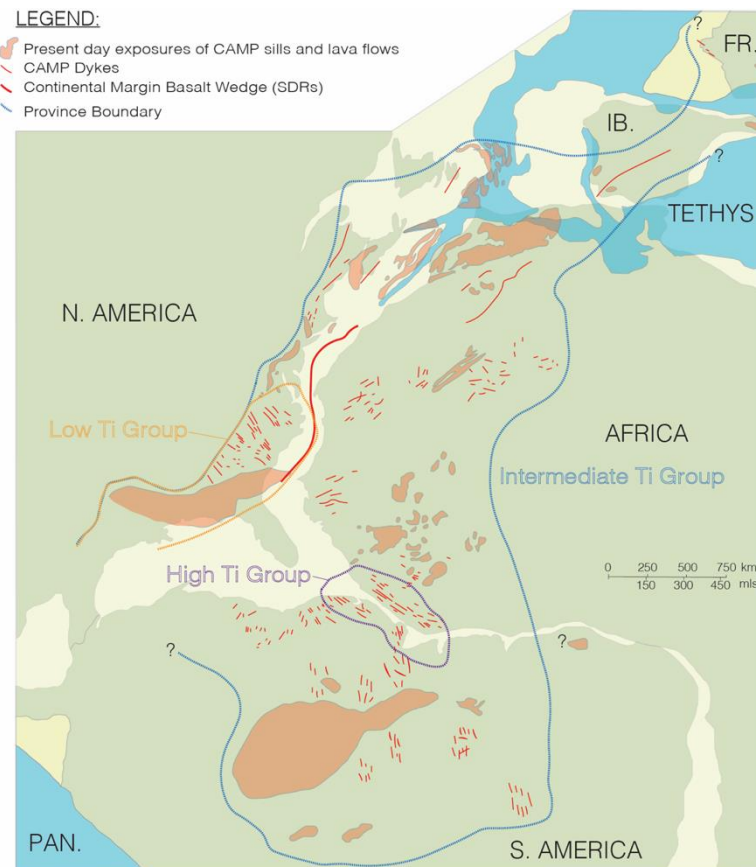


Figure 13:- Past and present extent of CAMP as represented through extrusive and intrusive volcanic deposits. Figure amended from Whiteside et al., (2007) and McHone, (2003). FR.- France, IB.- Iberia., PAN.- Panthalassic Ocean, TETHYS- Tethys Ocean, ?- uncertainty regarding the extent of province boundary, SDR- Seaward Dipping Reflector, mls- miles. Blue- areas submerged in water, darker green- the outline of existing landmasses, lighter green- interconnecting landmass.

Quantifying marine redox across the Triassic–Jurassic mass extinction

Upper Triassic CAMP initiation is further evidenced through the presence of intrusive volcanic units (dykes and sills) from Africa (Mauritania, Guinea, Morocco), South America (Brazil, Bolivia), southwest Europe (Spain) and North America (Canada) (*Fig. 4*) [*Blackburn et al., 2013; Davies et al., 2017*]. CAMP dykes and sills date the initiation of CAMP activity to 201.6 Ma at the latest (201.612 Ma- Tarabuco sill, Bolivia; 201.635 Ma- Kakoulima intrusion, Guinea) [*Davies et al., 2017*]. The dating of CAMP initiation to 201.6 Ma pre-dates the currently accepted lower boundary of the ETME (201.56- *Blackburn et al., 2013*) and therefore strongly correlates CAMP volcanism as a likely cause of the ETME.

Other proxies which have been used to support the Late Triassic initiation of volcanism include elemental studies, such as mercury (Hg) and osmium (Os). Mercury is a volcanic trace gas with a short residence time (0.5 - 2 years) and has therefore been used in the past to correlate LIPs to mass extinction events [*Percival et al., 2015; Font et al., 2016*].

Increased concentrations of mercury have been recorded in several pulses closely associated with the ETME [*Thibodeau et al., 2016; Percival et al., 2017; Tegner et al., 2020; Kovacs et al., 2020*]. Decreasing values of $^{187}\text{Os}/^{188}\text{Os}$ within Late Triassic seawater have also indicated an increasing supply of unradiogenic osmium throughout the Late Triassic and ETME [*Kuroda et al., 2010*]. Unradiogenic osmium is supplied through mantle upwelling and volcanism and may indicate the emplacement of a LIP (e.g., CAMP) [*Kuroda et al., 2010*]. Elemental proxies therefore strongly support the occurrence of Late Triassic volcanism in the form of a Large Igneous Province (CAMP) when collated with Upper Triassic volcanic units, elevated iridium concentrations and seismite deposits.

The extent and impact of CAMP volcanism: CAMP has been reconstructed as having an aerial extent of anywhere between 2×10^6 and 1×10^7 km² (*Fig. 13*) [*Marzoli et al., 1999*;

Chapter 2: The end-Triassic mass extinction event

McHone, 2003; Marzoli et al., 2004; Nomade et al., 2007; Whiteside et al., 2007; Schoene et al., 2010; Green et al., 2012]. However, precise reconstruction is made difficult due to $<1 \times 10^6 \text{ km}^2$ of CAMP deposits being preserved (*Fig. 13*) [*Marzoli et al., 1999; Nomade et al., 2007*]. The volume of flood basalt erupted from CAMP is estimated as between 2×10^6 and $4 \times 10^6 \text{ km}^3$ erupted over a timescale of 580 kyr to 2 Myr [*Holbrook & Kelemen, 1993; Marzoli et al., 1999; Wignall, 2001; McHone et al., 2003; Marzoli et al., 2004; Nomade et al., 2007; Kent & Olsen, 2008; Cirilli et al., 2009; Schoene et al., 2010; Schaller et al., 2011; Greene et al., 2012; Percival et al., 2017; Davies et al., 2017*]. Total volcanic emissions have been estimated as ranging between 1.11×10^{12} and 5.19×10^{12} metric tonnes [*McHone et al., 2003*], and Beerling and Berner (2002) estimate that as much as 3.3 Eg (3.3×10^{12} metric tonnes) of carbon may have been released as both CO_2 and CH_4 .

The large scale release of isotopically light carbon, such as that exuded by CAMP, is very widely evidenced within the Late Triassic carbon isotope record in the form of multiple $\delta^{13}\text{C}$ negative shifts of up to 8‰ [*Hallam & Goodfellow, 1990; Ward et al., 2001; Pálffy et al., 2001; Hesselbo et al., 2002; Guex et al., 2004; Galli et al. 2005; Pálffy et al., 2007; Korte et al., 2009; Ruhl et al., 2010; Kuroda et al., 2010; Črncić et al., 2011; Lindström et al., 2012; Muttoni et al., 2014; Hönig et al., 2016; Yager et al., 2017; Ge et al., 2018*].

Such large concentrations of isotopically light carbon will have been partially released through thermo-mechanical erosion and partial melt of the lithosphere [*Saunders, 2017*]. However, research has suggested that carbon released from flood basalts alone would be insufficient to cause the negative shifts in $\delta^{13}\text{C}$ observed during the Late Triassic [*Beerling & Berner, 2002; Payne & Kump, 2007*]. It is therefore believed that magma was also injected into carbon rich sediments which will have resulted in magmatic devolatilisation and enhanced carbon output [*Beerling & Berner, 2002; Pálffy et al., 2001; Svensen et al., 2009; Neumann et al., 2017*]. Furthermore, positive feedback mechanisms caused through

Quantifying marine redox across the Triassic–Jurassic mass extinction

a warming climate are believed to have resulted in the release of methane, potentially in the form of methane clathrates (hydrates) [Pálffy *et al.*, 2001; Beerling & Berner, 2002; Pálffy, 2003; Ruhl & Kürschner, 2011; Pálffy & Kocsis, 2014].

As well as increased concentrations of CO₂ and CH₄ being introduced to the atmosphere, there will also have been an increased concentration of SO₂. These greenhouse gases will have collectively resulted in global warming as well as possible acidification of the oceans [Črnek *et al.*, 2011]. Acidification of the Late Triassic and Early Jurassic oceans has been proposed by several geochemical studies as well as being inferred through the 'Late Triassic biocalcification crisis' (2.3.4.3) [Richoz *et al.*, 2012; Greene *et al.*, 2012; Honisch *et al.*, 2012; Ikeda *et al.*, 2015].

CAMP and marine anoxia- CAMP induced global warming will have also caused the expansion of oxygen minimum zones and the increased de-oxygenation of the oceans, which ultimately drives marine mass extinctions [Kasprak *et al.*, 2015]. However, marine redox evolution throughout the ETME remains relatively poorly understood. One of the first studies to recognise marine oxygen paucity during the Late Triassic was Richoz *et al.*, (2012) using organic biomarker isorenieretane. Isorenieretane, a C₄₀ diaryl isoprenoid, is a light harvesting pigment produced by green algae which live within the photic zone and require free sulphur [Richoz *et al.*, 2012]. Isorenieretane is therefore a proxy for Photic Zone Euxinia (PZE) [Richoz *et al.*, 2012]. Three subsequent studies from Bristol (England), Kennecott Point (Canada) and the Hebelmeer 2 core (North Germany) also noted the presence of isorenieretane [Jaraula *et al.*, 2013; Kasprak *et al.*, 2015; Blumenberg *et al.*, 2016]. However, all four studies recorded PZE at different stratigraphic levels and generally provided low resolution information regarding changes to marine redox through the ETME interval. Despite more recent research studying Triassic–Jurassic

Chapter 2: The end-Triassic mass extinction event

marine redox change at higher resolution, through the use of biomarker, isotopic and elemental proxies, spatio-temporal redox evolution during the TJB still remains poorly understood (Jost et al., 2017; He et al., 2020; Beith et al., 2021; Fox et al., 2022; He et al., 2022a, 2022b). There is also very little research which directly correlates shifts in marine biodiversity to changes in marine redox, nor research with studies controls on Triassic–Jurassic marine redox change. Given the prominent effect that Late Triassic spatio-temporal marine redox change may have had on Late Triassic marine biodiversity (2.3.4), it is therefore important that marine redox evolution is further researched from the ETME and its impact on marine biodiversity better understood.

2.3.6.3 Section summary: The presence of a LIP which developed on the supercontinent of Pangaea during the Late Triassic is strongly supported by extensive Rhaetian and Hettangian tholeiitic lava deposits; Rhaetian volcanic intrusions; volcanoclastic clay spherules; volcanically induced seismites; modest increases in iridium, mercury and unradiogenic osmium; multiple negative shifts within the carbon isotope record indicative of large-scale outpouring of isotopically light carbon. LIP activity, in the form of CAMP, during the Late Triassic is believed to have resulted in global warming, ocean acidification and the progressive de-oxygenation of marine environments. However, the initiation and spatio-temporal pattern of redox change during the Late Triassic, as well as its role in Late Triassic diversity depletions, remains poorly understood and therefore requires further study.

2.4 CHAPTER SUMMARY

The ETME is widely recognised as one of the largest mass extinction events throughout the Phanerozoic Eon, witnessing the extinction of ~76% of all species and ~12% of all families. The ETME is also exemplified by the disappearances of large numbers of marine

Quantifying marine redox across the Triassic–Jurassic mass extinction

invertebrates at multiple trophic levels. This includes the near-complete disappearance of ammonites and reef building corals, as well as spatio-temporal extinctions of marine bivalves, the asynchronous disappearance of conodonts, and diversity depletions amongst zooplankton and phytoplankton.

Marine invertebrate extinctions throughout the Late Triassic are thought to be the result of environmental perturbation and oceanic chemical changes caused by LIP activity. The presence of a Late Triassic LIP is supported through Upper Triassic and Lower Jurassic volcanic deposits, increases in iridium and mercury as well as negative shifts in $\delta^{13}\text{C}$ of up to 8‰ indicative of large-scale de-gassing of isotopically light carbon. LIP-induced environmental change is believed to have resulted in de-oxygenation and/or acidification of the oceans and subsequent Late Triassic marine extinctions. However, despite marine redox change being evidenced at the ETME, the initiation, spatio-temporal progression and drivers of marine de-oxygenation, as well as its role in the ETME, remain poorly understood.

The aim of this research is therefore to quantify spatio-temporal marine de-oxygenation as a result of environmental change throughout the ETME. This research will be undertaken through the study of isotopic and elemental proxies within Rhaetian and Hettangian sedimentary successions. Furthermore, it is through the study of biogeochemical relationships in geological time that future anthropogenic changes to marine environments may be better understood. However, it should be noted that both present and past environmental changes differ markedly in terms of both duration, palaeogeography and starting conditions. The next chapter will discuss elemental and isotopic techniques which have been used within this thesis to reconstruct palaeo-environmental conditions, including marine redox, during the Late Triassic and Early Jurassic.

3 GEOCHEMICAL ENVIRONMENTAL PROXIES

3.1 INTRODUCTION

In order to reconstruct changing environmental conditions, including marine redox, within marine settings during the Triassic–Jurassic boundary interval a selection of palaeo-environmental proxies has been chosen. These include elemental and isotopic proxies which have been used within this thesis to determine marine redox, weathering, and hydrography at the selected study sites. This chapter will discuss the chosen proxies used within this thesis as well as explaining their application. For more detailed reviews of the selected redox proxies refer to Appendix 2.

3.2 PALAEO-REDOX PROXIES

For this thesis a series of palaeo-redox proxies have been used to reconstruct marine oxygenation during the latest Triassic and earliest Jurassic on the Tethyan shelf. Such proxies include enrichment of redox sensitive trace metals within carbonates and mudrocks (Mo, Cd, Zn, Mn, U, V, Cr), redox indicative elemental ratios (Fe_T/Al , C_{org}/P), and molybdenum isotope compositions ($\delta^{98}Mo$).

Molybdenum (Mo) is a conservative element which primarily exists as the oxyanion MoO_4^{2-} within oxic waters. Under oxic conditions Mo may adsorb onto Fe-Mn oxyhydroxides and become fractionated by up to 3 per mil lighter than coeval seawater resulting isotopically light $\delta^{98}Mo$ and molybdenum concentrations up to and exceeding 100 ppm (Barling & Anbar, 2004; Scott & Lyons, 2012). Under sulfidic conditions Mo forms particle reactive thiomolybdates, as well as Mo-S species under progressively increasing H_2S concentrations, resulting in sedimentary Mo enrichment and isotopically heavy δMo values (Helz et al., 1996; Ericksen & Helz, 2000). Sediments accumulating in

Quantifying marine redox across the Triassic–Jurassic mass extinction

intermittently and permanently sulfidic environments may exhibit 2 to 3 times greater Mo concentrations (>100 ppm) than non-euxinic environments (<25 ppm) (Scott & Lyons, 2012) under modern ocean Mo concentrations of ~105 nM. Global redox changes may also be interpreted through δMo values with globally oxygenated conditions being reflected through isotopically heavy seawater δMo , due to isotopically light sedimentary Mo uptake via oxyhydroxides, and globally sulfidic conditions being reflected by isotopically light seawater δMo , due to isotopically heavy sedimentary Mo uptake via sulfides.

Under oxidising conditions cadmium (Cd) commonly exists as CdCl^+ in seawater (Morford & Emerson, 1999; Tribovillard et al., 2006). However, in the presence of sub $\mu\text{mol kg}^{-1}$ H_2S concentrations Cd forms insoluble CdS and is removed into bottom water sediments (Framson & Leckie, 1978; Rosenthal et al., 1995; Van Geen et al., 1995; Janssen et al., 2014). However, more recent studies interpret that Cd burial may be facilitated through burial via organic matter with a more minor sulfide component (de Souza et al., 2022). Suboxic and anoxic margin sediments consequently account for up to 93% of Cd output within the modern oceans (Bryan et al., 2021).

Zinc (Zn) exists in the form of ZnCl^+ and Zn^{2+} within oxygenated waters, however under reducing conditions forms insoluble ZnS (Daskalakis & Helz, 1993; Janssen et al., 2014; Sweere et al., 2018; Zhang et al., 2021). Zn is subsequently enriched within sediments underlying an anoxic/euxinic water column or bearing anoxic pore waters (Daskalakis & Helz, 1993; Algeo & Maynard, 2004; Tribovillard et al., 2006; Janssen et al., 2014).

Under oxygenated conditions manganese (Mn) predominantly exists as Mn (III) and Mn (IV) oxides, including Mn-oxyhydroxides (Calvert & Pedersen, 1993). Under anoxic

Chapter 3: Geochemical environmental proxies

conditions Mn undergoes reductive dissolution to Mn (II) (Rue et al., 1997; Tribovillard et al., 2006; Piper & Calvert, 2009; Algeo & Li, 2020). Where Mn reduction occurs below the sediment water interface, Mn (II) may freely migrate within the sediment as it is not taken up significantly into organic or sulfide phases (Algeo & Maynard, 2004; Tribovillard et al., 2006). Mn (II) may subsequently flux into the overlying water column within anoxic basins or re-precipitate upon encountering oxic conditions resulting in concentrations in excess of upper crustal abundance (Mangini et al., 2001; Algeo & Maynard, 2004; Brumsack, 2006; Piper & Calvert, 2009). Sedimentary Mn enrichment therefore typically occurs under oxygenated conditions. However, enrichment may also occur within anoxic sediment pore space or euxinic bottom waters through the formation of Mn carbonate and sulfide species (Force & Maynard, 1991; Calvert & Pedersen, 1993; Algeo & Maynard, 2004; Brumsack, 2006; Lenz et al., 2014, 2015; Häusler et al., 2018).

Uranium (U) is a conservative element which commonly exists within oxygenated marine environments as U(VI)[UO₂(CO₃)₃⁴⁻] (Calvert & Pedersen, 1993; Tribovillard et al., 2006). As a result of the unreactive nature of U(VI) within oxygenated seawater, U exhibits low sedimentary enrichment under oxic conditions (Andersen et al., 1989; Calvert & Pedersen, 1993). However, under oxygen poor conditions reduction of U(VI) to U(IV) leads to immobilisation and enrichment of U below the sediment-water interface (Crusius et al., 1996; Morford et al., 2001; McManus et al., 2005; Andersen et al., 2014, 2016). U enrichment is thought to occur primarily within bottom water sediments on account of U(VI) reduction occurring independent of H₂S availability and Fe-Mn cycling (Algeo & Maynard, 2004; McManus et al., 2005). U therefore operates as a proxy for pore water [O₂] below the Fe(II/III) redox couple.

Quantifying marine redox across the Triassic–Jurassic mass extinction

Chromium (Cr) and vanadium (V), much like uranium, become insoluble under reducing conditions and are strongly removed from anoxic pore waters (Calvert & Pedersen, 1993). Cr commonly exists under oxygenated conditions as Cr(VI) (CrO_4^{2-}), however under reducing conditions it forms Cr(III) ($\text{Cr}(\text{H}_2\text{O})_4(\text{OH})_2^+$), which becomes insoluble upon aging. Meanwhile, V commonly exists as HVO_4^{2-} and H_2VO_4^- being hydrolysed to insoluble $\text{VO}(\text{OH})_2$ under mildly reducing conditions.

Fe_T/Al is a proxy which measures authigenic iron (Fe) enrichment under oxygen-poor conditions relative to detrital input (Al) (Lyons et al., 2003). Fe_T/Al values are commonly elevated within euxinic and ferruginous sediments through syngenetic pyrite formation (>0.7) (Lyons et al., 2003; Lyons & Severmann, 2006; Poulton & Canfield, 2011; Dickson et al., 2014; Hardisty et al., 2016; Young et al., 2020). Conversely, Fe_T/Al values are relatively low within oxic environments (<0.55) (Lyons & Severmann, 2006; Raiswell et al., 2008; Sperling et al., 2013, 2016, 2018].

Upon the burial of organic matter, phosphorus (P) is preferentially remineralised through bacterial decomposition (Algeo & Ingall, 2007; Burkhardt et al., 2014). Where the surrounding pore waters are oxygenated, remineralised P may be retained through adsorption to mineral surfaces (Fe-Mn oxyhydroxides) or organic uptake (Ruttenberg & Berner, 1993; Davelaar, 1993; Slomp et al., 1996; Sannigrahi & Ingall, 2005). Conversely, where surrounding pore waters are anoxic/euxinic, remineralised phosphorous is released back into the water column due to oxyhydroxide instability under low oxygen conditions (Ingall & Jahnke, 1994; Van Cappellen & Ingall, 1996; Ingall et al., 2005; Algeo & Ingall, 2007). The ratio of C_{org}/P may therefore be used to reconstruct sedimentary $[\text{O}_2]$, with

Chapter 3: Geochemical environmental proxies

C_{org}/P becoming elevated above typical Redfield ratios of ~ 106 under anoxic conditions (50–300) and below this ratio under oxic conditions (<50) [Algeo & Ingall, 2007].

The Redox Ladder:

Many of the redox sensitive elements discussed above fall into a redox framework. This framework is called the redox ladder and it lists the idealised progression in elemental enrichment of redox sensitive elements with changing water oxygen and sulfur concentrations (see Figure 14) [Algeo & Li, 2020; Algeo & Lui, 2020]. Elements like chromium and manganese are more sensitive to changes in oxygen concentrations and are enriched under less reducing conditions than elements which rely on the presence of reduced sulfur (e.g., molybdenum). Each suite of elements is associated with a redox facies, and a range in oxygen/sulfur concentration, and therefore the proportional enrichment of a number of indicative, redox sensitive elements may be used to interpret relative oxygen or reduced sulfur concentrations within the water column and/or sedimentary pore waters (Fig. 14).

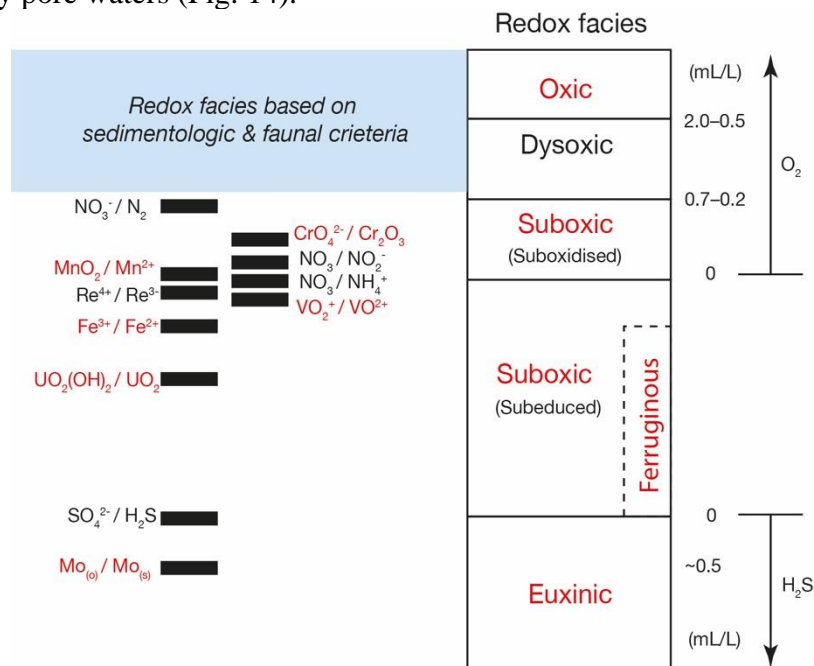


Figure 14:- An overview of ‘the redox ladder’. Redox facies and proxies used within this thesis in red. Figure amended from Algeo & Li, (2020).

Quantifying marine redox across the Triassic–Jurassic mass extinction

However, a strict calibration between elemental enrichment and oxygen conditions is not always possible. For example, the redox ladder does not take into consideration rapidly fluctuating and spatially variable redox conditions which could result in conflicting signals [Algeo & Li, 2020]. Nor does the redox ladder take into consideration reworking of marine sediments. It is for this reason that the redox ladder is often a theoretical framework that must be tailored for each study location.

Throughout this thesis redox classifications have been assigned according to the variable enrichment of redox sensitive elements (Fig. 15), using the redox ladder as a starting framework, and have been further informed through palaeobiological information where available. The elevated enrichment of Fe and/or Mn (1–10) alongside low enrichment of U, Cr, V, Mo, Cd and/or Zn (0–1) has been identified here as representing oxygenated marine conditions and therefore termed ‘oxic’ [Algeo & Maynard, 2004; Algeo & Tribovillard, 2009; Algeo & Lui, 2020]. The elevated enrichment of U, Cr, V, Mo, Cd, Fe, and/or Zn (1–10), whilst sometimes associated with the decreased enrichment of Mn, has been identified here as representing slightly decreased marine oxygenation and therefore termed ‘suboxic’ [Algeo & Maynard, 2004; Algeo & Li, 2020]. The elevated enrichment of elements which are particularly sensitive to sulfidic conditions (e.g., Mo, 2–20) over elements which do not rely on the presence of reduced sulfur (e.g., U, Cr, V; 1–10) has been used to specify suboxic conditions extending into the water column as sometimes represented through shoaling of the sulfate reduction zone [Algeo & Tribovillard, 2009]. Where elements which are sensitive to reduced sulfur (e.g., Mo) exhibit significantly elevated enrichment values (>20), suggesting significantly elevated $[HS^-]$ within the water column and the absence of oxygen, then this has been interpreted as representing ‘euxinic’ conditions with the extent of euxinia being interpreted based on absolute values [Algeo & Tribovillard,

Chapter 3: Geochemical environmental proxies

2009]. Meanwhile, in the rare circumstance that elements sensitive to anoxia exhibit little or no enrichment and elements sensitive to reduced sulfur exhibit variable enrichment this has been interpreted as reflecting ferruginous (low sulfur in the absence of oxygen) conditions.

		Analyte enrichment			
		Mn	U	V	Mo
Redox conditions	Oxic	~1 to 10	0 to ~1*	0 to ~1	0 to ~1 [^]
	Suboxic (p)	0 to ~1**	1 to 10	1 to 2	1 to 10
	Suboxic (w)	0 to ~1**	1 to 10	1 to 2	2 to 20
	Anox./Eux.	0 to ~1***	1 to >20 [^] *	2 to 5	>20

*U uptake into carbonate sediments can result in elevated values.

**Elevated Mn values can result from oxidation fronts and saturation with respect to rhodochrosite.

***Elevated Mn values can result from MnS precipitation.

[^] elevated Mo values can be due to Fe-Mn oxyhydroxides.

[^] U can be lost through post depositional loss.

Figure 15:- A quantitative framework to interpret redox conditions. Anox.- anoxic, Eux.- euxinic, (p)- pore water, (w)- water column. Redox boundaries and ranges based on data from Algeo & Maynard, (2004), Algeo & Tribovillard, (2009) and Algeo & Li, (2020). Footnotes based on Force & Maynard, (1991), Calvert & Pedersen, (1993), Tribovillard et al., (2006) and Kendall et al., (2017) for further information refer to Appendix 2.

3.3 PALAEO-WEATHERING/DETRITAL INPUT PROXIES

Palaeo-weathering conditions, when correlated to changes in marine redox, may be used to determine whether Triassic–Jurassic marine de-oxygenation may have been driven by localised changes in detrital input. Palaeo-weathering conditions during the latest Triassic and earliest Jurassic on the Tethyan shelf have been reconstructed using Ti/Al, Zr/Al, and CIA within this thesis to further understand this relationship.

Titanium (Ti) is commonly found within high-density Ti-bearing minerals within marine sediments, which are generally transported with coarser-grained silts and fine sands

Quantifying marine redox across the Triassic–Jurassic mass extinction

(Calvert & Pedersen, 2007). Aluminosilicates typically exhibit finer-grained clay and silt sized sediment within marine environments (Dickson et al., 2014). Therefore, when Ti is normalised to aluminosilicate input (Al), Ti may determine the proportion of coarse-grained sediment. Alternatively, Al (%) may be used on its own as a proxy for the detrital input or proportion of clay-sized sediment.

Zirconium (Zr) commonly exists within marine sediments as the mineral zircon (Calvert & Pedersen, 2007). Zr is resistant to weathering, has no cleavage and places just above quartz on Moh's hardness scale (7.5) (Calvert & Pedersen, 2007). Zr also exhibits a higher specific gravity than quartz meaning that unlike aluminosilicates (clay, silt) and Ti (silt, fine sand), Zr becomes concentrated with the fine to medium sand fraction of marine sediments (Calvert & Pedersen, 2007). Zr may therefore be used to determine the proportion of even coarser grained sediment when normalised to Al (Zr/Al).

The Chemical Index for Alteration (CIA) was initially developed by Nesbitt and Young (1982) as a proxy for palaeo-environmental reconstruction using soils and sediments and is expressed through the following equation: $CIA = [Al_2O_3 / (Al_2O_3 + CaO^* + Na_2O + K_2O)] \times 100$. Warmer and wetter environments produce higher CIA values due to higher mobilisation of cations, whilst colder and drier climates produce lower CIA values due to lower cation mobilisation (Wang et al., 2020). CIA has also been used a proxy for the chemical weathering of sedimentary rocks in order to determine changes in weathering intensity (Wang et al., 2020).

3.4 PALAEO-HYDROGRAPHIC PROXIES

Chapter 3: Geochemical environmental proxies

Hydrographic conditions, when correlated to changes in marine redox, may be used to determine whether marine redox changes during the TJB and ETME may have been driven by localised hydrographic changes. Palaeo-hydrographic conditions during the latest Triassic and earliest Triassic on the Tethyan shelf have been reconstructed here using Al (%), Ca (%) and Cobalt (ppm)*Manganese (%) (Co*Mn) to further understand the potential role of hydrography as a driver of marine de-oxygenation on the Triassic–Jurassic Tethyan shelf.

Al (%) is a proxy which can be used to determine the relative proportion of terrestrially derived, clastic material within an environmental setting. Lithic (rock) material is composed of compounds of Aluminium (Al) and Silica (Si) called aluminosilicates which form different arrangements and therefore different rock forming minerals. When rocks are weathered on land, they will accumulate within basins (e.g., seas and oceans) and remain in the sediment as Al and Si. Al is almost entirely bound within these terrestrial-derived aluminosilicates and has no biological function (Calver & Pederson, 2007). Therefore, the concentration of Al within a rock can be used to determine the proportion of terrestrially derived sediment within a certain stratigraphic layer. Al (%) may be used to determine basin proximity (i.e., higher Al (%) = more proximally positioned basin) when interpreted alongside other data (e. g. sedimentology, ichnofacies, palynology).

Co (ppm)*Mn (%) is a proxy for hydrographic restriction developed by Sweere et al., (2016). Within oceanic environments both cobalt (Co) and manganese (Mn) decrease in concentration with depth as they are scavenged into bottom water sediments (Knauer et al., 1982; Statham & Burton, 1986). Within unrestricted (open marine) environments the supply of Co and Mn into bottom water sediments is reduced through upwelling.

Furthermore, once Co and Mn are upwelled into coastal settings, they may exit the system

Quantifying marine redox across the Triassic–Jurassic mass extinction

through lateral advection (McArthur, 2019). Enrichment of Co and Mn is therefore reduced within the sediments of open marine, upwelling environments and can be characterised by Co (ppm)*Mn (%) of <0.4 (Sweere et al., 2016). However, within restricted settings movement of Co and Mn is more inhibited, and therefore Co and Mn largely remain within deeper waters. Any Co and Mn that does reach shallower waters within restricted settings cannot be removed from the system due to its closed nature. Co and Mn instead return to deeper waters through surface advection or are drawn into sediments through redox cycling (McArthur, 2019). The enrichment of Co and Mn is therefore greater within the sediments of restricted environments and can be characterised by Co (ppm)*Mn (%) of >0.4 (Sweere et al., 2016).

3.5 CHAPTER SUMMARY

Through the collection of both elemental and isotopic data, using the methods described in Chapter 5 of this thesis, it will therefore be possible to reconstruct a range of environmental changes through the proxies described within this chapter. Most notably it will be possible to reconstruct marine redox change at a local, regional, and global scale in order to further determine the role of marine redox change in marine extinction phases during the ETME, as well as to what extent marine redox may have been driven by detrital and hydrographic changes. The next chapter will discuss the materials which have been studied as part of this thesis from across the Tethyan shelf.

4 UPPER TRIASSIC AND LOWER JURASSIC CORE AND OUTCROP SAMPLES

4.1 INTRODUCTION

As discussed within chapter 2 of this thesis, it has only been within the past 12 years that a GSSP has been allocated for the Triassic–Jurassic boundary interval [Hillebrandt *et al.*, 2013]. However, in the lead up to a basal Hettangian GSSP being selected and ratified, many researchers were hard at work in a bid to further understand the stratigraphy of potential GSSP sites [Hesselbo *et al.*, 2002; Guex *et al.*, 2004; Ward *et al.*, 2004; Page, 2005; Hillebrandt *et al.*, 2007; Londridge *et al.*, 2007; Simms & Jeram, 2007; Ruhl *et al.*, 2009; Ruhl *et al.*, 2010]. GSSP candidate sites, which were stratigraphically poorly understood before, have subsequently become key locations for studies of end-Triassic marine mass extinction and recovery [Longridge *et al.*, 2007a, 2007b; van de Schootbrugge *et al.*, 2007; Mander & Twitchett, 2008; Mander *et al.*, 2008; Whiteside & Ward, 2011; McRoberts *et al.*, 2012; Jaraula *et al.*, 2013; Kasprak *et al.*, 2015; Atkinson & Wignall, 2019; Wignall & Atkinson, 2020; Du *et al.*, 2020]. Furthermore, several of these sites have also undergone recent drilling resulting in the extraction of sedimentary core sections. Core material provides an ideal record for geochemical analysis due to its relatively continuous and unweathered nature.

Core material has been retrieved from the Larne Basin in the form of the Carnduff-1 and Carnduff-2 cores [Boomer *et al.*, 2021, *this thesis*], the New York Canyon Section, Nevada [M. Ruhl 2019. *pers. comm.* 6 June] and St. Audrie’s Bay, Somerset [*this thesis*]. However, boreholes which intersect Upper Triassic and Lower Jurassic sections have also been drilled through other, less stratigraphically well understood, expanded localities.

Chapter 4: Upper Triassic and Lower Jurassic core and outcrop samples

These include the Hebelmeer-2, Schandelah-1 and Prees 2c cores [Blumenberg *et al.*, 2016; van de Schootbrugge *et al.*, 2019; *this thesis*]. The timing of this thesis therefore perfectly coincides with the emergence of several Upper Triassic and Lower Jurassic core sections from a range of Tethyan sites offering a potential new spatio-temporal understanding of Triassic-Jurassic marine redox evolution and its role in the end-Triassic mass extinction event.

Material has also been obtained from the Hungarian Csóvár Vár-hegy section, which is one of very few sites to exhibit continuous carbonate sedimentation through the Triassic–Jurassic boundary interval.

This chapter further discusses the core and outcrop material studied for this thesis including previous stratigraphic studies or geological background, the nature of the samples, the origin of the samples, sample collection, sample horizons, sample repository, and any other previous studies on the material where relevant.

4.2 CARNDUFF-2 CORE, LARNE BASIN, NORTHERN IRELAND

Previous stratigraphic studies- The Larne Basin, Northern Ireland became a site of particular interest in 1962 when the extraction of the Larne No.1 Borehole allowed for the detailed study of an expanded Triassic-Jurassic core section (Manning & Wilson, 1975; McCann, 1990). Palynological studies of the Larne No. 1 Borehole by Warrington & Harland (1975) revealed moderately diverse plankton and spore assemblages, with outcrop studies by Ivimey-Cook (1975) detailing invertebrate ranges throughout the Upper Triassic. The Larne Basin has subsequently undergone detailed study by Michael Simms & Andrew Jeram who endorsed Waterloo Bay as a candidate GSSP section based on detailed studies of ammonite biostratigraphy (Simms & Jeram, 2007). Simms & Jeram, (2007) also reconstructed cyclostratigraphy and carbon isotope stratigraphy for the Larne Basin. More

Quantifying marine redox across the Triassic–Jurassic mass extinction

recently (2013– 2014) two boreholes have been drilled within the Larne Basin by Gaelectric Energy Storage, the Carnduff-1 and Carnduff-2 cores, which have undergone detailed lithostratigraphic, biostratigraphic and chemostratigraphic study (*Boomer et al., 2021*). It is the Carnduff-2 core which has been studied as part of this thesis and will therefore be focussed on for the remainder of this section.

Nature of material studied- Sub-samples of the Carnduff-2 core

Origin of material- The Carnduff-2 core was drilled between October 31st, 2013, and March 21st, 2014, by Priority Drilling Ltd and Gaelectric Energy as part of a gas storage test. The borehole was drilled at 54.83882° N, 5.821264° W.

Sample collection- The Carnduff-2 core was sub-sampled by Micha Ruhl on 19/09/2018 at the Geological Survey of Northern Ireland (GSNI) core store.

Sample horizons & stratigraphy- 68 samples ranging from the base of the Westbury Formation to the lower Waterloo Mudstone Formation. For detailed stratigraphy see Boomer et al., (2021). For a summary of all the information within this chapter, refer to Appendix 3.1.

Sample repository- The Carnduff-2 core is archived at the GSNI core store, Round Tower Industrial Estate, Dargan Crescent, Belfast, BT3 9JP. Sub-samples may also be obtained from GSNI.

Previous studies of the Carnduff-2 core- The Carnduff-2 core was studied by Andeskie et al., (2018) who interpreted the Mercia Mudstone Group of the Larne Basin as representing

Chapter 4: Upper Triassic and Lower Jurassic core and outcrop samples

an arid depositional environment consisting of playa lake deposits and aeolian sediments. Recent work by Boomer et al., (2021) studied the detailed stratigraphy of both the Carnduff-1 and Carnduff-2 cores, correlating the cores to both each other and to St. Audrie's Bay, Somerset.

4.3 SOMERSET-1 & SOMERSET-2 CORES, ST. AUDRIE'S BAY, BRISTOL CHANNEL BASIN, SOMERSET, SW ENGLAND

Previous stratigraphic studies- The ammonite biostratigraphy of the Bristol Channel Basin has been studied for centuries, likely being a key tool used by William Smith during his mapping of the Jurassic strata of Southwest Britain (circa 1815). However, it has only been within the past 30 years that the Bristol Channel Basin has become more widely recognised as a key TJB locality. Detailed studies of ammonite biostratigraphy by Warrington et al., (1994) proposed the Triassic-Jurassic section at St. Audrie's Bay (SAB), Somerset as a candidate for the basal Hettangian GSSP based on the first appearance of ammonite *Psiloceras planorbis*. A ground-breaking study by Hesselbo et al., (2002) subsequently studied the biostratigraphy and carbon isotope stratigraphy from SAB allowing for the first correlation of marine (SAB, Kennecott Point, Csővár) and terrestrial (Astartekløft) TJB sites. Subsequent work by Hounslow et al., (2004) analysed biostratigraphy alongside magnetostratigraphy in order to further correlate SAB with terrestrial TJB sections (Newark Supergroup). Research by Ruhl et al., (2010) studied the Milankovitch cyclicity represented within the Lower Jurassic, interbedded, organic-rich shales and carbonates at SAB, further understanding the site's cyclostratigraphy. Meanwhile, a more recent study by Ruhl & Kürschner, (2011) uses carbon isotope stratigraphy to correlate SAB with both the GSSP (Kuhjoch) and terrestrial CAMP

Quantifying marine redox across the Triassic–Jurassic mass extinction

deposits from Morocco. However, the most interesting development from this site over the past decade has been the extraction of several core sections from the SAB foreshore in 2013. The Somerset core material will be further discussed here.

Nature of material studied- Sub-samples and archived core sections from the Somerset-1 and Somerset-2 cores.

Origin of material- The Somerset-1 and Somerset-2 cores were drilled on the foreshore at St. Audrie's Bay in early 2013 by a research group including Christian Bjerrum and Micha Ruhl. The cores were drilled at 51.18186° N, 3.286053° W, close to the site where Hesselbo and others (2002) previously logged the foreshore in outcrop and studied the stratigraphy in detail. A further two cores were drilled by Bjerrum and colleagues [C. Bjerrum, 2019. pers. comm. 13 May] covering the critical interval (Cotham to Langport Member) and mid-Westbury Formation.

Sample collection- The Somerset-1 and -2 cores were sub-sampled by Christian Bjerrum at the University of Copenhagen between 2018 and 2021.

Sample horizons & stratigraphy- 51 samples. Samples from the Somerset-2 core extend from the top of the Westbury Formation to the top of the Lilstock Formation. Samples from the Somerset-1 core extend from the base of the Lilstock Formation to the lower Lias. The sample horizons are reported relative to stratigraphic heights from Hesselbo et al., (2002) and have been correlated using carbon isotope stratigraphy by Christian Bjerrum [C. Bjerrum, 2021.pers. comm. 10 Aug]. For further information including core

Chapter 4: Upper Triassic and Lower Jurassic core and outcrop samples

descriptions, core photos and detailed sedimentary logs, which have been generated as part of this thesis, refer to Appendix 3.2.

Sample repository- The Somerset-1 and Somerset-2 cores are archived at the Geocenter, Copenhagen University, Øster Voldgade, Copenhagen, Denmark. Sample aliquots are stored at the Geocenter also.

Previous studies of the material- The work within this thesis is the first which formally studies the core material. Due to insufficient time, it has not been possible to obtain detailed biostratigraphy of the core material. However, detailed lithostratigraphy and carbon isotope stratigraphy has been used to correlate the cores to nearby outcrop sections studied by Hesselbo et al., (2002) [*C. Bjerrum, 2021. pers. comms. 10 Aug.*].

Biostratigraphy from Hesselbo et al., (2002) has subsequently been extrapolated for both cores.

4.4 THE PREES-2C CORE, CHESHIRE BASIN, ENGLAND

Previous stratigraphic studies- The Jurassic stratigraphy of North Wales, geographically proximal to the Cheshire Basin, is known in detail on account of numerous studies of the Mochras borehole (Hesselbo et al., 2013). The Mochras borehole, formally known as the Llanbedr (Mochras Farm) borehole, was drilled between 1967 and 1969 on the Cardigan Bay coast, North Wales (Woodland, 1971; Hesselbo et al., 2013). Approximately 1300m of core was recovered during drilling revealing a significantly expanded and relatively complete Jurassic succession (Ruhl et al., 2016; Hesselbo et al., 2013; Hollaar et al., 2021). Sub-samples of the Mochras borehole were subsequently processed for high resolution carbon isotope stratigraphy (Storm et al., 2020), and cyclostratigraphy (Ruhl et al., 2016)

Quantifying marine redox across the Triassic–Jurassic mass extinction

including the identification of a positive carbon isotopic excursion from the basal Jurassic in the Mochras core by Jenkyns & Clayton, (1997).

On account of the expanded nature of the Jurassic strata in North Wales and bordering Shropshire, as well as the unavailability to drill near the original Mochras site, the Cheshire Basin was subsequently chosen as the site for a combined NERC-ICDP project to further understand the Early Jurassic Timescale ('JET'). In late 2020 the 'JET' project retrieved 656m of Lower Jurassic and Upper Triassic core material from the Cheshire basin, known as the Prees-2c core. It is the Prees-2c core which has been studied as part of this thesis and will be the focus of the remainder of this section.

Nature of material studied- Sub-samples and archived core sections of the Prees-2c core.

Origin of material- The Prees-2c core was drilled between early November and 29th December 2020, just off the A49, ~1km north of the village of Prees, Whitchurch, north Shropshire, England. The core was drilled by a team of scientists led by Professor Stephen Hesselbo of the University of Exeter.

Sample collection- 125m of core material were logged at a centimetre scale at the British Geological Survey (BGS) (Appendix 3.3), Keyworth, Nottingham. Sub-samples of the core were collected by a team of JET scientists.

Sample horizons and stratigraphy- 38 samples. Samples span from the upper Hettangian to upper Rhaetian based on carbon isotope and ammonite stratigraphy [S. Hesselbo 2021. *pers. comm.* 7th July].

Chapter 4: Upper Triassic and Lower Jurassic core and outcrop samples

Sample repository- The Prees-2c core working and archive halves are housed at BGS.

Previous studies of the material- Given that the core material was only recovered in late 2020, and that initial processing of the material was only completed at the end of last year, there has been very little previous study of the material. Initial results were presented at the European Geophysical Union 2021 [Hesselbo *et al.*, 2022], however there are no formal publications as of yet on the Prees-2c core material.

4.5 CORE AND OUTCROP SAMPLES FROM THE CENTRAL EUROPEAN BASIN

Originally named the ‘Germanic Basin’, a large portion of mainland Europe is now thought to have formed an extensive marginal basin in the form of the ‘Central European Basin (CEB)’ or Southern Permian Basin [Blumenberg *et al.*, 2016]. The CEB has been reconstructed numerous ways by different studies [van de Schootbrugge *et al.*, 2009; Greene *et al.*, 2012; Richoz *et al.*, 2012; Lindström *et al.*, 2016; Blumenberg *et al.*, 2016]. However, in spite of the varied reconstructions of the CEB architecture, all studies agree that the CEB was connected to the Tethys Ocean during the Late Triassic and Early Jurassic. This connection was likely partly restricted on the account of several studies reporting brackish conditions from the CEB during this time [Bonis *et al.*, 2010; Blumenberg *et al.*, 2016; Barth *et al.*, 2018]. The CEB is subdivided into numerous sub-basins [Bense & Jähne-Klinberg, 2017] which include sites represented by the Hebelmeer-2 and Schandelah-1 cores as well as material from the Csővár Vár-hegy section, Hungary. The CEB sites studied within this thesis will be further discussed in the remainder of this chapter.

Quantifying marine redox across the Triassic–Jurassic mass extinction

4.5.1 Hebelermeer-2 core, Germany:

Geological Background- Despite the stratigraphy in the area of the Hebelermeer-2 core having been relatively unstudied prior to the core's extraction in 1955, the Hebelermeer-2 core represents the wealth of information that is available due to exploratory wells. The Hebelermeer-2 core was originally extracted for the purposes of hydrocarbon prospecting more than 65 years ago, however the archiving of such cores has allowed for their use in scientific research in the 21st century [see *Blumenberg et al., 2016*]. Archived cores may therefore represent an invaluable asset with regards to reconstructing spatio-temporal redox change and palaeoenvironmental conditions across ancient continental interiors.

Previous stratigraphic studies- see '*Previous studies of the material*' below

Nature of material studied- Sub-samples from Hebelermeer-2 core.

Origin of material- The Hebelermeer-2 core was drilled in 1955 by Deutsche Vacuum Öl, GEW Elwerath, Deutsche Schachtbau, Wintershall and KCA Deutag [*Schwarzenhölzer, 1955; Blumenberg et al., 2016*]. The core was drilled at 52.675842° N, 7.208970° E.

Sample horizons & stratigraphy- 7 samples. Samples extend from the lower to middle Rhaetian to the lower Hettangian based on *Blumenberg et al., (2016)*.

Sample repository- The Hebelermeer-2 core is archived at the core repository of BGR (Bundesanstalt für Geowissenschaften und Rohstoffe) and LBEG (Landesamt für Bergbau, Energie und Geologie), the Geocenter, Hannover [*Blumenberg et al., 2016*]. Further data on coring and stratigraphy of the whole core are available at the LBEG archive [*Blumenberg et al, 2016*].

Chapter 4: Upper Triassic and Lower Jurassic core and outcrop samples

Previous studies of the material- The core has been studied for its lithological characteristics as well as undergoing detailed micro and macrofossil studies [Schwarzenhölzer, 1995]. However, a more recent study, with particular relevance to this thesis, is the work undertaken on the Hebelmeer-2 core by Martin Blumenberg and colleagues (2016). Blumenberg et al., (2016) studied biomarker isorenieratane from the Hebelmeer-2 core and identified euxinic conditions from as early as the middle Rhaetian. A middle Rhaetian initiation of marine anoxia predates that of other Tethyan and Panthalassa sites [Richoz et al., 2012; Jaraula et al., 2013; Kasprak et al., 2015] and may suggest a more complex redox evolution during the Late Triassic than previously interpreted.

4.5.2 Schandelah-1 core, Germany:

Geological Background- Much like the Hebelemeere-2 core site, the Schandelah-1 core locality was relatively unstudied prior the Schandelah-1 core extraction in 2008. Very little existing data was available from this site, and the stratigraphy of the region was relatively poorly understood [van de Schootbrugge et al., 2019]. Therefore, archived core material may be supplemented by new, strategically placed boreholes in order to obtain new data, and fill potential gaps in knowledge. In this circumstance, the Schandelah-1 core was extracted with the aim of understanding Lower Jurassic black shale deposition from the CEB. Geochemical signatures of Upper Triassic and Lower Jurassic black shales from the CEB will be used to further understand redox conditions across mainland Europe during the ETME when studied alongside data from Hebelmeer-2 core.

Nature of material studied- Sub-samples from the Schandelah-1 core.

Quantifying marine redox across the Triassic–Jurassic mass extinction

Sample collection- Sub-samples from the Schandelah-1 core collected by Remco Bos and Bas van de Schootbrugge.

Origin of material- The Schandelah-1 core was drilled by Daldrup and Söhne between 5th August and 18th September 2008. The borehole was drilled at 52.30639° N, 10.71833° W.

Sample horizons & stratigraphy- 28 samples. Ranging from the Arnstadt Formation (upper Rhaetian) to the Angulatenton Formation (Planorbis Zone, Lower Hettangian) [*van de Schootbrugge et al., 2019*].

Sample repository- The Schandelah-1 core is archived in the German core repository for scientific drilling in Berlin Spandau [*van de Schootbrugge et al., 2019*]. Sample aliquots are stored at the Institute of Geosciences, Goethe University, Frankfurt.

Previous studies of the material- A study by Lindström et al., (2015) reports soft sediment deformation (SSD) from the Upper Triassic of Schandelah-1 core and correlates this SSD to similar sedimentary features from other Tethyan sites. Lindström et al., (2015) interprets that SSD across Tethyan sites is the result of CAMP seismicity and that seismite deposition may have played a role in the ETME across the CEB. Work by Lindström et al., (2017) correlates Schandelah-1 to other CEB sites, including the GSSP, using detailed palyno-, carbon isotope, ammonite, and dinoflagellate stratigraphy. A recent study by van de Schootbrugge et al., (2020) correlates increased reworking of terrestrial plant matter across several CEB sites (including Schandelah-1) and interprets this to be the result of deforestation and subsequent soil erosion in the proximity of the CEB. Research of Upper Triassic and Lower Jurassic sediments from the Schandelah-1 core is currently ongoing at

Chapter 4: Upper Triassic and Lower Jurassic core and outcrop samples

Utrecht University [B. van de Schootbrugge, 2020. pers. comm. 12 Feb; Bos, R. 2020. pers. comm. 26 Feb] including the correlation between aberrant pollen and spore composition and Late Triassic environmental changes, as well as isorenieratane studies. All previous and on-going studies will help to supplement the palaeo-environmental proxies studied from the Schandelah-1 core within this thesis.

4.5.3 Csővár Vár-hegy section, Hungary

Previous stratigraphic studies- Early research of the strata in the vicinity of Csővár, Hungary interpreted a Triassic or Jurassic age exclusively (Szabó, 1860; Vadász, 1910). However, later work by Pálffy and Dosztály (2000), supplemented by biostratigraphic studies by Kozur & Mostler (1973), Detre et al., (1988), Kozur & Mock, (1991), Kozur (1993) and Haas et al., (1997), determined that the Vár-hegy section near Csővár exhibited continuous sedimentation across the Triassic–Jurassic boundary. Pálffy and Dosztály (2000) identified the first Jurassic ammonite *ex situ* ~19m from the base of the section and interpreted its origin as being from several meters further up section. Meanwhile, Triassic Choristoceratid ammonites had already been identified from the base of the section (Detre et al., 1988). A Triassic–Jurassic age for the section was further confirmed by Pálffy et al., (2007) through the identification of a Late Triassic Radiolarian assemblage at ~1.5m and an Early Jurassic radiolarian assemblage at ~26.5m. Chemostratigraphic data from Pálffy et al., (2001, 2007) also identified a negative shift in carbon isotope data which has become indicative of the Triassic–Jurassic boundary interval and ETME globally (Hesselbo et al., 2007; Ruhl et al., 2020). Work by Haas & Tardy-Filác (2004), Pálffy et al., (2007) and Haas et al., (2010) has produced several detailed cyclostratigraphic frameworks for the Vár-hegy section with another study by Götz et al., (2009) analysing detailed palynofacies

Quantifying marine redox across the Triassic–Jurassic mass extinction

changes. Recent work by Kovács et al., (2020) has sampled the Vár-hegy section at high resolution, with powdered sample aliquots from that study being used here for marine redox reconstruction.

Nature of material studied- Outcrop samples from near to the village of Csővár, Hungary.

Sample collections- Samples collected from outcrop by Emma Blanka Kovács. 40 sub-samples (powdered sample aliquots) were obtained from Kovács for geochemical analyses.

Origin of material- Samples selected from an existing study from the Vár-hegy section, Csővár, Hungary (Kovács et al., 2020). ~50km north-north-east of Budapest.

Sample horizons & stratigraphy- 40 samples. Samples span from the upper Rhaetian to the basal Jurassic based on carbon isotope stratigraphy and biostratigraphy [Kovács et al., 2020].

Sample repository- Samples from the Vár-hegy section are housed at both Trinity College Dublin and Eötvös Loránd University, Hungary.

Previous studies of the material- Numerous studies have analysed the sediments of the Vár-hegy section however most have involved the collection of new samples from outcrop. This comes with the exception of this work which uses the same sample powder aliquots as those produced by Kovács et al., (2020). Kovács et al., (2020) identify increased concentrations of Hg/Fe directly coinciding with the main CIE and therefore suggest a

Chapter 4: Upper Triassic and Lower Jurassic core and outcrop samples

direct link between Late Triassic volcanism, carbon cycle perturbation and potentially Late Triassic extinction phases.

4.6 CHAPTER SUMMARY

The 232 core and outcrop samples studied within this thesis provide a representative selection of stratigraphically well-understood, Tethyan, TJB sites. Core material from Northern Ireland, in the form of Carnduff-2 core, and Southwest England, in the form of the Somerset-1 and Somerset-2 cores, provides a continuous sedimentary core record through the ETME from two GSSP candidate sections. The expanded nature of Carnduff-2 core makes this locality particularly unique, with an additional expanded section also being studied from the Cheshire Basin in the form of the Prees-2c core. Both of these sites will help to reconstruct high resolution redox changes during the Late Triassic and the ETME.

Core material from central Europe, in the form of the Schandelah-1 and Hebelmeer-2 cores, provides a window into marine redox change from the more distal, slightly restricted CEB. Past studies of PZE and black shale deposition from the CEB make these localities key for understanding spatio-temporal marine redox change across the European Continent during the TJB and ETME. Meanwhile, continuous carbonate deposition recorded in outcrop samples from the Vár-hegy section, Hungary may allow for the findings from the other localities to be understood in a broader context. The following chapter will discuss the methods used within this thesis for the powdering and digestion of core and outcrop samples in order to obtain elemental data for palaeoenvironmental proxies.

5 THE GEOCHEMICAL PROCESSING OF CORE AND OUTCROP SAMPLES

5.1 INTRODUCTION

Due to the low natural concentrations of the redox-informative elements being studied within this thesis (e.g., Mo, Cd), it was essential that samples were processed in such a way as to avoid contamination. This included the use of clean (metal free) labs, high purity acids, ultra-pure Milli-Q water, and the use of Class 100 laminar flow hoods. All Teflon, Teflon FEP and polypropylene vessels were acid cleaned to ensure low blanks, and lab suits and anti-static footwear were worn to limit sample contamination. Latex or nitrile gloves were also worn. This chapter details the procedures used within this thesis for milling and digesting samples as well as measuring the isotopic and elemental concentrations of sedimentary material. All care has been taken to limit sample contamination, the details of which can be found within this chapter and the detailed procedural guides (Appendix 4).

5.2 SAMPLE POWDERING

In order to reduce metal contamination, samples were powdered in either agate, tungsten carbide or carbon alloy (1.1740). Samples from the Hebelmeer-2 core were powdered in agate by Martin Blumenberg at the Federal Institute for Geosciences and Natural Resources, Hannover using a Siebtechnik Vibratory Disc Mill TS 750/ TS 1000. Samples from the Somerset-1 and -2 cores were powdered by Christian Bjerrum at the Geocentre, Copenhagen University using a tungsten carbide rotary mill. Select samples from the Carnduff-2 core were powdered in agate by Micha Ruhl using a pestle and mortar at the Department of Geology, Trinity College Dublin. Samples from the Csővár section were

Chapter 5: The geochemical processing of core and outcrop samples

powdered in agate by Emma Blanka Kovács at Eötvös Loránd University, Budapest (for further details see Appendix 4.1).

All other samples (Schandelah-1, Prees-2c and selected samples from the Carnduff-2 core) were powdered in carbon alloy (1.1740) using a Retsch RS200 Vibratory Disc Mill at the Department of Earth Sciences, Royal Holloway University of London. For further details of the milling procedure used within this thesis refer to Appendices 4.1–4.3.

5.3 LABWEAR CLEANING

All lab wear used for chemical analyses within this thesis were acid cleaned to ensure low levels of contamination. Teflon (PTFE) and Teflon FEP were cleaned by soaking in 30–50% HNO₃, followed by 30% HCl and ultra-pure Milli-Q water (x4 rinses). Polypropylene was cleaned by soaking in weak HCl and ultra-pure Milli-Q water (x4 rinses). For further details of the cleaning procedure used within this thesis refer to Appendix 4.4.

5.4 INORGANIC ELEMENTAL ANALYSES

5.4.1 Sample digestion (non-carbonate samples)

In order to obtain major, minor and trace element data for non-carbonate samples, approximately 50 mg of sample was precisely weighed into a 6 ml acid-cleaned, Teflon digestion vessel using a 4 d.p. balance and oxidised in inverse aqua regia (HNO₃: HCL, 3:1) at 150°C for 2–3 days. The samples were then dried down until residue and further digested in HF and HNO₃ (1:2) at 120°C for 1–2 days to promote dissolution of silicates and further oxidise the sample. The samples were dried down again and re-dissolved in ~5ml of 1M HNO₃ (120°C overnight) in preparation for ICP-AES and ICP-MS analyses. Non-carbonate samples were digested alongside PERN-1 and MAG-1 rock standards as

Quantifying marine redox across the Triassic–Jurassic mass extinction

well as a procedural blank to evaluate contamination and sample digestion as well as accuracy and precision of the data (Appendix. 5). For further details of the non-carbonate sample digestion procedure used within this thesis refer to Appendix 4.5.1.

5.4.2 Sample leaching (carbonate samples)

For inorganic elemental analysis, carbonate samples were washed in ultra-pure Milli Q water and then leached using 0.2M acetic acid (CH_3COOH) at room temperature. Acetic acid was used for carbonate digestion to avoid liberating non-carbonate Zn. For a detailed procedural guide refer to Appendix 4.5.2.

5.4.3 Sample measurement

Major elemental concentration data was measured using a Perkin Elmer Optima 3300RL ICP-AES in the Department of Earth Sciences, Royal Holloway University of London (RHUL). Samples were measured at ~150-fold dilution. A series of in-house standards ('M' and 50 ppm standard) were used to measure instrumental drift after every 8 samples throughout the run. A 5-point calibration line constructed from certified solution standards was used to convert elemental intensities to element concentrations (Appendix 4.5.1). Data processing was undertaken in Microsoft Excel.

Minor and trace elemental concentration data was partly measured using a Perkin Elmer NexION 350D ICP-MS at the University of Oxford. Samples were measured at ~2000-fold dilution. Each sample was doped with 1ppb Rh, In, Ir, and Re to correct for instrumental drift. Calibrations were obtained for each element on the instrument using an external calibration constructed from a 10 ppm custom-blend multi element standard produced by CPAchem Ltd. An external standard was also diluted and measured from a custom bought

Chapter 5: The geochemical processing of core and outcrop samples

QMX multi element solution. Minor and trace elemental concentration data was also measured using an Agilent 7500 ICP-MS at RHUL. Samples were run alongside a series of calibration standards (0.01, 0.5, 1, 10, 30 and 50 ppb) and, for carbonate samples, each sample was spiked with a Re standard to monitor drift throughout the run.

5.5 ORGANIC ELEMENTAL ANALYSES

5.5.1 Sample processing

Samples for organic elemental data were furnaceed at 450 °C overnight (15 hours) to remove organic matter and weighed into tin capsules. A second un-furnaced sample of the same powder aliquot was weighed into a second tin capsule. For detailed procedures of sample preparation for organic elemental analysis refer to Appendix 4.6.

5.5.2 C, N, S measurements

Carbon (%), nitrogen (%) and sulfur (%) were obtained using an Elementar Analyser Micro Vario Cube. Total carbon (TC, un-furnaced sample) and total inorganic carbon (TIC, furnaced sample) were used to calculate for total organic carbon (TOC%) using:

$$\text{TOC} = \text{TC} - \text{TIC}$$

Accuracy throughout the run was determined using a chemical standard (sulfanilamide) to correct for instrument drift. Precision of the batch was determined using in house Eocene shale and marl standards as well as sample triplicates.

5.6 ISOTOPIC ANALYSIS

5.6.1 Sample digestion (non-carbonate samples)

Non-carbonate samples for isotopic analysis were digested using inverse aqua regia at 150 °C (followed by 1 : 2 HF/HNO₃ for Zn isotopes). Prior to digestion a precise mass of

Quantifying marine redox across the Triassic–Jurassic mass extinction

double spike solution was added to each sample. For Mo isotope analyses a ^{100}Mo – ^{97}Mo spike was used and for Zn isotope analyses a ^{67}Zn – ^{64}Zn spike was used. For further details of spike calculation and digestion of non-carbonate samples for isotope analysis refer to Appendix 4.7.

5.6.2 Sample leaching (carbonate samples)

Carbonate samples for isotopic analysis were leached using 0.2M acetic acid at room temperature. Following removal of a small aliquot for elemental concentration measurements, samples were then spiked with a ^{67}Zn – ^{64}Zn enriched solution.

5.6.3 Anion Exchange Columns

Samples were processed for Mo-isotopes using a single pass anion exchange method described by Pearce et al., (2009) and Dickson et al., (2016) in order to remove potential sources of interference. For Zn isotopes samples were processed using a multi pass exchange method outlined in Sweere et al., (2020) and Dickson et al., (2020). For full details of the anion exchange column procedure used for this thesis refer to Appendix 4.7.

5.6.4 Measurement of Isotopic composition(s)

Isotopic compositions of Mo and Zn were measured using a Thermo Scientific Neptune Plus MC-ICP-MS within the Department of Earth Sciences, Royal Holloway University of London.

Set up and tuning- The Neptune Plus underwent a baseline calibration of 600 cycles prior to each run in order to correct for electronic noise. The ion beam was then tuned using a 10–20 ppb tuning solution for Mo and 100–200 ppb tuning solution for Zn. Whilst the

Chapter 5: The geochemical processing of core and outcrop samples

tuning solution was being measured, the sample gas flow rates (Ar and N₂ for Mo, Ar only for Zn), the position of the ICP torch, and the focus and shape of the ion beam were altered until a high intensity, stable signal was attained.

Sample introduction- Solutions for Mo isotope measurements were introduced as a dry plasma using a Teledyne Aridus III. Meanwhile solutions for Zn isotope measurements were introduced as a wet plasma using a quartz cyclonic spray chamber. Both sample introduction methods used a PFA nebuliser with a 100µl/min flow rate.

Concentration checks- After the instrument was tuned a 50-fold dilution of each sample was measured. The intensities measured from the diluted samples were used to dilute the stock solutions so that all samples were normalised to same intensity (10 or 20ppb for Mo, 100–200ppb for Zn). Measuring dilute solutions also allowed for spike/sample ratios to be determined which were used to make bracketing standards for Zn batches.

Isotope measurements- A blank of 3% HNO₃ was measured before each sample for background concentration. The intensity of each sample was then measured for between 50 and 80 sample integrations for an integration time of 8.4 seconds. The blank was then subtracted from the sample measurement and all samples were normalised to a zero-delta standard:

Molybdenum, NIST 3134:

$$\delta^{98/95}\text{Mo} = \left(\frac{(^{98}\text{Mo}/^{95}\text{Mo})_{\text{sample}}}{((^{98}\text{Mo}/^{95}\text{Mo})_{\text{NIST3134}} * 0.99975)} - 1 \right) * 1000$$

where $\delta^{98/95}\text{Mo}$ is in units of ‰

(Nägler et al., 2014)

Quantifying marine redox across the Triassic–Jurassic mass extinction

Zinc, AA-ETH:

$$\delta^{66/64}\text{Zn} = \left(\frac{(^{66}\text{Zn}/^{64}\text{Zn})_{\text{sample}}}{((^{66}\text{Zn}/^{64}\text{Zn})_{\text{AA-ETH}})} - 1 \right) * 1000$$

where $\delta^{66/64}\text{Zn}$ is in units of ‰

(Archer et al., 2017)

Isotopic correction- Final Mo isotope values were corrected by +0.25% (c.f. Nägler et al., 2014) and final Zn isotope values were corrected by +0.28 as per Archer et al., (2017) to provide values equivalent to Lyon Zn.

Primary and secondary standards- Accuracy was determined by measuring primary and secondary standards. These included OU Mo (open university molybdenum standard c.f Goldberg et al., 2013) and USGS SDO-1 for Mo (*Fig. 16*), and Spec Pure (Alfa Aesar Spec pure Zn concentration standard), USGS SDO-1, and a CRM standard for Zn. For further details of procedures used for the measurements of isotope ratios refer to Appendix 4.7.

5.6.5 Processing of isotopic data

Isotopic data was deconvolved offline using an Excel-based method.

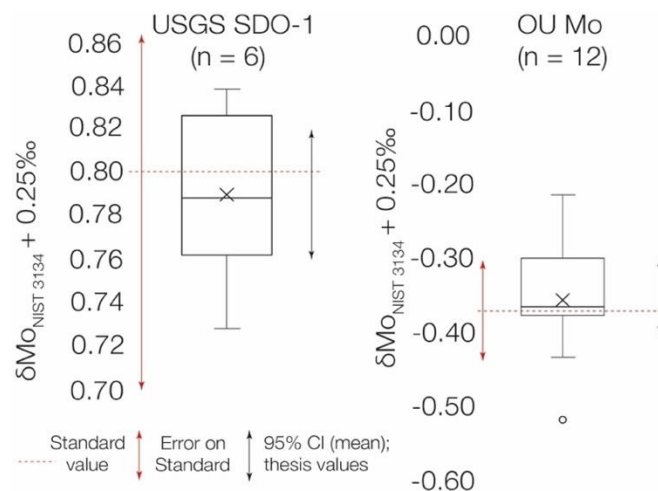


Figure 16:- A comparison of standard values from literature (red) and this thesis (black) for molybdenum isotopic ratios. Note how both datasets are indistinguishable.

6 MARINE REDOX CHANGE AND EXTINCTION IN TRIASSIC–JURASSIC BOUNDARY STRATA FROM THE LARNE BASIN, NORTHERN IRELAND

Andrew D. Bond, Alexander J. Dickson, Micha Ruhl and Robert Raine.

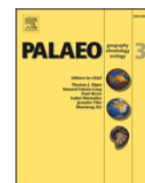
Published in *Palaeogeography, Palaeoclimatology, Palaeoecology* volume 598, 111018. <https://doi.org/10.1016/j.palaeo.2022.111018>.

Statement of lead author's contributions:

- Obtained samples from MR
- Milled a subset of the samples
- Digested the sample powders
- Prepared the samples for ICP-MS and ICP-AES analyses
- Prepared a subset of samples for Elementar Micro Vario Cube (EMVC) analysis
- Ran the sample subset on the EMVC
- Processed the ICP-MS, ICP-AES and EMVC data
- Interpreted the ICP-MS, ICP-AES and EMVC data
- Compiled palaeobiology data from literature
- Wrote the first draft of the manuscript
- Prepared all figures for the manuscript
- Made corrections to the manuscript and figures based on co-authors' and reviewers' comments

Contents lists available at [ScienceDirect](https://www.sciencedirect.com)

Palaeogeography, Palaeoclimatology, Palaeoecology

journal homepage: www.elsevier.com/locate/palaeo

Marine redox change and extinction in Triassic–Jurassic boundary strata from the Larne Basin, Northern Ireland

Andrew D. Bond^{a,*}, Alexander J. Dickson^a, Micha Ruhl^b, Robert Raine^c

^a Department of Earth Sciences, Royal Holloway University of London, Egham Hill, Egham, Surrey TW20 0EX, UK

^b Department of Geology, Trinity College Dublin, The University of Dublin, College Green, Dublin, Ireland

^c Geological Survey of Northern Ireland, Dundonald House, Upper Newtownards Road, Belfast BT4 3SB, Northern Ireland, United Kingdom

ARTICLE INFO

Editor: Lucia Angiolini

Keywords:

End-Triassic Mass Extinction (ETME)

Carnduff-2 borehole

Local extinction

Suboxia

Infaunal

Ichnotaxa

ABSTRACT

The de-oxygenation of marine environments is thought to have played a significant role in many of Earth's major mass extinction events. This includes the end-Triassic mass extinction event (ETME), which witnessed the disappearance of conodonts, the near extinction of ammonoids and the most significant reef crisis across the entirety of the Phanerozoic. However, there are few high-resolution redox studies across the ETME, including across the main pulse of marine extinction, and few studies that directly correlate marine redox conditions with the biotic record in the same sedimentary succession. Here we present a high-resolution multi-proxy redox record from an expanded Triassic–Jurassic boundary section (Carnduff-2 borehole) from the Larne Basin, Northern Ireland. Redox conditions within the Larne Basin during the latest Triassic and earliest Jurassic were oxic to suboxic with suboxia being mainly restricted to sedimentary pore fluids. Such conditions differ from the photic zone euxinia reported from this time in other basins. Despite the Larne Basin being relatively oxygenated during the latest Triassic (Rhaetian) to earliest Jurassic (Hettangian), subtle pulsed marine redox changes within the Larne Basin had a profound effect on infaunal marine organisms. Suboxia within the Larne Basin coincided with the disappearance of 62.5% of bivalve species, of which 90% were infaunal, and the temporary absence of bioturbation.

1. Introduction

Marine environments during the Triassic–Jurassic boundary interval (~201 Ma) are renowned for the widespread, pulsed extinction of numerous marine faunas at multiple trophic levels (Hallam, 2002; Kiessling et al., 2007; Whiteside and Ward, 2011; Ros et al., 2011; Hodges and Stanley, 2015; Dunhill et al., 2018). These pulsed extinctions are collectively referred to as the ‘end-Triassic mass extinction event’ (ETME), and notably include the asynchronous disappearance of conodonts, the near disappearance of ammonites, and the most significant reef crisis across the entirety of the Phanerozoic (Kozur and Mock, 1991; Flügel and Kiessling, 2002; Guex et al., 2004; Du et al., 2020).

Early studies attributed the ETME to an extra-terrestrial impact (Olsen et al., 2002; Tanner and Kyte, 2005). Subsequent research, however, has strongly endorsed the ETME as being caused through the onset of provincial volcanism associated with the emplacement of the Central Atlantic Magmatic Province (CAMP) (Hesselbo et al., 2002; Marzoli et al., 2004; Schoene et al., 2010; Whiteside et al., 2010; Ruhl

et al., 2011; Blackburn et al., 2013; Davies et al., 2017; Percival et al., 2017; Kovács et al., 2020; Ruhl et al., 2020). The CAMP activity has been linked to terrestrial wildfires (Marynowski and Simoneit, 2009; Belcher et al., 2010; Petersen and Lindström, 2012; Lindström et al., 2020) and marine acidification (Hautmann et al., 2008; Greene et al., 2012; Hönisch et al., 2012; Jost et al., 2017a), with strong evidence for marine anoxia and photic zone euxinia (PZE) being revealed in recent years (Van de Schootbrugge et al., 2007; Bonis et al., 2010; Richoz et al., 2012; Jaraula et al., 2013; Kasprak et al., 2015; Blumenberg et al., 2016; Jost et al., 2017b; He et al., 2020; Beith et al., 2021; Fox et al., 2022a). The expansion of Late Triassic marine anoxia into the photic zone, based on the occurrence of the biomarker isorenieratane, a light harvesting pigment formed by green sulfur bacteria in a sulfidic photic zone and found in sediments of that time (Summons and Powell, 1986; Richoz et al., 2012; Jaraula et al., 2013; Kasprak et al., 2015; Blumenberg et al., 2016; Beith et al., 2021; Fox et al., 2022a), adds to a growing body of evidence that marine redox change may have played a significant role in marine extinctions during the ETME (Barras and Twitchett, 2007;

* Corresponding author.

E-mail address: Andrew.Bond.2014@live.rhul.ac.uk (A.D. Bond).

<https://doi.org/10.1016/j.palaeo.2022.111018>

Received 13 January 2022; Received in revised form 22 April 2022; Accepted 24 April 2022

Available online 29 April 2022

0031-0182/© 2022 The Authors. Published by Elsevier B.V. This is an open access article under the CC BY license (<http://creativecommons.org/licenses/by/4.0/>).

Mander and Twitchett, 2008; Kasprak et al., 2015; Van de Schootbrugge and Wignall, 2015; He et al., 2020; He et al., 2022).

Despite strong evidence for marine anoxia as a mechanism for Late Triassic marine extinctions, there are currently very few high-resolution redox studies through this key extinction interval. Many Triassic–Jurassic redox-sensitive geochemical studies consist of data with temporal resolutions between ~25,000 and 200,000 years; thus, not resolving redox changes occurring at shorter temporal scales that are comparable to the C-cycle perturbations that characterise this period (Hesselbo et al., 2002; Richoz et al., 2012; Jaraula et al., 2013; Kasprak et al., 2015; Blumenberg et al., 2016). Other redox-related studies almost exclusively focussed on the Early Jurassic (Van de Schootbrugge et al., 2007; Quan et al., 2008; Jost et al., 2017b; Atkinson and Wignall, 2019) or did not directly assess relationships between marine redox changes and changes in marine biodiversity (Jaraula et al., 2013; Kasprak et al., 2015; Blumenberg et al., 2016).

To better understand variation in palaeo-marine redox conditions at a

high temporal resolution, and their possible role in marine extinctions during the ETME, this study presents new data from an expanded Upper Triassic to Lower Jurassic section in well-preserved core samples, that span the main extinction interval. We present a high-resolution multiproxy redox record, with a ~ 4500-year resolution, spanning late Rhaetian and earliest Hettangian strata of the Larne Basin (Northern Ireland), to determine the relationship between redox state and biodiversity change at a local, basinal scale.

2. Geological background

2.1. Previous geological study of the Triassic–Jurassic in the Larne Basin

Early detailed studies of the Larne Basin geology were aided by the drilling of the Larne No.1 borehole in 1962, 2 km SW of Waterloo Bay (Manning and Wilson, 1975; McCann, 1990) (Fig. 1). This core provided a record of 1284 m of Triassic and Jurassic strata in the basin and was



Fig. 1. The approximate location and extent of the Larne Basin: a) Basin location relative to the cities of Larne and Belfast (dashed line) and the supercontinent of Pangaea (star; bottom left-hand corner). The locations of the Waterloo Bay Foreshore (WB), Larne No.1 Borehole (L1), Carnduff-1 core (C1), and Carnduff-2 core (C2) relative to Larne are shown in the bottom right-hand corner of a. F- Larne Fault, P.- Panthalassic Ocean, T.- Tethys Ocean, white strata- Lias Group outcrop, black strata- Penarth Group outcrop. b) Basin location relative to the T/J Tethys shelf. The locations of key T/J Tethys basins and study sites (outcrops and core localities) have been included within b). A- Astartekløft section (Greenland), Ar- Argana Basin (Morocco), AM- Armorian Massif, B- Bristol Channel Basin (UK; St. Audrie's Bay section), B. M.- Bohemian Massif, C- Cheshire Basin (UK; Prees-2c core), CM.- Cornubian Massif, Cs- Csővár Basin (Hungary), E- Eiberg Basin (Austria), F- Fundy Basin (Canada), F. H.- Ferroscandian High, H- Hebelermee-2 core (Germany), IRE- Ireland, K- Kuhjoch Section (Austria; GSSP), L- Larne Basin (UK; this study; Carnduff-2 core), LBM- London Brabant Massif, Lo- Lombardy Basin (Italy), M- Mariental-1 core (Germany), MC.- Massif Central, Mi- Mingsolsheim core (Germany), N- Norra Albert Quarry (Sweden), R- Rosswinkel core (Luxembourg), R.- Rhenish Massif, S- Schandelah-1 core (Germany), St- Stenlille cores (Denmark; Danish Basin), WM.- Welsh Massif; a) modified from Mitchell (2004), Andeskie et al. (2018) and Boomer et al. (2021); b) modified from Fischer et al. (2012); Lindström et al. (2015) and Schobben et al. (2019); Basin and core location data from Whiteside et al. (2007); McElwain et al. (2007); McKie and Williams (2009); Ruhl et al. (2011); Richoz et al. (2012); Lindström et al. (2015); Casacci et al. (2016); Kovács et al. (2020) and Boomer et al. (2021); CAMP outcrop data from Whiteside et al. (2007).

the subject of a number of additional studies (Manning and Wilson, 1975; McCann, 1990). Warrington and Harland's (1975) palynological study of the Larne No.1 Borehole revealed moderately diverse assemblages of miospores, acritarchs and dinoflagellates from the Upper Triassic, and prompted Ivimey-Cook (1975) to examine the Rhaetian and Hettangian geology of east County Antrim at outcrop, which included studies of invertebrate diversity. Later studies by Reid and Bancroft (1986) identified the Larne foreshore as a promising site for ammonite biostratigraphy, and Simms and Jeram (2007) later proposed Waterloo Bay as a candidate for the basal Hettangian Global Stratotype Section and Point (GSSP) (Fig. 1). Studies of Waterloo Bay in outcrop by Simms (2003, 2007) identified seismite deposits from the Cotham Member, which have been correlated to other sites in SW England, and interpreted to be the result of tectonic activity (Simms, 2007; Laborde-Casadaban et al., 2021).

Between 2013 and 2014 two fully-cored boreholes were drilled within the Larne Basin by Gaelectric Energy Storage Ltd., reaching depths of 922.70 m (Carnduff-1) and 970 m (Carnduff-2) below ground level (Fig. 1). Detailed studies of the Mercia Mudstone Group section of the core from Carnduff-2 were undertaken by Andeskie et al. (2018), with a recent study by Boomer et al. (2021) documenting the uppermost Triassic and Lower Jurassic interval in both cores. A synthesis of the Triassic–Jurassic basins of Ireland, including the Larne Basin, was compiled by Raine et al. (2021). Meanwhile, recent work by Jeram et al. (2021) presented detailed carbon isotope data from the Larne Basin, and a study by Opazo and Page (2021) analysed changes in bivalve palaeocommunities across the Triassic–Jurassic boundary using material from the Waterloo Bay foreshore. Thus, there is now a wealth of (bio) stratigraphic data for this interval in the Larne Basin that can be utilised to test the role of redox on extinction.

2.2. Palaeoenvironmental and lithological change during the Late Triassic to Early Jurassic of the Larne Basin

The Larne Basin represents an epicontinental, extensional basin located on the Tethyan margin during Late Triassic to Early Jurassic times (Simms and Jeram, 2007) (Fig. 1). The Upper Triassic Mercia Mudstone Group is a red mudstone dominated succession deposited in a terrestrial setting (Howard et al., 2008; Andeskie et al., 2018). A study of the group by Andeskie et al. (2018) described the sedimentary facies, including the bedded halite and gypsum, along with other features such as mud cracks, rip-up clasts, and ripple cross-lamination. Intervening massive mudstone units in their study interval showed blocky beds, circumgranular cracks and soil slickensides suggesting the influence of pedogenic processes.

In contrast, the overlying Westbury Formation is dominated by dark grey to black, finely laminated mudstones, shales and subordinate silty claystones. At certain levels thin beds of ripple cross-laminated or bioturbated siltstones and sandstones are observed. Bioturbated limestones and sandy limestones are also present at certain horizons (Simms and Jeram, 2007; Boomer et al., 2021). The ichnotaxa *Planolites* and *Arenicolites* dominate the trace fossil assemblage, but bioturbation, although locally intense, is for the most part sporadic through the formation (Simms and Jeram, 2007; Boomer et al., 2021). Sediment deformation is common at the top of the Westbury Formation (Jeram et al., 2021; Laborde-Casadaban et al., 2021; Boomer et al., 2021). The fossil assemblages, trace fossils and facies of the Westbury Formation support deposition within a low-energy restricted marine setting which was subject to intermittent high energy events (MacQuaker, 1999; Simms, 2007; Laborde-Casadaban et al., 2021).

The Westbury Formation passes up into the Cotham Member (Lilstock Formation) which is dominated by silty mudstones and claystones, with common, thin, ripple cross-laminated sandstone beds, sandy siltstones, and towards the top of the member, silty limestones. Sedimentary structures include colour banding, pinstripes of silt and sand, lenticular bedding, current and wave ripple cross-lamination, rare mud

cracks in the claystones, and hummocky cross-stratification in some sandstones (Simms and Jeram, 2007; Boomer et al., 2021; Jeram et al., 2021). Soft sediment deformation is observed throughout the Cotham Member but is most intense around 370 m and 368 m and takes the form of folding and shearing (Simms and Jeram, 2007; Laborde-Casadaban et al., 2021; Boomer et al., 2021; Jeram et al., 2021). The ichnofauna of the Cotham Member is not well documented and for the most part the unit is unbioturbated with fine-scale sedimentary features being well preserved. However, at some levels there is sparse bioturbation with resting traces and surface trails recorded by Boomer et al. (2021). The member is widely regarded as having been deposited at least in part under freshwater conditions (Mayall, 1983), but the record of marine bivalves throughout the unit in the Larne Basin (Simms and Jeram, 2007; Opazo and Page, 2021) suggest that the Cotham Member retained a marine connection during its deposition.

The overlying Langport Member (upper part of the Lilstock Formation) largely comprises dark grey laminated claystones, silty claystones and ripple cross-laminated or bioturbated siltstones with local pinstripes of sandstone. Near the base of the unit, calcareous mudstones, argillaceous silty limestones, and sandy limestones are recorded, with bioclastic limestones higher in the member. Bioturbation is more common within the Langport Member and is dominated by *Planolites* and *Chondrites*. The presence of the ostracod *Darwinula* suggests brackish conditions at times and there are also marine reptiles recorded (Simms and Jeram, 2007; Boomer et al., 2021).

The Waterloo Mudstone Formation consists of laminated and bioturbated claystones and silty claystones with some intercalated calcareous claystones, muddy limestones, and limestones. Echinoids and the crinoid *Isocrinus* appear at the base of the Waterloo Mudstone Formation with ammonites appearing slightly further up section confirming a fully marine offshore setting for the unit (Simms and Jeram, 2007; Boomer et al., 2021; Opazo and Page, 2021).

3. Palaeo-redox proxies across the Triassic–Jurassic boundary interval in the Larne Basin

For this study we analysed a series of palaeo-redox proxies to reconstruct variations in the oxygenation state of the Larne Basin during the latest Triassic and earliest Jurassic, including the sedimentary enrichment of redox sensitive trace metals (Mo_{EF} , Cd_{EF} , Zn_{EF} , Mn_{EF} , U_{EF}) and redox indicative elemental ratios (Fe_T/Al , $\text{C}_{\text{org}}/\text{P}$).

Within oxygenated waters molybdenum (Mo), cadmium (Cd) and zinc (Zn) commonly exist as ionic species (MoO_4^{2-} , CdCl^+ , ZnCl^+) (Morford and Emerson, 1999; Tribouillard et al., 2006). However, under sulfidic conditions Mo, Cd and Zn form sulfide species resulting in sedimentary enrichment (Framson and Leckie, 1978; Daskalakis and Helz, 1993; Rosenthal et al., 1995; Van Geen et al., 1995; Helz et al., 1996; Erickson and Helz, 2000; Janssen et al., 2014; Sweere et al., 2018; Zhang et al., 2021). Uranium (U) commonly exists within oxygenated marine environments as U(VI) (Calvert and Pedersen, 1993; Tribouillard et al., 2006). U(VI) is unreactive under oxic conditions, resulting in low sedimentary U enrichment (Anderson et al., 1989; Calvert and Pedersen, 1993). Under oxygen poor conditions reduction of U(VI) to U(IV) leads to immobilisation and enrichment of U below the sediment-water interface (Morford et al., 2001; McManus et al., 2005).

Fe_T/Al values are commonly elevated within euxinic and ferruginous sediments through syngenetic pyrite formation (>0.7) (Lyons et al., 2003; Lyons and Severmann, 2006; Hardisty et al., 2016; Young et al., 2020). Conversely, Fe_T/Al values are relatively low within oxic environments (<0.55) (Lyons and Severmann, 2006; Raiswell et al., 2008; Sperling et al., 2013, 2016, 2018).

Organic phosphorus (P) is preferentially remineralised through bacterial decomposition (Algeo and Ingall, 2007; Burkhardt et al., 2014). Where the surrounding pore waters are oxygenated, remineralised P may be retained through adsorption to mineral surfaces (Fe–Mn oxyhydroxides) or organic uptake (Ruttenberg and Berner, 1993;

Davelaar, 1993; Slomp et al., 1996; Sannigrahi and Ingall, 2005). Conversely, in the presence of reducing pore waters, remineralised phosphorus is released back into the water column due to oxyhydroxide instability under low oxygen conditions (Ingall and Jahnke, 1994; Van Cappellen and Ingall, 1996; Ingall et al., 2005; Algeo and Ingall, 2007). C_{org}/P is consequently elevated under anoxic conditions (50–300) and reduced under oxic conditions (<50) (Algeo and Ingall, 2007).

Conversely to several of the proxies highlighted above, Mn is stabilised under oxidising depositional conditions. Under oxygenated conditions manganese (Mn) predominantly exists as Mn (III) oxyhydroxides (Calvert and Pedersen, 1993). Under low oxygen conditions Mn (III) undergoes reduction to Mn (II) (Rue et al., 1997; Tribouillard et al., 2006; Piper and Calvert, 2009; Algeo and Li, 2020). Mn may subsequently re-precipitate upon encountering oxic conditions resulting in concentrations in excess of upper crustal abundance (Shimmield and Price, 1986; Pruyssers et al., 1993; Piper and Calvert, 2009).

4. Materials and methods

4.1. Carnduff-2 core samples

Sixty-two samples were obtained from 378.2 m to 348.3 m depth from the Carnduff-2 core, County Antrim, N. Ireland (54.83882° N, 5.821264° W). The core was sampled at the Geological Survey of Northern Ireland (GSNI) core repository. The samples span the latest Triassic and earliest Jurassic based on ammonite biostratigraphy and palynology (Boomer et al., 2021).

4.2. Bulk inorganic geochemistry

Samples were milled in tungsten carbide and carbon alloy down to a grain size of ~60 µm. ~50 mg of each sample was digested using inverse aqua regia (1 HCl: 3 HNO₃) at 150 °C followed by digestion of silicates in 1: 2 HF/HNO₃ at 120 °C. Samples were diluted 150-fold for major element concentration measurements, which were undertaken with a Perkin Elmer Optima 3300RL ICP-AES. Aliquots of the same digests were diluted 2000-fold for minor and trace element concentration measurements, which were undertaken using a Perkin Elmer NexION 350D ICP-MS. Accuracy was assessed with full procedural digestions ($n = 3$) of MAG-1 and was ±4%. Precision was calculated as the 2 Standard Deviation (S.D.) of the MAG-1 digests and 3 digests of an in-house mudrock standard (PERN-1) as ±7 and 13%. Elemental enrichments were calculated using the following calculation: $(Mo_{sample}/Al_{sample}) / (Mo_{ucc}/Al_{ucc})$ as shown for Mo. Upper continental crust (ucc) concentrations were obtained from Rudnick and Gao (2003).

4.3. Bulk organic geochemistry

TOC data and C_{org}/N ratios were obtained using an Elementar Micro Vario Cube elemental analyser. Sample aliquots were furnace to 450 °C to remove organic matter and measured twice for total inorganic carbon (TIC) and total carbon (TC) in order to obtain total organic carbon (TOC) %. Precision was calculated using the 2 S.D. of an in-house mudrock standard (Eocene Shale, $n = 10$, C: ±0.16%, N: ±0.05%, S: ±0.22%) and an in-house marl standard ($n = 5$, C: ±0.12%, N: 0.03%, S: ±0.14%). Two samples were analysed in triplicate and yielded comparable precision to the reference materials (2 S.D. = C: ±0.04%, N: ±0.00%, S: ±0.03%, C: ±0.00%, N ± 0.03%, S: ±0.002%).

5. Results

5.1. The Westbury Formation

The basal Westbury Formation (378.2 m–377.3 m) exhibits moderate Mo_{EF} (6.25), Cd_{EF} (3.15) and Zn_{EF} (1.40) as well as elevated TOC (%) (2.79%), and high to very high Fe_T/Al (0.60) and C_{org}/P (453). U_{EF} and

Mn_{EF} exhibit low values (Fig. 2). Most proxies then decrease into the middle Westbury Formation (376.7 m–373.8 m) where Mo_{EF} exhibits low to moderate values (2.36) and Cd_{EF} (1.16), Zn_{EF} (0.66), U_{EF} (0.99), Mn_{EF} (0.48) and Fe_T/Al (0.45) all exhibit low values. Meanwhile, TOC (%) (2.67) and C_{org}/P (434) remain high (Fig. 2). Most proxies then observe an increase into the upper Westbury Formation (373.2 m–371.6 m). Mo_{EF} continues to exhibit low to moderate values (2.11) with Zn_{EF} (1.92) and Cd_{EF} (5.48) both exhibiting moderate values. U_{EF} meanwhile exhibits low average values (1.10) and Fe_T/Al (0.54) and C_{org}/P (273) exhibit high values.

5.2. The Lilstock Formation

5.2.1. The Cotham Member

The basal Cotham Member (371.0 m–369.4 m) is defined by low enrichment of Mo (0.52), U (0.81), Cd (1.21), Mn (0.60) and Zn (0.61), as well as low Fe_T/Al (0.39), C_{org}/P (72) and TOC (%) (0.59) (Fig. 2). An enriched horizon is then observed at 368.8 m extending to 368.5 m. The horizon exhibits increased U_{EF} (1.43), Cd_{EF} (1.57), Mn_{EF} (3.25), Fe_T/Al (0.57) and Zn_{EF} (0.98), whilst Mo_{EF} (0.34), TOC (%) (0.28) and C_{org}/P (35) decrease or remain low (Fig. 2). This horizon (368.8 m–368.5 m) is then overlain by a thick unit exhibiting moderate enrichment of redox sensitive elements (367.3 m–363.8 m), with values fluctuating. Most proxies fluctuate and gradually increase throughout this unit (367.3 m–365.0 m). This includes Mo_{EF} (0.32–2.04), U_{EF} (0.80–2.37), Cd_{EF} (0.60–1.35), Mn_{EF} (0.39–1.42), Fe_T/Al (0.34–0.63), Zn_{EF} (0.62–0.84), C_{org}/P (38–125) and TOC (%) (0.30–0.73). Enrichment eventually peaks at 364.8 m, exhibiting sharp increases for Mo_{EF} (1.60–9.34), U_{EF} (1.36–5.86), Cd_{EF} (1.14–7.42), Mn_{EF} (1.33–7.06), Fe_T/Al (0.54–1.35) and Zn_{EF} (0.79–1.44) (Fig. 2). Meanwhile C_{org}/P (81–70) and TOC (%) (0.55–0.44) both decrease before a peak at 364.6 m (200, 0.87). Values gradually decrease throughout the top 1 m of the unit, with a lesser peak being observed from 364 to 363.8 m.

5.2.2. The Langport Member

The basal Langport Member (363.1–362.9) is marked by a small enrichment in Mo (1.57), Cd (2.20) and Fe_T/Al (0.74), as well as a marked increase in TOC (%) (1.56) and C_{org}/P (250). Following this enriched horizon, all proxies remain low throughout the remainder of the Langport Member (362.5 m–357.4 m) (Fig. 2).

5.2.3. The Waterloo Mudstone Formation

The basal Waterloo Mudstone Formation (357.0 m–354.7 m) exhibits pulsed enrichment of Mo (1.51, 3.76, 3.25), U (1.30, 1.46, 1.30), Cd (2.01, 2.33, 1.11), Mn (2.20, 4.19, 2.24) and Zn (1.05, 1.87, 1.44) as well as elevated Fe_T/Al (1.13, 1.54, 0.69), TOC (%) (1.02, 0.99, 1.71) and C_{org}/P (138, 184, 156) (Fig. 2). The overlying unit (353.0 m to 353.8 m) exhibits enrichment of Mo (3.49) and Mn (1.31) as well as elevated Fe_T/Al (0.58), TOC (%) (1.84) and C_{org}/P (302). However, all other proxies remain low. The interval from 352.6 m to 350.6 m is marked by low enrichment of Mo (0.85), U (0.75), Cd (0.69), Mn (1.09), Zn (1.01) as well as relatively low Fe_T/Al (0.50), moderate to low TOC (%) (1.41) and C_{org}/P (126) (Fig. 2). This is then overlain by a horizon (350.4 m) with moderate values for Cd_{EF} (4.23) and Zn_{EF} (6.39) as well as slightly elevated TOC (%) (2.46) and Mo_{EF} (1.53) but little/no change for other proxies. Values then fluctuate within the remainder of the section with two further noteworthy horizons at 349.9 m and 349.7 m–349.3 m. At 349.9 m there is low enrichment of Mo (0.47), U (0.78), Cd (0.80) and Zn (0.90), as well as low values for TOC (%) (0.80) and C_{org}/P (64.48) but moderate enrichment of Mn (3.05) and Fe (0.70). Between 349.7 m and 349.3 m there is a pronounced increase of several proxies, notably Mo (5.37), TOC (%) (2.44) and C_{org}/P (188) whilst all other proxies remain low (Fig. 2).

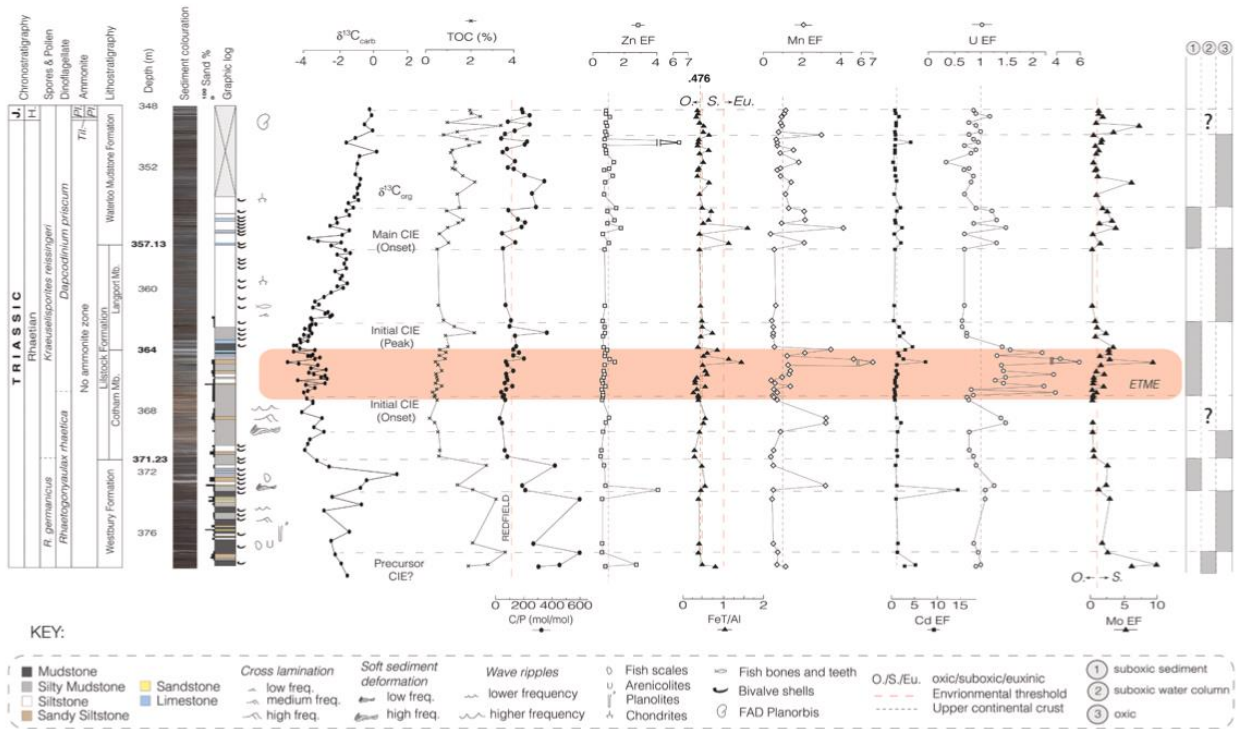


Fig. 2. A high resolution geochemical dataset from the Larne Basin plotted against stratigraphy. Upper continental crust values for elemental proxies are ‘1’ unless stated otherwise e.g., Fe_T/Al. Carbon (carbonate) isotope data (from Carduff-2 core samples), sedimentology, and stratigraphy from Boomer et al. (2021), Carbon (organic) isotope data from Boomer et al. (2021) and Jeram et al. (2021).

6. Discussion

6.1. Deciphering discrepancies between redox proxies

The low- to moderate enrichment of elements sensitive to reduced S within the Carduff-2 core suggests that the Larne Basin exhibited non-euxinic conditions during deposition of the Triassic–Jurassic boundary strata. However, whilst trace elements exhibit relatively little enrichment, Fe_T/Al and C_{org}/P exhibit high values that may be interpreted as representing euxinic conditions (Lyons and Severmann, 2006; Algeo and Ingall, 2007). One possible reason for this discrepancy between the different redox proxies is that the Larne Basin may have experienced strongly restricted conditions during the Late Triassic wherein the basinal seawater inventory of trace elements was significantly depleted (e.g. Algeo and Lyons, 2006; Helz and Vorlicek, 2019). Conversely, an average Co(ppm)*Mn(%) of 1.14 indicates that the Larne Basin was only weakly restricted (see Supplementary Information 1.) (Sweere et al., 2016). The Larne Basin is also not believed to have been positioned close to landmasses during the Triassic–Jurassic transition, unlike the geographically proximal Bristol Channel Basin, making severe hydrographic restriction unlikely (Lindström et al., 2015; Korte et al., 2019) (Fig. 1). Alternatively, persistent globally euxinic conditions on the timescale of 10⁵ to >10⁶ yr may have resulted in trace element depleted waters (e.g., Algeo, 2004; Owens et al., 2016). However, there is little evidence for widespread, persistent euxinia in the Late Triassic, with anoxic conditions being episodic only and likely confined to more restricted continental margin settings (Richoz et al., 2012; Jaraula et al., 2013; Jost et al., 2017b; Beith et al., 2021; Fox et al., 2022a).

Therefore, it is likely that both Fe_T/Al and C_{org}/P have been significantly elevated by non-redox related environmental factors. Given that the Larne Basin was weakly restricted during the latest Triassic, one

reason for elevated Fe_T/Al may be the removal of Fe into underlying sediments through a particulate shuttle (Raiswell et al., 2018). A Fe–Mn oxyhydroxide particulate shuttle operating within the water column may also result in sedimentary trace element enrichment due to metal adsorption and subsequent removal into underlying marine sediments (Berrang and Grill, 1974; Rosenthal et al., 1995; Hein et al., 1997; Wasylenki et al., 2011, 2014; Chen et al., 2021). Elevated Fe_T/Al may also be associated with coastal proximity due to biological remobilisation and concentration of Fe in near-shore settings (Aller et al., 1986; Canfield, 1989). The trace fossil assemblage recorded in the Westbury Formation of the Carduff-2 core represents the *Arenicolites* ichnofacies, which are strongly associated with intertidal, near shore environments (Gingras et al., 2012; Hofmann et al., 2012). Water and/or airborne deposition of proximal Fe-rich sediments into the Larne Basin during the late Triassic (e.g. exposures of Mercia Mudstone-type sediments) may have also contributed to locally high Fe_T/Al (Andeskie et al., 2018). Therefore, significantly elevated Fe_T/Al within the Late Triassic of the Larne Basin is likely associated with hydrographic and environmental concentration of Fe and is not indicative of euxinic conditions.

Meanwhile, the elevated C_{org}/P values within the Late Triassic of the Larne Basin may be associated with the varying source of organic matter entering the basin. Despite marine organisms having an average C_{org}/P < 1:165 (Redfield, 1958; Redfield et al., 1963; Takahashi et al., 1985; Anderson and Sarmiento, 1994; Ho et al., 2003; Martiny et al., 2014), terrestrial plant matter exhibits a C_{org}/P ratio > 1:800 (McGroddy et al., 2004). This includes C_{org}/P upper values of 1:4116 for tropical tree litter and 1:2352 for temperate coniferous tree litter (McGroddy et al., 2004). Between 76.4% and 84.6% of the miospore taxa in the Westbury Fm. are gymnosperms, including the following taxa: bisaccate pollen, *Classopollis meyeriana*, *Ovalipollis pseudoalatus* and *Ricciisporites tuberculatus* (Kürschner et al., 2013, 2014; van Eldijk et al., 2018; Li et al., 2018;

Boomer et al., 2021). However, just 10.5% of the miospore taxa in the basal Lilstock Fm. are gymnosperms. Therefore, the depleted C_{org}/P values within the basal Lilstock Formation compared to the Westbury Formation may be the result of a sudden change or reduction in the source of terrestrial organic matter (e. g. marine regression, wildfires, biological turnover etc.). A relationship between C_{org}/P values and organic matter type is further supported through a positive correlation between C_{org}/N and C_{org}/P from this site (Fig. 3). Why exactly C_{org}/P values are significantly higher within the Westbury Formation compared to the Waterloo Mudstone Formation is not clear despite both exhibiting high C_{org}/N values (Fig. 3). However, sedimentation rate is also known to affect C_{org}/P values (Ingall and Van Cappellen, 1990), as may proportion of terrestrial organic matter and persistence of terrestrial organic matter influx. Significantly elevated C_{org}/P values within the Late Triassic of the Larne Basin can subsequently be attributed to the influx of terrestrial organic matter from further inland instead of marine euxinia.

6.2. Possible alternative controls on elemental fluctuations throughout the Carnduff-2 core

Given that both Fe_T/Al and C_{org}/P both exhibit non-redox related, environmental controls, it is essential that the potential effect of such controls (e.g., detrital, diagenetic, hydrographic and/or depositional changes) on other redox proxies are also addressed.

Sedimentary trace metal enrichment can be related to the weathering of a trace-metal enriched parent lithology. However, elemental compositional data for the Carnduff-2 core samples suggests the weathering of a fresh, granitic parent rock which would exhibit low trace metal enrichment (Fig. 4a). Maturation can affect trace metal concentrations in mudrocks (Dickson et al., 2020, 2022). The sediments of the Carnduff-2 core are thermally immature based on vitrinite reflectance data (Fig. 4c) with aragonite shell material well-preserved in the claystones and contact metamorphism only being known from Waterloo Bay within the Larne Basin (Raine et al., 2021; Boomer et al., 2021). Therefore, there is little evidence for thermal alteration of the Carnduff-2 core sediments. The Larne Basin was weakly restricted–upwelling during the Triassic–Jurassic boundary interval with there being little correlation between the hydrographic restriction of the basin and trace element enrichment (Fig. 4b) Also, there is little correlation between elemental enrichment data, sequence stratigraphy, or sedimentary facies changes, suggesting that the depositional environment was an insignificant control on elemental enrichment (Fig. 2). Fluctuations in the elemental enrichment of redox sensitive proxies throughout

the Carnduff-2 core may instead therefore be attributed to redox change.

6.3. Interpreting Marine Redox Change from the Triassic–Jurassic of the Larne basin

In order to determine marine redox changes within the Larne Basin through the Triassic–Jurassic boundary a detailed analysis has been undertaken of trace element enrichment data

6.3.1. Westbury Formation

Moderate average values for Mo_{EF} , Cd_{EF} and Zn_{EF} within the basal Westbury Formation (378.2 m–377.3 m) when coupled with low average U_{EF} and Mn_{EF} suggests suboxic conditions with the chemocline extending above the sediment water interface (SWI) (Algeo and Tribouillard, 2009; Scott and Lyons, 2012; Tribouillard et al., 2012; Algeo and Liu, 2020)

Conditions became increasingly oxygenated during deposition of the middle Westbury Formation (376.7 m–373.8 m) as is suggested by low averages for Cd_{EF} , Zn_{EF} and U_{EF} , and low to moderate average Mo_{EF} . Oxidic conditions are also supported by an average Fe_T/Al which is similar to values interpreted as representing either oxidic or detrital concentrations (Lyons et al., 2003; Lyons and Severmann, 2006; Dickson et al., 2014).

Conditions then shifted to suboxic conditions once again during deposition of the upper Westbury Formation (373.2 m–371.6 m). Sub-oxic conditions with the chemocline at or just below the SWI are suggested by elevated averages for Cd_{EF} and Zn_{EF} , as well as low to moderate average Mo_{EF} (Algeo and Tribouillard, 2009; Tribouillard et al., 2012).

6.3.2. Lilstock Formation

Low mean values for Mo_{EF} , Zn_{EF} , Cd_{EF} and U_{EF} suggest a shift to oxidic conditions at the base of the Cotham Member (371.0–369.4 m). Oxidic conditions are further supported by an average Fe_T/Al which is similar to values interpreted as representing oxidic marine conditions (Lyons and Severmann, 2006; Sperling et al., 2013, 2016). Mean C_{org}/P suggests oxidic-suboxic conditions with values decreasing sharply through the Westbury–Lilstock Formation boundary (Algeo and Ingall, 2007; Algeo and Liu, 2020).

Low average values for Mo_{EF} , Zn_{EF} , TOC (%) and C_{org}/P throughout the middle Cotham Member (368.8 m–368.5 m) as well as elevated average values for Mn_{EF} and Fe_T/Al suggest oxygenated sedimentary pore waters at this time (Algeo and Ingall, 2007; Algeo and Liu, 2020). Elevated averages for Cd_{EF} and U_{EF} may be the result of increased carbonate export or adsorption onto oxides/oxyhydroxides (Tribouillard et al., 2006; Wang et al., 2013).

The most significant shift in trace element enrichment throughout the entire section is observed within the overlying upper Cotham Member (367.3 m–363.8 m). Conditions fluctuated and became increasingly oxygen poor throughout the deposition of the upper Cotham Member. This stratigraphic interval directly coincides with the initial carbon isotope excursion observed in the Carnduff-2 core as well as the main pulse of the ETME (Fig. 2) (Hesselbo et al., 2002; Guex et al., 2004; Whiteside et al., 2007, 2010; Ruhl et al., 2009, 2010, 2011; Lindström et al., 2017; Boomer et al., 2021). An increase in average Mo_{EF} , Cd_{EF} and Fe_T/Al alongside the highest average U_{EF} throughout the entire section suggests suboxic conditions restricted to sediment porewaters (Algeo and Tribouillard, 2009; Tribouillard et al., 2012; Algeo and Li, 2020) (Fig. 2). Trace element enrichments peak towards the top of the Cotham Member (364.8 m), coincident with the most negative carbon isotope values of the initial CIE. However, peak average values for Mo_{EF} , Cd_{EF} , Zn_{EF} and U_{EF} still suggest suboxic pore waters instead of anoxic pore waters or euxinic water column conditions. Significant enrichment of Mn coincident with peak trace metal enrichments may be due to carbonate saturation with respect to rhodochrosite or a Mn oxidation front (Mangini et al., 2001; Brumsack, 2006; Tribouillard

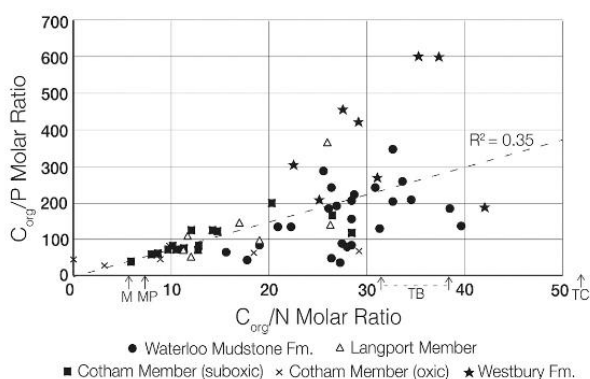


Fig. 3. C_{org}/P plotted against C_{org}/N from the Upper Triassic and lowermost Jurassic strata of the Larne Basin. Typical C_{org}/N ratios for marine organisms (M), marine phytoplankton (MP), temperate broadleaf litter (TB) and temperate coniferous litter (TC) plotted on x-axis based on Martiny et al. (2014), Ho et al. (2003) and McGroddy et al. (2004).

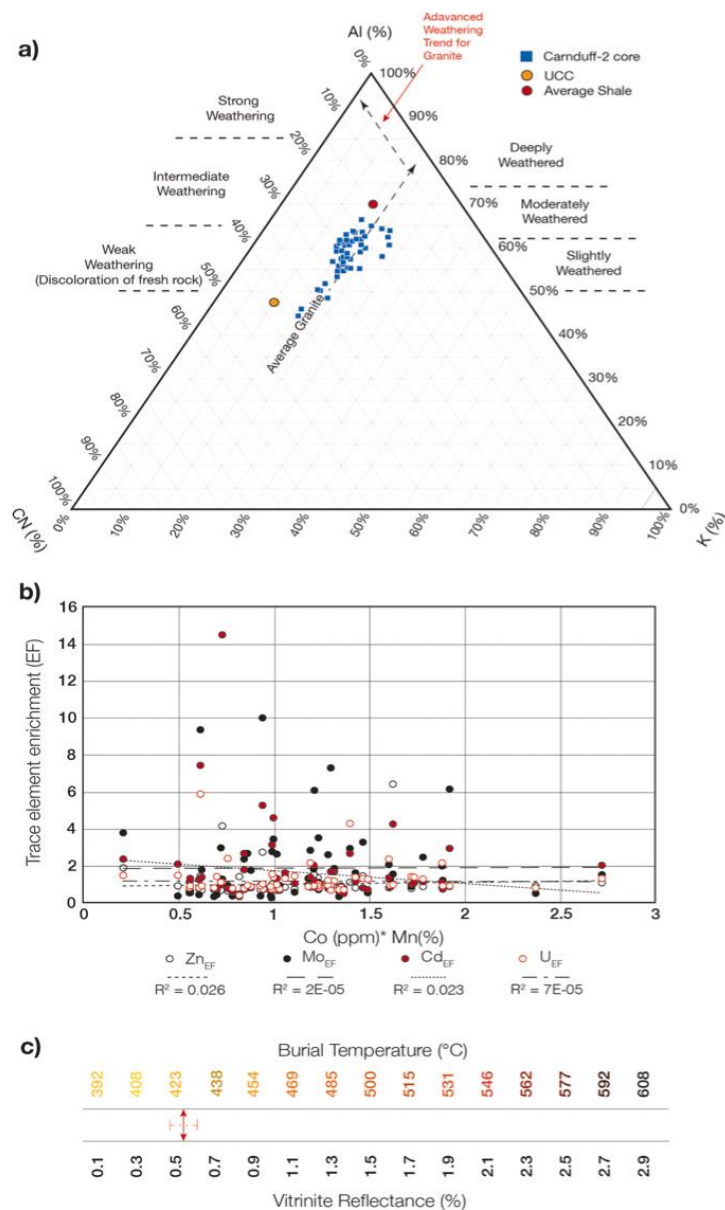


Fig. 4. Alternative controls on trace element enrichment through the Upper Triassic Carnduff-2 core, a) A-CN-K ternary plot denoting the parent lithology being weathered and transported into the Late Triassic Larne Basin, b) Trace element enrichment data plotted against palaeo-hydrography (Co*Mn), lines of best fit included in graph and R² values included in key c) Vitrinite reflectance data (GSNI unpublished data) with burial temperature conversion based on Evenick (2021).

et al., 2006).

Elevated averages for Mo_{EF}, Cd_{EF} and Fe_T/Al suggests suboxic conditions during deposition of the basal Langport Member (363.1 m–362.9 m) whilst low average Mo_{EF}, Cd_{EF}, Zn_{EF}, U_{EF}, Fe_T/Al, and C_{org}/P suggest oxic conditions throughout the deposition of the rest of the member.

6.3.3. Waterloo Mudstone Formation

Pulsed increases of Mo_{EF}, Cd_{EF}, Zn_{EF}, U_{EF} and Fe_T/Al through the basal Waterloo Mudstone Formation (357.0 m–354.7 m) suggest pulsed suboxic conditions to have occurred. Low averages for Cd_{EF}, U_{EF}, and

Zn_{EF} during the deposition of the overlying interval (353.0 m–353.8 m) would suggest more oxygenated conditions. A significant enrichment in average Mo_{EF} during this interval may be due to Mo adsorption to oxyhydroxides, however Fe_T/Al and Mn_{EF} remain relatively low on average (Berrang and Grill, 1974; Algeo and Maynard, 2004). Oxic conditions persisted during the deposition of the subsequent interval (352.6 m–350.6 m) as indicated by low sedimentary averages for Mo_{EF}, Cd_{EF}, U_{EF} and an average Fe_T/Al which is similar to oxic and detrital Fe_T/Al values as observed at other sites (Lyons et al., 2003; Lyons and Severmann, 2006; Raiswell et al., 2008; Dickson et al., 2014; Clarkson et al., 2014; Sperling et al., 2016, 2018).

Elevated Cd_{EF} , Zn_{EF} and TOC (%) alongside relatively low values for all other redox proxies at 350.4 m suggests that oxic conditions persisted through this interval alongside the increased burial of organic matter. Low average values for Cd_{EF} , Zn_{EF} , U_{EF} through to the top of the section (349.9 m–348.3 m) alongside elevated Mn_{EF} and Fe_T/Al also suggest oxic conditions. However, it remains uncertain which processes resulted in elevated Mo_{EF} towards the top of the study interval (349.7 m–349.3 m). TOC progressively increases throughout the Waterloo Mudstone Formation of the Carnduff-2 core as also noted by Jeram et al. (2021) based on outcrop studies (Fig. 2). Elevated TOC(%) values during the deposition of the Waterloo Mudstone Formation are intimately linked to increased C_{org}/P and are therefore likely related to organic matter source rather than increasingly oxygen-poor conditions.

Therefore, despite significantly elevated C_{org}/P and Fe_T/Al throughout the Late Triassic succession of the Larne Basin, conditions remained relatively oxygenated. Contrary to the photic zone euxinia reported from other Late Triassic and Early Jurassic sites, the Larne basin exhibited oxic to suboxic conditions with suboxia being mainly restricted to sedimentary pore fluids. However, redox fluctuations are observed throughout the section, including a notable shift in trace element enrichment coincident with the main pulse of the ETME.

6.4. Upper Triassic Biodiversity and extinction selectivity in the Larne Basin

To constrain the impact of Late Triassic redox fluctuations on marine organisms and ecosystem stability of the Larne Basin a palaeobiological dataset has been compiled from literature (Fig. S2) (Ivimey-Cook, 1975; Simms and Jeram, 2007; Wignall and Atkinson, 2020; Boomer et al.,

2021; Opazo and Page, 2021).

Here we use the compilation to identify two major and a single minor biodiversity change during the latest Triassic of the Larne Basin (Fig. 5). The two major biodiversity changes stratigraphically coincide with and corroborate the two major pulses of extinction identified by Wignall and Atkinson (2020) during the late Rhaetian from nine different sites globally. The first major biodiversity change occurred in the upper Westbury Formation where the temporary disappearance of ichnotaxa (*Chondrites*, *Arenicolites*, *Thalassinoides*, *Diplo craterion*, *Planolites*) is observed alongside the stepwise disappearance of 38% of bivalve taxa (8 out of 21 taxa) and a very minor miospore turnover (1 out of 8) (Fig. 5). Fish and marine reptile remains become sparse in stratigraphic deposits following this event while being common throughout the Westbury Formation. The minor biodiversity change is from the middle to the top of the Cotham member and is marked by the disappearance of 66% of dinoflagellate taxa (2 out of 3) as well as 9% of miospore taxa (1/11), and 8% (1/13) of bivalve taxa. Ichnotaxa begin to re-appear towards the top of the Cotham Member, albeit in dwarfed forms (Fig. 5). The second major biodiversity change stratigraphically spans the Langport Member where 66% of acritarch taxa disappear (2 out of 3 taxa) alongside 18% of bivalve taxa (4/22) and the disappearance of all prasinophycean taxa (2/2) (Fig. 5). The second major biodiversity reduction within the Larne Basin also coincided with the time-interval at which conodonts became extinct throughout the British Isles (Fig. 5). The upper Lilstock Formation to lower Waterloo Mudstone Formation stratigraphic interval is marked by the diversification of bivalve species with 74% of basal Jurassic species (20/27) having originated during this timeframe within the Larne Basin. Fish and marine reptile remains also become increasingly common throughout the upper Langport Member alongside the re-

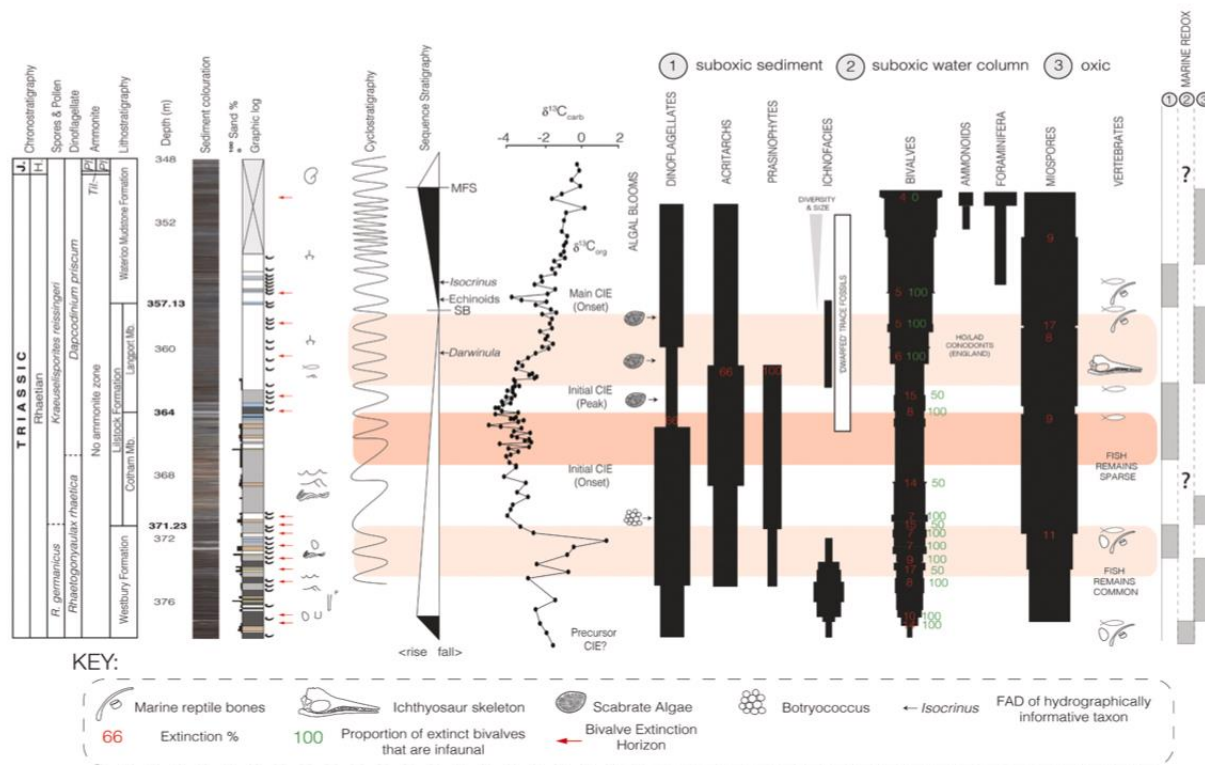


Fig. 5. Marine redox and biodiversity data spanning the Upper Triassic and lowermost Jurassic succession in the Carnduff-2 core of the Larne Basin. Carbon (carbonate) isotope data, sedimentology, and stratigraphy from Boomer et al. (2021). Carbon (organic) isotope data from Boomer et al. (2021) and Jeram et al. (2021). Cyclostratigraphy and sequence stratigraphy from Simms and Jeram (2007). For full key refer to figure 2.

appearance of echinoderm taxa (Fig. 5). Meanwhile, the lower Waterloo Mudstone Formation is marked by the re-appearance of foraminiferan and ammonoid taxa, as well as by trace fossils becoming larger and ichnofaunas more diverse (Fig. 5). Despite bivalve disappearances being generally grouped around the major extinction horizons, minor bivalve disappearances are also observed in the basal Westbury Formation, mid Cotham Member, and lower Waterloo Mudstone Formation (Fig. 5).

The majority of bivalves that went extinct in the Late Triassic Larne Basin were aragonitic (59%; 13 out of 22) with lesser extinction rates having occurred amongst bimineralic (36%; 8/22) and calcitic taxa (4.5%; 1/22). Infaunal bivalve taxa, including endobyssate bivalve species, were also disproportionately affected (77%; 17/22), whilst epibyssate (18%; 4/22) and epiplanktonic taxa (4.5%; 1/22) underwent minor extinctions. The high proportion of aragonitic bivalve species going extinct during the Late Triassic corroborates findings by Hautmann et al. (2008), who interpret the disproportionate extinction of aragonitic bivalve species to be the result of ocean acidification and aragonite undersaturation. Hautmann et al. (2008) note that infaunal species are invariably aragonitic and therefore also interpret the high extinction percentage amongst infaunal bivalves to be a function of shell mineralogy. Recent work by Opazo and Page (2021) similarly reported high extinction percentages amongst infaunal and aragonitic bivalves from the Larne Basin and, much like Hautmann et al. (2008), attribute bivalve extinction selectivity to shell mineralogy and marine acidification. However, Mander et al. (2008) interpreted shell mineralogy to be insignificant with regards to bivalve extinction selectivity during the ETME, and instead attributed high extinction percentages amongst aragonitic species to have been the result of either preservational bias, or oxygen-poor sedimentary conditions disproportionately affecting aragonitic taxa.

6.5. Linking redox change and extinction in the Late Triassic Larne Basin

In order to further test the possibility that sedimentary redox conditions directly affected bivalve biodiversity during the Triassic–Jurassic boundary interval, we analyse the correlation between bivalve disappearances and marine redox conditions based on the data acquired through this study. Of the 16 horizons involving the disappearance of bivalve taxa, 62.5% (10) occur during, immediately before, or immediately after suboxic intervals. The majority of these horizons (8) exclusively involve the disappearance of infaunal taxa, whilst the remaining horizons (2) involve the disappearance of 50% infaunal taxa (Fig. 5).

Suboxic conditions at the base of the Westbury Formation coincide with the disappearance of the shallow infaunal and semi infaunal bivalve species *Dacromya* sp. and *Gervillella* sp. Meanwhile, the basal Westbury Formation exhibits a low-diversity trace fossil assemblage consisting only of indistinct burrow mottling (Fig. 5). As the Larne Basin progressed towards oxic conditions, stratigraphically further up in the Westbury Formation, both ichnological and bivalve diversity increased sharply with bivalve origination including 71% infaunal taxa. Maximum ichnological diversity (*Planolites*, *Diplocraterion*, *Arenicolites*, *Rhizocorallium*, *Teichichnus*) is reached during stable oxic conditions, during deposition of the mid-Westbury Formation, but with ichnological diversity beginning to decrease shortly after, in the form of the disappearances of *Rhizocorallium* and *Teichichnus* (Fig. 5, Fig. 6). The reduction in trace fossil diversity directly coincided with the disappearance of infaunal bivalve taxa in the form of the semi-infaunal *Permorphus elongatus* and the shallow infaunal *Lyriomyophora postera* despite redox conditions being intrinsically oxic. These disappearances may have been due to low food/nutrient availability for infaunal species, as also suggested by McRoberts and Newton (1995), or small and/or intermittent changes in sediment redox conditions undetectable by geochemical proxies. As ichnofaunal diversity decreased during the deposition of the upper Westbury Formation (*Chondrites*, *Thalassinoides*, *Arenicolites*), sedimentary pore spaces progressed from oxic to suboxic.

Suboxic sediments also coincide with the disappearance of the shallow infaunal *Tutcheria* sp. and semi-infaunal *Modiolus sodburienis*. As suboxic conditions persisted, ichnofacies disappeared entirely whilst the shallow and deep infaunal bivalve taxa *Isocyprina ewaldi* and *Cercomya praecursor* disappeared (Fig. 5, Fig. 6, Fig. S2). The complete disappearance of the ichnotaxa *Planolites* and *Diplocraterion*, alongside the persistence of bivalve taxa may be due to differences in hypoxic sensitivity between trace makers and molluscs (Zhang and Cui, 2016) (Fig. 5). As soon as oxic conditions returned, shallow infaunal species like *Cardinia* sp. became absent. The absence of *Cardinia* sp. while conditions were intrinsically oxic may represent either a delayed response to changing marine redox conditions or one of reasons listed above (low nutrient availability, undetectable redox changes).

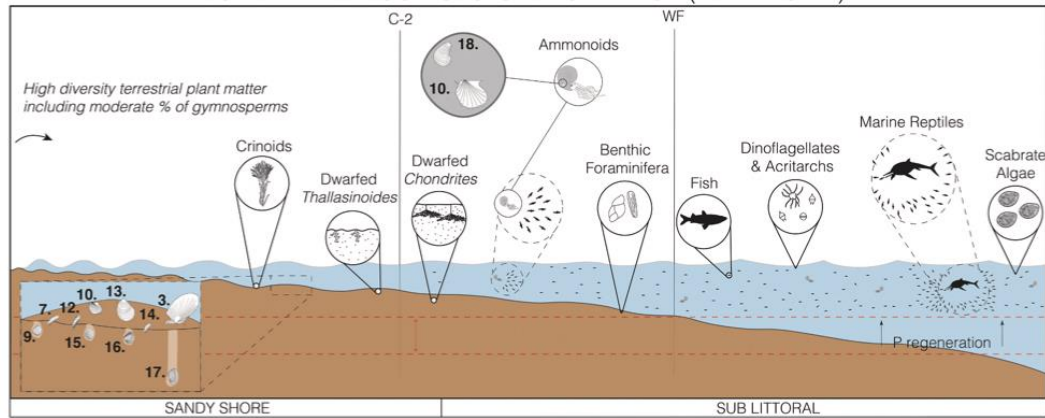
Oxic conditions returned during deposition of the basal Cotham Member with all new bivalve taxa originating during the deposition of the basal Cotham Member being infaunal (Fig. 5, Fig. 6, Fig. S2). Blooms of the freshwater algae *Botryococcus* spp. at the base of the Cotham member may suggest the increased influx of terrestrially derived material as a result of elevated run-off (Matthiessen et al., 2000), as also observed at other Tethyan sites (Van de Schootbrugge et al., 2020; Fox et al., 2022b). Alternatively, the presence of the ostracod *Darwinula*, branchiopod crustaceans and the liverwort *Naiadites* elsewhere within the formation could suggest a shift towards freshwater conditions due to a marine regression (Simms and Jeram, 2007; Boomer et al., 2021). Meanwhile, increases in prasinophycean diversity may suggest P-regeneration and potential stratification deeper within the basin (Fig. 6) (Slomp and van Cappellen, 2007; März et al., 2008; Lu et al., 2019). The semi-infaunal bivalve species *Mytilus cloacinus* is absent in the middle Cotham Member, coinciding with the enrichment of some redox sensitive proxies (U, Fe). At the same time, ichnofacies continue to be absent in the basin relative to earlier times (Fig. 5, Fig. 6). The upper Cotham Member to lower Langport Member exhibits a shift to progressively suboxic conditions within the sediments of the Larne Basin. Peak suboxic conditions within the sediment pore spaces coincided with the disappearance of the shallow infaunal bivalve species *Isocyprina concentricum*, the peak of the initial CIE, and the main pulse of the ETME (Fig. 5).

Dwarfed, low-diversity trace fossils began to re-appear during the deposition of the upper Cotham Member (Waterloo Bay Foreshore) to lower/mid Langport member (Carnduff-2 core) in the form of *Arenicolites*, *Planolites*, *Chondrites* and *Thalassinoides* (Fig. 5, Fig. 6, Fig. S2). The increased appearance of burrowing activity during the deposition of the lower/mid Langport member (Carnduff-2 core) directly preceded the return of sustained oxic conditions during deposition of the mid Langport Member (Fig. 5). Prasinophycean and acritarch taxa disappeared entirely during deposition of the mid Langport Member at the Carnduff-2 depositional locality, potentially suggesting increased oxygenation of the water column. Bivalve taxa continued to originate throughout the deposition of the Langport Member, with the majority (56%) of bivalve taxa originating at this time being infaunal. However, despite oxic conditions persisting, the shallow and semi-infaunal bivalve taxa *Pteryomya crowcombeia* and *Modiolus hillanoides* disappeared during this interval. Suboxic conditions returned during deposition of the basal Waterloo Mudstone Formation coinciding with the disappearance of *Chondrites* at the Carnduff 2 core palaeo-depositional locality (Fig. 5). The occurrence of suboxic conditions at this time also coincided with the disappearance of the shallow infaunal bivalve taxa *Protocardia rhaetica*. As sustained oxic conditions returned once again, as observed towards the top of the studied section, ichnofacies became larger and more diverse, benthic forams diversified and bivalves continued to increase in diversity with 64% of new bivalve taxa being infaunal (Fig. 5, Fig. 6, Fig. S2).

6.6. Depositional environment, facies changes and shell mineralogy controls on bivalve disappearances

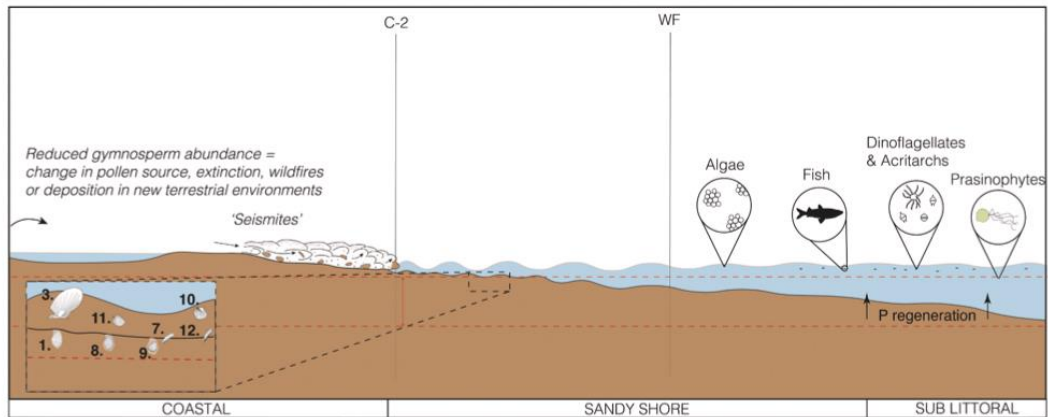
Bivalve disappearances within Upper Triassic successions of the

LOWER WATERLOO MUDSTONE FORMATION (HETTANGIAN)



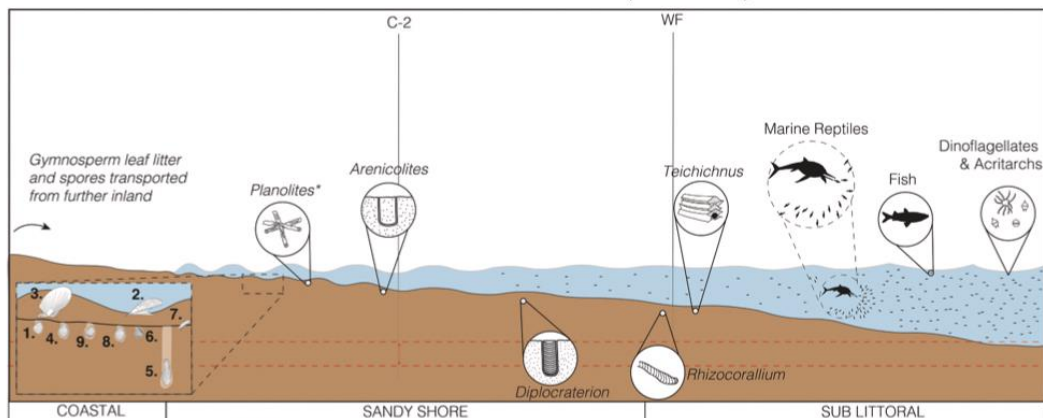
Sea level rise coupled with contraction of OMZ results in renewed biodiversity. Dwarfed ichnotaxa and geochemical data suggest chemocline still close to sediment-water boundary. However, benthic forams indicate oxic benthos near WF. Presence of ammonoids and larger nekton suggest sufficient oxygen within water column for biological function.

LOWER-MID COTHAM MEMBER (RHAETIAN)



Expansion of the OMZ and sea level fall resulted in pronounced environmental changes. Ichnotaxa disappeared due to suboxic/anoxic sediments. Persistence of bivalves may have been due to lower hypoxic sensitivity. Blooms of freshwater algae may have been due to increased run-off, and prasinophycean blooms may suggest P-regeneration, and therefore potential basin stratification.

MID WESTBURY FORMATION (RHAETIAN)



*Can range to outer shelf --- Chemocline

Oxic conditions within the water column and sediment as evidenced by geochemical data (this study) and abundance of nektonic (fish & marine reptiles), planktonic (dinoflagellates & acritarchs) and benthic organisms (bivalves, ichnotaxa).

(caption on next page)

Fig. 6. Palaeoenvironmental reconstruction of the Larne Basin throughout the latest Triassic (late Rhaetian) and earliest Jurassic (early Hettangian). The relative positions of the Carnduff-2 core (C-2), and Waterloo Bay Foreshore (WF) have been determined using ichnofacies. A representative range of bivalve taxa have been chosen for each time frame. 1- *Protocardia rhaetica*, 2- *Rhaeticicula contorta*, 3- *Chlamys valoniensis*, 4- *Isocyprina ewaldi*, 5- *Cercomya praecursor*, 6- *Lyriomyophora postera*, 7- *Modiolus hillanus*, 8- *Isocyprina concentricum*, 9- *Cardinia* sp., 10- *Oxytoma* sp., 11- *Plagiostoma punctatum*, 12- *Modiolus* sp., 13- *Plagiostoma giganteum*, 14- *Modiolus minimus*, 15- *Astarte* sp., 16- *Protocardia* sp., 17- *Pleuromya* sp., 18- *Liostrrea hisingeri*. Where exact morphology of bivalve taxa could not be found a representative specimen of the same genus has been used (e.g., 5, 8, 9, 11).

Larne Basin may therefore be associated with bivalve extinctions as a result of unfavourable marine redox conditions. Conversely, bivalve disappearances could also be associated with early shell dissolution amongst aragonitic bivalves, facies changes, and/or a shifting depositional environment (Wright et al., 2003; Hautmann et al., 2008; Opazo and Page, 2021).

Despite there being a greater proportion of aragonitic bivalves disappearing, numerous aragonitic bivalve taxa persist from the base of the section through to the Early Jurassic (e.g., *Cardinia regularis*, *Grammatodon* sp., *Modiolus hillanus*) (Fig. S2). Also, both aragonitic (59%) and bimineralic taxa (36%) undergo disappearances (Fig. S2). Therefore, bivalve disappearances are unlikely to be exclusively a function of shell mineralogy.

Meanwhile, the majority of bivalve disappearances do not correspond with changes to sedimentary facies and also include the disappearances of genera and species that undergo both regional and global extinctions (*Rhaeticicula contorta*, *Isocyprina concentricum*, *Permorpha elongatus*, *Protocardia rhaetica*, *Lyriomorpha postera*, *Mytilus cloacinus*, *Placunopsis alpina*) (Mander et al., 2008) (Fig. 5, Fig. S2). Despite there being little evidence for bivalve disappearances coinciding with a changing depositional environment, the progressive change in ichnofacies assemblage composition throughout the middle to upper Westbury Formation may be partially controlled by a falling sea level (Fig. 5, Fig. S2). However, there is little evidence that environmental or diagenetic factors are responsible for bivalve disappearances within the Upper Triassic Larne succession. Our findings therefore support the interpretations of Mander and Twitchett (2008) and suggest that the changes to infaunal biodiversity observed within the Larne Basin during the Late Triassic were caused, at least in part, by changes to marine redox state. Our findings therefore contradict, or at least complicate, interpretations by Hautmann et al. (2008) and Opazo and Page (2021) that the extinction of infaunal and aragonitic bivalve taxa was only a function of marine acidification.

7. Conclusions

Despite studies of other Upper Triassic basins recording episodic photic zone euxinia (PZE; Kasprak et al., 2015; Blumenberg et al., 2016; Fox et al., 2022a), the distribution of redox-sensitive metals in well-preserved core samples indicate that such conditions were not observed within the Larne Basin during this time. Redox conditions were oxidic to suboxic with oxygen poor conditions generally constrained to bottom water sediments. In spite of these conditions, the minor redox changes observed within the Larne Basin during the Late Triassic had a profound effect on infaunal marine organisms. Ichnofacies disappeared entirely during deposition of the upper Westbury Formation, coincident with suboxic conditions. Ichnofacies assemblages, as observed within the Carnduff-2 core, do not re-appear until those times at which sustained oxidic conditions return during deposition of the Langport Member, albeit then of low diversity and dwarfed in nature. Meanwhile, suboxic conditions within the Larne Basin consistently coincided with the extinction of infaunal bivalve taxa, whilst oxidic intervals were marked by infaunal bivalve origination. The disproportionate extinction of infaunal bivalve taxa during the ETME is often associated with shell mineralogy and ocean acidification, as infaunal bivalves are invariably aragonitic. However, the preferential extinction of infaunal organisms within the Larne Basin during the Late Triassic may be strongly associated with de-oxygenation of sedimentary pore fluids, suggesting redox change as a

possible driver of infaunal extinctions at this time.

Availability of data and materials

The datasets generated and analysed during the current study are available in the Supplementary Information of this paper.

Funding

This work was funded by a NERC DTP PhD Studentship NE/L002485/1 awarded to ADB. Sample collection at the Northern Ireland Geological Survey (GSNI) was funded through the Irish Centre for research in Applied Geoscience (iCRAG) (MR).

Declaration of Competing Interest

The authors declare that they have no competing interests.

Acknowledgements

We would like to thank Mr. James Brakeley and Mr. Philip Holdship for assisting with ICP-AES and ICP-MS measurements. We thank Giovanna Della Porta and an anonymous reviewer for their comments that improved the manuscript. This work was funded by the Natural Environmental Research Council (NE/L002485/1).

Appendix A. Supplementary data

Supplementary data to this article can be found online at <https://doi.org/10.1016/j.palaeo.2022.111018>.

References

- Algeo, T.J., 2004. Can marine anoxic events draw down the trace element inventory of seawater? *Geol* 32 (12), 1057–1060.
- Algeo, T.J., Ingall, E., 2007. Sedimentary C_{org}/P ratios, paleocean ventilation and Phanerozoic atmospheric pO_2 . *Palaeogeog., Palaeoclim., Palaeoecol.* 256, 130–155.
- Algeo, T.J., Li, C., 2020. Redox classification and calibration of redox thresholds in sedimentary systems. *Geochim. Cosmochim. Acta* 287, 8–26.
- Algeo, T.J., Liu, J., 2020. A re-assessment of elemental proxies for paleoredox analysis. *Chem. Geol.* 540, 119549.
- Algeo, T.J., Lyons, T.W., 2006. Mo-total organic carbon covariation in modern anoxic marine environments: Implications for analysis of paleoredox and paleohydrographic conditions. *Paleoceanograph.* 21 (1), 1–23.
- Algeo, T.J., Maynard, J.B., 2004. Trace-element behavior and redox facies in core shales of Upper Pennsylvanian Kansas-type cyclothems. *Chem. Geol.* 206, 289–318.
- Algeo, T.J., Tribouillard, N., 2009. Environmental analysis of paleoceanographic systems based on molybdenum-uranium covariation. *Chem. Geol.* 268, 211–225.
- Aller, R.C., Mackin, J.E., Cox, R.T., 1986. Diagenesis of Fe and S in Amazon inner shelf muds: apparent dominance of Fe reduction and implications for the genesis of ironstones. *Cont. Shelf Res.* 6, 263–289.
- Anderson, L.A., Sarmiento, J.L., 1994. Redfield ratios of remineralisation determined by nutrient data analysis. *Glob. Biogeochem. Cycles* 8 (1), 65–80.
- Anderson, R.F., Fleisher, M.Q., LeHuray, A.P., 1989. Concentration, oxidation state and particulate flux of uranium in the Black Sea. *Geochim. Cosmochim. Acta* 53, 2215–2224.
- Andeskie, A.S., Benison, K.C., Eichenlaub, L.A., Raine, R., 2018. Acid-saline-lake systems of the Triassic Mercia Mudstone Group, County Antrim, Northern Ireland. *J. Sediment. Res.* 88, 385–398.
- Atkinson, J.W., Wignall, P.B., 2019. How quick was marine recovery after the end-Triassic mass extinction and what role did anoxia play? *Palaeogeogr., Palaeoclimatol., Palaeoecol.* 528, 99–119.
- Barras, C.G., Twitchett, R.J., 2007. Response of marine infauna to Triassic–Jurassic environmental change: ichnological data from southern England. *Palaeogeogr., Palaeoclimatol., Palaeoecol.* 244, 223–241.

- Beith, S.J., Fox, C.P., Marshall, J.E.A., Whiteside, J.H., 2021. Recurring photic zone euxinia in the northwest Tethys impinged end-Triassic extinction recovery. *Palaeogeogr. Palaeoclimatol. Palaeoecol.* 584, 110680.
- Belcher, C.M., Mander, L., Rein, G., Jervis, F.X., Haworth, M., Hesselbo, S.P., Glasspool, I. J., McElwain, J.C., 2010. Increased fire activity at the Triassic/Jurassic boundary in Greenland due to climate-driven floral change. *Nat. Geosci.* 3, 426–429.
- Berrang, P.G., Grill, E.V., 1974. The effect of manganese oxide scavenging on molybdenum in Saanich Inlet, British Columbia. *Mar. Chem.* 2 (2), 125–148.
- Blackburn, T.J., Olsen, P.E., Bowring, S.A., McLean, N.M., Kent, D.V., Puffer, J., Kent, D. V., McHone, G., Rasbury, E.T., Et-Touhami, M., 2013. Zircon U-Pb geochronology links the end-Triassic extinction with the Central Atlantic Magmatic Province. *Sci.* 340 (6135), 941–945.
- Blumenberg, M., Heunisch, C., Lückge, A., Scheeder, G., Wiese, F., 2016. Photic zone euxinia in the central Rhaetian Sea prior the Triassic-Jurassic boundary. *Palaeogeogr., Palaeoclimatol. Palaeoecol.* 461, 55–64.
- Bonis, N.R., Ruhl, M., Kürschner, W.M., 2010. Climate change driven black shale deposition during the end-Triassic in the western Tethys. *Palaeogeogr. Palaeoclimatol. Palaeoecol.* 299, 151–159.
- Boomer, I., Copestake, P., Raine, R., Azmi, A., Fenton, J.P.G., Page, K.N., O'Callaghan, M., 2021. Stratigraphy, palaeoenvironments and geochemistry across the Triassic-Jurassic boundary transition at Carnduff, County Antrim, Northern Ireland. *Proc. Geol. Assoc.* 132 (6), 667–687.
- Brunsack, H.-J., 2006. The trace metal content of recent organic carbon-rich sediments: Implications for cretaceous black shale formation. *Palaeogeogr. Palaeoclimatol. Palaeoecol.* 232, 344–361.
- Burkhardt, B.G., Watkins-Brandt, K.S., Defforey, D., Paytan, A., White, A.E., 2014. Remineralization of phytoplankton-derived organic matter by natural populations of heterotrophic bacteria. *Mar. Chem.* 163, 1–9.
- Calvert, S.E., Pedersen, T.F., 1993. Geochemistry of recent oxic and anoxic marine sediments: Implications for the geological record. *Mar. Geol.* 13, 67–88.
- Canfield, D.E., 1989. Reactive iron in marine sediments. *Geochim. Cosmochim. Acta* 53, 619–632.
- Casacci, M., Bertinelli, A., Algeo, T.J., Rigo, M., 2016. Carbonate-to-biosilica transition at the Norian-Rhaetian boundary controlled by rift-related subsidence in the western Tethyan Lagonegro Basin (southern Italy). *Palaeogeogr. Palaeoclimatol. Palaeoecol.* 456, 21–36.
- Chen, L., Little, S.H., Kreissig, K., Severmann, S., McManus, J., 2021. Isotopically Light Cd in Sediments underlying Oxygen Deficient zones. *Front. Earth Sci.* 9, 623720.
- Clarkson, M.O., Poulton, S.W., Guilbaud, R., Wood, R., 2014. Assessing the utility of Fe/Al and Fe-speciation to record water column redox conditions in carbonate-rich sediments. *Chem. Geol.* 382, 111–122.
- Daskalakis, K.D., Helz, G.R., 1993. The solubility of sphalerite (ZnS) in sulfidic solutions at 25°C and 1 atm pressure. *Geochim. Cosmochim. Acta* 57 (20), 4923–4931.
- Davelaar, D., 1993. Ecological significance of bacterial polyphosphate metabolism in sediments. *Hydrobiol.* 253, 179–192.
- Davies, J.H.F.L., Marzoli, A., Bertrand, H., Youbi, N., Ernesto, M., Schaltegger, U., 2017. End-Triassic mass extinction started by intrusive CAMP activity. *Nat. Comm.* 8, 15596.
- Dickson, A.J., Rees-Owen, R.L., März, C., Coe, A.L., Cohen, A.S., Pancost, R.D., Taylor, K., Shcherbinina, E., 2014. The spread of marine anoxia on the northern Tethys margin during the Palaeocene-Eocene Thermal Maximum. *Paleoceanogr.* 29, 471–488.
- Dickson, A.J., Idiz, E., Porcelli, D., van den Boorn, S.H.J.M., 2020. The influence of thermal maturity on the stable isotope compositions and concentrations of molybdenum, zinc and cadmium in organic-rich marine mudrocks. *Geochim. Cosmochim. Acta* 287, 205–220.
- Dickson, A.J., Idiz, E., Porcelli, D., Murphy, M.J., Celestino, R., Jenkyns, H.C., Poulton, S. W., Hesselbo, S.P., Hooker, J.N., Ruhl, M., van den Boorn, S.H.J.M., 2022. No effect of thermal maturity on the Mo, U, Cd, and Zn isotope compositions of lower Jurassic organic-rich sediments. *Geology*. <https://doi.org/10.1130/G49724.1>.
- Du, Y., Chiari, M., Viktor, K., Nicora, A., Onoue, T., Pálffy, J., Roghi, G., Tomimatsu, Y., Rigo, M., 2020. The asynchronous disappearance of conodonts: New constraints from Triassic-Jurassic boundary sections in the Tethys and Panthalassa. *Earth Sci. Rev.* 203, 1–18.
- Dunhill, A.M., Foster, W.J., Sciberras, J., Twitchett, R.J., 2018. Impact of the late Triassic mass extinction on functional diversity and composition of marine ecosystems. *Palaeontol.* 61, 133–148.
- Eldijk, Van, Wappler, T., Strother, P.K., Van der Weijst, C.M.H., Rajaei, H., Visscher, H., Van de Schootbrugge, B., 2018. A Triassic-Jurassic window into the evolution of Lepidoptera. *Sci. Adv.* 4 (1), 1701568.
- Erickson, B.E., Helz, G.R., 2000. Molybdenum (VI) Speciation in Sulfidic Waters: Stability and Lability of Thiomolybdates. *Geochim. Cosmochim. Acta* 64, 1149–1158.
- Evenick, J.C., 2021. Examining the relationship between Tmax and vitrinite reflectance: an empirical comparison between thermal maturity indicators. *J. Nat. Gas Sci. Eng.* 91, 103946 <https://doi.org/10.1016/j.jngse.2021.103946>.
- Fischer, J., Voigt, S., Franz, M., Schneider, J.W., Joachimski, M.M., Tichomirowa, M., Götze, J., Furrer, H., 2012. Palaeoenvironments of the late Triassic Rhaetian Sea: implications from oxygen and strontium isotopes of hybridont shark teeth. *Palaeogeogr. Palaeoclimatol. Palaeoecol.* 353–355, 60–72.
- Flügel, E., Kiessling, W., 2002. Patterns of Phanerozoic Reef crises. *SEPM Spec. Pub.* 72, 691–733.
- Fox, C.P., Whiteside, J.H., Olsen, P.E., Cui, Xingqian, Summons, R.E., Idiz, E., Grice, K., 2022a. Two-pronged killing mechanism at the end-Triassic mass extinction. *Geol.* <https://doi.org/10.1130/G49560.1>.
- Fox, C.P., Whiteside, J.H., Olsen, P.E., Grice, K., 2022b. Flame out! End-Triassic mass extinction polycyclic aromatic hydrocarbons reflect more than just fire. *Earth Planet. Sci. Lett.* 584, 117418 <https://doi.org/10.1016/j.epsl.2022.117418>.
- Framson, P.E., Leckie, J.O., 1978. Limits of coprecipitation of cadmium and ferrous sulfides. *Environ. Sci. Technol.* 12, 465–469.
- Gingras, M.K., MacEachern, J.A., Dashtgard, S.E., 2012. The potential of trace fossils as tidal indicators in bays and estuaries. *Sediment. Geol.* 279, 97–106.
- Greene, S.E., Martindale, R.C., Ritterbush, K.A., Bottjer, D.J., Corsetti, F.A., Berelson, W. M., 2012. Recognising Ocean acidification in deep time: an evaluation of the evidence for acidification across the Triassic-Jurassic boundary. *Earth Sci. Rev.* 113 (1–2), 72–93.
- Guex, J., Bartolini, A., Atudorei, V., Taylor, D., 2004. High-resolution ammonite and carbon isotope stratigraphy across the Triassic-Jurassic boundary at New York Canyon (Nevada). *Earth Planet. Sci. Lett.* 225, 29–41.
- Hallam, A., 2002. How catastrophic was the end-Triassic mass extinction? *Lethaia* 35 (2), 147–157.
- Hardisty, D.S., Riedinger, N., Planavsky, N.J., Asael, D., Andrén, T., Jørgensen, B.B., Lyons, T.W., 2016. A Holocene history of dynamic water column redox conditions in the Landsort deep, Baltic Sea. *Am. J. Sci.* 316, 713–745.
- Hautmann, M., Benton, M.J., Tomašových, A., 2008. Catastrophic Ocean acidification at the Triassic-Jurassic boundary. *Neues Jahrb. Geol. Paläontol.* 249, 119–127.
- He, T., Dal Corso, J., Newton, R.J., Wignall, P.B., Mills, B.J.W., Di Todaro, S., Stefano, P., Turner, E.C., Jamieson, R.A., Randazzo, V., Rigo, M., Jones, R.E., Dunhill, A.M., 2020. An enormous sulfur isotope excursion indicates marine anoxia during the end-Triassic. *Sci. Adv.* 6 (37), eabb6704. <https://doi.org/10.1126/sciadv.abb6704>.
- He, T., Wignall, P.B., Newton, R.J., Atkinson, J.W., Keeling, J.F.J., Xiong, Y., Poulton, S. W., 2022. Extensive marine anoxia in the European epicontinental sea during the end-Triassic mass extinction. *Glob. Planet. Change* 210, 103771. <https://doi.org/10.1016/j.gloplacha.2022.103771>.
- Hein, J.R., Koschinsky, A., Halbach, P., Manheim, F.T., Bau, M., Kang, J.-K., Lubick, N., Nicklson, K., Hein, J.R., Bühn, B., Dasgupta, S. (Eds.), 1997. *Geol. Soc. Spec. Publ.* 199, 123–138.
- Helz, G., Vorlíček, T., 2019. Precipitation of molybdenum from euxinic waters and the role of organic matter. *Chem. Geol.* 509, 178–193.
- Helz, G.R., Miller, C.V., Charnock, J.M., Mosseimans, J.F.W., Patrick, R.A.D., Garner, C. D., Vaughan, D.J., 1996. Mechanism of molybdenum removal from the sea and its connections in black shales: EXAFS evidence. *Geochim. Cosmochim. Acta* 60 (19), 3631–3642.
- Hesselbo, S.P., Robinson, S.A., Surlyk, F., Piasecki, S., 2002. Terrestrial and marine mass extinction at the Triassic/Jurassic boundary synchronized with initiation of massive volcanism. *Geol.* 30 (3), 251–254.
- Ho, T.-Y., Quigg, A., Finkel, Z.V., Milligan, A.J., Wyman, K., Falkowski, P.G., Morel, F.M. M., 2003. The elemental composition of some marine phytoplankton. *J. Phycol.* 39, 1145–1159.
- Hodges, M.S., Stanley, G.D., 2015. North American coral recovery after the end-Triassic mass extinction, New York Canyon, Nevada, USA. *GSA Today* 25 (10), 4–9.
- Hofmann, R., Mángano, M.G., Elicki, O., Shinaq, R., 2012. Paleoclimatic and biostratigraphic significance of trace fossils from shallow- to marginal-marine environments from the middle Cambrian (stage 5) of Jordan. *J. Paleontol.* 86 (6), 931–955.
- Hönisch, B., Ridgwell, A., Schmidt, D.N., Thomas, E., Gibbs, S., Rias, J., Sluvis, A., Zeebe, R., Kump, L., Martindale, R.C., Greene, S.E., Kiessling, W., Ries, J., Zachos, J.C., Royer, D.L., Barker, S., Marchitto Jr., T.M., Moyer, R., Pelejero, C., Ziveri, P., Foster, G.L., Williams, B., 2012. The Geological Record of Ocean Acidification. *Sci.* 335 (6072), 1058–1063.
- Howard, A.S., Warrington, G., Ambrose, K., Rees, J.G., 2008. A formational framework for the Mercia Mudstone Group (Triassic) of England and Wales. In: *British Geological Survey, Research Report RR/08/04* (41 p).
- Ingall, E., Jahnke, R., 1994. Evidence for enhanced phosphorus regeneration from marine sediments overlain by oxygen depleted waters. *Geochim. Cosmochim. Acta* 58, 2571–2575.
- Ingall, E.D., Van Cappellen, P., 1990. Relation between sedimentation rate and burial of organic phosphorus and organic carbon in marine sediments. *Geochim. Cosmochim. Acta* 54, 373–386.
- Ingall, E., Kolowith, L., Lyons, T., Hurtgen, M., 2005. Sediment carbon, nitrogen and phosphorus cycling in an anoxic fjord, Effingham Inlet, British Columbia. *Am. J. Sci.* 305, 240–258.
- Ivimey-Cook, H.C., 1975. The stratigraphy of the Rhaetic and lower Jurassic in East Antrim. *Bull. Geol. Surv. G. B.* 50, 51–69.
- Janssen, D.J., Conway, T., John, S.G., Christian, J.R., Kramer, D.J., Pedersen, T.F., Cullen, J.T., 2014. Undocumented water column sink for cadmium in open ocean oxygen-deficient zones. *PNAS* 111 (19), 6888–6893.
- Jaraula, C.M.B., Grice, K., Twitchett, R.J., Böttcher, M.E., LeMetayer, P., Dastidar, A.G., Opazo, L.F., 2013. Elevated pCO₂ leading to Late Triassic extinction, persistent photic zone euxinia, and rising sea levels. *Geol.* 41 (9), 955–958.
- Jeram, A.J., Simms, M.J., Hesselbo, S.P., Raine, R., 2021. Carbon isotopes, ammonites and earthquakes: Key Triassic-Jurassic boundary events in the coastal sections of south-east County Antrim, Northern Ireland, UK. *Proc. Geol. Assoc.* 132, 702–725.
- Jost, A.B., Bachan, A., van de Schootbrugge, B., Brown, S.T., DePaolo, D.J., Payne, J.L., 2017a. Additive effects of acidification and mineralogy on calcium isotopes in Triassic/Jurassic boundary limestones. *Geochim. Geophys. Res.* 18 (1), 113–124.
- Jost, A.B., Bachan, A., van de Schootbrugge, B., Lau, K.V., Weaver, K.L., Maher, K., Payne, J.L., 2017b. Uranium isotope evidence for an expansion of marine anoxia during the end-Triassic extinction. *Geochim. Geophys. Res.* 18 (8), 3093–3108.

- Kasprak, A.H., Sepulveda, J., Price-Waldman, R., Williford, K.H., Schoepfer, S.D., Haggart, J.W., Ward, P.D., Summons, R.E., Whiteside, J.H., 2015. Episodic photoic zone euxinia in the northeastern Panthalassic Ocean during the end-Triassic extinction. *Geol.* 43, 307–310.
- Kiessling, W., Aberhan, M., Brenneis, B., Wagner, P.J., 2007. Extinction trajectories of benthic organisms across the Triassic-Jurassic boundary. *Palaeogeogr. Palaeoclimatol. Palaeoecol.* 244 (1–4), 201–222.
- Korte, C., Ruhl, M., Pálffy, J., Ullmann, C.V., Hesselbo, S.P., 2019. Chemostratigraphy across the Triassic–Jurassic boundary. In: Sial, A.N., Gaucher, C., Ramkumar, M., Ferreira, V.P. (Eds.), *Chemostratigraphy across Major Chronological Boundaries*, Geophysical Monograph, First edition. John Wiley & Sons, Inc., pp. 185–210.
- Kovács, E.B., Ruhl, M., Demény, A., Fórizs, I., Hegyi, I., Horváth-Kostva, Z.R., Mórincz, F., Vallner, Z., Pálffy, J., 2020. Mercury anomalies and carbon isotope excursions in the western Tethyan Csóvár section support the link between CAMP volcanism and the end-Triassic extinction. *Glob. Planet. Change* 194, 103291.
- Kozur, H., Mock, R., 1991. New Middle Carnian and Rhaetian conodonts from Hungary and the Alps, stratigraphic importance and tectonic implications for the Buda Mountains and adjacent areas. *J. Geol. Bundesanst.* 134, 271–297.
- Kürschner, W.M., Batenburg, S.J., Mander, L., 2013. Aberrant *Classopollis* pollen reveals evidence for unreduced (2n) pollen in the conifer family Cheirolepidiaceae during the Triassic–Jurassic transition. *Proc. R. Soc. B* 280, 20131708.
- Kürschner, W.M., Mander, L., McElwain, J.C., 2014. A gymnosperm affinity for *Ricciisporites tuberculatus* Lundblad: implications for vegetation and environmental reconstructions in the late Triassic. *Palaeobiodiv. Palaeoenviron.* 94 (2), 295–305.
- Laborde-Casadaban, M., Homberg, C., Schnyder, J., Borderie, S., Raine, R., 2021. Do soft sediment deformations in the late Triassic and early Jurassic of the UK record seismic activity during the break-up of Pangaea? *Proc. Geol. Assoc.* 132, 688–701.
- Li, L., Wang, Y., Vajda, V., Liu, Z., 2018. Late Triassic ecosystem variations inferred by palynological records from Hechuan, southern Sichuan Basin, China. *Geol. Mag.* 155 (8), 1793–1810.
- Lindström, S., Pedersen, G.K., van de Schootbrugge, B., Hansen, K.H., Kuhlmann, N., Thein, J., Johansson, L., Petersen, H.L., Alwmark, C., Dybkjær, K., Weibel, R., Erlström, M., Nielsen, L.H., Oschmann, W., Tegner, C., 2015. Intense and widespread seismicity during the end-Triassic mass extinction due to emplacement of a large igneous province. *Geol.* 43 (5), 387–390.
- Lindström, S., van de Schootbrugge, B., Hansen, K.H., Pedersen, G.K., Alsen, P., Thibault, N., Dybkjær, K., Bjerrum, C.J., Nielsen, L.H., 2017. *Palaeogeogr., Palaeoclimatol. Palaeoecol.* 478, 80–102.
- Lindström, S., Nytoft, H.P., Pedersen, G.K., Niedzwiedski, G., Dybkjær, K., Johansson, L., Petersen, H.L., Sanei, H., Tegner, C., Weibel, R., 2020. Land plants and terrestrial environmental changes during the onset of the end-Triassic event. *EGU General Assembly 2020, Online, (4–8 May 2020)*. <https://doi.org/10.5194/egusphere-egu2020-20732>.
- Lu, J., Zhu, B., Struewing, I., Xu, N., Duan, S., 2019. Nitrogen–phosphorus-associated metabolic activities during the development of a cyanobacterial bloom revealed by metatranscriptomics. *Sci. Rep.* 9, 2840. <https://doi.org/10.1038/s41598-019-38481-2>.
- Lyons, T.W., Severmann, S., 2006. A critical look at iron paleoredox proxies based on new insights from modern anoxic basins. *Geochim. Cosmochim. Acta* 70, 5698–5722.
- Lyons, T.W., Werne, J.P., Hollander, D.J., Murray, J.W., 2003. Contrasting sulfur geochemistry and Fe/Al and Mo/Al ratios across the last oxic-to-anoxic transition in the Cariaco Basin, Venezuela. *Chem. Geol.* 195, 131–157.
- MacQuaker, J.H.S., 1999. Aspects of the sedimentology of the Westbury Formation. In: Swift, A., Martill, D.M. (Eds.), *Fossils of the Rhaetian Penarth Group*. The Palaeontological Association, pp. 39–48.
- Mander, L., Twitchett, R.J., 2008. Quality of the Triassic–Jurassic bivalve fossil record in Northwest Europe. *Palaeontol.* 51 (6), 1213–1223.
- Mander, L., Twitchett, R.J., Benton, M.J., 2008. Palaeoecology of the late Triassic extinction event in the SW UK. *J. Geol. Soc.* 165, 319–332.
- Mangini, A., Jung, M., Laukenmann, S., 2001. What do we learn from peaks of uranium and of manganese in deep sea sediments? *Mar. Geol.* 177, 63–78.
- Manning, P.L., Wilson, H.E., 1975. The stratigraphy of the Larne Borehole, County Antrim. *Bull. Geol. Surv. G. B.* 50, 1–50.
- Martiny, A.C., Vrugt, J.A., Lomas, M.W., 2014. Concentrations and ratios of particulate organic carbon, nitrogen, and phosphorus in the global ocean. *Sci. Data* 1, 140048.
- Marynowski, L., Simoneit, B.R.T., 2009. Widespread Upper Triassic to lower Jurassic wildfire records from Poland: evidence from charcoal and pyrolytic polycyclic aromatic hydrocarbons. *Palaios* 24, 785–798.
- März, C., Poulton, S.W., Beckmann, B., Kuester, K., Wagner, T., Kasten, S., 2008. Redox sensitivity of P cycling during marine black shale formation: Dynamics of sulfidic and anoxic, non-sulfidic bottom waters. *Geochim. Cosmochim. Acta* 72, 3703–3717.
- Marzoli, A., Bertrand, H., Knight, K.B., Cirilli, S., Buratti, N., Vèrati, C., Nomade, S., Renne, P.R., Youbi, N., Martini, R., Allenbach, K., Neuwerth, R., Rapaille, C., Zaninetti, L., Bellieni, G., 2004. Synchrony of the Central Atlantic magmatic province and the Triassic–Jurassic boundary climatic and biotic crisis. *Geol.* 32 (11), 973–976.
- Matthiessen, J., Kunz-Pirrung, M., Mudie, P.J., 2000. Freshwater chlorophycean algae in recent marine sediments of the Beaufort, Laptev and Kara Seas (Arctic Ocean) as indicators of river runoff. *Int. J. Earth Sci.* 89, 470–485.
- Mayall, M.J., 1983. An earthquake origin for synsedimentary deformation in a late Triassic (Rhaetian) lagoonal sequence, Southwest Britain. *Geol. Mag.* 120, 613–622.
- McCann, N., 1990. The Subsurface Geology between Belfast and Larne, Northern Ireland. *Ir. J. Earth Sci.* 10, 157–173.
- McElwain, J.C., Popa, M.E., Hesselbo, S.P., Haworth, M., Surlyk, F., 2007. Macroecological responses of terrestrial vegetation to climatic and atmospheric change across the Triassic/Jurassic boundary in East Greenland. *Paleobiol.* 33 (4), 547–573.
- McGroddy, M., Daufresne, T., Hedin, L., 2004. Scaling of C:N:P stoichiometry in forests worldwide: implications of terrestrial Redfield-type ratios. *Ecol.* 85, 2390–2401.
- McKie, T., Williams, B., 2009. Triassic palaeogeography and fluvial dispersal across the northwest European Basins. *Geol. J.* 44, 711–741.
- McManus, J., Berelson, W.M., Klinkhammer, G.P., Hammond, D.E., Holm, C., 2005. Authigenic uranium: relationship to oxygen penetration depth and organic carbon rain. *Geochim. Cosmochim. Acta* 69, 95–108.
- McRoberts, C.A., Newton, C.R., 1995. Selective extinction among end-Triassic European bivalves. *Geol.* 23, 102–104.
- Mitchell, I., 2004. *The Geology of Northern Ireland: Our Natural Foundation*, 1st edition. British Geological Survey.
- Morford, J.L., Emerson, S., 1999. The geochemistry of redox sensitive trace metals in sediment. *Geochim. Cosmochim. Acta* 63 (11–12), 1735–1750.
- Morford, J.L., Russell, A.D., Emerson, S., 2001. Trace metal evidence for changes in the redox environment associated with the transition from terrigenous clay to diatomaceous sediments, Saanich Inlet, BC, Mar. Geol. 174, 355–369.
- Olsen, P.E., Kent, D.V., Sues, H.-D., Koeberl, C., Huber, H., Montanari, A., Rainforth, E.C., Fowell, S.J., Szajna, M.J., Hartline, B.W., 2002. Ascent of dinosaurs linked to an iridium anomaly at the Triassic–Jurassic boundary. *Sci.* 296 (5571), 1305–1307.
- Opazo, L.F., Page, K.N., 2021. Palaeoecological patterns of change in marine invertebrate faunas across the End-Triassic mass extinction event: evidence from Larne, Northern Ireland. *Proc. Geol. Assoc.* 132 (6), 726–742.
- Owens, J.D., Lyons, T.W., Hardisty, D.S., Lowery, C.M., Lu, Z., Lee, B., Jenkyns, H.C., 2016. Patterns of local and global redox availability during the Cenomanian–Turonian Boundary Event (Oceanic Anoxic Event 2) recorded in carbonates and shales from Central Italy. *Sedimentol.* 64 (1), 168–185.
- Percival, L.M.E., Ruhl, M., Hesselbo, S.P., Jenkyns, H.C., Mather, T.A., Whiteside, J.H., 2017. Mercury evidence for pulsed volcanism during the end-Triassic mass extinction. *PNAS USA* 114 (30), 7929–7934.
- Petersen, H.L., Lindström, S., 2012. Synchronous wildfire activity rise and mire deforestation at the Triassic–Jurassic boundary. *PLoS One* 7 (10), 47236.
- Piper, D.Z., Calvert, S.E., 2009. A marine biogeochemical perspective on black shale deposition. *Earth Sci. Rev.* 95, 63–96.
- Pruyters, P.A., de Lange, G.J., Middelburg, J.J., Hydes, D.J., 1993. The diagenetic formation of metal-rich layers in sapropel-containing sediments in eastern Mediterranean. *Geochim. Cosmochim. Acta* 57, 527–536.
- Quan, T.M., van de Schootbrugge, B., Field, M.P., Rosenthal, Y., Falkowski, P.G., 2008. Nitrogen isotope and trace metal analyses from the Mingolshiem core (Germany): Evidence for redox variations across the Triassic–Jurassic boundary. *Glob. Biogeochem. Cycles* 22 (2), 1–14.
- Raine, R., Copestake, P., Simms, M.J., Boomer, I., 2021. Uppermost Triassic to Lowermost Jurassic sediments of the island of Ireland and its surrounding basins. *Proc. Geol. Assoc.* 132 (6), 627–640.
- Raiswell, R., Newton, R., Bottrell, S.H., Coburn, P., Briggs, D.E.G., Bond, D.P.G., Poulton, S.W., 2008. Turbidite depositional influences on the diagenesis of Beecher's Trilobite Bed and the Hunsrück Slate: Sites of soft tissue preservation. *Am. J. Sci.* 308, 105–129.
- Raiswell, R., Hardisty, D.S., Lyons, T.W., Canfield, D.E., Owens, J.D., Planavsky, N.J., Poulton, S.W., Reinhard, C.T., 2018. The iron paleoredox proxies: a guide to the pitfalls, problems and proper practice. *Am. J. Sci.* 318, 491–526.
- Redfield, A.C., 1958. *The Biological Control of Chemical Factors in the Environment*. Am. Sci. 46, 205–221.
- Redfield, A.C., Ketchum, B.H., Richards, F.A., 1963. The Influence of Organisms on the Composition of the Sea Water. In: Hill, M.N. (Ed.), *The Sea*, vol. 2. Interscience Publishers, New York, pp. 26–77.
- Reid, C.G.R., Bancroft, A.J., 1986. The Irish lower Jurassic type ammonites of Major-General J.E. Portlock (1843): *Leptechioceras macdonnellii*, *Psiloceras (Caloceras) intermedium*, and *Psiloceras (Psiloceras) sampsoni*. *Ir. J. Earth Sci.* 8, 41–51.
- Richo, S., van de Schootbrugge, B., Pross, J., Püttmann, W., Quan, T.M., Lindström, S., Heinisch, C., Fiebig, J., Maquil, R., Schouten, S., Hauzenberger Wignall, P.B., 2012. Hydrogen sulphide poisoning of shallow seas following the end-Triassic extinction. *Nat. Geosci.* 5 (9), 662–667.
- Ros, S., De Renzi, M., Damborenea, S.E., Márquez-Aliaga, A., 2011. Coping between crises: early Triassic–early Jurassic bivalve diversity dynamics. *Palaeogeogr., Palaeoclimatol. Palaeoecol.* 311, 184–199.
- Rosenthal, Y., Lam, P., Boyle, E.A., Thomson, J., 1995. Authigenic cadmium enrichments in suboxic sediments: Precipitation and postdepositional mobility. *Earth Planet. Sci. Lett.* 132, 99–111.
- Rudnick, R.L., Gao, S., 2003. The Composition of the Continental Crust. In: Holland, H. D., Turekian, K.K. (Eds.), *Treatise on Geochemistry, The Crust*, vol. 3. Elsevier–Pergamon, Oxford, pp. 1–64.
- Rue, E.L., Smith, G.J., Cutter, G.A., Bruland, K.W., 1997. The response of trace element redox couples to suboxic conditions in the water column. *Deep-Sea Res.* 44 (1), 113–134.
- Ruhl, M., Kürschner, W.M., Krystyn, L., 2009. Triassic–Jurassic organic carbon isotope stratigraphy of key sections in western Tethys realm (Austria). *Earth Planet. Sci. Lett.* 281, 169–187.
- Ruhl, M., Veld, H., Kürschner, W.M., 2010. Sedimentary organic matter characterization of the Triassic–Jurassic boundary GSSP at Kuhjoch (Austria). *Earth Planet. Sci. Lett.* 292, 17–26.
- Ruhl, M., Bonis, N.R., Reichart, G.J., Damste, J.S.S., Kürschner, W.M., 2011. Atmospheric carbon injection linked to end-Triassic mass extinction. *Sci. Rep.* 333 (6041), 430–434.

- Ruhl, M., Hesselbo, S.P., Al-Suwaidi, A., Jenkyns, H.C., Damborenea, S.E., Mancenido, M.O., Storm, M., Mather, T.A., Riccardi, A.C., 2020. On the onset of Central Atlantic Magmatic Province (CAMP) volcanism and environmental and carbon cycle change at the Triassic–Jurassic transition (Neuquén Basin, Argentina). *Earth Sci. Res.* 208, 103229.
- Ruttenberg, K., Berner, R., 1993. Authigenic apatite formation and burial in sediments from non-upwelling, continental margin environments. *Geochim. Cosmochim. Acta* 57, 991–1007.
- Sannigrahi, P., Ingall, E., 2005. Polyphosphates as a source of enhanced P fluxes in marine sediments overlain by anoxic waters: evidence from ³¹P NMR. *Geochem. Trans.* 6, 52–59.
- Schobben, M., Gravendyck, J., Mangels, F., Struck, U., Bussert, R., Kürschner, W.M., Korn, D., Sander, P.M., Aberhan, M., 2019. A comparative study of total organic carbon-δ¹³C signatures in the Triassic–Jurassic transitional beds of the Central European Basin and western Tethys shelf seas. *Newsl. Stratigr.* 52 (4), 461–486.
- Schoene, B., Guex, J., Bartolini, A., Schaltegger, U., Blackburn, T.J., 2010. Correlating the end-Triassic mass extinction and flood basalt volcanism at the 100 ka level. *Geol.* 38 (5), 387–390.
- Scott, C., Lyons, T.W., 2012. Contrasting molybdenum cycling and isotopic properties in euxinic versus non-euxinic sediments and sedimentary rocks: refining the paleoproxies. *Chem. Geol.* 324–325, 19–27.
- Shimfield, G.B., Price, N.B., 1986. The behaviour of molybdenum and manganese during early sediment diagenesis—offshore Baja California. Mexico. *Mar. Chem.* 19, 261–280.
- Simms, M.J., 2003. Uniquely extensive seismite from the latest Triassic of the United Kingdom: evidence for bolide impact? *Geol.* 31 (6), 557–560.
- Simms, M.J., 2007. Uniquely extensive soft-sediment deformation in the Rhaetian of the UK: evidence for earthquake or impact? *Palaeogeogr. Palaeoclimatol. Palaeoecol.* 244 (1–4), 407–423.
- Simms, M.J., Jeram, A.J., 2007. Waterloo Bay, Larne, Northern Ireland: a candidate Global Stratotype Section and Point for the base of the Hettangian Stage and Jurassic System. *ISJS Newsl.* 34 (1), 50–68.
- Slopp, C.P., van Cappellen, P., 2007. The global marine phosphorus cycle: Sensitivity to oceanic circulation. *Biogeosci.* 4, 155–171.
- Slopp, C.P., Epping, E.H.G., Helder, W., Van Raaphorst, W., 1996. A key role for iron-bound phosphorus in authigenic apatite formation in North Atlantic continental platform sediments. *J. Mar. Res.* 54, 1179–1205.
- Sperling, E.A., Halverson, G.P., Knoll, A.H., Macdonald, F.A., Johnston, D.T., 2013. A basin redox transect at the dawn of animal life. *Earth Planet. Sci. Lett.* 371–372, 143–155.
- Sperling, E.A., Carbonne, C., Strauss, J.V., Johnston, D.T., Narbonne, G.M., Macdonald, F.A., 2016. Oxygen, facies, and secular controls on the appearance of Cryogenian and Ediacaran body and trace fossils in the Mackenzie Mountains of northwestern Canada. *Geol. Soc. Am. Bull.* 128, 558–575.
- Sperling, E.A., Balthasar, U., Skovsted, C.B., 2018. On the edge of exceptional preservation: insights into the role of redox state in Burgess Shale-type taphonomic windows from the Mural Formation, Alberta Canada. *Emerg. Top. Life Sci.* 1–13 <https://doi.org/10.1042/ETLS20170163>.
- Summons, R.E., Powell, T.G., 1986. *Chlorobiaceae* in Palaeozoic seas revealed by biological markers, isotopes and geology. *Nat.* 319, 763–765.
- Sweere, T., van den Boorn, S., Dickson, A.J., Reichert, G.-J., 2016. Definition of new trace-metal proxies for the controls on organic matter enrichment in marine sediments based on Mn, Co, Mo and Cd concentrations. *Chem. Geol.* 441, 235–245.
- Sweere, T.C., Dickson, A.J., Jenkyns, H.C., Porcelli, D., Elrick, M., van den Boorn, S.H.J.M., Henderson, G.M., 2018. Isotopic evidence for changes in the zinc cycle during Oceanic Anoxic Event 2 (late cretaceous). *Geol.* 46 (5), 463–466.
- Takahashi, T., Broecker, W.S., Langer, S., 1985. Redfield ratio based on chemical data from isopycnal surfaces. *J. Geophys. Res. Oceans* 90 (4), 6907–6924.
- Tanner, L., Kyte, F.T., 2005. Anomalous iridium enrichment at the Triassic–Jurassic boundary, Blomidon Formation, Fundy basin, Canada. *Earth Planet. Sci. Lett.* 240, 634–641.
- Tribouillard, N., Algeo, T.J., Lyons, T., Riboulleau, A., 2006. Trace metals as paleoredox and paleoproductivity proxies: an update. *Chem. Geol.* 232, 12–32.
- Tribouillard, N., Algeo, T.J., Baudin, F., Riboulleau, A., 2012. Analysis of marine environmental conditions based on molybdenum–uranium covariation—applications to Mesozoic paleoceanography. *Chem. Geol.* 324–325, 46–58.
- Van Cappellen, P., Ingall, E.D., 1996. Redox Stabilization of the Atmosphere and Oceans by Phosphorus-Limited Marine Productivity. *Sci.* 271, 493–496.
- Van de Schootbrugge, B., Wignall, P.B., 2015. A tale of two extinctions: converging end-Permian and end-Triassic scenarios. *Geol. Mag.*, 153. Special Issue 2, 332–354.
- Van de Schootbrugge, B., Tremolada, F., Rosenthal, Y., Bailey, T.R., Feist-Burkhardt, S., Brinkhuis, H., Kent, D.V., Falkowski, P.G., 2007. End-Triassic calcification crisis and blooms of organic-walled ‘disaster species’. *Palaeogeogr., Palaeoclimatol. Palaeoecol.* 244, 126–141.
- Van de Schootbrugge, B., van der Weijst, C.M.H., Hollaar, T.P., Vecoli, M., Strother, P.K., Kuhlmann, N., Thein, J., Visscher, H., van Konijnenburg-van Cittert, H., Schobben, M.A.N., Sluijs, A., Lindström, S., 2020. Catastrophic soil loss associated with end-Triassic deforestation. *Earth Sci. Rev.* 210, 103332 <https://doi.org/10.1016/j.earscirev.2020.103332>.
- Van Geen, A., McCorkle, D.C., Klinkhammer, G.P., 1995. Sensitivity of the phosphate-cadmium-carbon isotope relation in the ocean to cadmium removal by suboxic sediments. *Paleoceanograph.* 10 (2), 159–169.
- Wang, Z., Lee, S.-W., Catalano, J.G., Lezamo-Pacheco, J.S., Bargar, J.R., Tebo, B.M., Giammar, D.E., 2013. Adsorption of Uranium (VI) to Manganese Oxides: X-ray Adsorption Spectroscopy and Surface Complexation Modeling. *Environ. Sci. Technol.* 47 (2), 850–858.
- Warrington, G., Harland, R., 1975. Palynology of the Trias and lower Lias of the Larne Borehole. *Bull. Geol. Surv. G. B.* 50, 37–50.
- Wasylenki, L.E., Weeks, C.L., Bargar, J.R., Spiro, T.G., Hein, J.R., Anbar, A.D., 2011. The molecular mechanism of Mo isotope fractionation during adsorption to birnessite. *Geochim. Cosmochim. Acta* 75 (17), 5019–5031.
- Wasylenki, L.E., Swihart, J.W., Romaniello, S.J., 2014. Cadmium isotope fractionation during adsorption to Mn oxyhydroxide at low and high ionic strength. *Geochim. Cosmochim. Acta* 140, 212–226.
- Whiteside, J.H., Ward, P.D., 2011. Ammonoid diversity and disparity track episodes of chaotic carbon cycling during the early Mesozoic. *Geol.* 39 (2), 99–102.
- Whiteside, J.H., Olsen, P.E., Kent, D.V., Powell, S.J., Et-Touhami, M., 2007. Synchrony between the Central Atlantic magmatic province and the Triassic–Jurassic mass-extinction event? *Palaeogeogr., Palaeoclimatol., Palaeoecol.* 244, 345–367.
- Whiteside, J.H., Olsen, P.E., Eglinton, T., Brookfield, M.E., Sambrotto, R.N., 2010. Compound-specific carbon isotopes from Earth’s largest flood basalt eruptions directly linked to the end-Triassic mass extinction. *PNAS* 107 (15), 6721–6725.
- Wignall, P.B., Atkinson, J.W., 2020. A two-phase end-Triassic mass extinction. *Earth Sci. Rev.* 208, 103282.
- Wright, P., Chernes, L., Hodges, P., 2003. Missing molluscs: field testing taphonomic loss in the Mesozoic through early large-scale aragonite dissolution. *Geol.* 31 (3), 211–214.
- Young, S.A., Benayoun, E., Kozik, N.P., Hints, O., Martma, T., Bergström, S.M., Owens, J. D., 2020. Marine redox variability from Baltica during extinction events in the latest Ordovician-early Silurian. *Palaeogeogr., Palaeoclimatol. Palaeoecol.* 554, 1–17.
- Zhang, X., Cui, L., 2016. Oxygen requirements for the Cambrian explosion. *J. Earth Sci.* 27 (2), 187–195.
- Zhang, Y., Planavsky, N.J., Zhao, M., Ison, T., Asael, D., Wang, C., Wang, F., 2021. The isotopic composition of sedimentary organic zinc and implications for the global Zn isotope mass balance. *Geochim. Cosmochim. Acta* 314, 16–26.

Stratigraphic Level	Al (ppm)	Fe (ppm)	P (ppm)	Mn (ppm)	Co (ppm)	Zn (ppm)	Mo 98 (ppm)	Cd-1111 (ppm)	U-1 238 (ppm)	TOC (%)	TN (%)
348.3	92229.98	38819.82	281.02	1004.84	27.25	68.39	1.49	0.07	2.71	2.02	0.09
348.5	84037.63	36789.98	278.80	874.03	26.26	62.14	1.42	0.08	2.61	2.08	0.09
348.7	84653.87	34626.11	264.56	763.57	24.70	78.44	2.09	0.15	3.25	2.49	0.11
349.1	77947.40	38970.80	295.48	665.64	26.38	54.80	0.94	0.09	2.09	0.98	0.06
349.3	77134.51	42542.38	366.61	715.24	25.93	60.03	7.56	0.09	2.33	3.44	0.13
349.7	80879.19	43896.39	275.87	596.78	28.44	55.39	3.79	0.06	2.68	1.43	0.08
349.9	59885.21	41711.31	321.22	1737.48	20.08	44.51	0.38	0.05	1.54	0.80	0.06
350.2	88258.29	40438.08	1299.27	547.93	24.52	56.56	2.05	0.08	2.53	1.87	0.08
350.4	102829.97	45858.39	284.18	695.33	31.09	539.95	2.13	0.48	3.26	2.46	0.10
350.6	87333.29	37848.46	244.01	605.03	24.79	55.57	0.95	0.07	2.12	1.95	0.08
350.9	56879.32	38739.54	394.10	888.69	19.68	41.37	0.92	0.05	1.73	1.20	0.05
351.1	83312.46	40430.60	612.07	681.59	26.41	60.51	0.95	0.07	2.31	1.13	0.05
351.7	68311.47	38213.59	253.82	1212.40	19.87	78.37	0.42	0.02	0.90	1.33	0.07
352.1	82250.84	38526.87	373.51	712.23	24.23	71.61	0.98	0.06	2.16	1.22	0.05
352.2	84744.52	37617.12	267.82	581.99	25.59	53.07	0.81	0.07	1.95	1.34	0.05
352.6	83396.46	35062.03	212.20	716.39	22.47	90.80	1.21	0.07	2.42	1.68	0.06
353	63853.24	44929.42	166.91	882.09	18.52	43.77	5.23	0.08	1.81	2.24	0.08
353.8	74431.50	34004.26	143.51	821.46	17.81	44.76	0.92	0.05	1.80	1.44	0.05
354.7	69712.97	37218.58	137.52	889.21	19.88	85.41	1.70	0.15	2.09	1.53	0.07
354.9	50465.63	35968.33	274.47	1040.87	15.55	41.14	1.76	0.06	2.01	0.94	0.04
355.5	56571.27	38889.82	282.17	1206.49		67.15	2.49	0.05	2.43	1.71	0.07
355.7	75220.88	41587.92	183.10	695.05	22.37	59.99	1.32	0.07	2.16	1.48	0.05
356	13028.73	20007.24	138.88	518.96	4.29	20.03	0.66	0.03	0.63	0.99	0.03
356.4	96150.99	44617.27	366.33	329.49	34.22	53.73	0.48	0.06	2.33	0.61	0.04
357	55409.50	62521.16	191.24	1157.88	27.06	47.74	1.13	0.12	2.38	1.02	0.03
357.4	81194.71	37282.94	265.19	421.07	32.29	52.61	0.29	0.07	1.95	0.52	0.05
361.1	84867.04	40858.58	214.41	526.97	35.46	58.29	0.37	0.06	1.97	0.57	0.06
362.1	88806.95	45215.80	190.90	398.76	34.18	48.26	0.89	0.05	2.00	0.80	0.08
362.5	86771.19	44616.77	345.49	421.30	30.71	57.98	1.09	0.16	1.92	1.30	0.08
362.9	79206.30	59200.27	157.60	396.40	30.38	51.67	2.49	0.23	1.93	2.22	0.10
363.1	88603.73	41844.28	170.24	415.99	28.43	50.06	0.97	0.17	2.19	0.90	0.04
363.8	75458.03	32318.19	182.00	399.71	24.86	45.15	3.47	0.38	3.43	1.02	0.07
364	30675.70	25558.94	131.30	1029.07	9.57	24.92	1.14	0.11	1.56	0.63	0.05
364.2	43871.41	28078.16	141.32	925.85	12.84	30.07	1.67	0.07	3.09	0.91	0.04
364.4	57816.56	32238.27	126.41	686.00	20.41	38.54	1.10	0.10	2.51	0.61	0.05
364.6	32122.31	34549.56	112.06	1418.28	9.84	28.98	1.26	0.09	4.55	0.87	0.05
364.8	16977.41	22899.70	159.82	1139.97	5.35	20.15	2.14	0.14	3.29	0.44	0.04
365	56344.58	30292.33	175.38	711.61	20.03	36.60	1.22	0.07	2.53	0.55	0.05
365.4	60733.81	36206.88	148.54	820.81	20.91	36.91	0.69	0.06	2.82	0.72	0.07
365.6	57924.60	36321.58	162.02	734.39	21.79	37.08	1.59	0.09	4.47	0.45	0.05
365.8	64367.70	26770.45	164.77	575.63	19.21	38.69	0.47	0.07	3.07	0.49	0.05
366	80559.81	30243.76	162.70	302.14	49.26	38.84	0.57	0.06	3.40	0.52	0.06
366.2	68700.09	25725.56	184.75	365.50	19.09	38.25	0.37	0.05	3.18	0.44	0.06
366.4	56139.11	32892.49	160.67	753.38	24.92	38.65	1.49	0.07	4.00	0.73	0.03
366.6	75491.78	31468.53	168.49	364.33	26.87	38.56	0.34	0.06	2.13	0.50	0.06
366.8	70277.49	24082.75	204.70	466.29	16.15	36.54	0.87	0.06	5.51	0.30	0.06
367	80028.91	34498.19	206.15	376.99	30.92	44.57	0.38	0.08	2.34	0.41	0.06
367.1	79146.87	36351.78	208.41	407.26	19.09	41.64	0.38	0.05	2.02	0.38	0.05
367.3	76812.27	35107.07	195.33	523.69	19.66	42.56	0.33	0.07	2.03	0.50	0.02
368.5	46972.86	28367.18	154.00	1454.78	16.96	41.42		0.06	2.15	0.16	0.06
368.8	38187.40	20793.35	236.65	1179.51	8.20	27.59	0.18	0.09	1.87	0.40	0.00
369.4	68959.23	31851.57	258.84	594.99	16.59	40.04	0.39	0.09	1.77	0.55	0.02
370.6	75651.83	27154.35	187.64	371.05	21.34	39.06	0.53	0.09	1.96	0.63	0.04
371	83914.16	29609.22	168.17	297.57	26.33	34.71	0.69	0.12	2.46	0.59	0.07
371.6	91695.37	47816.71	197.97	444.92	26.69	59.34	3.26	0.08	2.85	2.75	0.11
372.9	49395.50	28985.59	264.65	1553.12	14.91	34.59	1.63	0.06	2.08	1.44	0.04
373.2	84724.29	42728.72	137.75	409.34	25.82	287.34	1.44	1.35	3.04	2.15	0.10
373.8	92974.81	41347.08	204.62	393.92	26.11	49.06	3.72	0.10	3.36	3.20	0.10
376.7	76833.68	35399.78	155.59	381.43	25.89	42.33	1.83	0.11	2.27	2.13	0.08
377.3	85031.03	38742.95	160.09	615.31	27.51	45.55	3.01	0.12	2.68	3.62	0.12
378.1	77093.80	40378.93	163.46	519.62	25.33	171.80	10.39	0.45	2.54	2.83	0.12
378.2	72530.18	59893.52	300.83	817.43	30.34	50.40	6.01	0.23	2.17	1.93	0.10
Upper Crustal Abundance (ppm) Rudnick & Gao (2003)	81500	38808	655	775	17.3	67	1.1	0.09	2.7		

Figure S1:- Larne Geochemical Data. For data in excel format:

https://www.sciencedirect.com/science/article/pii/S0031018222001882?ref=cra_js_challenge&fr=RR-1#s0150

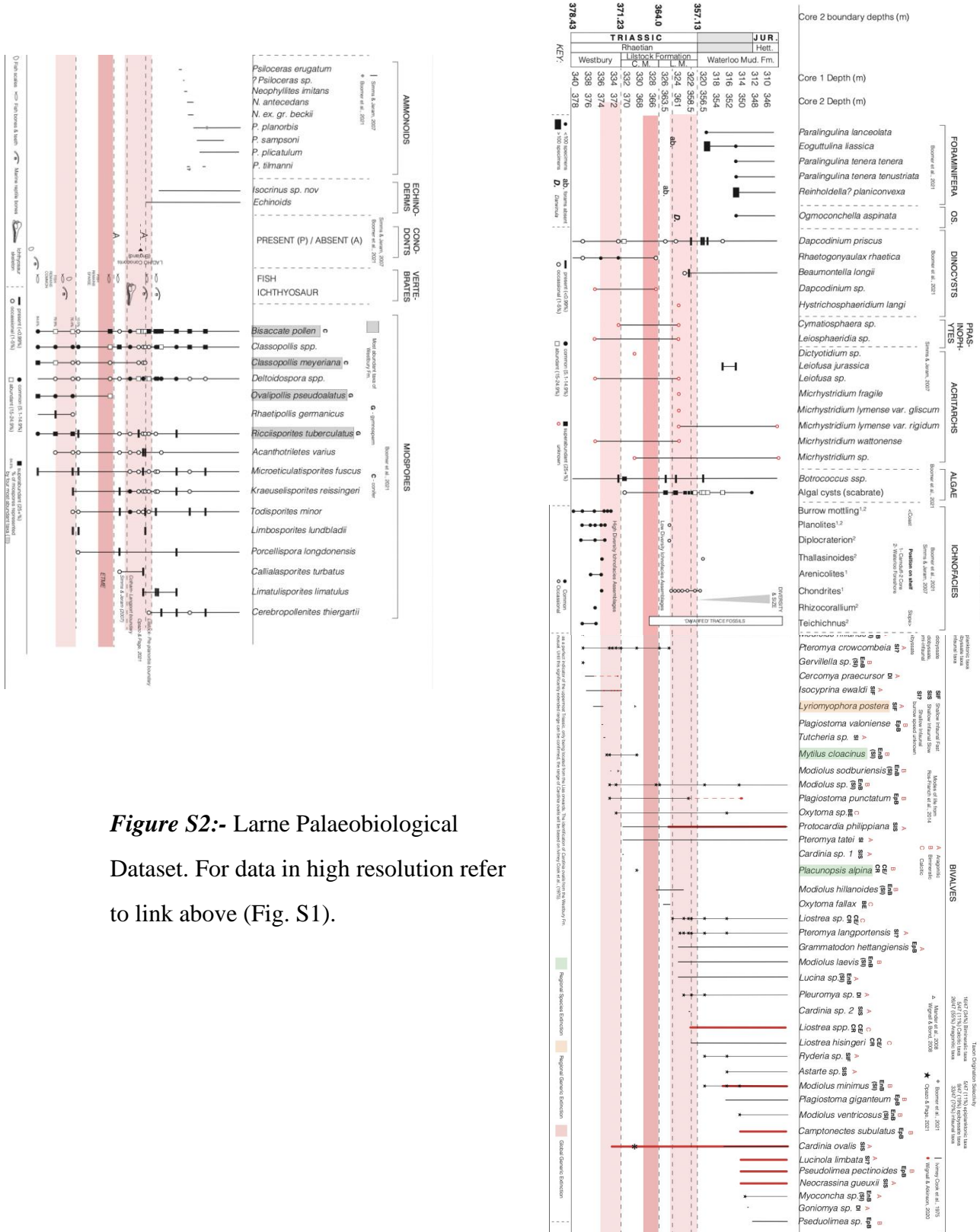


Figure S2:- Lerne Palaeobiological Dataset. For data in high resolution refer to link above (Fig. S1).

Chapter 6: Supplementary Information

Palaeobiological (stratigraphic) correlation and figure data:

This section of the supplementary information lists the data sources compiled to form the palaeobiological compilation (Fig. S2- Chapter 6) as well as detailing how the sources of information were correlated and how Figure 5 of Chapter 6 was designed through the use of the palaeobiological data.

Bivalve biodiversity data:

Bivalve biodiversity data from the Larne Basin was compiled from a number of sources from Larne sections in outcrop. These include studies by Ivimey-Cook, (1975), Wignall & Atkinson, (2020) and Opazo & Page, (2021) of the Waterloo Bay Foreshore section. Regional bivalve disappearances as noted by Wignall and Bond, (2008) and Mander et al., (2008) have been crudely correlated to the Larne Basin stratigraphy based on the Westbury and Lilstock Formations being considered to represent broadly equivalent intervals of sedimentary deposition across Northern Ireland and the southwest of England (Wignall & Bond, 2008; Boomer et al., 2021).

The earliest known detailed studies of bivalve data from the Larne Basin took the form of outcrop (Waterloo Bay Foreshore) and core (Larne No. 1 Borehole) studies by Ivimey-Cook, (1975) which were inspired by palaeobiological studies of the Larne No. 1 Borehole (Manning & Wilson, 1975; Warrington & Harland, 1975). Ivimey-Cook, (1975)'s bivalve compilation data is observed in Fig. S3 (Chapter 6) and has also been collated with observations by Simms & Jeram, (2007).

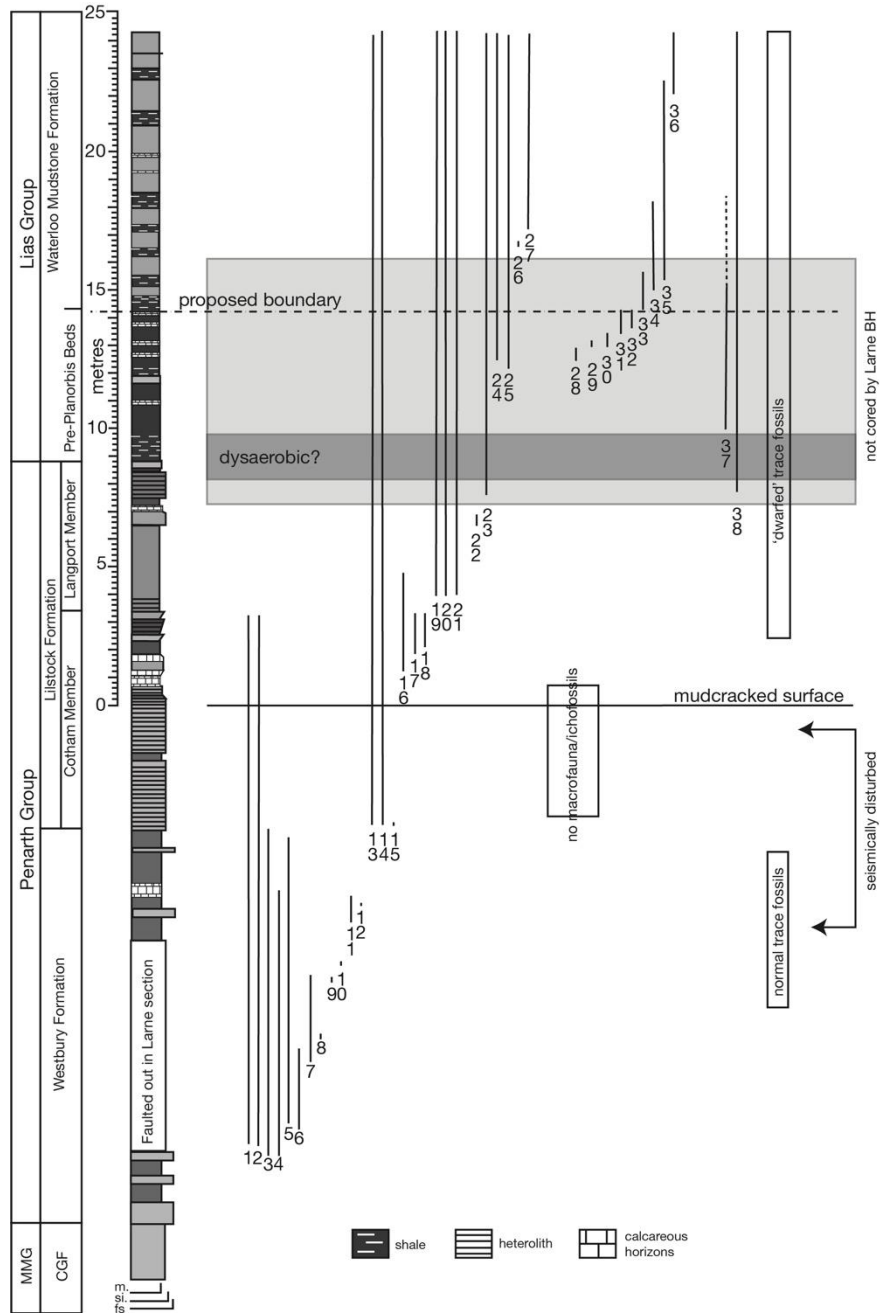


Figure S3:- Faunal biostratigraphy for the Penarth and basal Lias Groups of the Larne Basin). Palaeobiological data from Ivimey-Cook, (1975) and Simms & Jeram, 2007. Figure amended from Simms and Jeram, 2007, figure 7. 1- *Protocardia rhaetica*, 2- *Eotrapezium (Isocyprina) concentricum*, 3- *Rhaeticula contorta*, 4- *Chlamys valoniensis*, 5- *Isocyprina (Eotrapezium) ewaldi*, 6- *Cercomya praecursor*, 7- *Lyriomyophoria postera*, 8- *Pleurophorus (Permophorus) elongatus*, 9- *Plagiostoma valoniense*, 10- *Tutcheria* sp., 11- *Modiolus hillanus*, 12- *Modiolus sodburiensis*, 13- *Protocardia philippiana*, 14- *Pteromya tatei*, 15- *Cardinia* sp. 1, 16- *Modiolus hillanoides*, 17- *Pteromya crowcombei*, 18- *Oxytoma fallax*, 19- *Grammatodon (Cosmetodon) hettangiensis*, 20- *Modiolus laevis*, 21- *Lucina* sp., 22- *Cardinia* sp. 2, 23- *Liostrea hisingeri*, 24- *Plagiostoma giganteum*, 25- *Cardinia ovalis*, 26- *Goniomya*

sp., 27- *Pseudolimea* sp., 28- *Psiloceras erugatum*, 29- ? *Psiloceras* sp., 30- *Neophyllites imitans*, 31- *Neophyllites antecedans*, 32- *Neophyllites* ex. gr. *beckii*, 33- *Psiloceras planorbis*, 34- *Psiloceras sampsoni*, 35- *Psiloceras plicatulum*, 36- *Caloceras* spp., 37- *Isocrinus* sp. nov., 38- Echinoids. m.- mudstone, si.- silt, fs- fine sand, MMG- Mercia Mudstone Group, CGF- Colin Glen Formation.

A study of the bivalve fauna of the Waterloo Bay Foreshore by Wignall and Atkinson, (2020) was used to aid their interpretation that the end-Triassic mass extinction took place as two main pulses (Fig. S4- Chapter 6).

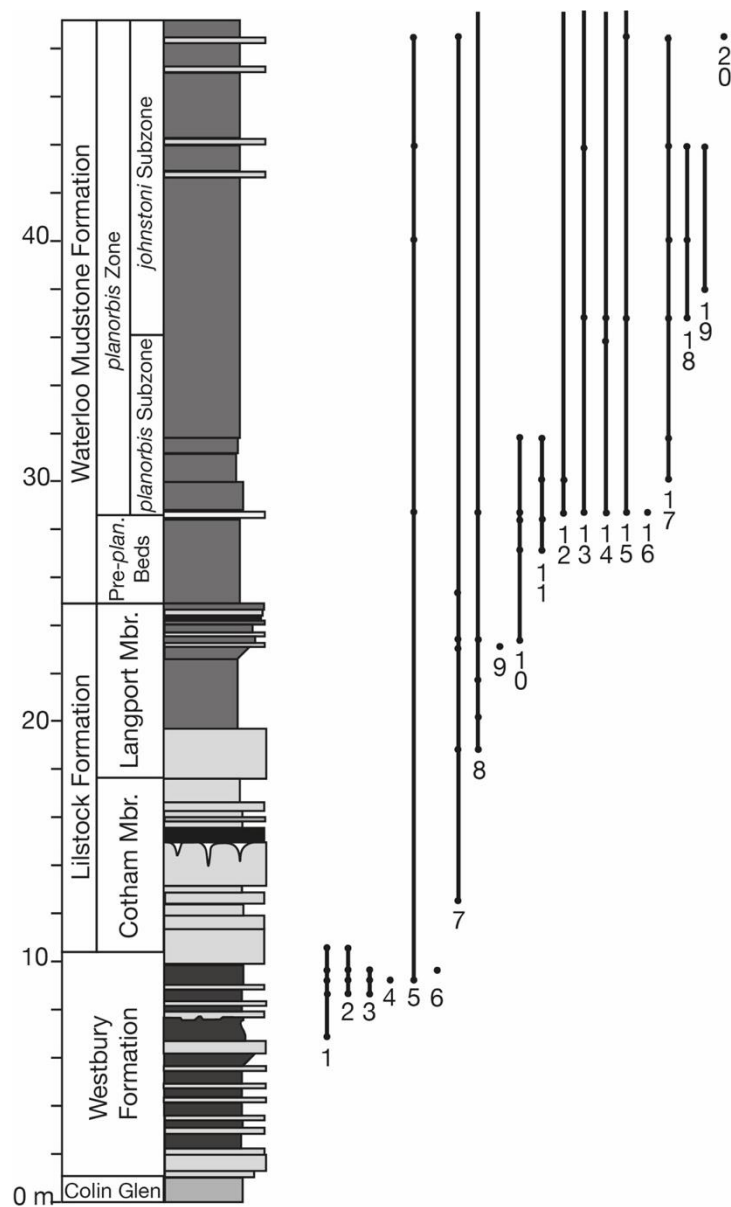


Figure S4:- Bivalve biostratigraphy for the Penarth and basal Lias Groups of the Larne Basin based on data from Wignall & Atkinson, 2020. Figure amended from Wignall & Atkinson, 2020, figure 2. 1- *Isocyprina ewaldi*, 2- *Rhaeticicula contorta*, 3- *Protocardia*

rhaetica, 4- *Chlamys valoniensis*, 5- *Cardinia ovalis*, 6- *Cercomya praecursor*, 7- *Pteromya crowcombeia*, 8- *Protocardia philippianum*, 9- *?Permophorus?* sp., 10- *Liostrea* spp., 11- *Modiolus minimus*, 12- *Camptonectes subulatus*, 13- *Lucinola limbata*, 14- *Pseudolimea pectinoides*, 15- *Neocrassina guexii*, 16- *Plagiostoma punctatum*, 17- *Modiolus hillanus*, 18- *Ryderia doris*, 19- *Palaeoneilo eliptica*, 20- *Grammatodon hettangiensis*, plan- *planorbis*.

More recent research of the invertebrate palaeobiological composition of the Waterloo Bay Foreshore sediments was undertaken by Opazo and Page, (2021). Their study focussed on the palaeoecological factors driving faunal changes within the Triassic-Jurassic Larne Basin with a particular focus on bivalve data (Fig. S5- Chapter 6).

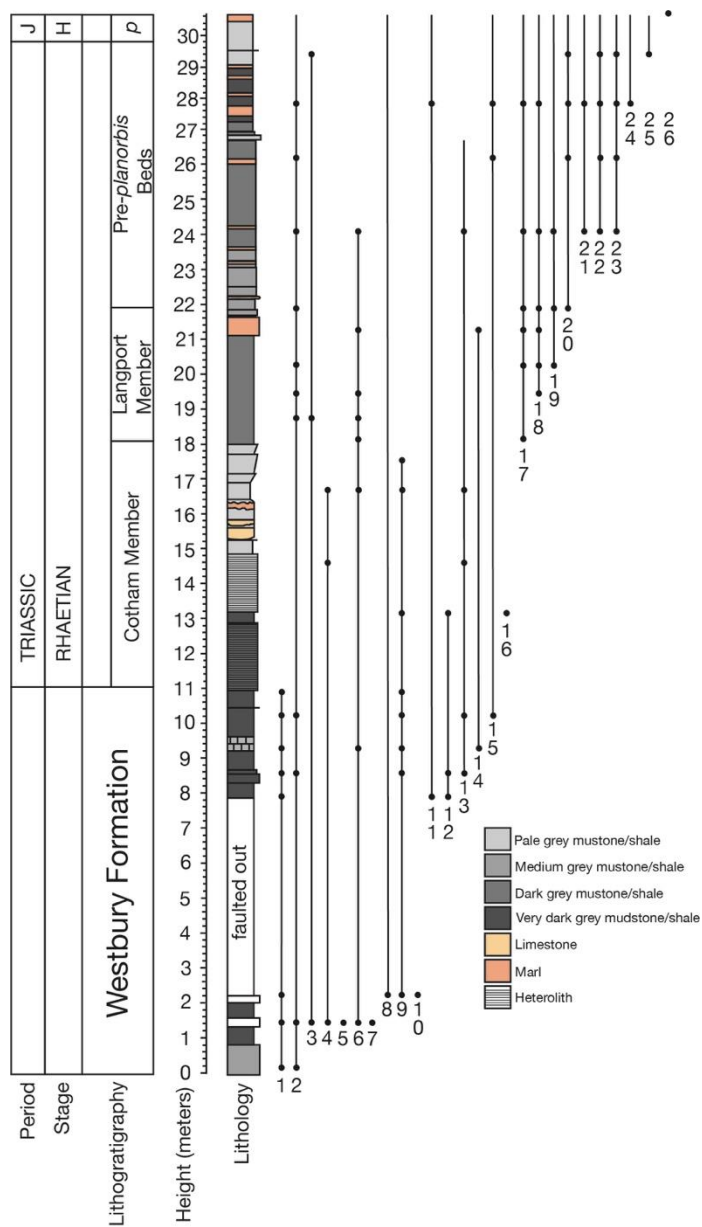


Figure S5 (above):- Invertebrate taxonomic range data from the Waterloo Bay Foreshore, Larne Basin, Ireland. Figure amended from Opazo & Page, 2021, figure 2. H- Hettangian, J- Jurassic, p- Planorbis Zone.

Ammonite and echinoderm biodiversity data:

Ammonite and echinoderm biodiversity data from the Larne Basin was obtained from Ivimey-Cook, (1975) and Simms & Jeram, (2007) (Fig. S3- Chapter 6), through studies of the Waterloo Bay Foreshore sediments, and was supplemented with observations from Boomer et al., (2021) regarding the first appearance of ammonite *Psiloceras planorbis* within the sediments of the Carnduff-1 and Carnduff-2 cores (see figure 3 and table 2 within Boomer et al., 2021).

Vertebrate biodiversity data:

Vertebrate biodiversity data from the Larne Basin has been obtained from qualitative data from Simms & Jeram, (2007) of the Waterloo Bay Foreshore. Particularly, regarding abundance of fish remains and occurrences of ichthyosaur bones. Refer to Simms and Jeram, 2007; 4.5.8 Vertebrates, p. 61 for more information.

Ichnofaunal biodiversity data:

Ichnofaunal biodiversity data from the Larne Basin has been obtained from Boomer et al., (2021) and Simms & Jeram, (2007). Data from Simms & Jeram, (2007) takes the form of qualitative data describing broad scale changes and observations regarding ichnofauna based on studies of the Waterloo Bay Foreshore (e.g., Fig. S3 Chapter 6; see also Simms & Jeram, (2007), figure 7 and Simms & Jeram, (2007); 4.5.7 Trace Fossils, p. 60). Data from Boomer et al., (2021) takes the form of ichnofaunal occurrences plotted against stratigraphy in the form of detailed sedimentary logs of the Carnduff-2 core (see figure 4 of Boomer et al., (2021) (Fig. S6- Chapter 6).

Miospore, dinocyst and algal biodiversity data:

Biodiversity data for miospore producing plants, dinoflagellates (in the form of dinocysts) and algae were obtained from Boomer et al., (2021) based on micropalaentological studies of the Carnduff-1 core (Fig. S7- Chapter 6).

Prasinophycean, dinocyst and acritarch biodiversity data was also obtained from Warrington and Harland, (1975) based on studies of the Larne No. 1 Borehole (Fig. S9- Chapter 6).

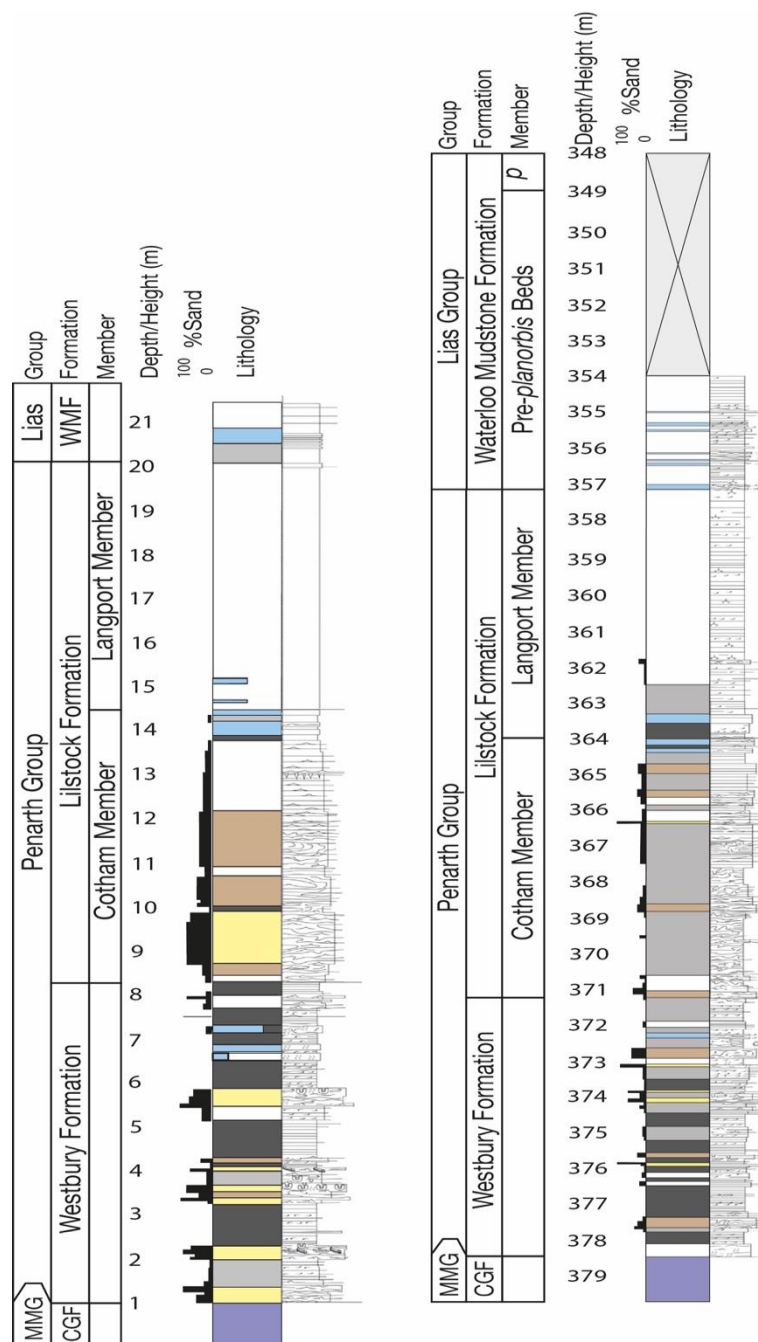


Figure S6 (above):- Sedimentary logs from the Waterloo Bay Foreshore (left) and Carnduff-2 core (right), including ichnofauna, from Boomer et al., (2021). For original, higher resolution logs and legend refer to Boomer et al., (2021), figure 4. For lithologies refer to main paper (this thesis). Dark blue lithology at base of sections- calcareous/dolomitic mudstone. CGF- Collin Glen Formation, Lias- Lias Group, MMG- Mercia Mudstone Group, *p*- Planorbis Zone, WMF- Waterloo Mudstone Formation.

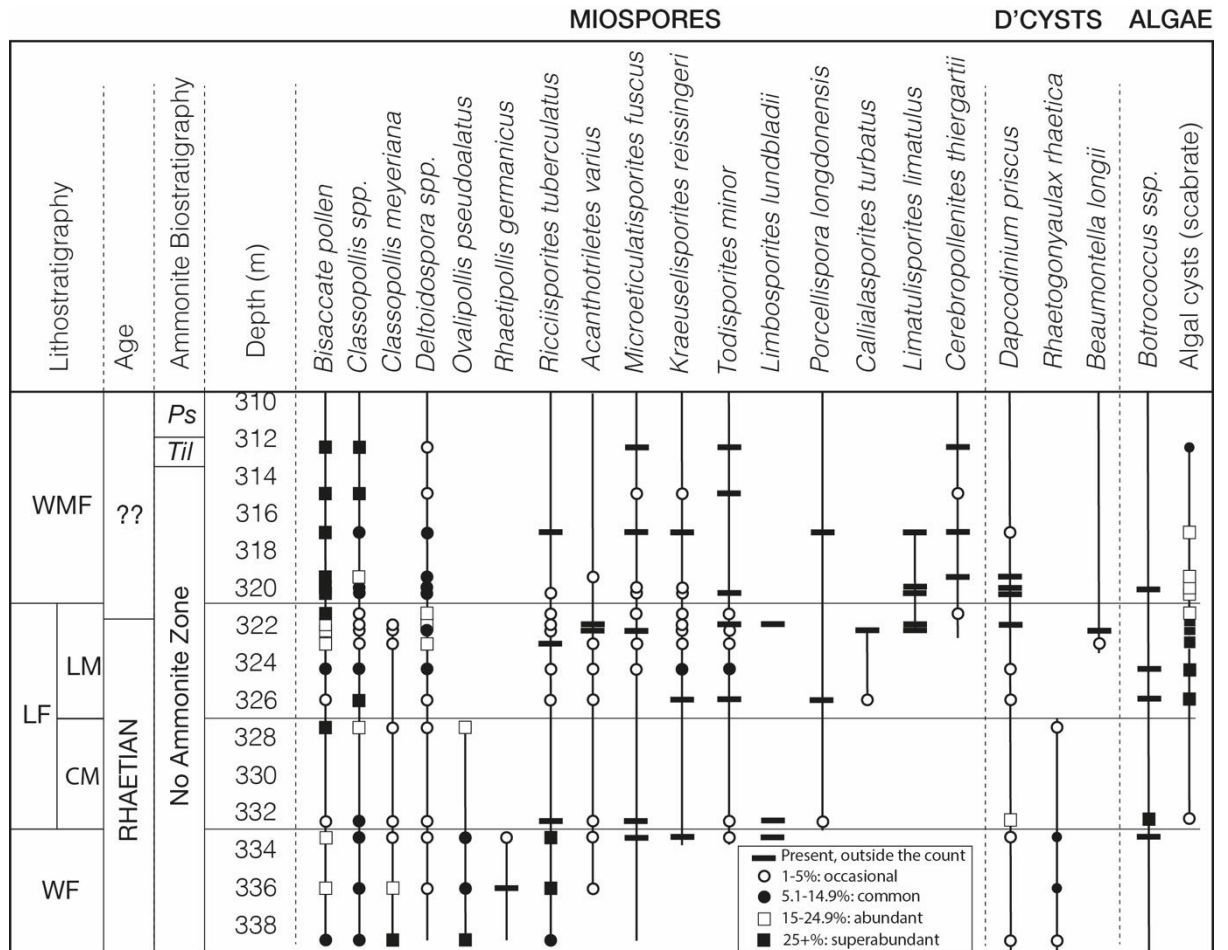


Figure S7:- Miospore, dinocyst and algal biodiversity data from Carnduff-1 core, Larne Basin, Northern Ireland. Figure amended from Boomer et al., (2021). Data from Boomer et al., (2021). CM- Cotham Member, D'CYSTS- dinocysts, LF- Lilstock Formation, LM- Langport Member, Ps- Planorbis Zone, Til- Tilmanni Zone, WF- Westbury Formation, WMF- Waterloo Mudstone Formation.

Foraminiferan, ostracod and conodont biodiversity data:

Foraminiferan and ostracod biodiversity data were obtained from Boomer et al., (2021), figure 6, based on studies of the Carnduff-1 core (Fig. S8- Chapter 6). Qualitative observations regarding the occurrence of conodont taxa have also been added to Fig. S2

(Chapter 6). Conodont biodiversity data as well as the horizon of regional conodont extinction in England were obtained from observations from Simms & Jeram, (2007; 4.5.6 Conodonts, p. 60).

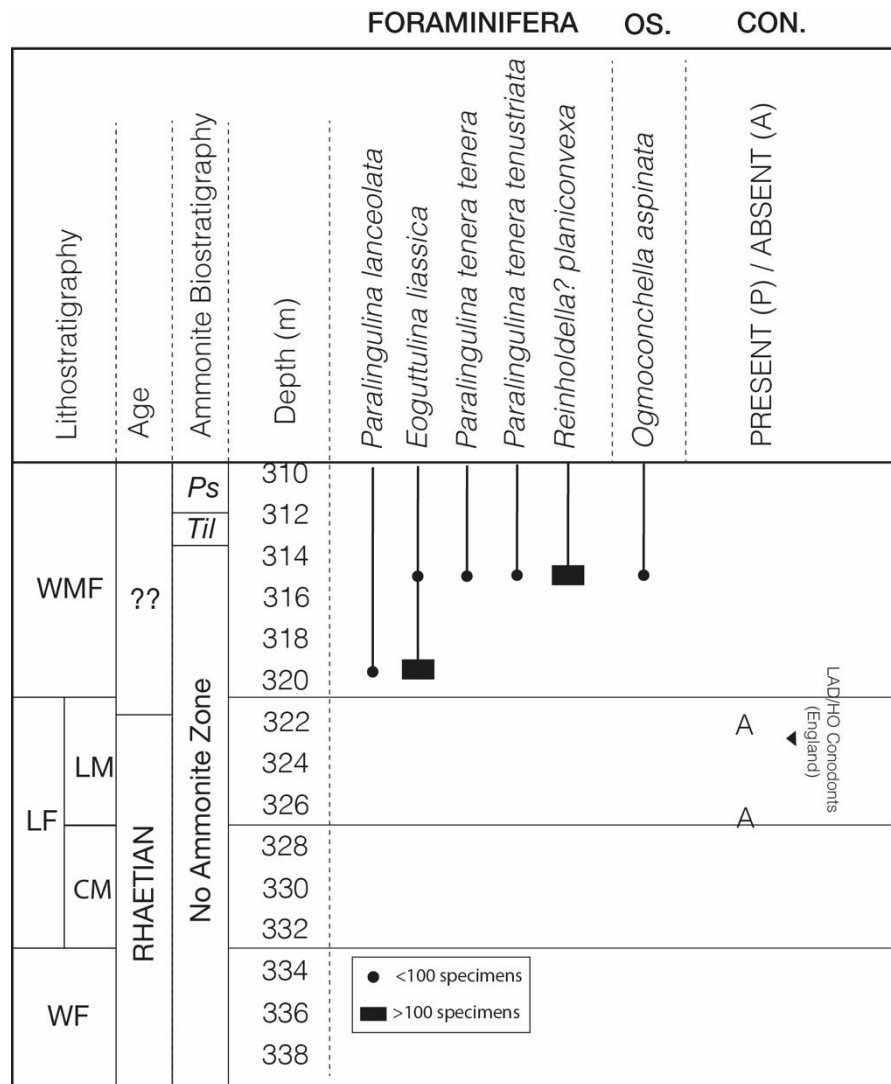


Figure S8:- Foraminiferan, ostracod and conodont biodiversity data from the Larne Basin, Northern Ireland. Foraminiferan and Ostracod data from Boomer et al., (2021), CM- Cotham Member, CON.- conodonts, LF- Lilstock Formation, LM- Langport Member, OS.- ostracods, Ps- Planorbis Zone, Til- Tilmanni Zone, WF- Westbury Formation, WMF- Waterloo Mudstone Formation.

Acritarch and prasinophyte biodiversity data:

Acritarch and prasinophycean biodiversity data has largely been obtained from Warrington and Harland, (1975) (Fig. S9- Chapter 6) with the range of *Leiofusa*

jurassica from the Carnduff-1 core (Boomer et al., 2021). The range of *L. jurassica* has therefore been correlated stratigraphically.

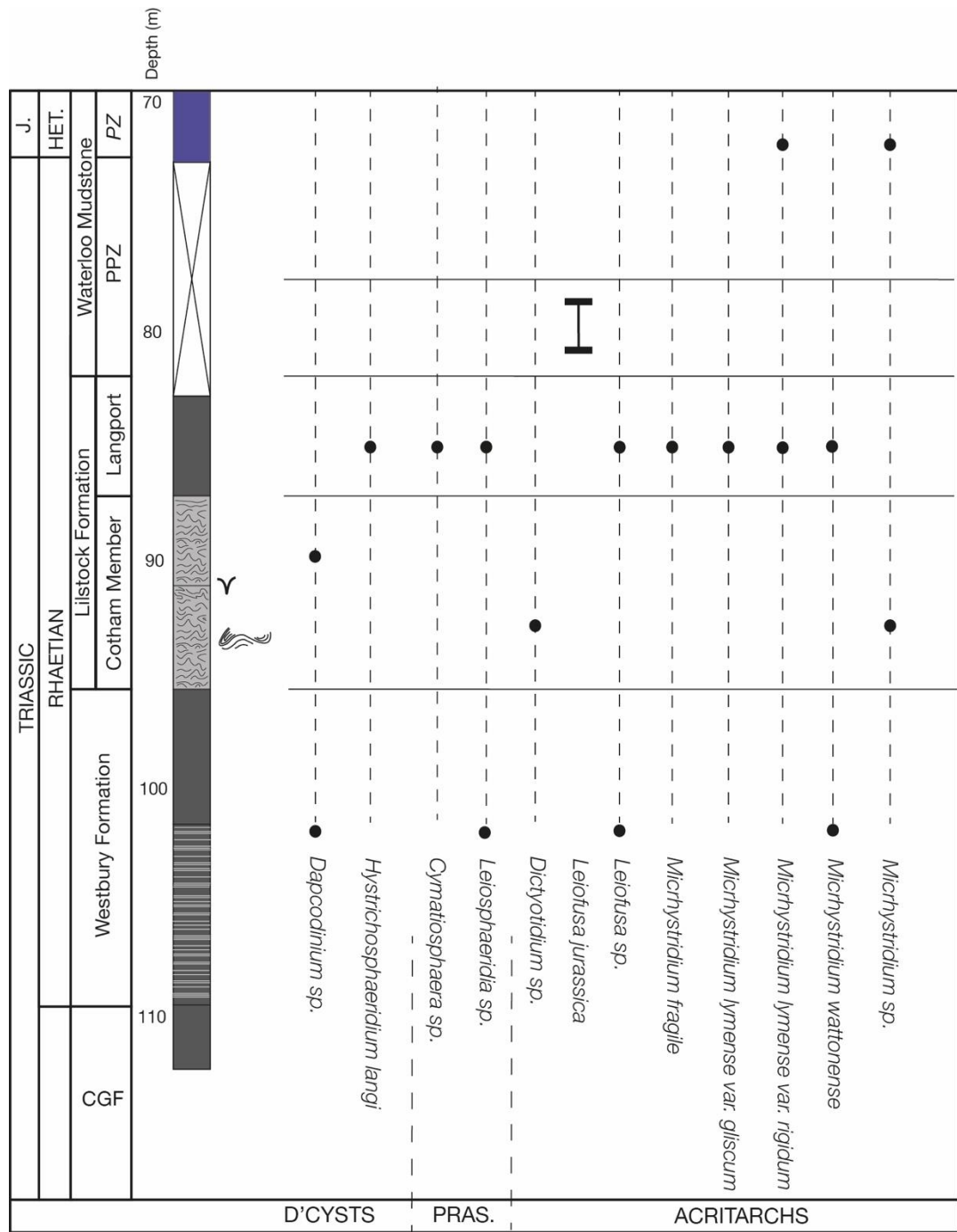
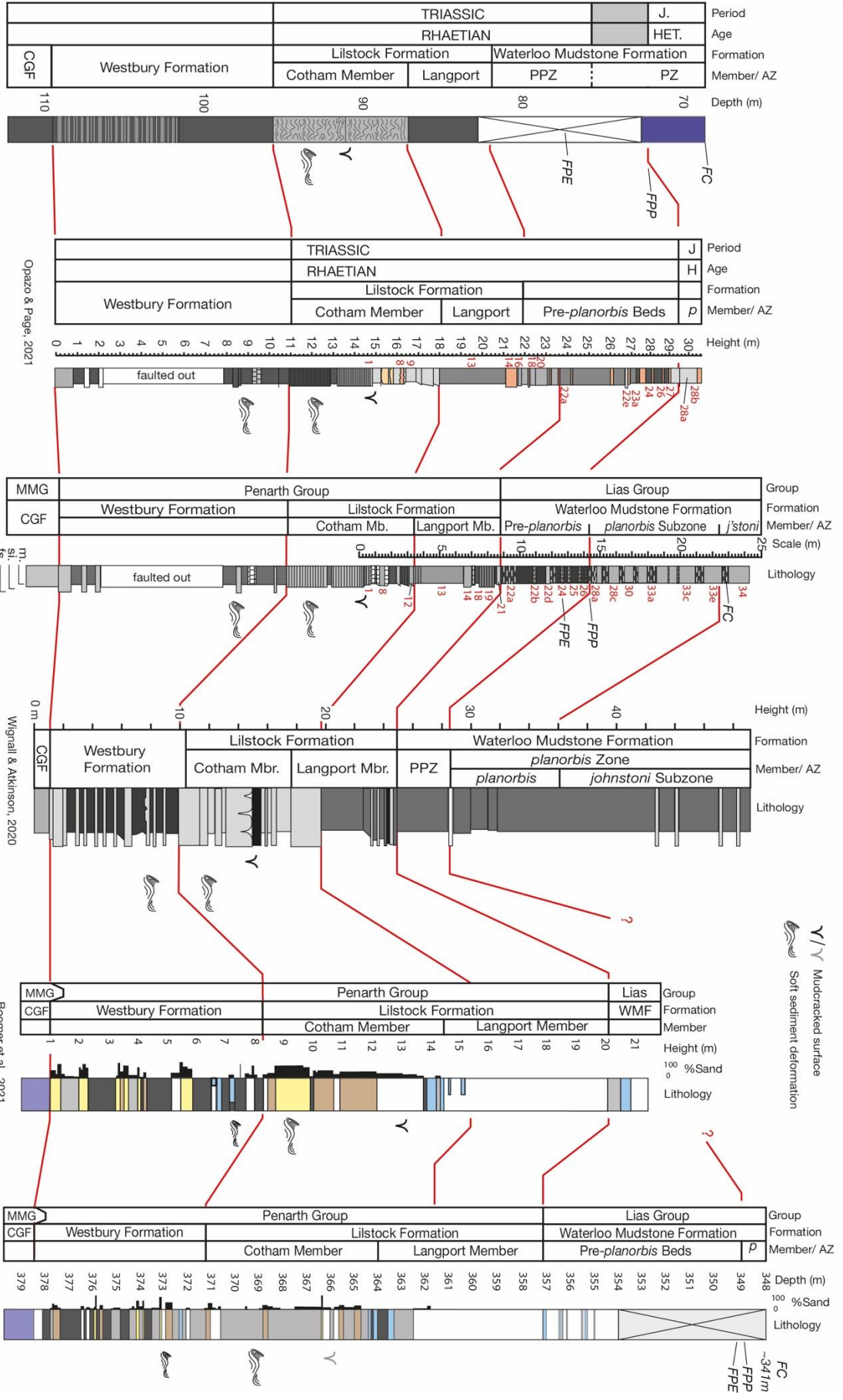


Figure S9:- Dinocyst, prasinophycean and acritarch biodiversity data from the Larne No.1 Borehole and Carnduff-1 core, Larne Basin, Northern Ireland. CGF- Collin Glen Formation, D'CYSTS- dinocysts, HET.- Hettangian, J.- Jurassic, PPZ- Pre-Planorbis Zone, PRAS.- Prasinophytes, PZ- Planorbis Zone. Data from Warrington & Harland, (1975) and Boomer et al., (2021). Figure amended from Simms & Jeram, (2007).



Manning & Wilson, 1975;
 Wmney-Cook, 1975
 Warrington & Harland, 1975

Opazo & Page, 2021
 Simms & Jeram, 2007;
 Wmney-Cook, 1975

Wignall & Atkinson, 2020
 Boomer et al., 2021

Boomer et al., 2021;
 this thesis.

Figure S10 (above):- A correlation of Larne foreshore and core sections. AZ- Ammonite Zone/Subzone, CGF- Collin Glen Formation, FC- First appearance datum of *Caloceras*, FPE- First appearance datum of *Psiloceras erugatum*, FPP- First appearance datum of *Psiloceras Planorbis*, H/HET.- Hettangian, J/J.- Jurassic, *j'stoni-johnstoni* Subzone, Mbr.- Member, PPZ- Pre Planorbis Zone, *p/PZ-* Planorbis Zone, WMF- Waterloo Mudstone Formation. Mudcracked surface symbol for Carnduff-2 core is paler in colour as mud cracks were not identified in the Carnduff-2 core however were noted at a correlative horizon within the Carnduff-1 core.

Stratigraphic correlation of Larne sections and associated uncertainties:

Larne sections from different studies were correlated using a combination of ammonite biostratigraphy and lithostratigraphy (Fig. S10- Chapter 6). Lithostratigraphic correlation was particularly aided through marker beds (e.g., seismite beds and mud cracks) and bed numbering. In light of the core and outcrop sections having been largely correlated through the use of lithostratigraphy there is some uncertainty, particularly where the lithology has been described in limited detail (e.g., Manning & Wilson, 1975). The correlation of prasinophycean, dinocyst and acritarch data from Warrington and Harland, (1975) may therefore be less precise than palaeobiological datasets correlated from other studies. Lithological data from the other studies is more detailed allowing for more accurate correlation of Larne sections (see Fig S10). However, in light of the varying amounts of detail which has been included within the sedimentary logs there still remains some uncertainty.

The correlation of the Carnduff-1 and Carnduff-2 cores:

The correlation of the Carnduff-1 and Carnduff-2 cores was based on detailed correlations undertaken by Boomer et al., (2021) using ammonite biostratigraphy and through correlating marker beds. The detailed correlation undertaken by Boomer et al., (2021) allowed for palynological and microfossil data to be correlated from the

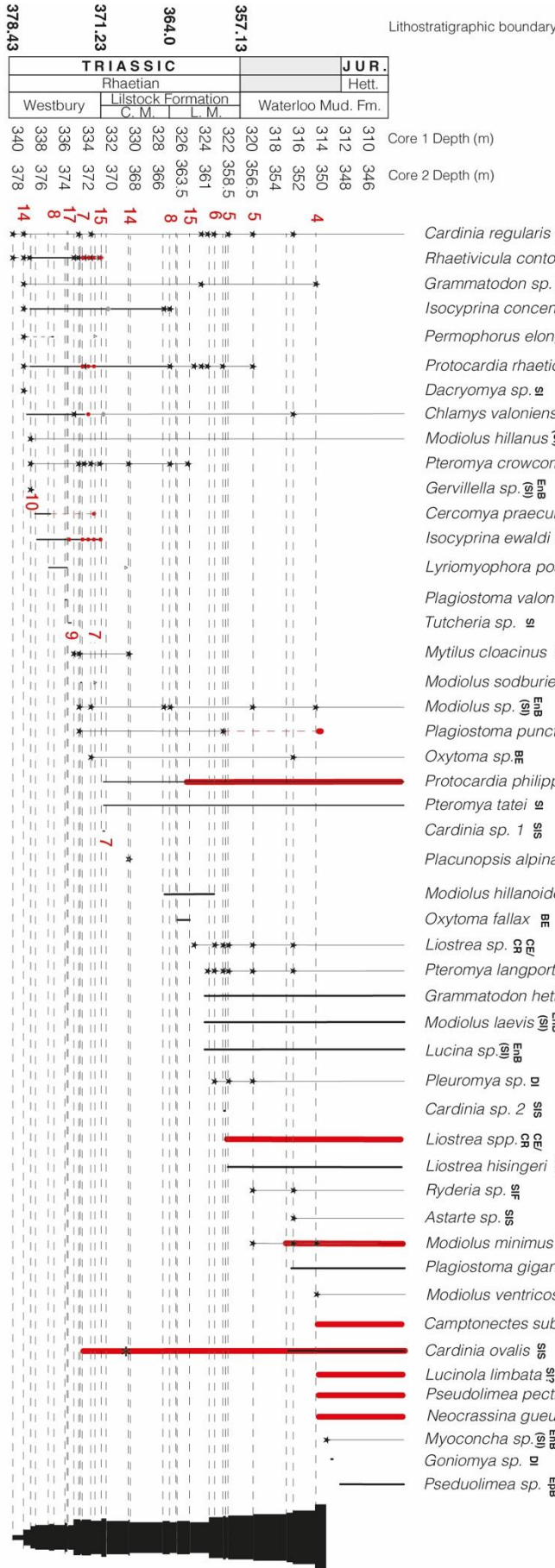
Carnduff-1 core to the Carnduff-2 core. It should be noted that the correlation of the Carnduff-1 and Carnduff-2 cores was largely based on lithostratigraphic correlation which may introduced some uncertainty due to lithological variations between the cores.

The use of stratigraphically correlated data to produce biodiversity bar plots:

Once the data had been stratigraphically correlated and plotted the data was overlain by construction lines and changes in biodiversity were identified. Where biodiversity, defined here by the number of taxa of a particular (palaeo)biological group, changes then the width of the bar changes accordingly. An increase in bar width indicates an increase in diversity and a decrease in bar width indicates a decrease in diversity (Fig. S11- Chapter 6). The width of the bars can only be interpreted for the same group of organisms as bar width cannot be directly extrapolated to species numbers. Despite a direct correlation between bar width and species numbers being more informative, this was not possible for this dataset due to the large range of taxonomic diversity observed from the least diverse groups (e.g., dinoflagellates- maximum diversity 2) to the most diverse groups (e.g., bivalves- maximum diversity 27).

Figure S11 (below):- Reconstructing changes in bivalve biodiversity throughout the Triassic–Jurassic Larne Basin. Numbers in red indicate horizons associate with percentage taxon extinction values (see also Fig. 5- Chapter 6).

Lithostratigraphic boundary depths (m)



The disappearances of taxa as proxies for extinction and the use of ichnotaxa in identifying specific species:

It should be acknowledged that the disappearance of taxa, including ichnotaxa, is not necessarily indicative of extinction. Taxa may disappear due to environmental changes or due to preservational changes. Furthermore, the loss of ichnotaxa in the Larne section are not indicative of species extinction as i) ichnotaxa cannot be directly related to species; they are records of animal behaviour and ii) the ichnotaxa named in this thesis from the Larne Basin re-occur in younger sediments. However, in light of all of the information which has been reviewed within this chapter there does appear to be a positive correlation between marine redox changes and changes to infaunal marine animal diversity/animal behaviour. Whether the biodiversity changes observed within this chapter could be in part related to other environmental changes have been partly addressed within this chapter, however there is scope for further study.

Redox facies interpretation:

The interpretation of redox facies within this chapter has been undertaken through reviewing elemental data from literature for select diagnostic redox sensitive elements in order to compile a quantitative redox framework (Chapter 3). This framework has acted as a guide with regards to the interpretation of redox conditions.

Sample contamination:

MAG-1 standards digested with the Larne batches fell within 4% of published values on average. Also, concentrations (ng) for procedural blanks digested with the Larne batches generally exhibit concentrations <1% of lower bound analyte values with all measured elements exhibiting sub ng concentrations.

7 AN OXYGENATED GLOBAL OCEAN DURING THE END-TRIASSIC MASS EXTINCTION EVENT

Andrew D. Bond, Alexander J. Dickson, Micha Ruhl, Remco Bos, and Bas van de Schootbrugge

In review in *Nature Geoscience*

Statement of lead author's contributions:

- Obtained samples from MR, BvdS, RB and Martin Blumenberg
- Milled a subset of the samples
- Digested the sample powders
- Prepared the samples for ICP-MS and ICP-AES analyses
- Processed the ICP-MS and ICP-AES data
- Calculated molybdenum double spike solution volumes and sample weights
- Weighed and digested samples with double spike solutions
- Processed sample solutions through anion exchange columns
- Processed samples on Neptune Plus MC-ICP-MS for concentration checks
- Diluted samples and ran for molybdenum isotope ratios
- Processed MC-ICP-MS data
- Interpreted MC-ICP-MS data
- Wrote the first draft of the manuscript
- Prepared all figures for the manuscript
- Made corrections to the manuscript and figures based on co-authors' comments
- Made corrections to the manuscript and figures based on the reviewer's comments

An oxygenated global ocean during the end-Triassic mass extinction event

Andrew D. Bond^{1*}, Alexander J. Dickson¹, Micha Ruhl², Remco Bos³, Bas van de Schootbrugge³.

¹Department of Earth Sciences, Royal Holloway University of London, Egham, Surrey, TW200EX, UK

² Department of Geology, Trinity College Dublin, The University of Dublin, Dublin, Ireland

³ Department of Earth Sciences, Utrecht University, Marine Palynology & Paleooceanography, Princetonlaan 8a, 3584, CB, Utrecht, the Netherlands

*Corresponding author: Andrew.Bond.2014@live.rhul.ac.uk

Abstract

One of the most severe extinctions of complex marine life in Earth's history occurred at the end of the Triassic Period. The end-Triassic extinction event was initiated by large igneous province volcanism and has tentatively been linked to oceanic redox change. However, the global-scale pattern of oceanic redox across the end-Triassic event is not well constrained. Here we use the sedimentary enrichment and isotopic composition of the redox-sensitive element molybdenum to reconstruct global–local marine redox conditions through the extinction interval. Peak $\delta^{98}\text{Mo}$ values indicate that the global distribution of sulfidic marine conditions was similar to the modern ocean during the extinction interval. Meanwhile, Tethyan shelf sediments record pulsed, positive $\delta^{98}\text{Mo}$ excursions indicative of locally oxygen-poor, sulfidic conditions. We suggest that pulses of marine de-oxygenation were largely restricted to marginal marine environments during the latest Triassic, playing a significant role in shallow marine extinction phases at that time, whilst the Late Triassic global ocean remained well-

oxygenated. Importantly, this shows that global marine biodiversity, and possibly ecosystem stability, were vulnerable to geographically localised anoxic conditions. Expanding present-day marine anoxia in response to anthropogenic marine nutrient supply and climate forcing may therefore have significant consequences for global biodiversity and wider ecosystem stability.

Main text

The Triassic–Jurassic boundary interval (TJB, ~201 Ma) is marked by one of the largest extinctions of complex marine life in Earth’s history: the End-Triassic mass extinction event (ETME) ¹. The ETME has been closely associated with provincial volcanism from the Central Atlantic Magmatic Province (CAMP) which has been linked to atmospheric carbon injection as evidenced through Triassic–Jurassic negative carbon isotope excursions ². CAMP activity is also thought to have caused Triassic–Jurassic marine acidification and marine de-oxygenation ^{2,3}. Studies of latest Triassic marine de-oxygenation indicate that locally sulfidic conditions were prominent within marginal marine surface waters of the Tethys and Panthalassic oceans around the TJB ^{3–8}. Oxygen-poor conditions have been further identified from blooms of prasinophycean algae ^{3,9}, a negative excursion in carbonate U isotopes ¹⁰, widespread Early Jurassic black shale deposition ^{9,11}, elemental redox proxies ^{3,12}, and Fe speciation data ¹³. Therefore, recent studies suggest that marine redox change may have played an important role in end-Triassic marine extinction phases. However, most existing Late Triassic redox studies are at a local, basinal scale or sub-regional scale, and do not provide information about the global-scale distribution of marine redox conditions. The unconstrained areal extent of globally sulfidic conditions during the ETME limits understanding of the role of spatial redox change in the Late Triassic marine extinctions.

The isotopic composition of molybdenum (Mo) in organic-rich sediments has been widely used to reconstruct the oxygenation of both local and global ancient marine environments^{14, 15}. Under oxic depositional conditions Mo typically exhibits low sedimentary enrichments and isotopically light compositions, due to (Mn)oxyhydroxide adsorption, with compositions ~3‰ lighter than coeval seawater^{15–17}. Under reducing conditions Mo exhibits higher sedimentary enrichments due to the formation of thiolated (poly)molybdate species that have smaller isotopic offsets from seawater than Mo adsorbed onto oxyhydroxides^{18, 19}. Generally well-oxygenated global marine conditions are therefore reflected by isotopically heavy $\delta^{98}\text{Mo}$ seawater values due to oxyhydroxide adsorption acting as the primary vector of Mo burial²⁰. Poorly oxygenated global marine conditions are represented by isotopically light $\delta^{98}\text{Mo}$ seawater values as global oxyhydroxide burial declines²⁰. However, studies of $\delta^{98}\text{Mo}$ from across the TJB and ETME remain undocumented.

Here we use the sedimentary enrichment (Mo_{EF}) and isotopic composition of Mo to examine the link between marine de-oxygenation and extinction during the ETME. We obtained material from the Carnduff-2 core (Northern Ireland), Hebelmeer-2 core (west Germany), and Schandelah-1 core (north Germany) which preserve lithological records of marine marls, sandstones, and organic-rich shales deposited on the Tethyan shelf before, during and after the ETME with little evidence for significant diagenetic alteration (Fig. 1; see Chapter 7 supplementary information). All three sites have undergone previous stratigraphic study and include detailed biotic records for correlation^{6, 21–23}. We identify little correlation between proxies for detrital sediment input and $\delta^{98}\text{Mo}$ or Mo_{EF} and therefore interpret stratigraphic variations in Mo as a

function of local redox conditions (see Chapter 7 supplementary data). The samples analysed in this study are therefore ideally suited to explore the relationship between marine extinction and de-oxygenation on the Tethyan shelf during the TJB.

Oxygenated global oceanic conditions prevailed during the Triassic–Jurassic transition

The $\delta^{98}\text{Mo}$ of coeval seawater ($\delta^{98}\text{Mo}_{\text{sw}}$) must be resolved to determine global redox conditions. However, in order to determine $\delta^{98}\text{Mo}_{\text{sw}}$, sedimentary $\delta^{98}\text{Mo}$ values must be corrected for isotopic fractionation, with the isotopic fractionation and sedimentary enrichment of Mo being dependent on local redox conditions²⁰. The maximum $\delta^{98}\text{Mo}$ compositions of Upper Triassic mudstones in the studied cores are $\sim 1.6\text{‰}$ (Carnduff-2: 1.56‰ ; Hebelmeer-2: 1.63‰ ; Fig. 2). These $\delta^{98}\text{Mo}$ values are obtained from sampling levels where trace metal distributions are indicative of non-euxinic depositional conditions (see supplementary information)¹². Non-euxinic conditions coinciding with upper-bound Carnduff-2 $\delta^{98}\text{Mo}$ values are further supported by oxic–anoxic iron speciation values from a correlative horizon within the Larne Basin¹³. Molybdenum sulfides forming in sedimentary porewaters underlying a non-euxinic water column are fractionated by a minimum of $\sim 0.7\text{‰}$ relative to coeval seawater^{24, 25}, with fractionation likely exceeding 0.7‰ within the Larne Basin on account of local redox conditions^{12, 13}. Therefore, Late Triassic $\delta^{98}\text{Mo}_{\text{sw}}$ was likely $>2.3\text{‰}$, similar to modern day seawater²⁶. A Late Triassic $\delta^{98}\text{Mo}_{\text{sw}}$ equal to or greater than the modern ocean is consistent with sulfidic conditions covering no more than $\sim 0.05\text{--}0.1\%$ of the Late Triassic seafloor, similar or even less than in the modern-day¹⁵.

The average upper bound $\delta^{98}\text{Mo}$ throughout the basal Jurassic of the Carnduff-2 core is $1.47 \pm 0.58\text{‰}$ ($n=3$) and characterises horizons with TM distributions that are not

indicative of localised euxinia¹². Predominantly non-euxinic conditions from the basal Jurassic of the Larnie Basin are further supported by iron speciation data¹³. Therefore, basal Jurassic $\delta^{98}\text{Mo}_{\text{SW}}$ was likely $>2.2\%$, also similar to the Late Triassic and modern global ocean. The persistence of a similar $\delta^{98}\text{Mo}_{\text{SW}}$ from the Late Triassic through to the basal Jurassic indicates that there was no significant long-term change in global marine redox conditions across the Triassic–Jurassic boundary interval, and that the basal Jurassic global open ocean remained generally well oxygenated. Our conclusion of a globally oxygenated open ocean during the basal Jurassic is further supported by pyrite framboid data from an open ocean Panthalassa site²⁷.

Regional de-oxygenation during the ETME

Oxygen-poor conditions were present across Tethyan and Panthalassa marginal marine environments during the main extinction interval^{5, 7, 12, 13}. Such conditions have been further identified here on the basis of $\delta^{98}\text{Mo}$ and M_{OEF} data with redox conditions varying according to both site and stratigraphy. The Schandelah-1 and Carnduff-2 cores both exhibit positive $\delta^{98}\text{Mo}$ shifts that directly coincide with the main extinction interval, as denoted by the “initial” negative carbon isotope excursion (CIE)^{2, 28, 29} (Fig. 2). The increase in $\delta^{98}\text{Mo}$ (and M_{OEF}) during the main extinction interval indicates an increased availability of reduced sulfur [HS^-], likely due to the shoaling of the sulfate reduction zone within sedimentary porewaters up to the sediment-water interface^{24, 25, 30}. Relatively high M_{OEF} alongside low $\delta^{98}\text{Mo}$ around the base of the main extinction interval within the Hebelmeer-2 core also indicates increased [HS^-], likely due to the expansion of the sulfate reduction zone into the water column, with the burial of intermediate thiomolybdate species at H_2S concentrations $<11\mu\text{M}$ ^{19, 31}. Isotopically light values are inconsistent with oxide adsorption given the

elevated TS (%) at this horizon ⁶. Weakly sulfidic conditions around the base of the initial CIE at Cloghan Point (Northern Ireland) and St. Audrie's Bay (Somerset, UK) are also suggested through positive $\delta^{34}\text{S}$ excursions ^{4,7}, and low sulfate within Late Triassic seawater of the Tethyan shelf has been interpreted through $\delta^{34}\text{S}$ data ⁷.

Pulsed de-oxygenation during the end-Triassic and earliest Jurassic

Multiple pulses of marine deoxygenation were prevalent on the Tethyan shelf during the latest Triassic and earliest Jurassic. Low to moderate M_{OEF} as well as isotopically heavy $\delta^{98}\text{Mo}$ in all three cores during deposition of the basal Westbury Formation and stratigraphically equivalent units, are suggestive of shoaling of the sulfate reduction zone towards the sediment-water interface ^{24,25,30}. Similar shoaling of the sulfate reduction zone is also observed within the Carnduff-2 and Hebelermeer-2 cores during the deposition of the uppermost Westbury Formation and equivalent units. Both phases of porewater de-oxygenation coincided with photic zone euxinia on the Tethyan shelf during the middle Rhaetian ⁶ (Fig. 3); the upper pulse also coincided with episodic photic zone euxinia within the Bristol Channel Basin ⁸, and de-nitrification within the Central European Basin at the Mingolsheim and Mariental-1 sites ^{3,32} (Fig. 3). $\delta^{98}\text{Mo}$ then decreases during the deposition of the lower Cotham member and stratigraphically equivalent units, as seen within both the Carnduff-2 and Schandelah-1 cores, with M_{OEF} decreasing or remaining low. Isotopically light $\delta^{98}\text{Mo}$ and low M_{OEF} are suggestive of a regional shift to more oxygenated conditions with high Mo fractionation likely being associated with Fe-Mn oxide formation and organic uptake ^{16,33}.

Multiple further positive shifts in $\delta^{98}\text{Mo}$ and M_{OEF} are observed within the basal Jurassic of the Carnduff-2 core suggestive of pulsed increases of $[\text{HS}^-]$ caused through periodic shoaling of the sulfate reduction zone. Correlative horizons within the Schandelah-1 core contain $\delta^{98}\text{Mo}$ and M_{OEF} shifts indicative of shoaling of the sulfate

reduction zone and low-sulfur, oxygen poor (ferruginous) conditions. The very low enrichment of elements sensitive to reduction (U) and variable enrichment of elements sensitive to HS⁻ availability (Mo, Cu, Zn) from this horizon within the Schandelah-1 core further supports ferruginous conditions (see supplementary information), as does overall low sulfate on the Triassic–Jurassic Tethyan shelf interpreted from $\delta^{34}\text{S}$ data⁷. Pulsed oxygen-poor conditions within the basal Jurassic of the Carnduff-2 and Schandelah-1 cores coincided with photic zone euxinia within the Bristol Channel Basin^{4, 8} (Fig. 3).

Periodically pulsed anoxia during the Late Triassic and Early Jurassic has previously been noted based on eccentricity modulated precession timescales in the Bristol Channel Basin (St. Audrie’s Bay) with laminated organic-rich black shales forming every precession cycle³⁴. Pulses of marine redox change have also been reported from the Larne Basin, largely coinciding with the disappearance of infaunal bivalve taxa¹². We similarly note a close relationship between redox pulses and Late Triassic extinction phases (Fig. 3).

Localised marine de-oxygenation as a driver of extinction during the ETME

The coincidental pulsed nature of marine de-oxygenation and end-Triassic marine extinction phases strongly suggests a causal relationship (Fig. 3, Fig. 4). However, the persistence of broadly oxygenated global marine conditions through the Triassic–Jurassic boundary interval inferred from our new Mo isotope datasets suggests that these pulses of marine de-oxygenation were largely limited to marginal marine environments. Geographically localised anoxic conditions on the Tethyan shelf are further supported by carbonate U isotope data¹⁰. We suggest that geographically

localised marine de-oxygenation, within Late Triassic marginal marine environments, therefore had major implications for Late Triassic biodiversity and ecosystem stability. Our inference of geographically localised marine de-oxygenation is consistent with recent studies indicating elevated weathering and erosion rates in Tethyan Shelf localities during the Late Triassic^{35, 36}. Localised marine de-oxygenation may have been driven by high run-off from the Late Triassic continents triggering eutrophication and stratification, with increased run-off being driven by a warming climate and the collapse of forest ecosystems³⁷. Open marine environments will have been significantly less affected by such perturbations and consequently the open oceans may have remained a refugia for marine life.

Modern, marginal marine environments are likely also particularly sensitive to changes in marine redox whilst also being some of the most biodiverse oceanic environments on Earth³⁸⁻⁴¹. Therefore, anthropogenically driven environmental change, including the expansion of marine anoxia and enhanced marine nutrient supply, may result in geographically localised, marine de-oxygenation, which could have major consequences for future marine biodiversity and ecosystem stability⁴², with particularly severe consequences for marginal marine corals, mangroves, and coastal fishes^{1, 40, 41}.

Methods

Bulk inorganic geochemistry 50mg of each sample was digested using inverse aqua regia (3:1 HNO₃/HCl) followed by digestion of silicates in 1:2 HF/HNO₃. Major elemental concentration data was measured using a Perkin Elmer Optima 3300RL ICP-AES and minor elemental concentration data was measured using a Perkin Elmer NexION 350D ICP-MS. Accuracy was determined using full procedural digests of MAG-1 (n=7) and was $\pm 2.5\%$ with Mo within uncertainty of the certified value.

Precision was calculated using the 2 S.D. of the MAG-1 digests as $\pm 17\%$ (Cr, Cu, Zn, Al $\pm < 10\%$), as well as 5 digests of an in-house mudrock standard (PERN-1) as $\pm 21\%$. Mo_{EF} was determined using: $((Mo_{sample}/Al_{sample}) / (Mo_{ucc}/Al_{ucc}))$. Upper continental crust (ucc) concentrations were taken from ref. 45. Procedural blanks digested with the ICP-MS batches exhibited blanks of between 0.02ng and 4.8ng total Mo.

Molybdenum concentrations and isotopes Samples were processed and measured under trace-metal clean laboratory conditions. Prior to molybdenum-isotope analysis each sample was weighed and spiked with a ^{97}Mo - ^{100}Mo double-spike solution and digested in 3:1 HNO_3/HCl . Mo samples were separated from matrix elements and interferences using an anion exchange column procedure detailed within refs. 46 and 47. $\delta^{98/95}Mo$ compositions were measured using a Thermo Scientific Neptune Plus MC-ICP-MS. Procedural blanks for Mo were between 0.5 and 5 ng. All $\delta^{98/95}Mo$ data were calculated relative to NIST SRM 3134 $+0.25\%$ ⁴⁸. Accuracy and precision were assessed using the Open University Mo solution standard (c.f. ref. 49) ($-0.35 \pm 0.15\%$, $n=12$, 2 S.D.) and multiple separate digests of USGS SDO-1 shale, which yielded an average $\delta^{98/95}Mo$ of $0.79 \pm 0.08\%$ (2.S.D., $n=6$) within uncertainty of published values ($0.8 \pm 0.1\%$)⁴⁹.

1. Dunhill, A. M., Foster, W. J., Sciberras, J. & Twitchett, R. J. Impact of the Late Triassic mass extinction on functional diversity and composition of marine ecosystems, *Palaeontol.* 61 (1), 133–148 (2018).
2. Ruhl, M., Bonis, N. R., Reichart, G.-J., Sinninghe Damsté, J. S. & Kürschner, W. M. Atmospheric carbon injection linked to end-Triassic mass extinction. *Sci. Rep.* 333, 430–434 (2011).
3. Richoz, S. *et al.* Hydrogen sulphide poisoning of shallow seas following the end-Triassic extinction. *Nat. Geosci.* 5, 662–667 (2012).

4. Jaraula, C. M. B *et al.* Elevated $p\text{CO}_2$ leading to Late Triassic extinction, persistent photic zone euxinia, and rising sea levels. *Geol.* 41 (9), 955–958 (2013).
5. Kasprak, A. H. *et al.* Episodic Photic Zone Euxinia in the Northeastern Panthalassic Ocean during the End-Triassic Extinction. *Geol.* 43 (4), 307–310 (2015).
6. Blumenberg, M., Heunisch, C., Lückge, A., Scheeder & Wiese, F. Photic zone euxinia in the central Rhaetian Sea prior the Triassic-Jurassic boundary. *Palaeogeog., Palaeoclimatol., Palaeoecol.* 461, 55–64 (2016).
7. He, T. *et al.* An enormous sulfur isotope excursion indicates marine anoxia during the end-Triassic mass extinction. *Sci. Adv.* 6 (37): eabb6704 (2020).
8. Fox, C. P. *et al.* Two-pronged kill mechanism at the end-Triassic mass extinction. *Geol.* <https://doi.org/10.1130/G49560.1> (2022)
9. Bonis, N. R., Ruhl, M. & Kürschner, W. M. Climate change driven black shale deposition during the end-Triassic in the western Tethys. *Palaeogeog., Palaeoclimatol., Palaeoecol.* 290, 151–159 (2010).
10. Jost, A. B. *et al.* Uranium isotope evidence for an expansion of marine anoxia during the end-Triassic extinction. *Geochem., Geophys., Geosyst.* 18 (8), 3093–3108 (2017).
11. Van de Schootbrugge, B.v.d., Bachan, A., Suan, G., Richoz, S. & Payne, J. L. Microbes, mud and methane: cause and consequence of recurrent Early Jurassic anoxia following the end-Triassic mass extinction. *Palaeontol.* 56 (4), 685–709 (2013).
12. Bond, A. D., Dickson, A. J., Ruhl, M. & Raine, R. Marine redox change and extinction in Triassic–Jurassic boundary strata from the Larne Basin, Northern Ireland. *Palaeogeog., Palaeoclimatol., Palaeoecol.* 598, 111018 (2022) <https://doi.org/10.1016/j.palaeo.2022.111018>.

13. He, T. *et al.* Extensive marine anoxia in the European epicontinental sea during the end-Triassic mass extinction. *Glob. Planet. Change* 210, 103771 (2022).
14. Dickson, A. J. A molybdenum-isotope perspective on Phanerozoic deoxygenation events. *Nat. Geosci.* 10, 721–726 (2017).
15. Kendall, B., Dahl, T. W. & Anbar, A. D. The stable isotope geochemistry of molybdenum. *Rev. Mineral. Geochem.* 82, 683–732 (2017).
16. Barling, J. & Anbar, A. D. Molybdenum isotope fractionation during adsorption by manganese oxides. *Earth Planet. Sci. Lett.* 217, 315–329 (2004).
17. Scott, C. & Lyons, T. W. Contrasting molybdenum cycling and isotopic properties in euxinic versus non-euxinic sediments and sedimentary rocks: Refining the paleoproxies. *Chem. Geol.* 324–325, 19–27 (2012).
18. Erickson, B. E. & Helz, G. R. Molybdenum(VI) speciation in sulfidic waters: Stability and lability of thiomolybdates. *Geochim. Cosmochim. Acta.* 64 (7), 1149–1158 (2000).
19. Nägler, T. F., Neubert, N., Böttcher, M. E., Dellwig, O. & Schmetger, B. Molybdenum isotope fractionation in pelagic euxinia: Evidence from the modern Black and Baltic Seas. *Chem. Geol.* 289, 1–11 (2011).
20. Dickson, A. J. *et al.* Isotopic constraints on ocean redox at the end of the Eocene. *Earth Planet. Sci. Lett.* 562, 116814 (2021).
21. Lindström, S. *et al.* A new correlation of Triassic–Jurassic boundary successions in NW Europe, Nevada and Peru, and the Central Atlantic Magmatic Province: A time-line for the end-Triassic mass extinction. *Palaeogeog., Palaeoclimatol., Palaeoecol.* 478, 80–102 (2017).
22. Schootbrugge, B.v.d. *et al.* The Schandelah Scientific Drilling Project: A 25-million year record of Early Jurassic palaeo-environmental change from northern Germany. *Newsl. Stratigr.* 52–53, 249–296 (2019).

23. Boomer, I. *et al.* Stratigraphy, palaeoenvironments and geochemistry across the Triassic–Jurassic boundary transition at Carnduff, County Antrim, Northern Ireland. *Proc. Geol. Assoc.* 132 (6), 667–687 (2021).
24. Poulson Brucker, R. L., McManus, J., Severmann, S. & Berelson, W. M. Molybdenum behaviour during early diagenesis: Insights from Mo isotopes. *Geochem. Geophys. Geosys.* 10 (6), Q06010 (2009).
25. Scholz, F., Siebert, C., Dale, A. W. & Frank, M. Intense molybdenum accumulation in sediments underneath a nitrogenous water column and implications for the reconstruction of paleo-redox conditions based on molybdenum isotopes. *Geochim. Cosmochim. Acta* 213, 400–417 (2017).
26. Nakagawa, Y. *et al.* The molybdenum isotope composition of the modern ocean. *Geochem. J.* 46, 131–141 (2012).
27. Wignall, P. B. *et al.* An 80 million year oceanic redox history from Permian to Jurassic pelagic sediments of the Mino-Tamba terrane, SW Japan, and the origin of four mass extinctions. *Glob. Planet. Change* 71(1–2), 109–123 (2010).
28. Hesselbo, S. P., Robinson, S. A., Surlyk, F. & Piasecki, S. Terrestrial and marine extinction at the Triassic–Jurassic boundary synchronized with major carbon-cycle perturbation: A link to initiation of massive volcanism? *Geol.* 30 (3), 251–254 (2002).
29. Wignall, P. B. & Atkinson, J. W. A two-phase end-Triassic mass extinction. *Earth Sci. Rev.* 208, 103282 (2020).
30. Siebert, C., McManus, J., Bice, A., Poulson, R. & Berelson, W. M. Molybdenum isotope signatures in continental margin marine sediments. *Earth Planet. Sci. Lett.* 241, 723–733 (2006).
31. Kerl, C. F., Lohmayer, R., Bura-Nakić, E., Vance, D. & Planer-Friedrich, B. Experimental confirmation of isotope fractionation in thiomolybdates using ion chromatographic separation and detection by multicollector ICPMS. *Anal. Chem.* 89 (5), 3123–3129 (2017).

32. Quan, T. M., Schootbrugge, B.v.d., Field, M. P. & Rosenthal, Y. Nitrogen isotope and trace metal analyses from the Mingolsheim core (Germany): Evidence for redox variations across the Triassic-Jurassic boundary. *Glob. Biogeochem. Cycles* 22 (2), <https://doi.org/10.1029/2007GB002981> (2008).
33. King, E. K., Perakis, S. S., & Pett-Ridge, J. C. Molybdenum isotope fractionation during adsorption to organic matter. *Geochim. Cosmochim. Acta.* 222, 584–598 (2018).
34. Ruhl *et al.* Astronomical constraints on the duration of the early Jurassic Hettangian stage and recovery rates following the end-Triassic mass extinction (St Audrie's Bay/East Quantoxhead, UK). *Earth Planet. Sci. Lett.* 295, 262–276 (2010).
35. Van de Schootbrugge, B.v.d *et al.* Catastrophic soil loss associated with end-Triassic deforestation. *Earth Sci. Rev.* 210, 103332 (2020).
36. Fox, C. P, Whiteside, J. H., Olsen, P. E., & Grice, K. Flame out! End-Triassic mass extinction polycyclic aromatic hydrocarbons reflect more than just fire. *Earth Planet. Sci. Lett.* 584, 117418, <https://doi.org/10.1016/j.epsl.2022.117418> (2022).
37. Van de Schootbrugge, B.v.d *et al.* Floral changes across the Triassic/Jurassic boundary linked to flood basalt volcanism. *Nat. Geosci.* 2, 589–594 (2009).
38. Schmidtko, S., Stramma, L. & Visbeck, M. Decline in global oceanic oxygen content during the past five decades. *Nat.* 542, 335–337 (2017).
39. Breitburg, D. L. *et al.* Declining oxygen in the global ocean and coastal waters. *Sci.* 359 (6371), eaam7240 (2018).
40. Renema, W. *et al.* Hopping Hotspots: Global Shifts in Marine Biodiversity. *Sci.* 321, 654–657 (2008).
41. Tittensor, D. P. *et al.* Global patterns and predictors of marine biodiversity across taxa. *Nat.* 466, 1098–1101 (2010).

42. IPCC *Climate Change 2021: The Physical Science Basis* (eds Masson-Delmotte, V. et al.) Cambridge Univ. Press 2021).
43. Barras, C. G. & Twitchett, R. J. Response of the marine infauna to Triassic–Jurassic environmental change: Ichnological data from southern England. *Palaeogeog., Palaeoclimatol., Palaeoecol.* 244, 223–241 (2007).
44. Hillebrandt, A.v. *et al.* The Global Stratotype Sections and Point (GSSP) for the base of the Jurassic System at Kuhjoch (Karwendel Mountains, Northern Calcareous Alps, Tyrol, Austria). *Episodes* 36 (3), 162–198 (2013).
45. Rudnick, R. L. & Gao, S. The composition of the Continental Crust *In* Holland, H. D. and Turekian, K.K., Eds., *Treatise on Geochemistry*, Vol. 3, The Crust, Elsevier-Pergamon, Oxford, 1–64. (2003).
46. Pearce, C. R., Cohen, A. S. & Parkinson, I. J. Quantitative separation of molybdenum and rhenium from geological materials for isotopic determination by MC-ICP-MS. *Geostand. Geoanal. Res.* 33 (2), 219–229 (2009).
47. Dickson, A. J., Jenkyns, H. C., Porcelli, D., van den Boorn, S. & Idiz, E. Basin-scale controls on the molybdenum-isotope composition of seawater during the Oceanic Anoxic Event 2 (Late Cretaceous). *Geochim. Cosmochim. Acta* 178, 291–306 (2016).
48. Nägler, T. F. *et al.* Proposal for an international molybdenum isotope measurement standard and data representation. *Geostand. Geoanal. Res.* 38 (2), 149–151 (2014).
49. Goldberg, T. *et al.* Resolution of inter-laboratory discrepancies in Mo isotope data: an intercalibration. *J. Anal. At. Spectrom.* 28 (5), 724–735 (2013).

Acknowledgements

We thank the Geological Survey of Northern Ireland (GSNI) for providing access to the Carnduff-2 core. We also thank Martin Blumenberg for generously providing the Hebelmeer-2 core material. We appreciate the help of J. Brakeley (RHUL) and P. Holdship (Oxford) for their assistance with ICP-MS and ICP-AES measurements. This work was funded through a NERC DTP PhD Studentship awarded to A.D.B (NE/L002485/1). MR acknowledges financial support from the Irish Centre for research in Applied Geoscience (iCRAG).

Author contributions

A.J.D, A.D.B and M.R designed the research. M.R sampled the Carnduff-2 core at the GSNI core repository. B.v.d.S and R.B provided access to material from the Schandelah-1 core. A.D.B carried out elemental and isotopic geochemical analyses with assistance from A.J.D. A.D.B and A.J.D interpreted the data with assistance from M.R, R.B. and B.v.d.S. A.D.B wrote the paper and designed the figures. All authors contributed to the text and figure amendments.

Additional Information

Supplementary information, including the dataset, will be available with the online version of the paper.

Competing financial interests

The authors declare no competing financial interests

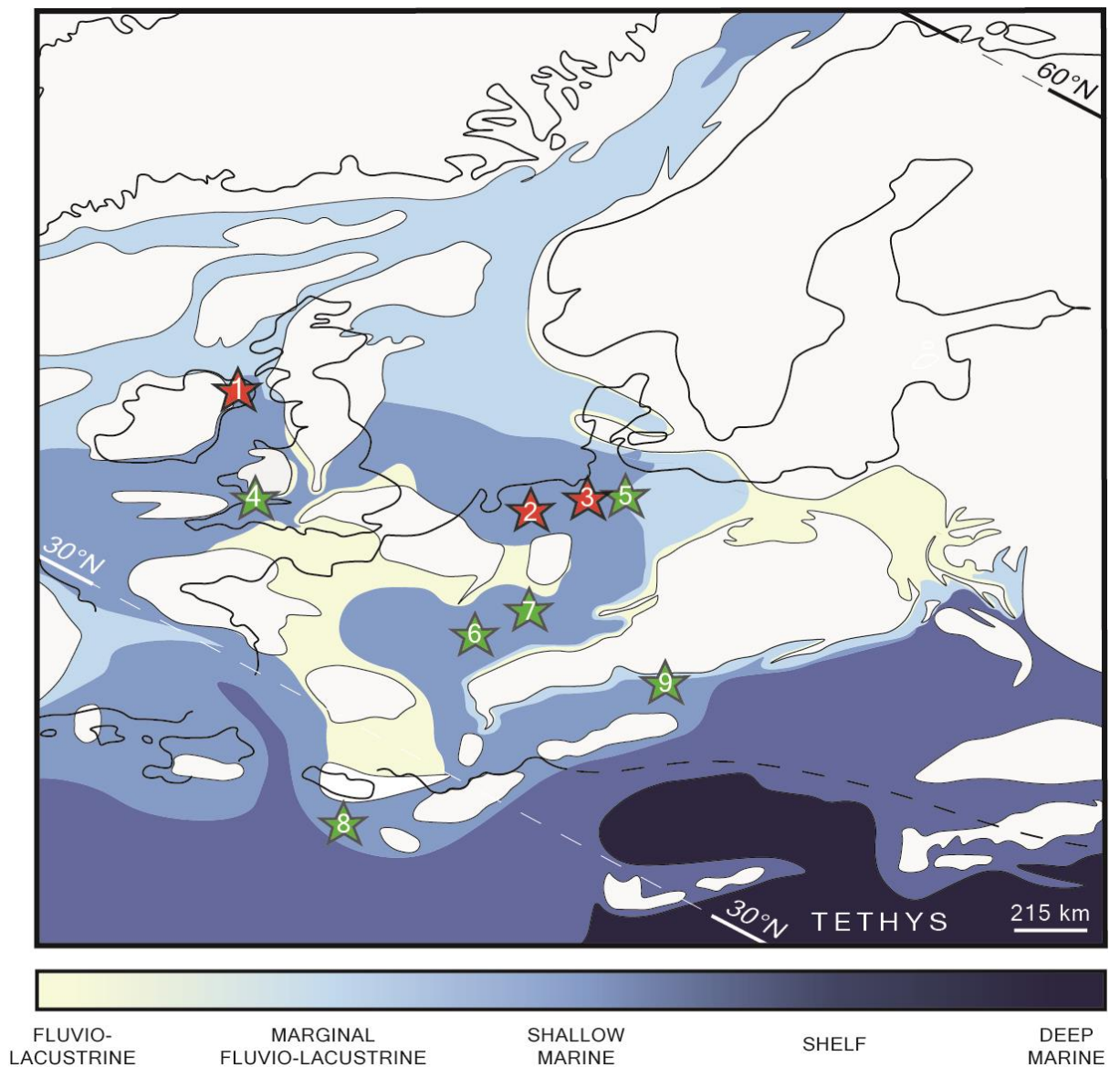


Figure 1: Triassic–Jurassic palaeogeography of the Tethyan shelf amended from ref. 12. 1- Carnduff-2 core, Larne Basin, 2- Hebelermeer-2 core, 3- Schandelah-1 core, 4- Bristol Channel Basin, 5- Marientel-1 core, 6- Rosswinkel FR 201-204 core, 7- Mingolsheim core, 8- Lombardy Alps, 9- Kuhjoch section (GSSP). Red stars- sites from this study. Green stars- sites of previous palaeo-redox studies and of stratigraphic importance.

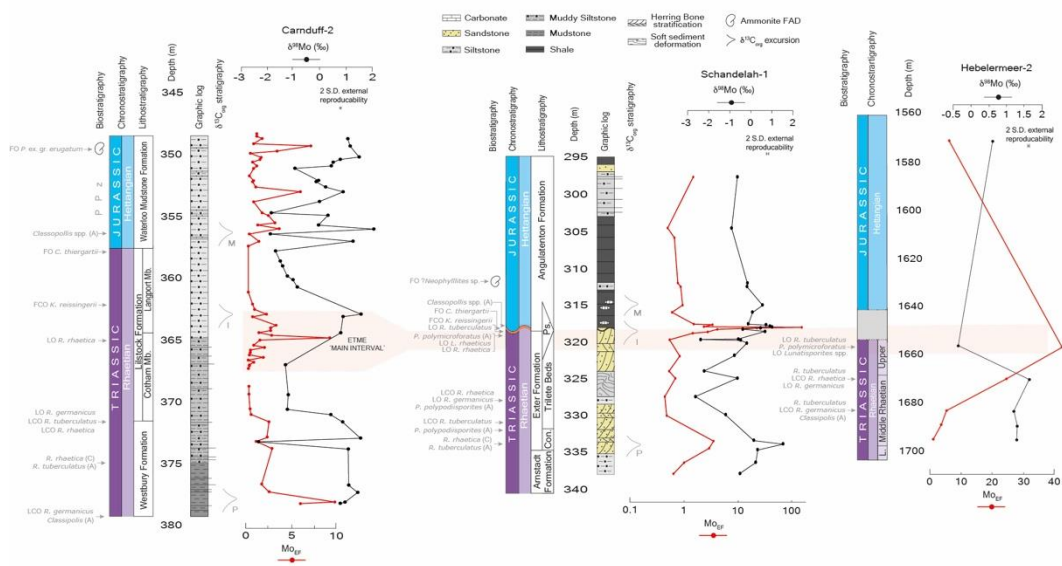


Figure 2:- Overview of key stratigraphic, lithological, and geochemical data for Carnduff-2, Schandelah-1, and Hebelermeer-2. Carnduff-2 stratigraphic and lithological data from refs. 12 and 23, Mo_{EF} data from ref. 12, Schandelah-1 stratigraphic and lithological data from refs. 21 and 22, Hebelermeer-2 stratigraphic data from ref. 6. (A)- Abundant, (C)- common, FCO- first common occurrence, FO- first occurrence, LCO, last common occurrence, LO- last occurrence. M- Main CIE, I- Initial CIE, P- Precursor CIE. The ETME ‘main interval’ coincides with the main phase of extinction at the GSSP. Correlative pulses of extinction are not currently known from the Schandelah-1 and Hebelermeer-2 core sections; however, this may partly be associated with uncertainty in the positioning of the ETME and CIE from the Hebelermeer-2 core section.

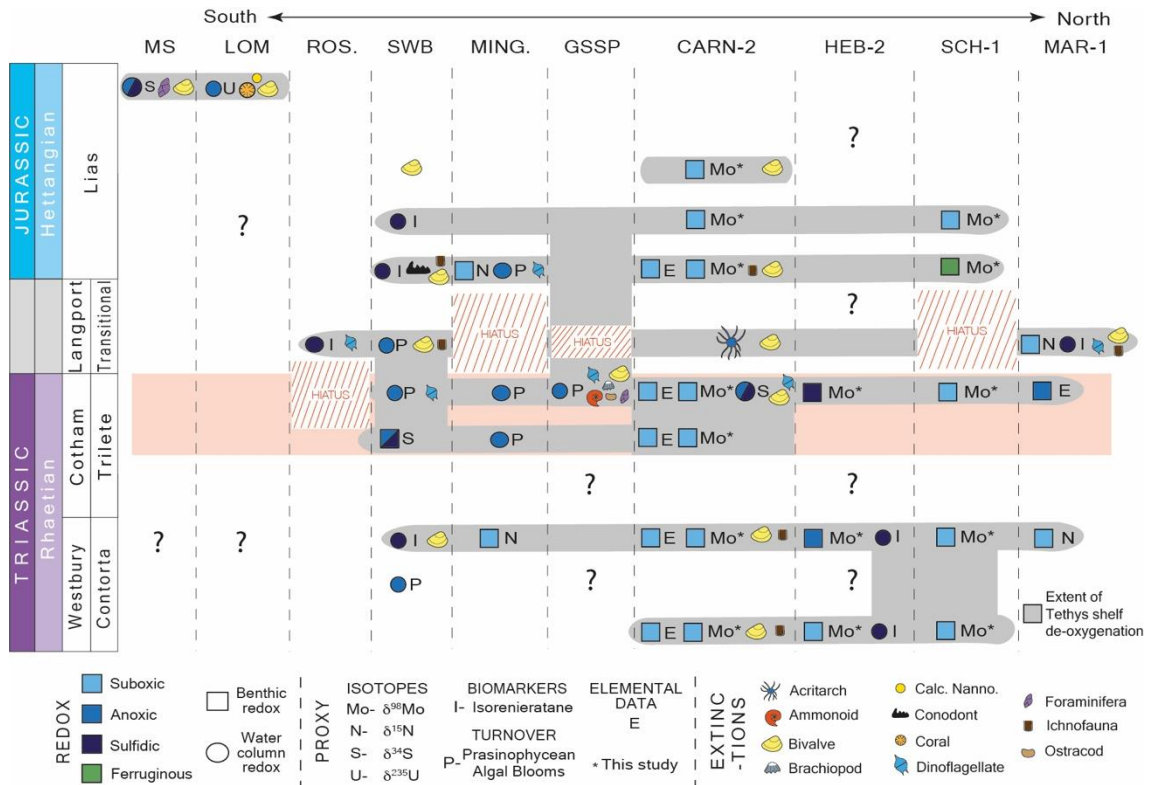


Figure 3:- Stepped evolution of marine de-oxygenation and extinction on the Tethyan shelf through the Late Triassic. CARN-2 – Carnduff-2 core, GSSP – Kuhjoch Section, Austria, HEB-2 – Hebelermeer-2 core, LOM. – Lombardy Basin, MAR-1- Marientel-1 core, MING. – Mingolsheim core, MS- Mount Sparagio section, Italy, ROS. – Rosswinkel FR 201-204 core, SCH-1 – Schandelah-1 core, SWB – Southwest Britain. $\delta^{15}\text{N}$ data from refs. 3 and 32, $\delta^{34}\text{S}$ data from refs. 4 and 7, $\delta^{235}\text{U}$ data from ref. 10., isorenieratane data from refs. 3, 4, 6, and 8, prasinophycean data from refs. 3 and 9, elemental data from refs. 3 and 12. Extinction data from refs. 3, 8, 9, 12, 29, 43, 44. Red shaded area- ETME Main Interval. Horizontal bars represent pulses of oxygen poor conditions. Vertical grey connections represent where oxygen poor conditions are more continuous in nature whereas gaps in the record represent either where the resolution of data is relatively low (question marks), or where the selected redox proxy represents a change in palaeodepositional conditions. For further information regarding the continuity of stratigraphic sections refer to Figs. S1 and S2 (Chapter 7).

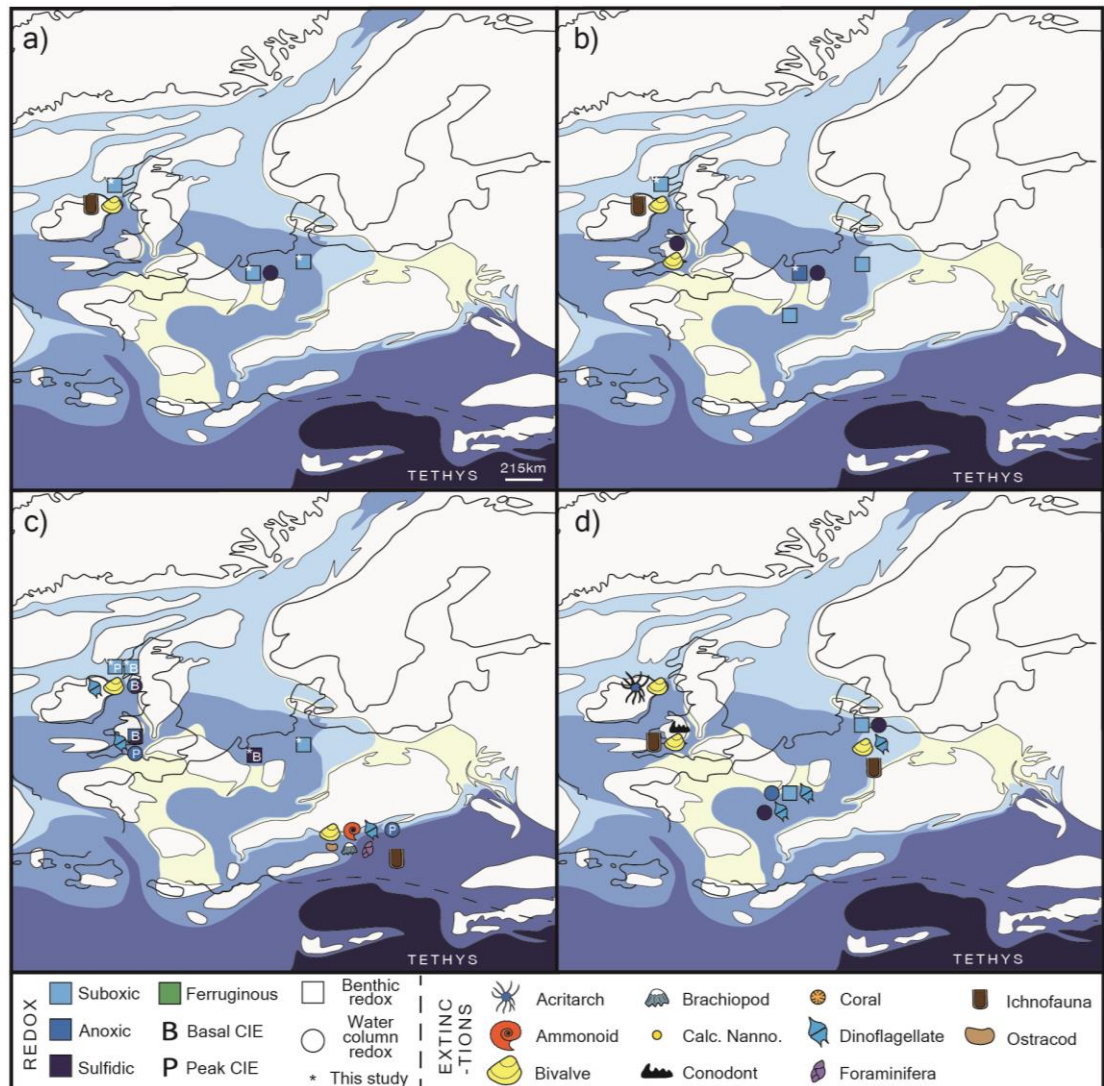


Figure 4:- Pulses of marine de-oxygenation and synchronous extinction during the latest Triassic and earliest Jurassic on the Tethyan shelf. a, b) pre-CIE (initial carbon isotope excursion), c) CIE d) post CIE. Extinction pictograms amended from ref. 29, palaeogeography amended from ref. 12. Calc. Nanno.- calcareous nannofossil. For data source(s) refer to Fig. 3.

Supplementary data – Raw data attached separately as an excel file ‘Supplementary Information : Chapter 7’

Chapter 7: Supplementary Information:

Correlation of stratigraphic sections within Chapter 7:

This section details how the stratigraphic sections within Chapter 7 of this thesis were correlated through a combination of carbon isotope data and biostratigraphic data (particularly for Figures 2 and 3 of chapter 7).

Chemostratigraphic data:

Carbon isotope data was obtained from the sources listed within the caption of Figure S1 (Chapter 7) with the assignment of ‘pre-cursor’, ‘initial’ and ‘main’ carbon isotope excursions being based on a brief review of the literature prior to chemostratigraphic correlation. The assignment of carbon isotope excursions from the Marientel-1 core is based on the excursions acknowledged by Lindström et al., (2017) with the ‘marshi’, ‘spelae’ and ‘tilmanni’ CIEs being re-named here as the precursor, initial and main CIEs respectively (Fig. S1- Chapter 7).

Excursion assignment has been undertaken previously for the Schandelah-1 core by van de Schootbrugge et al., (2019) but the assigned excursion names do not coincide with the typical nomenclature for the Triassic–Jurassic boundary interval carbon isotope excursions. The negative carbon isotope excursion at approximately 334m within the Schandelah-1 core has subsequently been assigned here as the precursor CIE and it is interpreted that the initial and main CIEs from the schandelah-1 core (~318m) are near continuous in nature due to a sedimentary hiatus during the deposition of the uppermost Rhaetian in the Schandelah-1 core section.

Insufficient carbon isotope data is present from the Hebelmeer-2 core for use in stratigraphic correlation and therefore carbon isotope data from the Hebelmeer-2 core has not been included here [*Blumenberg et al., 2016*].

The carbon isotope data and excursion assignment from the Carnduff-2 core has been obtained from the Boomer et al., (2021). It should be noted, however, that the precursor CIE is tenuously assigned on the basis of being a single data point spike (Fig S1- Chapter 7).

The carbon isotope stratigraphy from the GSSP is well established with the initial carbon isotope excursion being assigned to the negative CIE at the base of the Tiefengraben Member and the main carbon isotope excursion being positioned at ~200m [Ruhl et al., 2009, 2010] (Fig S1- Chapter 7). A precursor CIE has been assigned here based on Ruhl et al., (2010), albeit being based on a tenuous single point spike (Fig S1- Chapter 7). A recent study by Lindström et al., (2017) proposed that the initial CIE and main CIE at the GSSP may instead be re-identified as the precursor (“marshi”) and initial (“spelae”) equivalent CIEs respectively. Lindström et al., (2017) based this interpretation on palynostratigraphy and ammonite biostratigraphy, however, there are problems with their proposed re-identification. These problems mainly stem from Lindström et al., (2017)’s strong focus on palynological data which results in discrepancies in the ammonite biostratigraphic records [Kovács et al., 2020].

Palynological data, although proving a useful proxy where taxa occur/disappear at many different locations near simultaneously/ over a very short time period, is less informative when there are spatio-temporal variations. As a result, several recent studies have continued to adopt the original carbon isotope correlation for the GSSP [Korte et al., 2019; Kovács et al., 2020; Wignall & Atkinson 2020]. The established chemostratigraphic correlation for the GSSP has also continued to be used here pending further study.

Carbon isotope data from the Mingsolsheim core has been obtained from Quan et al., (2008). The precursor CIE has been assigned to a negative carbon isotope excursion at

~206m with the initial and main CIE being assigned here as the negative carbon isotope excursions at ~200m and ~197m respectively. However, due to the initial carbon isotope excursion being based on a single point spike its assignment is tenuous (Fig S1- Chapter 7).

Carbon isotope data from Somerset core material has been obtained from Hesselbo et al., (2002). Assignment of carbon isotope excursions from the Somerset section are well established with the precursor CIE spanning the base of the Westbury Formation, the initial CIE at the top of the Cotham Member and the onset of the main CIE within the lower Blue Lias Formation. Due to the uppermost Westbury Formation to basal Blue Lias Formation from the Somerset section having only been studied within this thesis the precursor and main CIEs have not been plotted, however, correlation lines have been drawn to denote their approximate horizons at ~7.5m (precursor) and ~16.5m (main) respectively (Fig S1- Chapter 7).

It is interpreted here that the carbon isotope record from the Val Adrara section is representative of the tail end of the main CIE on the basis of the pattern of the carbon isotope data as well as biostratigraphic data from the section (see Fig. S7, Chapter 8). Correlation of the Val Adrara and Mount Sparagio sections has been discussed in more detail within the supplementary information of Chapter 8. It should be noted that there may be uncertainties associated with correlating organic and carbonate derive carbon isotope data.

Carbon isotope data from the Rosswinkel core was not available during this study and therefore correlation has instead been achieved biostratigraphically.

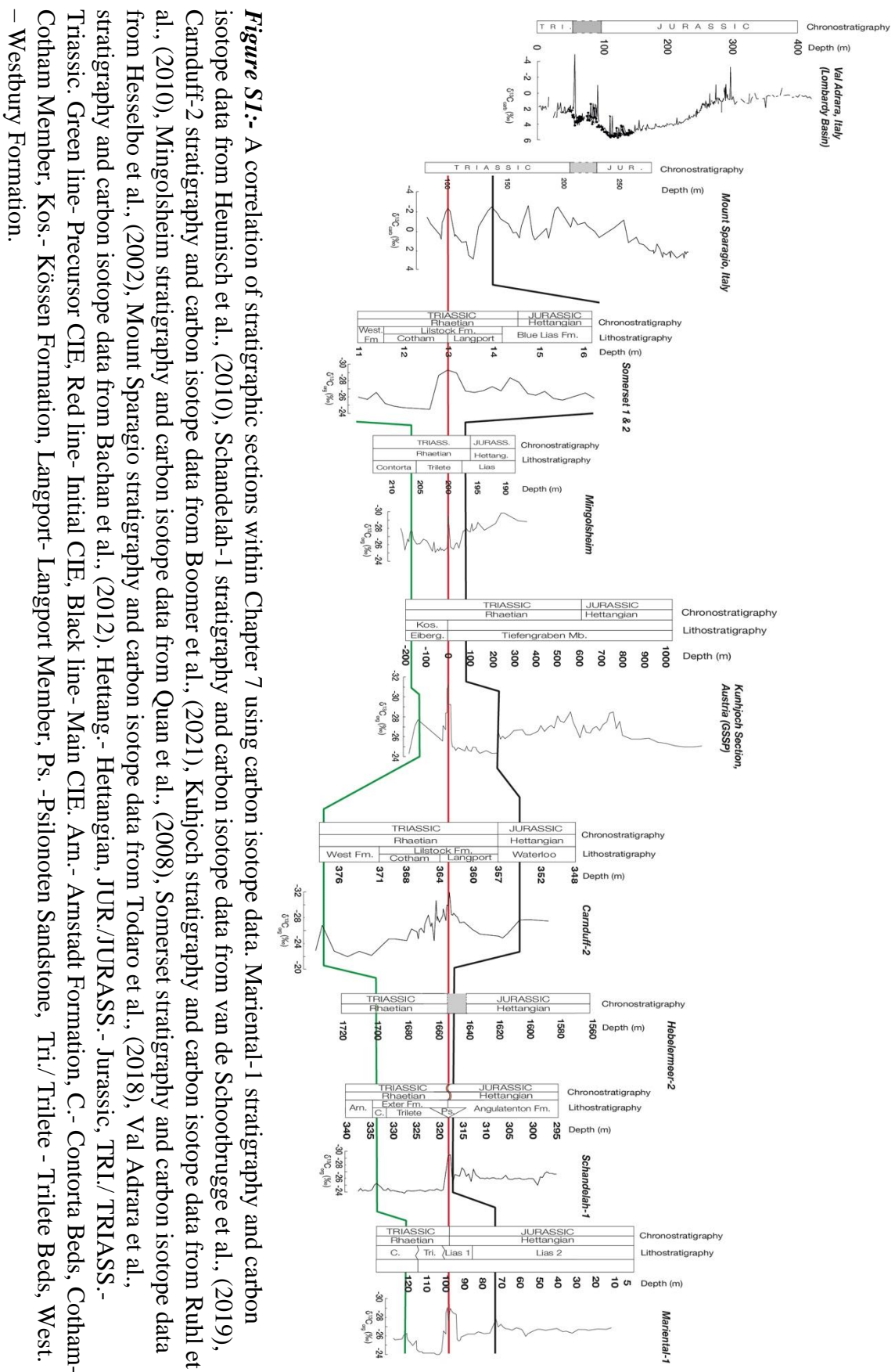


Figure S1: A correlation of stratigraphic sections within Chapter 7 using carbon isotope data. Mariental-1 stratigraphy and carbon isotope data from Heunisch et al., (2010), Schandelah-1 stratigraphy and carbon isotope data from van de Schootbrugge et al., (2019), Carnuff-2 stratigraphy and carbon isotope data from Boomer et al., (2021), Kuntjoch stratigraphy and carbon isotope data from Ruhl et al., (2010), Mingsolsheim stratigraphy and carbon isotope data from Quan et al., (2008), Somerset stratigraphy and carbon isotope data from Hesselbo et al., (2002), Mount Spargio stratigraphy and carbon isotope data from Todaro et al., (2018), Val Adara et al., stratigraphy and carbon isotope data from Bachan et al., (2012). Hettangian - Hettangian, JUR./JURASSIC - Jurassic, TRI./ TRIASSIC - Triassic. Green line- Precursor CIE, Red line- Initial CIE, Black line- Main CIE. Arn.- Arnstadt Formation, C.- Contorta Beds, Cotham- Cotham Member, Kos.- Kössen Formation, Langport- Langport Member, Ps.- Psilonoten Sandstone, Tri./ Trilete - Trilete Beds, West.- Westbury Formation.

Biostratigraphic data:

Biostratigraphic data has generally been used to supplement the chemostratigraphic data and limit potential uncertainties. The chemostratigraphic correlation of the

Marientel-1 core has been further supported through biostratigraphic correlation including the use of the polypodiisporites abundance interval [Lindström *et al.*, 2017].

Biostratigraphically informative palynotaxa further support that the equivalent of the Langport Member (in the British sedimentary succession) or Transitional Beds (in mainland Europe) is missing from the Schandelah-1 core and that the initial and main CIE form a single excursion (Chapter 7, Fig. S2).

Biostratigraphic data from Heblermeer-2 core has facilitated correlation of samples from the Rhaetian of the Heblermeer-2 core to the basal Westbury Formation/ basal Contorta beds, uppermost Westbury Formation/ uppermost contorta beds, and the uppermost Cotham Member/ uppermost Trilete beds. However, in light of the coarse nature of sampling from the Heblermeer-2 core as well as the absence of high-resolution carbon isotope data the correlation of the Heblermeer-2 core to other stratigraphic sections within this thesis exhibits some uncertainty (Chapter 7, Fig. S2).

Despite the Carnduff-2 core not exhibiting a polypodiisporites abundance interval biostratigraphic data has further supported the chemostratigraphic correlation of the core to other sections. The correlation of the Carnduff-2 core was particularly aided by the last common occurrence (LCO) and last occurrence (LO) of *Rhaetipollis germanicus* as well as the first occurrence of *Cerebropollenites thiergartii* and the first common occurrence (FCO) of *Kraeuselisporites reissingerii*. Biostratigraphic data also supports that the single point carbon isotope excursion towards the base of the Westbury Formation may represent the precursor CIE. However, further study would have to be undertaken to confirm this interpretation.

The biostratigraphic data from the GSSP exhibits definite inconsistencies when compared to correlations using chemostratigraphic data alone. However, considering that recent attempts to rectify such discrepancies using a palynotaxa dominant approach were relatively unsuccessful [Lindström *et al.*, 2017] it is perhaps pertinent that correlation of the GSSP to other sections is revisited to rectify these inconsistencies. Until then this chapter uses chemostratigraphic correlation only to correlate the GSSP to other sections with a caveat that potential uncertainty may be introduced as a result.

Despite the initial CIE from the Mingolsheim core being composed of a single point spike the biostratigraphic data from the Mingolsheim core would further support that the positioning of the excursion is coincident with the initial CIE from other sections.

The polydiisporites abundance interval from the Somerset section broadly coincides with the initial CIE, as seen from other sections (e.g., Schandelah-1, Mingolsheim, Marientel). Which would further support the Somerset chemostratigraphic correlation. Biostratigraphic correlation of the Somerset section is , however, complicated slightly by the persistence of *Rhaetogonyaulax rhaetica*. The LCO and LO of *R. rhaetica* has therefore not be used when correlating to other sections.

A limited biostratigraphic dataset has allowed for the correlation of the Rosswinkel core to other stratigraphic sections, however in light of the absence of carbon isotope data there exists some uncertainty in the correlation. Biostratigraphic data would suggest, however, that the Elvange Formation of the Rosswinkel core broadly coincides with the Cotham Member/ Trilete Beds from other sections.

The absence of useful biostratigraphic data from the Val Adrara and Mount Sparagio sections means that these sections may only be correlated with each other and tenuously with the other sections through the use of carbon isotope data only (see Figure S7,

Chapter 8). Further research should be undertaken to further understand the correlation of such carbonate dominant sections with other sedimentologies, particularly given the relative absence of biostratigraphically informative taxa.

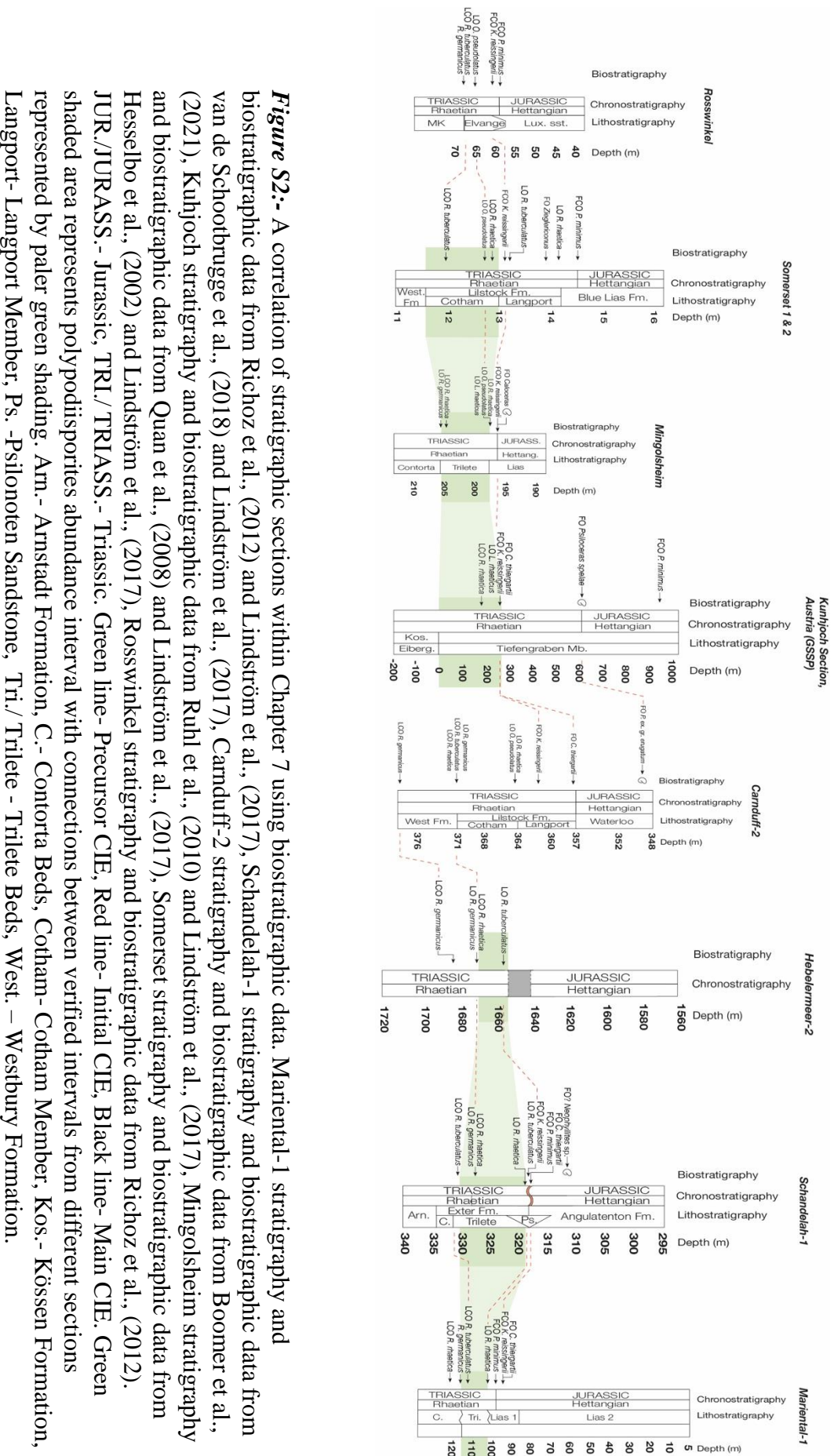


Figure S2: A correlation of stratigraphic sections within Chapter 7 using biostratigraphic data. Mariental-1 stratigraphy and biostratigraphic data from van de Schootbrugge et al., (2018) and Lindström et al., (2012) and Lindström et al., (2017), Schandelah-1 stratigraphy and biostratigraphic data from Boomer et al., (2021), Kuhnloch stratigraphy and biostratigraphic data from Ruhl et al., (2010) and Lindström et al., (2017), Mingolsheim stratigraphy and biostratigraphic data from Quan et al., (2008) and Lindström et al., (2017), Somersset stratigraphy and biostratigraphic data from Hesselbo et al., (2002) and Lindström et al., (2017), Rosswinkel stratigraphy and biostratigraphic data from Richoz et al., (2012). JUR./JURASS.- Jurassic, TRI./TRIASS.- Triassic. Green line- Precursor CIE, Red line- Initial CIE, Black line- Main CIE. Green shaded area represents polydispersities abundance interval with connections between verified intervals from different sections represented by paler green shading. Arn.- Arnstadt Formation, C.- Contorta Beds, Cotham- Cotham Member, Kos.- Kössen Formation, Langport- Langport Member, Ps.- Pylonoten Sandstone, Tri./Trilete - Trilete Beds, West.- Westbury Formation.

Diagenetic alteration of study sections:

Evidence for diagenetic and thermal alteration of the Larne Basin sediments has been evaluated in some detail by Bond et al., (2022a) (Chapter 6 of this thesis). Sediments of the Carnduff-2 core are thermally immature on the basis of vitrinite reflectance data where an average vitrinite reflectance of ~0.5% would suggest a burial temperature of ~423°C (immature to early oil window) [Bond et al., 2022a]. Also, aragonite shell material within the Larne Basin is noted to be well-preserved suggesting limited evidence for thermal alteration [Raine et al., 2021; Boomer et al., 2021; Bond et al., 2022a].

The sediments of the Hebelmeer-2 core record a vitrinite reflectance of 0.56%, similar to the immature to early oil window burial temperatures experienced by the Larne Basin sediments [Blumenberg et al., 2016]. T_{\max} values calculated by Blumenberg et al., (2016) for the Hebelmeer-2 core would also support lower oil window burial temperatures with a range between 424°C and 435°C [Blumenberg et al., 2016].

Organic matter in the form of palynomorphs are generally moderately good with poor preservation being observed for sample Heb-1 (1571.5m).

The sediments of the Schandelah-1 core are reported to exhibit a vitrinite reflectance of ~1% suggesting thermally immature sediments [van de Schootbrugge et al., 2019].

Relative thermal immaturity for the Schandelah-1 core sediments may also be interpreted on the basis of organic matter preservation including the preservation of non-biomineralised/ lightly sclerotised insect remains and excellent preservation of palynomorphs [van de Schootbrugge et al., 2019].

8 GLOBAL OCEAN DE-OXYGENATION PRECEDED END-TRIASSIC MARINE MASS EXTINCTION

Andrew D. Bond, Alexander J. Dickson, Emma Blanka Kovács, József Pálfy and Micha Ruhl

Submitted to *Geology*

Statement of lead author's contributions:

- Obtained samples from EBK
- Digested the sample powders
- Prepared the samples for ICP-MS analysis
- Processed the ICP-MS data
- Calculated sample dilutions for calcium concentrations
- Diluted samples for secondary ICP-MS analysis
- Processed ICP-MS data
- Interpreted ICP-MS data
- Ran t-tests for elements of interest
- Wrote the first draft of the manuscript
- Prepared all figures for the manuscript
- Made corrections to the manuscript and figures based on co-authors' comments

Global ocean de-oxygenation preceded end-Triassic marine mass extinction

Andrew D. Bond^{1,*}, Alexander J. Dickson¹, Emma Blanka Kovács², József Pálffy³,
Micha Ruhl²

¹ Centre of Climate, Ocean and Atmosphere, Department of Earth Sciences, Royal Holloway University of London, Egham Hill, Egham, Surrey, TW200EX, UK

² Department of Geology, Trinity College Dublin, The University of Dublin, College Green, Dublin, Ireland

³ Department of Geology, Eötvös Loránd University, and ELKH-MTM-ELTE Research Group for Paleontology Pázmány Péter sétány 1/C, Budapest, Hungary

*Corresponding author. E-mail address: Andrew.Bond.2014@live.rhul.ac.uk (A. D. Bond)

Abstract

The pulsed extinction of marine organisms during the latest Triassic (the end-Triassic mass extinction, ETME) represents one of the largest mass extinction events in geological history. The ETME is thought to have been driven by large igneous province volcanism which caused perturbations to ocean redox chemistry and surface temperatures. However, the timing and magnitude of redox change within open marine environments during the ETME remains largely unknown. Here, we present a high-resolution redox-element/calcium record that spans the ETME from the Hungarian Csővár, Vár-hegy section, one of the few known localities worldwide to exhibit continuous carbonate deposition throughout this interval. Our data evidence a large

reduction in V, Cr and U in seawater directly before the ETME that persisted through to the Early Jurassic. We suggest that the decreased concentrations of V, Cr and U in seawater were the result of the enhanced burial of these elements under expanded, open marine, suboxic–anoxic conditions. Our observations constitute the earliest known evidence for open marine redox change and contrast with recent evidence for relative stability in the distribution of sulfidic, epicontinental environments across the same time interval. Therefore, our data demonstrate that marine deoxygenation may have progressed from the open ocean to marginal marine locations.

Introduction

The Triassic–Jurassic boundary interval (~201 Ma) contained one of the largest extinction events in geological history: the end Triassic mass extinction event (ETME) (Raup & Sepkoski, 1982). The ETME is closely associated with an extended period of large igneous province volcanism in the form of the Central Atlantic Magmatic Province (CAMP) emplacement and is characterised by the pulsed disappearances of numerous marine organisms (Hesselbo et al., 2002; Ruhl et al., 2011; Wignall & Atkinson, 2020). Marine redox changes, when linked with a cascade of environmental feedbacks triggered by CAMP volcanism, are suggested to have played a significant role in marine extinction phases during the ETME. The development of sulfidic conditions within Late Triassic marginal marine environments is evidenced through elemental, isotopic and biomarker proxies (Richoz et al., 2012; Kasprak et al., 2015; He et al., 2020; Bond et al., 2022a). However, recent work by Bond et al., (2022a) suggests that sulfidic conditions were relatively rare outside of marginal marine environments. The timing and magnitude of redox change within Late Triassic open marine environments, therefore, remains largely unknown. Quantifying open marine redox

change during the Triassic–Jurassic boundary interval is essential to further understanding of the role that marine de-oxygenation played in subsequent ETME marine extinction phases.

The ratio of trace elements to calcium within biogenic and inorganic carbonates has been widely used as a proxy to reconstruct the concentrations of these elements in ancient oceans (Glock et al., 2016; Chen et al., 2017; Jenkyns et al., 2017; He et al., 2022a). Redox-sensitive trace elements (RSTEs) are substituted into the carbonate lattice from the surrounding water column or porewater fluids. Given the long oceanic residence times of many RSTEs (10^4 – 10^5 years), a reduction in their concentrations in carbonates (e.g., U, Cr, V normalised to Ca), which are formed in seawater, would indicate a reduction in their seawater concentration due to increased removal fluxes mainly into seafloor sediments. Unless the local environment is hydrographically restricted then fluctuations in seawater RSTEs will reflect global scale removal fluxes and therefore global-scale changes in marine redox.

Here, we present a high-resolution elemental record from an upper Rhaetian (uppermost Triassic) – lower Hettangian (lowermost Jurassic) carbonate succession at the Csővár, Vár-hegy section (Hungary). The Csővár Vár-hegy section is one of just a handful of Triassic–Jurassic boundary sections to exhibit continuous carbonate deposition. The succession was deposited in an intraplatform basin on the edge of the Tethyan shelf. Our data evidence a shift in marine redox directly preceding the ETME Main Interval which we suggest is associated with the de-oxygenation of Late Triassic, open marine environments.

Palaeoenvironmental context and stratigraphy

The sedimentary succession at Csővár [Fig. 1] was deposited on the foreslope of a Tethyan carbonate platform and is composed of laminated calcareous mudstones, platform-derived ooidal limestones, and bioclastic limestones with alternation between platform-derived and basinal facies (Haas & Tardy-Filácz, 2004). A Triassic–Jurassic age for the section was first confirmed through the compilation of biostratigraphic studies (Pálfy and Dosztály, 2000 and papers therein). Research by Pálfy et al., (2007) further constrained the Triassic–Jurassic boundary in the section through radiolarian biostratigraphy. Triassic and Jurassic sediments of the Csővár section are defined by the last and first appearances of Triassic and Jurassic ammonite taxa, respectively, with the main extinction horizon being identified through the negative carbon isotope excursion NCIE-3 [Fig. 1] (Pálfy et al., 2001, 2007; Kovács et al., 2020). Given the continuous nature of carbonate deposition observed across the Triassic–Jurassic boundary within the Csővár Vár-hegy section, as well as the section being stratigraphically well understood with a connection to the open Tethys Ocean based on palaeontological observations (Pálfy et al., 2007), samples from the section are well suited to reconstruct global marine redox changes.

Materials and methods:

Forty (40) fresh, unweathered carbonate samples were collected from the Csővár, Vár-hegy section and powdered by hand using an agate mortar and pestle. ~0.5g of each sample was then weighed and cleaned using Milli-Q water to remove fine clays and hydro-soluble salts. A random selection of samples (n=4) underwent an additional reductive cleaning step using 5 ml 0.15M citric acid + 12M ammonium solution as well

as an additional oxidative cleaning step using 5 ml NaOH-buffered H₂O₂ [Fig. S1] (Druce et al., 2022). All samples were then leached with 14 ml of 0.2M ultra-pure acetic acid. Between 8.9% and 12.8% of the carbonate was dissolved during the acetic acid step, with an average yield of 11.5%. Solutions were diluted to 20 ppm Ca, to suppress fluctuations in trace element concentration due to Ca matrix effects (de Villiers, 2003), and were measured using an Agilent 7500 ICP-MS. Each sample was internally spiked with a Re standard to correct for drift throughout the run. Accuracy and precision (2 S.D.) of X/Ca values were determined throughout the run using certified solution standards (n=7). For Cr/Ca and V/Ca precision and accuracy were $<6 \pm 0.5 \%$. For U/Ca precision and accuracy were $<21 \pm 0.8 \%$. Procedural blanks processed with the leachate batch generally exhibit sub ng concentrations including averages of -0.1ng for U, 0.02ng for V, and 1.45ng for Cr .

Results

Ratios of average U/Ca (0.95 $\mu\text{mol/mol}$), V/Ca (29.06 $\mu\text{mol/mol}$) and Cr/Ca (9.16) are elevated within the bottom half of the section (0–11.4m) [Fig. 2]. However, average U/Ca (0.28 $\mu\text{mol/mol}$), V/Ca (7.26 $\mu\text{mol/mol}$) and Cr/Ca (4.46 $\mu\text{mol/mol}$) undergo a significant decline after NCIE-2 (~11.4 m) [Fig. 2].

Triassic–Jurassic trends in redox elemental ratios from the Hungarian Csóvár section

Carbonate-hosted V, Cr and U contents could potentially have been altered/ changed by several different factors. One such process is the diagenetic incorporation of elements (e.g., U) post burial. However, a correlation of $\delta^{13}\text{C}$ and $\delta^{18}\text{O}$ by Kovács et al., (2020) finds little evidence for diagenetic alteration of the Csóvár sediments. Given that the

Csővár sediments are detrital in nature, and broadly matrix supported, there is little chance of elemental deviations through diagenetic alteration of carbonate cements (see SI). Also, samples from the Csővár section are low in organic matter (<0.1%) with only marginal thermal maturation based on previous studies (Pálffy et al., 2007). Moreover, the Csővár samples exhibit an average Mg/Ca of 0.01 mmol/mol and a range from 0.004 to 0.016 mmol/mol [Fig. 3a]. These Mg/Ca values fall within the range of Triassic–Jurassic, unaltered Mg/Ca reported by He et al., (2022a) and Ullmann et al., (2021), and fall outside of Sinemurian, diagenetic calcite values (Ullmann et al., 2021) [Fig. 3a]. Therefore, we find little evidence for dolomitization or diagenetic alteration through our data. Furthermore, there is little evidence for a strong correlation between trends in X/Ca data and carbonate grain composition (see SI).

Elemental ratios may also be affected by hydrographic restriction which can alter the concentrations of RSTEs in local seawater versus open ocean seawater. However, fluctuations in elemental ratios from the Csővár section occur independently of facies changes and cyclical changes in sea level inferred from local sequence stratigraphy [Fig. 2]. Furthermore, the paleogeographic reconstructions and the common fossil occurrences indicate that the basin retained an open marine connection during the Triassic–Jurassic boundary interval (Pálffy et al., 2007) [Fig. 2]. We find no correlation between the indices U/Ca, V/Ca or Cr/Ca and Al (ppb) in the leach solutions, suggesting little to no liberation of trace elements from aluminosilicates during chemical preparation [Fig. S2]. Therefore, we interpret the chemical compositions as primarily recording the concentration of RSTEs in the precipitating fluid, which we assume to be seawater that was well-mixed with the open ocean.

Within the lower half of the section (0–11.4 m), up to the top of NCIE-2, average U/Ca and Cr/Ca fall within the range of values recorded for modern biotic carbonates [Fig. 3c–d]. Therefore, assuming similar carbonate substitution as modern analogues, the concentration of these elements in seawater was similar to today. It may therefore be interpreted that global marine waters during the deposition of the base of the section were relatively oxygenated.

After NCIE-2 (11.41m–29.2 m) average U/Ca decreases to outside of the range of modern marine values [Fig. 3c–d]. A statistically significant decrease between average U/Ca, V/Ca and Cr/Ca before and after NCIE-2 is confirmed through a t-test with an alpha value of 0.05 [Fig. 3c–d; Fig. S4]. A statistically significant decrease in average V/Ca, Cr/Ca and U/Ca after NCIE-2 would suggest a decrease in trace element concentrations within the global seawater inventory and therefore a globally averaged increased removal flux of V, Cr and U, ostensibly into low oxygen sediments that constitute the main removal fluxes for these elements from global ocean waters. These observations imply that global marine redox change directly preceded the main extinction interval of the ETME.

Global redox change within open marine environments prior to the ETME

A global shift in marine redox shortly before the main interval of the ETME may have resulted from several different factors. For example, the observed shift to on average globally elevated low oxygen conditions directly coincides with more localised de-oxygenation within marginal marine and mid-oceanic environments on the Tethyan and Panthalassa margins (Kasprak et al., 2015; Blumenberg et al., 2016; Fox et al., 2020). Therefore, a reduction in global oceanic trace metal concentrations may have been the

result of trace metal burial in oxygen-poor conditions within epicontinental marine basins. However, multiple problems exist with this model. Firstly, water column de-oxygenation within epi-continental environments throughout the Triassic–Jurassic boundary interval, and during this time interval, was dominated by sulfidic conditions (Ricoz et al., 2012; Kasprak et al., 2015; He et al., 2020, 2022b; Fox et al., 2022). Mo isotope data suggests that global sulfidic conditions remained broadly constant during the latest Triassic (Bond et al., 2022a) and, therefore, increasingly sulfidic conditions cannot explain a significant decrease in V, Cr, and U during this interval, unlike expanding suboxic/anoxic conditions. Our data therefore suggest changes in the geographic extent of environments which are becoming suboxic–anoxic, but not sulfidic, unlike epicontinental basins during this time interval.

A de-coupling between our elemental carbonate data and redox changes within epicontinental, marine environments is further suggested by the relative timing of redox changes. V/Ca, Cr/Ca and U/Ca from the Csővár section decrease prior to major pulsed de-oxygenation within marginal marine environments (Bond et al., 2022a). Also, V, Cr and U normalised to Ca largely remained constant through to the Early Jurassic despite increasing de-oxygenation within epicontinental basins (Kasprak et al., 2015; Bond et al., 2022a, 2022b). However, V/Ca, Cr/Ca, and U/Ca from the Csővár section track changes in marine redox recorded from other open marine sections [Fig. 4]. Therefore, we suggest that the global redox shift shortly before the ETME (Main Interval) was the result of expanding suboxic–anoxic conditions within Late Triassic open marine environments.

Our data suggest that whilst sulfidic conditions persisted to some degree in restricted, continental basins, regions of the open ocean had already become increasingly oxygen-poor prior to the ETME (Main Interval), possibly in the form of expanding oxygen minimum zones. The development of open ocean de-oxygenation prior to the major pulsed de-oxygenation of restricted marine environments during the Late Triassic significantly predates all previous evidence for Late Triassic, open ocean de-oxygenation [Fig. 4]. The later de-oxygenation of marginal marine environments, relative to open-marine settings, may be associated with the variable onset of CAMP activity. The first major pulse of CAMP volcanism coincided with the ETME and may have caused increased weathering and nutrient input into restricted, marginal marine basins as well as subsequent water column stratification and potential eutrophication (Ruhl et al., 2011). However, early volcanic degassing from CAMP may have resulted in open ocean de-oxygenation from surface water warming. The idea of open ocean de-oxygenation occurring due to CAMP degassing is further supported by $p\text{CO}_2$ increasing prior to the ETME, coinciding with the so-called late Triassic ‘pre-cursor’ carbon isotope excursion (NCIE-2) (Bonis et al., 2010; Ruhl & Kürschner, 2011; Kovács et al., 2020).

Conclusion

Carbonate-hosted elemental abundance data from the Hungarian Csóvár section evidence a significant, global redox change within open marine environments shortly before the main phase of the ETME. This global redox change possibly took the form of expanding OMZs and the expansion of suboxic and anoxic conditions that controlled the burial of several redox-sensitive elements, as evidenced through significant reductions in the V/Ca, Cr/Ca, and U/Ca ratios of well-preserved marine carbonates.

The expansion of open marine, low oxygen environments evidenced here pre-dated the major, pulsed de-oxygenation of marginal marine environments during the latest Triassic extinction interval, demonstrating that marine deoxygenation may have progressed from the open ocean to marginal marine locations.

Declaration of Competing Interest

The authors declare that they have no competing financial interests or personal relationships that could have appeared to influence the work reported in this paper.

Acknowledgements

This work was funded by a NERC DTP PhD Studentship awarded to ADB (NE/L002485/1). We would like to thank the Wet Geochemistry Lab, Department of Earth Sciences, for assisting with ICP-MS measurements. JP acknowledges funding from NKFI Grant K135309. This is ELKH-MTM-ELTE Paleo contribution no. 3xx..

References

- Bachan, A. Schootbrugge, B. v. d., Fiebig, J., McRoberts, C. A., Ciarapica, G., and Payne, J. L., 2012, Carbon cycle dynamics following the end-Triassic mass extinction: Constraints from paired $\delta^{13}\text{C}_{\text{carb}}$ and $\delta^{13}\text{C}_{\text{org}}$ records: *Geochemistry, Geophysics, Geosystems*, v.13, Q09008, doi:10.1029/2012GC004150.
- Blumenberg, M., Heunisch, C., Lückge, A., Scheeder, G., and Wiese, F., 2016, Photic zone euxinia in the central Rhaetian Sea prior the Triassic-Jurassic boundary: *Palaeogeography, Palaeoclimatology, Palaeoecology*, v. 461, p. 55–64.
- Bond, A. D., Dickson, A. J., Ruhl, M., Bos, R., and Schootbrugge, B. v. d., 2022a, An oxygenated global ocean during the end-Triassic mass extinction event. [10.21203/rs.3.rs-1684412/v1](https://doi.org/10.21203/rs.3.rs-1684412/v1).
- Bond, A. D., Dickson, A.J., Ruhl, M., and Raine, R. 2022b, Marine redox change and extinction in Triassic–Jurassic boundary strata from the Larne Basin, Northern Ireland. *Palaeogeography, Palaeoclimatology, Palaeoecology*, v. 598, 111018, <https://doi.org/10.1016/j.palaeo.2022.111018>.

- Bonis, N. R., Van Konijnenburg-Van Cittert, J. H. A, and Kürchner, W. M., 2010, Changing CO₂ conditions during the end-Triassic inferred from stomatal frequency analysis on *Lepidopteris ottonis* (Goepfert) Schimper and *Ginkgoites taeniatus* (Braun) Harris: *Palaeogeography, Palaeoclimatology, Palaeoecology*, v. 295, p. 146–161. <https://doi.org/10.1016/j.palaeo.2010.05.034>.
- Chen, P., Yu, J., and Jin, Z., 2017, An evaluation of benthic foraminiferal U/Ca and U/Mn proxies for deep ocean carbonate chemistry and redox conditions: *Geochemistry, Geophysics, Geosystems*, v.18, p. 617–630. <http://dx.doi.org/10.1002/2016GC006730>.
- De Villiers, S., 2003, A 425 kyr record of foraminiferal shell weight variability in the western equatorial Pacific: *Paleoceanography*, v. 18. <https://doi.org/10.1016/j.palaeo.2010.05.034>.
- Druce, M., Stirling, C. H., Bostock, H. C., and Rolison, J. M., 2022, Examining the effects of chemical cleaning, leaching, and partial dissolution on zinc and cadmium isotope fractionation in marine carbonates: *Chemical Geology*, v. 592, 120738.
- Fox, C. P., Whiteside, J. H., Olsen, P. E., Cui, Xingqian, Summons, R. E., Idiz, E., Grice, K., 2022. Two-pronged killing mechanism at the end-Triassic mass extinction. *Geology*, v. 50, p. 448–453. <https://doi.org/10.1130/G49560.1>
- Glock, N., Liebetrau, V., Eisenhauer, A., and Rocholl, A., 2016, High resolution I/Ca ratios of benthic foraminifera from the Peruvian oxygen-minimum-zone: A SIMS derived assessment of a potential redox proxy: *Chemical Geology*, v. 447, p. 40–53. <http://doi.org/10.1016/j.chemgeo.2016.10.025>.
- Götz, A.E., Ruckwied, K., Pálffy, J., and Haas, J., 2009, Palynological evidence of synchronous changes within the terrestrial and marine realm at the Triassic/Jurassic boundary (Csövár section, Hungary): *Review of Palaeobotany and Palynology*, v. 156, p. 401-409.
- Greene, S. E., Martindale, R. C., Ritterbush, K. A., Bottjer, D. J., Corsetti, F. A., and Berelson, W. M., 2012, Recognising ocean acidification in deep time: An evaluation of the evidence for acidification across the Triassic-Jurassic boundary: *Earth Science Reviews*, v. 113, p. 72–93.
- Haas, J. and Tardy-Filácz, E., 2004, Facies changes in the Triassic–Jurassic boundary interval in and intraplatform basin succession at Csövár (Transdanubian Range, Hungary): *Sedimentary Geology*, v. 168, p. 19–48. [Doi:10.1016/j.sedgeo.2004.03.002](https://doi.org/10.1016/j.sedgeo.2004.03.002).
- Haas, J., Götz, A.E., and Pálffy, J., 2010, Late Triassic to Early Jurassic palaeogeography and eustatic history in the NW Tethyan realm: New insights from sedimentary and organic facies of the Csövár Basin (Hungary): *Palaeogeography, Palaeoclimatology, Palaeoecology*, v. 291, p. 456-468.
- He, T., Dal Corso, J., Newton, R. J., Wignall, P. B., Mills, B. J. W., Todaro, S. Di Stefano, P., Turner, E. C., Jamieson, R. A. Randazzo, V., Rigo, M., Jones, R. E., and Dunhill, A. M., 2020, An enormous sulfur isotope excursion indicates marine anoxia during the end-Triassic: *Science Advances*, v. 6, eabb6704, [10.1126/sciadv.abb6704](https://doi.org/10.1126/sciadv.abb6704).

He, T., Newton, R. J., Wignall, P. B., Reid, S., Dal Corso, J., Takahashi, S., Wu, H., Todaro, S., Di Stefano, P., Randazzo, V., Rigo, M., and Dunhill, A. M., 2022a, Shallow ocean oxygen decline during the end-Triassic mass extinction: *Global and Planetary Change*, v. 210, 103770. <https://doi.org/10.1016/j.gloplacha.2022.103770>.

He, T., Wignall, P. B., Newton, R. J., Atkinson, J. W., Keeling, J. F. J., Xiong, Y., and Poulton, S. W., 2022b, Extensive marine anoxia in the European epicontinental sea during the end-Triassic mass extinction: *Global and Planetary Change*, v. 210, 103771, <https://doi.org/10.1016/j.gloplacha.2022.103771>.

Hesselbo, S. P., Robinson, S. A., Surlyk, F., and Piasecki, S., 2002, Terrestrial and marine mass extinction at the Triassic/Jurassic boundary synchronized with initiation of massive volcanism: *Geology*, v. 30, p. 251–254.

Jaraula, C. M. B., Grice, K., Twitchett, R. J., Böttcher, M. E., LeMetayer, P., Dastidar, A. G., and Opazo, L. F., 2013, Elevated $p\text{CO}_2$ leading to Late Triassic extinction, persistent photic zone euxinia, and rising sea levels: *Geology*, v. 41, p. 955–958.

Jenkyns, H. C., Dickson, A. J., Ruhl, M., and van den Boorn, S. H. J. M., 2017, Basalt-seawater interaction, the Plenus Cold Event, enhanced weathering and geochemical change: deconstructing Oceanic Anoxic Event 2 (Cenomanian–Turonian, Late Cretaceous): *Sedimentology*, v. 64, p. 16–43. <https://doi.org/10.1111/sed.12305>.

Jost, A. B., Bachan, A., van de Schootbrugge, B., Lau, K. V., Weaver, K. L., Maher, K., and Payne, J. L., 2017, Uranium isotope evidence for an expansion of marine anoxia during the end-Triassic extinction: *Geochemistry, Geophysics, Geosystems*, v. 8, p.3093–3108.

Kasprak, A. H., Sepulveda, J., Price-Waldman, R., Williford, K. H., Schoepfer, S. D., Haggart, J. W., Ward, P. D., Summons, R. E., and Whiteside, J. H., 2015, Episodic photic zone euxinia in the northeastern Panthalassic Ocean during the end-Triassic extinction: *Geology*, v. 43, p. 307–310.

Kovács, E. B., Ruhl, M., Demény, A., Fórizs, I., Hegyi, I., Horváth-Kostka, Z. R., Móricz, F., Vallner, Z., and Pálffy, J., 2020, Mercury anomalies and carbon isotope excursions in the western Tethyan Csóvár section support the link between CAMP volcanism and the end-Triassic extinction: *Global and Planetary Change*, v. 194, 103291.

Pálffy, J. and Dosztály, L., 2000, A new marine Triassic–Jurassic boundary section in Hungary: preliminary results. In: Hall, R. L., Smith, P. I., (Eds.), *Advances in Jurassic Research 2000*. GeoResearch Forum, TransTech Publications, Zurich, p. 173–179.

Pálffy, J., Demény, A., Haas, J., Hetényi, M., Orchard, M. and Vető, I., 2001, Carbon isotope anomaly and other geochemical changes at the Triassic-Jurassic boundary from a marine section in Hungary: *Geology*, v. 29, p. 1047–1050.

Pálffy, J., Demény, D., Haas, J., Carter, E. S., Görög, Á., Halász, D., Oravecz-Scheffer, A., Hetényi, M., Márton, E., Orchard, M. J., Ozsvárt, P., Vető, I., and Zajzon, N., 2007,

Triassic–Jurassic boundary events inferred from integrated stratigraphy of the Csővár section, Hungary: *Palaeogeography, Palaeoclimatology, Palaeoecology*, v. 244, p. 11–33. [10.1016/j.palaeo.2006.06.021](https://doi.org/10.1016/j.palaeo.2006.06.021).

Raup, D. M. and Sepkoski, J. J., 1982, Mass extinctions in the Marine Fossil Record: *Science*, v. 215, p. 1501–1503. [10.1126/science.215.4539.1501](https://doi.org/10.1126/science.215.4539.1501).

Richoz, S., van de Schootbrugge, B., Pross, J., Püttmann, W., Quan, T. M., Lindström, S., Heunisch, C., Fiebig, J., Maquil, R., Schouten, S., Hauzenberger, and Wignall, P. B., 2012, Hydrogen sulphide poisoning of shallow seas following the end-Triassic extinction: *Nature Geoscience*, v. 5, p. 662–667.

Ruhl, M. and Kürschner, W. M., 2011, Multiple phases of carbon cycle disturbance from large igneous province formation at the Triassic–Jurassic transition: *Geology*, v. 39, p. 431–434. doi:10.1130/G31680.

Ruhl, M., Bonis, N. R., Reichert, G. J., Damste, J. S. S., and Kürschner, W. M., 2011, Atmospheric carbon injection linked to end-Triassic mass extinction: *Science Reports*, v. 333, p. 430–434.

Todaro, S., Rigo, M., Randazzo, V., and Di Stefano, P., 2018, The end-Triassic mass extinction: A new correlation between extinction events and $\delta^{13}\text{C}$ fluctuations from a Triassic–Jurassic peritidal succession in western Sicily: *Sedimentary Geology*, v. 368, p. 105–113.

Ullmann, C. V., Szűcs, D., Jiang, M., Hudson, A. J. L., and Hesselbo, S. P., 2021, Geochemistry of macrofossil, bulk rock, and secondary calcite in the Early Jurassic strata of the Llanbedr (Mochras Farm), drill core, Cardigan Bay Basin, Wales, UK: *Geology*, v. 179, <https://doi.org/10.1144/jgs2021-018>.

Wignall, P. B. and Atkinson, J. W., 2020, A two-phase end-Triassic mass extinction: *Earth Science Reviews*, v. 208, 103282.

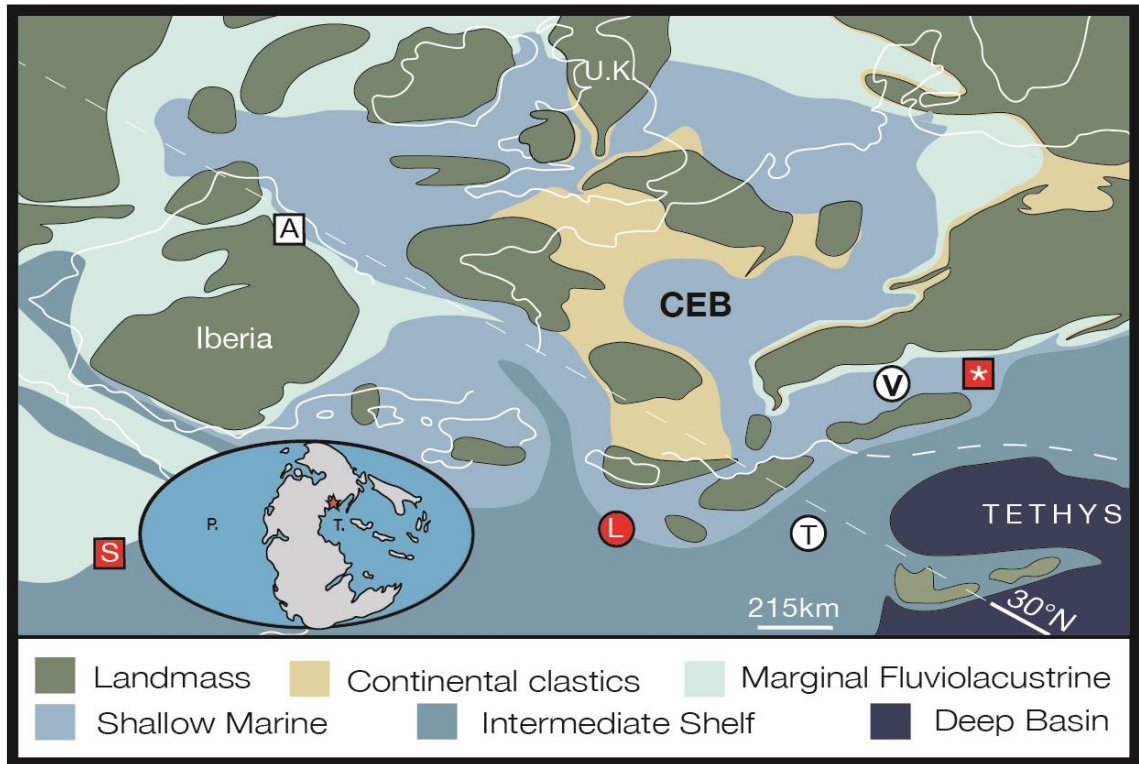


Figure 1:- Location of the Csővár section in relation to the Late Triassic palaeogeography of the Tethyan shelf (main figure) and the supercontinent of Pangaea (red star; bottom left). A- Asturias section (Northern Spain), V- Vár-hegy, Csővár section, (Hungary, this study), L- Lombardy Basins (including Val Adrara section, Northern Italy), S- Mount Sparagio section (Southern Italy), T- Tolmin Basin (Slovenia), *- Kuhjoch Section (Austria, Global Stratotype Section and Point (GSSP) for the base of the Jurassic). Red shapes- potential carbonate hiatus, white shapes- continuous carbonate deposition, circles- deeper basin localities, squares- shallower marine localities. CEB- Central European Basin. Inset (bottom left): P.- Panthalassa Ocean, T.- Tethys Ocean. Figure amended from Greene et al., (2012), and Bond et al.,

(2022b).

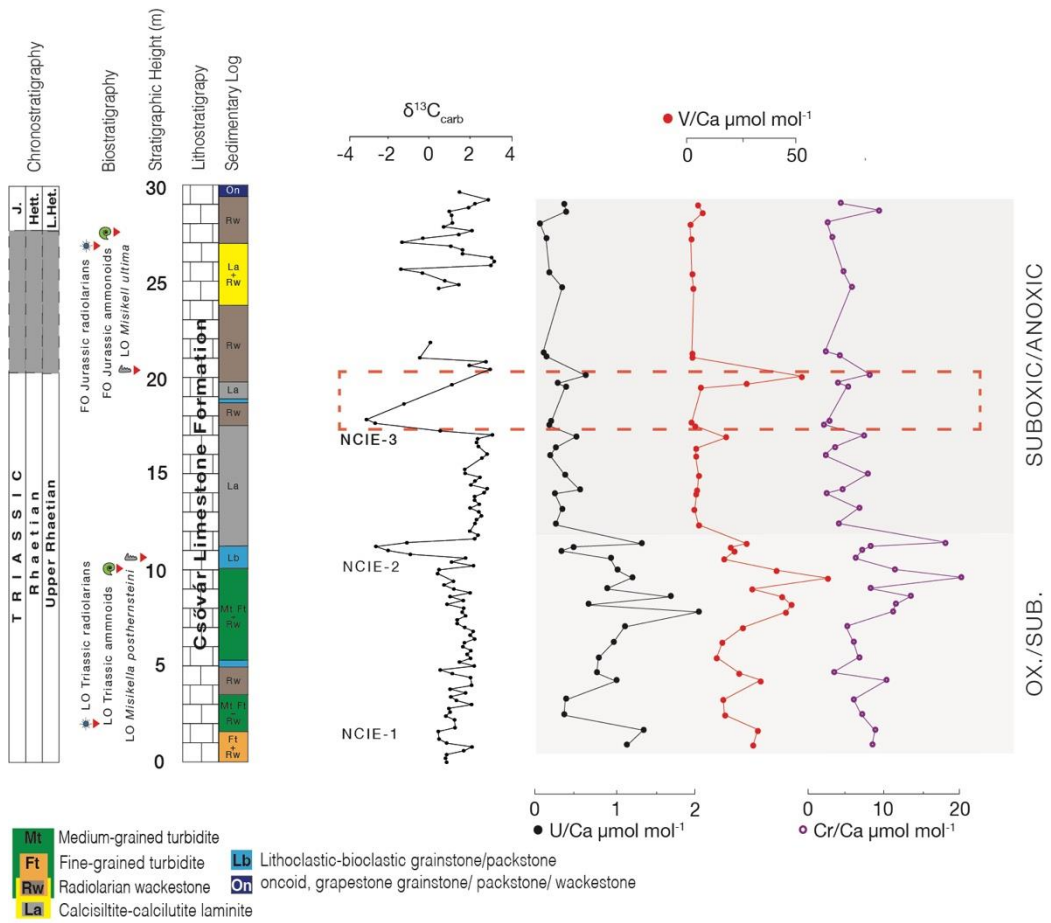


Figure 2:- Element/Calcium data from the Late Triassic Csővár section, Hungary.

Chronostratigraphy, biostratigraphy, lithostratigraphy and carbon isotope data from

Kovács et al., (2020) and sedimentology from Haas & Tady-Filácz (2004). Red, dashed

line- ETME Main Interval. FO- first occurrence, LO- last occurrence.

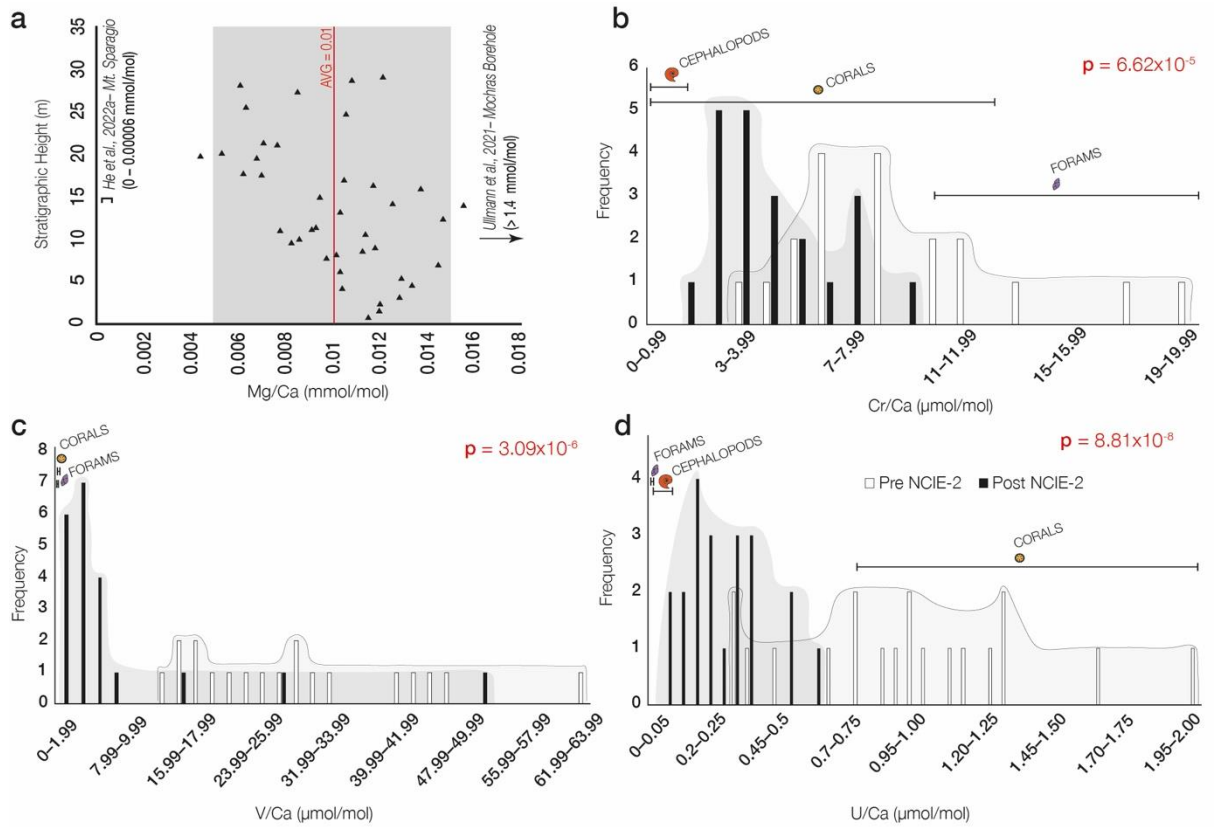


Figure 3:- A significant decline in carbonate trace element concentrations amongst unaltered Csővár samples. a) Mg/Ca data from Csővár samples compared to unaltered, Triassic–Jurassic Mg/Ca values from other, recent studies. Note that the Csővár Mg/Ca data falls within the range of unaltered values. Grey bar represent 2 S. D. of values, AVG.- Average. b – d) A global redox shift during the end Triassic mass extinction: Carbonate trace element data (X/Ca) reported from this study plotted before and after NCIE-2 and against modern marine X/Ca ratios. Two-tail P values (p) for a t-test with an alpha value of 0.05 displayed in top, right-hand corner of each histogram. See Fig. S3 for biogenic X/Ca data sources.

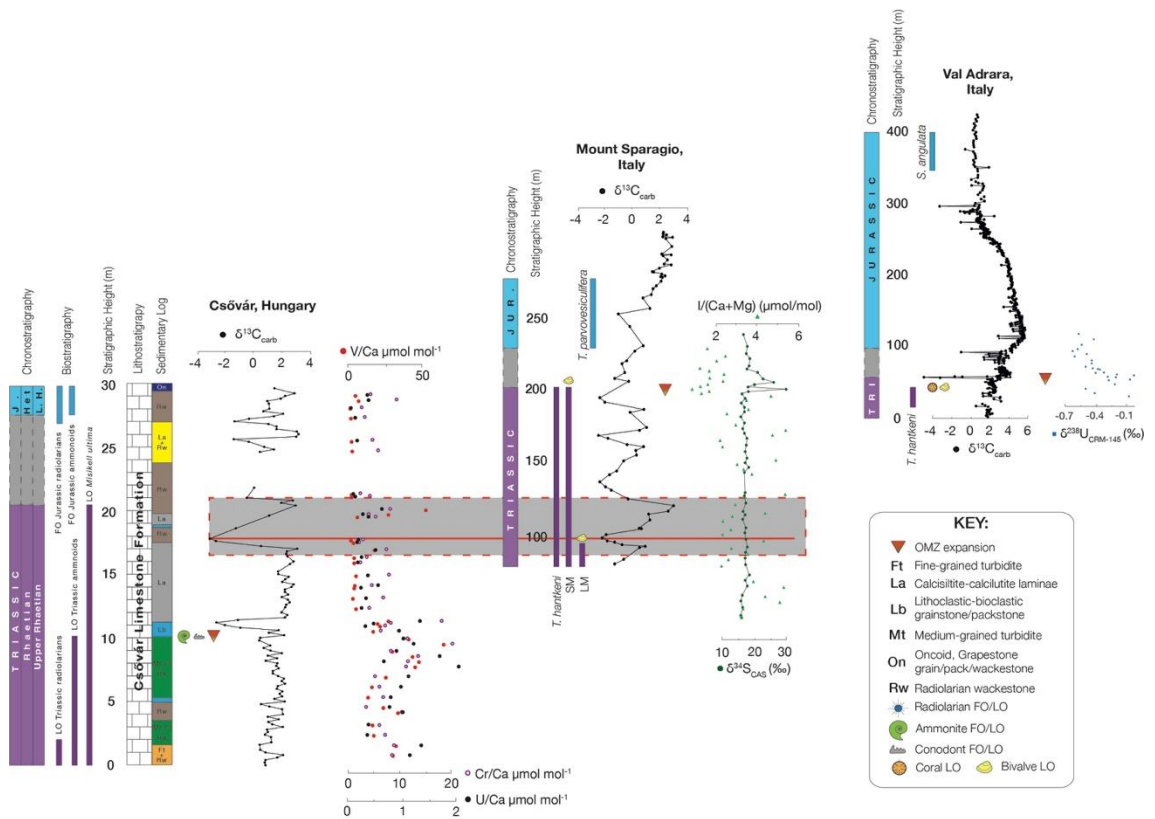


Figure 4:- A comparison of local and global hydrogenic redox data from across the Triassic–Jurassic boundary interval. Note the relative timing of open marine deoxygenation based on the carbonate trace element data. $I/(Ca+Mg)$ data from He et al., (2022a), $\delta^{34}S$ data from He et al., (2020), $\delta^{238}U$ data from Jost et al., (2017). Mt. Sparagio and Val Adrara stratigraphy from Bachan et al., (2012) and Todaro et al., (2018), stratigraphic correlation based on Todaro et al., (2018) and Kovács et al., (2020). Red dashed line with grey shading- ETME Main Interval; unlike at the GSSP no equivalent extinction is observed at the Vár-hegy section. Red solid line initial CIE correlation line.

Chapter 8: Supplementary Information

Leach tests:

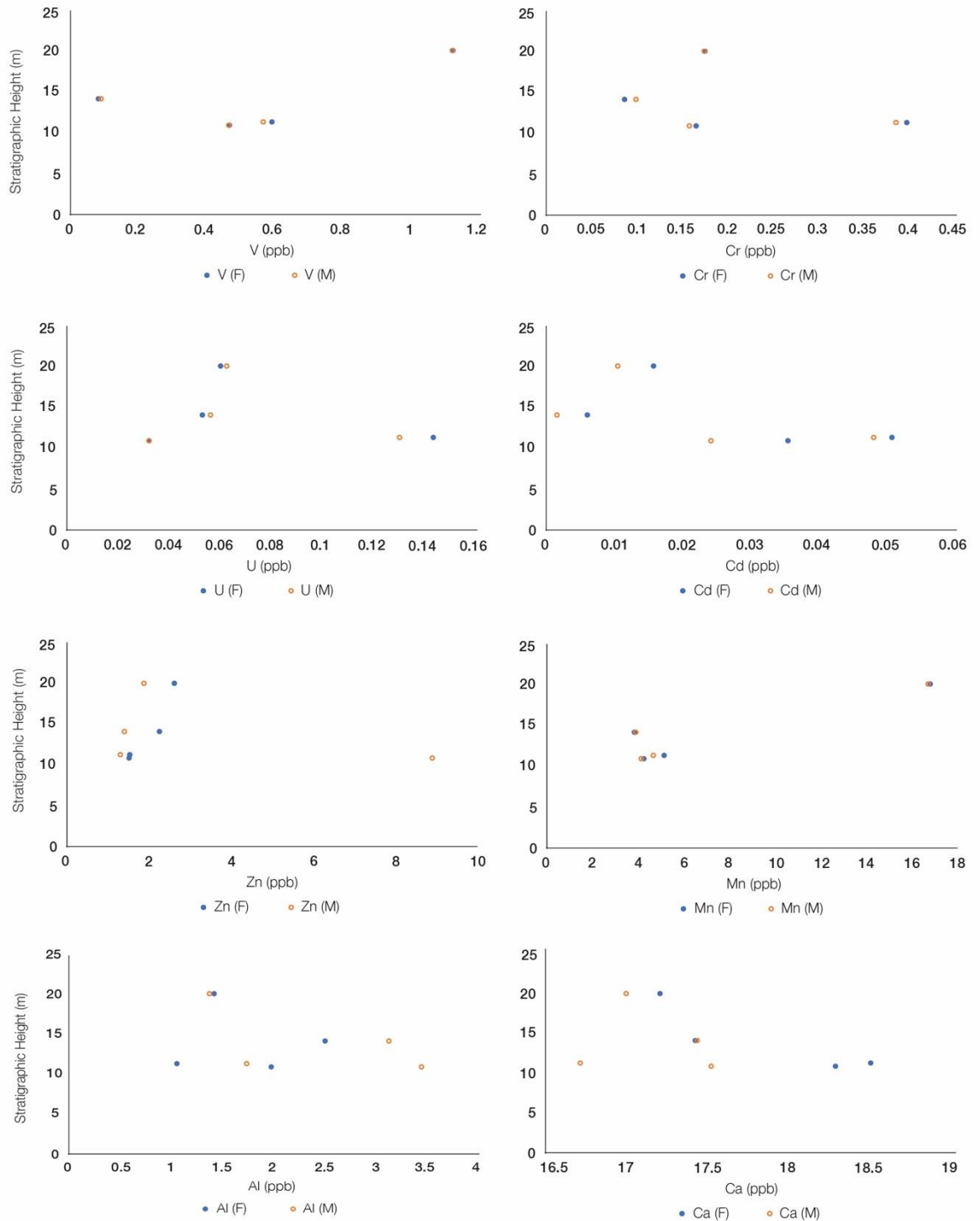


Figure S1: A comparison of samples which have undergone cleaning using milli-q water only (M) and the same samples which have undergone a reductive and oxidative cleaning step (F).

Four samples, at horizons 11 m, 11.4 m, 14.2 m, and 20.2 m, were cleaned using two different methods (see methods above) [Fig. S1]. We observe very little difference, on average, between the samples which were cleaned using milli-q water only (M) and those which underwent a full cleaning procedure using an oxidative and reductive cleaning step (F), particularly amongst the indices U/Ca, V/Ca, and Cr/Ca [Fig. S1]. We therefore interpret that the elemental concentration data is representative of authigenic trace element concentrations and not as a result of detrital material which failed to be removed during the milli-q cleaning procedure. The absence of detrital influence on element/calcium ratios is further supported through Fig. S2.

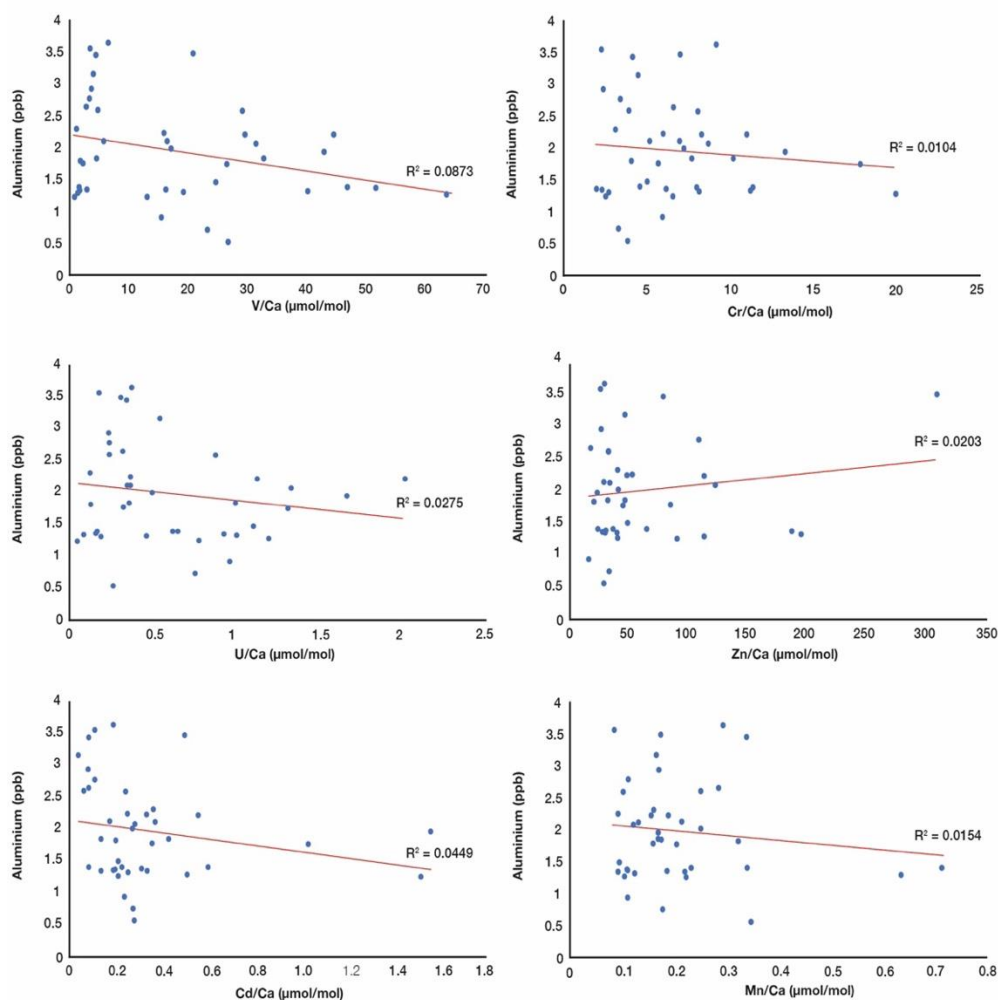


Figure S2: X/Ca ratios plotted against Aluminium (ppb). Low correlation amongst all elements indicates little to no siliciclastic/detrital control on X/Ca of redox sensitive elements..

X/Ca		CORALS $\mu\text{mol/mol}$		SQUID $\mu\text{mol/mol}$		FORAMS $\mu\text{mol/mol}$
U/Ca	Little et al., 2021 Jiang et al., 2017 Prouty et al., 2008 Carilli et al., 2009 Cardinal et al., 2001 Ourbak et al., 2005 Andersson et al., 2020	1.1–2.2 n/a 1.2–1.35 n/a 1.15–0.8 1.0–1.25 0.75–1.2	Liu et al., 2013	0.024–0.110	Chen et al., 2017 Russel et al., 2004 Allen et al., 2016 Salmon et al., 2016 Raitzch et al., 2011 Russel et al., 1996	0.003–0.015 0.005–0.017 0.003–0.012 0.005–0.025 0.005–0.022 0.005–0.013
Cr/Ca	Little et al., 2021 Jiang et al., 2017 Prouty et al., 2008 Carilli et al., 2009	n/a 1.31–12.59 0.05–0.6 0–0.5	Liu et al., 2013	0.16–2.21	Remmelzwaal et al., 2019 Schmidt et al., 2022**	0–0.0004 9–40
V/Ca	Little et al., 2021 Jiang et al., 2017 Prouty et al., 2008 Carilli et al., 2009	n/a n/a 0.11–0.21 n/a	Liu et al., 2013	n/a	Hastings et al., 1996 Saha et al., 2019	0–0.5 0.08–0.2
Zn/Ca	Little et al., 2021 Jiang et al., 2017 Prouty et al., 2008 Carilli et al., 2009 Chen et al., 2010 Ramos et al., 2004 Hanna & Muir, 1990	0.42–9.33 7.75–10.52 0–12 0–1 5–50 2.21–34.3 15.9	Liu et al., 2013	n/a	Schmidt et al., 2022** Marchitto et al., 2000	10–70 1–5
Cd/Ca	Little et al., 2021 Jiang et al., 2017 Prouty et al., 2008 Carilli et al., 2009 Carriguiry & Villaescusa, 2010 Matthews et al., 2008	0.05–1.59 0.01 0.5–3.5 n/a 0–0.06 0.01–0.03	Liu et al., 2013	n/a	Rickaby & Elderfield, 1999 Schmidt et al., 2022** Van Geen et al., 1992	0.025–0.12 0–20 0.25–0.55
Mn/Ca	Little et al., 2021 Jiang et al., 2017 Prouty et al., 2008 Carilli et al., 2009 Carriguiry & Villaescusa, 2010 Chen et al., 2010 Ramos et al., 2004 Hanna & Muir, 1990	0.06–0.48 mmol/mol 2.12–2.83 mmol/mol 0.2–1.2 mmol/mol 1.22–2.87 mmol/mol 0–0.12 mmol/mol 0.01–16.21 mmol/mol 0.172–7.58 mmol/mol 11 mmol/mol	Liu et al., 2013	2.70–6.57 mmol/mol	Remmelzwaal et al., 2019 Hastings et al., 1996 Schmidt et al., 2022**	0–0.0005 mmol/mol 0–40 mmol/mol 0.02–2.4 mmol/mol
** Removing anomalously high values						

Figure S3: Element/Calcium ratios for redox sensitive elements amongst calcifying marine organisms.

t-Test: Two-Sample Assuming Equal Variances		
	V/Ca	
	Variable 1	Variable 2
Mean	29.06282102	7.258810918
Variance	180.1366271	139.5750211
Observations	19	21
Pooled Variance	158.7884134	
Hypothesized Mean Difference	0	
df	38	
t Stat	5.464915134	
P(T<=t) one-tail	1.54199E-06	
t Critical one-tail	1.68595446	
P(T<=t) two-tail	3.08398E-06	
t Critical two-tail	2.024394164	

t-Test: Two-Sample Assuming Equal Variances		
	Cr/Ca	
	Variable 1	Variable 2
Mean	9.163882521	4.458343195
Variance	18.17429549	4.54233976
Observations	19	21
Pooled Variance	10.99958195	
Hypothesized Mean Difference	0	
df	38	
t Stat	4.481029156	
P(T<=t) one-tail	3.30826E-05	
t Critical one-tail	1.68595446	
P(T<=t) two-tail	6.61652E-05	
t Critical two-tail	2.024394164	

t-Test: Two-Sample Assuming Equal Variances		
	Mn/Ca	
	Variable 1	Variable 2
Mean	0.176195537	0.232344706
Variance	0.016102745	0.018193888
Observations	19	21
Pooled Variance	0.017203346	
Hypothesized Mean Difference	0	
df	38	
t Stat	-1.35205175	
P(T<=t) one-tail	0.092175749	
t Critical one-tail	1.68595446	
P(T<=t) two-tail	0.184351498	
t Critical two-tail	2.024394164	

t-Test: Two-Sample Assuming Equal Variances		
	Zn/Ca	
	Variable 1	Variable 2
Mean	74.25595887	53.28606334
Variance	5140.243941	1738.16629
Observations	19	21
Pooled Variance	3349.676756	
Hypothesized Mean Difference	0	
df	38	
t Stat	1.144329962	
P(T<=t) one-tail	0.129821973	
t Critical one-tail	1.68595446	
P(T<=t) two-tail	0.259643945	
t Critical two-tail	2.024394164	

t-Test: Two-Sample Assuming Equal Variances		
	Cd/Ca	
	Variable 1	Variable 2
Mean	0.402962623	0.262838605
Variance	0.122385096	0.099633727
Observations	19	21
Pooled Variance	0.110410691	
Hypothesized Mean Difference	0	
df	38	
t Stat	1.331875006	
P(T<=t) one-tail	0.095417551	
t Critical one-tail	1.68595446	
P(T<=t) two-tail	0.190835103	
t Critical two-tail	2.024394164	

t-Test: Two-Sample Assuming Equal Variances		
	U/Ca	
	Variable 1	Variable 2
Mean	0.959626643	0.279236195
Variance	0.197733977	0.022566252
Observations	19	21
Pooled Variance	0.105540438	
Hypothesized Mean Difference	0	
df	38	
t Stat	6.614624794	
P(T<=t) one-tail	4.10405E-08	
t Critical one-tail	1.68595446	
P(T<=t) two-tail	8.20809E-08	
t Critical two-tail	2.024394164	

Figure S4: T-tests for X/Ca before and after NCIE-2 with an alpha value of 0.05. Therefore P (two tail) of <0.05 is statistically significant. Differences between V/Ca, Cr/Ca, and U/Ca before and after NCIE-2 are statistically significant, whereas differences between Zn/Ca, Cd/Ca, and Mn/Ca before and after NCIE-2 are not statistically significant. Zn and Cd typically co-precipitate with sulfur under oxygen poor conditions resulting in sedimentary enrichment whereas U, V and Cr are more readily enriched within marine sediments under suboxic–anoxic conditions.

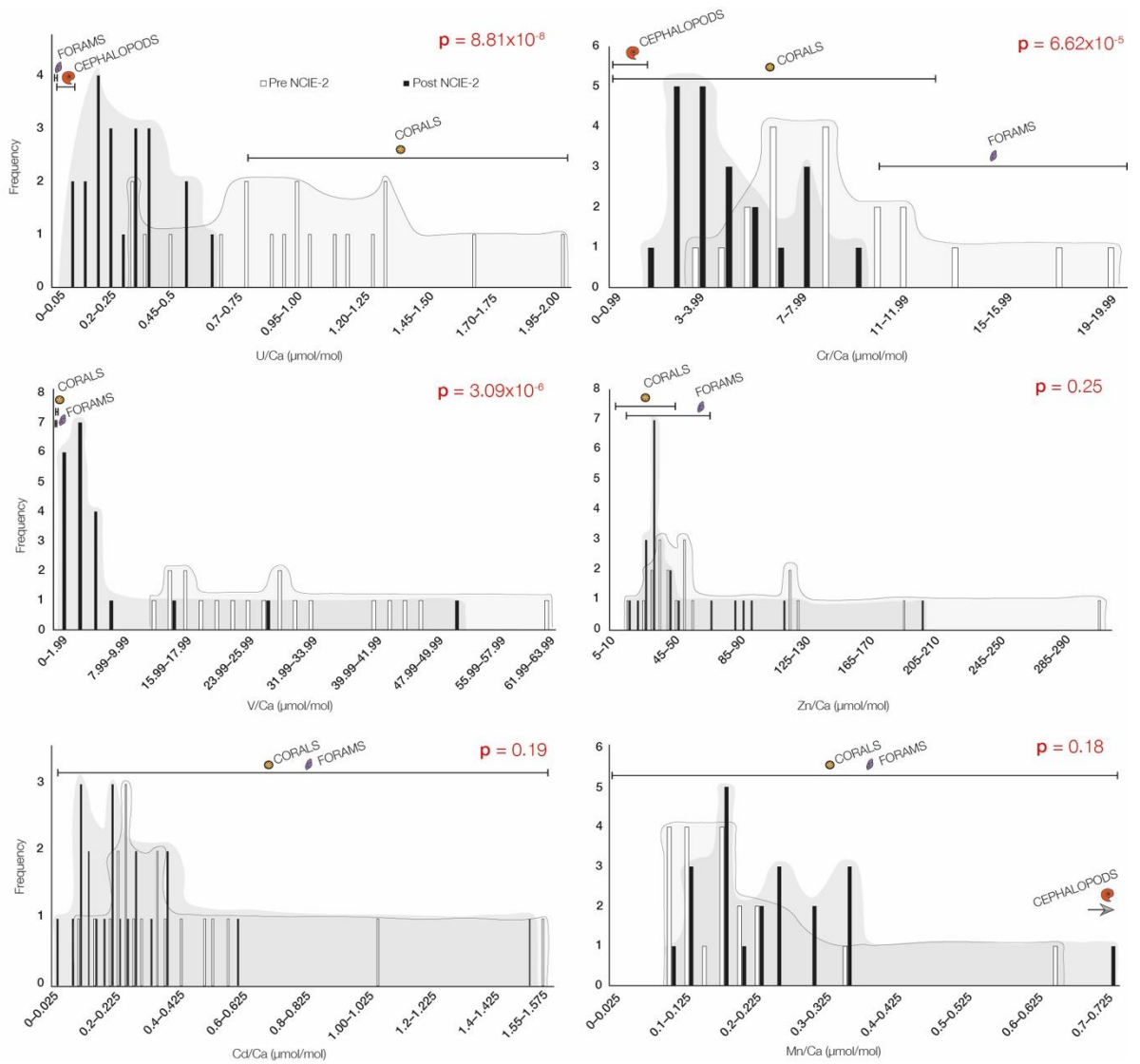


Figure S5:- Carbonate trace element data (X/Ca) for redox sensitive elements before and after NCIE-2. Note the statistically significant shift observed amongst Cr, V and U which is absent amongst other, redox sensitive elements.

Sedimentology and carbonate grain composition throughout the study section:

Given that the X/Ca values which have been recorded throughout the Csóvár Vár-hegy section fall within the bounds of biological values it is discussed here whether the X/Ca shift observed during NCIE-2 could be related to a change in carbonate grain composition. In order to establish whether this could be the case the sedimentology and carbonate grain composition of the study section is first described in detail.

The base of the section (0–12 m) is composed of a combination fine- and medium-grained calciturbidites as well as radiolarian wackestones and rare lithoclastic-bioclastic grainstone/packstone (Fig. 2, Chapter 8). The fine-grained calciturbidite is composed of laminated beds of alternating calcarenite packstones and wackestones (Haas & Tardy-Filácz, 2004). Peloidal echinoderm fragments (crinoids), molluscs and ostracods are common within the calcarenite laminae (Haas & Tardy-Filácz, 2004). Meanwhile, sponge spicules and radiolarians are common within the wackestone laminae (Haas & Tardy-Filácz, 2004). The medium-grained calciturbidite is composed of a graded packstone and coarse to fine-grained calcarenite (Haas & Tardy-Filácz, 2004). The primary component of the medium-grained calciturbidite beds is crinoid skeletal debris as well as common fragments of molluscs, benthic foraminifera, and microbial crusts (Haas & Tardy-Filácz, 2004). The radiolarian wackestone is composed of thinly bedded carbonates with local chert. The predominant component is radiolarians; however, sponge spicules, molluscs and echinoderm fragments are also common (Haas & Tardy-Filácz, 2004). The rare lithoclastic-bioclastic grainstone/packstone is composed of fine calciruditic to coarse calcarenitic facies (Haas & Tardy-Filácz, 2004). Fragments of echinoderms (crinoids and echinoderm spines) are common within the lithoclastic-bioclastic grainstone/packstone alongside molluscs, microbial crust, benthic foraminifera, and thick-shelled ostracods (Haas & Tardy-Filácz, 2004). The carbonate grain composition within the lower 12 m of the study section is therefore crinoid and echinoderm fragments, molluscs, ostracods, sponge spicules, microbial crusts, and benthic foraminifera with echinoderm skeletal debris being the most prominent component.

Towards the top half of the section (12–30 m) the lithology changes to calcisiltite–calcilutite laminite as well as radiolarian wackestone, rare lithoclastic-bioclastic grainstone/packstone and finally oncoid, grapestone grainstone/packstone/wackestone at the very top of the section. The calcisiltite-calcilutite laminite is composed of thinly bedded, platy and laminated fine-grained carbonates composed of radiolarians, sponge spicules and ostracods (Haas & Tardy-Filácz, 2004). The oncoid, grapestone grainstone/packstone/wackestone is composed of carbonate coated grains with rare bioclasts of molluscs, brachiopods and ostracods (Haas & Tardy-Filácz, 2004). The carbonate grain composition within the upper 18 m of the study section is therefore echinoderm fragments, molluscs, ostracods, sponge spicules and brachiopods.

Despite the overall carbonate grain composition varying very little from the bottom half to the top half of the section, the upper part of the study section exhibits a much lower proportion of echinoderm skeletal debris, no microbial fragments or benthic foraminifera, and common brachiopod debris at the very top of the study section. Given the very sparse nature of brachiopod skeletal debris throughout much of the section, its relative abundance is highly unlikely to have any control of X/Ca values throughout the section and, therefore, echinoderm, microbial mat and foraminiferan X/Ca values are most important here.

Published U/Ca values for sea urchins are very low (0.006–0.013 $\mu\text{mol/mol}$) (Ulrich et al., 2021). However, it should be noted that there is little other available data on the X/Ca composition of echinoderms. Microbial mats also have little available X/Ca data. Meanwhile, foraminiferan X/Ca values are low for V/Ca and U/Ca and high for Cr/Ca (see Fig. S3).

Despite the relative absence of X/Ca data for echinoderms and microbial mats, the foraminiferan and available sea urchin data as well as carbonate sedimentology do not strongly suggest that elevated X/Ca ratios towards the base of the section are the result of carbonate grain composition, with the possible exemption of Cr/Ca data based on foraminiferan Cr/Ca values. However, in order to further understanding of this relationship, it is essential that more X/Ca data is obtained from echinoderms and microbial mats.

Diagenesis of carbonate cement from the Csővár Vár-hegy section:

As discussed within the main text we observed little evidence of diagenetic alteration, thermal alteration or dolomitization on the basis of $\delta^{13}\text{C}$ and $\delta^{18}\text{O}$, Mg/Ca, and organic matter content. However, in order to further discern whether there may have been diagenetic alteration of the Vár-hegy carbonates we describe here the composition of carbonate cement as well as any evidence for re-mineralisation or dissolution.

The fine- and medium-grained calciturbidites do not exhibit a carbonate cement, meanwhile the radiolarian wackestone and lithoclastic-bioclastic grainstone/packstone exhibit a calcisiltite and calcilutite mudstone matrix alongside rare spirititic cement (Haas & Tardy-Filácz, 2004). Therefore, the base of the section (0–12m) is broadly non-cemented and is instead (mud) matrix supported.

The calcisiltite–calcilutite laminite and radiolarian wackestone within the top of the section (12–30 m) is non-cemented. Meanwhile the oncoid, grapestone grainstone/packstone/wackestone exhibits a spirititic cement. Therefore, the upper half of the section is also broadly non-cemented (Haas & Tardy-Filácz, 2004).

Given the detrital nature of the carbonate material, consisting of proximal to distal calciturbidites, the section is, therefore, generally non-cemented and as a result the shift in X/Ca values cannot be associated with a change in cement composition. There is little information on the mineralogy/composition of the individual grains which form the calci-turbidites and other detrital carbonate facies. However, based on $\delta^{13}\text{C}$ and $\delta^{18}\text{O}$ values there is little reason to interpret significant remineralisation of the carbonate grains. Further studies should be undertaken, however, to verify the mineralogy of the carbonate grains and the extent (if any) of diagenetic alteration.

Stratigraphic correlation of chapter 8 sections:

This section of the supplementary information discusses how the sections in chapter 8 were correlated, other potential ways of correlating the sections, and the uncertainties associated with the stratigraphic correlation(s).

One potential way of correlating the sections relies almost exclusively on carbon isotope data from literature and the assignment of specific ‘excursions’ to the fluctuations observed within the carbon datasets, as assigned by the original authors. Using this method results in the correlation observed within Fig. S6 (Chapter 8).

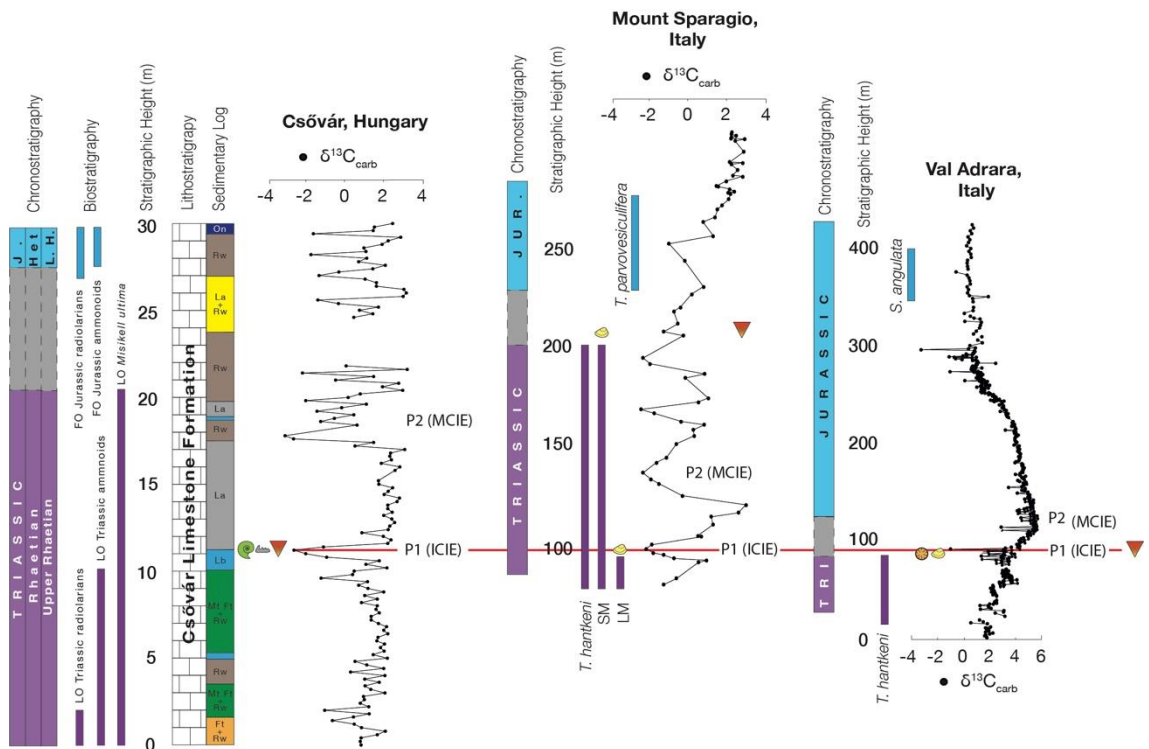


Figure S6:- Correlation of the chapter 8 sections using the assigned carbon isotope excursions. ICIE (P1)- initial carbon isotope excursion, MCIE (P2)- main carbon isotope excursion, PCIE (P0)- Precursor carbon isotope excursion. Refer to main text for additional abbreviations and data sources.

The issues that arise when using this method to correlate the three sections are largely underpinned by uncertainties regarding the assignment of the excursions. For the Csővár section the excursion at 10m (NCIE-2) has been identified as the pre-cursor CIE by Kovács et al., (2020), however, NCIE-2 may be tenuously identified as the initial CIE. The initial CIE at the GSSP coincides with the disappearance of choristoceratid ammonites as does the excursion at 10m from the Csővár section. However, disappearances of ammonite taxa may be spatially variable, and the carbon isotope fluctuations observed within the Csővár section most closely correlate with the CIE at 10m being identified as the precursor CIE when compared with carbon isotope fluctuations from other sites, particularly after the dataset has undergone screening (Kovács et al., 2020). A similar screening process was performed on the carbon isotope

data here through removing carbon isotope datapoints where the oxygen isotopes were $<-5\text{‰}$ and single point spikes, as suggested by the original authors [Kovács *et al.*, 2020].

The identified excursions for the Mount Sparagio section also coincide with the general carbon isotope trends observed from other Tr–J sections and therefore would agree with the excursion assignment for this section.

Conversely, the assignment of excursions to the carbon isotope data from the Val Adrara section does not coincide with similar identifications from other sites with excursions being identified based on single point spikes [Bachan *et al.*, 2012]. If single point spikes are discounted then the carbon isotope trends and biostratigraphy from the Val Adrara section suggest that the section comprises of uppermost Triassic and lowermost Jurassic sediments with the carbon isotope stratigraphy exhibiting the upper half of the main carbon isotope excursion.

Through the use of carbon isotope stratigraphy and biostratigraphy the excursion assignments from Kovács *et al.*, (2020) and Todaro *et al.*, (2018) have been deemed accurate for the Csővár Vár-hegy and Mount Sparagio sections, however the Val Adrara section excursion assignment has been updated here in light of carbon isotope trends and biostratigraphy (see Fig. S7- Chapter 8).

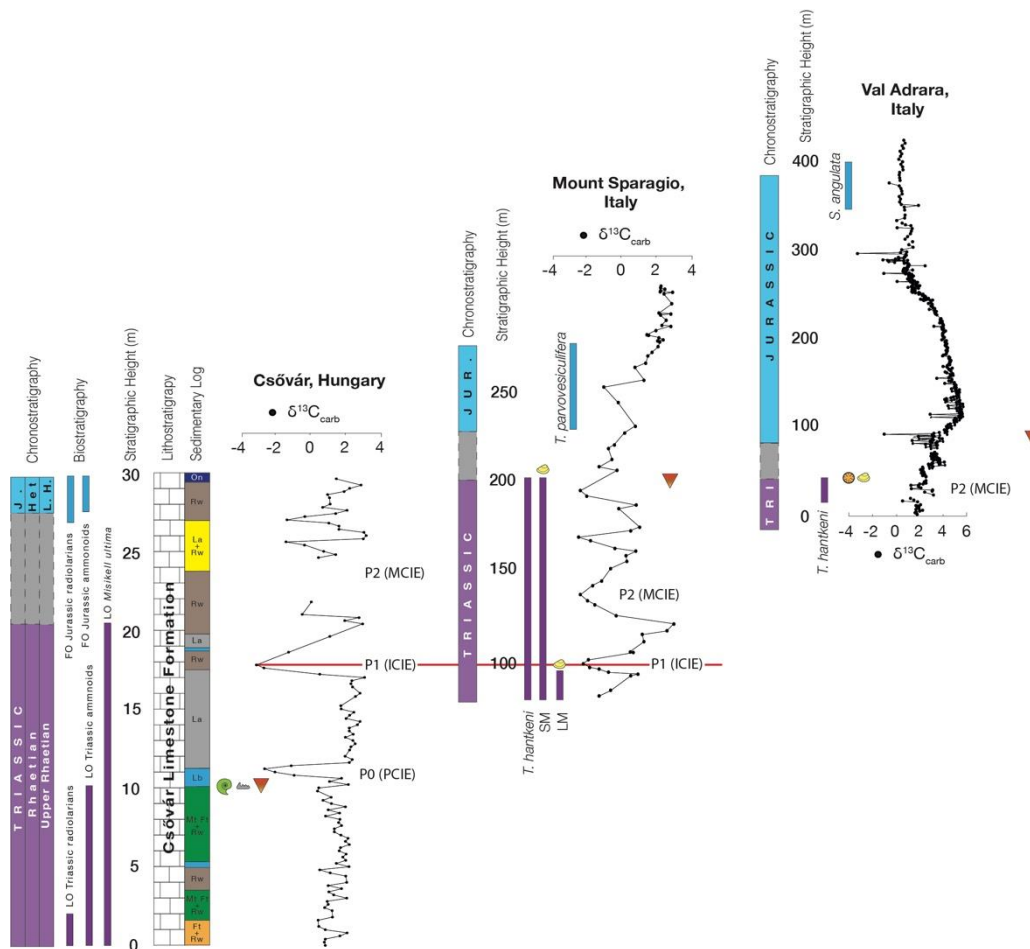


Figure S7:- Correlation of the chapter 8 sections using a revised carbon isotope excursion assignment and biostratigraphic correlation. Refer to Figure S6 for explanation of abbreviations.

The revised stratigraphic correlation used here would therefore confirm that open ocean marine redox change evidenced within this chapter significantly pre-dated open marine redox change evidenced through I/Ca+Mg) and U isotope data, which both postdate the main interval of the ETME.

Supplementary Information- Raw data attached separately as an excel file ‘Supplementary Information: Chapter 8’

REFERENCES

- Allen, K. A., Honisch, B., Eggins, S. M., Haynes, L. L., Rosenthal, Y., and Yu, J., 2016, Trace element proxies for surface ocean conditions: A synthesis of culture calibrations with planktic foraminifera: *Geochimica et Cosmochimica Acta*, v. 193, p. 197–221.
- Andersson, E. R., Stewart, J. A., Work, T. M., Woodley, C. M., Schock, T. B., and Day, R. D., 2020, Morphological, elemental, and boron isotopic insights into pathophysiology of diseased coral growth anomalies, 10, 8252.
- Cardinal, D., Hamelin, B., Bard, E., and Pätzold, J., 2001, Sr/Ca, U/Ca and $\delta^{18}\text{O}$ records in recent massive corals from Bermuda: relationships with sea surface temperature: *Chemical Geology*, v. 176, p. 213–233.
- Carilli, J. E., Prouty, N. G., Huguen, K.A., and Norris, R. D., 2009, Century-scale records of land-based activities recorded in Mesoamerican coral cores: *Marine Pollution Bulletin*, v. 58, p. 1835–1842.
- Carriquiry, J. D., and Villaescusa, J. A., 2010, Coral Cd/Ca and Mn/Ca records of ENSO variability in the Gulf of California: *Climate of the Past*, v. 6, p. 410–410.
- Chen, P., Yu, J., and Jin, Z., 2017, An evaluation of benthic foraminiferal U/Ca and U/Mn proxies for deep ocean carbonate chemistry and redox conditions: *Geochemistry, Geophysics, Geosystems*, v. 18, p. 617–630.
- Chen, T.-R., Yu, K.-F., Li, S., Price, G. J., Shi, Q., and Wei, G.-J., 2010, Heavy metal pollution recorded in *Porites* corals from Daya Bay, northern South China Sea: *Marine Environmental Research*, v. 70, p. 318–326.
- Hanna, R. G. and Muir, G. L., 1990, Red sea corals as biomonitors of trace metal pollution: *Environmental Monitoring and Assessment* 14, 211e222.
- Hastings, D. W., Emerson, S. R., Erez, J., and Nelson, B. K., 1996, Vanadium in foraminiferal calcite: Evaluation of a method to determine paleo-seawater vanadium concentrations: *Geochimica et Cosmochimica Acta*, v. 60, p. 3701–3715.
- Jiang, W., Yu, K.-F., Song, Y.-X., Zhao, J.-X., Feng, Y.-X., Wang, Y.-H., and Xu, S.-D., 2017, Coral trace metal of natural and anthropogenic influences in the northern South China Sea: *Science of the Total Environment*, v. 607–608, p. 195–203.
- Little, S. H., Wilson, D. J., Rehkämper, M., Adkins, J. F., Robinson, L. F., and van de Lierdt, T., 2021, Cold-water corals as archives of seawater Zn and Cu isotopes: *Chemical Geology*, v. 578, <https://doi.org/10.1016/j.chemgeo.2021.120304>.
- Liu, B., Chen, X., Chen, Y., and Tian, S., 2013. Geographic variation in statolith trace elements of the Humboldt squid, *Dosidicus gigas*, in high seas of Eastern Pacific Ocean: *Marine Biology*, v. 160, p. 2853–2862.
- Marchitto Jr., T. M., Curry, W. B., and Oppo, D. W., 2010, Zinc concentrations in benthic foraminifera reflect seawater chemistry: *Paleoceanography*, v. 15, p. 299–306.

- Matthews, K. A., Grottoli, A. G., McDonough, W. F., and Palardy, J. E., 2008, Upwelling, species, and depth defects on corals skeletal cadmium-to-calcium ratios (Cd/Ca): *Geochimica et Cosmochimica Acta*, v. 72, p. 4537–4550.
- Ourbak, T., Corrège, T., Malaizé, B., Le Cornec, F., Charlier, K., and Peypouquet, J. P., 2006, A high-resolution investigation of temperature, salinity, and upwelling activity proxies in corals: *Geochemistry, Geophysics, Geosystems*, v.7, doi:10.1029/2005GC001064.
- Prouty, N. G., Huguen, K. A., and Carilli, J., 2008, Geochemical signature of land-based activities in Caribbean coral surface samples: *Coral Reefs*, v. 27, p. 727–742.
- Raitzsch, M., Kuhnert, H., Hathorne, E. C., Groeneveld, J., and Bickert, T., 2011, U/Ca in benthic foraminifers: A proxy for the deep-sea carbonate saturation: *Geochemistry, Geophysics, Geosystems*, v. 12, doi:10.1029/2010GC003344.
- Ramos, A. A., Inoue, Y., and Ohde, S., 2004, Metal contents in *Porites* corals: anthropogenic input of river run-off into a coral reef from an urbanized area, Okinawa: *Marine Pollution Bulletin* 48, 281e294.
- Rommelzwaal, S. R. C., Sadekov, A. Y., Parkinson, I. J., Schmidt, D. N., Titelboim, D., Abramovich, S., Roepert, A., Kienhuis, M., Polerecky, L., Goring-Harford, H., Kimoto, K., Allen, K. A., Holland, K., Stewart, J. A., and Middelburg, J. J., 2019, Post-depositional overprinting of chromium in foraminifera: *Earth and Planetary Science Letters*, v. 15, p. 100-111.
- Rickaby, R. E. M., and Elderfield, H., 1999, Planktonic foraminiferal Cd/Ca: Paleonutrients or Paleotemperature?: *Paleoceanography*, v. 14, p. 293–303.
- Russell, A. D., Emerson, S., Mix, A. C., and Peterson, L. C., 1996, The use of foraminiferal uranium/calcium ratios as an indicator of changes in seawater uranium content: *Paleoceanography*, 1996, v. 11, p. 649–663.
- Russell, A. D., Hönisch, B., Spero, H. J., and Lea, D. W., 2004, Effects of seawater carbonate ion concentration and temperature on shell U, Mg, and Sr in cultured planktonic foraminifera: *Geochimica et Cosmochimica Acta*, v. 68, p. 4347–4361.
- Saha, N., Webb, G. E., Christy, A. G., and Zhao, J.-X., 2019, Vanadium in the massive coral *Porites*: A potential proxy for historical wood clearing and burning: *Earth and Planetary Science Letters*, v. 527, 115793.
- Salmon, K. H., Anand, P., Sexton, P. F., and Conte, M., 2016, Calcification and growth processes in planktonic foraminifera complicate the use of B/Ca and U/Ca as carbonate chemistry proxies: *Earth and Planetary Science Letters*, v. 449, 372–381.
- Schmidt, S., Hathorne, E. C., Schönfeld, J., and Garbe-Schönberg, D., 2022, Heavy metal uptake of nearshore benthic foraminifera during multi-metal culturing experiments: *Biogeosciences*, v. 19, p. 629–664.

Van Geen, A., Luoma, S. N., Fuller, C. C., Anima, T., Clifton, H. E., and Trumbore, S., 1992, Evidence from Cd/Ca ratios in foraminifera for greater upwelling off California 4,000 years ago: *Letters to Nature*, v. 358, p. 54–56.

9 WIDESPREAD PULSES OF BENTHIC DE-OXYGENATION ON THE TETHYAN SHELF DURING THE END-TRIASSIC MASS EXTINCTION

Andrew D. Bond, Alexander J. Dickson, Christian Bjerrum, Micha Ruhl, Remco Bos, Bas van de Schootbrugge

In preparation for *Earth and Planetary Science Letters*

Statement of lead author's contributions:

- Obtained samples from CB and MR
- Logged the sedimentology of the Somerset-1 and Somerset-2 cores
- Milled the samples from the Prees-2c core
- Digested the sample powders
- Prepared the samples for ICP-AES and ICP-MS analyses
- Processed the ICP-AES and ICP-MS data
- Interpreted the ICP-AES and ICP-MS data
- Ran t-tests
- Collated the final dataset
- Correlated data from the different sites using carbon isotope chemostratigraphy and palynostratigraphy
- Wrote the first draft of the manuscript
- Prepared all figures for the manuscript

Widespread pulses of benthic de-oxygenation on the Tethyan shelf during the end-Triassic mass extinction

Andrew D. Bond^{a*}, Alexander J. Dickson^a, Christian Bjerrum^b, Micha Ruhl^c, Bas van de Schootbrugge^d, Remco Bos^d

^a Centre of Climate, Ocean and Atmosphere, Department of Earth Sciences, Royal Holloway University of London, Egham Hill, Egham, Surrey, TW200ES, UK

^b Department of Geosciences and Natural Resource Management, University of Copenhagen, Øster Voldgade 10, Copenhagen, Denmark

^c Department of Geology, Trinity College Dublin, The University of Dublin, College Green, Dublin, Ireland

^d Department of Earth Sciences, Utrecht University, Marine Palynology & Paleocenography, Princetonlaan 8a, 3584, CD, Utrecht, the Netherlands

*Corresponding author: Andrew.Bond.2014@live.rhul.ac.uk

Abstract

The end-Triassic mass extinction event (ETME) is defined by the pulsed extinction of numerous marine organisms. The ETME has been widely attributed to large igneous province activity in the form of the Central Atlantic Magmatic Province (CAMP) which has been linked to marine acidification and de-oxygenation. Euxinic water column conditions, which have been widely reported from Triassic–Jurassic marginal marine environments, have subsequently been endorsed as a key driver of

marine extinctions during the Triassic–Jurassic boundary interval. However, recent elemental studies report the widespread, pulsed de-oxygenation of marine, sedimentary porewaters and bottom waters on the marginal marine Tethyan shelf with euxinic conditions being relatively localised. Here we use both new and existing elemental data from five sites on the Tethyan shelf to evaluate the geographic extent of sedimentary porewater and bottom water de-oxygenation during the ETME. We find that pulsed, sedimentary porewater and bottom water de-oxygenation was widespread on the Tethyan shelf whilst euxinic water column conditions were spatially limited. Moreover, pulses of porewater and bottom water de-oxygenation directly coincided with the three main pulses of the ETME, which largely included the extinction of benthic marine organisms and planktonic organism with a benthic resting stage. We therefore interpret benthic de-oxygenation as being a significant factor in the widespread extinction of marine organisms during the ETME whilst the localised development of sulfidic water column conditions may have driven the extinction of exclusively planktonic and nektonic taxa.

1. Introduction

The Triassic–Jurassic boundary interval coincided with one of the largest mass extinction events in geological history, the end-Triassic mass extinction event (ETME) (Raup & Sepkoski, 1982; Alroy, 2014). The ETME is characterised by the pulsed extinction of marine organisms with ammonites, bivalves and reefal organisms having been particularly affected (Hallam, 1981; Flügel & Kiessling, 2002; Guex et al., 2004; Kiessling et al., 2007; Whiteside & Ward, 2011; Dunhill et al., 2018; Wignall & Atkinson, 2020). The ETME also coincided with

disappearances amongst marine vertebrates, in the form of conodonts, as well as extinctions amongst phytoplankton groups including radiolarians and dinoflagellates (Carter & Hori, 2005; van de Schootbrugge et al., 2007; Hautmann, 2012; Onoue et al., 2016; Rigo et al., 2018; Du et al., 2020).

The ETME was initially thought to have been triggered by an extra-terrestrial impact based on the discovery of Late Triassic iridium anomalies and seismite deposits (Orth, 1989; McLaren & Goodfellow, 1990; Olsen et al., 2002; Simms, 2003; Tanner & Kyte, 2005). However, subsequent studies have closely associated Triassic–Jurassic iridium anomalies and seismite deposits with large igneous province volcanism (Lindström et al., 2015; Tanner et al., 2016; Lindström et al., 2020; Laborde-Casadaban et al., 2021). A large igneous province centred on the supercontinent of Pangaea, the Central Atlantic Magmatic Province (CAMP), was emplaced synchronously with the ETME and has consequently been closely associated with the Triassic–Jurassic extinction pulses (Marzoli et al., 1999; Whiteside et al., 2010; Schoene et al., 2010; Ruhl et al., 2011; Blackburn et al., 2013; Lindström et al., 2017; Davies et al., 2017; Marzoli et al., 2018; Kovács et al., 2020).

CAMP-induced environmental change has been strongly associated with marine acidification and marine de-oxygenation during the Triassic–Jurassic boundary interval (TJB) with marine redox change having been intensely studied from across the Triassic–Jurassic Tethyan shelf (Hautmann et al., 2008; Richoz et al., 2012; Greene et al., 2012; Jost et al., 2017a; 2017b; He et al., 2020; Bond et al., 2022a, 2022b, 2022c). Euxinic water column conditions have been widely reported from across Tethyan marginal marine environments during the TJB based on biomarker and isotope studies

(Richoz et al., 2012; Jaraula et al., 2013; Blumenberg et al., 2016; Jost et al., 2017b; He et al., 2020, 2022; Beith et al., 2021; Fox et al., 2022). However, recent research reports the pulsed deoxygenation of sedimentary porewater and bottom waters on the Triassic–Jurassic Tethyan shelf with euxinic water column conditions being spatially limited (Bond et al., 2022a, 2022b). We hypothesise that the pulsed de-oxygenation of sedimentary pore waters was widely distributed on the Tethyan shelf during the Triassic–Jurassic boundary interval whilst euxinic conditions were spatially constrained on the Tethyan shelf. This hypothesis has been previously difficult to test due to the lack of spatially extensive elemental redox data from across the Tethyan shelf.

In order to test this hypothesis, we present a compilation of elemental data from five sites across the Triassic–Jurassic Tethyan shelf. Trace metal data has been used to determine the magnitude and temporal pattern of marine redox change at each study site. The dataset used within this study includes previously published data from the upper Rhaetian (uppermost Triassic) and lower Hettangian (lowermost Jurassic) of the Carnduff-2 core (N. Ireland), Schandelah-1 core (N. Germany), and Hebelermeer-2 core (NW Germany) and new trace metal data from the Rhaetian and Hettangian of St. Audrie’s Bay (SW England) and the Prees-2c core (England) [Fig. 1]. The chosen study sections include a range of sites from different palaeolatitudes and palaeolongitudes throughout the Tethyan shelf from a range of palaeo-environmental settings [Blumenberg et al., 2016; van de Schootbrugge et al., 2019; Boomer et al., 2021; Bond et al., 2022]. The study sections are generally stratigraphically well understood, have undergone previous study for redox change using alternative proxies, and all occupy a similar stratigraphic range for direct comparison and stratigraphic correlation between sections to be made [Hesselbo et al., 2002; Blumenberg et al., 2016; Lindström et al.,

2017; van de Schootbrugge et al., 2019; Boomer et al., 2021, Hesselbo, S. 2022. Pers. comms. 30th July). The sedimentary records from each site are also relatively thermally immature and have undergone limited diagenetic alteration (see Chapter 9: supplementary information).

2. Materials and Methods

2.1 Prees 2c and Somerset core samples

Both the Somerset-1 and Somerset-2 cores were extracted from St. Audrie's Bay, Somerset, England (51.18186° N, 3.286053° W). The cores were sampled at The Geocenter, Copenhagen University, Denmark. The samples span the upper Rhaetian and lower Hettangian based on carbon isotope stratigraphy. Twenty-three samples were obtained from the Somerset-1 core between ~3.5 m and ~4.69 m depth. Twenty-eight samples were also obtained from the Somerset-2 core between 0 m and 3.32 m depth.

Thirty-eight samples were obtained between 607.57 m and 500.37 m depth from the Prees-2c core, Shropshire, England. The core was sampled at the British Geological Survey (BGS) core repository. The samples extend from the upper Rhaetian to the upper Hettangian based on ammonite biostratigraphy and carbon isotope stratigraphy (Hesselbo, S. 2022. Pers. comms. 30th July).

2.2 Bulk Inorganic Geochemistry

Samples from the Somerset-1, Somerset-2 and Prees-2c cores were milled in tungsten carbide and carbon alloy. ~50 mg of each sample was digested in 1:3 HCl/HNO₃ followed by digestion in 1:2 HF/HNO₃ using an identical method to Bond et al.,

(2022a). Samples were diluted 150-fold and were measured on a Perkin Elmer Optima 3300RL ICP-AES for major elemental concentration data. Aliquots of the same sample digests were diluted 2000-fold and were measured on a Perkin Elmer NexION 350D ICP-MS and Agilent 7500 ICP-MS for minor and trace elemental concentration data. Accuracy was determined using full procedural digestions (n=8) of MAG-1 and was better than $\pm 1\%$. Precision was assessed with digests of MAG-1 (n=8) and an in-house mudrock standard (PERN-1) (n=8) and was better than $\sim 21\%$ for all elements. Procedural blanks processed alongside each batch of samples generally exhibited sub ng (total) concentrations. Elemental enrichment data was obtained using the following calculation: $((X_{\text{sample}} / Al_{\text{sample}}) / (X_{\text{UCC}} / Al_{\text{UCC}}))$ where X is the trace metal analyte. Average upper continental crust (UCC) concentrations were obtained from Rudnick & Gao, (2003).

2.3 Chemical Index for Alteration

The Chemical Index for Alteration (CIA) was calculated using the following equation: $CIA = [Al_2O_3 / (Al_2O_3 + CaO^* + Na_2O + K_2O)] \times 100$. CaO^* was determined as the greater value between Na_2O and CaO' where $CaO' = Ca - 10/3 * \text{Phosphorus (P)}$. CaO^* therefore allowed for CIA to be corrected for non-silicate Ca.

3. Palaeo-redox proxies

In order to reconstruct palaeo-redox conditions at the new study sites a representative selection of palaeo-redox proxies has been chosen (Mo_{EF} , U_{EF} , Mn_{EF}).

Under oxygenated conditions molybdenum (Mo) and uranium (U) exist as the conservative species MoO_4^{2-} and U(VI) in seawater (Calvert & Pedersen, 1993;

Tribovillard et al., 2006). Under reducing conditions Mo co-precipitates with sulfur which results in sedimentary enrichment of Mo above crustal concentrations (Helz et al., 1996; Erickson & Helz, 2000; Scott & Lyons, 2012). Mo_{EF} is therefore a proxy for $[HS^-]$ when studied alongside other elements (e.g., Mn, U). Meanwhile, U(VI) is reduced to U(IV) around the Fe(III/II) redox couple, leading to immobilisation and subsequent sedimentary enrichment across the sediment-water interface. U_{EF} can therefore act as a proxy for pore water $[O_2]$ with U enrichment starting prior to sulfate reduction.

Manganese (Mn) exhibits a contrasting chemical behaviour to Mo and U. Under oxygenated conditions Mn is enriched within marine sediments through Mn (III) oxyhydroxide formation (Calvert & Pedersen, 1993). However, under reducing conditions Mn undergoes reductive dissolution to Mn (II) which may move freely within sedimentary porewaters. When Mn (II) encounters oxygenated conditions it may re-precipitate resulting in sedimentary enrichment (Shimmield & Price, 1986; Pruyssers et al., 1993; Piper & Calvert, 2009). Low enrichment of Mn, Mo and U have been defined here as EF 0–1, whilst moderate enrichment has been defined as EF 1–5, high enrichment as EF 5–15, and very high enrichment as EF 15+.

4. Localised, pulsed redox change on the Triassic–Jurassic Tethyan shelf

As part of this thesis a quantitative framework has been compiled from literature exhibiting the typical range in elemental enrichment for Mo, U and Mn under variable redox conditions (Chapter 3). This redox framework has been used here to interpret changing redox conditions at the selected Triassic–Jurassic boundary locations.

Somerset-1 and Somerset-2 cores, Bristol Channel Basin, SW England

The uppermost Westbury Formation, mid upper Cotham Member, basal Langport Member, mid upper Langport Member, and lower Blue Lias Formation of the Somerset cores exhibit moderate to high M_{OEF} and M_{NEF} as well as moderate to very high U_{EF} . The Somerset palaeodepositional site was therefore likely suboxic during the depositional of these sedimentary units with marine redox change being restricted to below the sediment-water interface [Fig. 2]. Very high M_{OEF} during the mid Cotham Member and uppermost Langport Member alongside moderate to high U_{EF} and moderate M_{NEF} is suggestive of sulfidic conditions extending into the water column at the Somerset palaeodepositional locality [Fig. 2]. Meanwhile, the uppermost Cotham Member exhibits high M_{OEF} alongside moderate U_{EF} and M_{NEF} which is suggestive of suboxic conditions extending into the water column.

Prees-2c core, Cheshire Basin, England

The upper Blue Anchor Formation and Westbury–Lilstock Formation within the Prees-2c core exhibit low M_{OEF} alongside moderate U_{EF} and low to moderate M_{NEF} . [Fig. 3]. The Prees-2c palaeodepositional site was therefore suboxic with oxygen poor conditions being restricted to sedimentary pore waters during the deposition of these sedimentary units. The Lower Redcar Mudstone Formation exhibits a horizon of high M_{OEF} as well as low U_{EF} and low to moderate M_{NEF} . The deposition of this interval therefore coincides with suboxic conditions extending into the water column. Throughout the remainder of the section U_{EF} , M_{NEF} and M_{OEF} fluctuate between low and moderate values [Fig. 3]. Redox conditions during the deposition of the remainder of the section therefore fluctuated between oxic conditions, suboxic conditions with marine redox change extending into the water column, and suboxic conditions restricted to sedimentary porewaters.

Carnduff-2 core, Larne Basin, Northern Ireland

The basal Westbury Formation of the Carnduff-2 core exhibits high M_{OEF} and low U_{EF} and M_{NEF} which was interpreted by Bond et al., (2022a) to reflect suboxic conditions extending into the water column [Fig. 4]. Throughout the remainder of the section M_{OEF} , U_{EF} , and M_{NEF} alternate between low and moderate values interpreted by Bond et al., (2022a) as reflecting alternating suboxic and oxic sedimentary pore waters [Fig. 4]. M_{OEF} , U_{EF} and M_{NEF} are particularly elevated throughout the upper Cotham member within the Carnduff-2 core [Fig. 4].

Schandelah-1 core, Lower Saxony Basin, N. Germany

The Contorta beds of the Schandelah-1 core exhibit high M_{OEF} , moderate U_{EF} and low M_{NEF} which was interpreted by Bond et al., (2022b) to represent shoaling of the sulfate reduction zone close to the sediment-water interface [Fig. 5]. Pulsed increases in U_{EF} within the upper Trilete beds alongside low to high M_{OEF} and moderate to high M_{NEF} are likely indicative of pulsed suboxic conditions which were restricted to sedimentary porewaters and extended into the water column [Fig. 5]. Very high M_{OEF} alongside moderate U_{EF} and high M_{NEF} within the Pilonoten beds were interpreted by Bond et al., (2022b) to represent ferruginous conditions during the deposition of the Pilonoten beds at the Schandelah-1 palaeodepositional site [Fig. 5]. Meanwhile, pulsed increases in M_{OEF} , U_{EF} and M_{NEF} throughout the Angulatenton Formation were interpreted by Bond et al., (2022b) to represent further shoaling of the sulfate reduction zone close to the sediment-water interface [Fig. 5].

Hebelermeer-2 core, Germanic Basin, NW Germany

Lower–Middle Rhaetian strata of the Hebelermeer-2 core (1695 m) exhibit moderate MO_{EF} and U_{EF} as well as low Mn_{EF} suggestive of suboxic conditions restricted to sedimentary porewaters [Fig. 6]. Middle Rhaetian strata of the Hebelermeer-2 core (1689 m, 1683 m) exhibit moderate to high MO_{EF} alongside moderate U_{EF} and low to moderate Mn_{EF} which was interpreted by Bond et al., (2022b) to represent shoaling of the sulfate reduction zone close to the sediment-water interface at the Hebelermeer-2 palaeodepositional site [Fig. 6]. Meanwhile, very high MO_{EF} alongside moderate U_{EF} and low Mn_{EF} within the middle to upper Rhaetian strata of the Hebelermeer-2 core (1670 m, 1657 m) were interpreted by Bond et al., (2022b) to reflect pulsed expansion of the sulfate reduction zone close to the sediment-water interface and into the water column [Fig. 6].

5. Localised drivers of pulsed marine redox change on the Tethyan shelf during the end Triassic mass extinction event

Pulses of sedimentary porewater and bottom water de-oxygenation were clearly prevalent at numerous sites on the Tethyan shelf during the Triassic–Jurassic boundary interval. However, it remains uncertain whether pulses of marine redox change on the Tethyan shelf may have been driven by localised environmental changes, particularly given that the five sites are geographically localised on the Tethyan shelf [Fig. 1]. To investigate local drivers of trace metal burial, the elemental redox proxies have been plotted against proxies for hydrography (Cobalt (ppm) * Manganese (%)) ($Co * Mn$) as well as detrital input, grain size and weathering intensity (Ti/Al, Zr/Al, Al (%), CIA) to determine whether redox changes may have been driven by localised environmental changes [Fig. 7, Fig. 8].

5.1 Palaeo-hydrography

Palaeo-hydrography has been determined at the study sites through the use of (Co*Mn). Within upwelling marine environments dissolved Co and Mn may be upwelled to shallower marine settings where they may leave the system through advection away from the upwelling cell (Sweere et al., 2016; McArthur, 2019). Sedimentary Co*Mn for upwelling, marine environments is therefore <0.4 (Sweere et al., 2016). Within restricted marine environments surface water advection into the open ocean is more limited and any dissolved Co or Mn that reaches the surface subsequently returns to deeper waters through diffusion and particle export. Sedimentary Co*Mn within restricted, marine environments is therefore >0.4 (Sweere et al., 2016).

The correlation between marine redox change and palaeo-hydrographic indicators is generally poor across all five study sites [Fig. 7]. Therefore, hydrographic changes are unlikely to have controlled marine redox change. However, given that trace element enrichment of <1 may have a detrital control, trace metal enrichment of >1 (Mo, U) was also compared for open marine (<0.4) and restricted sites (<0.4). Through the use of t-test with an alpha value of 0.05 open marine and restricted sites were found to exhibit no statistically significant difference for M_{OEF} and U_{EF} (Fig. S1). It is therefore unlikely that pulses of sedimentary porewater de-oxygenation across all five study sites were solely the function of changing hydrographic conditions.

5.2 Detrital input, grain size and weathering intensity

The correlation between marine redox change and detrital input is generally poor across all five sites. This is clearly observed through the poor correlations observed between M_{OEF} and Al (%), Ti/Al, and Zr/Al [Fig. 8].

Ti/Al and Zr/Al are also informative proxies with regards to grain size. Aluminium (Al) is generally bound within clay sized sediments, whereas high density Titanium (Ti)-bearing minerals are generally transported with silts and fine sands, and Zirconium (Zr) is concentrated within fine to medium sands due to its high specific gravity (Calvert & Pedersen, 2007). Changes in grain size may suggest changes in energy, as a result of a marine regression, or the increase input of coarser detrital material. Therefore, the poor correlation between Al (%), Ti/Al, Zr/Al and Mo_{EF} would suggest that changing redox conditions did not coincide with the influx of coarser material nor environmental changes due to changing sea-level.

A correlation between marine redox change and weathering intensity, or changing weathering catchment area, may also be ruled out due to the poor correlation between Mo_{EF} and CIA. The Chemical Index of Alteration (CIA) is defined through the equation: $CIA = [Al_2O_3 / (Al_2O_3 + CaO^* + Na_2O + K_2O)] \times 100$ and was initially developed as a proxy for palaeo-climate reconstruction (Nesbitt & Young, 1982). CIA measures the mobilisation of cations (e.g., K^+), which are more readily mobilised within warm, wet climates (Wang et al., 2020). CIA has also been used as a proxy for the chemical weathering of sedimentary rocks as well as changes in weathering intensity. However, CIA may equally determine changes in weathering catchment area. The poor correlation between CIA and Mo_{EF} across all five sites would therefore suggest that redox changes did not coincide with changes in the weathering intensity of rocks mobilised from nearby landmasses, nor with changes to the weathering catchment area as a result of eustatic or isostatic changes.

Given that the de-oxygenation of sedimentary porewaters and bottom waters were localised on the Tethyan shelf there was a possibility that these redox changes may have been generated by localised environmental changes instead of manifestations of spatially extensive phenomena. However, the poor correlation between palaeo-hydrographic, palaeo-weathering, palaeo-detrital proxies and marine redox change would give support to the null hypothesis. Therefore, there is no evidence that hydrographic, isostatic, eustatic, or detrital changes were significantly driving marine redox change on the Triassic–Jurassic Tethyan shelf. Therefore, sedimentary porewater and bottom water de-oxygenation on the Tethyan shelf was regionally extensive and was likely driven by regional-scale environmental changes. This may include regional changes to nutrient availability, marine temperature changes leading to stratification, and/or deep-water oxygen advection.

6. Pulsed suboxia throughout the Tethyan shelf during the ETME

Numerous, regionally extensive, widespread pulses of sedimentary porewater and bottom water de-oxygenation took place on the Tethyan shelf during the Triassic–Jurassic boundary interval. These pulses took place during the deposition of the upper Westbury Formation, mid–upper Cotham member, Triassic–Jurassic transition, and stratigraphically equivalent units [Fig. 9].

The uppermost Westbury Formation and stratigraphically equivalent units at four of the five study sites exhibit moderate to very high M_{OEF} alongside moderate to high U_{EF} [Fig. 9]. Tethyan shelf environments therefore underwent widespread de-oxygenation of sedimentary pore-waters during the deposition of the uppermost Westbury Formation with some extension of oxygen poor conditions into the water column. Sedimentary

porewater and bottom water de-oxygenation during the upper Westbury Formation coincided with one of the major pulses of the ETME (Wignall & Atkinson, 2020). This major pulse of the ETME is reflected in the study sections through the extinction of bivalves and ichnotaxa across the Bristol Channel and Larne Basins (Wignall & Atkinson, 2020; Fox et al., 2022; Bond et al., 2022a). A pulse of widespread marine redox change during the deposition of the uppermost Westbury Formation has also been suggested by Bond et al., (2022b) through a compilation of late Triassic redox proxy data, with suboxic benthic conditions also being observed at the Marientel-1 and Mingolsheim FR 204-201 palaeodepositional sites (Quan et al., 2008; Richoz et al., 2012). Euxinic conditions were largely restricted to marine photic zones during the deposition of the uppermost Westbury Formation and have only been reported from the Germanic and Bristol Channel Basins (Blumenberg et al., 2016; Fox et al., 2022; He et al., 2022).

Bond et al., (2022a) previously reported a major pulse of marine deoxygenation during the mid–upper Cotham member within the Carnduff-2 core of the Larne Basin, marked by a distinctive enrichment in sedimentary U. We are now able to correlate this pulse of U_{EF} to other pulses of U_{EF} at similar stratigraphic horizons from other Triassic–Jurassic sections. All five sites exhibit low to very high Mo_{EF} alongside moderate to very high U_{EF} around the base of the initial CIE [Fig. 9]. Tethyan shelf environments therefore underwent widespread de-oxygenation of sedimentary pore-waters alongside variable extension of the sulfate reduction zone into the water column coincident with the base of the initial CIE, which also coincided with the main extinction interval of the ETME. The main ETME interval is reflected within the study sections through dinoflagellate and bivalve disappearances as well as the absence of ichnofauna within the Larne Basin;

significant reductions in bivalve species richness and dinoflagellate diversity alongside prasinophycean blooms within the Bristol Channel Basin; dinoflagellate disappearances from the Lower Saxony Basin. Bond et al., (2022b) also suggested a widespread pulse of marine de-oxygenation during the mid to upper Cotham member, with anoxic benthic conditions also being reported from the Marientel-1 palaeodepositional site.

Geographically localised, euxinic water column conditions have been reported from the Germanic and Bristol Channel Basins during the deposition of the mid–upper Cotham member with similar conditions being supported by this study (Jaraula et al., 2013; He et al., 2022; Bond et al., 2022b). However, sulfidic conditions were not as widely distributed as suboxic sedimentary porewater conditions during this interval.

Pulsed moderate to very high M_{OEF} and moderate to high U_{EF} throughout the uppermost Triassic to basal Jurassic sediments of four out of the five sections are indicative of widespread de-oxygenation of sedimentary porewaters alongside variable extension of oxygen-poor conditions into the water column [Fig. 9]. The fifth site (Hebelmeer-2) is only not included as a result of low-resolution sampling, but still contains evidence for elevated U in the same stratigraphic succession. The Triassic–Jurassic transition also coincides with the second major pulse of the ETME which is reflected throughout the Larne and Bristol Channel Basin sections through the extinction of bivalves and conodonts, as well as dwarfed bivalve and ichnofaunal assemblages (Wignall & Atkinson, 2020 ; Fox et al., 2022; Bond et al. 2022a). Pulsed redox changes during the Triassic–Jurassic transition were also suggested by Bond et al., (2022b). A widespread pulse of photic zone euxinia in the early Jurassic has been inferred from the basal strata deposited in the Jurassic Central European Basin by Richoz et al., (2012). However, following this pulse of photic zone euxinia, sulfidic conditions on the Tethyan shelf are

generally localised to the Bristol Channel Basin (Jaraula et al., 2013; Fox et al., 2020; He et al., 2022). Therefore, sedimentary porewater de-oxygenation was more widely distributed than euxinic conditions on the Tethyan shelf during the basal Jurassic.

7. Pulsed suboxia as a driver of benthic marine extinctions during the ETME

Euxinic water column conditions were spatially constrained on the Tethyan shelf during the TJB. Meanwhile the de-oxygenation of sedimentary porewaters and bottom waters was widely distributed throughout the Tethyan shelf during the Triassic–Jurassic boundary interval and directly coincided with the three main pulses of the ETME [Fig. 10]. These three main ETME pulses are further evidenced in the form of benthic extinctions across a handful of the study sites [Fig. 10]. Despite dinoflagellates, which spend most of their lives as planktonic organisms, also being affected, this may be due to dinoflagellates having a benthic resting stage during their life cycle (Bravo & Figueroa, 2014). Therefore, significant disappearances amongst dinoflagellates may not be solely associated with Early Jurassic sulfidic conditions, as previously suggested by Richoz et al., (2012), but also with the widespread de-oxygenation of Tethyan, Triassic–Jurassic, bottom water environments. As nonflagellated, benthic resting cysts were pressured by widespread benthic de-oxygenation, planktonic, flagellated forms were affected by localised anoxic and euxinic conditions resulting in significant extinctions amongst dinoflagellates.

The widespread de-oxygenation of Tethyan sedimentary porewater and bottom water environments may be further evidenced through significant extinctions amongst benthic marine organisms on the Tethyan shelf, or organisms which exhibit a non-motile, benthic phase during their life cycle (i.e. dinoflagellates). Benthic de-oxygenation during the deposition of the uppermost Westbury Formation directly coincided with the

extinction of marine bivalves from across the British Isles and disappearances amongst marine ichnofauna (Mander et al., 2008; Wignall & Atkinson, 2020; Bond et al., 2022a) [Fig. 10]. Sedimentary porewater de-oxygenation, alongside the expansion of sulfate reduction zone into the water column, during the deposition of the mid to upper Cotham member coincided with global bivalve extinctions, particularly amongst infaunal species, as well as reductions in bivalve size, and reduced and/or dwarfed bioturbation (Simms & Jeram, 2007; Todaro et al., 2018; Mette et al., 2019; Atkinson & Wignall, 2020; Wignall & Atkinson, 2020; Opazo & Page, 2021). Marine de-oxygenation during the deposition of the mid-upper Cotham member also coincided with brachiopod extinctions at the GSSP, low foraminiferan and echinoid diversity regionally, and regional dinoflagellate extinctions (Hilledbrandt et al., 2013; Wignall & Atkinson, 2020; Boomer et al., 2021) [Fig. 10]. Pulsed sediment de-oxygenation, as well as some expansion of the oxygen-minimum zone into the water column, throughout the Triassi—Jurassic transition coincided with localised bivalve extinctions, bivalve size reduction, reduced depth, diameter, and diversity of ichnotaxa, the extinction of conodonts across the British Isles and the extinction of bivalves, sponges and corals within Italian TJB sections (Barras & Twitchett, 2007; Ruhl et al., 2011; Richoz et al., 2012; Mander et al., 2008; Todaro et al., 2018; Atkinson & Wignall, 2020; Wignall & Atkinson, 2020; Bond et al., 2022a) [Fig. 10]. The widespread de-oxygenation of sedimentary porewaters, as well as expansion of oxygen-poor conditions into the water column, will have therefore been a key driving factor in the extinction of organisms that lived exclusively or for a duration on the Tethyan benthos. Meanwhile the localised development of sulfidic water column conditions may have played a more significant role in the extinction of exclusively planktonic and nektonic marine organisms.

8. Conclusion

Sulfidic water column conditions are commonly regarded as being prominent within marginal marine environments during the TJB, as well as being a significant driver of marine extinctions during the ETME. However, recent studies report that marine redox changes were restricted to sedimentary porewaters and marine bottom waters with sulfidic conditions being relatively localised. Through compiling both new and existing elemental redox data from five different Tethyan, Triassic–Jurassic sites we identify that pulsed, sedimentary porewater and bottom water de-oxygenation was present within at least five different basins across the Tethyan shelf during the ETME. Despite these basins being geographically localised, there is no evidence for redox changes being correlated to localised environmental controls (e.g., hydrography, detrital input, cyclical sea level changes). Therefore, pulsed sedimentary porewater and bottom water de-oxygenation was likely widespread on the Tethyan shelf during the Triassic–Jurassic boundary interval. Widespread pulses of sedimentary porewater and bottom water de-oxygenation were particularly observed during the deposition of the upper Westbury Formation, the mid–upper Cotham member and the Triassic–Jurassic transition as well as stratigraphically equivalent horizons from other sites. Meanwhile, euxinic water column conditions during the same time intervals were relatively limited. Pulses of widespread sedimentary porewater and bottom water de-oxygenation on the Tethyan shelf directly coincided with the three main pulses of the ETME which were largely dominated by the widespread extinction of benthic marine organisms, or planktonic organisms with a non-motile, benthic resting stage. Therefore, we propose that widespread benthic de-oxygenation likely played a significant role in the extinction of marine organisms on the Tethyan shelf with the more localised development of water column euxinia having contributed to extinctions amongst exclusively planktonic and nektonic marine organisms.

Declaration of Competing Interest

The authors declare that they have no competing financial or personal relationships that could have appeared to influence the work reported in this paper

Acknowledgements

This work was funded by a NERC DTP PhD Studentship awarded to ADB (NE/L002485/1). We would like to thank Nathalie Grassineau and Phil Holdship for assisting with ICP-MS measurements.

References

- ALROY, J. 2014. Accurate and precise estimates of origination and extinction rates. *Paleobiology*, **40** (3), 374–397.
- ATKINSON, J. W. & Wignall, P. B. 2020. Body size trends and recovery amongst bivalves following the end-Triassic mass extinction, *Palaeogeography, Palaeoclimatology, Palaeoecology*, **538**, 109453.
- BARRAS, C. G. & Twitchett, R. J. 2007. Response of marine infauna to Triassic-Jurassic environmental change: Ichnological data from southern England. *Palaeogeography, Palaeoclimatology, Palaeoecology*, **244**, 223–241.
- BEITH, S. J., Fox, C. P., Marshall, J. E. A. & Whiteside, J. H., 2021. Recurring photic zone euxinia in the northwest Tethys impinged end-Triassic extinction recovery. *Palaeogeography, Palaeoclimatology, Palaeoecology*, **584**, 110680.
- BLACKBURN, T. J., Olsen, P. E., Bowring, S. A., McLean, N. M., Kent, D. V., Puffer J., McHone, G., Rasbury, E. T. & Et-Touhami, M. 2013. Zircon U-Pb geochronology links the end-Triassic extinction with the Central Atlantic Magmatic Province. *Science*, **340** (6135), 941–945.
- BLUMENBERG, M., Heunisch, C., Lückge, A., Scheeder, G. & Wiese, F., 2016. Photic zone euxinia in the central Rhaetian Sea prior the Triassic-Jurassic boundary. *Palaeogeography, Palaeoclimatology, Palaeoecology*, **461**, 55–64.
- BOOMER, I., Copestake, P., Raine, R., Azmi, A., Fenton, J. P. G., Page, K. N. & O’Callaghan, M., 2021. Stratigraphy, palaeoenvironments and geochemistry across the Triassic–Jurassic boundary transition at Carnduff, County Antrim, Northern Ireland. *Proceedings of the Geological Association*, **132** (6), 667–687.

- BOND, A. D., Dickson, A. J., Ruhl, M. & Raine, R. 2022. Marine redox change and extinction in Triassic–Jurassic boundary strata from the Larne Basin, Northern Ireland, *Palaeogeography, Palaeoclimatology, Palaeoecology*, **598**, 111018.
- BOND, A. D., Dickson, A. J., Ruhl, M., Bos, R. & Schoutbrugg, B. V. D. 2022b. An oxygenated global ocean during the end-Triassic mass extinction event. <https://doi.org/10.21203/rs.3.rs-1684412/v1>.
- BOND, A. D., Dickson, A. J., Kovács, E. B., Pálffy, J. & Ruhl, M. 2022c. Global ocean de-oxygenation preceded end-Triassic marine mass extinction.
- BRAVO, I. & Figueroa, R. I. 2014. Towards an ecological understanding of dinoflagellate cyst functions. *Microorganisms*, **2**, 11–32.
- CALVERT, S. E. & Pedersen, T. F. 1993. Geochemistry of Recent oxic and anoxic marine sediments: Implications for the geological record. *Marine Geology*, **13**, 67–88.
- CALVERT, S. E. & Pedersen, T. F. 2007. Chapter Fourteen: Elemental proxies for palaeoclimatic and palaeogeographic variability in marine sediments: interpretation and application in *Developments in Marine Geology*, vol. 1. Elsevier, p. 567–644.
- CARTER, E. & Hori, R. 2005. Global correlation of the radiolarian faunal change across the Triassic–Jurassic boundary. *Canadian Journal of Earth Sciences*, **42**, 777–790.
- DAVIES, J. H. F. L., Marzoli, A., Bertrand H., Youbi, N., Ernesto, M., & Schaltegger, U. 2017. End-Triassic mass extinction started by intrusive CAMP activity. *Nature Communications*, **8**, 15596.
- DU, Y., Chiari, M., Viktor, K., Nicora, A., Onoue, T., Pálffy, J., Roghi, G., Tomimatsu, Y. & Rigo, M. 2020. The asynchronous disappearance of conodonts: New constraints from Triassic–Jurassic boundary sections in the Tethys and Panthalassa. *Earth-Science Reviews*, **203**, 1–18.
- DUNHILL, A. M., Foster, W. J., Sciberras, J. & Twitchett, R. J. 2018. Impact of the late Triassic mass extinction on functional diversity and composition of marine ecosystems. *Palaeontology*, **61**, 133–148.
- ERICKSON, B. E. & Helz, G. R., 2000. Molybdenum (VI) Speciation in Sulfidic Waters: Stability and Lability of Thiomolybdates. *Geochimica et Cosmochimica Acta*, **64**, 1149–1158.
- FLÜGEL, E. & Kiessling, W. 2002. Patterns of Phanerozoic Reef Crises. *SEPM Special Publication*, **72**, 691–733.
- FOX, C. P., Whiteside, J. H., Olsen, P. E., Cui, Xingqian, Summons, R. E., Idiz, E. & Grice, K., 2022. Two-pronged killing mechanism at the end-Triassic mass extinction. *Geology*, **50** (4), 448–453.

- GREENE, S. E., Martindale, R. C., Ritterbush, K. A., Bottjer, D. J., Corsetti, F. A. & Berelson, W. M. 2012. Recognising ocean acidification in deep time: An evaluation of the evidence for acidification across the Triassic-Jurassic boundary. *Earth-Science Reviews*, **113** (1–2), 72–93.
- GUEX, J., Bartolini, A., Atudorei, V. & Taylor, D. 2004. High-resolution ammonite and carbon isotope stratigraphy across the Triassic–Jurassic boundary at New York Canyon (Nevada). *Earth and Planetary Science Letters*, **225**, 29–41.
- HALLAM, A. 1981. THE END-TRIASSIC BIVALVE EXTINCTION EVENT. *Palaeogeography, Palaeoclimatology, Palaeoecology*, **35**, 211–225.
- HAUTMANN, M., Benton, M. J. & Tomašových, A. 2008. Catastrophic ocean acidification at the Triassic–Jurassic boundary. *Neues Jahrbuch für Geologie und Palaöntologie Abhandlungen*, **249**, 119–127
- HAUTMANN, M. 2012. Extinction: end-Triassic mass extinction in eLS. John Wiley & Sons Ltd: Chichester. <https://doi.org/10.1002/9780470015902.a0001655.pub3>
- HE, T., Dal Corso, J., Newton, R. J., Wignall, P. B., Mills, B. J. W., Todaro, S. Di Stefano, P., Turner, E. C., Jamieson, R. A. Randazzo, V., Rigo, M., Jones, R. E. & Dunhill, A. M., 2020. An enormous sulfur isotope excursion indicates marine anoxia during the end-Triassic. *Science Advances*, **6** (37), eabb6704, 10.1126/sciadv.abb6704.
- HE. T., Wignall, P. B., Newton, R. J., Atkinson, J. W., Keeling, J. F. J., Xiong, Y. & Poulton, S. W., 2022. Extensive marine anoxia in the European epicontinental sea during the end-Triassic mass extinction. *Global and Planetary Change*, **210**, 103771, <https://doi.org/10.1016/j.gloplacha.2022.103771>.
- HELZ, G. R. Miller, C. V. Charnock, J. M., Mosselmans, J. F. W., Patrick, R. A. D., Garner, C. D. & Vaughan, D. J., 1996. Mechanism of molybdenum removal from the sea and its connections in black shales: EXAFS evidence. *Geochimica et Cosmochimica Acta*, **60** (19), 3631–3642.
- HESSELBO, S. P., Robinson, S. A., Surlyk, F. & Piasecki, S. 2002. Terrestrial and marine mass extinction at the Triassic/Jurassic boundary synchronized with initiation of massive volcanism. *Geology*, **30** (3), 251–254.
- HILLEBRANDT, A. v., Krystyn, L., Kürschner, W. M., Bonis, N. R., Ruhl, M., Richoz, S., Schobben, M. A. N., Urlichs, M., Bown, P. R., Kment, K., McRoberts, C. A., Simms, M. & Tomášových, A. 2013. The Global Stratotype Sections and Point (GSSP) for the base of the Jurassic System at Kuhjoch (Karwendel Mountains, Northern Calcareous Alps, Tyrol, Austria). *Episodes*, **36** (3), 162–198.
- JARAULA, C. M. B., Grice, K., Twitchett, R. J., Böttcher, M. E., LeMetayer, P., Dastidar, A. G. & Opazo, L. F., 2013. Elevated $p\text{CO}_2$ leading to Late Triassic extinction, persistent photic zone euxinia, and rising sea levels. *Geology*, **41** (9), 955–958.
- JOST, A. B., Bachan, A., van de Schootbrugge, B., Brown, S. T., DePaolo, D. J. &

- Payne, J. L., 2017a. Additive effects of acidification and mineralogy on calcium isotopes in Triassic/Jurassic boundary limestones. *Geochemistry, Geophysics, Geosystems*, **18** (1), 113–124.
- JOST, A. B., Bachan, A., van de Schootbrugge, B., Lau, K. V., Weaver, K. L., Maher, K. & Payne, J. L., 2017b. Uranium isotope evidence for an expansion of marine anoxia during the end-Triassic extinction. *Geochemistry, Geophysics, Geosystems*, **18** (8), 3093–3108.
- KIESSLING, W., Aberhan, M., Brenneis, B. & Wagner, P. J. 2007. Extinction trajectories of benthic organisms across the Triassic-Jurassic boundary. *Palaeogeography, Palaeoclimatology, Palaeoecology*, **244** (1–4), 201–222.
- KOVÁCS, E. B., Ruhl, M., Demény, A., Fórizs, I., Hegyi, I., Horváth-Kostva, Z. R., Móricz, F., Vallner, Z. & Pálffy, J. 2020. Mercury anomalies and carbon isotope excursions in the western Tethyan Csövár section support the link between CAMP volcanism and the end-Triassic extinction. *Global and Planetary Change*, **194**, 103291.
- LABORDE-CASADABAN, M., Homberg, C., Schnyder, J., Borderie, S. & Raine, R., 2021. Do soft sediment deformations in the Late Triassic and Early Jurassic of the UK record seismic activity during the break-up of Pangaea? *Proceedings of the Geological Association*, 132, 688–701.
- LINDSTRÖM, S., Pederson, G. K., van de Schootbrugge, B., Hansen, K. H., Kuhlmann, N., Thein, J., Johansson, L., Petersen, H. I., Alwmark, C., Dybkjær, K., Weibel, R., Erlström, M., Nielsen, H. N. Oschmann, W. & Tegner, C. 2015. Intense and widespread seismicity during the end-Triassic mass extinction due to emplacement of a large igneous province. *Geology*, **43**(5), 387–390.
- LINDSTRÖM, S., van de Schootbrugge, B., Hansen, K. H., Pedersen, G. K., Alsen, P., Thibault, N., Dybkjær, K., Bjerrum, C. J. & Nielsen, L. H. 2017. A new correlation of Triassic–Jurassic boundary successions in NW Europe, Nevada and Peru, and the Central Atlantic Magmatic province: A time-line for the end-Triassic mass extinction. *Palaeogeography, Palaeoclimatology, Palaeoecology*, **478**, 80–102.
- MANDER, L., Twitchett, R. J. & Benton, M. J., 2008. Palaeology of the Late Triassic extinction event in the SW UK. *Journal of the Geological Society*, **165**, 319–332.
- MARZOLI, A., Callegaro, S., Dal Corso, J., Davies, J. H. F. L., Massimo, C., Youbi, N., Bertrand, H., Resiberg, L., Merle, R. & Jourdan, F. 2018. The Central Atlantic Magmatic Province (CAMP): A Review. In: Tanner, L. (eds) *The Late Triassic World. Topics in Geobiology*, vol 46. Springer, Cham. https://doi.org/10.1007/978-3-319-68009-5_4.
- McLAREN, D. J., & Goodfellow, W. D. 1990. Geological and biological consequences of giant impacts. *Annual Review of Earth and Planetary Sciences*, **18**, 123–171.
- METTE, W., Clemence, M.-E., Thibault, N., Jore, C., Konrad, B. & Ullmann, C. V. 2019. Sedimentology, carbon isotope stratigraphy and micropalaeontology of the

- Rhaetian Zlambach Formation–Implications for the Dachstein carbonate platform development (Northern Calcareous Alps, Austria), *Sedimentary Geology*, **382**, 47–60.
- NESBITT, H. W. & Young, G. M. 1982. Early Proterozoic climates and plate motions inferred from major element chemistry of lutites, *Nature*, **299**, 715–717.
- OLSEN, P. E., Kent, D. V., Sues, H.-D., Koeberl, C., Huber, H., Montanari, A., Rainforth, E. C., Fowell, S. J., Szajna, M. J. & Hartline, B. W. 2002. Ascent of dinosaurs linked to an iridium anomaly at the Triassic-Jurassic boundary. *Science*, **296** (5571), 1305–1307.
- ONOUÉ, T., Sato, H., Yamashita, D., Ikehara, M., Yasukawa, K., Fujinaga, K., Kato, Y. & Matsuoka, A. 2016. Bolide impact triggered the Late Triassic extinction event in equatorial Panthalassa. *Scientific reports*, **6**, 29609.
- OPAZO, L. F. & Page, K. N., 2021. Palaeoecological patterns of change in marine invertebrate faunas across the End-Triassic mass extinction event: Evidence from Larne, Northern Ireland. *Proceedings of the Geological Association*, **132** (6), 726–742.
- ORTH, C. J. 1989. Geochemistry of the bio-event horizons. In S. K. Donovan (Ed.), *Mass Extinctions: Processes and Evidence*. Belhaven Press, London. pp. 37–72.
- PIPER, D. Z. & Calvert, S. E., 2009. A marine biogeochemical perspective on black shale deposition. *Earth-Science Reviews*, **95**, 63–96.
- PRUYERS, P. A., de Lange, G. J., Middelburg, J. J. & Hydes, D. J., 1993. The diagenetic formation of metal-rich layers in sapropel-containing sediments in eastern Mediterranean. *Geochimica et Cosmochimica Acta*, **57**, 527–536.
- RAUP, M. & Sepkoski, J. J. 1982. Mass Extinctions in the Marine Fossil Record. *Science*, **215** (4539), 1501–1503.
- RICHOZ, S., van de Schootbrugge, B., Pross, J., Püttmann, W., Quan, T. M., Lindström, S., Heunisch, C., Fiebig, J., Maquil, R., Schouten, S., Hauzenberger, C. A. & Wignall, P. B. 2012. Hydrogen sulphide poisoning of shallow seas following the end-Triassic extinction. *Nature Geoscience*, **5** (9), 662–667.
- RIGO, M., Mazza, M., Karádi, V. & Nicora, A. 2018. New Upper Triassic Conodont Biozonation of the Tethyan Realm In Tanner, L. H. (Ed.) *The Late Triassic World: Earth in a Time of Transition*, *Topics in Geobiology* 46, Springer. 186–236.
- Rudnick, R. L. & Gao, S., 2003. The Composition of the Continental Crust. In: Holland, H. D. and Turekian, K.K., Eds., *Treatise on Geochemistry*, Vol. 3, The Crust, Elsevier-Pergamon, Oxford, 1–64.
- RUHL, M., Bonis, N. R., Reichart, G. J., Damste, J. S. S. & Kurschner, W. M. 2011. Atmospheric carbon injection linked to end-Triassic mass extinction. *Science*, **333** (6041), 430–434.

- SCHOENE, B., Guex, J., Bartolini, A., Schaltegger, U. & Blackburn, T. J. 2010. Correlating the end-Triassic mass extinction and flood basalt volcanism at the 100 ka level. *Geology*, **38** (5), 387–390.
- SCOTT, C & Lyons, T. W., 2012. Contrasting molybdenum cycling and isotopic properties in euxinic versus non-euxinic sediments and sedimentary rocks: Refining the paleoproxies. *Chemical Geology*, **324–325**, 19–27.
- SHIMMIELD, G. B. & Price, N. B., 1986. The behaviour of molybdenum and manganese during early sediment diagenesis—offshore Baja California, Mexico. *Marine Chemistry*, **19**, 261–280.
- SIMMS, M. J. 2003. Uniquely extensive seismite from the latest Triassic of the United Kingdom: Evidence for bolide impact? *Geology*, **31**(6), 557–560.
- SIMMS, M. J. & Jeram, A. J., 2007. Waterloo Bay, Larne, Northern Ireland: a candidate Global Stratotype Section and Point for the base of the Hettangian Stage and Jurassic System. *ISJS Newsletter*, **34** (1), 50–68.
- SWEERE, T., van den Boorn, S., Dickson, A. J. & Reichart, G.-J., 2016. Definition of new trace-metal proxies for the controls on organic matter enrichment in marine sediments based on Mn, Co, Mo and Cd concentrations. *Chemical Geology*, **441**, 235–245.
- TANNER, L. & Kyte, F. T. 2005. Anomalous iridium enrichment at the Triassic–Jurassic boundary, Blomidon Formation, Fundy basin, Canada. *Earth and Planetary Science Letters*, **240**, 634–641.
- TANNER, L. H., Kyte, F. T., Richoz, S. & Krystyn, L. 2016. Distribution of iridium and associated geochemistry across the Triassic–Jurassic boundary in sections at Kuhjoch and Kendlbach, Northern Calcareous Alps, Austria. *Palaeogeography, Palaeoclimatology, Palaeoecology* **449**, 13–26.
- TODARO, S., Rigo, M., Randazzo, V. & Di Stefano, P. 2018. The end-Triassic mass extinction: A new correlation between extinction events and $\delta^{13}\text{C}$ fluctuations from a Triassic–Jurassic peritidal succession in western Sicily. *Sedimentary Geology*, **368**, 105–113.
- TRIBOVILLARD, N., Algeo T. J., Lyons, T. & Riboulleau, A., 2006. Trace metals as paleoredox and paleoproductivity proxies: An update. *Chemical Geology*, **232**, 12–32.
- VAN DE SCHOOTBRUGGE, B., Tremolada, F., Rosenthal, Y., Bailey, T. R., Feist-Burkhardt, S., Brinkhuis, H., Kent, D. V. & Falkowski, P. G. 2007. End-Triassic calcification crisis and blooms of organic-walled ‘disaster species’. *Palaeogeography, Palaeoclimatology, Palaeoecology*, **244**, 126–141.
- VAN DE SCHOOTBRUGGE, B., Richoz, S., Pross, J., Luppold, F. W., Hunze, S., Wonik, T., Blau, J., Meister, C., van der Weijst, C. M. H., Suan, G., Fraguas, A., Fiebig, J., Herrie, J. O., Guex, J., Little, C. T. S., Wignall, P. B., Püttmann, W. & Oschmann, W. 2019. The Schandelah Scientific Drilling Project: A 25-million year record of Early

Jurassic palaeo-environmental change from northern Germany. *Newsletters of Stratigraphy*, **53** (3), 249–296.

WANG, P., Du, Y., Yu., W., Algeo, T. J., Zhou, Q., Xu, Y., Qi, L., Yuan, L. & Pan, W. 2020. The chemical index of alteration (CIA) as a proxy for climate change during glacial-interglacial transitions in Earth history, *Earth-Science Reviews*, **201**, 103032.

WHITESIDE, J. H. & Ward, P. D. 2011. Ammonoid diversity and disparity track episodes of chaotic carbon cycling during the early Mesozoic. *Geology*, **39** (2), 99–102.

WHITESIDE, J. H., Olsen, P. E., Eglinton, T., Brookfield, M. E., & Sambrotto, R. N., 2010. Compound-specific carbon isotopes from Earth’s largest flood basalt eruptions directly linked to the end-Triassic mass extinction. *Proceedings of the National Academy of Sciences*, **107** (15), 6721–6725.

WIGNALL, P. B. & Atkinson, J. W., 2020. A two-phase end-Triassic mass extinction. *Earth-Science Reviews*, **208**, 103282.

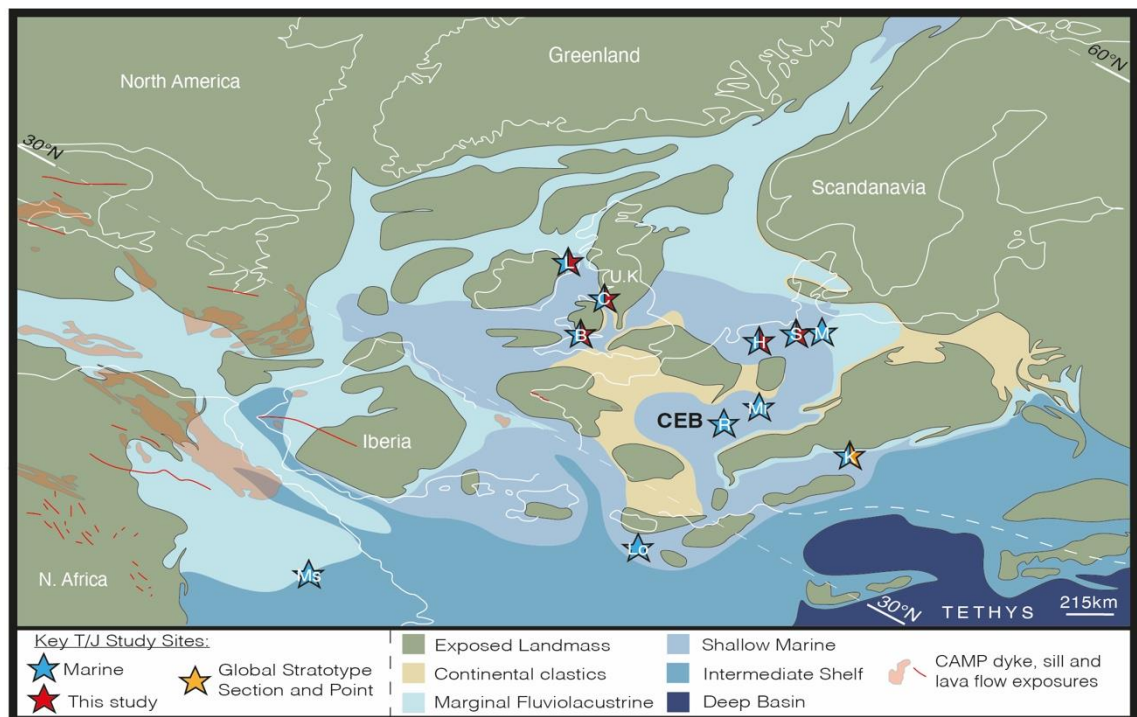


Figure 1:- Triassic–Jurassic palaeogeography of the Tethyan shelf showing key T–J study sites. B- Bristol Channel Basin (UK; St. Audrie’s Bay section; this study), C- Cheshire Basin (UK; Prees-2c core; this study), H- Hebelermeer-2 core (Germany; this study), K- Kuhjoch Section (Austria; GSSP), L- Lerne Basin (UK; Carnduff-2 core; this study), Lo- Lombardy Basin (Italy), M- Marientel-1 core (Germany), Mi- Mingolsheim

core (Germany), Ms- Mount Sparagio Section (Sicily, Italy), R- Rosswinkel core (Luxembourg), S- Schandelah-1 core (Germany; this study). Figure modified from Bond et al., (2022a).

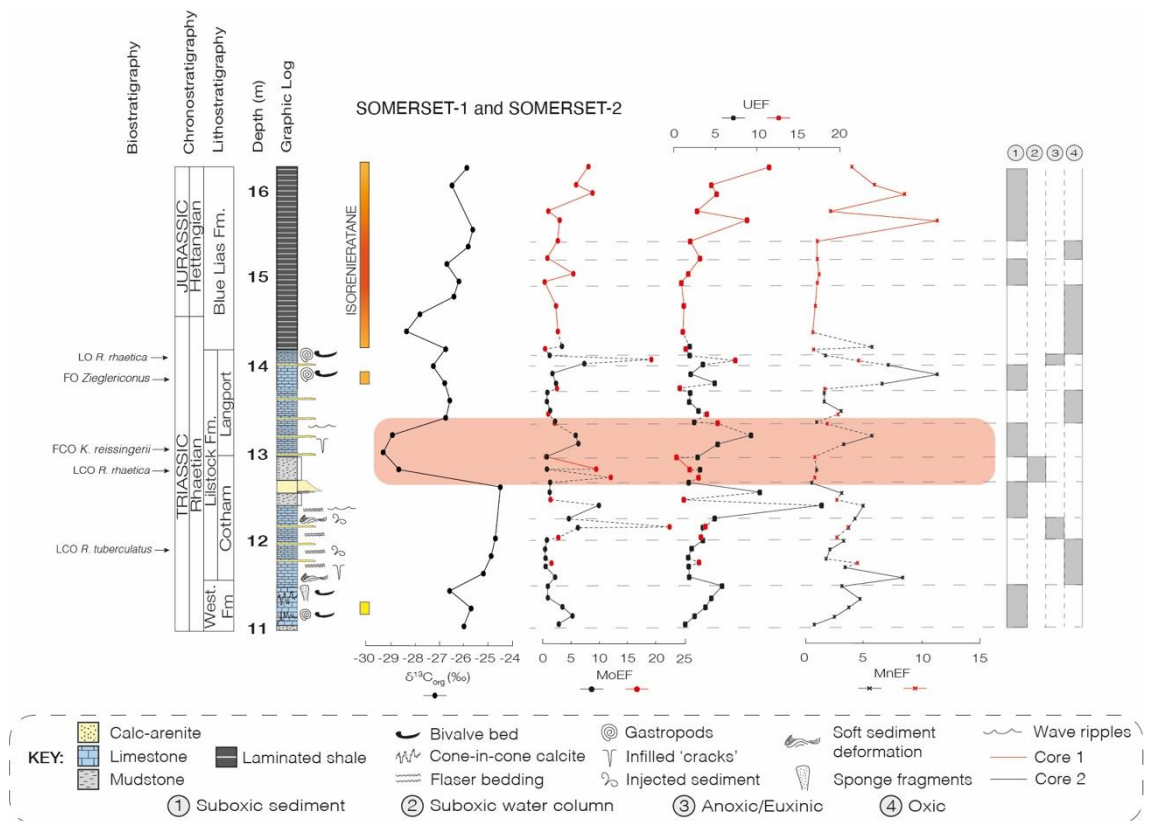


Figure 2:- Elemental marine redox data from the Somerset-1 and Somerset-2 cores, Bristol Channel Basin. Sedimentology from this study (see supplementary information). Core depths correlated to stratigraphic heights from Hesselbo et al., (2002) using carbon isotope stratigraphy. Carbon isotope stratigraphy from Hesselbo et al., (2002). Biostratigraphy extrapolated from Hesselbo et al., (2002). Isorenieratane based on data from Fox et al., (2020). ETME extinction pulses based on Wignall & Atkinson (2020) and Fox et al., (2022). Red band marks the ETME Main Interval as defined by carbon isotope chemostratigraphy.

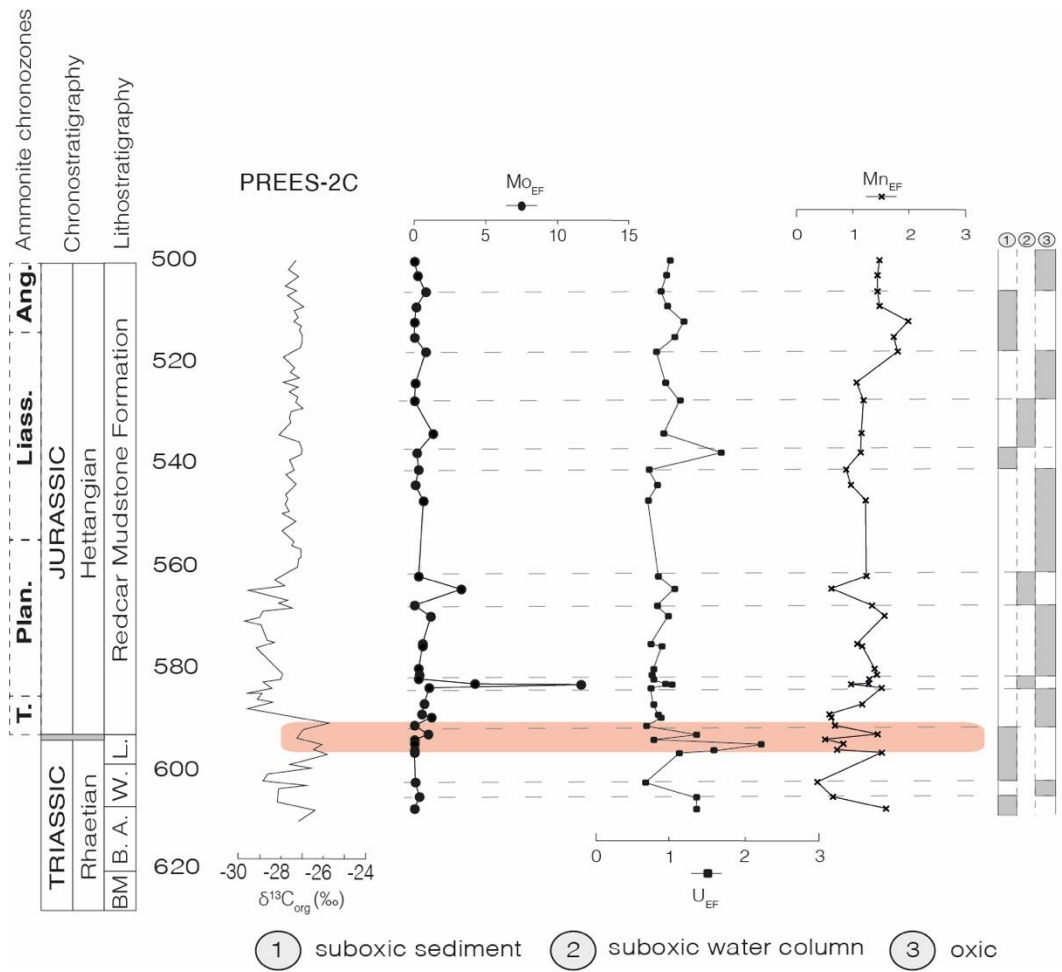


Figure 3:- Elemental marine redox data from the Prees-2c core, Cheshire Basin. Carbon isotope data and stratigraphy from Hesselbo et al., (unpublished). Red band marks the ETME Main Interval as defined by carbon isotope chemostratigraphy. No correlative pulse of extinction has yet been identified from the Prees-2c core section.

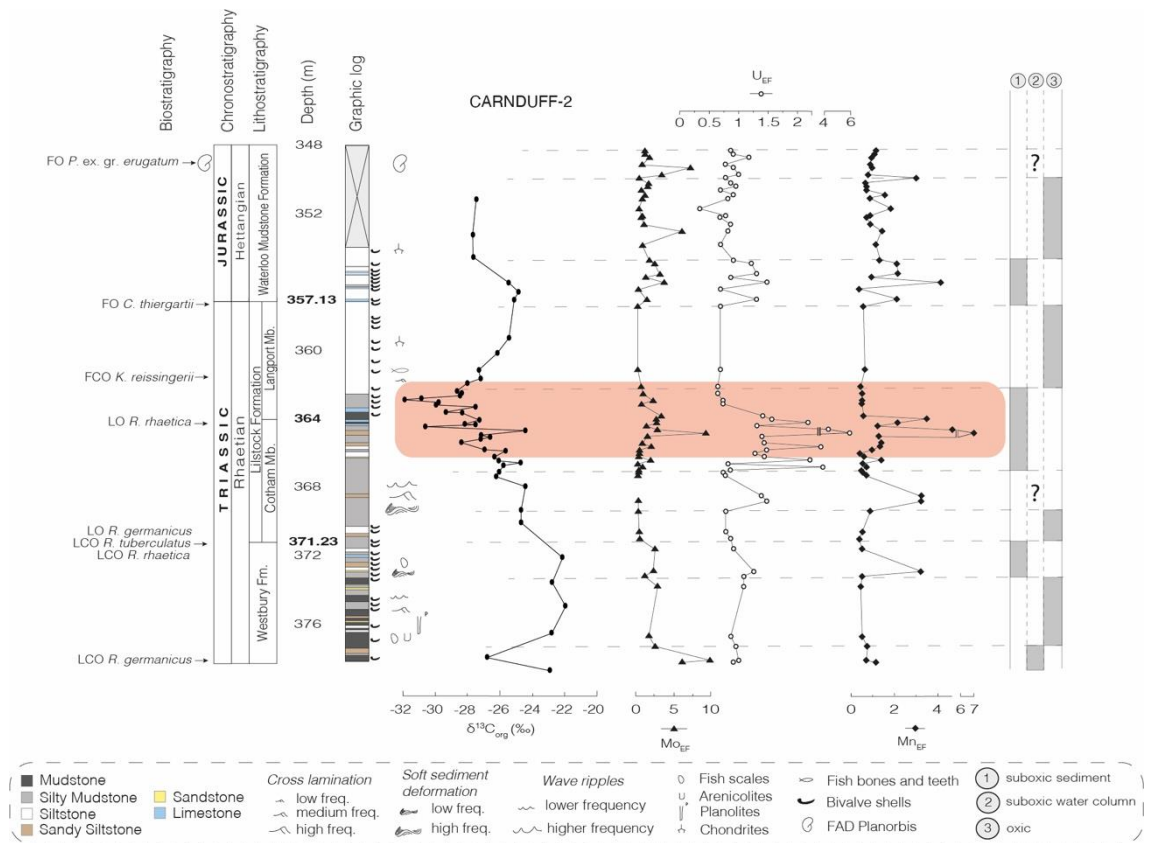


Figure 4:- Elemental marine redox data from the Carnduff-2 core, Larne Basin. Data from Bond et al., (2022a). Figure amended from Bond et al., (2022a), sedimentology and stratigraphy from Boomer et al., (2021). Red band marks the ETME Main Interval as defined by carbon isotope chemostratigraphy.

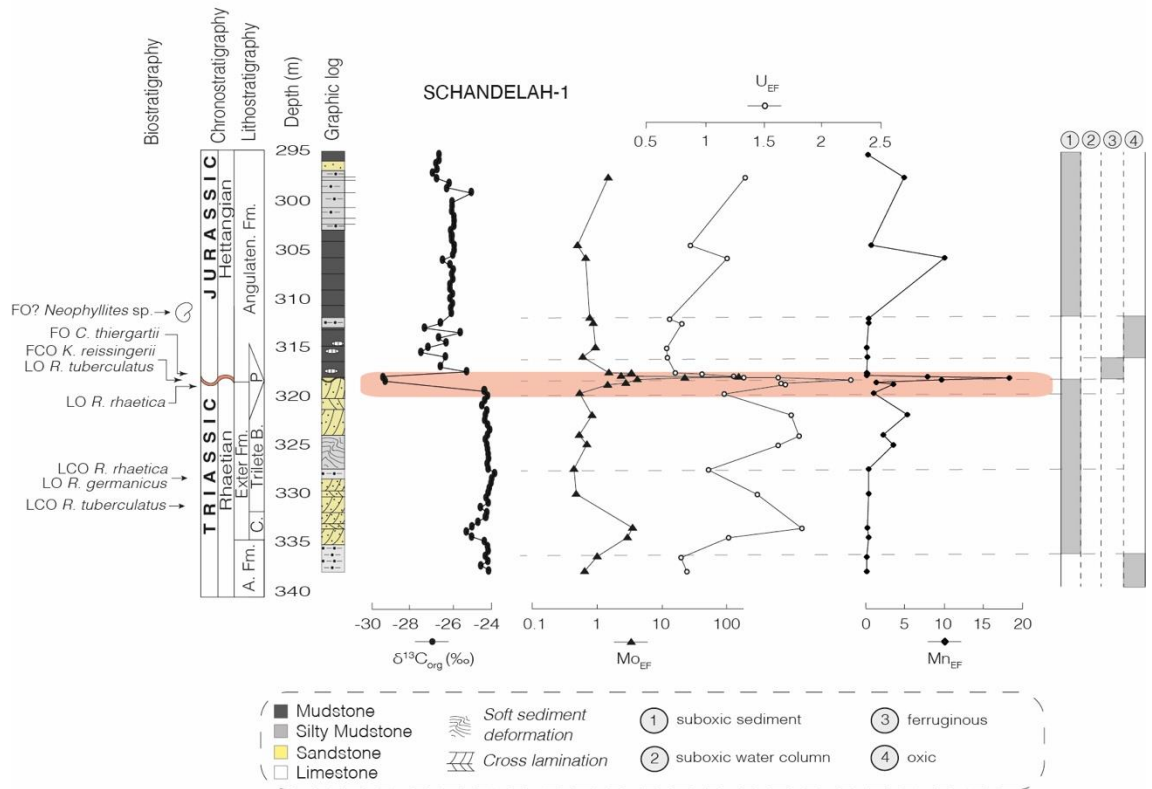


Figure 5:- Elemental marine redox data from the Schandelah-1 core, Lower Saxony Basin. Data from Bond et al., (2022b). Figure amended from Bond et al., (2022b), sedimentology and carbon isotope stratigraphy from van de Schootbrugge et al., (2019), palynostratigraphy from Lindström et al., (2017) and van de Schootbrugge et al., (2019). Red band marks the ETME Main Interval as defined by carbon isotope chemostratigraphy. No correlative pulse of extinction has yet been identified from the Schandelah-1 core section.

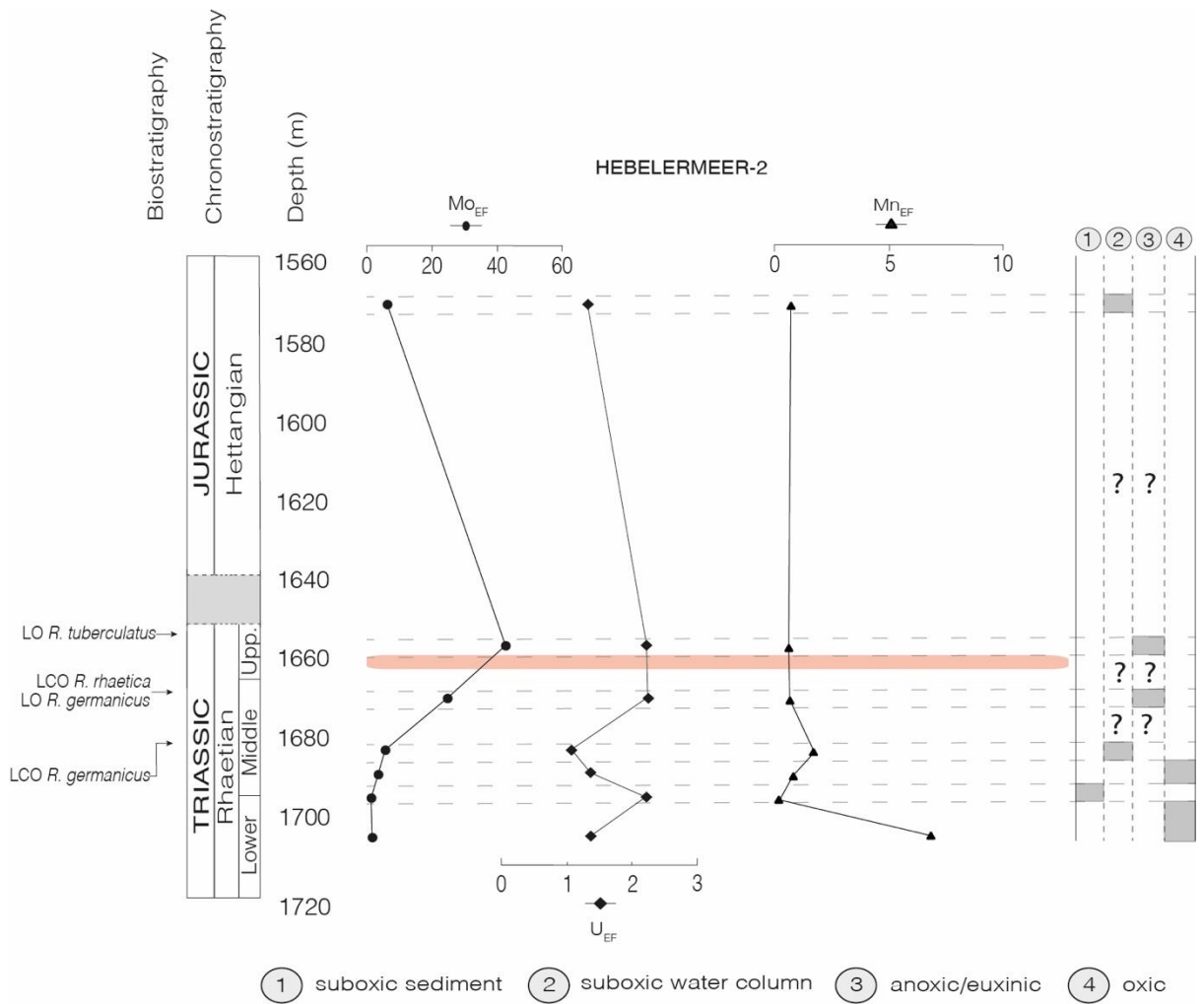


Figure 6:- Elemental marine redox data from the Hebelermeer-2 core, Germanic Basin. Data from Bond et al., (2022b). Figure amended from Bond et al., (2022b), palynostratigraphy from Blumenberg et al., (2016). Red band marks the ETME Main Interval as interpreted through palynostratigraphy. No correlative pulse of extinction has yet been identified from the Hebelermeer-2 core section. However, this may be partly associated with uncertainty in the positioning of the ETME and CIE.

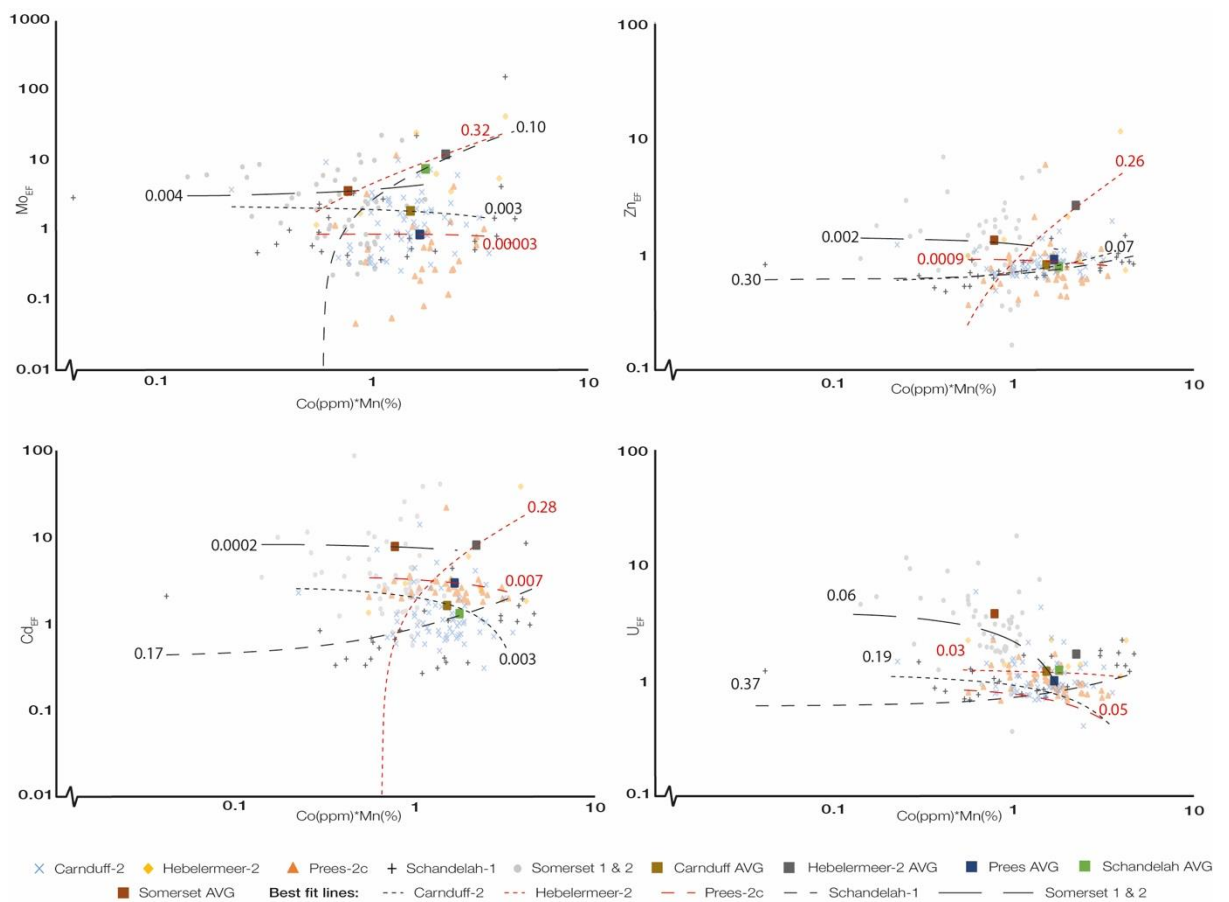


Figure 7:- The correlation between hydrography and marine redox data across the Bristol Channel, Cheshire, Germanic, Larne, and Lower Saxony Basins. Marine redox and hydrography data from the Carnduff-2, Hebelermeer-2, and Schandelah-1 cores from Bond et al., (2022a, 2022b). Lines on charts are best fit lines generated through the excel function “add chart element > trendline > linear”. Numbers next to best fit lines are r^2 values.

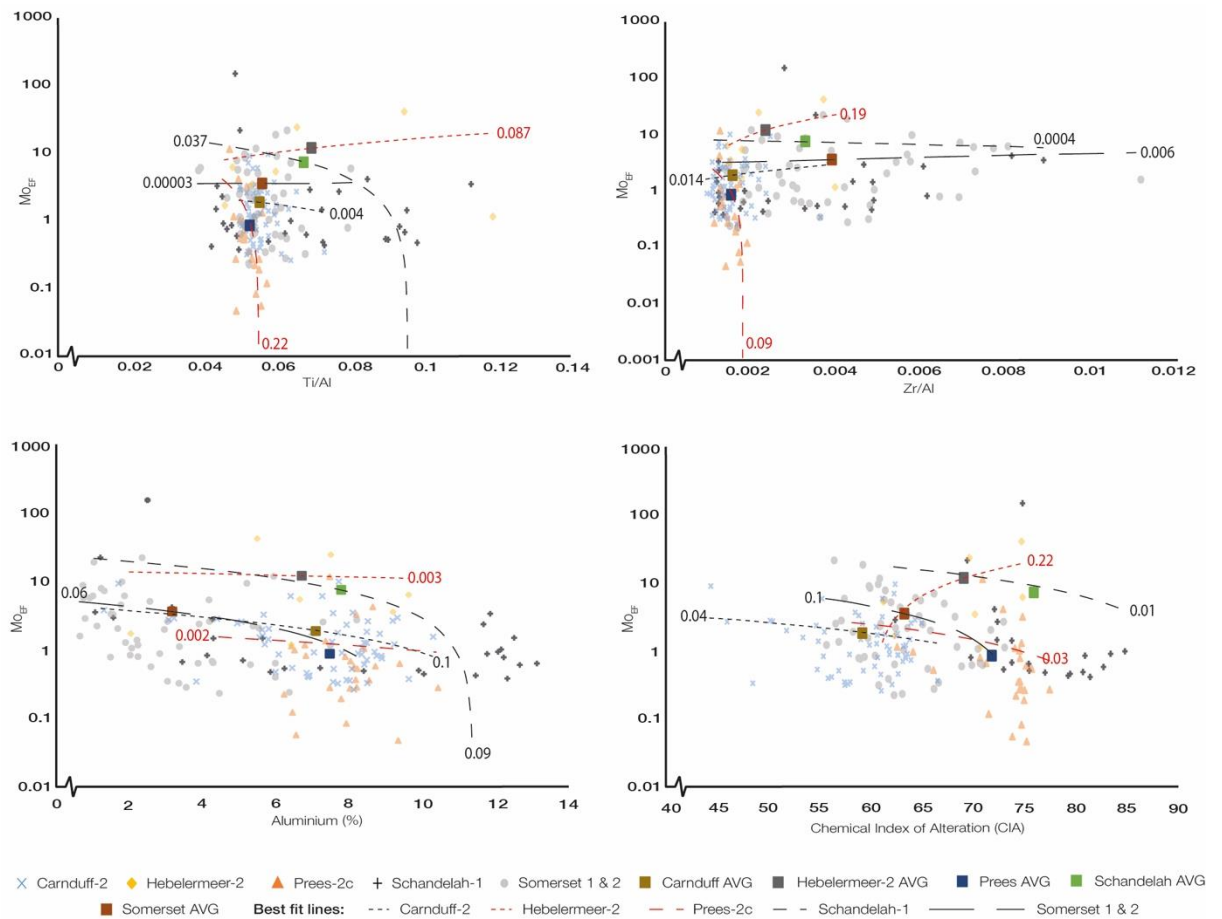


Figure 8:- The correlation between detrital input, grain size, weathering intensity and marine redox data across the Bristol Channel, Cheshire, Germanic, Larne, and Lower Saxony basins. Mo_{EF} , palaeo-weathering, grain size and detrital input data for the Carnduff-2, Hebelmeer-2, and Schandelah-1 cores from Bond et al. (2022a, 2022b). Lines on charts are best fit lines generated through the excel function “add chart element > trendline > linear”. Numbers next to best fit lines are r^2 values.

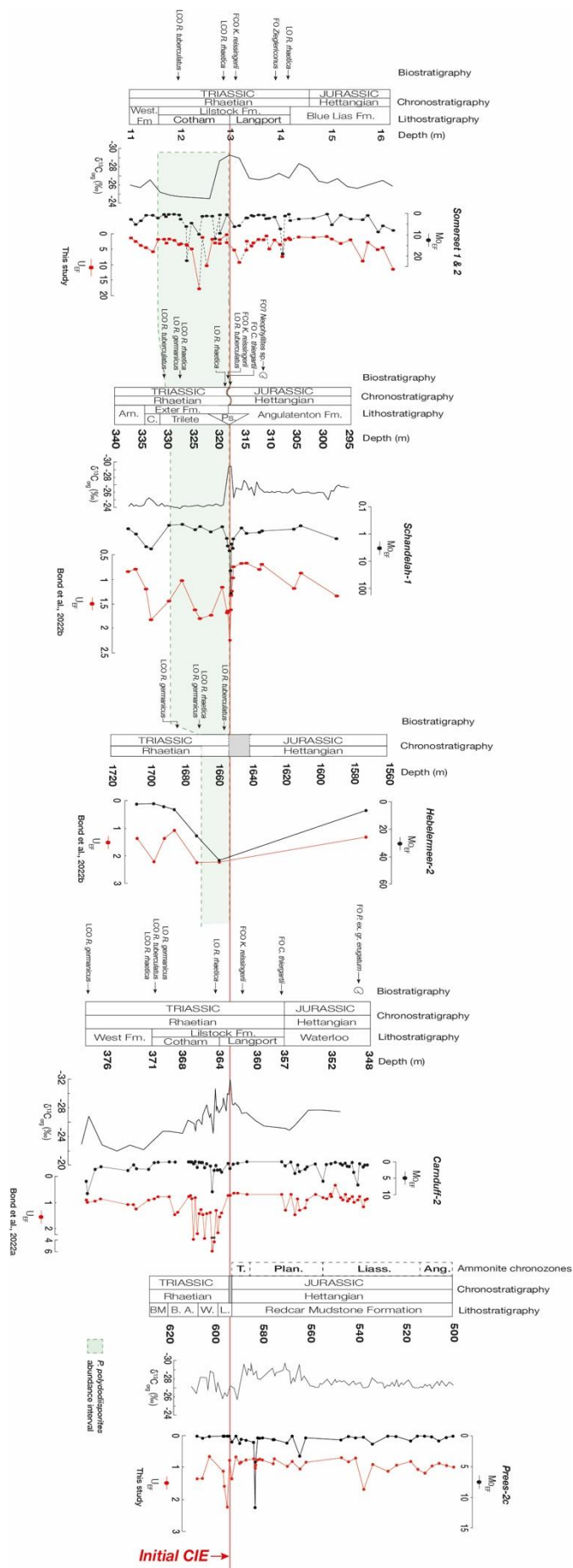


Figure 9:- A regional correlation of elemental marine redox data. Refer to figures 2–6 for stratigraphic sources. *P. polyodontisporites* interval (green, dashed outline) based on Lindström et al., (2017). Sites correlated through carbon isotope chemostratigraphy and palynostratigraphy (see supplementary information)

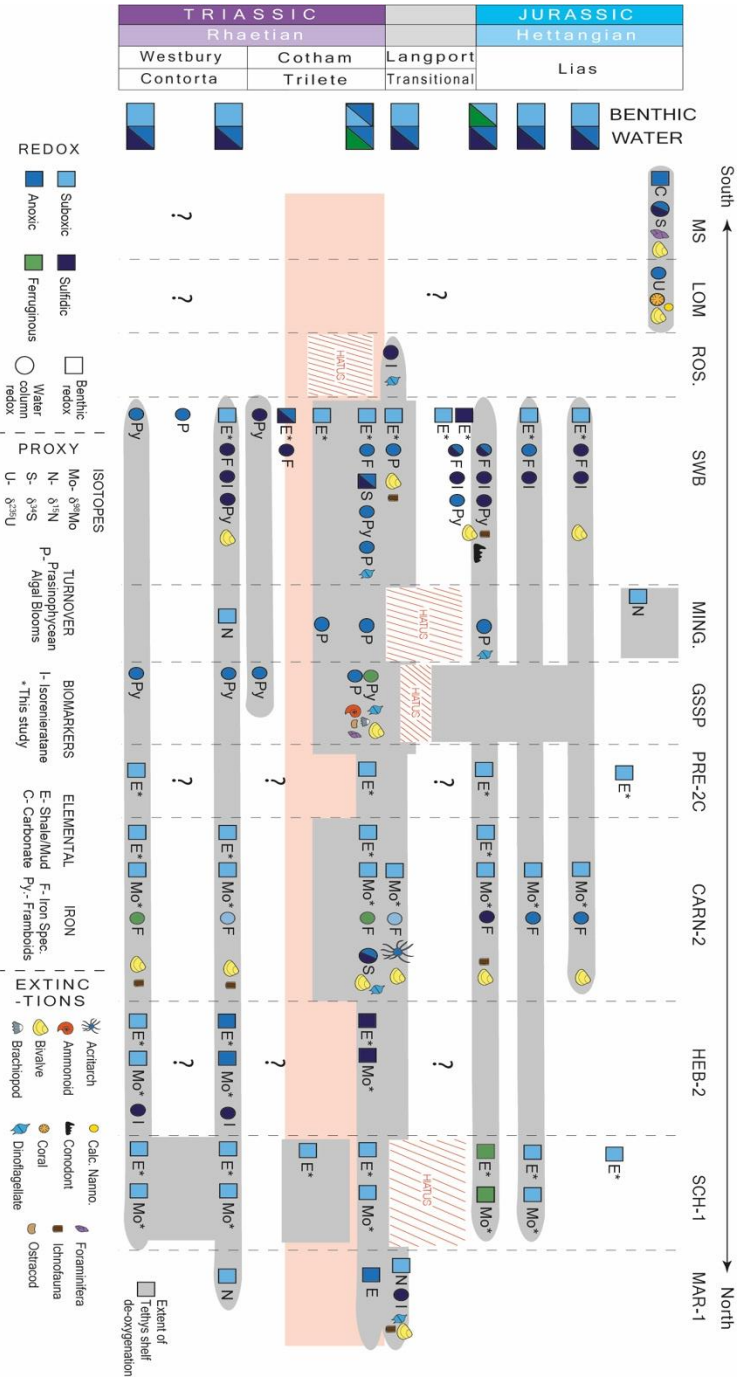


Figure 10:- Coincident pulses of benthic de-oxygenation and the extinction of partly and exclusively benthic marine organisms on the Tethyan shelf. Figure amended from Bond et al., (2022b). Red shaded area- ETME main interval. For further explanation of vertical and horizontal bars, connections and gaps refer to Chapter 7, Figure 3.

Supplementary Information:

t-Test: Two-Sample Assuming Equal Variances	Mo	
	<i>Variable 1</i>	<i>Variable 2</i>
Mean	6.4614976	4.61334393
Variance	315.068806	7.00944642
Observations	82	10
Pooled Variance	284.26287	
Hypothesized Mean Difference	0	
df	90	
t Stat	0.32725857	
P(T<=t) one-tail	0.37211615	
t Critical one-tail	1.66196108	
P(T<=t) two-tail	0.74423229	
t Critical two-tail	1.98667454	

t-Test: Two-Sample Assuming Equal Variances	U	
	<i>Variable 1</i>	<i>Variable 2</i>
Mean	2.66998468	1.23819115
Variance	6.20883706	0.00835829
Observations	106	3
Pooled Variance	6.09294026	
Hypothesized Mean Difference	0	
df	107	
t Stat	0.99075722	
P(T<=t) one-tail	0.16201967	
t Critical one-tail	1.65921931	
P(T<=t) two-tail	0.32403935	
t Critical two-tail	1.98238337	

Figure S1:- T-tests for open marine and restricted trace element enrichment >1. Note that the hypothesised mean different for both Mo and U is 0, and that both Mo and U exceed the alpha value of 0.05, suggesting that hydrography was not a significant controlling factor of Triassic–Jurassic marine redox change

Supplementary Data- Raw data attached as separate excel file ‘Supplementary Information: Chapter 9’

Stratigraphic correlation of T-J sections in chapter 9- Triassic-Jurassic boundary sections from chapter 9 of this thesis have been correlated using a combination of carbon isotope stratigraphy and biostratigraphy (using stratigraphically information dinocyst and palynological occurrences).

The carbon isotope data for the Prees-2c core has yet to be published and was obtained through personal communication with Stephen Hesselbo (30th June 2022). Formal identification of carbon isotope excursions from the Prees-2c core carbon isotope data has not been undertaken, however, the most likely candidates for the ‘initial’, ‘precursor’ and ‘main’ carbon isotope excursions have been identified here through correlating similar shifts in the carbon isotope data from other sections. The negative carbon isotope excursion observed at approximately 593m within the Prees-2c core is interpreted here as the initial CIE, the negative carbon isotope excursion observed at approximately 601m within the Prees-2c core is interpreted here as the precursor CIE, and the carbon isotope excursion observed at approximately 588m within the Prees-2c core is interpreted here as the main CIE. It should be noted that these assignments are only provisional pending more detailed biostratigraphic and chemostratigraphic study of the Prees-2c core material. Should the assignment of carbon isotope excursions change then the timing of marine redox shifts in the region of the Prees-2c core palaeodepositional localities will also have to be re-evaluated. The assignment of carbon isotope excursions for the Schandelah-1, Somerset-1 & 2 and Carnduff-2 core sections

is detailed in the supplementary information of Chapter 7 alongside a critical discussion of the other carbon isotope records correlated within Chapter 9.

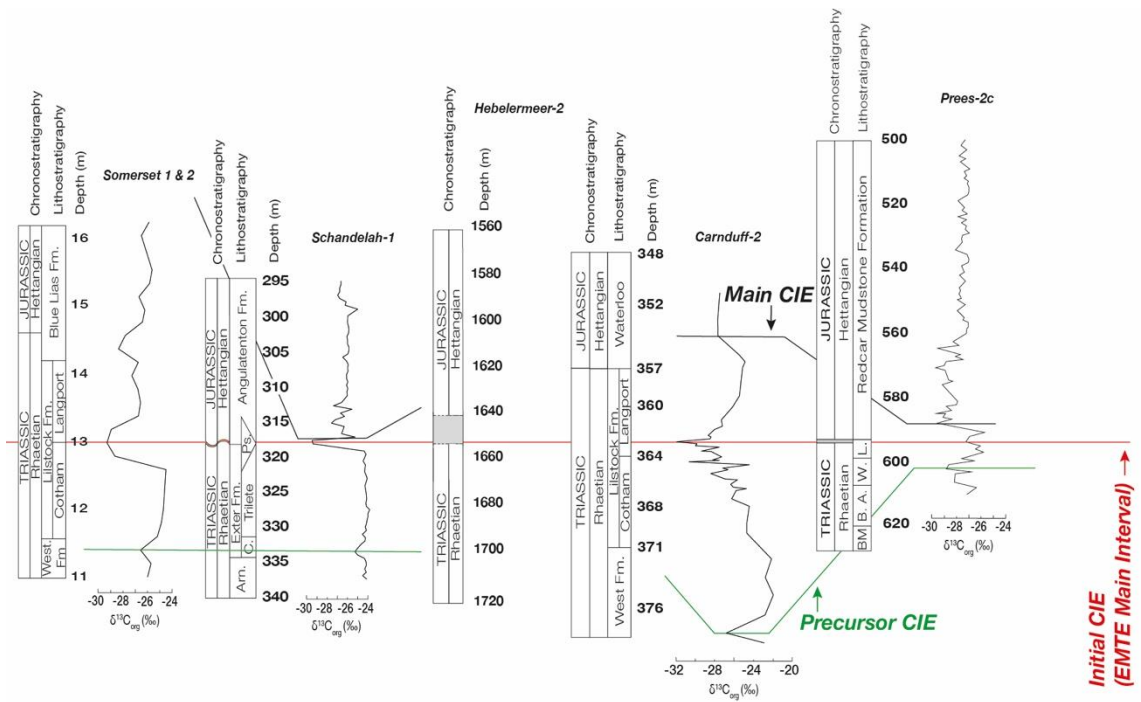


Figure S2:- Stratigraphic correlation of chapter 9 sections through the use of carbon isotope (organic) data. Refer to main figures for explanation of abbreviations.

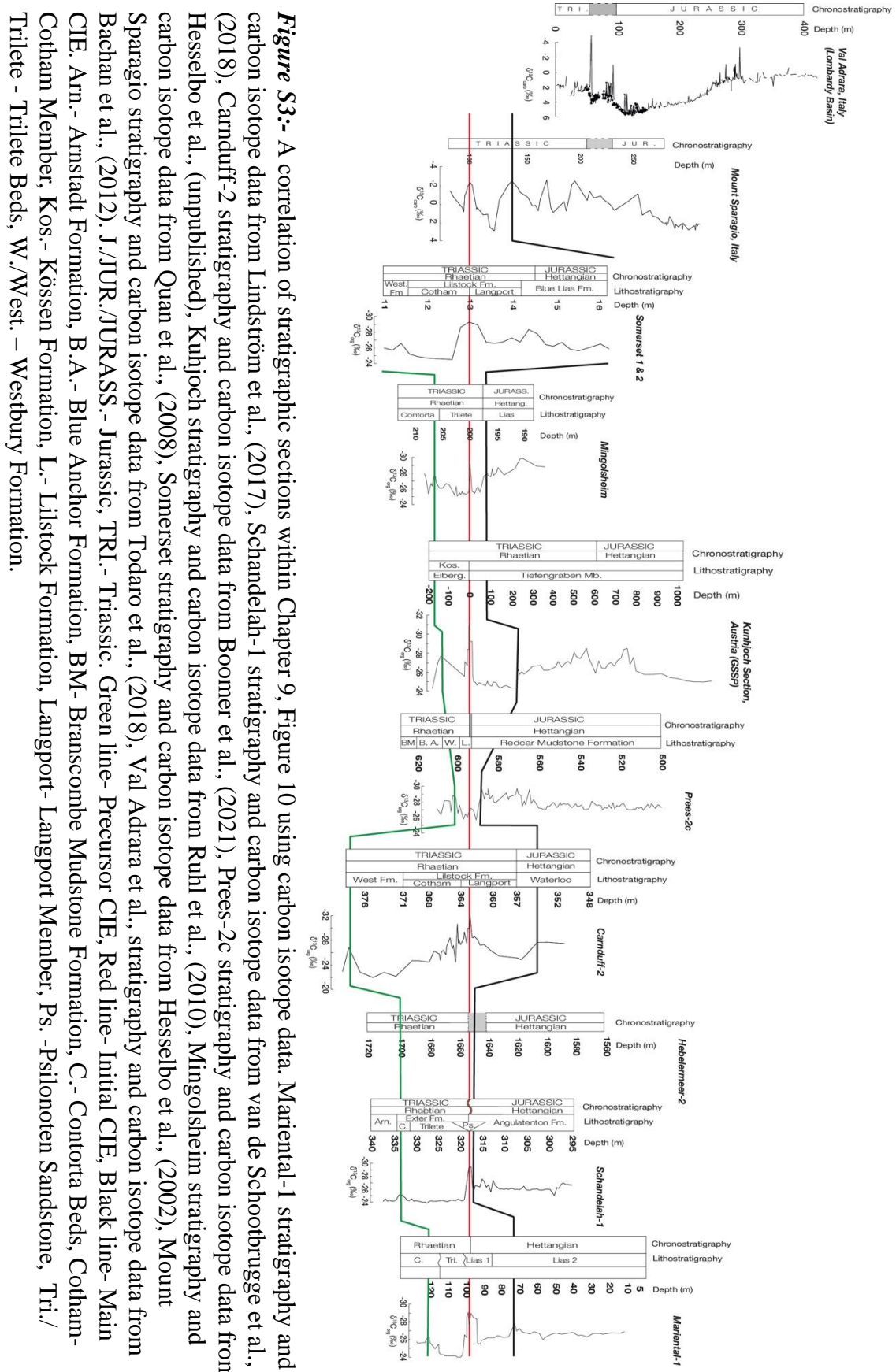


Figure S3:- A correlation of stratigraphic sections within Chapter 9, Figure 10 using carbon isotope data. Mariental-1 stratigraphy and carbon isotope data from Lindström et al., (2017), Schandela-1 stratigraphy and carbon isotope data from van de Schootbrugge et al., (2018), Carnduff-2 stratigraphy and carbon isotope data from Boomer et al., (2021), Prees-2c stratigraphy and carbon isotope data from Hesselbo et al., (unpublished), Kurnibach stratigraphy and carbon isotope data from Ruhl et al., (2010), Mingolsheim stratigraphy and carbon isotope data from Quan et al., (2008), Somerses stratigraphy and carbon isotope data from Hesselbo et al., (2002), Mount Sparagio stratigraphy and carbon isotope data from Todaro et al., (2018), Val Adra et al., stratigraphy and carbon isotope data from Bachan et al., (2012). J./JUR./JURASS.- Jurassic, TRI.- Triassic. Green line- Precursor CIE, Red line- Initial CIE, Black line- Main CIE. Arn.- Arnstadt Formation, B.A.- Blue Anchor Formation, BM- Branscombe Mudstone Formation, C.- Contorta Beds, Cotham- Cotham Member, Kos.- Kössen Formation, L.- Lilstock Formation, Langport- Langport Member, Ps.- Pylonoten Sandstone, Tri./Trilete - Trilete Beds, W./West. – Westbury Formation.

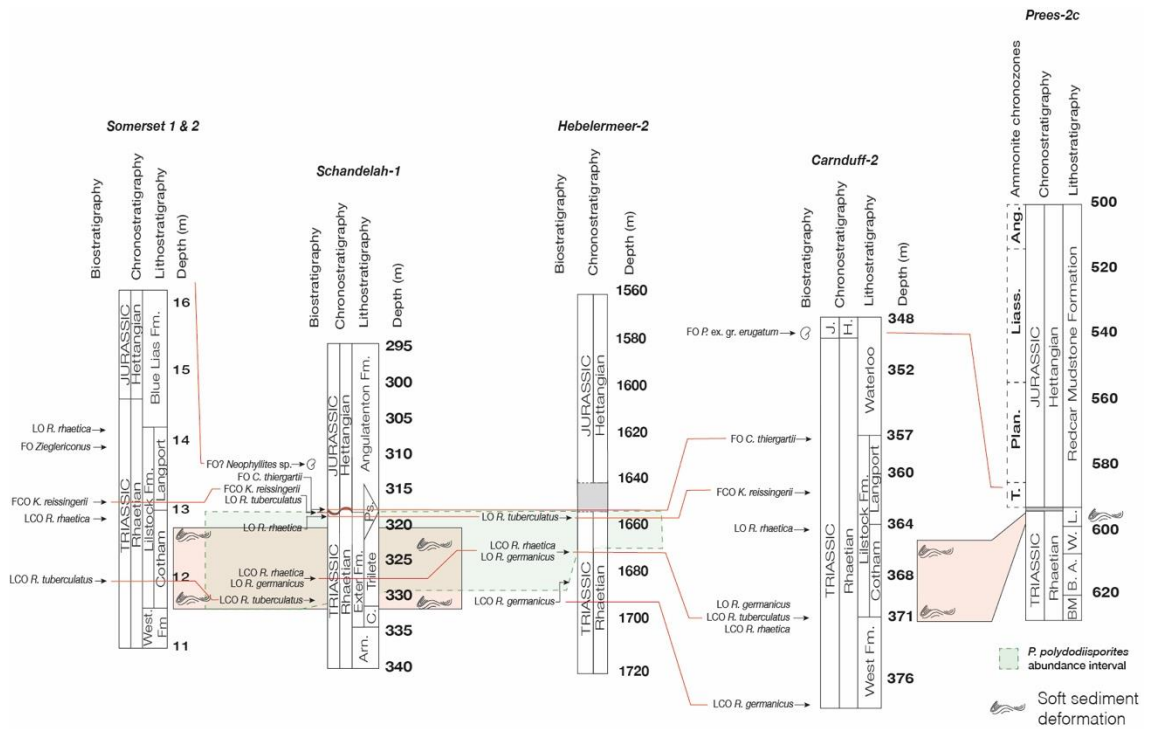


Figure S4:- Stratigraphic correlation of chapter 9 sections through the use of pollen and dinocyst occurrences.

Biostratigraphic data was obtained from the original data sources with the exception of the Prees-2c core for which such data was not available. Appearances and disappearances of diagnostic Triassic and Jurassic pollen and dinocysts were correlated across the remaining four sections with biostratigraphic correlations broadly supporting the correlation based on carbon isotope data (refer to Chapter 7, supplementary information for further discussion as well as biostratigraphic plots). The correlation of the Somerset 1 & 2 cores, Schandelah-1 core, Carnduff-2 core and Prees-2c core was further supported through using soft sediment deformation as a marker horizon.

Evidence for diagenetic alteration- As discussed within the previous chapters of this thesis there exists little evidence for significant diagenetic or thermal alteration of the selected study sections (see Chapters 6 and 7). There is limited evidence for significant

diagenetic and thermal alteration within the Carnduff-2 core on the basis of vitrinite reflectance data [Bond *et al.*, 2022a]. Furthermore, aragonite shell mineralogy is noted to be well-preserved within the Larne Basin suggesting thermally immature sediments [Raine *et al.*, 2021; Boomer *et al.*, 2021; Bond *et al.*, 2022a]. The sediments of the Hebelmeer-2 core exhibit a generally low vitrinite reflectance (%) value of 0.56% with T_{\max} values corroborating immature to early oil window maturation of organic matter [Blumenberg *et al.*, 2016]. The Schandelah-1 core sediments exhibit a vitrinite reflectance of ~1% suggesting thermally immature sediments [van de Schootbrugge *et al.*, 2019]. Organic matter within the Schandelah-1 core is also well-preserved suggesting relatively low thermal maturation [van de Schootbrugge *et al.*, 2019]. The Somerset-2 core exhibits beef calcite which may have been formed by dissolution [Kershaw & Guo, 2016]. However, Lower Jurassic limestones from SW England are interpreted to have only undergone marine burial diagenesis based on geochemical data [Arzani, 2004]. Samples from St. Audrie's Bay are also sufficiently thermally immature for the preservation of biomarkers and palynomorphs [van de Schootbrugge *et al.*, 2007; Jaraula *et al.*, 2013; Fox *et al.*, 2020; Beith *et al.*, 2021]. Sr/Ca, Mn/Ca, and Al/Ca ratios from the TJB at St. Audrie's Bay further evidence that 80% of oyster shells are diagenetically unaltered [van de Schootbrugge *et al.*, 2007]. Furthermore, ichnofabrics and fossil content of Lower Jurassic sediments at St. Audrie's Bay have survived the diagenetic redistribution of carbonate within the succession which would further suggest low diagenetic alteration [Hesselbo *et al.*, 2004]. The Prees-2c core has yet to undergo detail study, however, excellent preservation of sedimentary structures and ichnofabrics alongside well-preserved fossil material (see Appendix 3.3) would likely suggest relatively low thermal maturation.

10 DISCUSSION, CRITICAL EVALUATION, AND FUTURE WORK

At the beginning of this thesis I proposed five main research questions: i) ‘When did marine redox change initiate during the ETME?’, ii) ‘How did marine redox progress spatio-temporally during the ETME?’, iii) ‘How prevalent was de-oxygenation in the deep ocean during the ETME?’ iv) ‘What were the drivers of marine redox change during the ETME?’, v) ‘To what extent was marine redox change a driver of extinction during the ETME?’. In this chapter I will summarise the key findings from across chapters 6–9 to answer these questions.

10.1 DE-OXYGENATION OF THE TETHYAN SHELF DURING THE END TRIASSIC MASS EXTINCTION

10.1.1 Initiation of marine redox change during the ETME

Prior to the work undertaken within this thesis there was a lot of uncertainty regarding when marine redox change initiated during the Triassic–Jurassic boundary interval. Research by Blumenberg et al., (2016) on the Hebelmeer-2 core provided evidence for photic zone euxinia (PZE) as early as the lower middle Rhaetian based on the occurrence of the biomarker isorenieratane. However, PZE from the Hebelmeer-2 core considerably pre-dated any other evidence for marine redox change across the Triassic–Jurassic Tethyan shelf. In order to further understand the initiation of marine redox change within open marine environments and marginal marine Tethyan shelf environments I have studied carbonate-bound redox sensitive trace elements (Chapter 8), elemental and isotopic marine redox proxies (Chapters 6, 7 & 9), and a compilation of redox proxies from literature from across the Tethyan shelf (Chapter 7) (*Fig. 17*).

Quantifying marine redox across the Triassic–Jurassic mass extinction

Elemental and isotopic marine redox proxies as well as redox compilation data show that the earliest pulses of marine redox change on the Tethyan shelf were recorded during the lower middle Rhaetian (Chapters 6 and 7) (*Fig. 17*). Meanwhile, widespread sedimentary porewater de-oxygenation on the Tethyan shelf did not take place until the upper middle Rhaetian (Chapter 9) (*Fig. 17*). The expansion of suboxic/anoxic conditions within the open ocean broadly coincided with the deposition of the lower–middle Westbury Formation (lower to mid middle Rhaetian) on the basis of coinciding with the so-called ‘pre-cursor’ carbon isotope excursion (Chapter 8) [Kovács *et al.*, 2020] (*Fig. 17*). Therefore, the initiation of widespread, Triassic–Jurassic marine redox change may be dated to the middle Rhaetian becoming particularly widespread during the upper Middle Rhaetian.

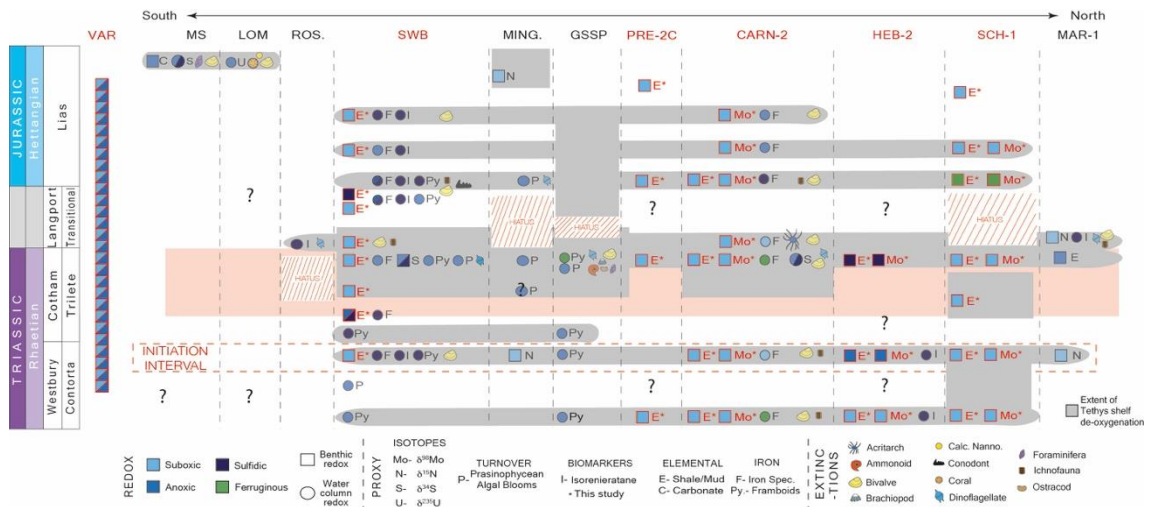


Figure 17:- Redox compilation data from the Triassic–Jurassic Tethyan shelf. Data from this thesis (in red) represents >50% of the known, published redox data from the Triassic–Jurassic Tethyan shelf including 100% of the known, published Triassic–Jurassic δMo data and >95% of the known, published, elemental, Triassic–Jurassic redox data from the Tethyan shelf. MS elemental carbonate data from He *et al.*, (2022b), iron speciation data from He *et al.*, (2022a), pyrite framboid data from Li *et al.*, (2022). VAR- Csóvár Vár-hegy section, Hungary. Refer to Chapter 7, Figure 3 for further information regarding abbreviations and data sources. For details regarding significance of questions marks, vertical grey bars and stratigraphic gaps see Ch. 7 Fig. 3.

10.1.2 Spatio-temporal redox progression during the ETME

The spatio-temporal progression of marine redox during the ETME was also poorly understood prior to the work undertaken within this thesis. Blumemberg et al., (2016) interpreted that marine redox change may have initiated with central basins of the Tethyan shelf before progressing to more marginal Tethyan basins. However, there has been no research since to supplement this theory. This thesis has used elemental and isotopic marine redox data (Chapters 6, 7 and 9) as well as compiled redox data (Chapter 7) from six Tethyan sites to understand the spatio-temporal progression of marine redox change during the Triassic–Jurassic boundary interval.

Elemental data from across the Triassic–Jurassic Tethyan shelf shows that marine redox change was temporally pulsed in nature (Chapters 6, 7 and 9) (*Fig. 17*). The research undertaken within this thesis was the first to identify pulses of marine redox change during the latest Triassic on the Tethyan shelf with redox fluctuations having been previously identified from the basal Jurassic of the Tethyan shelf (Ruhl et al., 2010; Richoz et al., 2012). There is no evidence for pulsed marine redox change from the open ocean record, with expanded suboxic/anoxic conditions persisting from shortly before the initial CIE through the basal Jurassic (Chapter 8) (*Fig. 17*).

The spatial progression of marine redox change on the Tethyan shelf is also pulsed in nature (Chapter 7). Early pulses of marine redox change are spatially constrained on the Tethyan shelf, to central and northern basins, and become more geographically extensive during the uppermost Rhaetian and lowermost Hettangian, extending into more southerly basins (Chapter 7) (*Fig. 17*). Therefore, the results from this thesis would partly support Blumenberg et al., (2016)'s interpretations.

Quantifying marine redox across the Triassic–Jurassic mass extinction

Mo isotope data presented in Chapter 7 of this thesis provide evidence that sulfidic conditions covered between ~0.05–0.1% of the Late Triassic seafloor. Given the numerous studies which have reported sulfidic marine conditions within Late Triassic, marginal marine environments, it has been interpreted here that sulfidic conditions were largely restricted to marginal marine environments during the TJB (Chapter 7). However, sulfidic water column conditions were not as spatially extensive as sedimentary porewater and bottom water de-oxygenation on the Tethyan shelf during the TJB (Chapter 9).

10.1.3 The prevalence of de-oxygenation in the deep ocean during the ETME

Molybdenum isotope and elemental data presented within chapters 7 and 8 of this thesis provide further information on the prevalence of de-oxygenation in the deep ocean during the ETME. As mentioned within section 10.1.2, Mo isotope data evidence that sulfidic conditions covered no more than 0.1% of the Late Triassic seafloor. Therefore, there is little evidence for persistent, sulfidic marine conditions within the open ocean during the ETME. The absence of sulfidic marine conditions within the open ocean is further supported by elemental carbonate data presented within chapter 8 of this thesis. Elemental carbonate data show little to no statistically significant change amongst elements which typically co-precipitate with sulfur (Cd, Zn) during the de-oxygenation of open marine environments (Chapter 8; *Figs S4 & S5*). However, elemental carbonate data do show a statistically significant decrease amongst elements which are particularly sensitive to suboxic and anoxic conditions (U, V, Cr). Given that Late Triassic deep marine environments show little evidence for de-oxygenation on the basis of pyrite framboid data [*Wignall et al., 2010*], it is likely that globally on average expanded anoxic and suboxic conditions are representative of expanded oxygen minimum zones

Chapter 10: Discussion, critical evaluation, and future work

during the TJB as previously suggest by other authors [*Kasprak et al., 2015; He et al., 2022*]. Therefore, the Late Triassic deep ocean is unlikely to have undergone prolonged de-oxygenation.

10.1.4 The drivers of marine redox change during the ETME

Elemental data within chapters 6, 7 and 9 of this thesis show no correlation with hydrography, weathering, and sedimentary facies changes. Therefore, it is unlikely that marine redox changes were driven by localised environmental changes. Instead, as suggested within chapter 8 of this thesis for the decoupling between open ocean and marginal marine de-oxygenation, marine redox change may be associated with pulsed volcanism and the thermal expansion of seawater. Thermal expansion can drive de-oxygenation as oxygen is less soluble in warmer waters [*Breitburg et al., 2018*]. Furthermore, warming of surface waters can result in stratification with warm, productive, well oxygenated surface waters underlain by cold, oxygen poor bottom waters [*Limburg et al., 2020*]. CAMP activity may have also resulted in changes to ocean circulation which can compromise ocean mixing causing stratification [*Palter & Trossman, 2018*] or regional changes in nutrient supply resulting in widespread eutrophication. However, these theories all require further study.

10.1.5 Marine redox change as a driver of extinction during the ETME

Until now the correlation between marine redox changes and intervals of extinction have been poorly constrained. Previous studies have suggested the correlation between Late Triassic marine extinctions and PZE, however many of these studies recorded PZE long before or after the main extinction level(s) [*Richoz et al., 2012; Jaraula et al., 2013; Blumenberg et al., 2016; Fox et al., 2020*]. Uranium and nitrogen isotope data

Quantifying marine redox across the Triassic–Jurassic mass extinction

interpreted as reflecting redox changes also pre- or post-date the main extinction interval [Quan *et al.*, 2008; Jost *et al.*, 2017]. Recent studies also correlate redox shifts, as denoted by sulfur isotope and element/calcium data, with minor Late Triassic extinction pulses [He *et al.*, 2020; 2022]. Therefore, prior to the work presented within this thesis, there are few studies which provide evidence for oxygen poor conditions coinciding with main extinction interval(s). Within this thesis I present numerous lines of evidence for the correlation between pulsed marine redox change and the extinction of marine organisms (Chapters 6, 7 and 9). Sedimentary porewater deoxygenation and the extinction of infaunal marine organisms are positively correlated within the Larne Basin, Northern Ireland (Chapter 6), regional pulses of de-oxygenation directly coincided with pulses of local and regional extinction on the Tethyan shelf (Chapter 7), and pulses of regional porewater and bottom water de-oxygenation directly coincided with the extinction of benthic marine organisms as well as planktonic organisms with a benthic resting stage (Chapter 9). The significant effect of marine de-oxygenation on marine organisms during the ETME is therefore evident.

10.2 UNCERTAINTY REGARDING LATE TRIASSIC STRATIGRAPHIC CORRELATION

As discussed within chapter 2 of this thesis there have historically been uncertainties regarding the correlation of Triassic–Jurassic boundary sections, which have proven to be an ongoing problem within this field of research. Despite carbon isotope stratigraphy proving a useful tool with regards to the correlation of Late Triassic sections [Hesselbo *et al.*, 2002; Ruhl *et al.*, 2010, 2011, Kovács *et al.*, 2020; Korte *et al.*, 2020], there are still some inconsistencies between correlations using carbon isotope records and palynostratigraphy [Jeram *et al.*, 2021; Lindstrom, 2021]. Furthermore, the carbon

Chapter 10: Discussion, critical evaluation, and future work

isotope stratigraphic correlation of TJB sites often results in multiple possible correlations [Wignall & Atkinson, 2020]. Therefore, more recent research has particularly used both carbon isotope stratigraphy and key palynofacies/palynotaxa as a ‘belt and braces’ approach to Triassic–Jurassic stratigraphic correlation [Lindström *et al.*, 2016; Lindström, 2021; Kovács *et al.*, 2020]. Where possible this approach has been used here to rule out the uncertainty caused through using palynostratigraphy or carbon isotope stratigraphy alone.

10.3 SAMPLE ALTERATION, GEOCHEMICAL OVERPRINTING AND PSEUDO-EXTINCTIONS

In order to rule out the possibility that the trends and patterns observed in this thesis were the result of alteration or environmental changes other than redox, these factors have consistently been investigated within the papers and manuscripts.

10.3.1 Thermal and/or diagenetic alteration

There is little evidence for thermal and/or diagenetic alteration within the outcrop or core sections studied within this thesis. The Carnduff-2 core is thermally immature with little thermal or diagenetic alteration on the basis of vitrinite reflectance data and aragonite preservation (Chapter 6). The Schandelah-1 and Hebelmeer-2 cores are also relatively thermally immature on the basis of palynomorph preservation, vitrinite reflectance data and T_{\max} (°C) estimates [Blumenberg *et al.*, 2016; van de Schootbrugge *et al.*, 2019]. The Vár-hegy section samples are well preserved on the basis of $\delta^{13}\text{C}$ vs. $\delta^{18}\text{O}$ correlation, organic matter %, and Mg/Ca ratios. The Prees-2c core exhibits low diagenetic alteration on the basis of very well-preserved fossil material and the preservation of original sedimentary textures (see Appendix 3.3). The Somerset core

Quantifying marine redox across the Triassic–Jurassic mass extinction

material is likely to have only undergone marine burial diagenesis based on geochemical analysis of Triassic–Jurassic limestones and shell material from SW Britain as well as preservation of biomarkers, palynomorphs, ichnofabrics and fossil content in light of diagenetic carbonate re-distribution [Arzani, 2004; Hesselbo *et al.*, 2004; van de Schootbrugge *et al.*, 2007; Jaraula *et al.*, 2013; Fox *et al.*, 2020; Beith *et al.*, 2021].

10.3.2 Palaeozoic shale weathering, detrital input, and hydrographic changes

As previously touched upon within this discussion (10.1.4) there is no correlation between proxies for detrital input or hydrography and marine redox change. Therefore, changes in elemental enrichment are unlikely to have been caused by the changing influx of detrital material at the study sites (Chapters 6, 7, 9). This has been further accounted for through the use of enrichment factors and elemental ratios instead of concentrations within the papers and manuscripts of this thesis. There is also no evidence that aluminosilicates have compromised the carbonate data presented in Chapter 8 of this thesis on the basis of the low correlation between redox sensitive elements and Al (ppb). There is no evidence that Mo isotope ratios were compromised by weathering of Palaeozoic, organic rich shales on the Tethyan shelf during the TJB on the basis of there being no correlation between detrital proxies and δMo (Chapter 7) [van de Schootbrugge *et al.*, 2020].

10.3.3 Organic matter input and near shore iron (Fe) remobilisation

The input of terrestrial organic matter and near shore Fe remobilisation have compromised the redox proxies C_{org}/P and Fe_T/Al within the Carnduff-2 core (Chapter

Chapter 10: Discussion, critical evaluation, and future work

6). Therefore, these proxies have been dismissed within this chapter and the enrichment of redox sensitive trace elements have been used instead.

10.3.4 Aragonite undersaturation

As discussed within Chapter 2 of this thesis, the ETME is represented by the disappearance of numerous different marine organisms. However, there is some uncertainty regarding the role of aragonite undersaturation in infaunal bivalve disappearances (Chapter 2). We find little evidence to suggest that the extinction/disappearance of infaunal marine organisms was the result of preferential dissolution of aragonitic shell material from the Larne Basin (Chapter 6). This is on the basis that both aragonitic (59%) and bimineralic taxa (36%) undergo disappearances and numerous aragonitic taxa persist from the base of the section through the basal Jurassic (Chapter 6).

10.3.5 Facies changes and/or sea level change

We also find little evidence to suggest that the disappearances of infaunal marine organisms from the Larne Basin were the result of changing sea level or sedimentary facies changes due to the fact that there is little correlation between these factors in the Larne Basin (Chapter 6).

10.4 SAMPLE CONTAMINATION, REPRESENTIVITY OF SAMPLE
MEASUREMENTS AND INSTRUMENTAL INTERFERENCE

As discussed in chapter 5, and in further detail in appendix 4, the samples processed for this thesis have been prepared in such a way as to avoid contamination and provide reproducible results. The samples were initially milled in tungsten carbide, agate, or carbon alloy to limit trace metal contamination and provide homogenous sample powders. Samples were weighed to 4 or 5 decimal places in a clean room and were digested using 2/3 x triple distilled acids in acid cleaned Teflon containers within class 100 fume cupboards. Samples were also spiked (for isotopic work) with Mo or Zn enriched solutions to track isotopic fractionation during sample processing. Samples were processed for isotopic data using an anion exchange column method to remove sources of isobaric interference and elements which may form argides with a similar m/z ratio to analytes. Isotope ratios were measured on the Neptune Plus MC-ICP-MS which initially underwent either a gain or background calibration to determine and subtract the noise from isotopic measurements. The Neptune was tuned to optimise and stabilise the signal. The samples were measured for between 50 and 80 integrations for an integration time of ~8 seconds each. Drift throughout the run was resolved using zero delta standards every 3 samples. Elemental and isotopic sample digests were processed alongside procedural blanks, external standards, and internal standards to determine contamination during digestion as well as the external and internal reproducibility of the sample batches (see Chapter 5 and Appendix 4 for further information).

10.5 REPRESENTIVITY/SUITABILITY OF STUDY SECTIONS AND PROXIES

The sections chosen for this thesis are generally very well understood stratigraphically (Chapters 2 and 4). Despite the Hebelmeer-2 core being less well understood and the Prees-2c core still undergoing detailed study, there is sufficient data available to correlate both of these sites with the other study sections. The sites have also undergone previous redox studies, which has allowed for some comparison of elemental, Mo isotope and other redox proxies [Jaraula *et al.*, 2013; Blumenberg *et al.*, 2016; Fox *et al.*, 2020; Beith *et al.*, 2021] (Fig. 17). The sites represent a broad range of latitudes, longitudes, sedimentology, and hydrographic settings on the Tethyan shelf. The sites, when collated with the chosen geochemical proxy data, also provide a broad range of local, regional, and global redox data allowing for a broad range of spatial redox information. The sections all span the TJB and ETME allowing for direct comparisons to be made between sections with considerable variability in expanded and condensed sections as well as stratigraphy above and below the TJB. The proxies chosen for this thesis are generally well established or in the case of newly developed proxies are well supported numerically. Figure 18 shows the use of Mo enrichment data plotted against uranium enrichment which has been used within previous studies to reconstruct marine redox conditions [Algeo & Tribovillard, 2009; He *et al.*, 2022a]. The redox conditions interpreted within this thesis, through the use of trace metal enrichment and Mo isotope data, are generally further supported by the Mo/U data.

Quantifying marine redox across the Triassic–Jurassic mass extinction

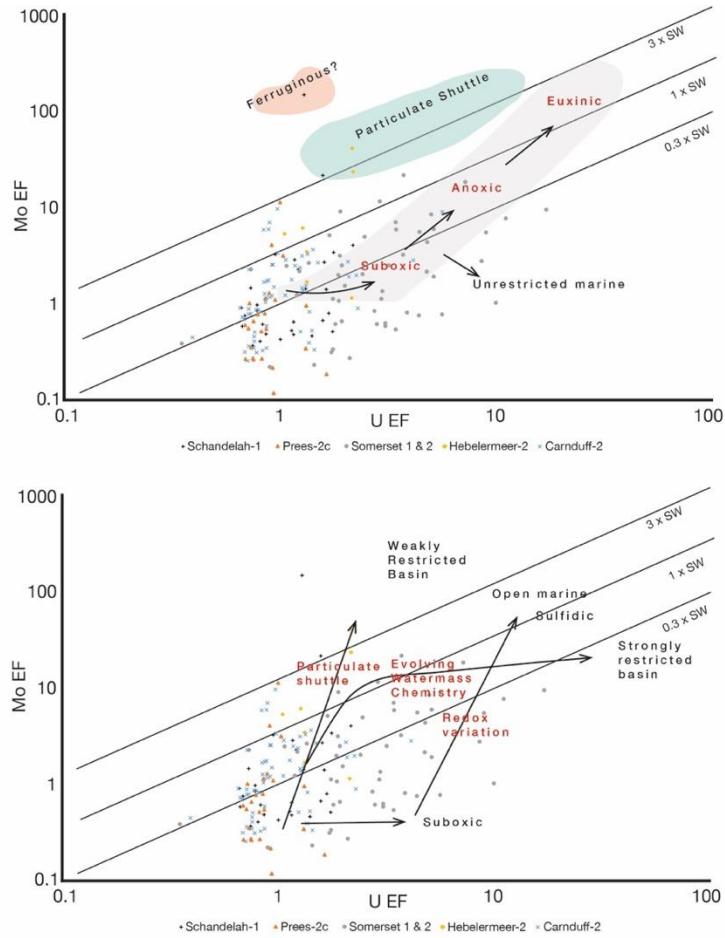


Figure 18:- Mo/U data from all five sites studied within this thesis showing how marine redox conditions may be evaluated and potential trace element enrichment processes compared.

10.6 COVID LIMITATIONS AND FUTURE WORK

The covid-19 pandemic severely changed the scope of this piece of research. Initially the thesis was also going to focus on material from Panthalassa GSSP candidate sites, including Haidi Gwaini and the New York Canyon section (see Chapters 2 and 4), as well as material from the Neuquén Basin, Argentina. Fieldwork was also going to be undertaken to Austria to collect material from the GSSP, to Argentina to study the

Chapter 10: Discussion, critical evaluation, and future work

Arroyo Malo section, and to Somerset to study the TJB at St. Audrie's Bay. Additional proxies were also to be included to further understanding of the role of weathering and volcanism in carbon cycle dynamics (such as lithium and osmium isotopes), but these were de-prioritised due to time limitations. Zinc isotopes were measured from the Larne Basin and prepared for measurement from Csővár (Appendix 6), but there has been insufficient time to finalise the Zn isotope data and subsequently formulate these data into a chapter. Large datasets were produced as a result of this work with only a fraction of this data having been studied in detailed throughout this thesis (Appendix 7). Future work may therefore wish to compile these datasets to further study spatial redox relationships alongside studying Panthalassa sites and material from the GSSP. These are all research avenues which would increase understanding of redox dynamics during the ETME and TJB.

11 CONCLUSIONS

Intervals of past, global environmental change, like the Triassic–Jurassic boundary interval and extinction event, may provide an analogue for the potential effect of anthropogenic carbon output on global marine ecosystems. However, many such intervals remain poorly understood in terms of marine redox change. This thesis evidences several new and exciting developments regarding marine redox change across the Triassic–Jurassic boundary interval. Some of these developments had been hypothesised but remained unproven whilst others were completely unknown:

- Marine redox change on the Tethyan shelf during the Triassic–Jurassic boundary was pulsed and was closely associated with pulses of marine extinction.
- The extinction of partly and exclusively benthic marine organisms during the ETME is closely associated, at both a regional and local extent, with sedimentary porewater and bottom water de-oxygenation.
- Sulfidic conditions only covered 0.05–0.1% of the late Triassic seafloor and were likely geographically restricted to marginal marine environments.
- Marine de-oxygenation in the open ocean largely preceded pulsed de-oxygenation on the Tethyan shelf, demonstrating that marine redox change may have progressed from the open ocean to marginal marine environments.
- Sulfidic water column conditions were spatially limited on the Tethyan shelf in comparison to sedimentary porewater and bottom water de-oxygenation, which was more widespread.

Further research should be undertaken, both during the Triassic–Jurassic boundary interval and during other mass extinction events, to further understand these spatio-temporal redox relationships and their effect on marine organisms.

REFERENCES

- ALDRIDGE, F., Smith, M. P., 1993. Conodonts. In: *Benton, M.J. (Ed.), The Fossil Record 2*. Chapman and Hall, London, pp. 563–572.
- ALGEO, T. J., 2004. Can marine anoxic events draw down the trace element inventory of seawater? *Geology*, **32** (12), 1057–1060.
- ALGEO, T. J. & Ingall, E. 2007. Sedimentary C_{org}/P ratios, paleocean ventilation and Phanerozoic atmospheric pO₂. *Palaeogeography, Palaeoclimatology, Palaeoecology*, **256**, 130–155.
- ALGEO, T. J. & Li, C. 2020. Redox classification and calibration of redox thresholds in sedimentary systems. *Geochimica et Cosmochimica Acta*, **287**, 8–26.
- ALGEO, T. J. & Liu, J., 2020. A re-assessment of elemental proxies for paleoredox analysis. *Chemical Geology*, **540**, 119549.
- ALGEO, T. J. & Lyons, T. W., 2006. Mo-total organic carbon covariation in modern anoxic marine environments: Implications for analysis of paleoredox and paleohydrographic conditions. *Paleoceanography*, **21** (1), 1–23.
- ALGEO, T. J. & Maynard, J. B. 2004. Trace-element behavior and redox facies in core shales of Upper Pennsylvanian Kansas-type cyclothems. *Chemical Geology*, **206**, 289–318.
- ALGEO, T. J. & Tribovillard, N., 2009. Environmental analysis of paleoceanographic systems based on molybdenum-uranium covariation. *Chemical Geology*, **268**, 211–225.
- ALLEN, B. J., Stubbs, T. L., Benton, M. J. & Puttick, M. N. 2018. Archosauromorph extinction selectivity during the Triassic–Jurassic mass extinction. *Palaeontology*, **62** (2), 211–224.
- ALLEN, K. A., Honisch, B., Eggins, S. M., Haynes, L. L., Rosenthal, Y., and Yu, J., 2016, Trace element proxies for surface ocean conditions: A synthesis of culture calibrations with planktic foraminifera, *Geochimica et Cosmochimica Acta*, **193**, 197–221.
- ALLER, R. C., Mackin, J. E. & Cox, R. T. 1986. Diagenesis of Fe and S in Amazon inner shelf muds: apparent dominance of Fe reduction and implications for the genesis of ironstones. *Continental Shelf Research*, **6**, 263–289.
- ALROY, J. 2008. Dynamics of origination and extinction in the marine fossil record. *PNAS*, **105** (1), 11536–11542.
- ALROY, J., Aberhan, M., Bottjer, D.J., Foote, M., Fürsich, F.T., Harries, P.J., Hendy, A.J.W., Holland, S.M., Ivany, L.C., Kiessling, W., Kosnik, M.A., Marshall, C.R., McGowan, A.J., Miller, A.I., Olszewski, T.D., Patzkowsky, M.E., Peters, S.E., Villier,

Quantifying marine redox across the Triassic–Jurassic mass extinction

- L., Wagner, P.J., Bonuso, N., Borkow, P.S., Brenneis, B., Clapham, M.E., Fall, L.M., Ferguson, C.A., Hanson, V.L., Krug, A.Z., Layou, K.M., Leckey, E.H., Nürnberg, S., Powers, C.M., Sessa, J.A., Simpson, C., Tomašových, A., Visaggi, C.C., 2008. Phanerozoic trends in the global diversity of marine invertebrates. *Science*, **321** (5885), 97–100.
- ALROY, J. 2010. Fair sampling of taxonomic richness and unbiased estimation of origination and extinction rates. *Palaeontology*, **53**, 1211–1235.
- ALROY, J. 2014. Accurate and precise estimates of origination and extinction rates. *Paleobiology*, **40** (3), 374–397.
- ALLASINAZ, A. 1992. The Late Triassic-Hettangian bivalve turnover in Lombardy (Southern Alps). *Rivista Italiana di Paleontologia e Stratigrafia*, **97**, 431–454.
- AL-SUWAIDI, A., Steuber, T. & Suarez, M. B. 2016. The Triassic–Jurassic boundary event from an equatorial carbonate platform (Ghalilah Formation, United Arab Emirates). *Journal of the Geological Society, London*, **173**, 949–953.
- ALVAREZ, L. W., Alvarez, W., Asaro, F., & Michel, H. V. 1980. Extraterrestrial Cause for the Cretaceous-Tertiary Extinction - Experimental Results and Theoretical Interpretation. *Science*, **208** (4448), 1095–1108.
- ANDERSEN, M. B., Romaniello, S., Vance, D., Little, S. H., Herdman, R., & Lyons, T. W. 2014, A modern framework for the interpretation of $^{238}\text{U}/^{235}\text{U}$ in studies of ancient ocean redox, *Earth and Planetary Science Letters*, **400**, 184–194.
- ANDERSEN, M. B., Vance, D., Morford, J. L., Buranaki, E., Breitenbach, S. F. M., & Och, L. 2016, Closing in on the marine $^{238}\text{U}/^{235}\text{U}$ budget, *Chemical Geology*, **420**, 11–22.
- ANDERSON, L. A. & Sarmiento, J. L. 1994. Redfield ratios of remineralisation determined by nutrient data analysis, *Glob. Biogeochemical Cycles*, **8** (1), 65–80.
- ANDERSON, R. F., Fleisher, M. Q., & LeHuray, A. P. 1989. Concentration, oxidation state, and particulate flux of uranium in the Black Sea. *Geochimica et Cosmochimica Acta*, **53**, 2215–2224.
- ANDERSSON, E. R., Stewart, J. A., Work, T. M., Woodley, C. M., Schock, T. B., and Day, R. D., 2020, Morphological, elemental, and boron isotopic insights into pathophysiology of diseased coral growth anomalies, *Scientific Reports*, **10**, 8252.
- ANDESKIE, A. S., Benison, K. C., Eichenlaub, L. A. & Raine, R. 2018. Acid-saline-lake systems of the Triassic Mercia Mudstone Group, County Antrim, Northern Ireland. *Journal of Sedimentary Research*, **88**, 385–398.
- ARCHER, C., Andersen, M. B., Cloquet, C., Conway, T. M., Dong, S., Ellwood, M., Moore, R., Nelson, J., Rehkämper, M., Rouxel, O., Samanta, M., Shin, K. C., Sohrin, Y., Takano, S., & Wasylenki, L. 2017. Inter-calibration of a proposed new primary

References

- reference standard AA-ETH Zn for zinc isotopic analysis. *Journal of analytical atomic spectrometry*, **32** (2), 415–419.
- ARZANI, N. 2004. Diagenetic Evolution of Mudstones : Black Shales to Laminated Limestones, An Example From the Lower Jurassic of SW Britain. *Journal of Sciences Islamic Republic of Iran*, **15** (3), 257–267.
- ATKINSON, J. W. & Wignall, P. B. 2019. How quick was marine recovery after the end-Triassic mass extinction and what role did anoxia play? *Palaeogeography, Palaeoclimatology, Palaeoecology*, **528**, 99–119.
- ATKINSON, J. W. & Wignall, P. B. 2020. Body size trends and recovery amongst bivalves following the end-Triassic mass extinction, *Palaeogeography, Palaeoclimatology, Palaeoecology*, **538**, 109453.
- BACHAN, A., van de Schootbrugge, B., Fiebig, J., McRoberts, C. A., Ciarapica, G. and Payne, J. L. 2012., Carbon cycle dynamics following the end-Triassic mass extinction: Constraints from paired $\delta^{13}\text{C}_{\text{carb}}$ and $\delta^{13}\text{C}_{\text{Corg}}$ records, *Geochemistry, Geophysics, Geosystems*, **13** (9), 1–24.
- BADJUKOV, D. D., Lobitzer, H., & Nazarov, M. A. 1987. Quartz grains with planar features in the Triassic-Jurassic boundary sediments from Northern Calcareous Alps, Austria. *Lunar and Planetary Science Letters*, **18**, 38–39.
- BAMBACH, R. K., Knoll, A. H., 2001. Is there a separate class of “mass” extinctions? Abstr. Programs-Geological Society of America, **33** (6), A141.
- BAMBACH, K. R., Knoll, A. H. & Wang, S. C. 2004. Origination, extinction and mass depletions of marine diversity. *Paleobiology*, **30** (4), 522–542
- BARATTOLO, F. & Romano, R. 2005. Shallow carbonate platform bioevents during the Upper Triassic-Lower Jurassic: an evolutive interpretation. *Bollettino Societa Geologica Italiana.*, **124**, 123–142.
- BARESEL, B., Bagherpour, B., Bucher, H., Guodun, K., Schaltegger, U., & Brosse, M. 2017. Timing of global regression and microbial bloom linked with the Permian-Triassic boundary mass extinction: implications for driving mechanisms. *Scientific Reports*, **7** (1), 3–10.
- BARLING, J. & Anbar, A. D. 2004. Molybdenum isotope fractionation during adsorption by manganese oxides. *Earth and Planetary Science Letters*, **217**, 315–329.
- BARRAS, C. G. & Twitchett, R. J. 2007. Response of marine infauna to Triassic-Jurassic environmental change: Ichthyological data from southern England. *Palaeogeography, Palaeoclimatology, Palaeoecology*, **244**, 223–241.
- BARTH, G., Franz, M. Heunisch, C. Ernst W. Zimmerman, J. & Wolfgramm, M. 2018. Marine and terrestrial sedimentation across the T-J transition in the North German Basin. *Palaeogeography, Palaeoclimatology, Palaeoecology*, **489**, 74–94.

Quantifying marine redox across the Triassic–Jurassic mass extinction

- BEERLING, D. J. & Berner, R. A. 2002. Biogeochemical constraints on the Triassic–Jurassic boundary carbon cycle event. *Global biogeochemical Cycles*, **16** (3), 1–13.
- BEITH, S. J., Fox, C. P., Marshall, J. E. A., Whiteside, J. H., 2021. Recurring photic zone euxinia in the northwest Tethys impinged end-Triassic extinction recovery. *Palaeogeography, Palaeoclimatology, Palaeoecology*, **584**, 110680.
- BELCHER, C. M., Mander, L., Rein, G., Jervis, F. X., Haworth, M., Hesselbo, S. P., Glasspool, I. J. & McElwain, J. C. 2010. Increased fire activity at the Triassic/Jurassic boundary in Greenland due to climate-driven floral change. *Nature Geoscience*, **3**, 426–429.
- BENSE, F. A. & Jähne-Klingberg, F. 2017. Storage potentials in the deeper subsurface of the Central North Sea. *Energy Procedia*, **114**, 4595–4622.
- BENTON, M. J. 1986. More than one event in the late Triassic mass extinction. *Nature*, **321**, 857–861.
- BENTON, M. J. 1993a. Late Triassic Extinctions and the Origin of the Dinosaur. *Science*, **260** (5109), 769–770.
- BENTON, M. J. (ed.) 1993b. *The Fossil Record 2*. 845 pp. Chapman & Hall, London.
- BENTON, M. J. 1995. Diversification and extinction in the history of life. *Science*, **268** (5207), 52–58.
- BERNECKER, M. 2005. Late Triassic reefs from the Northwest and South Tethys: distribution, setting, and biotic composition. *Facies*, **51**, 442–45.
- BERRANG, P. G. & Grill, E. V. 1974. The effect of manganese oxide scavenging on molybdenum in Saanich Inlet, British Columbia. *Marine Chemistry*, **2** (2), 125–148.
- BICE, D. M., Newton, C. R. McCauley, S. Reiners, P. W. & McRoberts C. A. 1992. Shocked Quartz at the Triassic–Jurassic Boundary in Italy. *Science*, **255**, 443–446.
- BLACKBURN, T. J., Olsen, P. E., Bowring, S. A., McLean, N. M., Kent, D. V., Puffer, J., McHone, G., Rasbury, E. T. & Et-Touhami, M. 2013. Zircon U–Pb geochronology links the end-Triassic extinction with the Central Atlantic Magmatic Province. *Science*, **340** (6135), 941–945.
- BLOME, C. D. 1986. Paleogeographic significance of Upper Triassic and Lower Jurassic Radiolaria from Cordilleran terranes. *Proceedings North American Paleontological Convention*, **4**, A5.
- BLOOS, G. & Page, K. 2000. The basal Jurassic ammonite succession in the North West European Province—review and new results. *Journal of Geological Research*, **6**, 27–40.

References

- BLUMENBERG, M., Heunisch, C., Lückge, A., Scheeder, G., & Wiese, F. 2016. Photic zone euxinia in the central Rhaetian Sea prior the Triassic-Jurassic boundary. *Palaeogeography, Palaeoclimatology, Palaeoecology*, **461**, 55–64.
- BOND, A. D. 2018. Phylogenetic and biological response of the arthropod group Naraoiidae to early- middle Cambrian environmental change- MSc Thesis- unpublished
- BOND, A. D. & Edgecombe, G. D. 2020. Phylogenetic response of naraoiid arthropods to early-middle Cambrian environmental change. *Palaeontology*, **64(1)**, 161–177.
- BOND, A. D., Dickson, A. J., Ruhl, M. & Raine, R. 2022. Marine redox change and extinction in Triassic–Jurassic boundary strata from the Larne Basin, Northern Ireland. *Palaeogeography, Palaeoclimatology, Palaeoecology*, **598**, 111018.
<https://doi.org/10.1016/j.palaeo.2022.111018>.
- BOND, D. P. G. & Grasby, S. E. 2017. On the causes of mass extinctions. *Palaeogeography, Palaeoclimatology, Palaeoecology*, **478**, 3–29.
- BONIS, N. R., Kürschner, W. M. & Krystyn, L. 2009. A detailed study of the Triassic-Jurassic transition in key sections of the Eiberg Basin (Northern Calcareous Alps, Austria). *Review of Palaeobotany and Palynology*, **156**, 376–400.
- BONIS, N. R., Ruhl, M. & Kürschner, W. M. 2010. Climate change driven black shale deposition during the end-Triassic in the western Tethys. *Palaeogeography, Palaeoclimatology, Palaeoecology*, **299**, 151–159.
- BONIS, N. R., Van Konijnenburg-Van Cittert, J. H. A, and Kürchner, W. M., 2010, Changing CO₂ conditions during the end-Triassic inferred from stomatal frequency analysis on *Lepidopteris ottonis* (Goeppert) Schimper and *Ginkgoites taeniatus* (Braun) Harris, *Palaeogeography, Palaeoclimatology, Palaeoecology*, **295**, 146–161.
<https://doi.org/10.1016/j.palaeo.2010.05.034>.
- BOOMER, I., Copestake, P., Raine, R., Azmi, A., Fenton, J. P. G., Page, K. N. & O' Callaghan, M. 2021. Stratigraphy, palaeoenvironments and geochemistry across the Triassic- Jurassic boundary transition at Carnduff, County Antrim, Northern Ireland. *Proceeding of the Geologists' Association*, **132** (6), 667–687.
- BOS, Remco, Lindström, S., van Konijnenburg-van Cittert, J., Hilgen, F., Hollaar, T. P., Aalpoel, H., van der Weijst, C., Sanei, H., Rudra, A., Sluijs, A., & van de Schootbrugge, B. 2023. Triassic–Jurassic Vegetation Response to Carbon Cycle Perturbations and Climate Change. (Pre-print). SSRN.
<https://ssrn.com/abstract=4371814> or <http://dx.doi.org/10.2139/ssrn.4371814>
- BOTTINI, C., Jadoul, F., Rigo, M., Zaffani, M., Artoni, C., Erba, E. 2016. Calcareous nannofossils at the Triassic/Jurassic boundary: stratigraphic and paleoceanographic characterization. *Rivista Italiana di Paleontologia e Stratigrafia*, **122** (3), 141–164.
- BRAYARD, A., Escarguel, G., Bucher, H., Monnet, C., Brühwiler, Goudemand, Galfetti, T., Guex, J. 2009. Good Genes and Good Luck: Ammonoid Diversity and the End-Permian Mass Extinction. *Science*, **325** (5944), 1118–1121.

- BRAVO, I. & Figueroa, R. I. 2014. Towards an ecological understanding of dinoflagellate cyst functions. *Microorganisms*, **2**, 11–32.
- BREITBURG, D. L., Levin, L. A., Oschlies, A., Grégoire, M., Chavez, F. P., Conley, D. J., Garçon, V., Gilbert, D., Gutiérrez, D., Isensee, K., Jacinto, G. S., Limburg, K. E., Montes, I., Naqvi, S. W. A., Pitcher, G. C., Rabalais, N. N., Roman, M. R., Rose, K. A., Seibel, B. A., Telszewski, M., Yasuhara, M. & Zhang, J. 2018. Declining oxygen in the global ocean and coastal waters. *Science*, **359** (6371), eaam7240.
- BRETZ, J. H. 1923. The Channeled Scablands of the Columbia Plateau. *Journal of Geology*, **31**, 617–649.
- BRUMSACK, H.-J. 2006. The trace metal content of recent organic carbon-rich sediments” Implications for Cretaceous black shale formation. *Palaeogeography, Palaeoclimatology, Palaeoecology*, **232**, 344–361.
- BRYAN, A. L., Dickson, A. J., Dowdall, F., Homoky, W. B., Porcelli, D. & Henderson, G. M. 2021. Controls on the cadmium isotope composition of modern marine sediments. *Earth and Planetary Science Letters*, **565**, 116946.
- BURKHARDT, B. G., Watkins-Brandt, K. S., Defforey, D., Paytan, A. & White, A. E. 2014. Remineralization of phytoplankton-derived organic matter by natural populations of heterotrophic bacteria. *Marine Chemistry*, **163**, 1–9.
- CALVERT, S. E. & Pedersen, T. F. 1993. Geochemistry of Recent oxic and anoxic marine sediments: Implications for the geological record. *Marine Geology*, **13**, 67–88.
- CALVERT, S. E. & Pedersen, T. F. 2007. Chapter Fourteen: Elemental proxies for palaeoclimatic and palaeogeographic variability in marine sediments: interpretation and application in *Developments in Marine Geology*, vol. 1. Elsevier, p. 567–644.
- CANFIELD, D. E. 1989. Reactive iron in marine sediments. *Geochimica et Cosmochimica Acta*, **53**, 619–632.
- CARDINAL, D., Hamelin, B., Bard, E. & Pätzold, J. 2001. Sr/Ca, U/Ca and $\delta^{18}\text{O}$ records in recent massive corals from Bermuda: relationships with sea surface temperature. *Chemical Geology*, **176**, 213–233.
- CARILLI, J. E., Prouty, N. G., Huguen, K.A. & Norris, R. D. 2009. Century-scale records of land-based activities recorded in Mesoamerican coral cores. *Marine Pollution Bulletin*, **58**, 835–1842.
- CARRIQUIRY, J. D. & Villaescusa, J. A., 2010. Coral Cd/Ca and Mn/Ca records of ENSO variability in the Gulf of California. *Climate of the Past*, **6**, 410–410.
- CARMICHAEL, M. J., Inglis, G. N., Badger, M. P. S., Naafs, B. D. A., Behrooz, L., Rimmelzwaal, S., Monteiro, F. M., Rohrssen, M., Farnsworth, A., Buss, H. L., Dickson, A. J., Valdes, P. J., Lunt, D. J. & Pancost, R. D. 2017. Hydrological and associated biogeochemical consequences of rapid global warming during the Paleocene-

References

- Eocene Thermal Maximum. *Global and Planetary Change*, **157**, 114–138.
- CARTER, E. S. 1994. Evolutionary trends in latest Norian through Hettangian radiolarians from the Queen Charlotte Islands, British Columbia. *Geobios Mémoire Spécial*, **17**, 111–119.
- CARTER, E. S. & Tipper, W. H. 1999. Proposal of Kunga Island, Queen Charlotte Islands, British Columbia, Canada as Triassic/Jurassic global boundary stratotype. *ISJS Newsletter*, **27**, 20.
- CARTER, E. & Hori, R. 2005. Global correlation of the radiolarian faunal change across the Triassic-Jurassic boundary. *Canadian Journal of Earth Sciences*, **42**, 777–790.
- CARTER, E. S. 2007. Global distribution of Rhaetian radiolarian faunas and their contribution to the definition of the Triassic-Jurassic boundary. *New Mexico Museum of Natural History and Science Bulletin*, **41**, 27–31.
- CASACCI, M., Bertinelli, A., Algeo, T. J. & Rigo, M. 2016. Carbonate-to-biosilica transition at the Norian–Rhaetian boundary controlled by rift-related subsidence in the western Tethyan Lagonegro Basin (southern Italy). *Palaeogeography, Palaeoclimatology, Palaeoecology*, **456**, 21–36.
- CHANNELL, J. E. T., Kozur, H. W., Sievers, T., Mock, R., Aubrecht, R. & Sykora, M. 2003. Carnian –Norain biomagnetostratigraphy at Silická Brezová (Slovakia): correlation to other Tethyan sections and to the Newark Basin. *Palaeogeography, Palaeoclimatology, Palaeoecology*, **191**, 65–109.
- CHEN, L., Little, S. H., Kreissig, K., Severmann, S. & McManus, J. 2021. Isotopically Light Cd in Sediments Underlying Oxygen Deficient Zones. *Frontiers in Earth Science*, **9**, 623720.
- CHEN, M., Koeberl, C. Xiao, W. Xie, X. & Tan, D. 2011. Planar deformation features in quartz from impact-produced polymict breccia of the Ziuyan crater China. *Meteoritics & Planetary Science*, **46**, 729–736.
- CHEN, P., Yu, J. & Jin, Z., 2017, An evaluation of benthic foraminiferal U/Ca and U/Mn proxies for deep ocean carbonate chemistry and redox conditions. *Geochemistry, Geophysics, Geosystems*, **18**, 617–630. <http://dx.doi.org/10.1002/2016GC006730>.
- CHEN, T.-R., Yu, K.-F., Li, S., Price, G. J., Shi, Q. & Wei, G.- J. 2010, Heavy metal pollution recorded in *Porites* corals from Daya Bay, northern South China Sea. *Marine Environmental Research*, **70**, 318–326.
- CIRILLI, S., Marzoli, A., Tanner, L., Bertrand, H., Buratti, N., Jourdan, F., Bellieni, G., Kontak, D. and Renne, P. R. 2009. Latest Triassic onset of the Central Atlantic Magmatic Province (CAMP) volcanism in the Fundy Basin (Nova Scotia): new stratigraphic constraints. *Earth and Planetary Science Letters*, **286**, 514–525.

Quantifying marine redox across the Triassic–Jurassic mass extinction

- CLAPHAM, M. E. & Renne, P. R. 2019. Flood basalts and mass extinctions. *Annual Review of Earth and Planetary Sciences*, **47**, 275–303.
- CLARK, D. L., 1980. Rise and fall of Triassic conodonts. *American Association of Petroleum Geologists Bulletin*. **64**, 691.
- CLARK, D. L., 1981. Extinction of Triassic conodonts. *Abhandlungen der Geologischen Bundesanstalt*, **35**, 193–195.
- CLARK, D. L. 1983. Extinction of conodonts. *Journal of Palaeontology*, **57**, 652–661.
- CLARKSON, M. O., Poulton, S. W., Guilbaud, R. & Wood, R., 2014. Assessing the utility of Fe/Al and Fe-speciation to record water column redox conditions in carbonate-rich sediments. *Chemical Geology*, **382**, 111–122.
- CLÉMENCE, M.-E., Gardin, S., Bartolini, A., Paris, G., Beaumont, V. & Guex, J. 2010. Benthic-planktonic evidence from Austrian Alps for a decline in sea-surface carbonate production at the end of the Triassic. *Swiss Journal of Geoscience*, **103** (2), 293–315.
- COHEN, B. E., Mark, D. F., Lee, M. R. & Simpson, S. L. 2017. A new high-precision $^{40}\text{Ar}/^{39}\text{Ar}$ age for the Rochechouart impact structure: At least 5 Ma older than the Triassic–Jurassic boundary. *Meteoritics & Planetary Science*, **52**(8), 1600–1611.
- COLBERT, E.H., 1949. Progressive adaptations as seen in the fossil record. In: *Jepsen, G.L., Mayr, E., Simpson, G.G. (Eds.), Genetics, Paleontology and Evolution*. Princeton Univ. Press, Princeton, NJ, 390–402.
- COLBERT, E.H., 1958. Triassic tetrapod extinction at the end of the Triassic period. *Proceedings of the National Academy of Science U. S. A.*, **44**, 973–977.
- ČRNE, A. E., Weissert, H., Goričan, S. & Bernasconi, M. 2011. A biocalcification crisis at the Triassic–Jurassic boundary recorded in the Budva Basin (Dinarides, Montenegro). *Geological Society of America Bulletin*, **123**, 40–50.
- CRUSIUS, J., Calvert, S., Pedersen, T. & Sage, D. 1996. Rhenium and molybdenum enrichment in sediments as indicators of oxic, suboxic and sulfidic conditions of deposition. *Earth and Planetary Science Letters*, **145**, 65–78.
- CUVIER, G. 1800. Mémoires sur les espèces d'éléphants vivants et fossiles. Mémoires de l'Institut des Sciences et Arts. Sciences math. et phys. v. 2.
- CUVIER, G. 1813. Essay on the Theory of the Earth, translated by Robert Kerr; With mineralogical notes and an account of Cuvier's geological discoveries by Professor Jameson. Edinburgh, Printed for W. Blackwood; London, J. Murray, R. Baldwin.
- CUVIER, G. 1818. Essay on the Theory of the Earth. New York; Kirk & Marcein.
- CUVIER, G. 1827. Essay on the Theory of the Earth (5th ed.) London: T Cadell.

References

- CUVIER, G. 1831. A discourse on the revolutions of the surface of the globe, and the changes thereby produced in the animal kingdom. Philadelphia : Carey & Lea.
- CUVIER, G. & Brongniart, A. 1808. Essay on the mineralogical geography of the surroundings of Paris. *Annals of the Museum of Natural History*, **11**, 329–375.
- CUVIER, G. & Brongniart, A. 1811. Essay on the mineralogical geography of the Paris area, with a geognostic map, and field sections. Baudouin, Paris, viii, 278 p., 2 pl., 1 card.
- CUVIER, G. & Brongniart, A. 1822. Geological description of the surroundings of Paris, by MM. G. Cuvier and Alex. Brongniart. 428 p., 16 pl., 2 cards.
- DAL CORSO, J., Marzoli, A., Tateo, F., Jenkyns, H. C., Bertrand, H., Youbi, N., Mahmoudi, A., Font, E., Buratti, N. & Cirilli, S. 2014. The dawn of CAMP volcanism and its bearing on the end-Triassic carbon cycle disruption. *Journal of the Geological Society, London*, **171** (2), 153–164.
- DARWIN, C. 1859. On the origin of species by means of natural selection, or preservation of favoured races in the struggle for life. London, John Murray
- DASKALAKIS K. D. & Helz G. R. 1993 The solubility of sphalerite (ZnS) in sulfidic solutions at 25°C and 1 atm pressure. *Geochimica et Cosmochimica Acta*, **57**, 4923–4932.
- DAVELAAR, D. 1993. Ecological significance of bacterial polyphosphate metabolism in sediments, *Hydrobiologia*, **253**, 179–192.
- DAVIES, J. H. F. L., Marzoli, A., Bertrand, H., Youbi, N., Ernesto, M., & Schaltegger, U. 2017. End-Triassic mass extinction started by intrusive CAMP activity. *Nature Communications*, **8**, 15596.
- DE RENZI, M., Budurov, K. & Sudar, M. 1996. The extinction of conodonts- in terms of discrete elements- at the Triassic- Jurassic boundary. *Cuadernos de Geologica Iberica*, **20**, 25–34.
- DE SOUZA, G. F., Vance, D., Sieber, M., Conway, T. M. & Little, S. H. 2022. Reassessing the influence of particle-hosted sulphide precipitation on the marine cadmium cycle. *Geochemica et Cosmochemica Acta*, **322**, 274–296.
- DE VILLIERS, S. 2003, A 425 kyr record of foraminiferal shell weight variability in the western equatorial Pacific *Paleoceanography*, **18**, 146–161.
<https://doi.org/10.1016/j.palaeo.2010.05.034>.
- DEENEN, M. H. L., Ruhl, M., Bonis, N. R., Krijgsman, W., Kuerschner, W. M., Reitsma, M. & van Bergen, M. J. 2010. A new chronology for the end-Triassic mass extinction. *Earth and Planetary Science Letters*, **291**, 113–125.

Quantifying marine redox across the Triassic–Jurassic mass extinction

DETRE, Cs., Dosztály, L. & Hermann, V. 1988. A csővári felső-nóri, sevati fauna (The Upper Norian (Sevatan) fauna of Csővár). A Magyar Állami Földtani Intézet Évi Jelentése az 1986. Evről (Annual Report of the Hungarian Geological Institute, 1986): 53–67.

DICKSON, A., Rees-Owen, R., Maerz, C., Cohen, A., Coe, A. L., Gavrillov, Y., Pancost, R. D. & Shcherbinina, E. 2014, 'The spread of marine anoxia on the Northern Tethys margin during the Paleocene-Eocene Thermal Maximum'. *Paleoceanography*, **29** (6), 471–488.

DICKSON, A. J., Jenkyns, H. C., Porcelli, D., van den Boorn, S. & Idiz, E. 2016. Basin-scale controls on the molybdenum-isotope composition of seawater during the Oceanic Anoxic Event 2 (Late Cretaceous). *Geochimica et Cosmochimica Acta*, **178**, 291–306.

DICKSON, A. J., Bagard, M.-L., Katchinoff, J. A. R., Davies, M., Poulton, S. W. & Cohen, A. S. 2017. A molybdenum-isotope perspective on Phanerozoic deoxygenation events. *Nature Geoscience*, **10**, 721–726.

DICKSON, A. J., Idiz, E., Porcelli, D., & van den Boorn, S. H. J. M., 2020, The influence of thermal maturity on the stable isotope compositions and concentrations of molybdenum, zinc and cadmium in organic-rich marine mudrocks. *Geochimica et Cosmochimica Acta*, **287**, 205–220.

DICKSON, A. J. *et al.* 2021. Isotopic constraints on ocean redox at the end of the Eocene. *Earth and Planetary Science Letters* 562, 116814.

DICKSON, A. J., Idiz, E., Porcelli, D., Murphy, M. J., Celestino, R., Jenkyns, H. C., Poulton, S. W., Hesselbo, S. P., Hooker, J. N., Ruhl, M. & van den Boorn, S. H. J. M., 2022. No effect of thermal maturity on the Mo, U, Cd, and Zn isotope compositions of Lower Jurassic organic-rich sediments. *Geology*, **50** (5), 598–602.
<https://doi.org/10.1130/G49724.1>

DRUCE, M., Stirling, C. H., Bostock, H. C. & Rolison, J. M. 2022, Examining the effects of chemical cleaning, leaching, and partial dissolution on zinc and cadmium isotope fractionation in marine carbonates: *Chemical Geology*, **592**, 120738.

DRUCKENMILLER, P. S., Kelley, N. P., Metz, E. T. & Baichtal, J. 2020. An articulated Late Triassic (Norian) thalattosauroid from Alaska and ecomorphology and extinction of Thalattosauria. *Scientific Reports*, **10**, 1746.

DU, Y., Chiari, M., Viktor, K., Nicora, A., Onoue, T., Pálffy, J., Roghi, G., Tomimatsu, Y. & Rigo, M. 2020. The asynchronous disappearance of conodonts: New constraints from Triassic–Jurassic boundary sections in the Tethys and Panthalassa. *Earth-Science Reviews*, **203**, 1–18.

DUNHILL, A. M., Foster, W. J., Sciberras, J. & Twitchett, R. J. 2018. Impact of the late Triassic mass extinction on functional diversity and composition of marine ecosystems. *Palaeontology*, **61**, 133–148.

References

- EL SHAARAWY, Z. 1981: Foraminifera and ostracods of the topmost Triassic and basal Jurassic of England, Wales and Austria. Unpublished PhD thesis. University of Birmingham.
- ERICKSON, B. E. & Helz, G. R., 2000. Molybdenum (VI) Speciation in Sulfidic Waters: Stability and Lability of Thiomolybdates. *Geochimica et Cosmochimica Acta*, **64**, 1149–1158.
- ERNST, R. E. & Youbi N. 2017. How Large Igneous Provinces affect global climate, sometimes cause mass extinctions, and represent natural markers in the geological record. *Palaeogeography, Palaeoclimatology, Palaeoecology*, **478**, 30–52.
- EVENICK, J. C., 2021. Examining the relationship between Tmax and vitrinite reflectance: An empirical comparison between thermal maturity indicators. *Journal of Natural Gas Science and Engineering*, 91, 103946, <https://doi.org/10.1016/j.jngse.2021.103946>.
- FAZZUOLI, M. & Orti, L. 2009. Remarks on the supposed bolide impacts at the T/J boundary in the Corfino Section (Northern Apennines, Italy). *Volumina Jurassica*, **7**, 3–8.
- FISCHER, J., Voigt, S., Franz, M., Schneider, J.W., Joachimski, M.M., Tichomirowa, M., Götze, J. & Furrer, H., 2012. Palaeoenvironments of the late Triassic Rhaetian Sea: implications from oxygen and strontium isotopes of hybodont shark teeth. *Palaeogeography, Palaeoclimatology, Palaeoecology*, **353–355**, 60–72.
- FLÜGEL, E., 1975. Fossile Hydrozoan-Kenntnisse und Probleme. *Palaöntologie Z.* **49**, 369 – 406.
- FLÜGEL, E. 2002. Triassic Reef Patterns. *SEPM Special Publication*, **72**, 391–463.
- FLÜGEL, E. & Kiessling, W. 2002. Patterns of Phanerozoic Reef Crises. *SEPM Special Publication*, **72**, 691–733.
- FONT, E., Adatte, T., Sial, A., N., Drude de Lacerda, L., Keller, G., & Punekar, J. 2016. Mercury anomaly, Deccan volcanism, and the end-Cretaceous mass extinction. *Geology*, **44** (2), 171–174.
- FOOTE, M. 1999. Morphological diversity in the evolutionary radiation of Paleozoic and post-Paleozoic crinoids. *Paleobiology*, **25** (suppl.), 1–115.
- FOOTE, M. 2000. Origination and extinction components of taxonomic diversity; generally problems. p. 74–102 In D. H. Erwin and S. L. Wing (eds.), *Deep Time: Paleobiology's Perspective*. *Paleobiology*, **26** (suppl.).
- FOOTE, M. 2003. Origination and Extinction through the Phanerozoic: A New Approach. *The Journal of Geology*, **111** (2), 125–148.
- FOOTE, M. 2005. Pulsed Origination and Extinction in the Marine Realm. *Paleobiology*, **31** (1), 6–20.

Quantifying marine redox across the Triassic–Jurassic mass extinction

FOOTE, M. 2007. Extinction and quiescence in marine animal genera. *Paleobiology*, **33** (2), 261–272.

FORCE, E. R. & Maynard, J. B. 1991. Manganese: Syngenetic deposits on the margins of anoxic basins In: Force, E. R., Eidel, J. J. & Maynard, J. B. (Eds.) *Sedimentary and Diagenetic Mineral Deposits, a Basin Analysis Approach to Exploration, Reviews in Economic Geology*, 5, 147–161.

FOSTER, W. J. & Twitchett, R. J. 2014. Functional diversity of marine ecosystems after the Late Permian mass extinction event. *Nature Geoscience*, **7**, 233–238

FOWELL, S. J., Cornet, B. & Olsen, P. E. 1994. Geologically rapid Late Triassic extinctions: Palynological evidence from the Newark Supergroup in Klein, G. D., ed., *Pangea: Paleoclimate, Tectonics, and Sedimentation During Accretion, Zenith, and Breakup of a Supercontinent*: Boulder, Colorado, *Geological Society of America*, Special Paper 288, 197–206.

FOX, C. P., Cui, X., Whiteside, J. H., Olsen, P. E., Summons, R. E. & Grice, K. 2020. Molecular and isotopic evidence reveals the end-Triassic carbon isotope excursion is not from massive exogenous light carbon. PNAS, article info pending
FOX, C. P., Whiteside, J. H., Olsen, P. E., Grice, K., 2022a. Flame out! End-Triassic mass extinction polycyclic aromatic hydrocarbons reflect more than just fire. *Earth and Planetary Science Letters*, **584**, 117418, <https://doi.org/10.1016/j.epsl.2022.117418>.

FOX, C. P., Whiteside, J. H., Olsen, P. E., Cui, Xingqian, Summons, R. E., Idiz, E., Grice, K., 2022b. Two-pronged killing mechanism at the end-Triassic mass extinction. *Geology*, 50 (4), 448–453, <https://doi.org/10.1130/G49560.1>.

FRAMSON, P. E. & LECKIE, J. O. 1978. Limits of coprecipitation of cadmium and ferrous sulfides, *Environmental Science and Technology*, **12**, 465–469.

FRENCH B. M. 1998. *Traces of Catastrophe: A Handbook of Shock-Metamorphic Effects in Terrestrial Meteorite Impact Structures*. LPI Contribution 954. Houston, Texas: Lunar and Planetary Institute. 120 p.

GALLET, Y., Krystyn, L., Besse, J. & Marcoux, J. 2003. Improving the Upper Triassic numerical time scale from cross-correlation between Tethyan marine sections and the continental Newark basin sequence. *Earth and Planetary Science Letters*, **212**, 255–261.

GALLET, Y., Krystyn, L., Marcoux, J. & Besse, J. 2007. New constraints on End-Triassic (Upper Norian–Rhaetian) magnetostratigraphy. *Earth and Planetary Science Letters*, **255**, 458–470.

GALLI, M. T., Jadoul, F., Bernasconi, S. M. & Weissert, H. 2005. Anomalies in global carbon cycling and extinction at the Triassic/Jurassic boundary: evidence from a marine C-isotope record. *Palaeogeography, Palaeoclimatology, Palaeoecology*, **216**, 203–214.

GALLI, M. T., Jadoul, F., Bernasconi, S. M., Cirilli, S. & Weissert, H. 2007. Stratigraphy and palaeoenvironmental analysis of the Triassic–Jurassic transition in the

References

western Southern Alps (Northern Italy). *Palaeogeography, Palaeoclimatology, Palaeoecology*, **244**, 52–70.

GE, Y., Shi, M., Steuber, T., Al-Suwaidi, A. H. & Suarez, M. B. 2018. Environmental change during the Triassic-Jurassic boundary interval of an equatorial carbonate platform: Sedimentology and chemostratigraphy of the Ghalilah Formation, United Arab Emirates. *Palaeogeography, Palaeoclimatology, Palaeoecology*, **502**, 86–103.

GINGRAS, M. K., MacEachern, J. A. & Dashtgard, S. E. 2012. The potential of trace fossils as tidal indicators in bays and estuaries. *Sediment. Geology*, **279**, 97–106.

GLASS, B., Koeberl, C., Kirkham, A. 2003. Invited comments on Kirkham's 'Glaucinitic spherules from the Triassic of the Bristol Area, SW England: probable microtektite pseudomorphs'. *Proceedings of the Geologists' Association*, **114**, 11–21.

GLOCK, N., Liebetrau, V., Eisenhauer, A. & Rocholl, A. 2016. High resolution I/Ca ratios of benthic foraminifera from the Peruvian oxygen-minimum-zone: A SIMS derived assessment of a potential redox proxy *Chemical Geology*, **447**, 40–53.
<http://doi.org/10.1016/j.chemgeo.2016.10.025>.

GOLBRANT, O., Leroux, H., Doukhan, J.-C. & Cordier, P. 1992. Formation mechanisms of planar deformation features in naturally shocked quartz. *Physics of the Earth and Planetary Interiors*, **74** (3-4), 219–240.

GOLDBERG, T., Gordon, G., Izon, G., Archer, C., Pearce, C. R., McManus, J., Anbar, A. D., & Rehkämper, M. 2013. Resolution of inter-laboratory discrepancies in Mo isotope data: an intercalibration. *Journal of Analytical Atomic Spectrometry*, **28** (5), 724–735.

GÖTZ, A. E., Ruckwied, K., Pálffy, J. & Haas, J. 2009. Palynological evidence of synchronous changes within the terrestrial and marine realm at the Triassic/Jurassic boundary (Csövár section, Hungary). *Review of Palaeobotany and Palynology*, **156**, 401–409.

GREENE, S. E., Martindale, R. C., Ritterbush, K. A., Bottjer, D. J., Corsetti, F. A. & Berelson, W. M. 2012. Recognising ocean acidification in deep time: An evaluation of the evidence for acidification across the Triassic-Jurassic boundary. *Earth-Science Reviews*, **113** (1–2), 72–93.

GRETZ, M., Lathuilière, B., & Martini, R. 2015. A new coral with simplified morphology from the oldest known Hettangian (Early Jurassic) reef in southern France. *Acta Palaeontologica Polonica*, **60** (2), 277–286.

GRICE, K., Cao, C., Love, G. D., Böttcher, M. E., Twitchet, R. J., Grosjean, E., Summons, R. E., Turgeon, S. C., Dunning, W. & Jin, Y. 2005. Photic Zone Euxinia During the Permian-Triassic Superanoxic Event. *Science*, **307**, 706–709.

GUEX, J. 1995. Ammonites hettangiennes de la Gabbs Valley Range (Nevada). *Mémoires de Géologie, Lausanne*, **27**, 1–130.

Quantifying marine redox across the Triassic–Jurassic mass extinction

GUEX, J., Rakus, M., Taylor, D. & Bucher H. 1997. The Triassic-Jurassic boundary: proposal for a stratotype defined in the Gabbs Valley Range (Nevada), *ISJS Newsletter*, **24**, 26–30.

GUEX, J., Bartolini, A., Taylor, D. 2002. Discovery of Neophyllites (Ammonita, Cephalopoda, Early Hettangian) in the New York Canyon sections (Gabbs Valley Range, Nevada) and discussion of the $\delta^{13}\text{C}$ negative anomalies located around the Triassic–Jurassic boundary. *Bulletin de la Société Vaudoise des Sciences Naturelles*, **88(2)**, 247–255.

GUEX, J., Bartolini, A., Atudorei, V. & Taylor, D. 2003. Two negative $\delta^{13}\text{C}$ excursions near the Triassic–Jurassic boundary in the New York Canyon area (Gabbs Valley Range, Nevada). *Bulletin de Géologie, Université Lausanne*, **1–4** (Special Issue).

GUEX, J., Bartolini, A., Atudorei, V. & Taylor, D. 2004. High-resolution ammonite and carbon isotope stratigraphy across the Triassic–Jurassic boundary at New York Canyon (Nevada). *Earth and Planetary Science Letters*, **225**, 29–41.

GUEX, J., Schoene, B., Bartolini, A., Spangenberg, J., Schaltegger, U., O’Dogherty, L., Taylor, D., Bucher, H. & Atudorei, V. 2012. Geochronological constraints on post-extinction recovery of the ammonoids and carbon cycle perturbations during the Early Jurassic. *Palaeogeography, Palaeoclimatology, Palaeoecology*, **346–347**, 1–11.

GUEX, J. (ed.) 2016. Heteromorph Ammonites and Uncoiling of Nautilus Above the Permian Triassic Boundary In Retrograde Evolution During Major Extinction Crises, Springer, Switzerland, 89 pp.

HAAS, J., TARDI-FILÁ CZ, E., ORAVE CZ-SCHEFFER, A., GÓ CZÁN, F. & DOSZTÁ LY, L. 1997. Stratigraphy and sedimentology of an Upper Triassic toe-of-slope and basin succession at Csővár, Hungary. *Acta Geologica Hungarica*, **40** (2), 111–177.

HAAS, J. and Tardy-Filá cz, E., 2004, Facies changes in the Triassic–Jurassic boundary interval in and intraplatform basin succession at Csővár (Transdanubian Range, Hungary): *Sedimentary Geology*, **168**, 19–48. Doi:10.1016/j.sedgeo.2004.03.002.

HAAS, J., Götz, A. E. & Pál fy, J., 2010, Late Triassic to Early Jurassic palaeogeography and eustatic history in the NW Tethyan realm: New insights from sedimentary and organic facies of the Csővár Basin (Hungary). *Palaeogeography, Palaeoclimatology, Palaeoecology*, **291**, 456–468.

HALLAM, A. 1981. THE END-TRIASSIC BIVALVE EXTINCTION EVENT. *Palaeogeography, Palaeoclimatology, Palaeoecology*, **35**, 211–225.

HALLAM, A. 1995: Major bio-events in the Triassic and Jurassic. In Walliser, O.H. (ed.): *Global events and Event Stratigraphy*, 265–283. Springer-Verlag, Berlin.

HALLAM, A. & Wignall P. B. 1997. Mass Extinctions and their Aftermath. Oxford University Press, Oxford, 320 pp.

References

- HALLAM, A. 2002. How catastrophic was the end-Triassic mass extinction? *Lethaia*, **35** (2), 147–157.
- HALLAM, A., & Goodfellow, W. D. 1990. Facies and Geochemical Evidence Bearing on the End-Triassic Disappearance Of the Alpine Reef Ecosystem. *Historical Biology*, **4**, 131–138.
- HANNA, R. G. & Muir, G. L. 1990, Red sea corals as biomonitors of trace metal pollution. *Environmental Monitoring and Assessment*, **14**, 211e222.
- HARDISTY, D. S., Riedinger, N., Planavsky, N. J., Asael, D., Andrén, T., Jørgensen, B. B. & Lyons, T. W. 2016. A Holocene history of dynamic water column redox conditions in the Landsort Deep, Baltic Sea. *American Journal of Science*, **316**, 713–745.
- HARPER, D. A. T., Brunton, C. H. C., Cocks, L. R. M., Copper, P., Doyle, E. N., Jeffrey, A. L., Owen, E. F., Parkes, M. A., Popov, L. E., Prosser, C. D. 1993. Brachiopoda. In: Benton, M.J. (Ed.), *The Fossil Record*, vol. 2. Chapman and Hall, London, pp. 427–462.
- HARPER, E. M., Palmer, T. J. & Alpey, J. R., 1997. Evolutionary response by bivalves to changing Phanerozoic sea-water chemistry. *Geological Magazine*, **134**, 403–407.
- HARPER, E. M. 2005. Fossil Invertebrates: Bivalves: In *Encyclopedia of Geology eds. Selley, E. C., Cocks, E. M. & Plimer, I. R.* 369–378.
- HART, M. B. & Williams, C. L. 1993. Protozoa. In: Benton, M.J. (Ed.), *The Fossil Record*, vol. 2. Chapman and Hall, London, pp. 43–70.
- HASTINGS, D. W., Emerson, S. R., Erez, J. & Nelson, B. K. 1996, Vanadium in foraminiferal calcite: Evaluation of a method to determine paleo-seawater vanadium concentrations. *Geochimica et Cosmochimica Acta*, **60**, 3701–3715.
- HÄUSLER, K., Dellwig, O., Schnetger, B., Feldens, P., Leipe, T., Moros, M., Pollehne, F., Schönke, Wegwerth, A., & Arz, H. W. 2018. Massive Mn carbonate formation in Landsort Deep (Baltic Sea): Hydrographic conditions, temporal succession, and Mn budget calculations. *Marine Geology*, **395**, 260–270.
- HAUTMANN, M. 2004. Effect of end-Triassic CO₂ maximum on carbonate sedimentation and marine mass extinction. *Facies*, **50**, 257–261.
- HAUTMANN, M. 2006. Shell mineralogical trends in epifaunal Mesozoic bivalves and their relationship to seawater chemistry and atmospheric carbon dioxide concentration. *Facies*, **52**, 417–433.
- HAUTMANN, M., Benton, M. J. & Tomašových, A. 2008a. Catastrophic ocean acidification at the Triassic-Jurassic boundary. *Neues Jahrbuch für Geologie und Palaöntologie Abhandlungen*, **249**, 119–127

Quantifying marine redox across the Triassic–Jurassic mass extinction

HAUTMANN, M., Stiller, F., Huawei, C. & Jingeng, S. 2008b. Extinction-recovery pattern of level-bottom faunas across the Triassic–Jurassic boundary in Tibet: Implication for potential killing mechanisms. *Palaios*, **23**, 711–718.

HAUTMANN, M. 2012. Extinction: end-Triassic mass extinction in eLS. John Wiley & Sons Ltd: Chichester. <https://doi.org/10.1002/9780470015902.a0001655.pub3>

HE, T., Dal Corso, J., Newton, R. J., Wignall, P. B., Mills, B. J. W., Todaro, S., Di Stefano, P., Turner, E. C., Jamieson, R. A., Randazzo, V., Rigo, M., Jones, R. E. & Dunhill, A. M. 2020. An enormous sulfur isotope excursion indicates marine anoxia during the end-Triassic mass extinction. *Science Advances*, **6**, 1–8.

HE, T., Wignall, P. B., Newton, R. J., Atkinson, J. W., Keeling, J. F. J., Xiong, Y., Poulton, S. W., 2022a. Extensive marine anoxia in the European epicontinental sea during the end-Triassic mass extinction. *Global and Planetary Change*, **210**, 103771, <https://doi.org/10.1016/j.gloplacha.2022.103771>.

HE, T., Newton, R. J., Wignall, P. B., Reid, S., Dal Corso, J., Takahashi, S., Wu, H., Todaro, S., Di Stefano, P., Randazzo, V., Rigo, M., and Dunhill, A. M., 2022b, Shallow ocean oxygen decline during the end-Triassic mass extinction, *Global and Planetary Change*, **210**, 103770. <https://doi.org/10.1016/j.gloplacha.2022.103770>.

HEBDON, N., Ritterbush, K. & Choi, Y. 2020. Computational fluid dynamics modelling of fossil ammonoid shells. *Palaeontologica Electronica*, **23** (1), 1–18

HEIN, J. R., Koschinsky, A., Halbach, P., Manheim, F. T., Bau, M., Kang, J.-K. & Lubick, N. In Nicklson, K., Hein, J. R., Bühn, B., Dasgupta, S. (eds), 1997, *Manganese Mineralization: Geochemistry and Mineralogy of Terrestrial Deposits*, Geological Society Special Publication, **199**, 123–138.

HELZ, G., Vorliceck, T. 2019. Precipitation of molybdenum from euxinic waters and the role of organic matter. *Chemical Geology*, **509**, 178–193.

HELZ, G. R. Miller, C. V. Charnock, J. M., Mosselmans, J. F. W., Patrick, R. A. D., Garner, C. D. & Vaughan, D. J., 1996. Mechanism of molybdenum removal from the sea and its connections in black shales: EXAFS evidence. *Geochimica et Cosmochimica Acta*, **60** (19), 3631–3642.

HESSELBO, S. P., Robinson, S. A., Surlyk, F., & Piasecki, S. 2002. Terrestrial and marine mass extinction at the Triassic/Jurassic boundary synchronized with initiation of massive volcanism. *Geology*, **30** (3), 251–254.

HESSELBO, S. P., Robinson, S. A. & Surlyk, F. 2004. Sea-level change and facies development across potential Triassic–Jurassic boundary horizons, SW Britain. *Journal of the Geological Society, London*, **161**, 365–379.

HESSELBO, S. P. Bjerrum, C. J., Hinnov, L. A., MacNicaill, C., Miller, K. G., Riding, J. B., van de Schootbrugge, B., and the Mochras Revisited Science Team. 2013. Mochras borehole revisited: a new global standard for Early Jurassic earth history. *Scientific Drilling*, **16**, 81–91.

References

- HESSELBO, S. P., Belcher, C. M., Bjerrum, C. J., Condon, D. J., Hinnov, L. A., Leng, M. J., Lenton, T. M., Little, C. T. S., Mac Niocaill, C., Miller, K. G., Newton, R. J., Poulton, S., Riding, J. B., Ullmann, C. V., Van De Schootbrugge, B., Wignall, P., Wonik, T., Bogus, K., Al-Suwaidi, A., Baker, S., Boomer, I., Bos, R., Browning, J., Butcher, A., Copestake, P., Daines, S., Damaschke, M., Damborenea, S., Deconinck, J. F., Dickson, A., Donnadieu, Y., Elson, A., Fendley, I., Fraguas, A., Frieling, J., Gibson, T. A., He, T., Holford, S., Hollaar, T. P., Huang, C. J., Hudson, A., Idiz, E., Jenkyns, H. J., Jiang, M., Johnson, B., Korte, C., Kovacs, E., Krijgsman, W., Leu, K., Mancenido, M., Mather, T., Mattioli, E., Meister, C., O'Keeffe, C., Page, K., Palfy, J., Pienkowski, G., Riccardi, A., Robinson, E. J., Roper, A., Ruhl, M., Stanley, J. N., Storm, M., Suan, G., Szűcs, D., Teichert, B., Thibault, N., Turner, J., Uchman, A., Vickers, M., Wadas, S., Whiteside, J. & Xu, W. (19–30 April, 2021). Initial results from coring at Prees, Cheshire Basin, UK, and future plans for the Early Jurassic Earth System and Timescale Project (JET). [Conference Presentation]. EGU 2021, Online.
- HEUNISCH, C. Luppold, F. W., Reinhardt, L. & Röhling, H.G. 2010. Palynofazies, Bio- und Lithostratigrafie im Grenzbereich Trias/Jura in der Borung Mariental (Lappwaldmulde, Ostniedersachsen). *Zeitschrift der Deutschen Gesellschaft für Geowissenschaften*, **161**, 51–98.
- HILDEBRAND, A. R. Penfield, G. T., Kring, D. A., Pilkington, M., Camargo-Zanoguera, A., Jacobsen, S. B. & Boynton, W. B. 1991. Chicxulub Crater: A possible Cretaceous/Tertiary boundary impact crater on the Yucatán Peninsula, Mexico. *Geology*, **19** (9), 867–871.
- HILLEBRANDT, A. v., Krystyn, L. & Kuerschner, W. M. 2007. A candidate GSSP for the base of the Jurassic in the Northern Calcareous Alps (Kuhjoch section, Karwendel Mountains, Tyrol, Austria). *ISJS Newsletter*, **34** (1), 2–20.
- HILLEBRANDT, A. v. & Krystyn, L. 2009. On the oldest Jurassic ammonite of Europe (Northern Calcareous Alps, Austria) and their global significance. *Neues Jahrbuch für Geologie und Paläontologie, Abh.* **253** (2-3), 163–195.
- HILLEBRANDT, A. v., Krystyn, L., Kürschner, W. M., Bonis, N. R., Ruhl, M., Richoz, S., Schobben, M. A. N., Urlichs, M., Bown, P. R., Kment, K., McRoberts, C. A., Simms, M. & Tomášovych, A. 2013. The Global Stratotype Sections and Point (GSSP) for the base of the Jurassic System at Kuhjoch (Karwendel Mountains, Northern Calcareous Alps, Tyrol, Austria). *Episodes*, **36** (3), 162–198.
- HO, T.-Y., Quigg, A., Finkel, Z. V., Milligan, A. J., Wyman, K., Falkowski, P. G. & Morel, F. M. M., 2003. The elemental composition of some marine phytoplankton. *Journal of Phycology*, **39**, 1145–1159.
- HODGES, M. S., & Stanley, G. D. 2015. North American coral recovery after the end-Triassic mass extinction, New York Canyon, Nevada, USA. *GSA Today*, **25**(10), 4–9.
- HODYCH, J. & Dunning, G. 1992. Did the Manicouagan impact trigger end-of-Triassic mass extinction? *Geology*, **20** (51), 51–54.

Quantifying marine redox across the Triassic–Jurassic mass extinction

- HOFMANN, R., Mángano, M. G., Elicki, O. & Shinaq, R. 2012. Paleoecologic and biostratigraphic significance of trace fossils from shallow- to marginal-marine environments from the middle Cambrian (Stage 5) of Jordan. *Journal of Paleontology*, **86** (6), 931–955.
- HOLBROOK, W. S. & Kelemen, P. B. 1993. Large igneous province on the US Atlantic margin and implications for magmatism during continental breakup. *Nature*, **364**, DOI: 10.1038/364433a0.
- HOLLAAR, T. P., Baker, S. J., Hesselbo, S. P., Deconinck, J.-F., Mander, L., Ruhl, M. & Belcher, C. M. 2021. Wildfire activity enhanced during phases of maximum orbital eccentricity and precessional forcing in the Early Jurassic. *Communication Earth and Environment*, **2**, 247.
- HÖNIG, M. R., John, C. M. & Manning, C. 2017. Development of an equatorial carbonate platform across the Triassic–Jurassic boundary and links to global palaeoenvironmental changes (Musandam Peninsula, UAE/Oman). *Gondwana Research*, **45**, 100–117.
- HÖNISCH, B., Ridgwell, A., Schmidt, D. N., Thomas, E., Gibbs, S. J., Sluijs, A., Zeebe, R., Kump, L., Martindale, R. C., Greene, S. E., Kiessling, W., Ries, J., Zachos, J. C., Royer, D. L., Barker, S., Marchitto Jr., T. M., Moyer, R., Pelejero, C., Ziveri, P., Foster, G. L. & Williams, B. 2012. The Geological Record of Ocean Acidification. *Science*, **335** (6072), 1058–1063.
- HORI, R. 1992. Radiolarian biostratigraphy at the Triassic/Jurassic period boundary in bedded cherts from the Inuyama area, central Japan. *J. Geoscience Osaka City University*, **35**, 53–65.
- HORI, R. S., Fujiki, T., Inoue, E., Kimura, J.-I., 2007. Platinum group element anomalies and bioevents in the Triassic–Jurassic deep-sea sediments of Panthalassa. *Palaeogeography, Palaeoclimatology, Palaeoecology*, **244**, 391–406.
- HORNUNG, T., Krystyn, L., & Brandner, R. 2007. A Tethys-wide mid-Carnian (Upper Triassic) carbonate productivity crisis: Evidence for the Alpine Reingraben Event from Spiti (Indian Himalaya)?, *Journal of Asian Earth Sciences*, **30**, 285–302
- HOUNSLOW, M. W., Posen, P. E. & Warrington, G. 2004. Magnetostratigraphy and biostratigraphy of the Upper Triassic and lowermost Jurassic succession, St. Audrie's Bay UK. *Palaeogeography, Palaeoclimatology, Palaeoecology*, **213**, 331–358.
- HOUSE, M. R. 1963. Burst in evolution. *Advances in Science*, **19**, 499–507.
- HOUSE, M. R. 1989. Ammonoid extinction events. *Philosophical Transactions of the Royal Society B London*, **325**, 307–326.
- HOWARD, A. S., Warrington, G., Ambrose, K. & Rees, J. G., 2008, A formational framework for the Mercia Mudstone Group (Triassic) of England and Wales: British Geological Survey, Research Report RR/08/04, 41 p.

References

- HUTTON, J. 1788. Theory of the Earth. Transactions of the Royal Society of Edinburgh, Vol. 1., Part 2, 209–304.
- IBARRA, Y., Corsetti, F. A., Greene, S. E. & Bottjer, D. J. 2016. A microbial carbonate response in synchrony with the end-Triassic mass extinction across the SW UK. *Scientific Reports*, **6**, 19808.
- IKEDA, M., Hori, R., Okada, Y. & Nakada, R. 2015. Volcanism and deep-ocean acidification across the end-Triassic extinction event. *Palaeogeography, Palaeoclimatology, Palaeoecology*, **440**, 725–733.
- INGALL, E. & Jahnke, R. 1994. Evidence for enhanced phosphorus regeneration from marine sediments overlain by oxygen depleted waters. *Geochimica et Cosmochimica Acta*, **58**, 2571–2575.
- INGALL, E. D. & Van Cappellen, P., 1990. Relation between sedimentation rate and burial of organic phosphorus and organic carbon in marine sediments. *Geochimica et Cosmochimica Acta*, **54**, 373–386.
- INGALL, E., Kolowith, L., Lyons, T. & Hurtgen, M. 2005. Sediment carbon, nitrogen and phosphorus cycling in an anoxic fjord, Effingham Inlet, British Columbia. *American Journal of Science*, **305**, 240–258.
- IPCC *Climate Change 2021: The Physical Science Basis* (eds Masson-Delmotte, V. et al.) Cambridge Univ. Press 2021).
- IVIMEY-COOK, H. C. 1975. The stratigraphy of the Rhaetic and Lower Jurassic in East Antrim. *Bulletin of the Geological Survey of Great Britain*, **50**, 51–69.
- JADOUL, F., & Galli, M. T. 2008. The Hettangian shallow water carbonates after the Triassic/Jurassic biocalcification crisis: The albenza formation in the Western Southern ALPS. *Rivista Italiana Di Paleontologia e Stratigrafia*, **114** (3), 453–470.
- JANSSEN, D. J., CONWAY, T., JOHN, S. G., CHRISTIAN, J. R., KRAMER, D. I., PEDERSEN, T. F. & CULLEN, J. T. 2014. Undocumented water column sink for cadmium in open ocean oxygen-deficient zones. *PNAS*, **111**(19), 6888–6893.
- JARAULA, C. M. B., Grice, K., Twitchett, R. J., Böttcher, M. E., LeMetayer, P., Dastidar, A. G. & Opazo, L. F., 2013. Elevated $p\text{CO}_2$ leading to Late Triassic extinction, persistent photic zone euxinia, and rising sea levels. *Geology*, **41** (9), 955–958.
- JENKYNS, H. C. & Clayton, C. J. 1997. Lower Jurassic epicontinental carbonates and mudstones from England and Wales: chemostratigraphic signals and the early Toarcian anoxic event. *Sedimentology*, **44**, 687–706.
- JENKYNS, H. C., Dickson, A. J., Ruhl, M., & van den Boorn, S. H. J. M., 2017, Basalt-seawater interaction, the Plenus Cold Event, enhanced weathering and geochemical change: deconstructing Oceanic Anoxic Event 2 (Cenomanian–Turonian, Late Cretaceous), *Sedimentology*, **64**, 16–43. <https://doi.org/10.1111/sed.12305>.

Quantifying marine redox across the Triassic–Jurassic mass extinction

JERAM, A. J., Simms, M. J., Hesselbo, S. P. & Raine, R., 2021. Carbon isotopes, ammonites and earthquakes: Key Triassic–Jurassic boundary events in the coastal sections of south-east County Antrim, Northern Ireland, UK. *Proceedings of the Geological Association*, **132**, 702–725.

JIANG, W., Yu, K.-F., Song, Y.-X., Zhao, J.-X., Feng, Y.-X., Wang, Y.-H. & Xu, S.-D. 2017. Coral trace metal of natural and anthropogenic influences in the northern South China Sea. *Science of the Total Environment*, **607–608**, 195–203.

JOST, A. B., Bachan, A., van de Schootbrugge, B., Brown, S. T., DePaolo, D. J., Payne, J. L., 2017a. Additive effects of acidification and mineralogy on calcium isotopes in Triassic/Jurassic boundary limestones. *Geochemistry, Geophysics, Geosystems*, **18** (1), 113–124.

JOST, A. B., Bachan, A., van de Schootbrugge, B., Lau, K. V., Weaver, K. L., Maher, K., Payne, J. L., 2017b. Uranium isotope evidence for an expansion of marine anoxia during the end-Triassic extinction. *Geochemistry, Geophysics, Geosystems*, **18** (8), 3093–3108.

JOURDAN, F., Marzoli, A., Bertrand, H., Cirilli, S., Tanner, L. H., Kontak, D. J., McHone, G., Renne, P. R. & Bellieni, G. 2009. $^{40}\text{Ar}/^{39}\text{Ar}$ ages of CAMP in North America: Implications for the Triassic–Jurassic boundary and the ^{40}K decay constant bias. *Lithos*, **110**, 167–180.

KARÁDI, V., Cau, A., Mazza, M. & Rigo, M. 2020. The last phase of conodont evolution during the Late Triassic: Integrating biostratigraphic and phylogenetic approaches. *Palaeogeography, Palaeoclimatology, Palaeoecology*, **549**, 1–12.

KASPRAK, A. H., Sepulveda, J., Price-Waldman, R., Williford, K. H., Schoepfer, S. D., Haggart, J. W., Ward, P. D., Summons, R. E., Whiteside, J. H., 2015. Episodic photic zone euxinia in the northeastern Panthalassic Ocean during the end-Triassic extinction. *Geology*, **43**, 307–310.

KENDALL, B., Dahl, T. W. & Anbar, A. D. 2017. The stable isotope geochemistry of molybdenum. *Reviews in Mineralogy and Geochemistry*, **82**, 683–732.

KENNEDY, W. J. 1977. Ammonite evolution. In: *Hallam A (ed) Patterns of evolution as illustrated in the fossil record*. Elsevier, Amsterdam, pp 251–304.

KENT, D. V. & Olsen, P.E., 2008. Early Jurassic magnetostratigraphy and paleolatitudes from the Hartford continental rift basin (eastern North America): Testing for polarity bias and abrupt polar wander in association with the central Atlantic magmatic province. *Journal of Geophysical Research B: Solid Earth*, **113** (6), 1–24.

KERL, C. F., Lohmayer, R., Bura-Nakić, E., Vance, D. & Planer-Friedrich, B. 2017. Experimental confirmation of isotope fractionation in thiomolybdates using ion chromatographic separation and detection by multicollector ICPMS. *Analytical Chemistry*, **89** (5), 3123–3129.

References

- KERSHAW, S. & GUO, L. 2016. Beef and cone-in-cone calcite fibrous cements associated with the end-Permian and end-Triassic mass extinctions: Reassessment of processes of formation. *Journal of Palaeogeography*, **5** (1), 28–42.
- KIDDER, D. L. & Erwin D. H. 2001. Secular distribution of biogenic silica through the Phanerozoic: comparison of silica-replaced fossils and bedded cherts at the series level. *Journal of Geology*, **109**, 509–522.
- KIESSLING, W., Flugel, E., & Golonka, J. 2000. Fluctuations in the carbonate production of Phanerozoic reefs. *Geological Society, London, Special Publications*, **178**, 191–215.
- KIESSLING, W., Aberhan, M., Brenneis, B., & Wagner, P. J. 2007. Extinction trajectories of benthic organisms across the Triassic-Jurassic boundary. *Palaeogeography, Palaeoclimatology, Palaeoecology*, **244** (1–4), 201–222.
- KIESSLING, W., Roniewicz, E., Villier, L., Léonide, P., & Struck, U. 2009. An early Hettangian coral reef in southern France: Implications for the end-Triassic reef crisis. *Palaios*, **24** (10), 657–671.
- KIESSLING, W., & Danelian, T. 2011. Trajectories of late Permian - Jurassic radiolarian extinction rates: No evidence for an end-Triassic mass extinction. *Fossil Record*, **14** (1), 95–101.
- KIESSLING, W., & Simpson, C. 2011. On the potential for ocean acidification to be a general cause of ancient reef crises. *Global Change Biology*, **17**(1), 56–67.
- KING, E. K., Perakis, S. S., & Pett-Ridge, J. C. 2018. Molybdenum isotope fractionation during adsorption to organic matter. *Geochimica et Cosmochimica Acta*. **222**, 584–598.
- KIRKHAM, A. 2002. Triassic microtektite pseudomorphs of the Bristol area. *Geoscientist*, **12**, 17–18.
- KIRKHAM, A. 2003. Glauconitic spherules from the Triassic of the Bristol Area, SW England: probable microtektite pseudomorphs. *Proceedings of the Geologists' Association*, **114**, 11–21.
- KNAUER, G., Martin, J. & Gordon, R., 1982. Cobalt in north-east Pacific waters. *Nature*, **297**, 49–51.
- KOCSIS, Á. T., Kiessling, W. & Pálffy, J. 2014. Radiolarian diversity dynamics through the Triassic and Jurassic: implications for proximate causes of the end-Triassic mass extinction. *Paleobiology*, **40**(4), 625–639.
- KOLAR-JURKOVŠEK, T. 2011. Latest Triassic conodonts of the Slovenian Basin and some remarks on their evolution. *Geologija*, **54**(1), 81–90.
- KORTE, C., Hesselbo, S. P., Jenkyns, H. C., Rickaby, R. E. M. & Spötl, C. 2009. Palaeoenvironmental significance of carbon- and oxygen-isotope stratigraphy of marine

Quantifying marine redox across the Triassic–Jurassic mass extinction

Triassic–Jurassic boundary sections in SW Britain. *Journal of the Geological Society, London*, **166**, 431–445.

KORTE, C., Ruhl, M., Pálffy, J., Ullmann, C. V. & Hesselbo, S. P., 2019. Chemostratigraphy Across the Triassic–Jurassic Boundary, *Geophysical Monograph*, **240**, 183–210.

KOVÁCS, E. B., Ruhl, M., Demény, A., Fórizs, I., Hegyi, I., Horváth-Kostva, Z. R., Móricz, F., Vallner, Z. & Pálffy, J. 2020. Mercury anomalies and carbon isotope excursions in the western Tethyan Csővár section support the link between CAMP volcanism and the end-Triassic extinction. *Global and Planetary Change*, **194**, 103291.

KOZUR, H. 1993. First evidence of Liassic in the vicinity of Csővár (Hungary), and its paleogeographic and paleotectonic significance. *Jahrbuch der Geologischen Bundesanstalt*, **136** (1), 89–98.

KOZUR, H., & Mock, R. 1991. New Middle Carnian and Rhaetian conodonts from Hungary and the Alps, stratigraphic importance and tectonic implications for the Buda Mountains and adjacent areas. *J. Geol. Bundesanst.* **134**, 271–297.

KOZUR, H. & Mostler, H. 1973. Mikrofaunistische Untersuchungen der Triasschollen im Raume Csővár, Ungarn. *Verhandlungen der Geologischen Bundesanstalt*, **2**, 291–325.

KRYSTYN, L., Gallet, Y., Besse, J. & Marcoux, J. 2002. Integrated Upper Carnian to Lower Norian biochronology and implications for the Upper Triassic magnetic polarity time scale. *Earth and Planetary Science Letters*, **203**, 343–351.

KUERSCHNER, W. M., Bonis, N. R. & Krystyn, L. 2007. Carbon-isotope stratigraphy and palynostratigraphy of the Triassic–Jurassic transitions in the Tiefengraben section — Northern Calcareous Alps (Austria). *Palaeogeography, Palaeoclimatology, Palaeoecology*, **244** (1–4), 257–280.

KUMMEL, B. 1957. Triassic Ammonoidea. In: Arkell, W. J., Furnish, W. M., Kummel, B., Miller, A. K., Moore, R. C., Schindewolf, O., Sylvester-Bradley, P. C., Wright, C. W. (eds) *Treatise on invertebrate paleontology, Part L, Mollusca 4, Cephalopoda*. Geol Soc Amer. University of Kansas Press, Denver, University of Kansas

KÜRSCHNER, W. M., Batenburg, S. J. & Mander, L., 2013. Aberrant *Classopollis* pollen reveals evidence for unreduced ($2n$) pollen in the conifer family Cheirolepidiaceae during the Triassic–Jurassic transition. *Proceedings of the Royal Society B*, **280**, 20131708.

KÜRCHNER, W. M., Mander, L. & McElwain, J. C., 2014. A gymnosperm affinity for *Ricciisporites tuberculatus* Lundblad: implications for vegetation and environmental reconstructions in the Late Triassic. *Palaeobiodiversity and Palaeoenvironments*, **94** (2), 295–305.

References

- KURODA, J., Hori, R. S., Suzuki, K., Gröcke, D. R., & Ohkouchi, N. 2010. Marine osmium isotope record across the Triassic-Jurassic boundary from a Pacific pelagic site. *Geology*, **38** (12), 1095–1098.
- LABORDE-CASADABAN, M., Homberg, C., Schnyder, J., Borderie, S. & Raine, R., 2021. Do soft sediment deformations in the Late Triassic and Early Jurassic of the UK record seismic activity during the break-up of Pangaea? *Proceedings of the Geological Association*, **132**, 688–701.
- LEE, J.-H. & Riding, R. 2018. Marine oxygenation, lithistid sponges, and the early history of Paleozoic skeletal reefs. *Earth-Science Reviews*, **18**, 98–121
- LEINFELDER, R. R., Schmid D. U., Nose, M. & Werner W. 2002. Jurassic reef patterns-the expression of a changing globe. In: *Kiessling W, Flügel E, Golonka J (eds) Phanerozoic reef patterns*, SEPM Special Publication 72, Tulsa. pp. 465–520.
- LENZ, C., Behrends, T., Jilbert, T., Silveira, M. & Slomp, C. P. 2014. Redox-dependent changes in manganese speciation in Baltic Sea sediments from the Holocene Thermal Maximum: An EXAFS, XANES and LA-ICP-MS study, *Chem. Geol.*, **370**, 49–57.
- LENZ, C., Jilbert, T., Conley, D. J., Wolthers, M & Slomp., C. P. 2015. Are recent changes in sediment manganese sequestration in the euxinic basins of the Baltic Sea linked to the expansion of hypoxia. *Biogeosciences*, **12**, 4875–4894.
- LI, J., Song, H., Tian, L., Bond, D. P. G., Song, H., Du, Y., Zhang, C., Chu, D., Wignall, P. B. & Tong, J. 2022. Dynamic ocean redox conditions during the end-Triassic mass extinction: Evidence from pyrite framboids. *Global and Planetary Change*, **218**, 103981.
- LI, L., Wang, Y., Vajda, V. & Liu, Z., 2018. Late Triassic ecosystem variations inferred by palynological records from Hechuan, southern Sichuan Basin, China. *Geological Magazine*, **155** (8), 1793–1810.
- LIMBURG, K. E., Breitburg, D., Swaney, D. P. & Jacinto, G. 2020. Ocean Deoxygenation: A Primer. *One Earth*, **2** (1), 24–29.
- LINDSTRÖM, S. 2021. Two-phased Mass Rarity and Extinction in Land Plants During the End-Triassic Climate Crisis. *Frontiers in Earth Science*, **9**, 780343.
- LINDSTRÖM, S., van de Schootbrugge, B., Dybkjaer, K., Pederson, G. K., Fiebig, J., Nielsen, L. H. & Richoz, S. 2012. No causal link between terrestrial ecosystem change and methane release during the end-Triassic mass extinction. *Geological Society of America*, **40** (6), 531–534.
- LINDSTRÖM, S. 2015. Palynofloral patterns of terrestrial ecosystem change during the end-Triassic event – a review. *Geological Magazine*, **153**, Special Issue 2: Mass Extinctions, March 2016, 223–251.

Quantifying marine redox across the Triassic–Jurassic mass extinction

LINDSTRÖM, S. 2021. Two-phased Mass Rarity and Extinction in Land Plants During the End-Triassic Climate Crisis. 2021. *Frontiers in Earth Science*, **9**, 780343.

LINDSTRÖM, S., Pederson, G. K., van de Schootbrugge, B., Hansen, K. H., Kuhlmann, N., Thein, J., Johansson, L., Petersen, H. I., Alwmark, C., Dybkjær, K., Weibel, R., Erlström, M., Nielsen, H. N. Oschmann, W. & Tegner, C. 2015. Intense and widespread seismicity during the end-Triassic mass extinction due to emplacement of a large igneous province. *Geology*, **43(5)**, 387–390.

LINDSTRÖM, S., van de Schootbrugge, B., Hansen, K. H., Pedersen, G. K., Alsen, P., Thibault, N., Dybkjær, K., Bjerrum, C. J. & Nielsen, L. H. 2017. A new correlation of Triassic–Jurassic boundary successions in NW Europe, Nevada and Peru, and the Central Atlantic Magmatic province: A time-line for the end-Triassic mass extinction. *Palaeogeography, Palaeoclimatology, Palaeoecology*, **478**, 80–102.

LINDSTRÖM, S., Sanei, H., van de Schootbrugge, B., Pederson, G. K., Leshner, C. E., Tegner, C., Heunisch, C., Dybkjær, K. & Outridge, P. M. 2019. Volcanic mercury mutagenesis in land plants during the end-Triassic mass extinction. *Science Advances*, **5**, 1–13.

LINDSTRÖM, S., Nytoft, H. P., Pederson, G. K., Niedzwiedski, G., Dybkjær, K., Johansson, L., Peterson, H. I., Sanei, H., Tegner, C., Weibel, R. (2020, May 3-8). Land plants and terrestrial environmental changes during the onset of the end-Triassic event [Conference Presentation]. EGU 2020, Online.

LITTLE, S. H., Wilson, D. J., Rehkämper, M., Adkins, J. F., Robinson, L. F., and van de Lierdt, T. 2021. Cold-water corals as archives of seawaters Zn and Cu isotopes. *Chemical Geology*, **578**, 120304. <https://doi.org/10.1016/j.chemgeo.2021.120304>.

LIU, B., Chen, X., Chen, Y. & Tian, S. 2013. Geographic variation in statolith trace elements of the Humboldt squid, *Dosidicus gigas*, in high seas of Eastern Pacific Ocean. *Marine Biology*, **160**, 2853–2862.

LOEBLICH, A. R. & TAPPAN, H. 1988. Foraminiferal Genera and Their Classification. 1. Text and Indices. New York: Van Nostrand 970 pp.

LONGRIDGE, L. M., Carter, E. S., Haggart, J. W. & Smith, P. L. 2007a. The Triassic–Jurassic transition at Kunga Island, Queen Charlotte Islands, British Columbia, Canada. *ISJS Newsletter*, **34** (1), 21–33

LONGRIDGE, L. M., Carter, E. S., Smith, P. L. & Tipper, H. W. 2007b. Early Hettangian ammonites and radiolarians from the Queen Charlotte Islands, British Columbia and their bearing on the definition of the Triassic–Jurassic boundary. *Palaeogeography, Palaeoclimatology, Palaeoecology*, **244** (1–4), 142–169.

LU, J., Zhu, B., Struewing, I., Xu, N., Duan, S., 2019. Nitrogen–phosphorus-associated metabolic activities during the development of a cyanobacterial bloom revealed by metatranscriptomics. *Science Reports*, **9**, 2840, <https://doi.org/10.1038/s41598-019-38481-2>.

References

- LUCAS, S. G. & Tanner, L. H. 2004. Late Triassic extinction events. *Albertiana*, **31**, 31–40.
- LUCAS, S. G., Taylor, D. G., Guex, J., Tanner, L. H. & Krainer, K. 2007. Updated proposal for the Global Stratotype Section and Point for the base of the Jurassic System in the New York Canyon area, Nevada, USA. *ISJS Newsletter*, **34** (1), 34–42.
- LUCAS, S. G. & Tanner, L. H. 2008. Reexamination of the end-Triassic mass extinction. In: *Mass Extinction A. M. T. Elewa (ed.)*, Springer Verlag, 68–103.
- LUCAS, S. G., Tanner, L. H., Donohoo-Hurley, L. L., Geissman, J. W., Kozur, H. W., Heckert, A. B. & Weems, R. E. 2011. Position of the Triassic–Jurassic boundary and timing of the end-Triassic extinctions on land: Data from the Moenave Formation on the southern Colorado Plateau, USA. *Palaeogeography, Palaeoclimatology, Palaeoecology*, **302** (3–4), 194–205.
- LUCAS, S. G. 2018. Late Triassic Ammonoids: Distribution, Biostratigraphy and Biotic Events. In *Tanner, L. H. (Ed.) The Late Triassic World: Earth in a Time of Transition*, Topics in Geobiology 46, Springer, 237–261.
- LYELL, C. 1830. Principles of geology, being an attempt to explain the former changes of the Earth's surface, by reference to causes now in operation. London: John Murray. Volume 1.
- LYONS, T.W. & Severmann, S. 2006. A critical look at iron paleoredox proxies based on new insights from modern anoxic basins. *Geochimica et Cosmochimica Acta*, **70**, 5698–5722.
- LYONS, T. W., Werne, J. P., Hollander, D. J. & Murray, J. W. 2003. Contrasting sulfur geochemistry and Fe/Al and Mo/Al ratios across the last oxic-to-anoxic transition in the Cariaco Basin, Venezuela. *Chemical Geology*, **195**, 131–157.
- MACQUAKER, J. H. S., 1999. Aspects of the sedimentology of the Westbury Formation In *Swift, A., Martill, D. M. (Eds.) Fossils of the Rhaetian Penarth Group, The Palaeontological Association*, p. 39–48.
- MANDER, L. & Twitchett, R. J. 2008. Quality of the Triassic- Jurassic bivalve fossil record in northwest Europe. *Palaeontology*, **51** (6), 1213–1223.
- MANDER, L., Twitchett, R. J. & Benton, M. J. 2008. Palaeoecology of the late Triassic extinction event in the SW UK. *Journal of the Geological Society, London*, **165**, 319–332.
- MANGINI, A., Jung, M. & Laukenmann, S. 2001. What do we learn from peaks of uranium and manganese in deep sea sediments? *Marine Geology*, **177**, 63–78.
- MANNING, P. I., Wilson, H. E. 1975. The stratigraphy of the Larne Borehole, County Antrim. *Bulletin of the Geological Survey of Great Britain*, **50**, 1–50.

Quantifying marine redox across the Triassic–Jurassic mass extinction

- MARTINY, A. C., Vrugt, J. A. & Lomas, M. W. 2014. Concentrations and ratios of particulate organic carbon, nitrogen, and phosphorous in the global ocean, *Scientific Data*, **1**:140048.
- MARCHITTO Jr., T. M., Curry, W. B. & Oppo, D. W. 2010. Zinc concentrations in benthic foraminifera reflect seawater chemistry. *Paleoceanography*, **15**, 299–306.
- MARYNOWSKI, L. & Simoneit, B. R. T. 2009. Widespread Upper Triassic to Lower Jurassic wildfire records from Poland: Evidence from charcoal and pyrolytic polycyclic aromatic hydrocarbons. *Palaios*, **24**, 785–798.
- MÄRZ, C., Poulton, S. W., Beckmann, B., Kuester, K., Wagner, T. & Kasten, S. 2008. Redox sensitivity of P cycling during marine black shale formation: Dynamics of sulfidic and anoxic, non-sulfidic bottom waters, *Geochimica et Cosmochimica Acta*, **72**, 3703–3717.
- MARZOLI, A., Renne, P. R., Piccirillo, E. M., Ernesto, M., Bellieni, G., & De Min, A. 1999. Extensive 200-Million-Year-Old Continental Flood Basalts of the Central Atlantic Magmatic Province. *Science Reports*, **284**, 616–618.
- MARZOLI, A., Bertrand, H., Knight, K. B., Cirilli, S., Buratti, N., Vérati, C., Nomade, S., Renne, P. R., Youbi, N., Martini, R., Allenbach, K., Neuwerth, R., Rapaille, C., Zaninetti, L. & Bellieni, G. 2004. Synchrony of the Central Atlantic magmatic province and the Triassic-Jurassic boundary climatic and biotic crisis. *Geology*, **32** (11), 973–976.
- MARZOLI, A., Jourdan, F., Puffer, J. H., Cuppone, T., Tanner, L. H., Weems, R. E., Bertrand, H., Cirilli, S., Bellieni, G. & De Min, A. 2011. Timing and duration of the Central Atlantic magmatic province in the Newark and Culpeper basins, eastern USA. *Lithos*, **122**, 175–188.
- MARZOLI, A., Callegaro, S., Dal Corso, J., Davies, J. H. F. L., Massimo, C., Youbi, N., Bertrand, H., Resiberg, L., Merle, R. & Jourdan, F. 2018. The Central Atlantic Magmatic Province (CAMP): A Review. In: Tanner, L. (eds) *The Late Triassic World. Topics in Geobiology*, vol 46. Springer, Cham. https://doi.org/10.1007/978-3-319-68009-5_4.
- MATTHEWS, K. A., Grottoli, A. G., McDonough, W. F. & Palardy, J. E. 2008. Upwelling, species, and depth defects on corals skeletal cadmium-to-calcium ratios (Cd/Ca). *Geochimica et Cosmochimica Acta*, **72**, 4537–4550.
- MATTHIESSEN, J., Kunz-Pirrung, M. & Mudie, P. J., 2000. Freshwater chlorophycean algae in recent marine sediments of the Beaufort, Laptev and Kara Seas (Arctic Ocean) as indicators of river runoff. *International Journal of Earth Sciences*, **89**, 470–485.
- MAYALL, M. J., 1983. An earthquake origin for synsedimentary deformation in a late Triassic (Rhaetian) lagoonal sequence, southwest Britain. *Geological Magazine*, **120**, 613–622.

References

- McARTHUR, J. M. 2019. Early Toarcian black shales: A response to an oceanic anoxic event or anoxia in marginal basins? *Chemical Geology*, **522**, 71–83.
- McCANN, N., 1990. The Subsurface Geology between Belfast and Larne, Northern Ireland. *Irish Journal of Earth Sciences*, **10**, 157–173.
- McCARTNEY, K., Huffman, A. R., & Tredoux, M. 1990. A paradigm for endogenous causation of mass extinctions. In V. L. Sharpton, & P. D. Ward (Eds.), *Global Catastrophes in Earth History: An Interdisciplinary Conference on Impacts, Volcanism, and Mass Mortality*. Geological Society of America, Boulder, CO. pp. 125–138.
- McELWAIN, J. C., Popa, M. E., Hesselbo, S. P., Haworth, M. & Surlyk, F., 2007. Macroecological responses of terrestrial vegetation to climatic and atmospheric change across the Triassic/Jurassic boundary in East Greenland. *Paleobiology*, **33** (4), 547–573.
- McGHEE, G.R., Sheehan, P.M., Bottjer, D.J., Droser, M.L., 2004. Ecological ranking of Phanerozoic biodiversity crises: ecological and taxonomic severities are decoupled. *Palaeogeography, Palaeoclimatology, Palaeoecology*, **211**, 289–297.
- McGHEE, G. R. Clapham, M. E., Sheehan, P. M., Botther, D. J. & Droser, M. L. 2013. A new ecological-severity ranking of major Phanerozoic biodiversity crises. *Palaeogeography, Palaeoclimatology, Palaeoecology*, **370**, 260–270
- McGRODDY, M., Daufresne, T. & Hedin, L., 2004 Scaling of C:N:P stoichiometry in forests worldwide: implications of terrestrial Redfield-type ratios. *Ecology*, **85**, 2390–2401.
- McHONE, J. G. 2003. Volatile emissions of Central Atlantic Magmatic Province basalts: Mass assumptions and environmental consequences. In HAMES, W. E. (ed.). *The Central Atlantic Magmatic Province*. American Geophysical Union Monograph 136, p. 241–254.
- McKIE, T. & Williams, B. 2009. Triassic palaeogeography and fluvial dispersal across the northwest European Basins, *Geological Journal*, **44**, 711–741.
- McLAREN, D. J., & Goodfellow, W. D. 1990. Geological and biological consequences of giant impacts. *Annual Review of Earth and Planetary Sciences*, **18**, 123–171.
- McMANUS, J., Berelson, W.M., Klinkhammer, G.P., Hammond, D.E. & Holm, C., 2005. Authigenic uranium: relationship to oxygen penetration depth and organic carbon rain. *Geochimica et Cosmochimica Acta*, **69**, 95–108.
- McMANUS, J., Berelson, W. M., Severmann, S., Poulson, R. L., Hammond, D. E., Klinkhammer, G. P., & Holm, C., 2006. Molybdenum and uranium geochemistry in continental margin sediments: paleoproxy potential. *Geochimica et Cosmochimica Acta* **70** (18), 4643–4662.
- McROBERTS, C. A., & Newton, C. R. 1995. Selective extinction among end-Triassic European bivalves. *Geology*, **23** (2), 102–104.

Quantifying marine redox across the Triassic–Jurassic mass extinction

- McROBERTS, C. A., Newton C. R., Allasinaz A. 1995. End-Triassic bivalve extinction: Lombardian Alps, Italy. *Historical Biology*, **9**, 297–317.
- McROBERTS, C. A., WARD, P. D. & HESSELBO, S. 2007. A proposal for the base Hettangian Stage (= base Jurassic System) GSSP at New York Canyon (Nevada, USA) using carbon isotopes. *ISJS Newsletter*, **34** (1), 43–49.
- McROBERTS, C. A., Krystyn, L., & Hautmann, M. 2012. Macrofaunal Response to the End-Triassic Mass Extinction in the West-Tethyan Kossen Basin, Austria. *Palaios*, **27** (9), 607–616.
- MELOTT, A. L. & Bambach R. K. 2014. Analysis of periodicity of extinction using the 2012 geological timescale. *Paleobiology*, **40**, 177–96.
- MERLE, R. Marzoli, A., Reisberg, L., Bertrand, H., Nemchin, A., Chiaradia, M., Callegaro, Jourdan, F., Bellieni, G., Kontak, D., Puffer, J. & McHone, J. G. Sr Nd, Pb and Os Isotope Systematics of CAMP Tholeiites from Eastern North America (ENA) Evidence of a Subduction-enriched Mantle Source. *Journal of Petrology*, **55** (1), 133–180.
- METTE, W., Clemence, M.-E., Thibault, N., Jore, C., Konrad, B. & Ullmann, C. V. 2019. Sedimentology, carbon isotope stratigraphy and micropalaeontology of the Rhaetian Zlambach Formation—Implications for the Dachstein carbonate platform development (Northern Calcareous Alps, Austria), *Sedimentary Geology*, **382**, 47–60.
- MITCHELL, I., 2004. *The Geology of Northern Ireland: Our Natural Foundation*, 1st edition, British Geological Survey.
- MORBEY, J. S. 1975. The palynostratigraphy of the Rhaetian stage, Upper Triassic in the Kendelbachgraben, Austria. *Palaeontograph B*, **152**, 1–75
- MORFORD, J. L & EMERSON, S. 1999. The geochemistry of redox sensitive trace metals in sediments. *Geochimica et Cosmochimica Acta*, **63** (11-12), 1735–1750.
- MORFORD, J. L., Russell, A. D., & Emerson S., 2001. Trace metal evidence for changes in the redox environment associated with the transition from terrigenous clay to diatomaceous sediment, Saanich Inlet, BC. *Marine Geology*, **174** (1), 355–369.
- MORTON, N. 2012. Inauguration of the GSSP for the Jurassic System. *Episodes*, **35** (2), 328–332.
- MOSSMAN, D. J., Grantham, R. G., & Langenhorst, F. 1998. A search for shocked quartz at the Triassic-Jurassic boundary in the Fundy and Newark basins of the Newark Supergroup. *Canadian Journal of Earth Sciences*, **35**(2), 101–109.
- MOSTLER, H., Scheuring, R. & Ulrichs, M. 1978. Zur Mega-, Mikrofauna und Mikroflora der Kossen Schichten (alpine Obertrias) von Weissloferbach in Tirol unter besonderer Berücksichtigung der in der suessi- und marshi- Zone auftretenden Conodonten. *Österreich Akad Wissensch Erdwissensch Komm Schriften*, **4**, 141–174.

References

- MUSCENTE, A. D., Prabhu, A., Zhong, H., Eleish, A., Meyer, M. B., Fox, P., Hazen, R. M. & Knoll, A. H. 2018. Quantifying ecological impacts of mass extinctions with network analysis of fossil communities. *Proceedings of the National Academy of Sciences*, **115** (20), 5217–5222.
- MUTTONI, G., Kent, D. V., Olsen, P. E., Di Stefano, P., Lowrie, W., Bernasconi, S. M. & Hernández, F. M. 2004. Tethyan magnetostratigraphy from Pizzo ondello (Sicily) and correlation to Late Triassic Newark astrochronological polarity time scale. *Geological Society of American Bulletin; September/October 2004*, **116** (9/10), 1043–1058.
- MUTTONI, G., Kent, D. V., Jadoul, F., Olsen, P. E., Rigo, M., Galli, M. T., & Nicora, A. 2010. Rhaetian magneto-biostratigraphy from the Southern Alps (Italy): Constraints on Triassic chronology, *Palaeogeography, Palaeoclimatology, Palaeoecology*, **285** (1–2), 1–16.
- MUTTONI, G., Mazza, M., Mosher, D., Katz, M. E., Kent, D. V. & Balini, M. 2014. A Middle-Late Triassic (Ladinian-Rhaetian) carbon and oxygen record from the Tethyan Ocean. *Palaeogeography, Palaeoclimatology, Palaeoecology*, **399**, 246–259.
- NÄGLER, T. F., Neubert, N., Böttcher, M. E., Dellwig, O. & Schnetger, B. 2011. Molybdenum isotope fractionation in pelagic euxinia: Evidence from the modern Black and Baltic Seas. *Chemical Geology*, **289**, 1–11.
- NÄGLER, T. F., Anbar, A. D., Archer, C., Goldberg, T., Gordon, G. W., Greber, N. D., Siebert, C., Yoshiki, S. & Vance, D. 2014. Proposal for an international molybdenum isotope measurement standard and data representation. *Geostandards and Geoanalytical Research*, **38** (2), 149–151.
- NAKAGAWA, Y., Takano, S., Lutfi Firdaus, M., Norisuye, K., Takafumi, H., Vance, D. & Sohrin, Y. 2012. The molybdenum isotopic composition of the modern ocean. *Geochemical Journal*, **46** (2), 131–141.
- NESBITT, H. W. & Young G. M. 1982. Early Proterozoic climates and plate motions inferred from major element chemistry of lutites. *Nature*, **299**, 715–717.
- NEUMANN, E.-R., Svensen, H. H., Polozov, A. G. & Hammer, Ø. 2017. Formation of Si-Al-Mg-Ca-rich zoned magnetite in an end Permian phreatomagmatic pipe in the Tunguska Basin, East Siberia, *Mineralium Deposita*, **52**, 1205–1222.
- NEWELL, N. D. 1963. Crises in the history of life. *Scientific American*, **208** (2), 76–95.
- NEWELL, N. D. 1967. Revolutions in the history of life. *Geological Society of America Special Paper*, **89**, 63–92.
- NOMADE, S., Knight, K. B., Beutel, E., Renne, P. R., Verati, C., Féraud, G., Marzoli, A., Youbi, N. & Bertrand, H. 2007. Chronology of the Central Atlantic Magmatic Province: Implications for the Central Atlantic rifting process and the Triassic- Jurassic biotic crisis. *Palaeogeography, Palaeoclimatology, Palaeoecology*, **244**, 326–344.

Quantifying marine redox across the Triassic–Jurassic mass extinction

- O'DOGHERTY, L., Carter E. S., Gorican, S. & Dumitrica P. 2010. Triassic radiolarian biostratigraphy. *Geological Society, London, Special Publications*, **334**, 163–200.
- OLSEN, P. E., Shubin, N. H., & Anders, M. H. 1987. New early Jurassic tetrapod assemblages constrain Triassic-Jurassic tetrapod extinction event. *Science*, **237** (4818), 1025–1029.
- OLSEN, P. E., Fowell, S. J. & Cornet, B. 1990. The Triassic- Jurassic boundary in continental rocks of the eastern North America; A progress report. *Geological Society of America, Special Paper* 247, 585–593.
- OLSEN, P. E., Kent, D. V., Sues, H.-D., Koeberl, C., Huber, H., Montanari, A., Rainforth, E. C., Fowell, S. J., Szajna, M. J. & Hartline, B. W. 2002. Ascent of dinosaurs linked to an iridium anomaly at the Triassic-Jurassic boundary. *Science*, **296** (5571), 1305–1307.
- OLSEN, P. E., Whiteside, J. H. & Huber, P. 2003. Causes and consequences of the Triassic-Jurassic mass extinction as seen from the Hartford basin. Skinner, B. J. and Cheney, J. T. (eds.) In *Guidebook for Field Trips in the Five College Region, 95th New England Intercollegiate Geological Conference*. Department of Geology, Smith College, Northampton, Massachusetts. B5.1-B5.41.
- ONOUE, T., Sato, H., Nakamura, T., Noguchi, T., Hidaka, Y., Shirai, N., Ebihara, M., Osawa, T., Hasukawa, Y., Toh, Y., Koizumi, M., Harada, H., Orchard, M. J. & Nedachi, M. 2012. Deep-sea record of impact apparently unrelated to mass extinction in the Late Triassic. *PNAS*, **109** (47), 19134–19139.
- ONOUE, T., Sato, H., Yamashita, D., Ikehara, M., Yasukawa, K., Fujinaga, K., Kato, Y., & Matsuoka, A. 2016. Bolide impact triggered the Late Triassic extinction event in equatorial Panthalassa. *Scientific reports*, **6**, 29609.
- OPAZO, L. F. & Page, K. N. 2021. Palaeoecological patterns of change in marine invertebrate faunas across the End-Triassic mass extinction event: Evidence from Larne, Northern Ireland. *Proceedings of The Geological Association*, **132** (6), 726–742.
- ORCHARD, M. J., 1991. Upper Triassic conodont biochronology and new index species from the Canadian Cordillera. *Geological Survey of Canada Bulletin*, **417**, 299–335.
- ORTH, C. J. 1989. Geochemistry of the bio-event horizons. In S. K. Donovan (Ed.), *Mass Extinctions: Processes and Evidence*. Belhaven Press, London. pp. 37–72.
- OWENS, J. D., Lyons, T. W., Hardisty, D. S., Lowery, C. M., Lu, Z., Lee, B. & Jenkyns, H. C. 2016. Patterns of local and global redox availability during the Cenomanian-Turonian Boundary Event (Oceanic Anoxic Event 2) recorded in carbonates and shales from central Italy. *Sedimentology*, **64** (1), 168–185.
- PAGE, K. N. 2005. The Hettangian ammonite faunas of the West Somerset coast (south west England) and their significance for the correlation of the candidate GSSP (Global

References

- Stratotype and Point) for the base of the Jurassic System at St. Audries Bay. In: Hanzo, M. (coord.), *Colloque Hettangien à Hettange, de la science au patrimoine, Hettange, 1-3 avril 2005*: 15-19. Université Henri Poncaré, Nancy.
- PÁLFY, J. & Dosztály, L. 2000. A New Marine Triassic–Jurassic Boundary Section in Hungary. *GeoResearch Forum*, **6**, 173–180.
- PÁLFY, J., Demény, A., Haas, J., Hetényi, M., Orchard, M., & Vető, I. 2001. Carbon isotope anomaly and other geochemical changes at the Triassic–Jurassic boundary from a marine section in Hungary. *Geology*, **29** (11), 1047–1050.
- PÁLFY, J. 2003. Volcanism of the Central Atlantic magmatic province as a potential driving force in the end-Triassic mass extinction, in Hames, W.E., McHone, J.G., Renne, P.R., and Ruppel, C., eds., *The Central Atlantic Magmatic Province: Insights from Fragments of Pangea*: American Geophysical Union Geophysical Monograph 136, p. 255–267.
- PÁLFY, J., Demény, A., Haas, J., Carter, E. S., Görög, A., Halász, D., Oravecz-Scheffer, K., Hetényi, M., Márton, E., Orchard, M. J., Ozsvárt, P., Vető, I. & Zajzon, N. 2007. Triassic–Jurassic boundary events inferred from integrated stratigraphy of the Csővár section, Hungary. *Palaeogeography, Palaeoclimatology, Palaeoecology*, **244**, 11–33.
- PÁLFY, J. & Kocsis, Á, T. 2014. Volcanism of the Central Atlantic Magmatic province as the trigger of environmental and biotic changes around the Triassic–Jurassic boundary. *Geological Society of America Special Papers*, **505**, 245–261.
- PALTER, J. B. & Trossman, D. S. 2018. The Sensitivity of Future Ocean Oxygen to Changes in Ocean Circulation. *Global Biogeochemical Cycles*, **32** (5), 738–751.
- PANFILI, G., Cirilli, S., Dal Corso, J., Bertrand, H., Medina, F., Youbi, N. & Marzoli, A. 2019. New biostratigraphic constraints show rapid emplacement of the Central Atlantic Province (CAMP) during the end-Triassic mass extinction interval. *Global and Planetary Change*, **172**, 60–68.
- PAYNE, J. L. & Kump, L. R. 2007. Evidence for recurrent Early Triassic massive volcanism from quantitative interpretation of carbon isotope fluctuations. *Earth and Planetary Science Letters*, **256**, 264–277.
- PEARCE, C. R., Cohen, A. S., & Parkinson, I. J. 2009. Quantitative separation of molybdenum and rhenium from geological materials for isotopic determination by MC-ICP-MS. *Geostandards and Geoanalytical Research*, **33** (2), 219–229.
- PEARSON, D. A. B. 1977. Rhaetian brachiopods of Europe. *Denkschriften Naturhistorisches Museum Wien*, **1**, 1–70.
- PENMAN, D. E., Turner, S. K., Sexton, P. F., Norris, R. D., Dickson, A. J., Boulila, S., Ridgwell, A., Zeebe, R. E., Zachos, J. C., Cameron, A., Westerhold, T. & Röhl, U. 2016. 'An abyssal carbonate compensation depth overshoot in the aftermath of the Palaeocene–Eocene Thermal Maximum'. *Nature Geoscience*, **9** (8), 575–580.

Quantifying marine redox across the Triassic–Jurassic mass extinction

- PERCIVEL, L. M. E., Witt, M. L. I., Mather, T. A., Hermoso, M., Jenkyns, H. C., Hesselbo, S. P., Al-Suwaidi, A. H., Storm, M. S. & Ruhl, M. 2015. Globally enhanced mercury deposition during the end-Pliensbachian extinction and Toarcian OAE: A link to the Karoo–Ferrar Large Igneous Province, *Earth and Planetary Science Letters*, **428**, 267–280.
- PERCIVAL, L. M. E., Ruhl, M., Hesselbo, S. P., Jenkyns, H. C., Mather, T. A., & Whiteside, J. H. 2017. Mercury evidence for pulsed volcanism during the end-Triassic mass extinction. *Proceedings of the National Academy of Sciences of the United States of America*, **114** (30), 7929–7934.
- PETERS, S. E. 2008. Environmental determinants of extinction selectivity in the fossil record. *Nature*, **454**, 626–629.
- PETERSEN, H. I. & Lindström, S. 2012. Synchronous wildfire activity rise and mire deforestation at the Triassic–Jurassic boundary. *PLOS One*, **7** (10), 47236.
- PIPER, D. Z. & Calver, S. E. 2009. A marine biogeochemical perspective on black shale deposition. *Earth Science Reviews*, **95**, 63–96.
- PITRAT, C.W., 1970. Phytoplankton and the Late Paleozoic wave of extinction. *Palaeogeography, Palaeoclimatology, Palaeoecology*, **8**, 49–66.
- POULSON BRUCKER, R. L., McManus, J., Severmann, S. & Berelson, W. M. 2009. Molybdenum behaviour during early diagenesis: Insights from Mo isotopes. *Geochemistry, Geophysics, Geosystems*, **10** (6), Q06010.
- POULTON, S. W. & Canfield, D. E. 2011. Ferruginous conditions: a dominant feature of the ocean through Earth’s history. *Elements*, **7**, 107–112.
- PROUTY, N. G., Huguen, K. A. & Carilli, J. 2008. Geochemical signature of land-based activities in Caribbean coral surface samples. *Coral Reefs*, **27**, 727–742.
- PRUYERS, P. A., de Lange, G. J., Middelburg, J. J. & Hydes, D. J., 1993. The diagenetic formation of metal-rich layers in sapropel-containing sediments in eastern Mediterranean. *Geochimica et Cosmochimica Acta*, **57**, 527–536.
- QUAN, T. M., van de Schootbrugge, B., Field, M. P., Rosenthal, Y. & Falkowski, P. G., 2008. Nitrogen isotope and trace metal analyses from the Mingolshiem core (Germany): Evidence for redox variations across the Triassic–Jurassic boundary. *Global Biogeochemical Cycles*, **22** (2), 1–14.
- RAINE, R., Copestake, P., Simms, M. J. & Boomer, I. 2021. Uppermost Triassic to Lowermost Jurassic sediments of the island of Ireland and its surrounding basins. *Proceedings of the Geological Association*, **132** (6), 627–640.
- RAISWELL, R., Newton, R. , Bottrell, S. H., Coburn, P., Briggs, D. E. G., Bond, D. P. G., & Poulton, S. W., 2008, Turbidite depositional influences on the diagenesis of

References

- Beecher's Trilobite Bed and the Hunsrück Slate: Sites of soft tissue preservation. *American Journal of Science*, **308**, 105–129.
- RAISWELL, R., Hardisty, D. S., Lyons, T. W., Canfield, D. E., Owens, J. D., Planavsky, N. J., Poulton, S. W. & Reinhard, C. T., 2018. The iron paleoredox proxies: a guide to the pitfalls, problems and proper practice. *American Journal of Science*, **318**, 491–526.
- RAITZSCH, M., Kuhnert, H., Hathorne, E. C., Groeneveld, J. & Bickert, T. 2011. U/Ca in benthic foraminifers: A proxy for the deep-sea carbonate saturation. *Geochemistry, Geophysics, Geosystems*, **12**, Q06019. doi:10.1029/2010GC003344.
- RAMEZANI, J., Bowring, S. A., Pringle, M. S., Winslow III, F. D. & Rasbury, E. T., 2005. The Manicouagan impact melt rock: A proposed standard for the intercalibration of U-Pb and ⁴⁰Ar/³⁹Ar isotopic systems. *Geochimica et Cosmochimica Acta*, **69**, A321.
- RAMOS, A. A., Inoue, Y. & Ohde, S. 2004. Metal contents in Porites corals: anthropogenic input of river run-off into a coral reef from an urbanized area, Okinawa. *Marine Pollution Bulletin*, **48**, 281e294.
- RAMPINO, M. R. & Stothers, R. B. 1998. Flood Basalt Volcanism During the Past 250 Million Years. *Science Articles*, **241**, 663–668.
- RAMPINO, M. R. & Caldeira, K. 2017. Correlation of the largest craters, stratigraphic impact signatures, and extinction events over the past 250 Myr. *Geoscience Frontiers*, **8**, 1241–1245.
- RAUP, M., & Sepkoski, J. J. 1982. Mass Extinctions in the Marine Fossil Record. *Science*, **215** (4539), 1501–1503.
- RAUP, M. & Sepkoski, J. J. 1986. Periodic Extinction of Families and Genera. *Science*, **231**, 833–836.
- RAUP, D. 1992. Large-body impact and extinction in the Phanerozoic. *Paleobiology*, **18** (1), 80–88.
- REDFIELD, A. C., 1958. The Biological Control of Chemical Factors in the Environment. *American Scientist*, **46**, 205–221.
- REDFIELD, A. C., Ketchum, B. H. & Richards, F. A. 1963. The Influence of Organisms on the Composition of the Sea Water. In Hill, M.N., Ed., *The Sea*, Vol. 2, Interscience Publishers, New York, 26–77.
- REID, C.G.R., Bancroft, A.J. 1986. The Irish Lower Jurassic type ammonites of Major-General J.E. Portlock (1843): *Leptechioceras macdonnelli*, *Psiloceras (Caloceras) intermedium*, and *Psiloceras (Psiloceras) sampsoni*. *International Journal of Earth Sciences*, **8**, 41–51.
- REMMELZWAAL, S. R. C., Sadekov, A. Y., Parkinson, I. J., Schmidt, D. N., Titelboim, D., Abramovich, S., Roepert, A., Kienhuis, M., Polerecky, L., Goring-

Quantifying marine redox across the Triassic–Jurassic mass extinction

- Harford, H., Kimoto, K., Allen, K. A., Holland, K., Stewart, J. A. & Middelburg, J. J. 2019. Post-depositional overprinting of chromium in foraminifera. *Earth and Planetary Science Letters*, **15**, 100–111.
- RENEMA, W., Bellwood, D. R., Braga, J. C., Bromfield, K., Johnson, K. G., Lunt, P., Meyer, C. P., McMonagle, L. B., Morley, R. J., O’Dea, A., Wesselingh, F. P., Wilson, M. E. J. & Pandolfi, J. M. .2008. Hopping Hotspots: Global Shifts in Marine Biodiversity. *Science*, **321**, 654–657.
- RENNE, P. R., Balco, G., Ludwig, K. R., Mundil, R., Min, K., 2011. Response to the comment by W.H. Schwarz et al. on “Joint determination of ^{40}K decay constants and $^{40}\text{Ar}^*/^{40}\text{K}$ for the Fish Canyon sanidine standard, and improved accuracy for $^{40}\text{Ar}/^{39}\text{Ar}$ geochronology” by P.R. Renne et al. (2010). *Geochimica et Cosmochimica Acta*, **75**, 5097–5100.
- RICHOZ, S., van de Schootbrugge, B., Pross, J., Püttmann, W., Quan, T. M., Lindström, S., Heunisch, C., Fiebig, J., Maquil, R., Schouten, S., Hauzenberger & Wignall, P. B. 2012. Hydrogen sulphide poisoning of shallow seas following the end-Triassic extinction. *Nature Geoscience*, **5** (9), 662–667.
- RICKABY, R. E. M. & Elderfield, H. 1999. Planktonic foraminiferal Cd/Ca: Paleonutrients or Paleotemperature?. *Paleoceanography*, **14**, 293–303.
- RIGO, M., Mazza, M., Karádi, V. & Nicora, A. 2018. New Upper Triassic Conodont Biozonation of the Tethyan Realm *In Tanner, L. H. (Ed.) The Late Triassic World: Earth in a Time of Transition, Topics in Geobiology*, **46**, Springer. 186–236.
- RIGO, M., Onoue, T., Tanner, L. H., Lucas, S. G., Godfrey, L., Katz, M. E., Zaffani, M., Grice, K., Cesar, J., Yamashita, D., Maron, M., Tackett, L. S., Campbell, H., Tateo, F., Concheri, G., Agnini, C., Chiara, M. & Bertinelli, A. 2020. The late Triassic Extinction at the Norian/Rhaetian boundary: Biotic evidence and geochemical signature. *Earth-Science Reviews*, **204**, 103180
- RITTERBUSH, K. A., Bottjer, D. J., Corsetti, F. A. & Rosas, S. 2014. New evidence on the role of siliceous sponges in ecology and sedimentary facies development in eastern Panthalassa following the Triassic–Jurassic mass extinction. *Palaios*, **29** (12), 652–668.
- RITTERBUSH, K. A., Rosas, S. Corsetti, F. A., Bottjer, D. J. & Joshua West, A. 2015. Andean sponges reveal long-term benthic ecosystem shifts following the end-Triassic mass extinction. *Palaeogeography, Palaeoclimatology, Palaeoecology*, **420**, 193–209.
- ROS, S., De Renzi, M., Damborenea, S. E. & Márquez-Aliaga, A. 2011. Coping between crises: Early Triassic- early Jurassic bivalve diversity dynamics. *Palaeogeography, Palaeoclimatology, Palaeoecology*, **311**, 184–199.
- ROSENTHAL, Y., LAM, P., BOYLE, E. A. & THOMSON, J. 1995. Authigenic cadmium enrichments in suboxic sediments: Precipitation and postdepositional mobility. *Earth and Planetary Science Letters*, **132**, 99–111.

References

RUDNICK, R. L. & Gao, S., 2003. The Composition of the Continental Crust. *In: Holland, H. D. and Turekian, K.K., Eds., Treatise on Geochemistry*, Vol. 3, The Crust, Elsevier-Pergamon, Oxford, 1–64.

RUDWICK, M. J. S. 1972. The meaning of fossils: Episodes in the History of Palaeontology. Chicago, Illinois: University of Chicago Press.

RUE, E. L., Smith, G. J., Cutter, G. A. & Bruland, K. W. 1997. The response of trace element redox couples to suboxic conditions in the water column. *Deep-Sea Research*, **44(1)**, 113–134.

RUHL, M., Kürschner, W. M., & Krystyn, L. 2009. Triassic-Jurassic organic carbon isotope stratigraphy of key sections in the western Tethys realm (Austria). *Earth and Planetary Science Letters*, **281** (3–4), 169–187.

RUHL, M. 2010. Carbon cycle changes during the Triassic- Jurassic transition. PhD thesis.

RUHL, M., Veld, H., & Kürschner, W. M. 2010. Sedimentary organic matter characterization of the Triassic-Jurassic boundary GSSP at Kuhjoch (Austria). *Earth and Planetary Science Letters*, **292** (1–2), 17–26.

RUHL, M., & Kürschner, W. M. 2011. Multiple phases of carbon cycle disturbance from large igneous province formation at the Triassic-Jurassic transition. *Geology*, **39** (5), 431–434.

RUHL, M., Bonis, N. R., Reichart, G. J., Damste, J. S. S., & Kürschner, W. M. 2011. Atmospheric carbon injection linked to end-Triassic mass extinction. *Science*, **333** (6041), 430–434.

RUHL, M., Hesselbo, S. P., Hinnov, L., Jenkyns, H. C., Xu, W., Riding, J. B., Storm, M., Minisini, D., Ullmann, C. V. & Leng, M. J. Astronomical constraints on the duration of the Early Jurassic Pliensbachian Stage and global climatic fluctuations. *Earth and Planetary Science Letters*, **455**, 149–165.

RUHL, M., Hesselbo, S. P., Al-Suwaidi, A., Jenkyns, H. C., Damborenea, S. E., Manceñido, M. O., Storm, M., Mather, T. A. & Riccardi, A. C. 2020. On the onset of Central Atlantic Magmatic Province (CAMP) volcanism and environmental and carbon cycle change at the Triassic Jurassic transition (Neuquén Basin, Argentina). *Earth-Science Reviews*, **208**, 103229.

RUSSELL, A. D., Emerson, S., Mix, A. C. & Peterson, L. C., 1996, The use of foraminiferal uranium/calcium ratios as an indicator of changes in seawater uranium content. *Paleoceanography*, **11**, 649–663.

RUSSELL, A. D., Hönisch, B., Spero, H. J. & Lea, D. W., 2004, Effects of seawater carbonate ion concentration and temperature on shell U, Mg, and Sr in cultured planktonic foraminifera. *Geochimica et Cosmochimica Acta*, **68**, 4347–4361.

Quantifying marine redox across the Triassic–Jurassic mass extinction

RUTTENBERG, K. & Berner, R. 1993. Authigenic apatite formation and burial in sediments from non-upwelling, continental margin environments. *Geochimica et Cosmochimica Acta*, **57**, 991–1007.

SAHA, N., Webb, G. E., Christy, A. G. & Zhao, J.-X. 2019. Vanadium in the massive coral *Porites*: A potential proxy for historical wood clearing and burning. *Earth and Planetary Science Letters*, **527**, 115793.

SALMON, K. H., Anand, P., Sexton, P. F. & Conte, M. 2016. Calcification and growth processes in planktonic foraminifera complicate the use of B/Ca and U/Ca as carbonate chemistry proxies. *Earth and Planetary Science Letters*, **449**, 372–381.

SANNIGRAHI, P., & E. Ingall. 2005. Polyphosphates as a source of enhanced P fluxes in marine sediments overlain by anoxic waters: Evidence from ^{31}P NMR, *Geochemical Transactions*, **6**, 52–59.

SATO, H., Onoue, T., Nozaki, T., & Suzuki, K. 2013. Osmium isotope evidence for a large Late Triassic impact event. *Nature Communications*, **4**, 1–7.

SAUNDERS, A. D. 2016. Two LIPs and two Earth-system crises: the impact of the North Atlantic Igneous Province and the Siberian Traps on the Earth-surface carbon cycle, *Geological Magazine*, **153**, 201–222.

SAUNDERS, A. D. 2017. Carbon and its role in mass extinctions. University Seminar, Royal Holloway University of London, 20/09/2017- unpublished.

SCHALLER, M. F., Wright, J. D. & Kent, D.V., 2011. Atmospheric pCO_2 perturbations associated with the Central Atlantic Magmatic Province. *Science*, **331** (6023), 1404–1409.

SCHALLER, M. F., Wright, J. D., Kent, D. V., & Olsen, P. E. 2012. Rapid emplacement of the Central Atlantic Magmatic Province as a net sink for CO_2 . *Earth and Planetary Science Letters*, **323–324**, 27–39.

SCHMIDT, S., Hathorne, E. C., Schönfeld, J. & Garbe-Schönberg, D. 2022. Heavy metal uptake of nearshore benthic foraminifera during multi-metal culturing experiments. *Biogeosciences*, **19**, 629–664.

SCHMIDTKO, S., Stramma, L. & Visbeck, M. 2017. Decline in global oceanic oxygen content during the past five decades. *Nature*, **542**, 335–337.

SCHMIEDER, M., Buchner, E., Schwarz, W. H., Trieloff, M. & Lambert, P. 2010. A Rhaetian $^{40}\text{Ar}/^{39}\text{Ar}$ age for the Rochechouart impact structure (France) and implications for the latest Triassic sedimentary record. *Meteoritics and Planetary Science*. **45**, 1225–1242.

SCHOBEN, M., Gravendyck, J., Mangels, F., Struck, U., Bussert, R., Kürschner, W. M., Korn, D., Sander, P. M. & Aberhan, M., 2019. A comparative study of total organic carbon- $\delta^{13}\text{C}$ signatures in the Triassic–Jurassic transitional beds of the Central

References

- European Basin and western Tethys shelf seas. *Newsletters on Stratigraphy*, **52** (4), 461–486.
- SCHOENE, B., Guex, J., Bartolini, A., Schaltegger, U., & Blackburn, T. J. 2010. Correlating the end-Triassic mass extinction and flood basalt volcanism at the 100 ka level. *Geology*, **38** (5), 387–390.
- SCHOLZ, F., Siebert, C., Dale, A. W. & Frank, M. 2017. Intense molybdenum accumulation in sediments underneath a nitrogenous water column and implications for the reconstruction of paleo-redox conditions based on molybdenum isotopes. *Geochimica et Cosmochimica Acta*, **213**, 400–417.
- SCHWARSENHÖLZER, W., 1955. Schichtenverzeichnis der Bohrung Hebelermeer 2 (German; unpublished). *LBEG-Archiv BV-Ordner 3009*, **66**, 1–38. (in German).
- SCOTT, C. & Lyons, T. W. 2012. Contrasting molybdenum cycling and isotopic properties in euxinic versus non-euxinic sediments and sedimentary rocks: Refining the paleoproxies. *Chemical Geology*, **324–325**, 19–27.
- SEPHTON, M. A., Amor, K., Franchi, I., Wignall, P. B., Newton, R. J. Zonneveld, J.-P. 2002. Carbon and nitrogen isotope disturbances and an end-Norian (Late Triassic) extinction event. *Geology*, **30** (12), 1119–1122.
- SEPKOSKI, J. J. Jr. 1982. Mass extinctions in Phanerozoic oceans: a review. In *Geological implications of impacts of large asteroids and comets on the earth*, eds Silver, L. T., Schultz, P. H. *Geological Society of America Special Paper*, **190**, 283–289.
- SEPKOSKI, J. J. Jr. 1986. Phanerozoic overview of mass extinction In *Patterns and Processes in the History of Life*, ed. DM Raup, D Jablonski, pp. 277–95. Berlin: Springer Verlag
- SEPKOSKI, J. J. Jr., and Raup, D. M. 1986. Periodicity in marine extinction events In *Dynamics of Extinction*, edited by David K. Elliott, 3–36. New York: John Wiley & Sons.
- SEPKOSKI, J. J. Jr. 1989. Periodicity in extinction and the problem of catastrophism in the history of life. *Journal of the Geological Society, London*, **146**, 7–19.
- SEPKOSKI, J. J. Jr. 1996. Patterns of Phanerozoic Extinction: a Perspective from the Global Data Bases. In *Global Events and Event Stratigraphy in the Phanerozoic*, O. H. Walliser (ed.), Springer-Verlag Berlin Heidelber.
- SEPKOSKI, J. J. Jr. 2002. A compendium of fossil marine animal genera. *Bulletins of American Paleontology*, **363**, 1–560
- SHEPHERD, H. M. E. 2013. Nearing the end: Reef building corals and bivalves in the late Triassic and comparing corals and bivalves before and after the End Triassic Mass Extinction using a taxonomic database. *Theses, Dissertations, Professional Papers*.

Paper 1403.

SHEVYREV, A. A. 2005. Heteromorph Ammonoids of the Triassic: A Review. *Palaeontological Journal*, **39** (5), S614–S628.

SHIMMIELD, G. B. & Price, N. B. 1986. The behaviour of molybdenum and manganese during early sediment diagenesis—offshore Baja California, Mexico. *Marine Chemistry*, **19**, 261–280.

SIEBERT, C., McManus, J., Bice, A., Poulson, R. & Berelson, W. M. 2006. Molybdenum isotope signatures in continental margin marine sediments. *Earth and Planetary Science Letters*, **241**, 723–733.

SIMMS, M. J. 2003. Uniquely extensive seismite from the latest Triassic of the United Kingdom: Evidence for bolide impact? *Geology*, **31** (6), 557–560.

SIMMS, M. J. 2007. Uniquely extensive soft-sediment deformation in the Rhaetian of the UK: Evidence for earthquake or impact? *Palaeogeography, Palaeoclimatology, Palaeoecology*, **244** (1–4), 407–423.

SIMMS, M. J. & Jeram, A. J. 2007. Waterloo Bay, Larne, Northern Ireland: a candidate Global Stratotype Section and Point for the base of the Hettangian Stage and Jurassic System. *ISJS Newsletter*, **34** (1), 50–68.

SIMPSON, G. G. 1944. *Tempo and Mode in Evolution*. New York; Columbia Univ. Press.

SKELTON, P. W. & Benton M. J. 1993 Mollusca: Rostroconchia, Scaphopoda and Bivalvia. In: Benton MJ (ed) *The fossil record 2*. Chapman & Hall, London, 237- 263

SLOMP, C. P. & van Cappellen, P., 2007, The global marine phosphorous cycle: Sensitivity to oceanic circulation, *Biogeosciences*, **4**, 155–171.

SLOMP, C. P., Epping, E. H. G., Helder, W. & Van Raaphorst, W. 1996. A key role for iron-bound phosphorus in authigenic apatite formation in North Atlantic continental platform sediments. *Journal of Marine Research*, **54**, 1179–1205.

SMALLEY, I. 2020. Work on *The Principle of Geology* is “interrupted,” and Charles Lyell investigates the nature and formation of loess deposits. *Endeavour*, **44**, 1–5.

SPERLING, E. A., Halverson, G. P., Knoll, A. H., Macdonald, F. A. & Johnston, D. T. 2013. A basin redox transect at the dawn of animal life. *Earth and Planetary Science Letters*, **371-372**, 143–155.

SPERLING, E. A., Carbonne, C., Strauss, J. V., Johnston, D. T., Narbonne, G. M. & Macdonald, F. A. 2016. Oxygen, facies, and secular controls on the appearance of Cryogenian and Ediacaran body and trace fossils in the Mackenzie Mountains of northwestern Canada. *Geological Society of America Bulletin*, **128**, 558–575.

References

- SPERLING, E. A., Balthasar, U. & Skovsted, C. B. 2018. On the edge of exceptional preservation: insights into the role of redox state in Burgess Shale-type taphonomic windows from the Mural Formation, Alberta Canada. *Emerging Topics in Life Sciences*, 1–13. <https://doi.org/10.1042/ETLS20170163>.
- STATHAM, P.J. & Burton, J., 1986. Dissolved manganese in the North Atlantic Ocean, 0–35 N. *Earth and Planetary Science Letters*, **79** (1), 55–65.
- STORDAL, F., Svensen, H. H., Aarnes, I., Roscher, M. 2017. Global temperature response to century-scale degassing from the Siberian Traps Large igneous province. *Palaeogeography, Palaeoclimatology, Palaeoecology*, **471**, 96–107.
- STORM, M. S., Hesselbo, S. P., Jenkyns, H. C., Ruhl, M., Ullmann, C. V., Xu, W., Leng, M. L. & Gorbanenko, O. 2020. Orbital pacing and secular evolution of the Early Jurassic carbon cycle. *PNAS*, **117** (8), 3974–3982.
- SUMMONS, R. E. & Powell, T. G., 1986. *Chlorobiaceae* in Palaeozoic seas revealed by biological markers, isotopes and geology. *Nature*, **319**, 763–765.
- SVENSEN, H. H., Planke, S., Polozov, A. G., Schmidbauer, N., Corfu, F., Podladchikov, Y. Y. & Jamtveit, B. 2009. Siberian gas venting and the end-Permian environmental crisis. *Earth and Planetary Science Letters*, **277** (3), 490–500
- SWEERE, T., van den Boorn, S., Dickson, A. J. & Reichart, G.-J., 2016. Definition of new trace-metal proxies for the controls on organic matter enrichment in marine sediments based on Mn, Co, Mo and Cd concentrations. *Chemical Geology*, **441**, 235–245.
- SWEERE, T. C., Dickson A. J., Jenkyns, H. C., Porcelli, D., Elrick, M., Van Den Boorn, S. H. J. M., & Hendersen, G. M. 2018. Isotopic evidence for changes in the zinc cycle during Oceanic Anoxic Event 2 (Late Cretaceous). *Geology*, **46** (5), 463–466.
- SWEERE, T. C., Dickson, A. J., Jenkyns, H. C., Porcelli, D., Ruhl, M., Murphy, M. J., Idiz, E., Van Den Boorn, S. H. J. M., Eldrett, J. S. & Henderson, G. M. 2020b. Controls on the Cd-isotope composition of the Upper Cretaceous (Cenomanian Turonian) organic-rich mudrocks from south Texas (Eagle Ford Group). *Geochimica et Cosmochimica Acta*, **287**, 251–262.
- SWEET, W. C. 1988. The Conodonta. Clarendon Press, New York, 212 pp
- SZABO, J. 1860. Geologische Detailkonte des Grenzgebietes des Nograder und Pesther Comitates. Jahrbuch des kaiserlich-koniglichen geologischen Reichanstalt, Sitzungberichte (Sitzung am 10. Janner 1860): 41–44.
- TAKAHASHI T., Broecker, W. S. & Langer, S., 1985. Redfield ratio based on chemical data from isopycnal surfaces. *Journal of Geophysical Research: Oceans*, **90** (4), 6907–6924.
- TANNER, L. H., Lucas, S. G., & Chapman, M. G. 2004. Assessing the record and causes of Late Triassic extinctions. *Earth-Science Reviews*, **65** (1–2), 103–139.

Quantifying marine redox across the Triassic–Jurassic mass extinction

- TANNER, L. & Kyte, F. T. 2005. Anomalous iridium enrichment at the Triassic–Jurassic boundary, Blomidon Formation, Fundy basin, Canada. *Earth and Planetary Science Letters*, **240**, 634–641.
- TANNER, L. H., Kyte, F. T., Richoz, S. & Krystyn, L. 2016. Distribution of iridium and associated geochemistry across the Triassic–Jurassic boundary in sections at Kuhjoch and Kendlbach, Northern Calcareous Alps, Austria. *Palaeogeography, Palaeoclimatology, Palaeoecology*, **449**, 13–26.
- TAYLOR, D. G., Smith, P. L., Laws, R. A. & Guex, J. 1983. The stratigraphy and biofacies trends of the lower Mesozoic Gabbs and Sunrise formations, west-central Nevada. *Canadian Journal of Earth Sciences*, **20**, 1598–1680.
- TAYLOR, D. G., Boelling K., Guex, J. 2000. The Triassic/Jurassic System boundary in the Gabbs Formation, Nevada. In: Hall R. L., Smith P. L. (eds) *Advances in Jurassic research*, Trans Tech Publications Ltd, Zurich, pp 225–236.
- TEGNER, C., Marzoli, A., McDonald, I., Youbi, N. & Lindström, S. 2020. Platinum-group elements link the end-Triassic mass extinction and the Central Atlantic Magmatic Province. *Scientific Reports*, **10**: 2482.
- TEICHERT, C., 1988. Crises in cephalopod evolution. In: Marois, M. (Ed.), *L'évolution dans sa Réalité et ses Diverses Modalités*. Fondation Singer-Polignac, Paris, pp. 7–64.
- TEKIN, U. K. 1999. Biostratigraphy and systematics of late Middle and late Triassic radiolarians from the Taurus Mountains and Ankara region, Turkey. *Geologisch–Palaöntologisch Mitteilungen, Sonderband*, **5**, 1–296.
- THIBODEAU, A. M., Ritterbush, K., Yager, J. A., Joshua West, A., Idarra, Y., Bottjer, D. J., Berelson, W. M., Bergquist, B. A. & Corsetti, F. A. 2016. Mercury anomalies and the timing of biotic recovery following the end-Triassic mass extinction. *Nature Communications*, **7**, 11147.
- TIPPER, H. W., Carter, E. S., Orchard, M. J. & Tozer, E. T. 1994. The Triassic–Jurassic (T–J) boundary in Queen Charlotte Islands, British Columbia defined by ammonites, conodonts and radiolarians. *Geobios*, **17**, 485–492.
- TITTENSOR, D. P., Mora, C., Jetz, W., Lotze, H. K., Ricard, D., Berghe, E. V. & Worm, B. 2010. Global patterns and predictors of marine biodiversity across taxa. *Nature*, **466**, 1098–1101.
- TODARO, S., Rigo, M., Randazzo, V. & Di Stefano, P. 2018. The end-Triassic mass extinction: A new correlation between extinction events and $\delta^{13}\text{C}$ fluctuations from a Triassic–Jurassic peritidal succession in western Sicily. *Sedimentary Geology*, **368**, 105–113.
- TOMAŠOVYCH A. & Siblík, M. 2007. Evaluating compositional turnover of brachiopod communities during the end-Triassic mass extinction (Northern Calcareous

References

- Alps): Removal of dominant groups, recovery and community reassembly. *Palaeogeography, Palaeoclimatology, Palaeoecology*, **244**, 170–200.
- TOZER, E. T. 1981. Triassic Ammonoidea: Classification, evolution and relationship with Permian and Jurassic forms. In: House MJ, Senior JR (eds) *The Ammonoidea, Systematics Association Special*, **18**, 65–100.
- TRIBOVILLARD, N., Algeo, T. J., Lyons, T. & Riboulleau, A. 2006. Trace metals as paleoredox and paleoproductivity proxies: An update. *Chemical Geology*, **232**, 12–32.
- TRIBOVILLARD, N., Algeo, T. J., Baudin, F. & Riboulleau, A., 2012. Analysis of marine environmental conditions based on molybdenum–uranium covariation—Applications to Mesozoic paleoceanography. *Chemical Geology*, **324–325**, 46–58.
- ULLMANN, C. V., Szűcs, D., Jiang, M., Hudson, A. J. L., & Hesselbo, S. P., 2021, Geochemistry of microfossil, bulk rock, and secondary calcite in the Early Jurassic strata of the Llanbedr (Mochras Farm), drill core, Cardigan Bay Basin, Wales, UK, *Geology*, **179**, jgs2021-018. <https://doi.org/10.1144/jgs2021-018>.
- URRUTIA-FUCUGAUCHI, J., Camargo-Zanoguera, A., Pérez-Cruz, L. & Pérez-Cruz, G. 2011. The Chixulub multi-ring impact crater, Yucatan carbonate platform, Gulf of Mexico. *Geofísica Internacional*, **50** (1), 99–127.
- VADASZ, E. 1910. A Duna-balparti idosebb rokok oslenytani es foldtani viszonyai [Paleontology and geology of older blocks on the left side of Danube]. Magyar Kinilyi Foldtani Intezet Evkonyve *Annals of the Royal Hungarian Geological Institute*, **18**(2): 101–171 .
- VAN CAPPELLEN, P. & Ingall, E. D. 1996. Redox Stabilization of the Atmosphere and Oceans by Phosphorus-Limited Marine Productivity. *Science*, **271**, 493–496.
- VAN DE SCHOOTBRUGGE, B. & Wignall, P. B., 2015. A tale of two extinctions: converging end-Permian and end-Triassic scenarios. *Geological Magazine*, **153**, Special Issue 2, 332–354.
- VAN DE SCHOOTBRUGGE, B., Tremolada, F., Rosenthal, Y., Bailey, T. R., Feist-Burkhardt, S., Brinkhuis, H., Kent, D. V. & Falkowski, P. G. 2007. End-Triassic calcification crisis and blooms of organic-walled ‘disaster species’. *Palaeogeography, Palaeoclimatology, Palaeoecology*, **244**, 126–141.
- VAN DE SCHOOTBRUGGE, B., Quan, T. M., Lindström, S., Püttmann, W., Heunisch, C., Pross, J., Fiebig, J., Petschick, R., Röhling, H.-G., Richoz, S., Rosenthal, Y. & Falkowski, P. G. 2009. Floral changes across the Triassic/Jurassic boundary linked to flood basalt volcanism. *Nature Geoscience*, **2**, 589–594.
- VAN DE SCHOOTBRUGGE, B., Bachan, A., Suan, G., Richoz, S. & Payne, J. L. 2013. Microbes, mud and methane: Cause and consequence of recurrent early Jurassic anoxia following the end-Triassic mass extinction. *Palaeontology*, 1–25, doi: 10.1111/pala.12034.

Quantifying marine redox across the Triassic–Jurassic mass extinction

- VAN DE SCHOOTBRUGGE, B., Richoz, S., Pross, J., Luppold, F. W., Hunze, S., Wonik, T., Blau, J., Meister, C., van der Weijst, C. M. H., Suan, G., Fraguas, A., Fiebig, J., Herrie, J. O., Guex, J., Little, C. T. S., Wignall, P. B., Püttmann, W. & Oschmann, W. 2019. The Schandelah Scientific Drilling Project: A 25-million year record of Early Jurassic palaeo-environmental change from northern Germany. *Newsletters of Stratigraphy*, **53** (3), 249–296.
- VAN DE SCHOOTBRUGGE, B. van der Weijst, C. M. H., Hollaar, T. P., Vecoli, M., Strother, P. K., Kuhlmann, N., Thein, J., Visscher, H., van Konijnenburg-van Cittert, H., Schobben, M. A. N., Sluijs, A. & Lindström, S. 2020. Catastrophic soil loss associated with end-Triassic deforestation. *Earth-Science Reviews*, **210**, 103332.
- VAN ELDIJK, Wappler, T., Strother, P. K., Van der Weijst, C. M. H., Rajaei, H., Visscher, H. & Van de Schootbrugge, B., 2018. A Triassic–Jurassic window into the evolution of Lepidoptera. *Science Advances*, **4** (1), 1701568.
- VAN GEEN, A., Luoma, S. N., Fuller, C. C., Anima, T., Clifton, H. E. & Trumbore, S. 1992. Evidence from Cd/Ca ratios in foraminifera for greater upwelling off California 4,000 years ago. *Letters to Nature*, **358**, 54–56.
- VAN GEEN, A., McCORKLE, D. C. & KLINKHAMMER, G. P. 1995. Sensitivity of the phosphate-cadmium-carbon isotope relation in the ocean to cadmium removal by suboxic sediments. *Paleoceanography*, **10**(2), 159–169.
- VISHNEVSKAYA, V. 1997. Development of Palaeozoic-Mesozoic Radiolaria in the northwestern Pacific rim. *Marine Micropalaeontology*, **30**, 79–95.
- WALKDEN, G., Parker, J., Kelley, S. 2002. A Late Triassic Impact Ejecta Layer in Southwestern Britain. *Science*, **298**, 2185–2188.
- WANG, Z., Lee, S.-W., Catalano, J. G., Lezamo-Pacheco, J. S., Bargar, J. R., Tebo, B. M. & Giammar, D. E. 2013. Adsorption of Uranium (VI) to Manganese Oxides: X-ray Adsorption Spectroscopy and Surface Complexation Modeling. *Environmental Science and Technology*, **47** (2), 850–858.
- WANG, P., Du, Y., Yu, W., Algeo, T. J., Zhou, Q., Xu, Y., Qi, L., Yuan, L., & Pan, W. 2020. The chemical index of alteration (CIA) as a proxy for climate change during glacial-interglacial transitions in Earth history. *Earth-Science Reviews*, **201**, 103032.
- WARD, P. D., Haggart, J. W. Carter, E. S., Wilbur, D., Tipper, H. W. & Evans, R. 2001. Sudden productivity collapse associated with the Triassic-Jurassic boundary mass extinction. *Science*, **292**, 1148–1151.
- WARD, P. D., Garrison, G. H., Haggart, J. W., King, D. A. & Beattie, M. J. 2004. Isotopic evidence bearing on Late Triassic extinction events, Queen Charlotte Islands, British Columbia, and implications for the duration and cause of the Triassic/Jurassic mass extinction. *Earth and Planetary Science Letters*, **224**, 589–600.

References

- WARD, P. D., Garrison, G. H., Williford, K. H., Kring, D. A., Goodwin, D., Beattie, M. J. & McRoberts, C. A. 2007. *Palaeogeography, Palaeoclimatology, Palaeoecology*, **244**, 281–289.
- WARRINGTON, G., Harland, R. 1975. Palynology of the Trias and Lower Lias of the Larne Borehole. *Bulletin of the Geological Survey of Great Britain*, **50**, 37–50.
- WARRINGTON, G., Cope, J. C. W. & Ivimey-Cook, H. C. 1994. St. Audrie's Bay, Somerset, England: a candidate Global Stratotype Section and Point for the base of the Jurassic System. *Geological Magazine*, **133**, 191–200.
- WASYLENKI, L. E., Weeks, C. L., Bargar, J. R., Spiro, T. G., Hein J. R. & Anbar, A. D. 2011. The molecular mechanism of Mo isotope fractionation during adsorption to birnessite. *Geochimica et Cosmochimica Acta*, **75** (17), 5019–5031.
- WASYLENKI, L. E., Swihart, J. W. & Romaniello, S. J. 2014. Cadmium isotope fractionation during adsorption to Mn oxyhydroxide at low and high ionic strength. *Geochimica et Cosmochimica Acta*, **140**, 212–226.
- WHITESIDE, J. H. & Ward, P. D. 2011. Ammonoid diversity and disparity track episodes of chaotic carbon cycling during the early Mesozoic. *Geology*, **39** (2), 99–102.
- WHITESIDE, J. H., & Grice, K. 2016. Biomarker Records Associated with Mass Extinction Events. *Annual Review of Earth and Planetary Sciences*, **44** (1), 581–612.
- WHITESIDE, J. H., Olsen, P. E., Kent, D. V., Fowell, S. J., & Et-Touhami, M. 2007. Synchrony between the Central Atlantic magmatic province and the Triassic-Jurassic mass-extinction event? *Palaeogeography, Palaeoclimatology, Palaeoecology*, **244** (1–4), 345–367.
- WHITESIDE, J. H., Olsen, P. E., Eglinton, T., Brookfield, M. E., & Sambrotto, R. N., 2010. Compound-specific carbon isotopes from Earth's largest flood basalt eruptions directly linked to the end-Triassic mass extinction. *Proceedings of the National Academy of Sciences*, **107** (15), 6721–6725.
- WIGNALL, P. B. 2001. Large igneous provinces and mass extinctions. *Earth-Science Reviews*, **53** (1-2), 1–33.
- WIGNALL, P. B. & Bond, D. P. G. 2008. The end-Triassic and Early Jurassic mass extinction records in the British Isles. *Proceedings of the Geologists' Association*, **119** (1), 73–84.
- WIGNALL, P. B. & Atkinson, J. W. 2020. A two-phase end-Triassic mass extinction. *Earth-Science Reviews*, **208**, 103282.
- WIGNALL, P. B., Bond, D. P. G., Kuwuhara, K., Newton, R. J. & Poulton, S. W.. 2010. An 80 million year oceanic redox history from Permian to Jurassic pelagic sediments of the Mino-Tamba terrane, SW Japan, and the origin of four mass extinctions. *Global and Planetary Change*, **71**(1–2), 109–123.

Quantifying marine redox across the Triassic–Jurassic mass extinction

WOODLAND, A. W. (Ed.), The Llanbedr (Mochras Farm) Borehole (1971)
Institute of Geological Sciences Report No. 71/18, 115 pp.

WOTZLAW, J.-F., Guex, J., Bartolini, A., Gallet, Y., Krystyn, L., McRoberts, C. A., Taylor, D., Schoene, B. & Schaltegger, U. 2014. Towards accurate numerical calibration of the Late Triassic: High-precision U-Pb geochronology constraints on the duration of the Rhaetian. *Geology*, **42**, 571–574.

WRIGHT, P. Chernes, L & Hodges, P. 2003. Missing mollusks: field testing taphonomic loss in the Mesozoic through early large-scale aragonite dissolution. *Geology*, **31**, 211–214.

YAGER, J. A., West, A. J., Corsetti, F. A., Berelson, W. M., Rollins, N. E., Rosas, S., & Bottjer, D. J. 2017. Duration of and decoupling between carbon isotope excursions during the end-Triassic mass extinction and Central Atlantic Magmatic Province emplacement. *Earth and Planetary Science Letters*, **473**, 227–236.

YOUNG, S. A., Benayoun, E., Kozik, N. P., Hints, O., Martma, T., Bergström, S. M. & Owens, J. D. 2020. Marine redox variability from Baltica during extinction events in the latest Ordovician-early Silurian. *Palaeogeography, Palaeoclimatology, Palaeoecology*, **554**, 1–17.

ZAFFANI, M., Jadoul, F. & Rigo, M. 2018. A new Rhaetian $\delta^{13}\text{C}_{\text{org}}$ record: Carbon cycle disturbances, volcanism, End-Triassic mass Extinction (ETE). *Earth Science Reviews*, **178**, 92–104.

ZAJZON, N., Kristály, F., Pálffy, J. & Németh, T. 2012. Detailed clay mineralogy of the Triassic-Jurassic boundary section at Kendlbachgraben (Northern Calcareous Alps, Austria). *Clay Minerals*, **47**, 177–189.

ZEEBE, R. E., Ridgwell, A., & Zachos, J. C. 2016. Anthropogenic carbon release rate unprecedented during the past 66 million years. *Nature Geoscience*, **9**, 325.

ZHANG, W., Shi, X., Jiang, G., Tang, D. & Wang, X. 2015. Mass-occurrence of oncoids at the Cambrian Series 2-Series 3 transition: Implications for microbial resurgence following an Cambrian Series 2 extinction. *Gondwana Research*, **28**, 432–450.

ZHANG, X & Cui, L., 2016. Oxygen requirements for the Cambrian explosion. *Journal of Earth Sciences*, **27** (2), 187–195.

ZHANG, Y., Planavsky, N. J., Zhao, M., Isson, T., Asael, D., Wang, C., & Wang, F. 2021. The isotopic composition of sedimentary organic zinc and implications for the global Zn isotope mass balance. *Geochimica et Cosmochimica Acta*, **314**, 16–26.

FIGURE REFERENCES:

References

Figure 1a- <https://wellcomecollection.org/works/wswygfdh>

Figure 1c- <https://pixabay.com/photos/charles-robert-darwin-scientists-62911/>

GLOSSARY

anoxia (anoxic)- *A condition in which an environment is deprived of oxygen*

BGR- *Bundesanstalt für Geowissenschaften und Rohstoffe; Federal Institute for Geosciences and Natural Resources*

BGS- *British Geological Survey; repository for the Prees 2-c core*

biocalcification crisis- *The proposed reduction in biocalcification across the Triassic-Jurassic boundary as evidence by a shift to siliciclastic sediments during the late Triassic in many sections [Greene et al. 2012].*

boundary-crosser rate equation- *A rate equation which considers counts of taxa either crossing the bottom and top of an interval or crossing one boundary but not the other [Alroy, 2014].*

CAMP- *The Central Atlantic Magmatic Province; a large igneous province (LIP) which occupied North Africa, the East portion of North America and parts of Southwest Europe during the latest Triassic and earliest Jurassic. It is believed to have played a significant role in the ETME.*

Carbon isotope stratigraphy- *The use of carbon isotope fluctuations (from carbonate or organic samples) to correlate marine and/or terrestrial sections.*

Carnian- *the oldest stage of the Upper Triassic Series; ~237 to ~227 Ma*

catastrophism- *The theory that many now extinct organisms were wiped out by catastrophic events known as ‘revolutions’; counter-argument to uniformitarianism.*

C_{DEF}- *Cadmium enrichment; a palaeo-redox proxy.*

CEB- *Central European Basin; an ancient Tethyan shelf basin which was situated over modern central Europe.*

Choristoceratidae- *A family of Late Triassic and earliest Jurassic ceratitid ammonites; the member *Choristoceras crickmayi* marks the lower margin of the ETME.*

CIA- *Chemical Index for Alteration; a palaeo-weathering proxy initially developed by Nesbitt & Young, (1982).*

continuous time rates- *A rate equation which considers turnover to be occurring continuously over a given time period.*

Glossary

Co*Mn- *The ratio of Cobalt (ppm) to Manganese (%); a palaeo-hydrography proxy developed by Sweere and others (2016).*

Cyclostratigraphy- *The use of cyclical changes in sedimentary facies, as a result of sea-level changes, to correlate marine sections.*

delta (δ)- *A scientific notation which denotes the isotopic ratio of an element, expressed in the form: ((the ratio of the heavy isotope to light isotope in the sample/ the same ratio of a standard) -1) x 1000 ‰*

ECME- *End-Cretaceous mass extinction event; a major extinction event ~65 Ma that is notable for leading to the final demise of avian dinosaurs. Rudist bivalves, diatoms, ammonoids and marine reptiles were also severely affected.*

EDME- *End-Devonian mass extinction event; a series of extinctions which occurred around the Frasnian-Famennian boundary (~370Ma) and the end-Devonian (~360Ma). Tabulate corals, brachiopods, trilobites, and jawless fishes were severely affected.*

EOME- *End-Ordovician mass extinction event; a series of extinctions which occurred at the Ordovician- Silurian boundary. Bryozoans, graptolites, brachiopods, and trilobites were severely affected.*

Endobysate- *A bivalve which bears a byssus/byssus threads for attaching to the sediment; the byssus in this case is used to anchor the bivalve within a burrow or boring (see Epibysate).*

Endolithic- *An organism which lives within a rock, a coral, a shell or in the pore space of a rock.*

Epibysate- *A bivalve which bears a byssus/byssus threads for attaching to seaweed or a rock.*

EPME- *End-Permian mass extinction event; the largest mass extinction event within geological history, known for the extinction of 96% of all marine species and 99% of all species. Rugose corals, crinoids, acanthodians and fusulinids were severely affected.*

ETME- *End-Triassic mass extinction event; a series of extinctions which occurred around the late Triassic. Bivalves, ammonoids, marine reptiles, conodonts and Triassic reefal organisms were particularly affected.*

Quantifying marine redox across the Triassic–Jurassic mass extinction

ETME (Main Interval)- *The term assigned within this thesis to the ‘main’ interval of the end-Triassic mass extinction. The main interval is interpreted to coincide with the main pulse of the ETME at the GSSP which correlates with a large pulses of extinction from other marine sections.*

euxinia (euxinic)- *A condition in which an environment is both anoxic and sulfidic.*

FAD- *First appearance datum; the first recorded appearance of an organism within a stratigraphic sequence.*

Fe_T/Al- *Total Iron: Aluminium ratio; a palaeo-redox proxy.*

functional redundancy- *The ecological circumstance that multiple different organisms and/or species share the same role within an ecosystem (e.g., scavenger/grazer)*

gap-filler rate equation- *A rate equation which considers counts of taxa that occupy the upper and lower intervals of a four-interval moving window, regardless of whether the taxa are found within the two intervals in-between.*

GSNI- *The Geological Society of Northern Ireland*

GSSP- *Global Stratotype Section and Point; a section of strata which is globally representative of a certain geological boundary.*

Heteromorph ammonites- *Uncoiled ammonite forms which largely proliferated during the Jurassic and Cretaceous Periods, however, are also observed during the late Triassic.*

Hettangian- *The first stage of the Jurassic Period; 201.3±0.2 to 199.3±0.3 Ma.*

ICDP- *Intercontinental Drilling Programme; co-funders of the JET project*

JET- *The Early Jurassic Earth Systems and Timescale Project; Drillers of Prees-2c core*

LAD- *Last appearance datum; the last recorded appearance of an organism within a stratigraphic sequence.*

LBEG- *Landesamt f. Bergbau, Energie u. Geologie; Office for Mining, Energy & Geol.*

Ladinian- *The last stage of the Middle Triassic Series; ~242 to ~237 Ma.*

Glossary

Lilstock Formation- *A late Triassic (Rhaetian) formation in the Southwest of Britain which is the upper formation of the Penarth Group. The Formation is underlain by the Westbury Formation and overlain by the Blue Lias Formation (Lias Group).*

LIPs- *Large Igneous Provinces- substantial areas of flood basalt volcanism which produce large volumes of greenhouse gases and can persist for millions of years.*

Magnetostratigraphy- *The use of reversals in magnetic polarity to correlate marine and/or terrestrial sections.*

Mass extinction event- *The widespread and rapid disappearance of a globally distributed higher taxa typically including both marine and terrestrial species.*

M_{NEF}- *Manganese enrichment; a palaeo-redox proxy*

Mo_{EF}- *Molybdenum enrichment; a palaeo-redox proxy*

NERC- *National Environmental Research Council; co-funders of JET and this thesis*

Norian- *The second stage of the Upper Triassic Series; ~227 to ~208.5 Ma.*

origination (rate)- *The rate at which new organisms are evolving/originating*

Palynostratigraphy- *The use of changes in pollen and spore abundance and diversity to correlate marine and/or terrestrial sections.*

part-timer rate equation- *A rate equation which considers counts of taxa that occur directly before or after an interval (within a four-window moving interval window), yet are not found within the interval itself.*

PETM- *The Palaeocene- Eocene Thermal Maximum; a hyperthermal event which occurred at the boundary between the Palaeocene and Eocene Series.*

per mille (‰)- *a unit of scientific measurement denoting a value out of 1000; commonly used for isotopic ratios (see δ)*

Phanerozoic- *The current Eon, which proceeded the Proterozoic; 541.0±1.0 to present day*

PPZ- *The Pre-Planorbis Zone; a late Triassic zone of ammonite stratigraphy in Northwestern Europe distinguished by the absence of ammonites.*

Quantifying marine redox across the Triassic–Jurassic mass extinction

Psiloceratidae- *A family of ammonites which were in existence from the Jurassic to Cretaceous Period; member Psiloceras Spelae marks the upper margin of the ETME and base of the TJB.*

pulsed turnover- *A turnover which occurs in sequential pulses over a period of time as opposed to all at once or continuously.*

PZE- *Photic Zone Euxinia*

revolutions- *The term applied by Georges Cuvier (founder of catastrophism) to extinction or turnover events.*

Rhaetian- *The last stage of the Upper Triassic Series; ~208.5 to 201.3±0.2 Ma.*

SAB- *St. Audrie's Bay; site of the Somerset-1 and Somerset-2 core extraction.*

scablands- *Large-scale channelised plains formed through catastrophic outflows during the last glacial maximum; term coined by J. Harlen Bretz.*

Serpenticone ammonites- *A common shell type during the latest Triassic which is coiled, with all previous whorls visible. The more sedentary, pelagic mode of life associated with this shell type is believed to have been very successful during the ETME.*

Sinemurian- *The second stage of the Jurassic Period (and Lower Jurassic Series); 199.3±0.3 to 190.8±1.0 Ma*

SSD- *Soft sediment deformation; e.g., Late Triassic seismite deposits*

three-timer extinction rate equation- *A rate equation which considers counts of taxa that are sampled across at least three out of four consecutive intervals within a four interval moving window.*

Ti/Al- *Titanium: Aluminium ratio; a palaeo-detrital proxy*

TJB- *The boundary between the Triassic and Jurassic Periods; dated to 201.36Ma; denounced biostratigraphically by the FAD of ammonite Psiloceras Spelae*

turnover proportions- *A rate equation which uses first and last appearance counts divided by diversity count to create a proportion [Alroy, 2008].*

U_{EF}- *Uranium enrichment; a palaeo-redox proxy*

Glossary

Uniformitarianism (Gradualism)- *The theory that life and landforms change gradually over long time periods of time through steady state processes; counter-argument to catastrophism.*

Westbury Formation- *A late Triassic (Rhaetian) formation in the South West of England which is the lower formation of the Penarth Group. The Formation is underlain by the Blue Anchor Formation and overlain by the Cotham Member (Lilstock Formation).*

X/Ca- *Trace Element/Calcium Ratio within marine carbonates; a palaeo-redox proxy*

Zn_{EF}- *Zinc enrichment; a palaeo-redox proxy*

Zr/Al- *Zirconium: Aluminium ratio; a palaeo-detrital proxy*

APPENDICES

APPENDIX 1: MASS EXTINCTION SEVERITY RANKING DATA

	ESR	FDL	GE	BXE	PE	PCE-1	PCE-2	HWR	
K-T	II	14.85	37%	40%					
T-J	III	21.7	37%	73%	0.7				
P-T	I	48.75	58%	83%	0.73				
E Dev	IV	24.4	29%	40%	0.58				
E Ord	V	23	46%	52%	0.63				
K-T	2	5	3	4	?	5	5		5 (4.0)
T-J	3	4	3	2	2	2	2		2 (2.6)
P-T	1	1	1	1	1	1	1		1 (1.0)
E Dev	4	2	5	4	4	4	4		4 (3.6)
E Ord	5	3	2	3	3	3	3		3 (3.5)
K-T	2	5	3	4	?	5	5	5	4
T-J	3	4	3	2	2	2	2	4	3
P-T	1	1	1	1	1	1	1	1	1
E Dev	4	2	5	4	4	4	4	3	3.67
E Ord	5	3	2	3	3	3	3	2	3

Figure 1:- A revised ranking for the severity of major Phanerozoic mass extinction events. ESR- ecological severity ranking, FDL- Familial diversity loss, GE- percentage genus extinction, BXE- boundary crosser extinction rates, PE- pulsed extinction rate, PCE- per capita extinction, HWR- Hallam & Wignall, 1997. ESR averaged from McGhee et al., 2004, 2013; Bambach and Knoll, 2001. FDL averaged from Benton, 1995; Sepkoski, 1982. GE averaged from Sepkoski et al., 1996, 2002; Bambach et al., 2004; Bond & Grasby, 2017. BXE from Alroy, 2010. PE from Foote, (2005). PCE-1 from Peters, (2008). Final rankings in bottom right hand corner. For further information see the attached excel file (Appendix 1).

APPENDIX 2: DETAILED GEOCHEMICAL REVIEWS

APPENDIX 2.1: CADMIUM

Introduction to Cadmium- Cadmium (Cd) is concentrated within the Earth's crust as sulfide deposits and is transported to the oceans through rivers ($0.04\text{--}0.15 \times 10^8 \text{molyr}^{-1}$), dust ($0.02\text{--}0.11 \times 10^8 \text{molyr}^{-1}$) and hydrothermal sources ($0.02\text{--}0.26 \times 10^8 \text{molyr}^{-1}$) (Calvert & Pedersen, 1993; Morford & Emerson, 1999; Bryan et al., 2021). Under oxidising conditions Cd exists in the oceans as $\text{Cd}^{2+}_{(\text{aq})}$, commonly in the form of $\text{CdCl}^{+}_{(\text{aq})}$ (Emerson et al., 1983; Calvert & Pedersen, 1993; Morford & Emerson, 1999; Tribovillard et al., 2006). Unlike some other redox-indicative transitional elements (e. g. Mo), Cd is very readily recycled within the water column over shorter time scales due to its role as a micronutrient (Bruland 1980; Boyle 1981, 1988; Calver & Pedersen, 1993; Piper & Perkins, 2004; Tribovillard et al., 2006; Bruland et al., 2014; Conway & John, 2015). Cd consequently has a relatively short residence time within the oceans ($\sim 50\text{kyr}$), and a relatively low dissolved abundance amongst redox indicative trace elements ($\sim 0.6 \text{nmol/kg}$) (Boyle, 1992; Morford & Emerson, 1999; Tribovillard et al., 2006). However, despite some inconsistencies between Cd and other redox proxies, Cd is consistently identified as exhibiting high levels of enrichment within anoxic sediments (Calvert & Pedersen, 1993; Van Geen et al., 1995; Tribovillard et al., 2006). This would suggest a removal mechanism for Cd specific to low oxygen conditions (Van Geen et al., 1995). The remainder of this section will further discuss Cd removal mechanisms and the role of Cd as both a palaeoredox proxy and micronutrient.

Cadmium and its micronutrient behaviour- Early studies of dissolved Cd within the oceans noted that Cd exhibits a similar spatial distribution to the micronutrient

Appendices

'phosphate' (Boyle, et al., 1976; Bruland et al., 1978; Bruland, 1980, 1983). These early studies, alongside subsequent research revealing similar results, have led researchers to conclude that Cd is taken up by marine organisms within the water column (Calvert & Pedersen, 1993; Van Geen et al., 1995; Morford & Emerson, 1999; Piper & Perkins, 2004, Tribovillard et al., 2006; Bruland et al., 2014; Janssen et al., 2014; Conway & John, 2015; Chen et al., 2021). However, biological uptake of Cd is contrary to its status as a toxic element, and the function of Cd as a nutrient remains poorly understood (Chen et al., 2021). The only biological function identified for Cd so far is the replacement of Zn in carbonic anhydrase (Price & Morel, 1990; Lee & Morel, 1995; Xu et al., 2008; Lionetto et al., 2016; Chen et al., 2021). Studies have also revealed that Cd uptake increases when other metals are not readily bioavailable (Lee & Morel, 1995; Xu et al., 2007).

The spatial distribution of dissolved Cadmium- Despite the exact function of Cd as a nutrient being poorly understood, biological uptake is known to be a major control on the spatial distribution of dissolved Cd. Cd is removed quantitatively in the photic zone through biological uptake resulting in the photic zone being Cd depleted (Boyle et al., 1976; Bruland et al., 1978; Bruland, 1980, 1983; Bruland & Coale, 1985; Saager et al., 1992; Calvert & Pedersen, 1993; Tribovillard et al., 2006; Janssen et al., 2014; Conway & John, 2015; Bryan et al., 2021). Cd is then delivered to marine sediments in association with organic matter (OM) and is liberated by OM decay (McCorkle & Klinkhammer, 1991; Calvert & Pedersen, 1993; Piper & Perkins, 2004; Tribovillard et al., 2006). The top few centimetres of bottom water sediments subsequently exhibit sharp increases in dissolved cadmium (Emerson et al., 1984; Gobeil et al., 1987; McCorkle & Klinkhammer, 1991). A study by Westerlund et al., (1986) revealed that

Quantifying marine redox across the Triassic–Jurassic mass extinction

the release rate of dissolved cadmium is directly proportional to oxygen availability. However, despite OM providing a source of Cd accumulation, Cd is not thought to scavenge to OM and therefore must be removed into marine sediments through alternative pathways (Guy & Chakrabarti, 1976; Pedersen et al., 1989; Conway & John, 2015).

Adsorption onto mineral surfaces- One such pathway is through the adsorption of Cd onto pelagic clays and mineral surfaces under oxic to anoxic conditions (e. g. Fe oxides, Fe-Mn oxyhydroxides and Fe-Mn biochar). Morford & Emerson, (1999) interpret that Cd accumulation may be possible through adsorption onto freshly precipitated Fe oxides, an interpretation which was mirrored by Chen et al., (2021), based on organic rich sediments from the Pacific margin, and Davies-Colley et al., (1984), based on aerobic, estuarine sediments. Lee et al., (2018) suggest that Cd may adsorb onto Fe-oxyhydroxide phases in the lower Peru margin oxygen minimum zone (OMZ). Janssen et al., (2014) and Conway & John (2015) similarly suggest that CdS forming within reducing, open marine sub-environments of the OMZ is scavenged onto Fe-oxyhydroxides. McCorkle & Klinkhammer, (1991) interpret Cd adsorption onto Fe-oxyhydroxides with the suboxic sediment pore space of the Californian Margin despite a low correlation between iron and Cd in their dataset. Whilst Dong et al., (2000) and Tessier et al., (1985, 1996) suggest that Fe-oxides and oxyhydroxides play an important role in the removal of Cd within oxic lake waters and sediments.

Rosenthal et al., (1995) meanwhile suggest that there may be an association between Cd and Mn-oxides and downplay the importance of Fe mineral phases in Cd removal. A connection between Cd and Mn is also supported by cadmium adsorption onto deep

Appendices

ocean Fe-Mn crusts as well as studies of Cd isotopic fractionation during Mn-oxyhydroxide adsorption (Schmitt et al., 2009; Horner et al., 2010, 2011; Wasylenki et al., 2014). Davies-Colley et al., (1984) also suggest that manganese phases may contribute to Cd binding and Yin et al., (2020) suggest that Fe-Mn binary oxide-biochar may act as an effective adsorbent for Cd removal from aqueous solutions. Whilst recent research by Groeningen et al., (2020) reports that the surface precipitation of Mn^{2+} onto clay minerals enhances Cd^{2+} adsorption under anoxic conditions. However, Gobeil et al., (1997) conversely report sedimentary Cd enrichment alongside Mn depletion.

Despite surface adsorption clearly representing a valid removal pathway for Cd, the outflux flux of Cd through pelagic clays and Fe-Mn oxides combined is <4% of the global ocean cadmium output (Schmitt et al., 2009; Horner et al., 2010; Bryan et al., 2021). Oxidic surface sediments are also reported to be an insignificant output flux in the global ocean mass balance of Cd (Little et al., 2015; Bryan et al., 2021). Whilst carbonates account for between 2.5% and ~2.8% of the global ocean Cd output (Horner et al., 2011; Bryan et al., 2021). Hydrothermal sources account for between 12.5% and ~40% of oceanic Cd output, although these figures are based on quantitative removal around the vent site (Bryan et al., 2021).

Cadmium removal under oxygen poor conditions- However, by far the most significant global ocean output for Cd is suboxic and anoxic margin sediments which account for ~93% of global oceanic Cd output. Based on studies of ancient and existing oxygen-poor marine environments, Cd is known to form an insoluble particulate phase under reducing conditions (Elderfield et al., 1981; McCorkle & Klinkhammer, 1991; Calvert & Pedersen, 1993; Tribovillard et al., 2006; Bryan, 2018; Sweere et al., 2020). In anoxic

Quantifying marine redox across the Triassic–Jurassic mass extinction

basins dissolved Cd decreases from a factor of 2 to a factor of 10 from oxic to anoxic water masses (Calvert & Pedersen, 1993). Pronounced depletions of dissolved Cd are exhibited in anoxic basins (Jacobs & Emerson, 1982; Jacobs et al., 1985, 1987), and Cd is also enriched in both mildly and strongly reducing sediments, with low dissolved Cd concentrations being observed in anoxic and suboxic pore waters (Elderfield et al., 1981; Gobeil et al., 1987; McCorkle & Klinkhammer, 1991; Tribovillard et al., 2006). Oil shales can exhibit greater levels of enrichment for Cd than classic redox-diagnostic elements (Mo and U) and geological intervals indicative of anoxic oceanic conditions exhibit Cd concentrations far in excess of crustal concentrations when normalised to detrital input (El-Hasan, 2008; Sweere et al., 2020).

Cadmium-sulfide formation- Under oxygen-poor conditions dissolved Cd is primarily removed through the formation of CdS (Calvert & Pedersen, 1993; Van Geen et al., 1995; Morford & Emerson, 1999; Tribovillard et al., 2006). The removal of Cd through CdS formation is supported by solid phase Cd concentrations increasing in the presence of acid volatile sulfides (AVS) (Gobeil et al., 1997). Cd also exhibits a strong, positive correlation with sulfur in oil shales (El-Hasan, 2008) and Conway and John (2015) report negative Cd* within low oxygen waters, also supporting CdS precipitation.

CdS formation occurs under reducing conditions just below the level of oxygen detection (Van Geen et al., 1995). This can be within suboxic, open marine environments in the presence of sinking organic matter (Janssen et al., 2014; Conway & John, 2015; Bianchi et al., 2018; Guinoiseau et al., 2019), in bottom waters of reducing continental margins near to the sediment-water interface (Gendron et al., 1986; Xie et

Appendices

al., 2019; Plass et al., 2020), in suboxic to anoxic pore waters of marine sediments (Elderfield et al., 1981; Rosenthal et al., 1995), or within a euxinic water column (Jacobs et al., 1985; Takéré et al., 2001).

The formation of CdS within marine sediments has been particularly well studied. In suboxic to anoxic pore waters free sulfur co-precipitates with dissolved cadmium to form CdS or an alternative sulfide phase (e. g. $\text{Cd}(\text{HS})_2$, $\text{Cd}(\text{HS})_3$, $\text{Cd}(\text{HS})_4$) (Elderfield et al., 1981; Jacobs & Emerson, 1982; Jacobs et al., 1985; Calvert & Pedersen, 1993; Davies-Collet et al., 1995; Tribovillard et al., 2006). Laboratory experiments have determined that CdS may equally form through surface exchange with ferrous monohydride at sub μmolkg^{-1} H_2S concentrations (Framson & Leckie, 1978). However, other studies have found iron to be insignificant in Cd removal and instead suggest that Cd likely forms a separate insoluble sulfide phase (Huerta-Diaz & Morse, 1992; Rosenthal et al., 1995; Tribovillard et al., 2006). Framson & Leckie (1978)'s observations regarding low H_2S concentrations have however been corroborated by subsequent research. A study by Rosenthal et al., (1995) has revealed that significant Cd removal, through CdS precipitation, can occur under very low H_2S concentrations. Rosenthal et al., (1995) estimate the upper limit of H_2S for Cd removal to be between $1\mu\text{molkg}^{-1}$ and $4\mu\text{molkg}^{-1}$. Therefore, significant CdS precipitation can occur under suboxic conditions where H_2S concentrations are un-detectable. Research by Van Geen et al., (1995) similarly concludes that Cd accumulation is enhanced under suboxic conditions and that suboxic sediments form a major sink for Cd.

Rosenthal et al., (1995) also find that the contribution of organic Cd to the formation of insoluble Cd phases is negligible and that authigenic Cd in marine sediments must

Quantifying marine redox across the Triassic–Jurassic mass extinction

largely originate from overlying seawater. Dickson et al., (2020) corroborate Rosenthal et al., (1995) through their calculation that organically bound Cd only accounts for 3.6% of authigenic Cd within the Posidonia Shale. Therefore, it is widely agreed upon that authigenic Cd is largely diffused from the overlying water column (Framson & Leckie, 1978; Davis-Colley et al., 1984, 1985; Gobeil et al., 1987; Pedersen et al., 1989; Rosenthal et al., 1995; Davies-Colley et al., 1995; Gobeil et al., 1997; Bryan et al., 2021). This would suggest that cadmium accumulates under oxygenated conditions and is removed under anoxic conditions (Calvert & Pedersen, 1993; Piper & Perkins, 2004).

Despite significant Cadmium removal being observed under low H₂S concentrations (Rosenthal et al., 1995; Van Geen et al., 1995), the opposite is true for high H₂S concentrations (~10⁻³M) (Calvert & Pedersen, 1993). Under high sulfide concentrations Cd may form complexes in association with bisulfides, polysulfides and elemental sulfur which complex with organic ligands to form soluble complexes (Jacobs & Emerson, 1982; Emerson et al., 1983; Jacobs et al., 1985; Davies-Colley et al., 1985; Pedersen et al., 1989). Therefore, deep sea sediments may act as a Cd source due to an increase in Cd solubility (Klinkhammer et al., 1982; Emerson et al., 1984; Jacobs et al., 1985; Davies-Colley et al., 1985; Gobeil et al., 1987). Despite there being no evidence to support CdS-ligand complexation, Gobeil et al., (1987) have provided evidence for the existence of soluble, electrochemically inactive cadmium complexes in deeper pore waters through UV irradiation experiments and Jacobs et al., (1985) believe that CdS-ligand complexation may play an important role in Cd thermodynamic equilibrium equations.

Appendices

- BIANCHI, D., WEBER, T. S., KIKO, R. & DEUTSCH, C. 2018. Global niche of marine anaerobic metabolisms expanded by particle microenvironments. *Nat. Geosci.*, **11**, 263–268.
- BOYLE, E. A., SCLATER, F. & EDMOND, J. M. 1976. On the marine geochemistry of cadmium. *Nature*, **263**, 42–44.
- BOYLE, E. A., 1981. Cadmium, zinc, copper and barium in foraminifera tests. *Earth and Planetary Science Letters*, **53**, 11–35.
- BOYLE, E. A., 1988. Cadmium: chemical tracer of deep water paleoceanography. *Paleoceanography*, **3**, 471–489.
- BOYLE, E. A. 1992. Cadmium and $\delta^{13}\text{C}$ paleochemical ocean distributions during the stage 2 glacial maximum, *Annu. Rev. Earth Planet. Sci.*, **20**, 245–287.
- BRULAND, K. W., KNAUER, G. A. & MARTIN, J. H. 1978. Cadmium in northeast Pacific waters. *Limnol. Oceanogr.*, **23**(4), 618–625.
- BRULAND, K. W. 1980. Oceanographic distributions of cadmium, zinc, nickel and copper in the north Pacific. *Earth and Planetary Science Letters*, **47**, 176–198.
- BRULAND, K. W. 1983. Trace metals in seawater *In Chemical Oceanography* (eds. J. P. RILEY and R. CHESTER) **8**, Ch. 45, 157–215. Academic Press.
- BRULAND, K. W., MIDDAG, R. & LOHAN, M. C. 2014. Controls of trace metals in Seawater *In Treatise of Geochemistry* 2nd edition (H. D. Holland, K. K. Turekian (eds.)), Oxford, Elsevier, **8**, 19–51.
- BRYAN, A. 2018. Investigation of the controls on the cadmium isotope composition of modern marine sediments. PhD Thesis.
- BRYAN, A. L., DICKSON, A. J., DOWDALL, F., HOMOKY, W. B., PORCELLI, D. & HENDERSON, G. M. 2021. Controls on the cadmium isotope composition of modern marine sediments. *Earth and Planetary Science Letters*, **565**, 116946.
- CALVERT, S. E. & PEDERSEN, T. F., 1993. Geochemistry of Recent oxic and anoxic marine sediments: Implications for the geological record. *In: R.J. Parkes, P. Westbroek and J.W. de Leeuw (Editors)*, Marine Sediments, Burial, Pore Water Chemistry, Microbiology and Diagenesis. *Mar. Geol.*, **113**, 67–88.
- CHEN, L., LITTLE, S. H., KREISSIG, K., SEVERMANN, S & McMANUS, J. 2021. Isotopically Light Cd in Sediments Underlying Oxygen Deficient Zones. *Frontiers in Earth Science*, **9**, 623720.
- CONWAY, T. M. & JOHN, S. G. 2015. The cycling of iron, zinc, cadmium in northeast Pacific Ocean – Insights from stable isotopes. *Geochimica et Cosmochimica Acta*, **164**, 262–283.

Quantifying marine redox across the Triassic–Jurassic mass extinction

- DAVIS-COLLEY, R. J., NELSON, P. O. & Williamson, K. J., 1984. Copper and cadmium uptake by estuarine sedimentary phases. *Environ. Sci. Technol.*, **18**, 491–499.
- DAVIES-COLLEY, R. J., NELSON, P. O. & WILLIAMSON, K. J. 1985. Sulfide control of cadmium and copper concentrations in an anaerobic estuarine sediment. *Mar. Chem.*, **16**, 173–186. *Geochimica et Cosmochimica Acta*, **287**, 205–220.
- DICKSON, A. J., IDIZ, E., PORCELLI, D. & VAN DEN BOORN, S. H. J. M. 2020. The influence of thermal maturity on the stable isotope compositions and concentrations of molybdenum, zinc and cadmium in organic-rich marine mudrocks.
- DONG, D., NELSON, Y. M., LION, L. W., SHULER, M. L. & GHORSE, W. C. 2000. Adsorption of Pb and Cd onto metal oxides and organic material in natural surface coatings as determined by selective extractions: New evidence for the importance of Mn and Fe oxides. *Water Research*, **34(2)**, 427–436
- ELDERFIELD, H., McCAFFREY, R. J., LUEDTKE, N., BENDER, M. & TRUESDALE, V. W. 1981. Chemical diagenesis of Narragansett Bay sediments. *Am. J. Sci.*, **281**, 1021–1055.
- EL-HASAN, T. 2008. Geochemistry of redox-sensitive trace elements and its implication on the mode of formation of the Upper Cretaceous oil shales, Central Jordan. *N. Jb. Geol. Paläont. Abh.*, **249(3)**, 333–344.
- EMERSON, S., JACOBS, L., & TEBO, B. 1983. The behavior of trace metals in marine waters: solubilities at the oxygen-hydrogen sulfide interface *In Trace Metals in Seawater* (eds. C. S. WONG et al.). Plenum, New York.
- EMERSON, S., JAHNKE, R. & HEGGIE, D. 1984. Sediment-water exchange in shallow water estuarine sediments. *J. Mar. Res.*, **42**, 709–730.
- FRAMSON, P. E. & LECKIE, J. O. 1978. Limits of coprecipitation of cadmium and ferrous sulfides, *Environ. Sci. Technol.*, **12**, 465–469.
- GOBEIL, C., SILVERBERG, N., SUNDBY, B. & COSSA, D. 1987. Cadmium diagenesis in Laurentian Trough sediments. *Geochimica et Cosmochimica Acta*, **51**, 589–596.
- GOBEIL, C., MACDONALD, R. W., & SUNDBY, B. 1997. Diagenetic separation of cadmium and manganese in suboxic continental margin sediments. *Geochim. Cosmochim. Acta*, **61**, 4647–4654.
- GROENINGEN, N. V., GLÜCK, B., CHRISTL, I. & KRETZCHMAR, R. 2020. Surface precipitation of Mn²⁺ on clay minerals enhances Cd²⁺ sorption under anoxic conditions. *Environmental Science: Processes & Impacts*, **22**, 1654.
- GUINOISEAU, D., GALER, S. J. G., ABOUCHAMI, W., FRANK, M., ACHTERBERG, E. P., and HAUG, G. H. 2019. Importance of cadmium sulfides for biogeochemical cycling of Cd and its isotopes in oxygen deficient zones-A case study of the Angola basin. *Glob. Biogeochem. Cycles*, **33**, 1746–1763.

Appendices

GUY, R. D. & CHAKRABARTI, C. L., 1976. Studies of metal-organic interactions in modern systems pertaining to natural waters. *Can. J. Chem.*, **16**, 2600–2611.

HORNER, T. J., SCHÖNBÄCHLER, M., REHKÄMPER, M., NIELSEN, S. G., WILLIAMS, H., HALLIDAY, A. N., XUE, Z. & HEIN, J. R. 2010. Ferromanganese crusts as archives of deep water Cd isotope compositions. *Geochem. Geophys. Geosyst.* **11**, 121. doi:10.1029/2009gc002987.

HORNER, T. J., RICKABY, R. E. M., HENDERSON, G. M. 2011. Isotopic fractionation of cadmium into calcite. *Earth Planet. Sci. Lett.*, **312**, 243–253.

HUERTA-DIAZ, M. A. & MORSE, J. W. 1992. Pyritisation of trace metals in anoxic marine sediments. *Geochim. Cosmochim. Acta*, **56**, 2681–2702.

JACOBS, L., & EMERSON, S. 1982. Trace metal solubility in an anoxic fjord, *Earth Planet. Sci. Lett.*, **60**, 237–252.

JACOBS, L., EMERSON, S. & SKEI, J. 1985. Partitioning and transport of metals across the O₂/H₂S interface in a permanently anoxic basin: Framvaren Fjord, Norway. *Geochim. Cosmochim. Acta*, **49**, 1433–1444.

JACOBS, L., EMERSON, S. & HUESTED, S. S. 1987. Trace metal geochemistry in the Cariaco Trench, *Deep Sea Res.*, **34**, 965–981.

JANSSEN, D. J., CONWAY, T., JOHN, S. G., CHRISTIAN, J. R., KRAMER, D. I., PEDERSEN, T. F. & CULLEN, J. T. 2014. Undocumented water column sink for cadmium in open ocean oxygen-deficient zones. *PNAS*, **111**(19), 6888–6893.

KLINKHAMMER, G. HEGGIE, D. T. & GRAHAM, D. W. 1982. Metal diagenesis in oxic marine sediments. *Earth Planet Sci. Lett.*, **61**, 211–219.

LEE, J. G. & MOREL, F. M. M. 1995. Replacement of zinc by cadmium in marine phytoplankton. *Marine Ecology Progress Series*, **127**, 305–309.

LEE, J.-M., HELLEr, M. I., & LAM, P. J. 2018. Size distribution of particulate trace elements in the U.S. GEOTRACES eastern pacific zonal transect (GP16). *Mar. Chem.*, **201**, 108–123.

LIONETTO, M. G., CARICATO, R., GIORDANO, M. E. & SCHETTINO, T. 2016. The Complex Relationship between Metals and Carbonic Anhydrase: New Insights and Perspectives. *International Journal of Molecular Sciences*, **17**, 127, doi:10.3390/ijms17010127.

LITTLE, S. H., VANCE, D., LYONS, T. W. & McMANUS, J. 2015. Controls on trace metal authi- genic enrichment in reducing sediments: insights from modern oxygen-deficient settings. *Am. J. Sci.*, **315**, 77–119.

McCORKLE, D. C. & KLINKHAMMER, G. P. 1991. Porewater cadmium geochemistry and the pore water cadmium relation. *Geochimica et Cosmochimica Acta*, **55**, 161–168.

Quantifying marine redox across the Triassic–Jurassic mass extinction

- MIDDAG, R., VAN HEUVEN, S. M. A. C., BRULAND, K. W. & DE BAAR, H. J. W. 2018. The relationship between cadmium and phosphate in the Atlantic Ocean unravelled, *Earth and Planetary Science Letters*, **492**, 79–88,
- MORFORD, J. L & EMERSON, S. 1999. The geochemistry of redox sensitive trace metals in sediments. *Geochimica et Cosmochimica Acta*, **63(11-12)**, 1735–1750.
- PEDERSEN, T. F., WATERS, R. D. & MACDONALD, R. W. 1989. On the natural enrichment of cadmium and molybdenum in the sediments of Ucluelet Inlet, British Columbia. *Sci. Total Environ.*, **79**, 125–139.
- PIPER, D. Z., PERKINS, R. B., 2004. A modern vs. Permian black shale— the hydrography, primary productivity, and water-column chemistry of deposition. *Chem. Geol.*, **206**, 177–197.
- PRICE, N. M. & MOREL, F. M. M. 1990. Cadmium and cobalt substitution for zinc in a marine diatom. *Nature*, **344**, 658–660.
- ROSENTHAL, Y., LAM, P., BOYLE, E. A. & THOMSON, J. 1995. Authigenic cadmium enrichments in suboxic sediments: Precipitation and postdepositional mobility. *Earth and Planetary Science Letters*, **132**, 99–111.
- SAAGER, P. M., DE BAAR, H. J. W. & HOWLAND, R. J. 1992. Cd, Zn, Ni and Cu in the Indian Ocean. *Deep Sea Research, Part A: Oceanographic Research Papers*, **39(1)**, 9–35.
- SCHMITT, A.-D., GALER, S. J. G. & ABOUCHAMI, W. 2009. Mass-dependent cadmium isotopic variations in nature with emphasis on the marine environment. *Earth Planet. Sci. Lett.*, **277**, 262–272.
- SWEERE, T. C., DICKSON, A. J., JENKYNS, H. C. & PORELLI, D. 2020a. Zinc- and Cadmium-isotope evidence for redox driven perturbations to global micronutrient cycles during Oceanic Anoxic Event 2 (Late Cretaceous). *Earth and Planetary Science Letters*, **546**, 116427.
- SWEERE, T. C., DICKSON, A. J., JENKYNS, H. C., PORCELLI, D., RUHL, M., MURPHY, M. J., IDIZ, E., VAN DEN BOORN, S. H. J. M., ELDRETT, J. S. & HENDERSON, G. M. 2020b. Controls on the Cd-isotope composition of the Upper Cretaceous (Cenomanian Turonian) organic-rich mudrocks from south Texas (Eagle Ford Group). *Geochimica et Cosmochimica Acta*, **287**, 251–262.
- TANKÉRÉ, S. P. C., MULLER, F. L. L., BURTON, J. D., STATHAM, P. J., GUIEU, C. & MARTIN, J.-M. 2001. Trace metal distributions in shelf waters of the northwestern Black Sea. *Continental Shelf Res.*, **21**, 1501–1532.
- TESSIER, A., RAPIN, F. & CARIGNAN, R. 1985. Trace metals in oxic lake sediments: possible adsorption onto iron oxyhydroxides. *Geochimica et Cosmochimica Acta*, **49**, 183–194.

Appendices

- TESSIER, A., FORTIN, D., BELZILE, N., DEVITRE, R. R. & LEPPARD, G. G. 1996. Metal sorption to diagenetic iron and manganese oxyhydroxides and associated organic matter: Narrowing the gap between field and laboratory measurements. *Geochimica et Cosmochimica Acta*, **60(3)**, 387–404.
- TRIBOVILLARD, N., ALGEO, T. J., LYONS, T. & RIBOULLEAU, A. 2006. Trace metals as paleoredox and paleoproductivity proxies: An update. *Chemical Geology*, **232**, 12–32.
- VAN GEEN, A., McCORKLE, D. C. & KLINKHAMMER, G. P. 1995. Sensitivity of the phosphate-cadmium-carbon isotope relation in the ocean to cadmium removal by suboxic sediments. *Paleoceanography*, **10(2)**, 159–169.
- WASYLENKI, L. E., SWIHART, J. W. & ROMANIELLO, S. J. 2014. Cadmium isotope fractionation during adsorption to Mn oxyhydroxide at low and high ionic strength. *Geochimica et Cosmochimica Acta*, **140**, 212–226.
- WESTERLUND, S. G., ANDERSON, L. G., HALL, P. O. J., IVER-FELDT, A., RUTGERS VAN DER LOEFF, M. M. & SUNDBY B. 1986. Benthic fluxes of cadmium, copper, nickel, zinc, and lead in the coastal environment. *Geochimica et Cosmochimica Acta*, **50**, 1289–1296.
- XIE, R. C., REHKÄMPER, M., GRASSE, P., VAN DE FLIERDT, T., FRANK, M. & XUE, Z. 2019. Isotopic evidence for complex biogeochemical cycling of Cd in the eastern tropical South Pacific. *Earth Planet. Sci. Lett.*, **512**, 134–146.
- XU, Y., FENG, L., JEFFREY, P., SHU, Y. & MOREL, F. M. M. 2008. Structure and metal exchange in the cadmium carbonic anhydrase of marine diatoms. *Nature*, **452**, 56–61.
- XU, Y., TANG, D., SHAKED, Y. & MOREL, F. M. M. 2007. Zinc, cadmium, and cobalt interreplacement and relative use efficiencies in the coccolithophore *Emiliania huxleyi*. *Limnol. Oceanogr.*, **52**, 2294–2305.
- YIN, G., SONG, X., TAO, L., SARKAR, B., SARMAH, A. K., ZHANG, W., LIN, Q., XIAO, R., LIU, Q. & WANG, H. 2020. Novel Fe-Mn binary oxide-biochar as an adsorbent for removing Cd(II) from aqueous solutions. *Chemical Engineering Journal*, **389**, 124465.

APPENDIX 2.2: IRON

Early palaeo-redox techniques- Prior to the use of Fe speciation as a palaeo-redox proxy, studies used micropalaeontology, geochemical indicators, carbon-sulfur relationships and isotopes studied alongside mineralogy [Raiswell *et al.*, 2018].

However, each of these techniques comes with its own limitations. Interpretations of redox conditions through the use of micropalaeontology are complicated if the fossil material is poorly preserved or absent, and may be insensitive to ecological shifts in the conditions of interest; geochemical indicators often require a minimum sample weight for analysis, and isotope techniques involve time consuming elemental separations and expensive instrumentation [Raiswell *et al.*, 2018].

Degree of Pyritisation (DOP)- However, with the initiation of pyrite formation studies during the 1980s, there was suddenly an easy solution with regards to reconstructing palaeo-environmental redox conditions [Berner, 1970; Berner, 1984; Raiswell & Berner, 1985; Raiswell *et al.*, 1988]. This came in the form of the ‘Degree of Pyritisation’ (DOP). Initially developed by Bob Berner to study the limitations on pyrite genesis [Berner, 1970], DOP was later used to better understand marine redox conditions and their effect on iron pyrite formation [Raiswell & Berner, 1985, 1986; Raiswell *et al.*, 1988; Canfield *et al.*, 1992].

Iron pyrite is known to be formed in oxygen-poor bottom waters and pore waters, where sulphate (SO_4^{2-}) is reduced to sulphur (H_2S) by anaerobic bacteria. Anaerobic sulphate reduction by microbial organisms occurs through the metabolism of labile organic matter (Fig.1) [Berner, 1970; Lyons & Severmann, 2006]. However, the reaction between H_2S and Fe primarily forms iron monosulphide compounds (e.g., greigite), and elemental sulphur is consequently required for efficient pyrite formation [Feld, 1911;

Appendices

Berner, 1970; Berner 1984]. Therefore, under oxygen-poor, normal marine bottom waters and pore waters in the presence of labile organic matter (where sulphate reduction is occurring in pore waters it has to be due to organic matter) reactive sedimentary Fe will bond with free H₂S and S to form FeS₂ (iron pyrite) [Berner, 1970]. Bob Berner's work was therefore partly interested in quantifying the proportion of H₂S reactive Fe remaining within the sediment (DOP), with later studies using Berner (1970)'s methodology to interpret bottom water oxygen conditions [Berner, 1970; Raiswell & Berner, 1985, 1986; Raiswell et al., 1988].

DOP was defined by Berner (1970) as:

$$\text{DOP} = \text{Fe}_{\text{py}} / (\text{Fe}_{\text{py}} + \text{Fe}_{\text{HCl-soluble}}) \quad (1)$$

Berner (1970) consequently devised a method which would digest H₂S reactive Fe phases whilst removing only small amounts of Fe from silicates. This method involved digesting the sediment in boiling concentrated HCl. The concentrated HCl completely dissolves iron carbonates, magnetite and fine-grained iron oxyhydroxides as well as only partially extracting iron from some silicates [Leventhal & Taylor, 1990; Raiswell et al., 1994; Raiswell et al., 2018]. HCl-soluble iron was thought to provide a rough estimation of H₂S reactive iron remaining within the sediment [Berner, 1970]. Based on Berner (1970)'s DOP equation (1), if the amount of H₂S reactive iron within the sediment was low then DOP would be greater. However, if the amount of H₂S reactive iron within the sediment was high then DOP would be lower. A higher DOP is indicative of more oxygen-poor conditions, and a lower DOP indicative of more oxygenated conditions.

Research by Raiswell et al., (1988) further developed Berner's DOP proxy through introducing constraints for low (<0.45), intermediate (0.46 < DOP < 0.80) and high

Quantifying marine redox across the Triassic–Jurassic mass extinction

($0.55 < \text{DOP} < 0.93$) degrees of pyritization. These constraints were calibrated using independent palaeo-environmental proxies on TOC-rich sediments as well as ancient marine shales [Raiswell & Berner, 1985, 1986; Raiswell et al., 1988]. Low DOP was interpreted by Raiswell et al., (1988) to denote aerobic bottom water conditions with intermediate and high DOP representing restricted and ‘inhospitable’ bottom conditions. Conversely, later research by Canfield et al., (1992) revealed that inhospitable sites can exhibit low DOP values (~ 0.40) if there is insufficient available reactive iron. Canfield et al., (1996) similarly identify iron reactivity as a factor in achieving high DOP values, revealing that Black Sea sediments had up to 3x more readily pyritized iron than continental margin sediments. Later work by Lyons & Berner, (1992) revealed that rapid sedimentation within a euxinic setting can also result in reduced DOP values. These issues have resulted in DOS (Degree of Sulfidation) being measured as well as DOP [Raiswell et al., 2018 and references therein].

Furthermore, Aller et al., (1986) and Canfield, (1989) have revealed that high DOP values may also be exhibited within oxic near-shore settings through biological remobilisation and concentration (Lyons & Severmann, 2006). Lyons & Severmann, (2006) therefore suggest that iron proxies are studied alongside sedimentological and palaeoecological data in order to distinguish biological iron enrichment in oxic settings.

Fe_{HR}/Fe_T – In light of previous work on iron reactivity by Canfield et al., (1992, 1996), Raiswell & Canfield (1998) studied the proportion of highly reactive iron (Fe_{HR}) to total iron (Fe_T) within modern marine sediments. Raiswell & Canfield (1998) defined Fe_{HR} as the sum of dithionite-extractable iron oxyhydroxide and Fe already present as FeS_2 (Fe_{py}). This definition of Fe_{HR} was inspired by the measurement of sedimentary Fe oxyhydroxide through citrate-dithionite extraction by Canfield, (1988, 1989). Raiswell

Appendices

& Canfield (1998) considered this proxy an 'indicator of anoxicity'. Whilst marginal and deep sea environments recorded a mean of 0.26 ± 0.08 , being closely allied to modern dysoxic or fluctuating redox sediments (0.28 ± 0.10), the euxinic and anoxic Black Sea (0.70 ± 0.19) and Cariaco Basin (0.51 ± 0.03) recorded significantly higher values. A threshold of 0.38 was introduced to distinguish the upper bound of oxic values and lower bound of anoxic values [Raiswell & Canfield, 1998]. Subsequent work by Poulton & Raiswell (2002) on Phanerozoic sediments similarly recorded low Fe_{HR} / Fe_T values (0.14 ± 0.08) from oxic marine sediments.

Fe_{HR} / Fe_T has been amended in recent years based on an improved understanding of highly reactive iron [Poulton *et al.*, 2004; Raiswell *et al.*, 2018]. This particularly includes the identification that ferruginous conditions also observe significant sedimentary iron enrichment through highly reactive ferric and/or ferrous iron minerals (e.g., magnetite, siderite and ankerite) (Poulton *et al.*, 2004; Poulton & Canfield, 2005). However, Poulton & Canfield, (2005) identified that euxinic and ferruginous conditions could not be distinguished using the existing analytical method. In order to measure the iron present within ferruginous iron minerals, and to distinguish sediments deposited under euxinic and ferruginous conditions, Poulton & Canfield, (2005) developed a new analytical method for iron extraction, leading to the redefinition of Fe_{HR} (as $Fe_{carb} + Fe_{ox} + Fe_{mag} + Fe_{py}$). Once Fe_{HR} was re-defined, later work by Poulton & Canfield, (2011) developed a cross plot to distinguish oxic, anoxic, ferruginous and euxinic conditions. Poulton & Canfield (2011) used an upper bound (Fe_{HR} / Fe_T) of 0.22 for oxic conditions based on Poulton & Raiswell (2002), and a lower bound (Fe_{HR} / Fe_T) of 0.38 for anoxic conditions based on Raiswell & Canfield (1998). Poulton & Canfield (2011) also used a threshold of 0.8 (Fe_{py} / Fe_{HR}) to distinguish ferruginous and euxinic conditions based on

Quantifying marine redox across the Triassic–Jurassic mass extinction

Andersen & Raiswell, (2004). However, all of the threshold values used by Poulton & Canfield (2011) were established using the previous analytical technique, which does not fully quantify Fe_{mag} and Fe_{carb} . Therefore, an Fe_{py}/Fe_{HR} of 0.7 may be more appropriate to distinguish ferruginous and euxinic conditions based on März et al., (2008).

Fe_T/Al- Recent studies of iron enrichment have resulted in the development of two new proxies for identifying marine anoxia and euxinia. These are Fe_T/Ti (Werne et al., 2002) and Fe_T/Al (Lyons et al., 2003). However, it is Fe_T/Al which has proven to be most widely used within recent years [Lyons & Severmann, 2006; Raiswell et al., 2018]. Fe_T/Al removes the effects of carbonate and opal dilution and allows iron enrichment to be compared to average detrital input [Lyons et al., 2003]. Fe_T/Al is also decoupled from the relative fraction of skeletal biological material [Lyons & Severmann, 2006]. However, unlike Fe_{HR}/Fe_T , Fe_T/Al cannot distinguish enrichment that may arise from an unreactive Fe fraction [Raiswell et al., 2018]. Nor can Fe_T/Al identify repartitioning of iron minerals in the absence of iron gain [Lyons & Severmann, 2006]. For these reasons Fe_T/Al is always studied alongside other redox proxies within this thesis.

Fe_T/Al , much like Fe_{HR}/Fe_T , assumes that the sedimentary increase in highly reactive iron, associated with redox change, can be sufficiently distinguished from detrital iron [Lyons et al., 2003; Lyons & Severmann, 2006; Raiswell et al., 2018]. Fe_T/Al values are commonly elevated within euxinic sediments through syngenetic pyrite formation [Lyons et al., 2003; Lyons & Severmann, 2006]. However, despite suggestions from Lyons & Severmann, (2006) to the contrary, syngenetic pyrite formation within the water column is not unique to euxinic environments, as this can also be observed under

Appendices

ferruginous conditions [Lyons & Severmann, 2006; Poulton & Canfield, 2011]. Lyons et al., (2003) similarly failed to mention the distinction of ferruginous and euxinic conditions when interpreting Fe_T/Al . This will be determined within this thesis through the study of redox sensitive elements which whilst enriched under oxic and/or euxinic conditions are relatively conservative under ferruginous conditions.

Detrital values for Fe_T/Al of 0.4-0.5 may be interpreted based on data from Lyons et al., (2003), whilst a detrital baseline of 0.75 is reported by Hardisty et al., (2016) from the Holocene of the Baltic Sea. Values in the range of 0.30 to 0.66 have been quoted as representing oxic marine conditions from both Palaeozoic and modern marine sediments [Lyons & Severmann, 2006; Raiswell et al., 2008; Sperling et al., 2013; Dickson et al., 2014; Clarkson et al., 2014; Sperling et al., 2016; Sperling et al., 2018; Zhang et al., 2019]. However, oxic values as low as 0.20 have been quoted for both the Neoproterozoic fifteen mile group and Windermere Supergroup [Sperling et al., 2013; Sperling et al., 2016]. Meanwhile, Casacci et al., (2016) quote Fe_T/Al of 2.4 from a Norian-Rhaetian shelf setting with no evidence of sulfur (<0.03%). Therefore, the oxic and detrital thresholds must be individually evaluated for each site according to palaeo-environmental conditions [Raiswell et al., 2018]. This includes sedimentation rate which cannot be distinguished by any of the existing iron proxies [Lyons & Severmann, 2006].

Euxinic values may be equally difficult to identify due to siliciclastic dilution, net retention of reactive iron or diminished iron delivery [Lyons & Severmann, 2006; Scholz, 2017]. However, early studies have provided promising results. Cole et al., (2017) define enrichment of Fe_T/Al as >0.77 based on data from 4850 soil samples

Quantifying marine redox across the Triassic–Jurassic mass extinction

[Raiswell *et al.*, 2018]. Meanwhile, Raiswell *et al.*, (2018) consider Fe_T/Al of >0.66 as ‘conservatively diagnostic of enrichment’ based on the sediment database threshold with a limit of one standard deviation. Euxinic Black Sea basin values record significant enrichment compared to margin and shelf settings, with 2-3 times greater Fe_T/Al (0.4-0.6 vs. 0.6-1.2) [Lyons & Severmann, 2006]. Meanwhile, euxinic conditions from the Orca Basin and Effingham Inlet range between 0.55-0.75 and 0.8-0.9 [Lyons & Severmann, 2006]. Hardisty *et al.*, (2016) report euxinic Holocene sapropels as exhibiting Fe_T/Al up to 1.4, whilst Zhang *et al.*, (2019) report euxinic values up to 1.9 within Guadalupian mudstones of the Yangtze Basin with significant enrichment compared to adjacent oxic horizons. Dickson *et al.*, (2014) report euxinic values of 0.7 and 1.0 from mudstones around the Palaeocene-Eocene boundary, and euxinic Fe_T/Al values as high as 3.1 and 4.6 have been reported from Toarcian OAE sections [Baroni *et al.*, 2018]. A recent study by Young *et al.*, (2020) records Fe_T/Al of ~ 0.75 from anoxic/euxinic strata of the Ordovician-Silurian Aizpute-41 and Röstånga-1 drill cores.

ALLER, R. C., Mackin, J. E. & Cox, R. T. 1986. Diagenesis of Fe and S in Amazon inner shelf muds: apparent dominance of Fe reduction and implications for the genesis of ironstones. *Cont. Shelf Res.*, **6**, 263–289.

ANDERSEN, T. & RAISWELL, R. 2004. Sources and mechanisms for the enrichment of highly reactive iron in euxinic Black Sea sediments. *American Journal of Science*, **304**(3), 203–231.

BARONI, I. R., Pohl, A., van Helmond, N. A. G. M., Papadomanolaki, N. M., Coe, A. L., Cohen, A. S., van de Schootbrugge, B., Donnadieu, Y. & Slomp, C. P. 2018. Ocean Circulation in the Toarcian (Early Jurassic): A Key Control on Deoxygenation and Carbon Burial on the European Shelf. *Paleoceanography and Paleoclimatology*, **33**, 994–1012.

BERNER, R. A. 1970. Sedimentary pyrite formation. *American Journal of Science*, **268**, 1–23.

BERNER, R. A. 1984. Sedimentary pyrite formation: An update*. *Geochimica et Cosmochimica Acta*, **48**, 605–615.

Appendices

- CANFIELD, D. E. 1988. Sulfate reduction and the diagenesis of iron in anoxic marine sediments. Ph.D. thesis, Yale Univ.
- CANFIELD, D. E., 1989. Reactive iron in marine sediments. *Geochimica et Cosmochimica Acta*, **53**, 619–632.
- CANFIELD, D. E., Raiswell, R. & Bottrell, S. 1992, The reactivity of sedimentary iron minerals toward sulfide. *American Journal of Science*, **292**, 659–683.
- CANFIELD, D. E., Lyons, T.W., & Raiswell, R., 1996, A model for iron deposition to euxinic Black Sea sediments: *American Journal of Science*, **296**, 818–834.
- CASACCI, M., Bertinelli, A., Algeo, T. J. & Rigo, M. 2016. Carbonate-to-biosilica transition at the Norian-Rhaetian boundary controlled by rift-related subsidence in the western Tethyan Lagonegro Basin (southern Italy). *Palaeogeog., Palaeoclimatol., Palaeoecol.*, **456**, 21–36.
- CLARKSON, M. O., Poulton, S. W., Guilbaud, R. & Wood, R. 2014. Assessing the utility of Fe/Al and Fe-speciation to record water column redox conditions in carbonate-rich sediments. *Chemical Geology*, **382**, 111–122.
- COLE, D. B., Zhang, S., and Planavsky, N. J., 2017, A new estimate of detrital redox-sensitive metal concentrations and variability in fluxes to marine sediments. *Geochimica et Cosmochimica Acta*, **215**, 337–353.
- DICKSON, A. J., Rees-Owen, R. L., März, C., Coe, A. L., Cohen, A. S., Pancost, R. D., Taylor, K. & Shcherbinina, E. 2014. The spread of marine anoxia on the northern Tethys margin during the Paleocene-Eocene Thermal Maximum. *Paleoceanography*, **29**, 471–488.
- FELD, W. 1911. Über die Bildung von Eisenbisulfid (FeS₂) in Lösungen und die Entstehung der natürlichen Pyritlager: *Zeitschr. Für angew. Chemie*, **24**, 97–103.
- HARDISTY, D. S., Riedinger, N., Planavsky, N. J., Asael, D., Andrén, T., Jørgensen, B. B. & Lyons, T. W. 2016. A Holocene history of dynamic water column redox conditions in the Landsort Deep, Baltic Sea. *American Journal of Science*, **316**, 713–745.
- LEVENTHAL, J. & Taylor, C. 1990. Comparison of methods to determine degree of pyritization. *Geochimica et Cosmochimica Acta*, **54**, 2621–2625.
- LYONS, T.W. & Berner, R. A. 1992. Carbon-sulfur-iron systematics of the uppermost deep-water sediments of the Black Sea. *Chemical Geology*, **99**, 1–27.
- LYONS, T. W., Werne, J. P., Hollander, D. J. & Murray, J. W. 2003. Contrasting sulfur geochemistry and Fe/Al and Mo/Al ratios across the last oxic-to-anoxic transition in the Cariaco Basin, Venezuela. *Chemical Geology*, **195**, 131–157.
- LYONS, T.W. & Severmann, S. 2006. A critical look at iron paleoredox proxies based on new insights from modern anoxic basins. *Geochimica et Cosmochimica Acta*, **70**,

Quantifying marine redox across the Triassic–Jurassic mass extinction

5698–5722.

MÄRZ, C., Poulton, S. W., Beckmann, B., Kuster, K., Wagner, T. & Kasten, S. 2008. Redox sensitivity of P cycling during marine black shale formation: dynamics of sulfidic and anoxic, non-sulfidic bottom waters. *Geochimica et Cosmochimica Acta*, **72**, 3703–3717.

POULTON, S. W. & Raiswell, R. 2002. The low- temperature geochemical cycle of iron: From continental fluxes to marine sedi- ment deposition. *American Journal of Science*, **302**, 774–805.

POULTON, S. W., Fralick, P. W., & Canfield, D. E. 2004. The transition to a sulfidic ocean ~1.84 billion years ago. *Nature*, **431**, 173–177.

POULTON, S. W. & Canfield, D. E. 2005. Development of a sequential extraction procedure for iron: implications for iron partitioning in continentally derived particulates: *Chemical Geology*, **214**, 209–211.

POULTON, S. W. & Canfield, D. E. 2011. Ferruginous conditions: a dominant feature of the ocean through Earth’s history. *Elements*, **7**, 107–112.

RAISWELL, R. & Berner, R. A. 1985. Pyrite formation in euxinic and semi euxinic sediments. *American Journal of Science*, **285**, 710–724.

RAISWELL, R. & Berner, R. A. 1986. Pyrite and organic matter in Phanerozoic normal marine shales. *Geochimica et Cosmochimica Acta*, **50**, 1967–1976.

RAISWELL, R. Buckley, F., Berner, R. A. & Anderson, T. F. 1988. Degree of pyritization of iron as a paleoenvironmental indicator of bottom-water oxygenation. *Journal of Sedimentary Petrology*, **58(5)**, 812–819.

RAISWELL, R., Canfield D. E. & Berner R. A. 1994. A comparison of iron extraction methods for the determination of degree of pyritisation and the recognition of iron-limited pyrite formation. *Chem. Geol.*, **111(1–4)**, 101–110.

RAISWELL, R. & Canfield, D. E. 1998, Sources of iron for pyrite formation in marine sediments. *American Journal of Science*, **298**, 219–243.

RAISWELL, R., Newton, R. , Bottrell, S. H., Coburn, P., Briggs, D. E. G., Bond, D. P. G., & Poulton, S. W., 2008, Turbidite depositional influences on the diagenesis of Beecher’s Trilobite Bed and the Hunsruck Slate: Sites of soft tissue preservation. *American Journal of Science*, **308**, 105–129.

RAISWELL, R., Hardisty, D. S., Lyons, T. W., Canfield, D. E., Owens, J. D., Planavsky, N. J., Poulton, S. W. & Reinhard, C. T. 2018. The iron paleoredox proxies: a guide to the pitfalls, problems and proper practice. *American Journal of Science*, **318**, 491–526.

SCHOLZ, F., Siebert, C., Dale, A. W. & Frank, M. 2017. Intense molybdenum accumulation in sediments underneath a nitrogenous water column and implications for

Appendices

the reconstruction of paleo-redox conditions based on molybdenum isotopes. *Geochimica et Cosmochimica Acta*, **213**, 400–417.

SPERLING, E. A., Halverson, G. P., Knoll, A. H., Macdonald, F. A. & Johnston, D. T. 2013. A basin redox transect at the dawn of animal life. *Earth and Planetary Science Letters*, **371-372**, 143–155.

SPERLING, E. A., Carbonne, C., Strauss, J. V., Johnston, D. T., Narbonne, G. M. & Macdonald, F. A. 2016. Oxygen, facies, and secular controls on the appearance of Cryogenian and Ediacaran body and trace fossils in the Mackenzie Mountains of northwestern Canada. *Geological Society of America Bulletin*, **128**, 558–575.

SPERLING, E. A., Balthasar, U. & Skovsted, C. B. 2018. On the edge of exceptional preservation: insights into the role of redox state in Burgess Shale-type taphonomic windows from the Mural Formation, Alberta Canada. *Emerging Topics in Life Sciences*, 1–13. <https://doi.org/10.1042/ETLS20170163>.

WERNE, J. P., Sageman, B. B., Lyons, T. W. & Hollander, D. J. 2002. An integrated assessment of a type ‘euxinic’ deposit: evidence for multiple controls on black shale deposition in the Middle Devonian Oatka Creek Formation. *American Journal of Science*, **302**, 110–143.

YOUNG, S. A., Benayoun, E., Kozik, N. P., Hints, O., Martma, T., Bergström, S. M. & Owens, J. D. 2020. Marine redox variability from Baltica during extinction events in the latest Ordovician-early Silurian. *Palaeogeog., Palaeoclimatol., Palaeoecol.*, **554**, 1–17.

ZHANG, B., Yao, S., Hu, W., Ding, H., Liu, B. & Ren, Y. 2019. Development of high-productivity and anoxic-euxinic conditions during the late Guadalupian in the Lower Yangtze region: Implications for the mid-Capitanian extinction event. *Palaeogeog., Palaeoclimatol., Palaeoecol.*, **531**, 1–16.

APPENDIX 2.3: MANGANESE

The enrichment of Manganese (Mn) within marine environments is highly redox dependent (*Calvert & Pedersen, 1993; Algeo & Maynard, 2004; Tribovillard et al., 2006*). The dominant species of Manganese (Mn) in seawater are Mn(II) and MnCl^+ . (*Calvert & Pedersen, 1993*). However, Mn(II) is thermodynamically unstable under oxic conditions and is therefore oxygenated to insoluble Mn(III) and, predominantly, Mn(IV) oxides (*Calvert & Pedersen, 1993*). Mn(IV) oxides commonly take the form of insoluble MnO_2 (manganese dioxide/ pyrolusite) and MnOOH “oxyhydroxides” (manganite) and are most abundant just above the oxic/anoxic boundary (*Brewer & Spencer, 1974; Shimmield & Price, 1986; Calvert & Pedersen, 1993; Piper & Calvert, 2009*).

Under anoxic conditions MnO_2 and MnOOH undergo sluggish reductive dissolution to Mn(II) (*Rue et al., 1997; Algeo & Maynard, 2004; Tribovillard et al., 2006; Piper & Calvert, 2009; Algeo & Li, 2020*). This is principally chemically driven; however, Mn reduction is also due to the use of Mn as an electron acceptor in microbially mediated reactions under suboxic conditions (*Froelich et al., 1979; Rue et al., 1997; Algeo & Li, 2020*). Where insoluble Mn-oxides undergo reduction in the water column, Mn(II) is exported to the deep ocean where it is scavenged (*Calvert & Pedersen, 1993*).

Meanwhile, where Mn-oxide reduction occurs below the sediment-water interface, Mn(II) may freely migrate within the sediment as it is not taken up significantly into organic or sulfide phases (*Algeo & Maynard, 2004*).

Downward sedimentary migration of Mn(II) may result in MnCO_3 (rhodochrosite/ kutnohorite) precipitation, particularly where anoxic pore waters are supersaturated with

Appendices

respect to rhodochrosite, and there is a sufficient supply of Mn(IV) to be reduced (Pedersen & Price, 1982; Calvert & Pedersen, 1993; Tribovillard *et al.*, 2006). Upward sedimentary migration of Mn(II) can result in re-precipitation of MnO₂ and MnOOH in oxygenated sediment overlying anoxic pore waters and subsequent enrichment above crustal/detrital background levels (~850ppm) (Siebert *et al.*, 2006; Tribovillard *et al.*, 2006; Boyer *et al.*, 2011). In the absence of oxygenated sediments Mn(II) undergoes flux into the overlying water column resulting in relatively Mn depleted sediments (Calvert & Pederson, 1993; Mangini *et al.*, 2001; Algeo & Maynard, 2004; Brumsack, 2006). In alkaline, anoxic/euxinic bottom waters of a highly restricted basin Mn(II) may become enriched, eventually reaching Mn(II) carbonate saturation, or potentially forming sulfide phases (alabandite/rambergite) (Force & Maynard, 1991; Calvert & Pedersen, 1993; Algeo & Maynard, 2004; Brumsack, 2006; Lyons & Severmann, 2006; Lenz *et al.*, 2014; Lenz *et al.*, 2015; Häusler *et al.*, 2018). However, the MnS mineral alabandite is highly soluble and therefore uncommon, even within euxinic sediments (Force & Maynard, 1991).

Despite Mn(VI) and Mn(II) being considered the two most important Mn species with regards to aqueous redox reactions, a recent study of modern marine sediments by Madison *et al.*, (2013) has revealed that soluble Mn (III), stabilised by organic and/or inorganic ligands, is highly abundant just below the oxic-suboxic boundary through oxidation of Mn(II).

ALGEO, T. J., Li, C. 2020. Redox classification and calibration of redox thresholds in sedimentary systems. *Geochimica et Cosmochimica Acta*, 287, 8–26.

ALGEO, T. J. & Maynard, J. B. 2004. Trace-element behavior and redox facies in core shales of Upper Pennsylvanian Kansas-type cyclothems. *Chemical Geology*, 206, 289–318.

Quantifying marine redox across the Triassic–Jurassic mass extinction

BOYER, D. L., Owens, J. D., Lyons, T. W. & Droser, M. L. 2011. Joining forces: Combined biological and geochemical proxies reveal a complex but refined high-resolution palaeo-oxygen history in Devonian epeiric seas. *Palaeogeography, Palaeoclimatology, Palaeoecology*, **306**, 134–146.

BREWER, P. G., Spencer, D. W., 1974. Distribution of some trace elements in Black Sea and their flux between dissolved and particulate phases. In: *Degens, E. T., Ross, D. A. (Eds.), The Black Sea—Geology, Chemistry, and Biology. Memoir, 20*. American Association of Petroleum Geologists, Tulsa, 137–143.

BRUMSACK, H.-J. 2006. The trace metal content of recent organic carbon-rich sediments” Implications for Cretaceous black shale formation. *Palaeogeography, Palaeoclimatology, Palaeoecology*, **232**, 344–361.

CALVERT, S. E. & Pedersen, T. F. 1993. Geochemistry of Recent oxic and anoxic marine sediments: Implications for the geological record. *Marine Geology*, **13**, 67–88.

FORCE, E. R. & Maynard, J. B. 1991. Manganese: Syngenetic deposits on the margins of anoxic basins In: *Force, E. R., Eidel, J. J. & Maynard, J. B. (Eds.) Sedimentary and Diagenetic Mineral Deposits, a Basin Analysis Approach to Exploration, Reviews in Economic Geology*, 5, 147–161.

FROELICH, P. N., Klinkhammer, G. P., Bender, M. L., Luedtke, N. A., Heath, G. R., Cullen, D., Dauphin, P., Hammond, D., Hartman, B. & Maynard, V. 1979. Early oxidation of organic matter in pelagic sediments of the eastern equatorial Atlantic: suboxic diagenesis. *Geochimica et Cosmochimica Acta*, **43**, 1075–1090.

LENZ, C., Behrends, T., Jilbert, T., Silveira, M. & Slomp, C. P. 2014. Redox-dependent changes in manganese speciation in Baltic Sea sediments from the Holocene Thermal Maximum: An EXAFS, XANES and LA-ICP-MS study, *Chem. Geol.*, **370**, 49–57.

LENZ, C., Jilbert, T., Conley, D. J., Wolthers, M & Slomp., C. P. 2015. Are recent changes in sediment manganese sequestration in the euxinic basins of the Baltic Sea linked to the expansion of hypoxia. *Biogeosciences*, **12**, 4875–4894.

LYONS, T. W. & Severmann, S. 2006. A critical look at iron paleoredox proxies: New insights from modern euxinic marine basins. *Geochimica et Cosmochimica Acta*, **70**, 5698–5722.

MADISON, A. S., Tebo, B. M., Mucci, A., Sundby & Luther III, G. W. 2013. Abundant Porewater Mn(III) Is a Major Component of the Sedimentary Redox System. *Science*, **341**, 875–878.

MANGINI, A., Jung, M. & Laukenmann, S. 2001. What do we learn from peaks of uranium and manganese in deep sea sediments? *Marine Geology*, **177**, 63–78.

PEDERSEN, T. F. and Price, N. B., 1982. The geochemistry of manganese carbonate in Panama Basin sediments. *Geochimica et Cosmochimica Acta*, **46**, 59–68.

Appendices

PIPER, D. Z. & Calvert, S. E. 2009. A marine biogeochemical perspective on black shale deposition. *Earth Science Reviews*, **95**, 63–96.

RUE, E. L., Smith, G. J., Cutter, G. A. & Bruland, K. W. 1997. The response of trace element redox couples to suboxic conditions in the water column. *Deep-Sea Research*, **44(1)**, 113–134.

SIEBERT, C., McManus, J., Bice, A., Poulson, R. & Berelson, W. M. 2006. Molybdenum isotope signatures in continental margin marine sediments. *Earth and Planetary Science Letters*, **241**, 723–733.

TRIBOVILLARD, N., Algeo, T. J., Lyons, T. & Riboulleau, A. 2006. Trace metals as paleoredox and paleoproductivity proxies: An update. *Chemical Geology*, **232**, 12–32.

APPENDIX 2.4: MOLYBDENUM

Introduction to Molybdenum and Mo-O species- Molybdenum (Mo) has been studied as a potential palaeo-redox proxy for decades on account of its bipolar redox behaviour (Brumsack, 1989; Emerson & Huested, 1991; Calvert & Pedersen, 1993; Crusius et al., 1996; Helz et al., 1996; Goldberg et al., 1998; Ericksen & Helz, 2000; Zheng et al., 2000; Adelsen et al., 2001; Bostick et al., 2003; Vorcilek et al., 2004; Algeo & Lyons, 2006; Tribovillard et al., 2006; Chappaz et al., 2008; Helz et al., 2011; Dahl et al., 2013; Chappaz et al., 2014; Dahl et al., 2017; Wagner et al., 2017). Under oxygenated conditions, organic shales and sulfide deposits, which are abundant in Mo, are weathered and transported to marine environments (Miller et al., 2011; Scott & Lyons, 2012). Mo (VI) is easily oxidised, and is the most common Mo species, occupying the largest area of Eh-Ph phase space (Kendall et al., 2017). Within oxygenated seawater and freshwater Mo (VI) forms the oxyanion molybdate (MoO_4^{2-}) (Broecker & Peng, 1982; Kendall et al., 2017). Molybdate is a highly mobile, conservative oxyanion; it only coordinates weakly with other environmentally common ligands (e.g., Cl^- , OH^-) and is not readily adsorbed by most natural or clay particles (Collier, 1985; Brumsack, 1989; Calvert & Pedersen, 1993; Goldberg et al., 1998; Kendall et al., 2017). This conservative behaviour may be due to the strong covalent bonds between the Mo and O atoms (Ozeki et al., 1996). The tetrahedrally coordinated Mo (VI) (MoO_4^{2-}) subsequently dominates aqueous Mo speciation (Kendall et al., 2017). However, recent work by Wang et al., (2011) suggests that the cationic Mo(V) species MoO_2^+ may play a more significant role than previously interpreted, albeit an intermediate role.

The conservative behaviour of molybdate results in Mo being the most abundant transition metal in oxygenated marine waters, with relatively high concentrations for a trace metal (~10ppb), and a long residence time (450 to 800kyr) (Collier, 1985;

Appendices

Morford & Emersen, 1999; Algeo, 2004; Algeo & Maynard, 2004; Algeo & Maynard, 2008; Miller et al., 2011; Scott & Lyons, 2012; Smedley & Kinniburgh, 2017). Where molybdenum concentrations exceed 1mM, and where pH >8, polymolybdates (polynuclear molybdate species) dominate Mo speciation (*Wasylenki et al., 2011; Kendall et al., 2017*). Despite such high Mo concentrations being rare in nature, polymolybdates have been associated with adsorption onto mineral surfaces (e.g., Fe-Mn oxides) (*Kendall et al., 2017*). Where pH <6, acidic Mo species may become quantitatively significant, this includes HMoO_4^- and H_2MoO_4 (“molybdic acid”) (*Kendall et al., 2017*). Meanwhile, molybdate should dominate at concentrations below 100 μM and pH >4 (*Kendall et al., 2017*).

Sedimentary Mo uptake through mineral adsorption- Under oxygenated conditions Mo may bind to oxides and Fe-Mn oxyhydroxides (Fe-Mn OOH) close to the sediment water interface where they are removed into the underlying sediment, this is known as a ‘particle shuttle’ (*Berrang & Grill, 1974; Murray, 1975; François, 1988; Emersen & Husted, 1991; Magyar et al., 1993; Crusius et al., 1996; Goldberg et al., 1996; Goldberg et al., 1998; Zheng et al., 2000; Adelsen et al., 2001; Morford et al., 2005; Tribovillard et al., 2006; Chappaz et al., 2008*). The particle shuttling of Mo into marine sediments has been revealed through significant enrichment of Mo in ferromanganese nodules and Fe-Mn OOH from marine sediments; the strong relationship between Mo concentration and Mn cycling; sediment trap data; elevated Mo enrichment in brines where a particle shuttle is interpreted to be absent (*Berrang & Grill, 1974; Calvert & Price, 1977; Shimmiel & Price, 1986; François, 1988; Zheng et al., 2000*). Experimental data shows that although Mo can adsorb to Fe OOH, the main host for Mo in ferromanganese crusts/nodules is MnOOH (manganite) (*Goldberg*

Quantifying marine redox across the Triassic–Jurassic mass extinction

et al., 2009; Kashiwabara *et al.*, 2009). Up to 35% of Mo is removed through adsorption on MnOOH. (Scott & Lyons, 2012). Studies by Goldberg *et al.*, (1996, 1998) find that greater absorption of Mo onto gibbsite is observed by surface area, although greater absorption of Mo onto amorphous Al oxides is observed by weight. Meanwhile, crystalline Al oxides show the least Mo adsorption (Goldberg *et al.*, 1996, 1998). However, as discussed by Scott & Lyons, (2012) Fe-Mn OOH are not permanent sinks for Mo over geological timescales.

Sedimentary Mo uptake through biological function- Mo plays a significant role as a biological nutrient, particularly amongst diazotrophs (Anbar & Knoll, 2002; Anbar, 2004). Nitrogen fixation can be achieved in the absence of Mo, through alternative nitrogenase metalloenzyme systems (Anbar & Knoll, 2002). However, the best known metalloenzyme system, present in all diazotrophs, requires bioavailable Mo to form a Fe_7MoS_9 cluster (Anbar *et al.*, 2002). Mo is therefore essential for an efficient nitrogenase enzyme (Falkowski *et al.*, 1983; Anbar *et al.*, 2002; Anbar, 2004; Glass *et al.*, 2009; Boyd *et al.*, 2011). Mo is also required for the formation of nitrate reductase enzymes (Glass *et al.*, 2009; Boyd *et al.*, 2011). Despite the importance of Mo for nitrogen fixing organisms, biological activity represents a very small flux compared to other removal pathways (e.g., Fe-Mn OOH) (Tribovillard *et al.*, 2006). Studies have also quoted little evidence to suggest significant biological cycling of Mo, or significant biological uptake (Collier, 1985; Nameroff *et al.*, 2002). Mo is also not thought to be concentrated by ordinary plankton (Tribovillard *et al.*, 2006).

Sedimentary Mo uptake under oxic conditions (summary)- Despite up to one third of marine Mo being removed through Mn OOH adsorption within oxygenated waters, geologically permanent Mo enrichment is limited in oxic marine settings due to

Appendices

diagenetic Mn dissolution (*Algeo & Tribovillard, 2009; Scott & Lyons, 2012*).

Biological uptake also represents a small flux for Mo into marine sediments, and therefore sedimentary Mo concentrations of <25ppm have been associated with oxygenated waters (*Scott & Lyons, 2012*).

Sedimentary Mo uptake through thiolation- Despite the relatively low enrichment of Mo under oxic conditions, up to 65% of Mo removal is thought to occur under anoxic conditions through the formation and fixation of Mo sulfide complexes (*Algeo & Maynard, 2004, Algeo & Lyons, 2006; Scott & Lyons, 2012*). Mo concentrations under intermittently and permanently sulfidic conditions (25-100ppm, 100ppm+) are 2-3 times greater those observed under oxic conditions (<25ppm) (*Algeo & Lyons, 2006; Scott & Lyons, 2012*). This is despite anoxic facies forming just 0.3% of the total seafloor area (*Algeo & Lyons, 2006*). Molybdenum sulfide (Mo-S) formation under oxygen poor conditions has therefore been interpreted as the main flux of Mo over geological timescales (*Calvert & Pedersen, 1993; Crusius et al., 1996; Tribovillard et al., 2006; Algeo & Lyons, 2006; Scott & Lyons, 2012*).

With the exception of highly sulfidic, 'euxinic' environments (e.g., The Black Sea), most Mo-S formation occurs within the sediment or close to the sediment water interface (*François, 1988; Emersen & Huested, 1991; Crusius et al., 1996; Ericksen & Helz, 2000; Zheng et al., 2000; Adelsen et al., 2001; Chappaz et al., 2008*).

Sedimentary Mo-S formation may be due to sedimentary Mo enrichment from MnOOH adsorption, with Mo being remobilised upon diagenetic Mn dissolution; transfer to bottom water sediments through humic substances; eddy diffusion; longer residence time on the seafloor; the positioning of the chemocline below the sediment-water interface; the presence of sedimentary brønsted acids and clay mineral surfaces which

Quantifying marine redox across the Triassic–Jurassic mass extinction

may catalyse sulfidation and hydrolysis (*Brumsack, 1989; Magyar et al., 1993; Helz et al., 1996; Morford & Emerson, 1999; Eriksen & Helz, 2000; Adelsen et al., 2001; Algeo & Tribovillard, 2009; Helz et al., 2011; Scott & Lyons, 2012*).

Early studies of Mo reduction believed molybdenite (MoS_2) to be one of the main Mo-S phases, and that the chemical shift from molybdate to molybdenite occurs through a single reduction reaction (*François, 1988; Emersen & Husteded, 1991; Calvert & Pedersen, 1993; Crusius et al., 1996; Zheng et al., 2000*). However, molybdenite is kinematically hindered in most surface environments, and such a reaction has only been observed within the Black Sea (*Eriksen & Helz, 2000; Kendall et al., 2017*).

Subsequent work by Helz et al., (1996) used Extended X-ray Adsorption Fine-Structure Spectrometry (EXAFS) to identify that the short-term exposure of molybdenum to H_2S does not form molybdenite or other molybdenum sulfide species (e.g., Jordisite (MoS_2) or Castaignite (Mo_2S_5)) but an intermediate species with shorter Mo-S bonds.

Molybdate or another Mo-O form was interpreted by Helz et al., (1996) to acquire some first shell sulfur resulting in the formation of a Mo-O-S species ‘oxythiomolybdate’ ($\text{MoO}_{4-y}\text{S}_y$). Helz et al., (1996) further proposed that the oxygen atoms of Mo-O species must therefore be susceptible to replacement by soft ligands, e.g., S, which subsequently form particle reactive (oxy)thiomolybdates capable of adsorbing onto particles containing transition metals (e.g., Fe-S). Thiols, including humic bound thiols, were also interpreted by Helz et al., (1996) to switch Mo behaviour, however they interpreted that Fe-Mo-S compounds, which were also identified through their study, were more important for the geological enrichment of Mo. Previous research by Coveney & Glascock, (1989) observed Mo near the surface of pyrite framboids using scanning electron microscopy (SEM), and Huerta-Diaz & Morse, (1992) interpret sedimentary pyrite to be an important sink for Mo. Bertine (1972) and Brumsack (1989) interpret

Appendices

that the most efficient short-term removal of Mo is through co-precipitation with FeS. Therefore, Helz et al., (1996)'s interpretation of Fe-Mo-S formation through thiomolybdate adsorption corroborated previous Mo research.

A subsequent study by Ericksen & Helz, (2000) further studied the formation of thiomolybdates and reported that a key reaction in their genesis is the thiolation of molybdate. Ericksen & Helz, (2000) also revealed that each subsequent stage of thiolation is one order of magnitude slower than the preceding stage, e.g., dithiomolybdate → trithiomolybdate will be 100 times slower than molybdate → thiomolybdate. Therefore, tetrathiomolybdate formation may not be reached in seasonally sulfidic waters (Ericksen & Helz, 2000). Ericksen & Helz (2000) also reported that a sulfide concentration of $>11\mu\text{M}$ is required for thiomolybdate formation, whilst coinciding work by Zheng et al., (2000) reports that a pore water sulfide concentration of $>0.1\mu\text{M}$ is required for Mo precipitation as a Mo-Fe-S species, with concentrations $>100\mu\text{M}$ required for Mo precipitation in the absence of Fe.

Experimental studies by Vorcilek et al., (2004) revealed that tri- and tetrathiomolybdate may be removed into pyrite under mildly alkaline pH, further supporting the results of previous studies regarding the close relationship between Mo, Fe and S. However, Vorcilek et al., (2004) also revealed that the majority of Mo removed under mildly alkaline pH is a byproduct of trithiomolybdate reduction by zero-valent sulfur.

Therefore, stoichiometric replacement of one thiomolybdate species for the succeeding thiomolybdate species does not occur, and instead the reduction of thiomolybdates by zero-valent sulfur forms highly reactive Mo (IV) polysulfide compounds which adsorb onto FeS₂ (Vorcilek et al., 2004). Similar results regarding Mo (IV) polysulfide complexes have been reported by Dahl et al., (2013), and the adsorption of Mo onto

Quantifying marine redox across the Triassic–Jurassic mass extinction

FeS₂ was also reported by Bostick et al., (2003) who identified Mo clusters on pyrite surfaces.

Despite studies by Vorcilek et al., (2004) and Dahl et al., (2013) reporting highly reactive Mo (IV) polysulfides as a major component of sediment Mo fixation, other works have continued to report the adsorption of thiomolybdates onto iron sulfide compounds. This includes work by Helz et al., (2004) who also revealed the adsorption of thiomolybdates onto clay mineral surfaces (e.g., illite, kaolinite and montmorillonite), and Helz et al., (2011) who identified nanoscale Fe (II)-Mo (VI) S complexes from Rogoznica Lake, Croatia.

Moreover, despite the binding of Molybdenum onto pyrite surfaces identified by Coveney & Glascock, (1989), Bostick et al., (2003) and Vorcilek et al., (2004), research by Chappaz et al., (2014) reveals that the majority of Mo (80-100%) is not found in the pyrite matrix. This also corroborates Lyons et al., (2003) and Algeo & Maynard, (2004) who identify little correlation between pyrite S and Mo within anoxic environments. However, a strong correlation is observed between Mo and TOC (*Brumsack, 1989; Tribovillard et al., 2005; Algeo & Lyons, 2006; McManus et al., 2006; Anbar et al., 2007*). This may suggest that the main removal pathway of Mo is through scavenging with particulate organic matter (*see Biswas et al., 2009*) or ligand substitution (*see Wagner et al., 2017*). A Mo-Fe-S polysulfide species identified by Dahl et al., (2013) exhibited a similar oxidation state, coordination environment and oxygen sensitivity to Mo-Fe-S cubane found within the Mo nitrogenase enzyme. Also, Dahl et al., (2017) have identified that Mo removal can occur in the absence of Fe through particulate organic matter. These discoveries further support the theory that Mo may be fixed into the sediment by biological uptake. Despite uncertainties expressed by Adelsen et al.,

Appendices

(2001) regarding the immobility of organic-bound Mo over geological timescales, Tribovillard et al., (2004) have identified enhanced trapping of Mo in the presence of sulfurised organic matter which they interpret as an indication of Mo immobility.

Sedimentary Mo uptake through thiolation (summary)- Mo is predominantly removed through the formation of Mo-S complexes under sulfidic conditions. Despite early studies interpreting that this may be through the reduction of molybdate to molybdenite, subsequent research of Mo-S formation and fixation has revealed a much more complex removal pathway. Pioneering research by Helz et al., (1996) has revealed that particle reactive thiomolybdates account for early-stage removal of molybdenum.

Thiomolybdates bind onto FeS, FeS₂, and clay minerals. However, there is a poor correlation between pyrite sulfur and Mo, and therefore, thiomolybdate adsorption onto pyrite may be disregarded as the main form of Mo fixation. Subsequent research has revealed that thiomolybdate reduction in the presence of zero valent sulfur forms more highly reactive Mo (IV) polysulfides. Mo (IV) polysulfides may scavenge onto Fe and form compounds that may be used as metalloenzymes. Mo fixation may therefore be the result of biological uptake within sulfidic pore waters.

Molybdenum summary- Molybdenum (Mo) is a useful tool for reconstructing palaeo-redox conditions within marine environments on account of its bi-polar redox behaviour and conservative nature. Under oxic conditions Mo is largely removed in smaller concentrations through adsorption onto Fe-Mn OOH particles near to the sediment water interface. However, Fe-Mn OOH is thermodynamically unstable under oxygen poor conditions, and therefore does not serve as a permanent geological store for molybdenum. Geologically stable sedimentary molybdenum is instead believed to be

Quantifying marine redox across the Triassic–Jurassic mass extinction

removed from the water column and sediment pore space under sulfidic conditions. In the presence of free sulfur Mo forms particle reactive thiomolybdates which may subsequently undergo reduction in the presence of zero valent sulfur to form more highly reactive Mo (IV) polysulfides. The exact removal pathway of these polysulfides remains uncertain, however there is a growing amount of data which would suggest a final removal pathway via biological uptake e.g., an Fe-Mo metalloenzyme.

ADELSON, J. M., HELZ, G. R. & MILLER, C. V. 2001. Reconstructing the rise of recent coastal anoxia; molybdenum in Chesapeake Bay sediments. *Geochimica et Cosmochimica Acta*, **65**, 237–252.

ALGEO, T. J. 2004. Can marine anoxic events draw down the trace element inventory of seawater? *Geology*, **32**(12), 1057–1060.

ALGEO, T. J. & LYONS, T. W. 2006. Mo-total organic carbon covariation in modern anoxic marine environments: Implications for analysis of paleoredox and paleohydrographic conditions. *Paleoceanography*, **21**, PA1016.

ALGEO, T. J. & MAYNARD, J. B. 2004. Trace-element behavior and redox facies in core shales of the Upper Pennsylvanian Kansas-type cyclothems. *Chemical Geology*, **206**, 289–318.

ALGEO, T. J. & MAYNARD, J. B. 2008. Trace-metal covariation as a guide to water-mass conditions in ancient anoxic marine environments. *Geosphere*, **4**(5), 872–887.

ALGEO, T. J. & TRIBOVILLARD, N. 2009. Environmental analysis of palaeoceanographic systems based on molybdenum-uranium covariation. *Chemical Geology*, **268**, 211–225.

ANBAR, A. D. & KNOLL, A. H. 2002. Proterozoic Ocean Chemistry and Evolution: A Bioinorganic Bridge? *Science*, **297**, 1137–1142.

ANBAR, A. D. 2004. Molybdenum Stable Isotopes: Observations, Interpretations and Directions. *Reviews in Mineralogy and Geochemistry*, **55**, 429–545.

ANBAR, A. D., DUAN, Y., LYONS, T. W., ARNOLD, G. L., KENDAL, B., CREASER, R. A., KAUFMAN, A. J., GORDON, G. W., SCOTT, C., GARVIN, J. & BUICK, R., 2007. A whiff of oxygen before the Great Oxidation Event. *Science*, **317**, 1903–1906.

BERRANG, P. G. & GRILL, E. V. 1974. The effect of manganese oxide scavenging on molybdenum in Saanich Inlet, British Columbia. *Marine Chemistry*, **2**(2), 125–148.

Appendices

- BERTINE, K. K. 1972. The deposition of molybdenum in anoxic waters. *Mar. Chem.* **1**, 43–53.
- BISWAS, K. C., WOODARDS, N. A., XU, H., & BARTON, L. L. 2009. Reduction of molybdate by sulfate-reducing bacteria. *BioMetals*, **22**, 131–139.
- BOSTICK, B. C., FENDORF, S. & HELZ, G. R. 2003. Differential adsorption of molybdate and tetrathiomolybdate on pyrite (FeS₂). *Environmental Science & Technology*, **37**, 285–291.
- BOYD, E. S., ANBAR A. D., MILLER, S., HAMILTON, T. L., LAVIN, M. & PETERS, J. W. 2011. A late methanogen origin for molybdenum-dependent nitrogenase. *Geobiol*, **9**, 221–232.
- BROECKER, W. S. & PENG, T.-H. 1982. Tracers in the Sea, Eldigio, Columbia Univ., Palisades, N. Y.
- BRUMSACK, H.-J. 1989. Geochemistry of recent TOC-rich sediments from the Guld of California and the Black Sea. *Geologische Rundschau*, **78** (3), 851–882.
- CALVERT, S. E. & PRICE, N. B. 1977. Geochemical variation in ferromanganese nodules and associated sediments from the Pacific Ocean. *Marine Chemistry*, **5**(1), 43–74.
- CALVERT, S. E. & PEDERSEN, T. F. 1993. Geochemistry of Recent oxic and anoxic marine sediments: Implications for the geological record. *Marine Geology*, **113**, 67–88.
- CHAPPAZ, A., GOBEIL, C. & TESSIER, A. 2008. Geochemical and anthropogenic enrichments of Mo in sediments from perennially oxic and seasonally anoxic lakes in eastern Canada. *Geochimica et Cosmochimica Acta*, **72**(1), 1149–1158.
- CHAPPAZ, A. LYONS, T. W., GREGORY, D. D., REINHARD, C. T., GILL, B. C., LI, C & LARGE, R. R. 2014. Does pyrite act as an important host for molybdenum in modern and ancient euxinic sediments? *Geochimica et Cosmochimica Acta*, **126**, 112–122.
- COLLIER, R. W. 1985. Molybdenum in the Northeast Pacific Ocean. *Limnol. Oceanogr.*, **30** (6), 1351–1354.
- COVENEY, R. M., Jr., & GLASCOCK, M. D. 1989. A review of the origins of metal-rich Pennsylvanian black shales, central U.S.A., with an inferred role for basinal brines. *Appl. Geochem.* **4**, 347–367.
- CRUSIUS, J., CALVERT, S., PEDERSEN, T. & SAGE, D. 1996. Rhenium and molybdenum enrichment in sediments as indicators of oxic, suboxic and sulfidic conditions of deposition. *Earth and Planetary Science Letters*, **145**, 65–78.
- DAHL, T. W., CHAPPAZ, A. FITTS, J. P & LYONS, T. W. 2013. Molybdenum reduction in a sulfidic lake: Evidence from X-ray adsorption fine-structure spectroscopy

Quantifying marine redox across the Triassic–Jurassic mass extinction

and implications for the Mo paleoproxy. *Geochimica et Cosmochimica Acta*, **103**, 213–231.

DAHL, T. W., CHAPPAZ, A., HOEK, J., MCKENZIE, C. J., SVANE, S. & CANFIELD, D. E. 2017. Evidence of Molybdenum association with particulate organic matter under sulfidic conditions. *Geobiology*, **15**, 311–323.

EMERSON, S. R. & HUESTED, S. S. 1991. Ocean anoxia and the concentrations of molybdenum and vanadium in seawater. *Marine Chemistry*, **34**, 177–196.

ERICKSON, B. E. & HELZ, G. R. 2000. Molybdenum (VI) Speciation in Sulfidic Waters: Stability and Lability of Thiomolybdates. *Geochimica et Cosmochimica Acta*, **64**, 1149–1158.

FALKOWSKI, P. G. 1983. Enzymology of nitrogen assimilation. In: Carpenter, E. J., Capone, D. G. (eds.) Nitrogen in the marine environment. Academic Press, New York, p. 839–868.

FRANCOIS, R. 1988. A study on the regulation of the concentrations of some trace metals (Rb, Sr, Zn, Pb, Cu, V, Cr, Ni, Mn and Mo) in Saanich Inlet sediments, British Columbia, Canada, *Marine Geology*, **83**, 285–308.

GLASS, J. B., WOLFE-SIMON F. & ANBAR, A. D. 2009. Coevolution of metal availability and nitrogen assimilation in cyanobacteria and algae. *Geobiol*, **7**, 100–123.

GOLDBERG, S., FORSTER, H. S. & GODFREY, C.L. 1996. Molybdenum Adsorption on Oxides, Clay Minerals, and Soils. *Soil Science Society of America Journal*, **60**, 425–432.

GOLDBERG, S., SU, C., & FORSTER, H. S. 1998. Sorption of molybdenum on oxides, clay minerals, and soils: Mechanisms and models. In: Adsorption of Metals by Geomedia: Variables, Mechanisms, and Model Applications, Proc. Am. Chem. Soc. Symp. E. A. Jenne (ed.). Academic Press, San Diego, CA, pp. 401Y426.

GOLDBERG, T., ARCHER, C., VANCE, D. & POULTON, S. W. 2009. Mo isotope fractionation during adsorption of Fe (oxyhydr)oxides. *Geochimica et Cosmochimica Acta* **73**, 6502–6516.

HELZ, G. R. MILLER, C. V. CHARNOCK, J. M., MOSSELMANS, J. F. W., PATTRICK, R. A. D., GARNER, C. D. & VAUGHAN, D. J. 1996. Mechanism of molybdenum removal from the sea and its connections in black shales: EXAFS evidence. *Geochimica et Cosmochimica Acta*, **60** (19), 3631–3642.

HELZ, G. R., VORLICEK, T. P., KAHN, M. D., 2004. Molybdenum scavenging by iron monosulfide. *Environ. Sci. Technol.* **38**, 4263–4268.

HELZ, G. R., BURA-NAKIĆ, E., MIKAC, N. & CIGLENEČKI, I. 2011. New model for molybdenum behavior in euxinic waters. *Chemical Geology*, **284**(3-4), 323–332.

Appendices

- HUERTA-DIAZ, M. A. & MORSE, J. W. 1992. Pyritisation of trace metals in anoxic marine sediments. *Geochim. Cosmochim. Acta*, **56**, 2681–2702.
- KASHIWABARA, T., TAKAHASHI, Y. & TANIMIZU, M., 2009. A XAFS study on the mechanism of isotopic fractionation of molybdenum during its adsorption of ferromanganese oxides. *Geochemical Journal*, **43**, 31–36.
- KENDALL, B., DAHL, T. W. & ANBAR, A. D. 2017. Good Golly, Why Moly? The stable isotope geochemistry of molybdenum. *Reviews in Mineralogy and Geochemistry*, **82**, 683–732.
- LYONS, T. W., WERNE, J. P., HOLLANDER, D. J. & MURRAY, R. W. 2003. Contrasting sulfur geochemistry and Fe/Al and Mo/Al ratios across the last oxic-to-anoxic transition in the Cariaco Basin, Venezuela, *Chem. Geol.*, **195**, 131–157.
- MAGYAR, B., MOOR, H. C. & SIGG, L. 1993. Vertical distribution and transport of molybdenum in a lake with a seasonally anoxic hypolimnion. *Limnology and Oceanography*, **38(3)**, 521–531.
- McMANUS, J., BERELSON, W. M., SEVERMANN, S., POULSON, R. L., HAMMOND, D. E., KLINKHAMMER, G. P. & HOLM, C. 2006. Molybdenum and uranium geochemistry in continental margin sediments: Paleoproxy potential. *Geochim. Cosmochim. Acta*, **70**, 4643–4679.
- MILLER, C. A., PEUCKER-EHRENBRINK, B., WALKER, B. D. & MARCANTONIO, F. 2011. Re-assessing the surface cycling of molybdenum and rhenium. *Geochimica et Cosmochimica Acta*, **75**, 7146–7179.
- MORFORD, J. L. & EMERSON, S. 1999. The geochemistry of redox sensitive trace metals in sediment. *Geochimica et Cosmochimica Acta*, **63 (11-12)**, 1735–1750.
- MORFORD, J. L., EMERSON, S. R., BRECKEL, E. J. & HYUN KIM, S. 2005. Diagenesis of oxyanions (V, U, Re, Mo) in pore waters and sediments from a continental margin. *Geochimica et Cosmochimica Acta*, **69(21)**, 5021–5032.
- MURRAY, J. W. 1975. The interaction of metal ions at the manganese dioxide-solution interface, *Geochimica et Cosmochimica Acta*, **43**, 1011–1026.
- NAMEROFF, T. J., BALISTRIERI, L. S. & MURRAY, J. W. 2002. Suboxic trace metal geochemistry in eastern tropical North Pacific. *Geochimica et Cosmochimica Acta*, **66(7)**, 1139–1158.
- OZEKI, T., ADACHI, H. & SHIGERO, I. 1996. Estimation of the dissolved structures and condensation reactivities of mononuclear molybdenum (VI) species in solution using the UV-vis absorption spectra and molecular orbital calculation DV-X. *Bull. Chem. Soc. Japan*, **69**, 619–625.
- SCHOLZ, F., SIEBERT, C., DALE, A. W. & FRANK, M. 2017. Intense molybdenum accumulation in sediments underneath a nitrogenous water column and implications for

Quantifying marine redox across the Triassic–Jurassic mass extinction

the reconstruction of paleo-redox conditions based on molybdenum isotopes.

Geochimica et Cosmochimica Acta, **213**, 400–417.

SCOTT, C & LYONS, T. W. 2012. Contrasting molybdenum cycling and isotopic properties in euxinic versus non-euxinic sediments and sedimentary rocks: Refining the paleoproxies. *Chemical Geology*, **324-325**, 19–27.

SHIMMIELD, G. B. & PRICE, N. B. 1986. The behaviour of molybdenum and manganese during early sediment diagenesis — offshore Baja California, Mexico. *Marine Chemistry*, **19(3)**, 261–280.

SMEDLEY, P. L. & KINNIBURGH, D. G. 2017. Molybdenum in natural waters: A review of occurrence, distributions and controls. *Applied Geochemistry*, **84**, 387–432.

TRIBOVILLARD, N., RIBOULLEAU, A., LYONS, T. & BAUDIN, F. 2004. Enhanced trapping of molybdenum by sulfurized marine organic matter of marine origin in Mesozoic limestones and shales. *Chemical Geology*, **213**, 385–401.

TRIBOVILLARD, N., ALGEO, T. J., LYONS, T. & RIBOULLEAU, A. 2006. Trace metals as paleoredox and paleoproductivity proxies: An update. *Chemical Geology*, **232**, 12–32.

TURNER, D. R., WHITFIELD, M. & DICKSON, A. G. 1981. The equilibrium speciation of dissolved components in freshwater and sea water at 25°C and 1 atm pressure. *Geochimica et Cosmochimica Acta*, **45 (6)**, 855–881.

VORLICEK, T. P., KAHN M. D., KASUYA, Y. & HELZ, G. R. 2004. Capture of molybdenum in pyrite-forming sediments: role of ligand-induced reduction by polysulfides. *Geochim Cosmochim Acta*, **68**, 547–556.

WAGNER, M., CHAPPAZ, A. & LYONS, T. W. 2017. Molybdenum speciation and burial pathway in weakly sulfidic environments: Insights from XAFS. *Geochimica et Cosmochimica Acta*, **206**, 18–29.

WANG, D., ALLER, R. C. & SAÑUDO-WILHELMY, S. A. 2011. Redox speciation and early diagenetic behavior of dissolved molybdenum in sulfidic muds. *Marine Chem.*, **125**, 101–107

WASYLENKI, L. E., WEEKS, C. L., BARGAR, J. R. SPIRO, T. G., HEIN, J. R. & ANBAR, A. D. 2011. The molecular mechanism Mo isotope fractionation during adsorption to birnessite. *Geochimica et Cosmochimica Acta*, **75**, 5019–5031.

ZHENG, Y., ANDERSON, R. F., VAN GEEN, A. & KUWUBARA, J. 2000. Authigenic molybdenum formation in marine sediments: A link to pore water sulfide in the Santa Barbara Basin. *Geochimica et Cosmochimica Acta*, **64 (24)**, 4165–4178.

APPENDIX 2.5: ORGANIC CARBON/PHOSPHORUS

The ground-breaking studies of Alfred Redfield determined that the atomic ratio of carbon (C) to phosphorous (P) within marine organisms conforms to a specific ratio (Redfield 1934, 1958; Redfield et al., 1963). Redfield quantified this ratio as 106 atoms of C for every atom of P (106:1). However, subsequent studies, particularly those during the later portion of the 20th century, contest this ratio (Lenton & Watson, 2000 and references therein). Anderson & Sarmiento (1994) quote a value of 117:1±14 based on data from 20 ‘neutral surfaces’ across the South Atlantic, Pacific and Indian Basins, between 400m and 4000m depth. Takahashi et al., (1985) record a value between 103:1 and 140:1 based on chemical data from isopycnal surfaces of the Indian and Atlantic Oceans. Meanwhile, recent work by Martiny et al., (2014) quotes a global marine C:P of 163:1 based on 100,605 individual measurements.

There is also variability of the ‘Redfield ratio’ amongst individual groups of organisms e. g. C:P has been found to vary between 50:1 and 150:1 within marine phytoplankton with Ho et al., (2003) quoting an average of 124:1 based on 9 taxa (Ho et al., 2003; Algeo & Ingall, 2007 and references therein). Also, Martiny et al., (2013) have noted C:P variation according to latitude and basin restriction, and Ingall & Van Cappellen, (1990) note elevated C:P ratios in localities with intermediate rates of sedimentation. In spite of these inconsistencies and the variability of C:P under different environmental regimes, the Redfield ratio can prove a useful palaeo-environmental indicator when studied alongside a selection of other proxies.

Algeo & Ingall (2007) particularly highlighted the use of sedimentary C:P as a potential proxy for palaeo-redox conditions. Upon the burial of organic matter within marine

Quantifying marine redox across the Triassic–Jurassic mass extinction

sediments, P is preferentially remineralised in the form of proteins and nucleic acids by bacterial decomposition (Algeo & Ingall and references therein). Preferential P remineralisation is thought to be the result of rapid P solubilisation from internal stores as well as faster remineralisation of P than Nitrogen (N). (Burkhardt et al., 2014).

Where the surrounding pore waters are oxygenated, remineralised P may be retained through microorganismal polyphosphate storage (Davelaar, 1993; Sannigrahi & Ingall, 2005), or sorption on mineral complexes e. g. Fe-Mn oxyhydroxides (Slomp et al., 1996) and carbonate fluorapatite (Ruttenberg & Berner, 1993). Despite most P under oxic conditions being lost through flux into the overlying water column (Ingall et al., 2005; Guilbaud et al., 2020), the collective processes listed above result in a 2 to 10 fold increase in sedimentary P and reduced sedimentary C:P values (Algeo & Ingall, 2007; Marynowski et al., 2017).

However, where surrounding pore waters are anoxic/sulfidic, remineralised phosphorous is release back into the water column due to the instability of oxyhydroxides under low oxygen conditions (Canfield et al., 1992; Dos Santos et al., 1992; Ingall & Jahnke, 1994; Van Cappellen & Ingall, 1996; Ingall et al., 2005; Algeo & Ingall, 2007). Oxygen poor conditions within the overlying water column also result in greater P remineralisation and reduced P burial which in turn can result in a positive feedback cycle of P regeneration and productivity (Van Cappellen & Ingall, 1994, 1996; Ingall & Jahnke, 1997; Lenton & Watson 2000). Anoxic/Sulfidic bottom water conditions therefore result in elevated C:P values.

Meanwhile ferruginous conditions, such as those reported from the Proterozoic, are also thought to result in a distinct retention of P (Reinhard et al., 2017; Bowyer et al., 2020;

Appendices

Guilbaud et al., 2020). Under ferruginous conditions P is partly recycled back into the water column (Bowyer et al., 2020), however P also fixes to Fe oxides (Thompson et al., 2019), Fe phosphates, such as vivianite (Egger et al., 2015; Xiong et al., 2019), and ferrihydrite (Guilbaud et al., 2020 and references therein). P limitation within the photic zone has also been hypothesised through an Fe-P trap within ferruginous deep water environments (Reinhard et al., 2017). These recent studies further highlight the need to study C:P alongside other proxies e.g. Fe speciation and metal enrichment, in order to distinguish ferruginous and oxic conditions.

ALGEO, T. J. & Ingall, E. 2007. Sedimentary C_{org}/P ratios, paleocean ventilation and Phanerozoic atmospheric pO_2 . *Palaeogeog., Palaeoclim., Palaeoecol.*, **256**, 130–155.

ANDERSON, L. A. & Sarmiento, J. L. 1994. Redfield ratios of remineralisation determined by nutrient data analysis, *Global Biogeochemical Cycles*, **8(1)**, 65–80.

BOWYER, F. T., Shore, A. J., Wood, R. A., Alcott, L. J., Thomas, A. L., Butler, I. B., Curtis, A., Hainanan, S., Curtis-Walcott, S., Penny, A. M. & Poulton, S. W. 2020. Regional nutrient decrease drove redox stabilisation and metazoan diversification in the late Ediacaran Nama Group, Namibia. *Scientific Reports*, 10: 2240.

BURKHARDT, B. G., Watkins-Brandt, K. S., Defforey, D., Paytan, A. & White, A. E. 2014. Remineralization of phytoplankton-derived organic matter by natural populations of heterotrophic bacteria. *Marine Chemistry*, **163**, 1–9.

CANFIELD, D. E., Raiswell, R. & Bottrell, S. H. 1992. The reactivity of sedimentary iron minerals toward sulfide. *Am. J. Sci.* **292**, 659–683.

DAVELAAR, D. 1993. Ecological significance of bacterial polyphosphate metabolism in sediments, *Hydrobiologia*, **253**, 179–192.

DOS SANTOS AFONSO, M. & Stumm, W. 1992. Reductive dissolution of iron(III) (hydr)oxides by hydrogen sulfide. *Langmuir* **8**, 1671–1675.

EGGER, M., Jilbert, T., Behrends, T., Rivard, C. & Slomp, C. P. 2015. Vivianite is a major sink for phosphorus in methanogenic coastal surface sediments. *Geochim. Cosmochim. Acta*, **169**, 217–235.

GUILBAUD, R., Poulton, S. W., Thompson, J., Husband, K. F., Zhu, M., Zhou, Y., Shields, G. A. & Lenton, T. M. 2020. Phosphorus-limited conditions in the early

Quantifying marine redox across the Triassic–Jurassic mass extinction

Neoproterozoic ocean maintained low levels of atmospheric oxygen. *Nature Geoscience*, **13**, 296–301.

HO, T.-Y., QUIGG, A., FINKEL, Z. V., MILLIGAN, A. J., WYMAN, K., FALKOWSKI, P. G. & MOREL, F. M. M. 2003. The elemental composition of some marine phytoplankton. *J. Phycol.*, **39**, 1145–1159.

INGALL, E. D. & Van Cappellen, P. 1990. Relation between sedimentation rate and burial of organic phosphorus and organic carbon in marine sediments. *Geochimica et Cosmochimica Acta*, **54**, 373–386.

INGALL, E. & Jahnke, R. 1994. Evidence for enhanced phosphorus regeneration from marine sediments overlain by oxygen depleted waters. *Geochim. Cosmochim. Acta*, **58**, 2571–2575.

INGALL, E., Kolowith, L., Lyons, T. & Hurtgen, M. 2005. Sediment carbon, nitrogen and phosphorus cycling in an anoxic fjord, Effingham Inlet, British Columbia. *American Journal of Science*, **305**, 240–258.

LENTON, T. M. & Watson A. J. 2000. Redfield revisited 1. Regulation of nitrate, phosphate, and oxygen in the ocean. *Global Biogeochemical Cycles*, **14(1)**, 225–248.

MARTINY, A. C., Pham, C. T. A., Primeau, F. W., Vrugt, J. A., Keith More, J., Levin, S. A. & Lomas, M. W. 2013. Strong latitudinal patterns in the elemental ratios of marine plankton and organic matter. *Nature Geoscience*, **6**, 279–283.

MARTINY, A. C., Vrugt, J. A. & Lomas, M. W. 2014. Concentrations and ratios of particulate organic carbon, nitrogen, and phosphorus in the global ocean, Scientific Data, 1:140048.

MARYNOWSKI, L., Piszczowska, A., Derkowski, A., Rakociński, M., Szaniawski, R., Środoń, J. & Cohen, A. S. 2017. Influence of palaeoweathering on trace metal concentrations and environmental proxies in black shales. *Palaeogeog. Palaeoclim. Palaeoecol.*, **472**, 177–191.

REDFIELD, A. C. 1934. On the proportions of organic derivatives in sea water and their relation to the composition of plankton. James Johnstone Memorial Volume, University Press of Liverpool, 176–192.

REDFIELD, A. C. 1958. The Biological Control of Chemical Factors in the Environment. *American Scientist*, **46**, 205–221.

REDFIELD, A. C., Ketchum, B. H. & Richards, F. A. **1963**. The Influence of Organisms on the Composition of the Sea Water. In Hill, M.N., Ed., *The Sea*, Vol. **2**, Interscience Publishers, New York, 26–77.

RUTTENBERG, K. & Berner, R. 1993. Authigenic apatite formation and burial in sediments from non-upwelling, continental margin environments. *Geochim. Cosmochim. Acta*, **57**, 991–1007.

Appendices

SANNIGRAHI, P., and E. Ingall. 2005. Polyphosphates as a source of enhanced P fluxes in marine sediments overlain by anoxic waters: Evidence from ^{31}P NMR, *Geochem. Trans.*, **6**, 52–59.

SLOMP, C. P., Epping, E. H. G., Helder, W. & Van Raaphorst, W. 1996. A key role for iron-bound phosphorus in authigenic apatite formation in North Atlantic continental platform sediments. *J. Mar. Res.*, **54**, 1179–1205.

TAKAHASHI, T., BROECKER, W. S. & LANGER, S. 1985. Redfield ratio based on chemical data from isopycnal surfaces. *Journal of Geophysical Research: Oceans*, **90(4)**, 6907–6924.

THOMPSON, J., Poulton, S. W., Guilbaud, R., Doyle, K. A., Reid, S. & Krom, M. D. 2019. Development of a modified SEDEX phosphorus speciation method for ancient rocks and modern iron-rich sediments. *Chem. Geol.* **524**, 383–393.

VAN CAPPELLEN, P. & Ingall, E. D. 1994. Benthic phosphorus regeneration, net primary production, and ocean anoxia: A model of the coupled marine biogeochemical cycles of carbon and phosphorus. *Palaeoceanography*, **9(5)**, 677–692.

VAN CAPPELLEN, P. & Ingall, E. D. 1996. Redox Stabilization of the Atmosphere and Oceans by Phosphorus-Limited Marine Productivity. *Science*, **271**, 493–496.

XIONG, Y., Guilbaud, R., Peacock, C. L., Cox, R. P., Canfield, D. E., Krom, M. D. & Poulton, S. W. 2019. Phosphorus cycling in Lake Cadagno, Switzerland: a low sulfate euxinic ocean analogue. *Geochim. Cosmochim. Acta* **251**, 116–135.

APPENDIX 2.6: ZINC

Introduction to Zinc- Zinc exhibits a very similar chemistry to cadmium due to both elements being chalcophilic transition metals occupying the 12th column of the periodic table (Calvert & Pedersen, 1993). Like Cd, Zinc (Zn) is concentrated within the Earth's Crust as sulfide deposits and is transported to the oceans through rivers (3.74×10^{16} kg yr^{-1} ; 92%), dust (4.5×10^{14} kg yr^{-1} ; 8%) and hydrothermal fluids (3.0×10^{13} kg yr^{-1} ; <1%) (Little et al., 2014, 2016; Vance et al., 2016; Sweere et al., 2018; Isson et al., 2018). However, unlike Cd, Zn may also be delivered to the oceans through benthic inputs and the release of Zn from bottom water sediments (Conway & John, 2015; Vance et al., 2016; Little et al., 2016; Sweere et al., 2018). Under oxygenated conditions Zn is present in the form of soluble ionic species Zn^{2+} (major) and ZnCl^+ (minor) (Calvert & Pedersen, 1993; Tribovillard et al., 2006; Vance et al., 2016). Small concentrations of Zn are also incorporated into/onto calcite or form independent carbonate species (ZnCO_3) (Vance et al., 2016; Sweere et al., 2018; Isson et al., 2018; Mavromatis et al., 2019). Meanwhile, Zn humate and fulvate complexes have been revealed as particularly common within oxic freshwater and marine environments (Bruland 1989; Achterberg et al., 1997; Aristilde et al., 2012).

Zn, like Cd, plays an important role as a micronutrient, particularly through the formation of carbonic anhydrase (Calvert & Pedersen, 1993; Shaked et al., 2006; Conway & John, 2015; Zhang et al., 2021). Zn is subsequently very readily recycled within the water column and has a residence time of just 11ky within modern oceans (Little et al., 2014). Most importantly, Zn, like Cd, is enriched within organic rich sediments and is concentrated under oxygen-poor conditions (Jacobs & Emerson, 1985; Algeo & Maynard, 2004; Tribovillard et al., 2006; Vance et al., 2016; Oculalidet et al.,

Appendices

2018; Dickson et al., 2020; Dickson, 2022). The remainder of this section will discuss Zn removal pathways and the use of Zn as a palaeo-redox proxy.

The importance of Zinc as a micronutrient- Studies of Zn distribution within the water column have determined that Zn exhibits a very similar spatial distribution to both phosphate and silica (Bruland et al., 1978; Bruland, 1980; Lohan et al., 2002; Bruland & Lohan, 2003; Conway & John, 2015). It is widely agreed upon that this distribution is due to Zn behaving as a micronutrient and that Zn is taken up by marine organisms in the photic zone (Calvert & Pedersen, 1993; Morel & Price, 2003; Tribovillard et al., 2006; Little et al., 2014; Conway & John, 2015; Vance et al., 2016; Zhao et al., 2021). Zinc is an important co-factor for hundreds of enzymes, including carbonic anhydrase and alkaline phosphatase, and is essential for a range of basic cellular functions (Anderson et al., 1978; Bruland et al., 1991; Morel et al., 2004; Anbar & Rouxel, 2007; Supuran, 2011; Scott et al., 2013; Zhao et al., 2021). Zn may also be a limiting factor for primary productivity (Anderson et al., 1978; Morel et al., 2004; Shaked et al., 2006).

The spatial distribution of dissolved zinc- Due to the important role that Zn plays as a micronutrient, the distribution of Zn within the water column is largely governed by biochemical reactions (Anderson et al., 1978; Calvert & Pederson, 1993; Morel et al., 2004; Shaked et al., 2006; Little et al., 2014). Zn is quantitatively removed in the photic zone by biological uptake and ligand complexation resulting in the photic zone being depleted in Zn (<0.1nM) (Bruland et al., 1978; Bruland, 1980; Bruland, 1989; Calvert & Pedersen, 1993; Lohan et al., 2002; Bruland & Lohan, 2003; Morel & Price, 2003; Anbar & Rouxel, 2007; Little et al., 2014 and papers therein; Wyatt et al., 2014; Conway & John, 2015; Vance et al., 2016). Zn is then delivered to bottom water

Quantifying marine redox across the Triassic–Jurassic mass extinction

sediments in association with organic matter (OM) where it is released through OM decay resulting in Zn regeneration (2-10nM) (Bruland, 1980; Calvert & Pedersen, 1993; Lohan et al., 2002; Bruland & Lohan, 2003; Tribovillard et al., 2006; Conway & John, 2014; Little et al., 2014; Zhang et al., 2021).

Zinc removal under oxic conditions- Upon sediment delivery Zn may be incorporated into carbonate and biogenic silica (Vance et al., 2016; Sweere et al., 2018; Isson et al., 2018; Mavromatis et al., 2019), or ferromanganese crusts and nodules, particularly amongst manganese-rich deposits (Hein et al., 1997). Zn may equally be fractionated directly from seawater in each of these situations without the need for biogenic delivery (Vance et al., 2016; Isson et al., 2018; Mavromatis et al., 2019; He et al., 2021).

However, Ferromanganese crusts, carbonates, and siliceous sediments only account for 27% of all sedimentary Zn removal (Isson et al., 2018). Furthermore, all are isotopically heavy removal mechanisms for Zn (Vance et al., 2016; Isson et al., 2018; Sweere et al., 2018; He et al., 2021), and recent studies suggest that isotopically light removal mechanisms for Zn are particularly significant within modern marine environments for maintaining an isotopically heavy (>0.5) δZn within the deep oceans (Little et al., 2014; Vance et al., 2016; Isson et al., 2018; Sweere et al., 2018).

Zinc removal under oxygen-poor conditions- Organic-rich deposits, formed under oxygen poor conditions, are commonly enriched in Zn and are isotopically light (Little et al., 2016; Zhang et al., 2021; Dickson et al., 2020, Dickson 2022). Therefore, given that 62% of zinc is delivered to marine sediments in association with organic matter, and the important role that Zn plays both as a micronutrient as well as in organic complexation, one possibility is that the majority of Zn is removed into sediments

Appendices

through scavenging to organic matter and/or biological uptake (Morel & Price, 2003; Shaked et al., 2006; Scott et al., 2013; Little et al., 2014 and papers therein; Conway & John, 2015; Isson et al., 2018; Zhang et al., 2021). However, the vast majority of biological Zn uptake within the marine photic zone is governed by diatoms which are not known to fractionate Zn (Vance et al., 2016 and references therein). Therefore, it is unlikely that biological uptake alone may account for such a significant isotopically-light removal pathway. Conversely, as noted by Vance et al., (2016), unfractionated Zn may be delivered in large concentrations to the seafloor through sinking organic matter and become subsequently removed through a secondary isotopically-light removal pathway (e. g. zinc sulfide formation).

Zinc sulfide formation- In anoxic basins, dissolved Zn decreases from a factor of 2 to a factor of 10 from the upper oxic to the lower anoxic water mass (Calvert & Pedersen, 1993). This is observed within the Black Sea and Framraven Fjord where sulfidised Zn species are dominant at dissolved sulfide levels (Daskalakis & Helz, 1993). The formation of insoluble Zn sulfide complexes within sulfidic, oxygen poor environments result in the quantitative removal of Zn from the water column into the underlying sediments and represents an important sink for Zn (Brumsack, 1980; Jacobs & Emerson 1985; Jacobs et al., 1987; Algeo & Maynard, 2004; Tribovillard et al., 2006; Little et al., 2014 and papers therein; Vance et al., 2016). Moreover, zinc sulfides are an isotopically light removal pathway for Zn (Sweere et al., 2018; Zhang et al., 2021).

Zinc sulfide species- Brumsack, (1980) and Morse & Luther, (1999) interpret that Zn may precipitate in solid solution with pyrite under oxygen poor conditions. However, Huerta-Diaz & Morse, (1992) report Zn incorporation into pyrite to be ‘unimportant’.

Quantifying marine redox across the Triassic–Jurassic mass extinction

Brumsack, (1980) and Morse & Luther, (1999) also propose that Zn may precipitate as an independent authigenic sphalerite phase. However, Daskalakis & Helz (1993) report anoxic basins like the Black Sea and the Framraven Fjord to be undersaturated with respect to sphalerite and instead report that the dominant species of zinc within sulfidic waters is ZnS(HS)^- which is subsequently scavenged into underlying sediments. Huerta-Diaz & Morse, (1992) report low DTMP (degree-of-trace-metal-pyritization) of Zn from a number of anoxic basin sediments, which would reflect the ultimate residence of Zn within a non-sulfidic or organic phase (Algeo & Maynard, 2004). A strong association between Zn and TOC within non-sulfidic, anoxic facies has also been noted by Algeo & Maynard (2004) through the study of Carboniferous sediments. Therefore, one potential removal pathway is the scavenging of ZnS(HS)^- by organic matter.

Zinc sulfide formation in open-marine environments- Despite ZnS formation commonly being associated with restricted, euxinic environments (e. g. The Black Sea), a recent study by Janssen et al., (2014) suggests that Zn co-precipitates with sulfur in the OMZ of open marine environments, much like Cd. These findings would suggest that ZnS formation under oxygen poor conditions represents a significant, global, isotopically light removal mechanism for Zn and an important palaeo-redox proxy.

ACHTERBERG, E. P., Van Den Berg, C. M. G., Boussemart, M., & Davison, W. 1997. Speciation and cycling of trace metals in Esthwaite water : a productive English lake with seasonal deep-water anoxia. *Geochimica et Cosmochimica Acta*, **61** (24), 5233-5253.

ALGEO, T. J. & Maynard, J. B. 2004. Trace-element behavior and redox facies in core shales of Upper Pennsylvanian Kansas-type cyclothems. *Chemical Geology*, **206**, 289–318.

ANBAR, A. D. & ROUXEL, O. 2007. Metal Stable Isotopes in Paleoceanography. *Annual Review of Earth and Planetary Science*, **35**, 717–746.

Appendices

- ANDERSON, M. A. Morel, F. M. M., & Guillard, R. R. L. 1978. Growth limitation of a coastal diatom by low zinc ion activity. *Nature*, **276**, 70–71
- ARISTILDE, L., Xu, Y., & Morel, F. M. M. 2012. Weak organic ligands enhance zinc uptake in marine phytoplankton. *Environmental Science and Technology*, **46**, 5438–5445.
- BRULAND, K. W. 1980. Oceanographic distributions of cadmium, zinc, nickel and copper in the north Pacific. *Earth and Planetary Science Letters*, **47**, 176–198.
- BRULAND, K. W. 1989. Complexation of zinc by natural organic ligands. in the central North Pacific. *Limnology and Oceanography*, **34**, 269–285.
- BRULAND, K. W., Donat, J. R., & Hutchins, D. A. 1991. Interactive influence of bioactive trace metals on biological production in oceanic waters. *Limnology and Oceanography*, **36** (8), 1555–1577.
- BRULAND, K. W. & Lohan, M. C. 2003. Controls of Trace Metals in Seawater, in K. W. Bruland & Lohan, M. C. (2004) Controls on trace metals in seawater, in the Oceans and Marine Geochemistry H. Elderfield (ed.) Vol. 6, Treatise on Geochemistry H. D. Holland and K.K. Turekian (eds.) pp. 23–49. London: Elsevier.
- BRULAND, K. W., Knauer, G. A., & Martin, J. H. 1978. Zinc in northeast Pacific water. *Nature*, **271**, 741–743.
- BRUMSACK, H.J., 1980. Geochemistry of Cretaceous black shales from the Atlantic Ocean (DSDP Legs 11, 14, 36, and 41). *Chemical Geology*, **31**, 1–25.
- CALVERT, S. E. & Pedersen, T. F. 1993. Geochemistry of Recent oxic and anoxic marine sediments: Implications for the geological record. *Marine Geology*, **13**, 67–88.
- CONWAY, T. M. & John, S. G. 2015. The cycling of iron, zinc and cadmium in the North East Pacific Ocean – Insights from stable isotopes. *Geochimica et Cosmochimica Acta*, **164**, 262–283.
- DASKALAKIS K. D. & Helz G. R. 1993 The solubility of sphalerite (ZnS) in sulfidic solutions at 25°C and 1 atm pressure. *Geochimica et Cosmochimica Acta*, **57**, 4923–4932.
- DICKSON, A. J., Idiz, E., Porcelli, D., & van den Boorn, S. H. J. M., 2020, The influence of thermal maturity on the stable isotope compositions and concentrations of molybdenum, zinc and cadmium in organic-rich marine mudrocks. *Geochimica et Cosmochimica Acta*, **287**, 205–220.
- DICKSON, A. J., 2022. The zinc isotope composition of late Holocene open-ocean marine sediments. *Chemical Geology*, **605**, 120971.

Quantifying marine redox across the Triassic–Jurassic mass extinction

HE, L., Liu, J., Zhang, H., Gao, J., Zhu, A., & Zhang, Y. 2021. Copper and zinc isotope variations in ferromanganese crusts and their isotopic fractionation mechanism. *Acta Oceanologica Sinica*, **40**, 43–52.

HEIN, J. R., Koschinsky, A., Halbach, P., Manheim, F. T., Bau, M., Kang, J.-K., & Lubick, N. 1997. Iron and manganese oxide mineralisation in the Pacific, in Nicholson, K., Hein, J. R., Bühn, B. & Dasgupta, S. (eds.), 1997, Manganese Mineralisation: Geochemistry and Mineralogy of Terrestrial and Marine Deposits, *Geological Society Special Publications*, **119**, 123–138.

HUERTA-DIAZ, M. A. & MORSE, J. W. 1992. Pyritisation of trace metals in anoxic marine sediments. *Geochim. Cosmochim. Acta*, **56**, 2681–2702.

ISSON, T. T., Love, G. D., Dupont, C. I., Reinhard, C. T., Zumberge, A. J., Asael, D., Gueguen, B., McCrow, J., Gill, B. C., & Owens, J., 2018. Tracking the rise of eukaryotes to ecological dominance with zinc isotopes. *Geobiology*, **16**, 341–352.

JACOBS, L., & Emerson, S. 1985. Partitioning and transport of metals across the O₂/H₂S interface in a permanently anoxic basin: Framvaren Fjord, Norway. *Geochimica et Cosmochimica Acta*, **49**, 1433–1444.

JACOBS, L., Emerson, S., & Husteded, S. S. 1987. Trace metal geochemistry in the Cariaco Trench. *Deep-Sea Research*, **34** (5–6), 965–981.

JANSSEN, D. J., CONWAY, T., JOHN, S. G., CHRISTIAN, J. R., KRAMER, D. I., PEDERSEN, T. F. & CULLEN, J. T. 2014. Undocumented water column sink for cadmium in open ocean oxygen-deficient zones. *PNAS*, **111**(19), 6888–6893.

LITTLE, S. H., Vance, D., Walker-Brown, C. & Landing, W. M. 2014. The oceanic mass balance of copper and zinc isotopes, investigated by analysis of their inputs, and outputs to ferromanganese oxide sediments. *Geochimica et Cosmochimica Acta*, **125**, 673–693.

LITTLE, S. H., Vance, D., McManus, J., & Severmann, S. 2016. Key role of continental margin sediments in the oceanic mass balance of Zn and Zn isotopes. *Geology*, **44** (3), 207–210.

LOHAN, M. C., Statham, P. J., & Crawford D. W. 2002. Dissolved zinc in the upper water column of the subarctic North East Pacific. *Deep-Sea Research II*, **49**, 5793–5808.

MAVROMATIS, V., González, A. G., Dietzel, M., & Schott, J. 2019. Zinc isotope fractionation during the inorganic precipitation of calcite – Towards a new pH proxy. *Geochimica et Cosmochimica Acta*, **244**, 99–112.

MOREL, F. M. M. & Price, N. M. 2003. The Biogeochemical Cycles of Trace Metals in the Oceans. *Science*, **300**, 944–947.

Appendices

- MOREL, F. M., Milligan A. J., & Saito M. A. 2004. Marine bioinorganic chemistry: the role of trace metals in the oceanic cycles of major nutrients. In *Treatise on Geochemistry*, ed. HD Holland, KK Turekian, 6:113–143. Amsterdam: Elsevier
- MORSE, J. W. & Luther III, G.W. 1999. Chemical influences on trace metal-sulfide interactions in anoxic sediments. *Geochimica et Cosmochimica Acta*, **63**, 3373–3378.
- OCUBALIDET, S. G., Rimmer, S. M., & Conder, J. A. 2018. Redox conditions associated with organic carbon accumulation in the Late Devonian New Albany Shale, west-central Kentucky, Illinois Basin, *International Journal of Coal Geology*, **190**, 42–55.
- SCOTT, C., Planavsky, N. J., Dupont, C. L., Kendall., B., Gill, B. C., Robbins, L. J., Husband, K. F., Arnold, G. L., Wing, B. A., Poulton, S. W., Bekker, A., Anbar, A. D., Konhauser, K. O., & Lyons, T. W. 2013. Bioavailability of zinc in marine systems through time. *Nature Geoscience*, **6**, 125–128.
- SHAKED, Y., Xu, Y., Leblanc, K., & Morel, F.M.M. 2006. Zinc availability and alkaline phosphatase activity in *Emiliania huxleyi*: Implications for Zn-P co-limitation in the ocean. *Limnology and Oceanography*, **51**, 299–309.
- SUPURAN, C. T. 2011. Carbonic anhydrase inhibition with natural products: novel chemotypes and inhibition mechanisms. *Molecular Diversity*, **15**, 305–316.
- SWEERE, T. C., Dickson A. J., Jenkyns, H. C., Porcelli, D., Elrick, M., Van Den Boorn, S. H. J. M., & Hendersen, G. M. 2018. Isotopic evidence for changes in the zinc cycle during Oceanic Anoxic Event 2 (Late Cretaceous). *Geology*, **46** (5), 463–466.
- TRIBOVILLARD, N., Algeo T. J., Lyons, T. & Riboulleau, A., 2006. Trace metals as paleoredox and paleoproductivity proxies: An update. *Chemical Geology*, **232**, 12–32.
- VANCE, D., Little, S. H., Archer, C., Vyllinniskii, C., Andersen, M. B., Rijkenberg, M. J. A., & Lyons, T. W. 2016. *Philosophical Transactions of the Royal Society A*, 374, 20150294.
- WYATT, N. J., Milne, A., Woodward, E.M.S., Rees, A.P., Browning, T.J., Bouman, H.A., Worsfold, P.J., & Lohan, M.C., 2014, Biogeochemical cycling of dissolved zinc along the Geotraces South Atlantic transect GA10 at 40°S: *Global Biogeochemical Cycles*, **28**, 44–56.
- ZHANG, Y., Planavsky, N. J., Zhao, M., Isson, T., Asael, D., Wang, C., & Wang, F. 2021. The isotopic composition of sedimentary organic zinc and implications for the global Zn isotope mass balance. *Geochimica et Cosmochimica Acta*, **314**, 16–26.
- ZHAO, M., Tarhan, L. G., Zhang, Y., Hood, A., Asael, D., Reid, R. P., & Planavsky, N. J. 2021. Evaluation of shallow-water carbonates as a seawater zinc isotope archive. *Earth and Planetary Science Letters*, **553**, 116599.

APPENDIX 3: MATERIALS APPENDIX

APPENDIX 3.1: MATERIALS COMPILATION

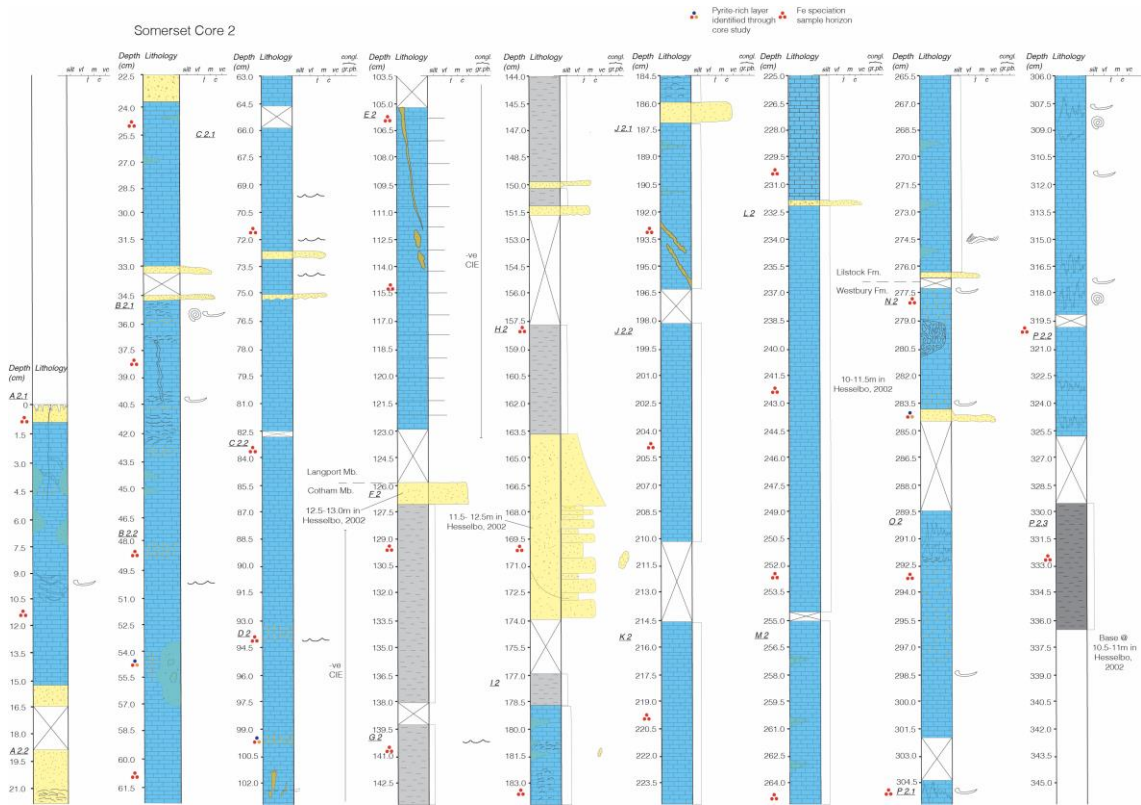
Attached as a separate excel file online.

APPENDIX 3.2: SOMERSET CORE DESCRIPTION

What follows is a detailed description and/or logs of two cores drilled in the foreshore at St. Audrie’s Bay (Somerset, Southwest England, UK) in 2013. The cores are currently held in the Department of Earth Sciences and Natural Resource Management, The Geocenter (Gefion Gymnasium) at the University of Copenhagen. One core section (Somerset Core-2) was studied in detail over the course of two days, from 1st July to the 2nd July 2019, totalling ~12 hours of study. Due to time constraints another core section (Somerset Core-1) was studied in less detail resulting in a digitised log only. Permission to use this material has been granted by Dr. Jonathan Larwood (Palaeontologist, Natural England) and Mrs Lucy Topham (Somerset, Avon & Wiltshire Adviser Support Team, Natural England).

Description of Core II:

Core 2 has been divided into logical sections according to breaks in the core or changes in sedimentology. What follows are detailed lithological descriptions of the 21 sections that compose the 336 centimetres of the core.

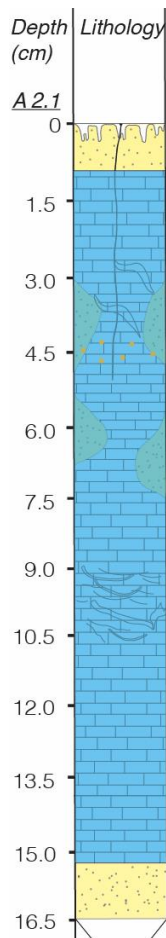


Appendices



Quantifying marine redox across the Triassic–Jurassic mass extinction

A 2.1:



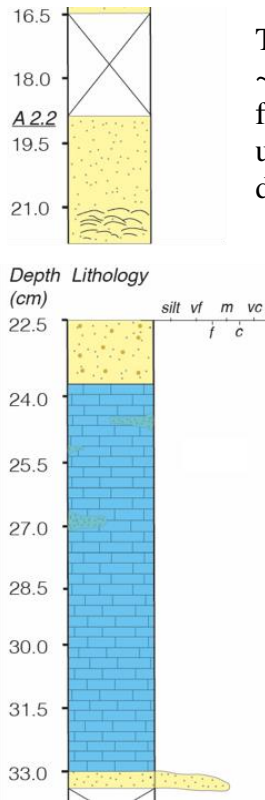
The core section is 16.5 cm in length. The upper 2 cm of the core is marked by modern bioturbation. A crack extends from the top of the core to a depth of ~5.7 cm. The top 6 cm of the core is pale grey in colour with no discernible grain size. The lithology is very fine, potentially crystalline, interpreted here as a fine carbonate lithology (Mudstone/micrite). Around 1 cm depth are inclusions of clastic, coarser material (very fine sand - fine sand). Similar inclusions may be observed at a depth of 3.5-4.5 cm. The inclusions are sometimes sinuous and are discontinuous. At ~4.5 cm are small, well-rounded globular inclusions which are dark yellow/gold in colour. The inclusions are ~1 mm across and are mostly likely authigenic pyrite. More fine sandstone inclusions however, is still very fine sand to fine sand. Oxidised patches are observed ~7 cm down to 13 cm. These may be more recent. Calcareous/mineralised valves are present from ~9.0 cm for 1 cm (Floatstone). The valves are thin, <1 mm thick, and 0.8 to 1.4 cm in length. The valves may preserve original calcite, however this is difficult to determine based on the core material. It is more than likely that the

valves may be re-mineralised. One of the valves exhibits taxodont dentition along its inner edges. One valved specimen still has both valves attached and the valves are opened. This would firstly suggest, along with the dentition, that the specimen is a bivalve and secondly that the depositional conditions were moderately calm. The base of section is a fine grained sand however exhibits indications of coarsening. The carbonate mudstone, described in line 4, makes up the majority of the section.



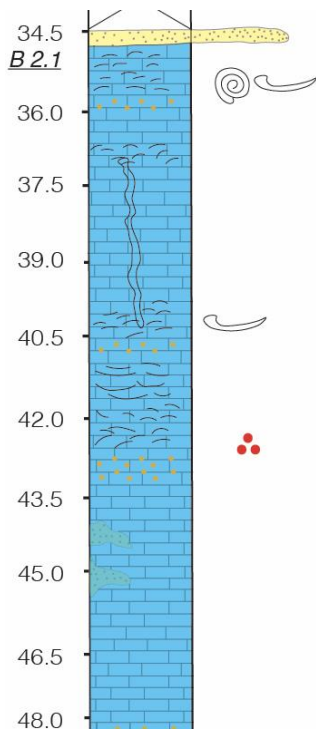
Appendices

A 2.2:



The core section is 14.5 cm in length and is separated by a gap of ~25mm from the base of section A 2.1. The top of the section follows on lithologically from the base of A 2.1. The top of A 2.2 is upper end of fine, lower end of medium grained sandstone. At 2 cm depth is a concentrated layer of numerous, small, crescentic valves which are dark in colour. These may be bivalves as observed within section A 2.1. At 2.7 to 3.4 cm depth are small rounded clasts/ nodules. The nodules are ~1mm in diameter and exhibit a dark, golden yellow colouration. These are likely to be pyrite globules as seen in section A 2.1 (4.5 cm depth). There are some signs of iron oxidation at 6.5cm depth as represented through reddened patches. Below the clastic sediments at the top of the section is a fine grained, dark grey lithology. The lithology is smooth with no visible grain size (micritic limestone). The lithology may be a fine grained carbonate, as interpreted from the previous section. At ~5 to 10.5 cm the section exhibits fine inclusions of clastic material, this is particularly common at 7 cm depth- fine sand. Coarse sandstone inclusions are also present just below 7cm depth. The bottom 3 cm of the core displays variably spaced parallel laminations/ thin interbeds. The base of the section is characterised by a brittle fine sandstone layer.

B 2.1:

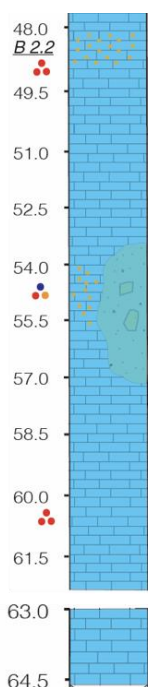


Section B 2.1 is separated from the base of A 2.2 by a 10mm gap. Section B 2.1 is 13 cm in length. The core section is distinct in its colouration exhibiting a slightly darker lithology. The lithology is still for the most part a very fine crystalline lithology-carbonate (packstone to floatstone). The very top of the core section is a 5mm layer of medium-coarse sandstone. The sandstone is poorly sorted, exhibiting angular grains and exhibits a mud/carbonate matrix. This sandstone is texturally similar to that at the based of A 2.2. Below this sandstone layer the core section is very fine carbonate (micrite), with fine calcitic crystalline inclusions of an



irregular morphology. These may represent the infilling of a burrow or fracture. Small valves and a helispiral gastropod shell can be seen at ~1.5 cm depth. Below this layer of valves and shell material is a thin section exhibiting rounded globules of what may be pyrite (based on that found within previous core sections). The globules are of similar size and colouration. A second bivalve layer is seen at ~2-2.5 cm. The layer exhibits dark, golden yellow globules 1-2mm in diameter (pyrite). A sinuous burrow/crack runs from ~2 cm to ~5 cm depth. The void is filled with medium-coarse crystalline calcite. The basal 1.5cm of the void is marked by bivalve rich strata. Below this bivalve layer (~5-5.6 cm) are fibrous and globular pyrite inclusions. These number 6/7 in total and are 1mm to 5mm in length. The next 1.5 cm of the core section in marked by coarse, crystalline infilled valves in a matrix of micrite. This bivalve layer also exhibits small (1mm) pyrite inclusions. The next 1cm contains valve fragments and globular, irregular pyrite crystals 0.5 to 3mm in diameter and numbering 8 in total. The basal 3.5 cm of the core section is a dark carbonate with less common coarse inclusions (e.g. fossil material). The upper 1.5 cm of this section exhibits relatively more common inclusions. Meanwhile the lower 2 cm exhibits very few inclusions but some globular pyrite 0.5 to 3mm in diameter. There is a possible stylolite 2 cm from the base with microcrystalline pyrite precipitated along this fracture. The core section exhibits a slight green colouration. This may be due to the presence of shallow marine mineral, glauconite.

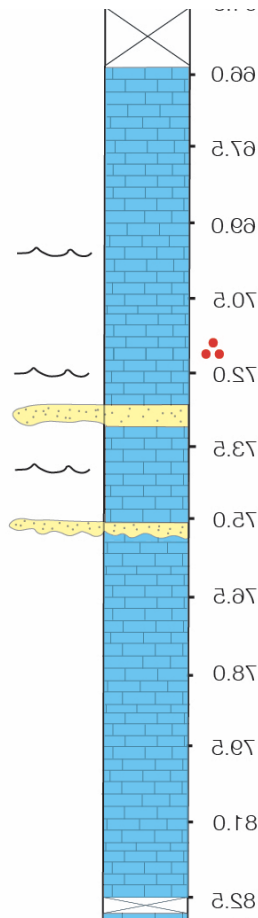
B 2.2:



Section B 2.2 continues directly on from section B 2.1 and was likely grouped separately due to breaking from the overlying section. The core section is 17cm in length. The upper 6cm of the core is peppered with pyrite and at closer study globular pyrite can be observed throughout the section. The pyrite in the upper 6 cm is .1mm to 1mm in size. The section is pale grey in colour and very fine, no grain size seen- likely very fine crystalline (micrite/lime mud). Within the carbonate matrix are light, lenticular patches ~1cm in size from 2.5 to 4 cm depth. These are associated with pinch and swell structures. From 6 cm to 10 cm on the right hand side of the core is a large patch of medium grained sandstone. Several large, well-rounded granules are also seen within this coarser section More lenses of light material are found around this horizon. The lenses decrease in size towards the base of the core section (~10cm). The bottom 7 cm of the core exhibits intermittent lenses of gradually reducing size (1cm). The lenses are commonly observed with a darker nucleus, but not always. May suggest pyrite with an alteration halo? The core section exhibits a slight green colouration. This may be due to the presence of shallow marine mineral, glauconite.



C 2.1:

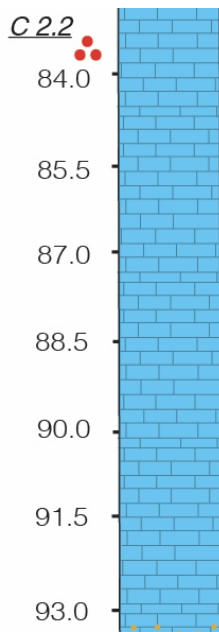


Section C 2.1 continues on from B 2.2, after a 15mm gap. Section C 2.1 is 17 cm in length. The top 15mm is a fine grained limestone (micrite) with some finer inclusions. Fine white lenses and pinch and swell structures are present within the next 35mm (lenticular bedding). These are similar to features observed towards the base of B 2.2. Some of these lenses are surrounding small dark inclusions. There is a medium to coarse sandstone layer at 6.5cm, ~5mm long. This is followed by 2 cm of lensed carbonate. Below this is a vf sandstone layer with a fine sandstone basal scour. Towards the bottom half of the core section the lithology transitions to micrite with fine interbeds of very fine sandstone.



Appendices

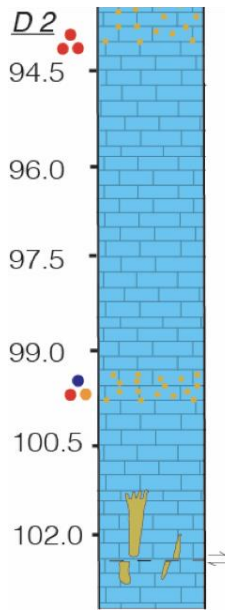
C 2.2:



Section C 2.2 continues on from C 2.1 after a 5mm gap. The section is 10.5 cm in length. The lithology is a grey, fine grained carbonate (micritic limestone) with dark inclusions. The dark inclusions are surrounded by halos, slightly less lenticular here. There are smaller interbeds of fine clastic lithology. The bottom 2cm exhibits interbedded lenticular micrite with fine to medium interbeds.



D 2:



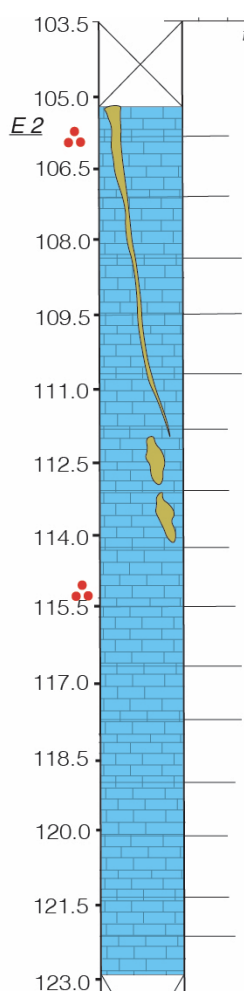
Section D 2 is 10cm in length and carries on directly from C 2.2. Section D is slightly darker than B 2.2 and much darker than A and C, which have a lighter grey colouration. The section contains rare cubic pyrite within the top 15mm. However, much of the pyrite observed within the section is micro-granular. The section is composed of fine grained (micritic) limestone. More brittle carbonate/mudstone ~2- 4 cm down. Approximately 7 cm down the core section is a pyrite rich layer exhibiting more than 10 crystals of pyrite, ranging in size



from .1 to .5mm in size. The pyrite crystals are of irregular size- large variation in sizes. The bottom 35mm is largely massif carbonate in structure. A long, thin pyrite vein 15mm long cross cuts bedding ~20mm from the base of the core section. An infilled cavity w/ pyrite and crystalline calcite is observed within the bottom 30mm with evidence of small scale slip of beds. Pyrite is injected along bedding/ a fracture ~8mm from the base.

Appendices

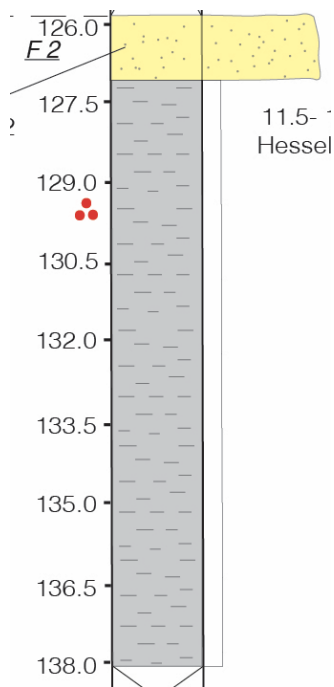
E 2:



Section E2 is separated from the base of D2 by a 15 mm gap. The section is 17.5 cm in length. The core section is composed of a pale grey fine grain limestone (micrite) exhibiting fine laminations. These laminations are fine to very fine sandstone. The sandstone layers are discontinuous in places and form along weaknesses/ fractures in the limestone. It is therefore interpreted here that the sandstone has been injected into the limestone during rapid deposition/emplacment. The section exhibits a crystalline and pyritic infill of voids and cracks. These voids may have been formed under stress and represent later pyrite. Or were formed through injection.



F 2:

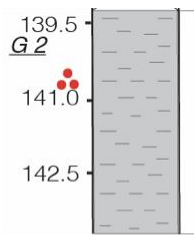


Core section F2 is separated from overlying section E2 by a 3 cm gap. The core section is 12.5 cm in length. The top 1 cm is medium to fine grained sandstone potentially in a calcareous matrix. The remaining core section is a finely laminated, homogeneous mudstone. Towards the base of the section there is some lensing potentially representing coarser intervals.

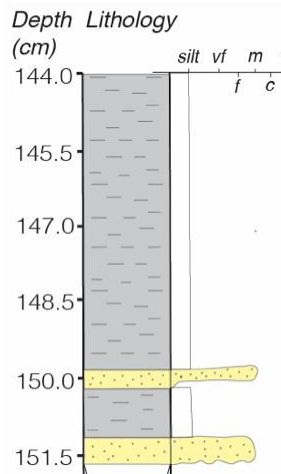


Appendices

G 2:



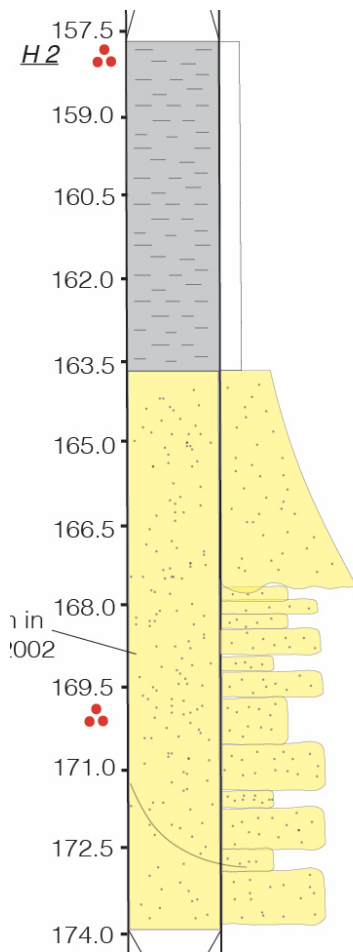
Core section G2 is 13 cm in length and is separated from core section F2 by a 10mm gap. The core is composed of a light grey, finely laminated homogenous mudstone. The mud facies observed within this core is very similar to that seen within section F2. There are two



coarser layers that can be observed at 10 cm and 12.5 cm. Both layers are composed of very fine sandstone. The upper layer exhibits irregular pyrite ~1mm in diameter (speckled layer to left of '1' in photo). The lower layer (globular layer directly to the left of bottom corner of grain size card) consists of more consistently sized rounded, globular pyrite ~2mm in diameter.



H 2:

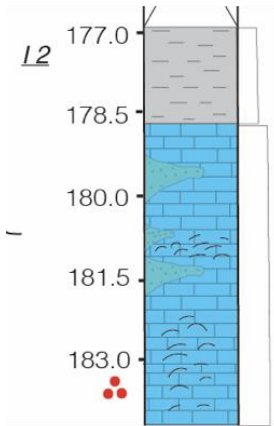


Core Section H2 follows on from core section G2 after a 6 cm gap. The soft and more brittle nature of the mudstone may have resulted in material being more poorly preserved. This section is 16 cm long. The upper 6 cm of the core are finely laminated mudstones which are brittle and pale grey. These are similar texturally to those observed in section G2. The core then transitions to coarser clastic material. At 7 cm is a medium sandstone bed ~5mm thick. This then gradually transitions into 30mm of coarse sandstone at 9cm. The sandstone is poorly sorted with angular grains and a muddy matrix. Towards the base of the section are interbedded coarse and very fine sandstone beds with rare pebble clasts (2 cm long). There are also potential channelised features. However this may also be the result of core rotation.

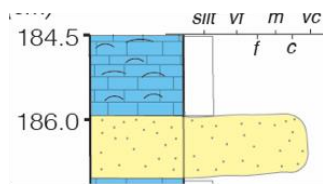


Appendices

I2:



Core section I2 begins 3 cm below the base of core section H2. The section is 10 cm in length. The top of the core section is composed of 2 cm of mudstone which exhibits very few structures. The rest of the core is very oxidised (hence the yellow/orange colouration of the section). From 3 to 6 cm the lithology is a fine grained limestone with medium sandstone inclusions/beds. Very coarse sandstone inclusions may be observed at 5 cm depth.

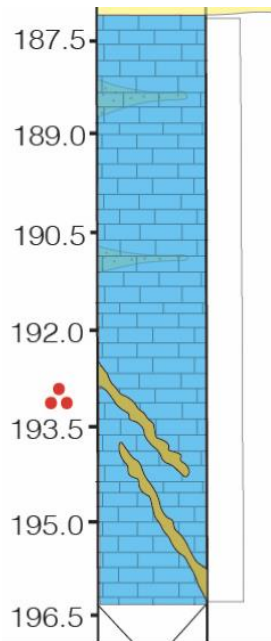


There are thin, dark, lenticular inclusions from 5.5 to 7 cm depth (floatstone). These extend to 15mm from the base of the section. These are most probably bivalves. There is also a thin valved layer at 4.5 cm depth ~ 2/3mm wide (floatstone). The base of the section exhibits medium to coarse sandstone.

The base of the section exhibits medium to coarse sandstone.



J2.1:

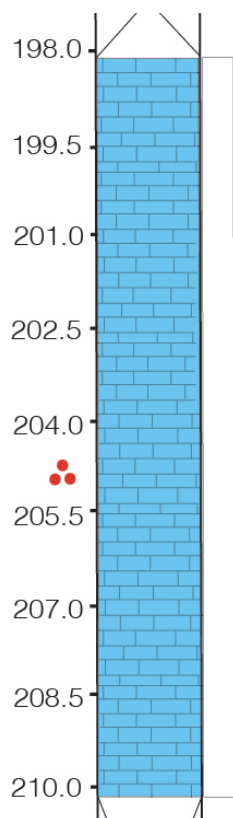


Core section J2.1 continues straight on from the base of section I2. The section is 9.5 cm in length. The sample is oxidised along the right hand side of the core section, particularly concentrated around a fracture. The section is composed of pale grey, fine grained limestone (micrite). There are also interbeds of very fine sandstone. The sandstone beds exhibit rippled surfaces which are particularly clearly seen near the base. Two veins cross cut bedding at an angle of ~315 degrees. The veins are filled with microcrystalline pyrite and sparitic calcite.



Appendices

J 2.2:



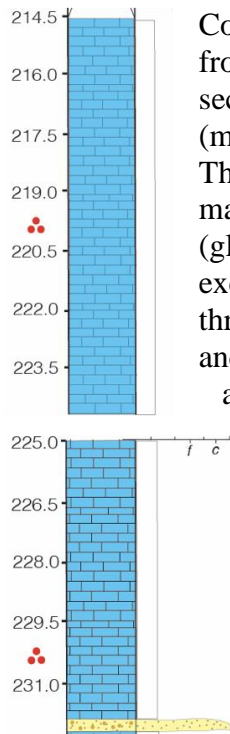
Core section J2.2 follows on from section J2.1 after a 2cm gap. The section is 12 cm in length and is generally composed of a very fine grained (grain size not visible), pale grey (fine limestone-micrite). The core section is very yellow in colouration. This is similar to portions of I2 and J2.1. As interpreted within these previous sections, this may be due to oxidation. The section exhibits lenticular fine sst ripples/ channelised infills throughout. This may be once again influence by core rotation. However these features and much clearer towards the base of the section and show little evidence of rotation during drilling. The features within this core are very similar to feature observed within the base of the overlying core section. The

'ripples' are largest at the top and decrease in size towards the base- shallowing upwards.



Quantifying marine redox across the Triassic–Jurassic mass extinction

K2:



Core section K2 is 18 cm in length and is separated from the overlying section by a 45mm gap. The core section is composed of a pale green limestone (micrite) interbedded with very fine sandstone beds. The core section exhibits a slight green hue which may suggest a shallow marine depositional setting (glaucanite). The core is featureless with the exception of rippled features that can be found throughout the core. The features are discontinuous and symmetrical. The rippled features observed here are very similar, if not identical, to those observed in sections J. A coarser, sandstone layer is present at the base of the section exhibiting globular pyrite.

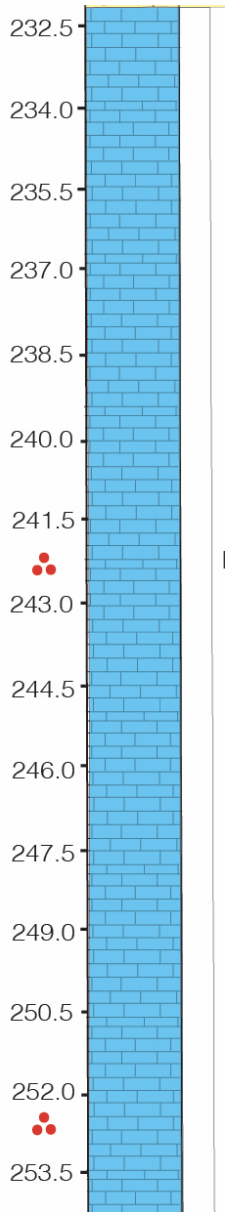


Crest/peak of ripple

Trough/bottom of ripple

Appendices

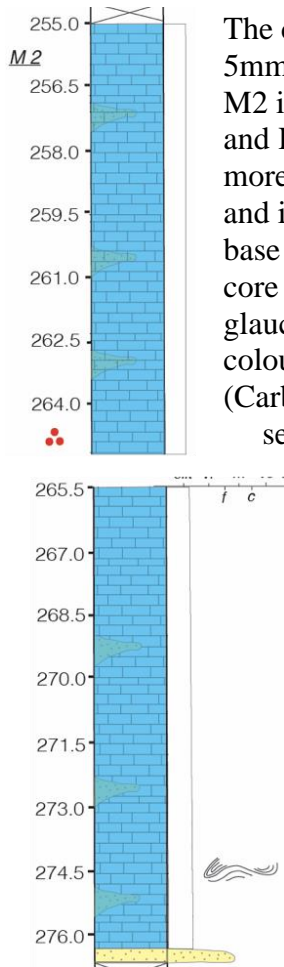
L 2:



Core section L2 is 20.5 cm in length and follows on directly from the base of section K2. The upper 14.5 cm of the core is marked by lenticular beds. The beds are greenish and white in colour with the white lithology forming ripples and lenses. The core is generally composed of a carbonate mudstone/fine grained limestone. The greenish colouration of the core, as also seen in sections B and K, is potentially from glauconite. Some of the discontinuous features may be injected sediment, as seen towards the base of the core section. Within the bottom 6 cm of the the carbonate is interbedded with darker fine sandstone layers.



M 2:



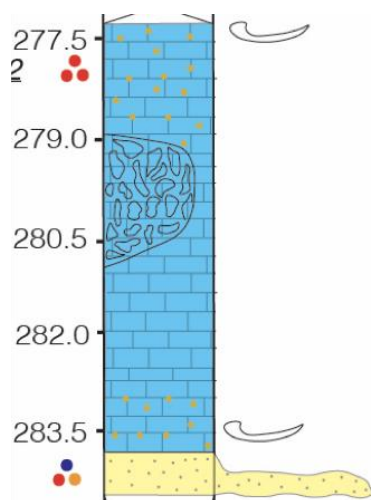
The core section is 20 cm in length and begins 5mm from the base of section L2. Core section M2 is very similar in appearance to sections L and K. However, within section M there are more lenses (lenticular bedding), ripple marks and injected sediment. This is similar to the base of L2. The slight green colouration of the core once again suggests the presence of glauconite. The lithology is a pale grey-green colour with no discernible grain size (Carbonate Mudstone). Some oxidation of the sediment can be observed along fractures.

The bottom 2 cm of the core section show rip up clasts and evidence of sediment disturbance. This may be due to soft sediment deformation under rapid sediment deposition. The base of the core section is a very fine to fine sandstone layer.



Appendices

N 2:



Core section N 2 is 7.5 cm in length and begins ~5-10mm down from the base of section M2. The core is dark in colour and different to the colouration seen in core sections K, L and M. The section is closer to the facies observed in B and A. The top 9 cm of the core section is abundant in globular pyrite. >9 pyrite globules observed up to .8mm in size. There are also many lenticular and scalloped thin, dark features which probably represent bivalves. The



scalloped edge representing the external ribbing intersecting the edge of the shell. The lithology here is identified as a floatstone.

The valves continue to be present towards the base of the core section but are decreasingly common below this abundant upper layer (transition to Mudstone/Wackestone). Within this upper portion of the core is a large organism. Little of the original mineralogy appears to have been preserved but the organism appears to be a sponge/ coral. The organism exhibits small, cylindrical pores/openings. The pores are both isolated and interconnected. There is no evidence of septa or any other features within the pores/voids. The interconnection of the voids resembles that of mural pores within extinct tabulate corals. This organism may therefore be a sponge as interconnected pores/ corallites are not known from scleractinian corals where pores within sponges are/may be connected. The lithology within this section of the core may be identified as a boundstone. However, this is difficult to determine based on this single core section.

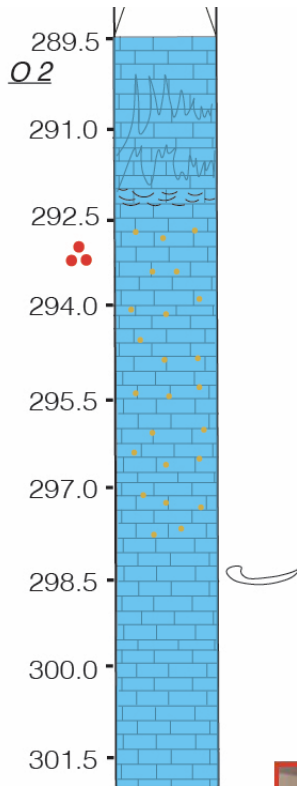


At the base of the core section is a very coarse, calcareous sandstone layer which is texturally immature (poorly sorted, angular to sub-rounded grains). The basal 15mm of the core section is also abundant in pyrite. 20+ pyrite globules are present within the basal 15mm with a size range from 1mm to 8mm. There are also bivalve casts infilled

Quantifying marine redox across the Triassic–Jurassic mass extinction

with microcrystalline pyrite. But not all calcite has been dissolved. Some original calcite appears to be present below this layer.

O 2:

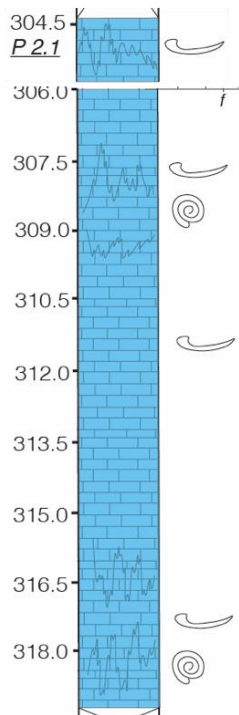


Core section O2 is 12.5 cm in length and continues from the base of N2 after a 5mm gap. The upper 3 cm of the core section is defined by a cone-in-cone texture. The lithology here is darker grey that the previous sections (K-N). At the base of the stylolitic section is a thin valve bed. The next 5cm is carbonate with with small <1mm pyrite inclusions. The entire core section is rich in bivalves and bivalve casts. The lithology is predominantly a floatstone due to the fine grained carbonate matrix and regular valved inclusions of >2mm.

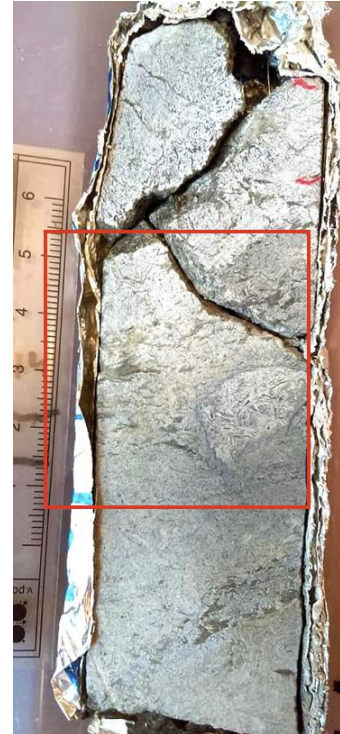


Appendices

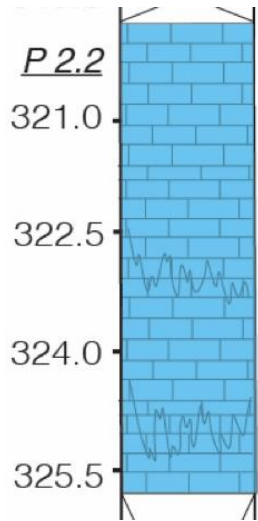
P 2.1:



Core section P2.1 begins 25mm from the base of O2. The section is 15cm in length and is similar lithologically to O2. The core sections bears cone-in-cone textures within the top 5 cm and the bottom 5 cm. The lithology is calcareous and fine grained. The grain size is not distinguishable. The core section is rich in bivalves and gastropods. The lithology is interpreted here as predominantly being a bioclastic packstone.



P 2.2:

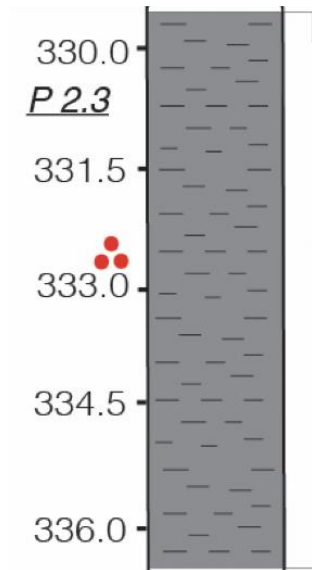


Core section P2.2 begins .5 to 1cm below P2.1. The section is once again defined by a clear cone-in-cone texture. However, unlike the two overlying sections, section P2.2 exhibits very little fossil material, similar to the very top of section O2. This may be due to carbonate recrystallisation. The lithology is a fine grained carbonate and is interpreted here as a carbonate mudstone due to the absence of any clear fossil material.



Appendices

P 2.3:



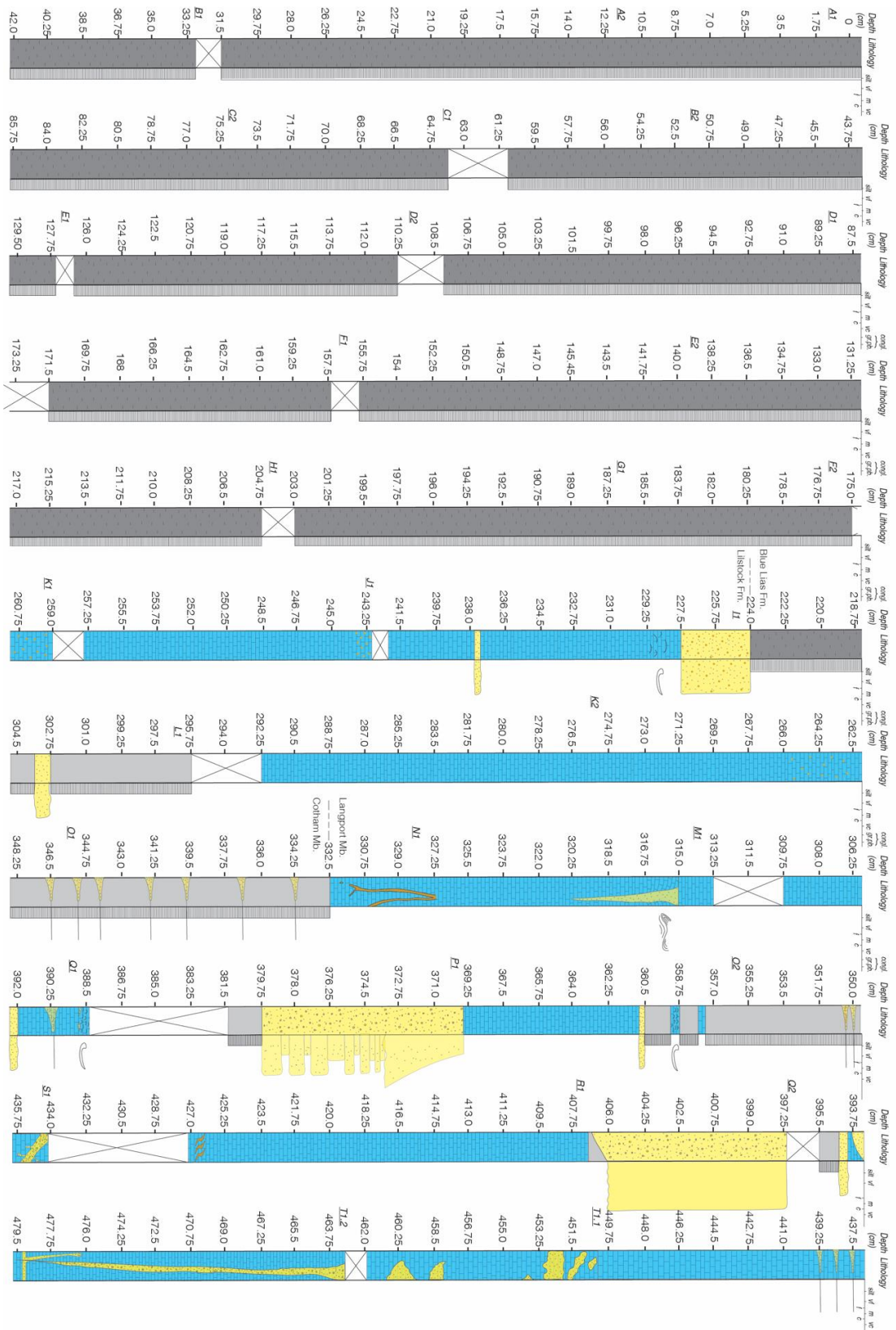
The final section of core 2 is section P2.3. The core section is 6-7 cm in length and it begins ~35mm from the base of P2.2. The section is composed of brittle, dark grey laminated mudstone. The lithology is very organic rich yet exhibits no indication of shell fragments/ fossil material. The mudstones are assumed here to be siliciclastic.



Quantifying marine redox across the Triassic–Jurassic mass extinction

Somerset Core 1

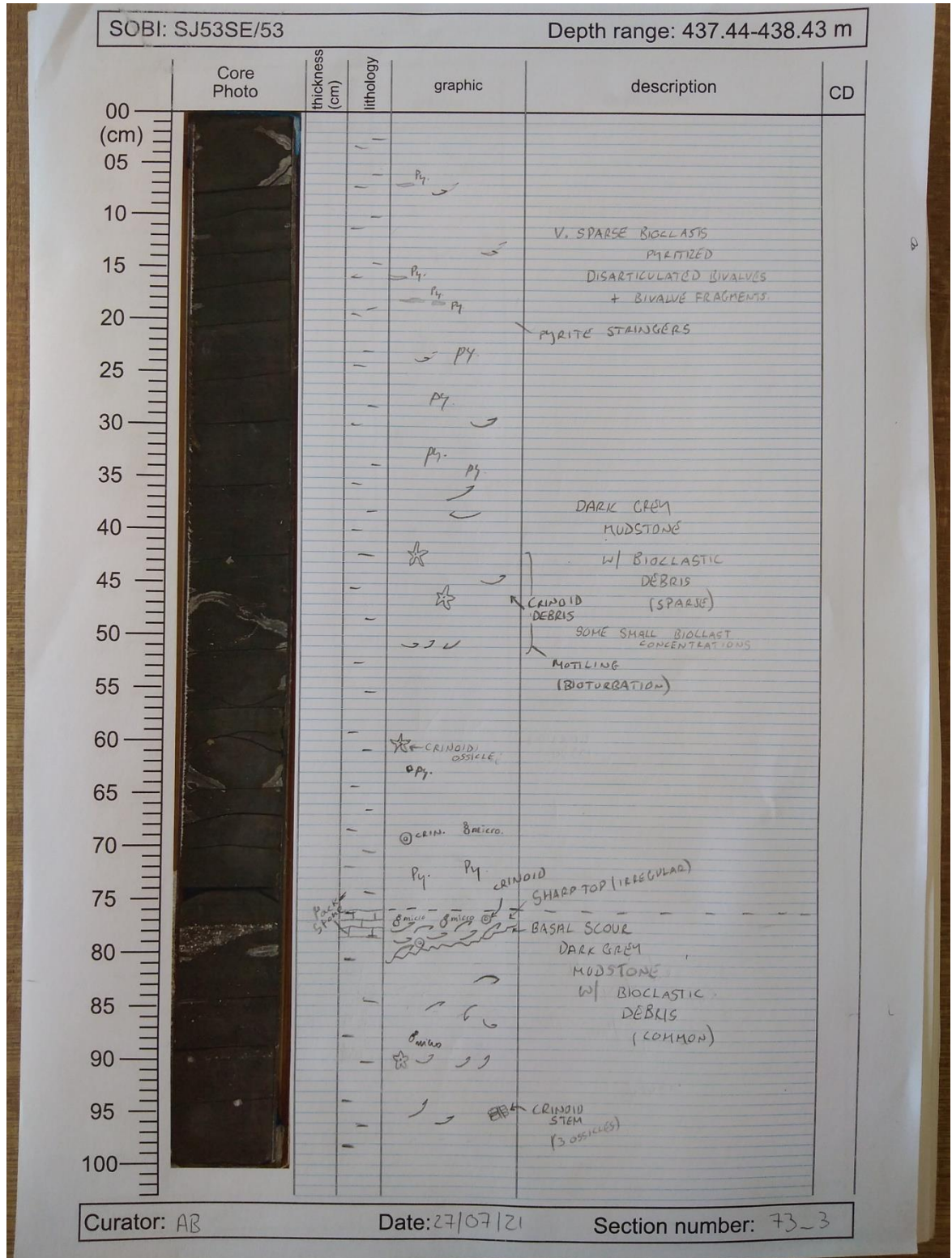
Digitised Core 1 Log:



Appendices

APPENDIX 3.3: PREES-2C SEDIMENTARY LOGGING

This section details the sedimentary logging of 125m of Hettangian–Sinemurian sediments of the Prees-2c core undertaken at the British Geological Survey, Keyworth.



Appendices

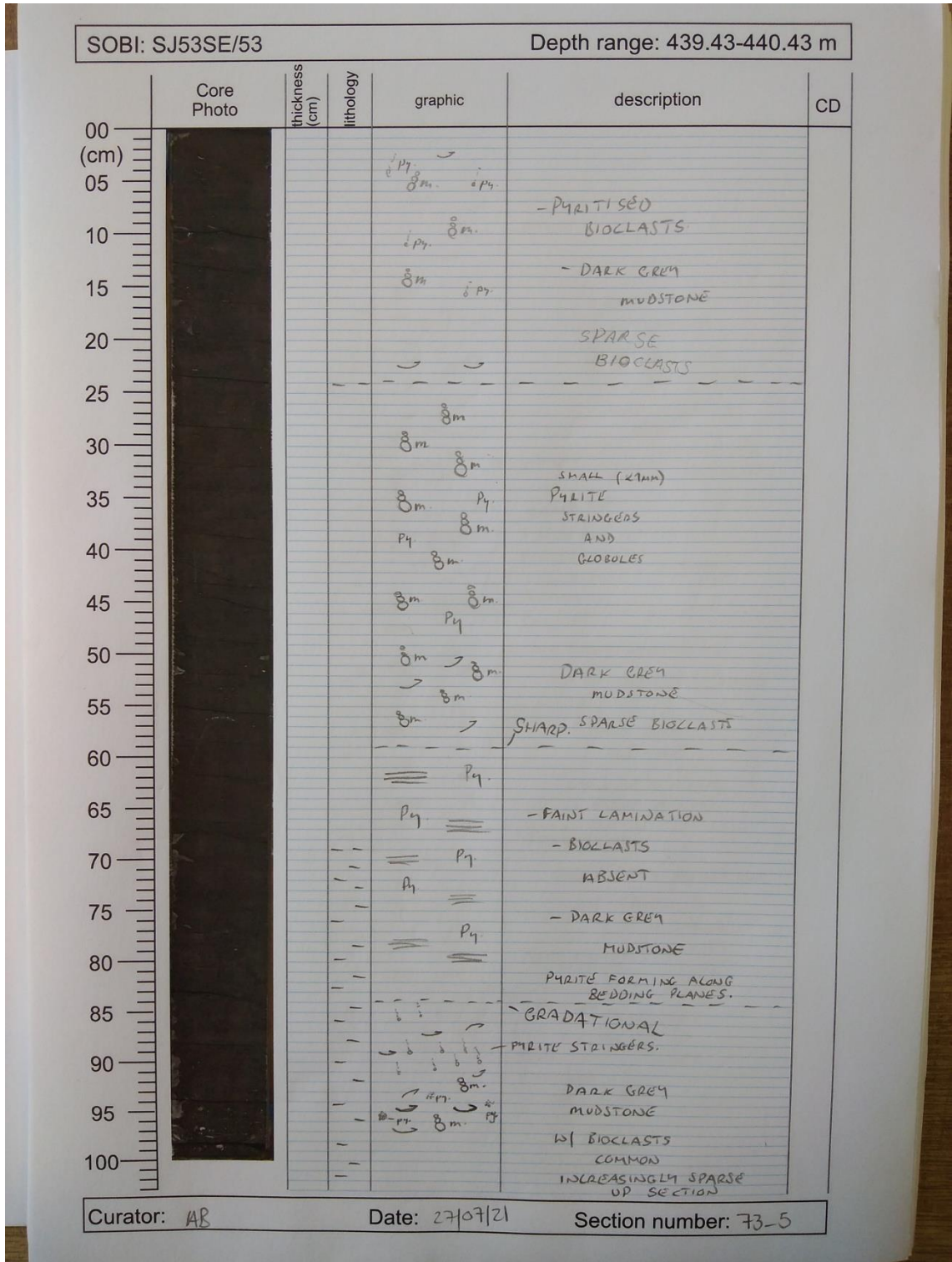
SOBI: SJ53SE/53		Depth range: 438.43-439.43 m				
Core Photo	thickness (cm)	lithology	graphic	description	CD	
	00 (cm)		δ_m δ_m			
	05		δ_m	MOTTLED (BIOTUBATED)		
	10		δ_m			
	15		δ_m	DARK GREY MUDSTONE		
	20		δ_m	w/ COMMON BIOCLASTIC DEBRIS		
	25		δ_m			
	30		CAINOID			
	35		CAINOID δ_{micro}			
	40		δ_{micro}	SHARP CHANGE		
	45		PHALLO STAINING	DARK GREY MUDSTONE		
	50		δ_{micro}	w/ BIOCLASTIC DEBRIS (SLIGHTLY MORE SPARSE)		
	55			SHARP CHANGE		
	60					
	65		CAINOID OSSICLE	DARK GREY MUDSTONE		
	70			w/ COMMON BIOCLASTIC DEBRIS		
	75			AMMONITE (PARITIZED) DEFORMED CAINOID OSSICLE (COMPACTED) + PARITISED.		
	80					
85						
90			δ_{micro}			
95						
100						

Curator: AB

Date: 27/07/21

Section number: 73_4

Quantifying marine redox across the Triassic–Jurassic mass extinction



Appendices

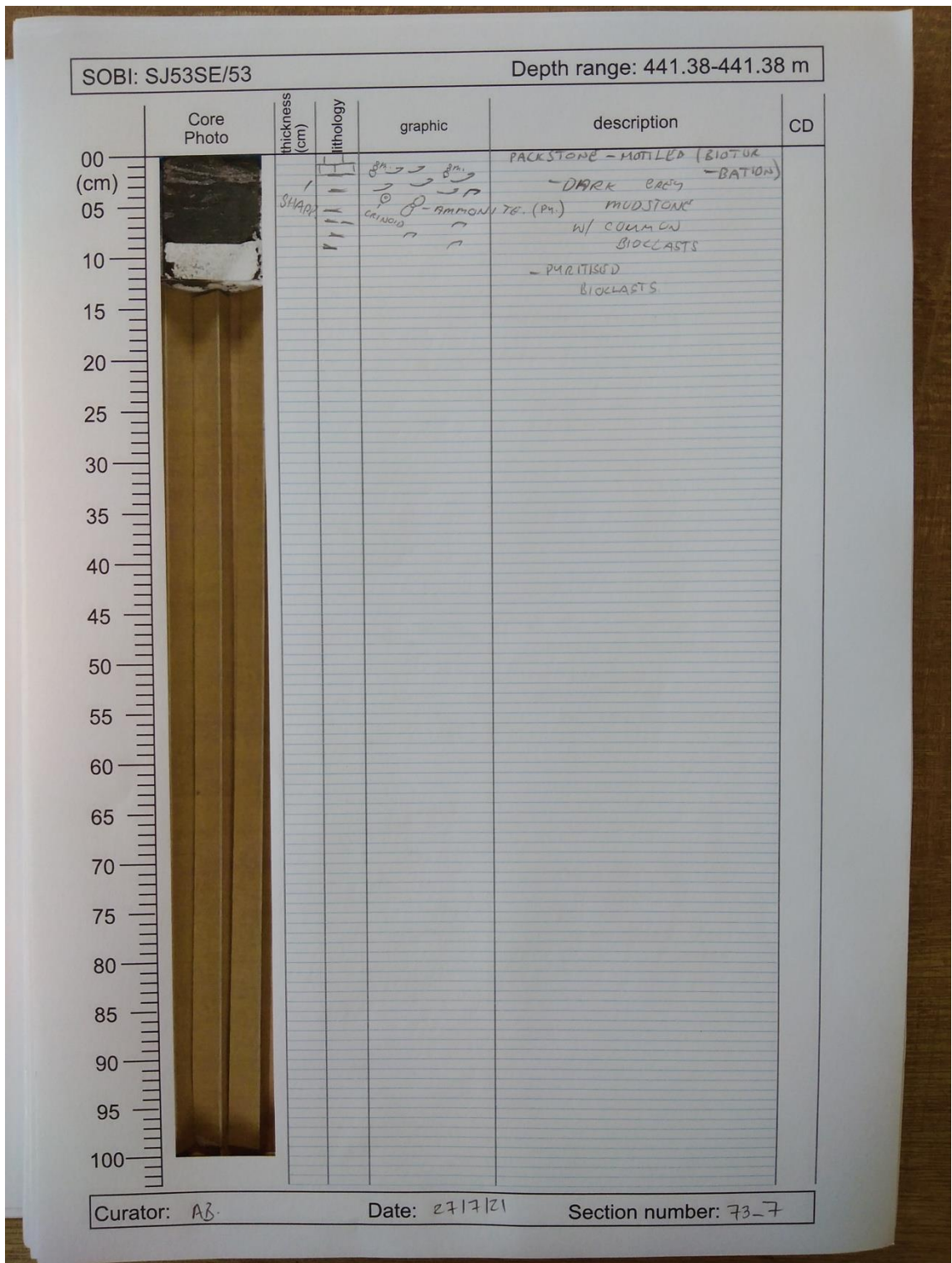
SOBI: SJ53SE/53		Depth range: 440.43-441.30 m				
Core Photo	thickness (cm)	lithology	graphic	description	CD	
	00					
	05					
	10				BIVALVE	
	15				- DARK GREY MUDSTONE	
	20				w/ COMMON BIOCLASTS	
	25				SOME MOTTLING BETWEEN	
	30				AMMONITE? gastropod 4cm and 2cm - BIOTURBATED	
	35				SHARP TOP	
	40				3 FINE BIOBLAST LAYERS. MOTTLED (BIOTURB.) COMPACTED. SHARP BASE	
	45				AMMONITE	
	50				SHARP.	
	55				- V. FAINT LAMINATION - BIOCLASTS V.V. SPARSE	
	60				- DARK GREY MUDSTONE	
	65				- PYRITE FORMING ALONG BEDDING PLANE	
	70				GRADATIONAL	
	75				DARK GREY MUDSTONE w/ SPARSE - V. SPARSE BIOCLASTS.	
	80				PYRITE STRINGERS + GLOBULES.	
	85				bivalve LAM. clamoid SHARP IRREGULAR TOP.	
	90				MUD MATRIX PACKSTONE V. CONCENTRATED BIOBLAST LAYER	
	95					
100						

Curator: AB

Date: 27/7/21

Section number: 73-6

Quantifying marine redox across the Triassic–Jurassic mass extinction



Appendices

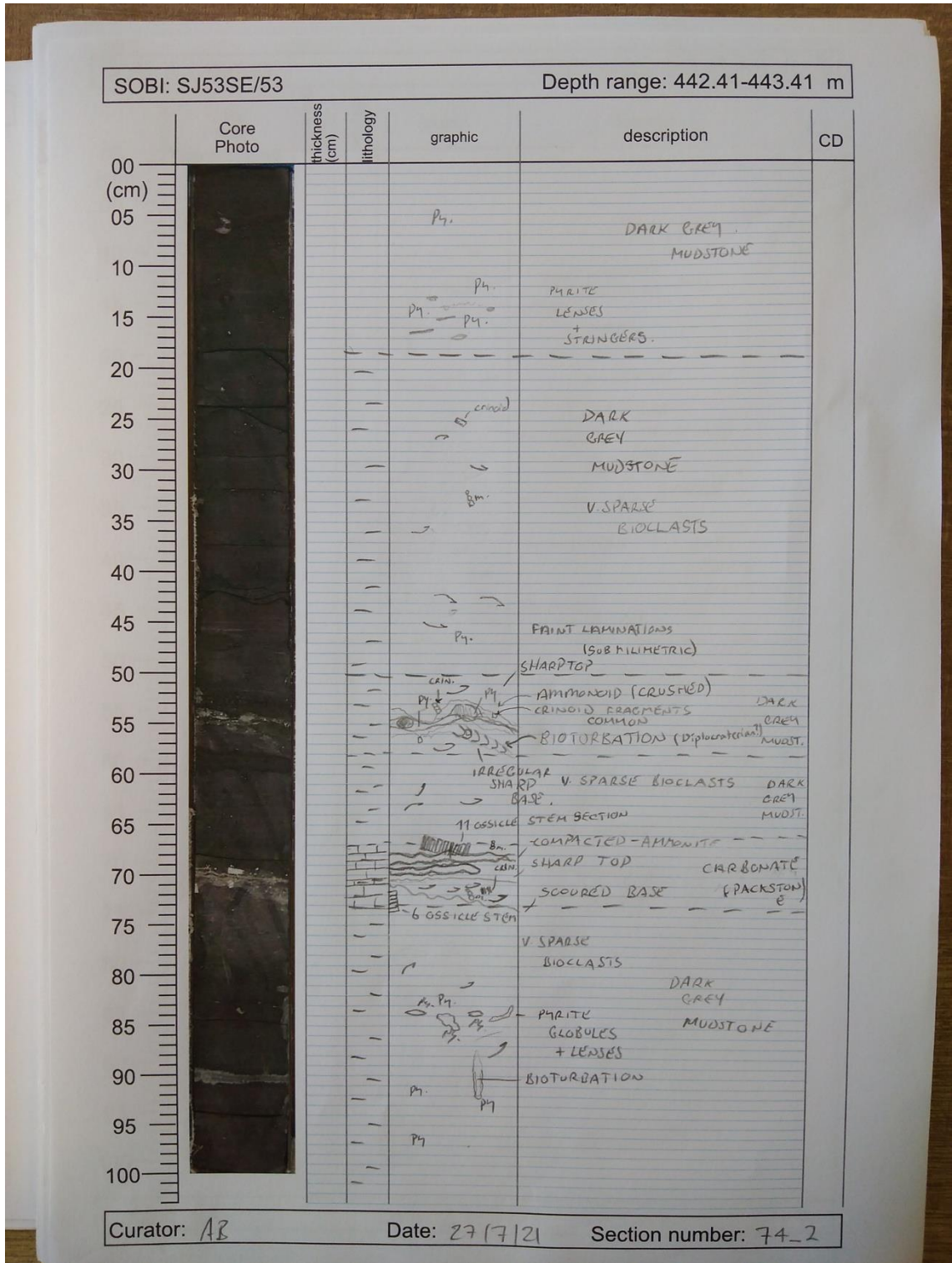
SOBI: SJ53SE/53		Depth range: 441.42-442.41 m				
Core Photo	thickness (cm)	lithology	graphic	description	CD	
	00					
	05					
	10				DARK GREY MUDSTONE	
	15				SPARSE - V. SPARSE	
	20				MOTTLED BIOCLASTS (BIOTURBATION), 4 OSSICLES	
	25				CRINOID STEM CRINOID OSICLE (P1)	
	30					
	35					
	40					
	45					
50				DARK GREY MUDSTONE		
55				CRIN. MOTTLED STILL BIOCLAST^ SPARSE BUT SOME CONCENTRATIONS		
60						
65						
70						
75				DARK GREY MUDSTONE BIOCLASTS		
80				* SPARSE TO V. SPARSE		
85						
90						
95						
100						

Curator: AB

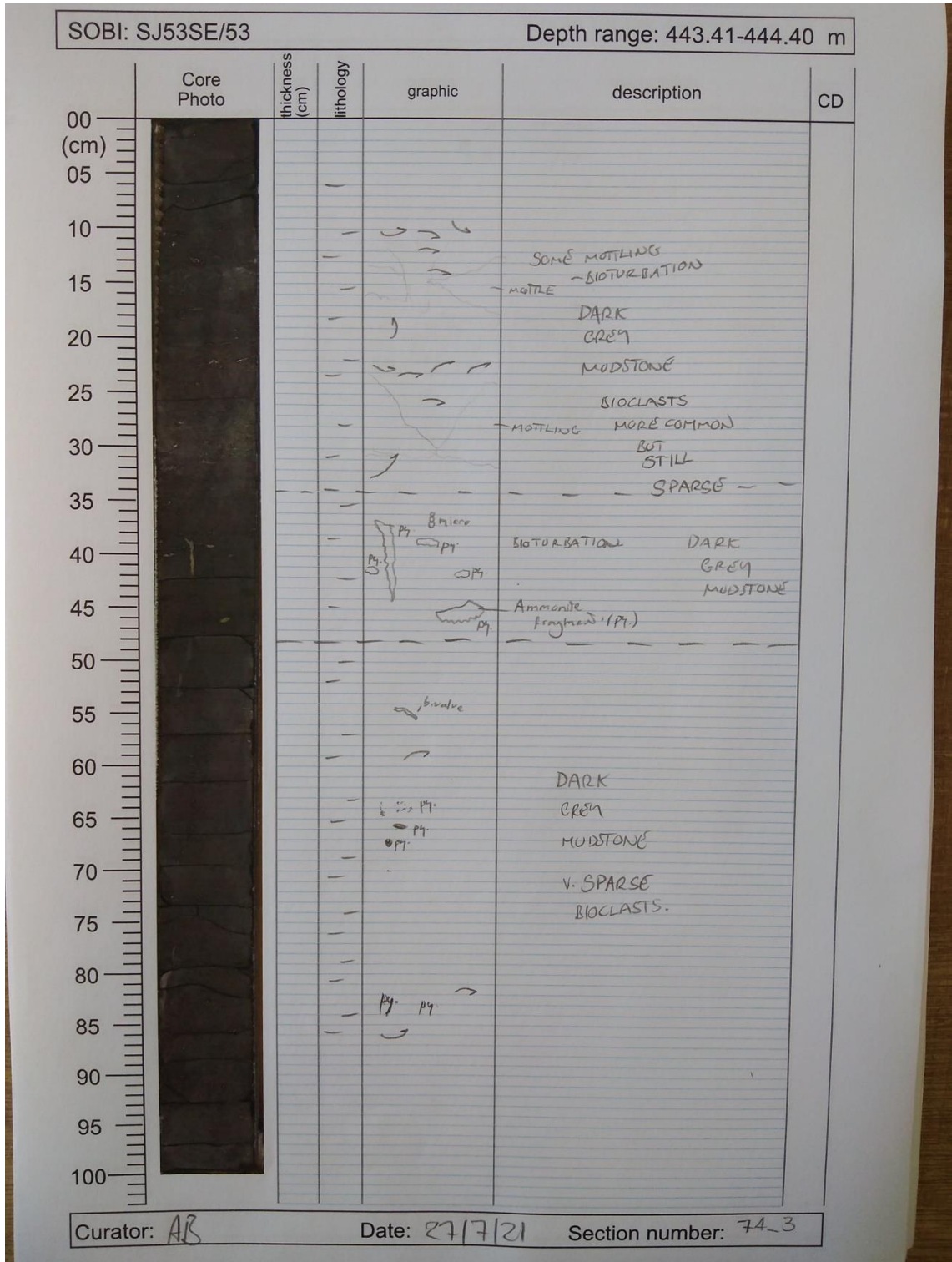
Date: 27/7/21

Section number: 74-1

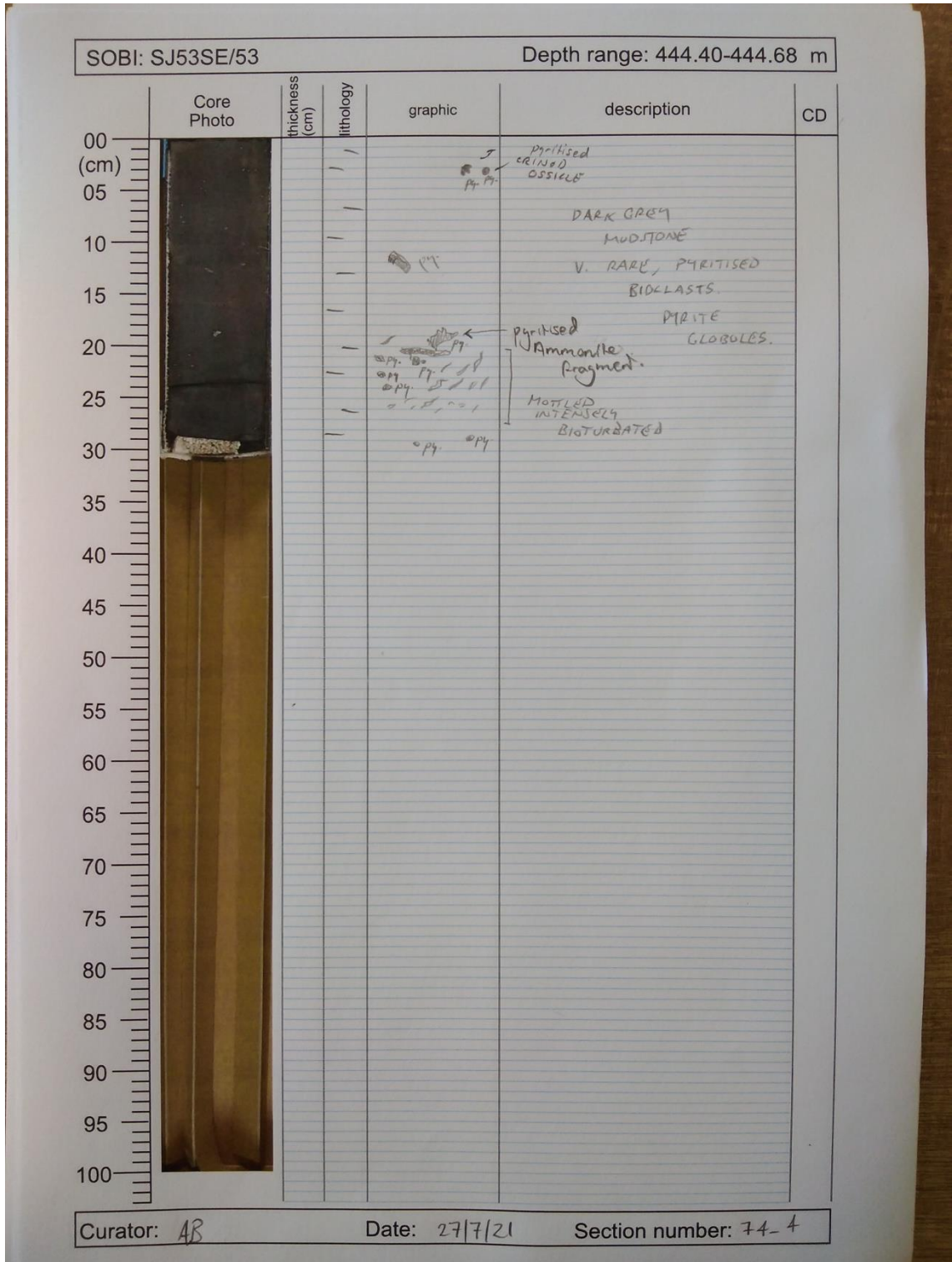
Quantifying marine redox across the Triassic–Jurassic mass extinction



Appendices



Quantifying marine redox across the Triassic–Jurassic mass extinction

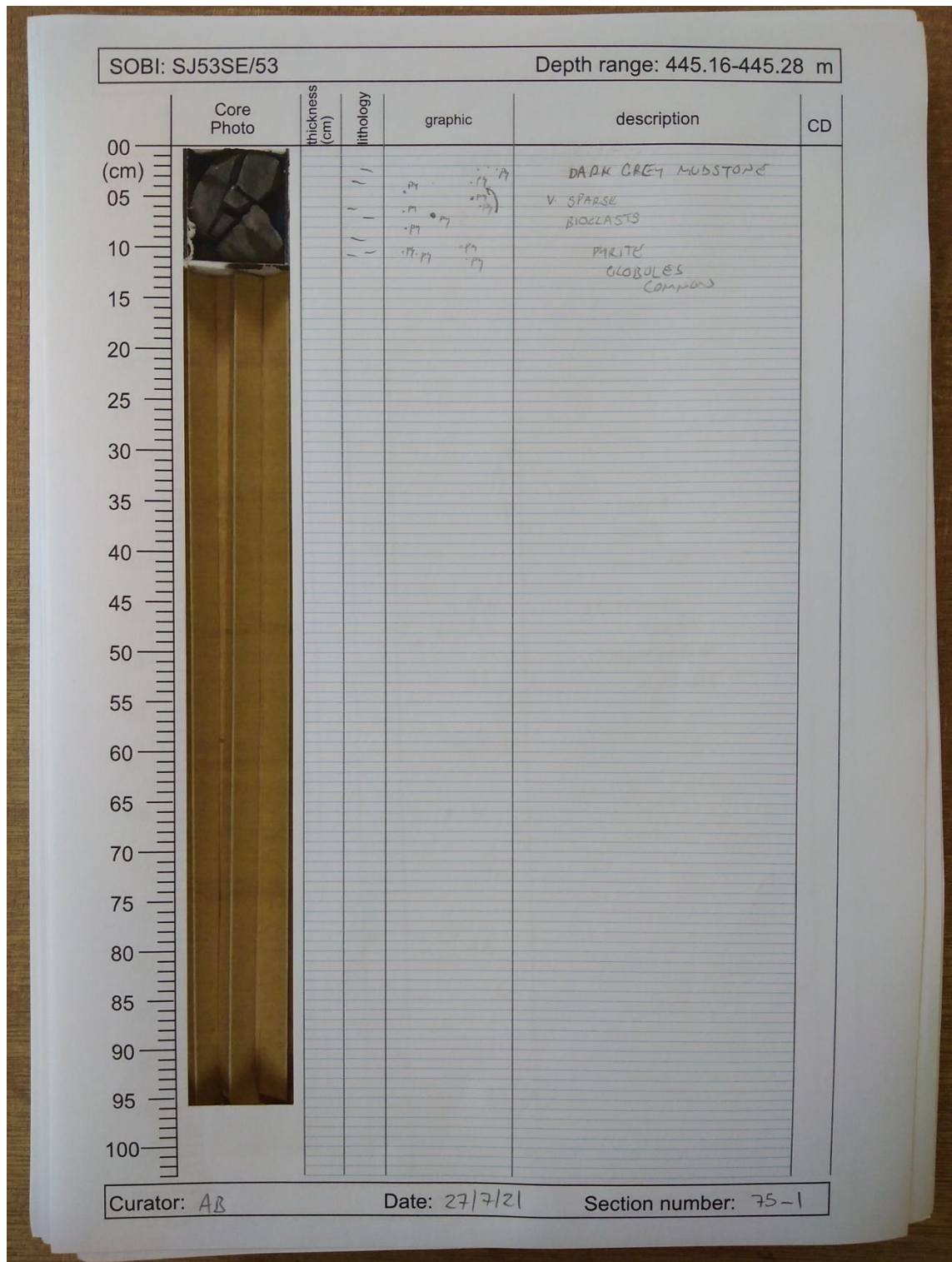


Appendices

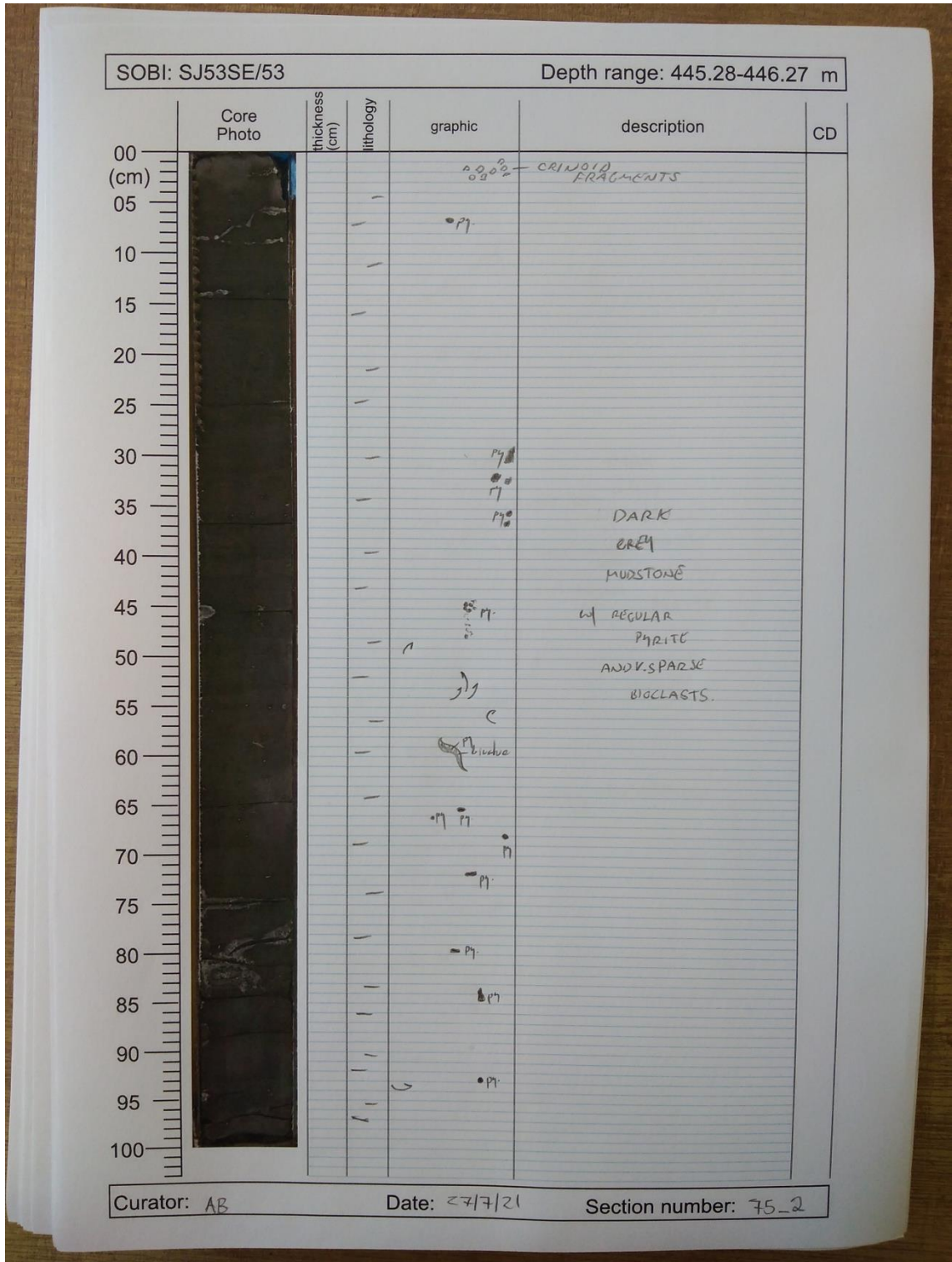
SOBI: SJ53SE/53		Depth range: 444.68-444.81 m				
Core Photo	thickness (cm)	lithology	graphic	description	CD	
	00			MOTILING - BIOTURBATION		
	05		•••••	DARK GREY		
	10		•••••	MUDSTONE		
	15		•••••	NO BIOCLASTS.		
	20					
	25					
	30					
	35					
	40					
	45					
50						
55						
60						
65						
70						
75						
80						
85						
90						
95						
100						

Curator: AB Date: 27/7/21 Section number: 74-5

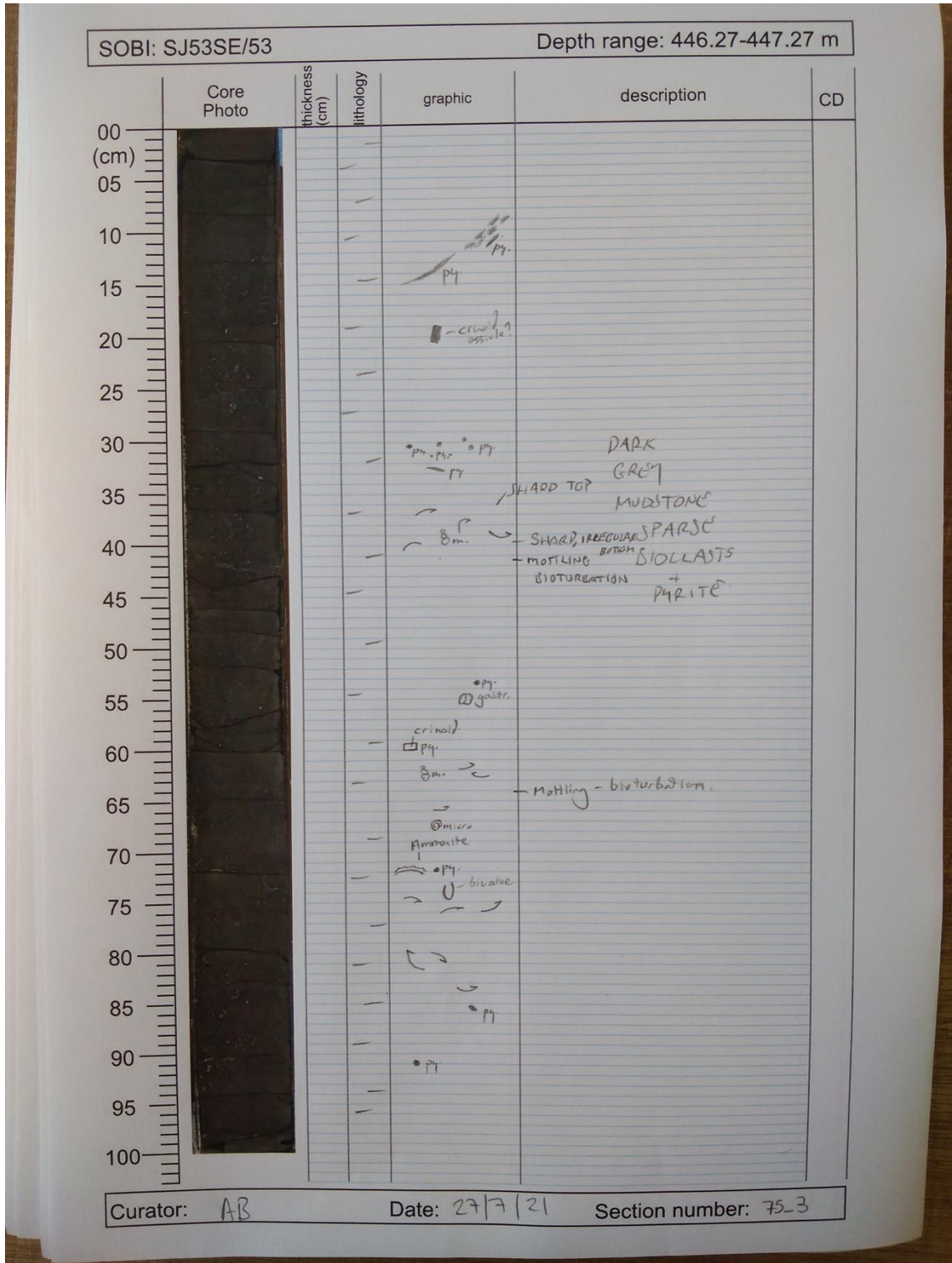
Quantifying marine redox across the Triassic–Jurassic mass extinction



Appendices



Quantifying marine redox across the Triassic–Jurassic mass extinction



Appendices

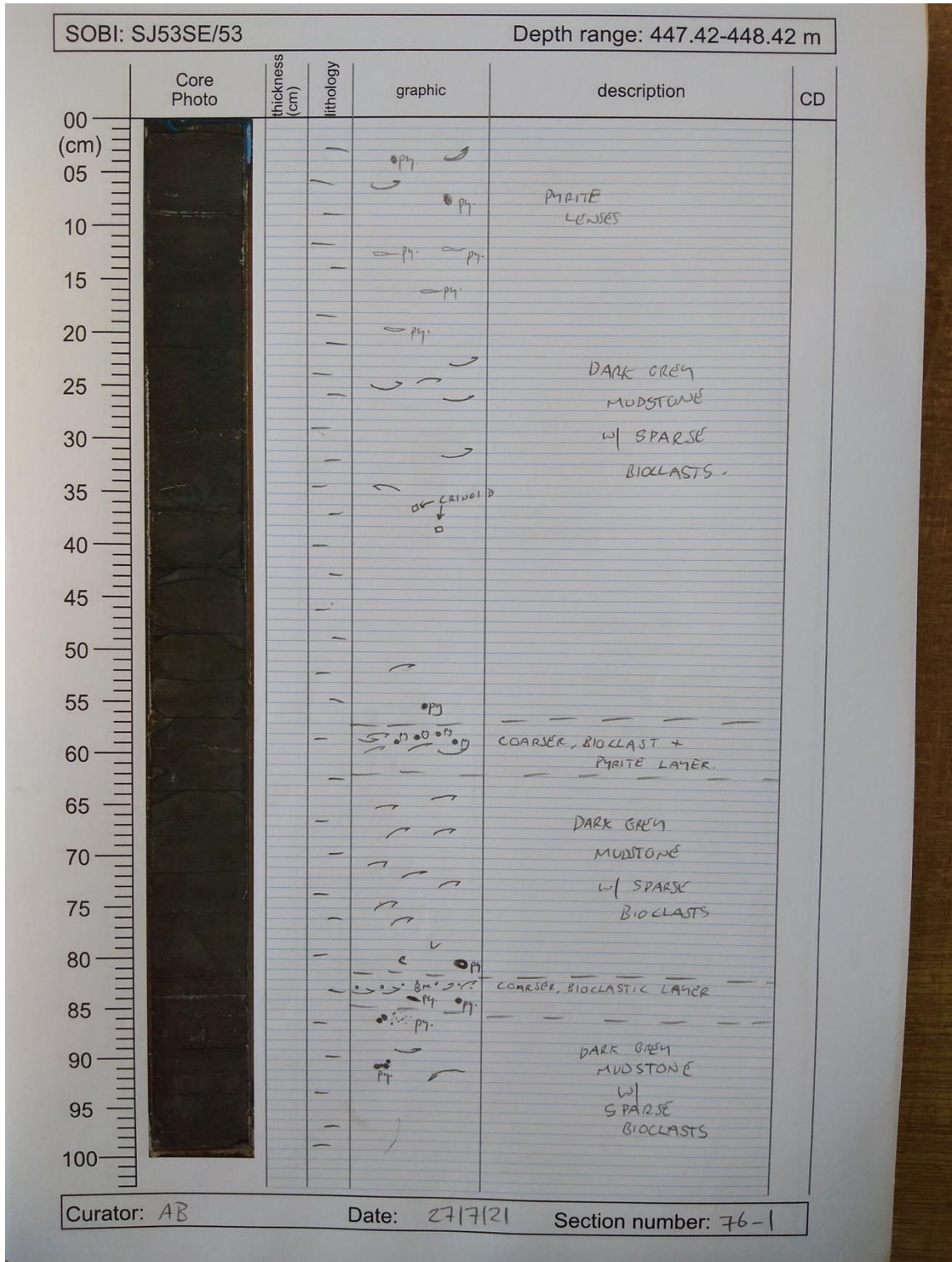
SOBI: SJ53SE/53		Depth range: 447.27-447.63 m			
Core Photo	thickness (cm)	lithology	graphic	description	CD
	00				
	05				
	10				DARK GREY MUDSTONE
	15				BIVALVE
	20				CRINOID
	25				CRINOID
	30				CRINOID OSICLE
	35				CRINOID OSICLE
	40				
	45				
50					
55					
60					
65					
70					
75					
80					
85					
90					
95					
100					

Curator: AB

Date: 27/7/21

Section number: 75-4

Quantifying marine redox across the Triassic–Jurassic mass extinction



Appendices

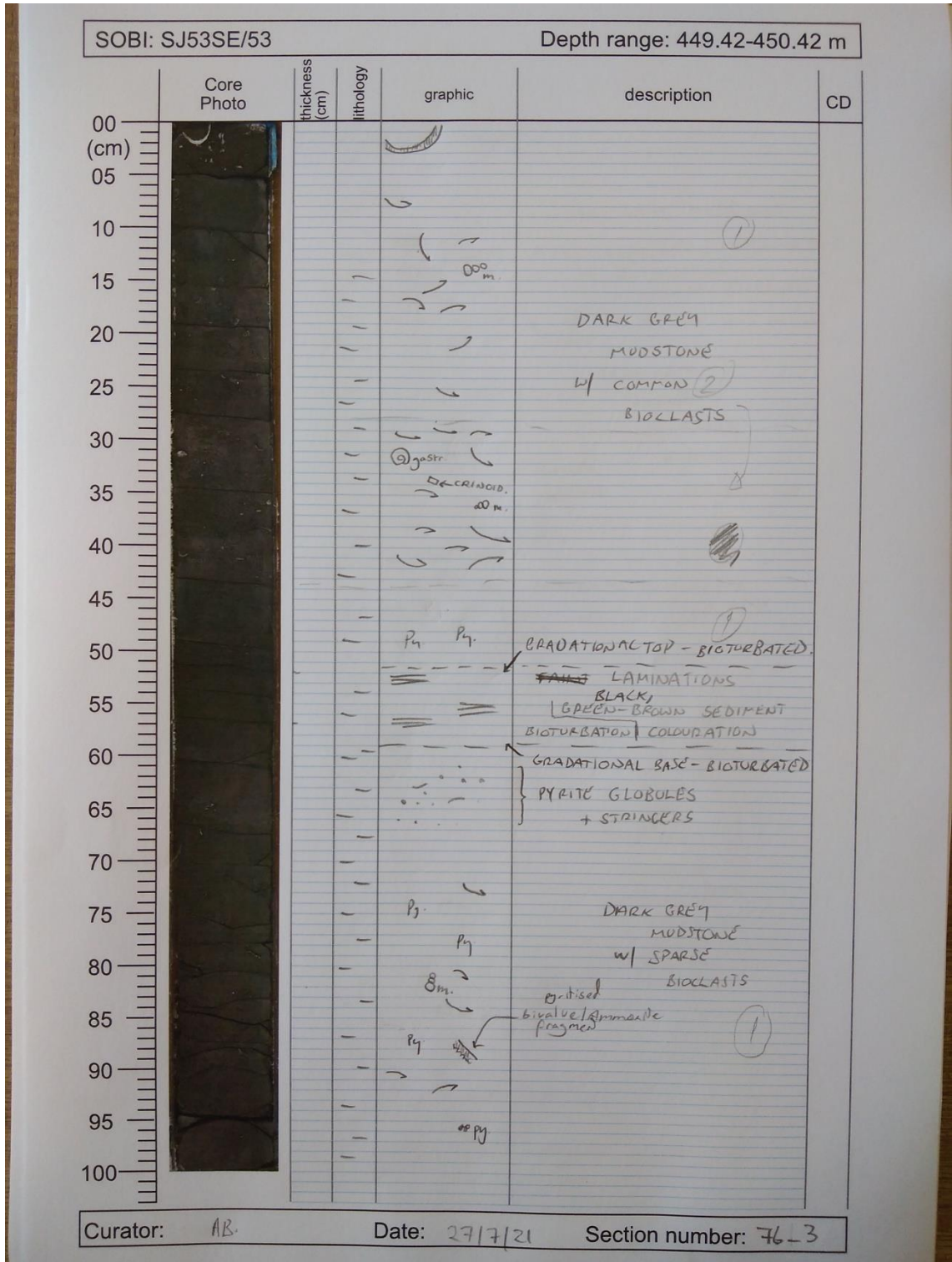
SOBI: SJ53SE/53		Depth range: 448.42-449.42 m				
	Core Photo	thickness (cm)	lithology	graphic	description	CD
00						
(cm)						
05						
10						
15					py.	
20						
25						
30						CALCITE SPAR LARGE RECLINING BIVALVE MUD FILL (GEOPETAL) VALVE FRAGMENT
35						
40						
45				py.		
50				py.	- DARK GREY MUDSTONE	
55				py.	- U SPARSE BIOCLASTS	
60				pyritised burrow	- PYRITISED THROUGHOUT	
65						
70				py.		
75				py.		
80				py.		
85				py.	- microcryst. pyrite	
90				py.		
95				py.	- microcrystalline pyrite	
100					- pyritised valves	

Curator: AB

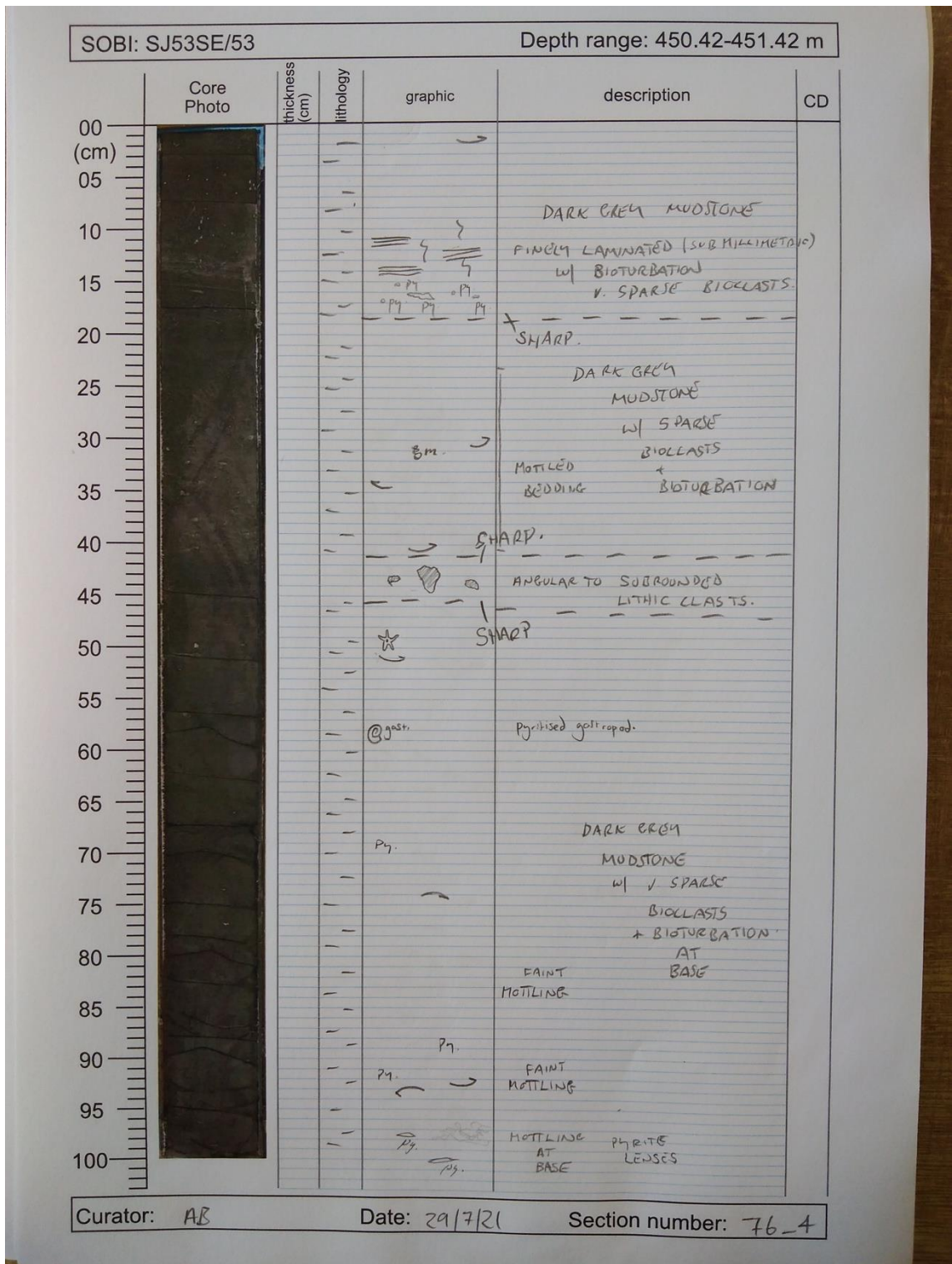
Date: 27/7/21

Section number: 76-2

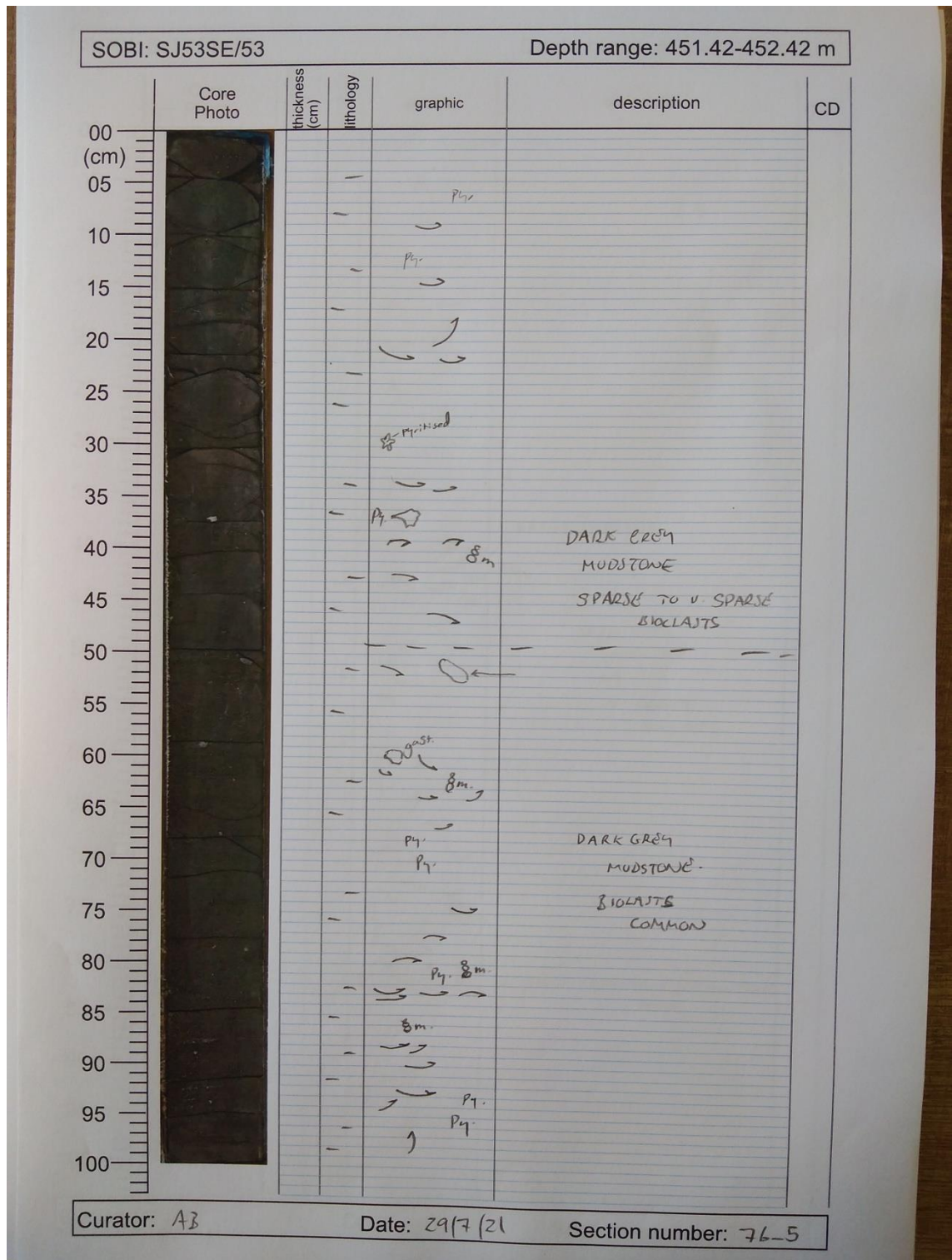
Quantifying marine redox across the Triassic–Jurassic mass extinction



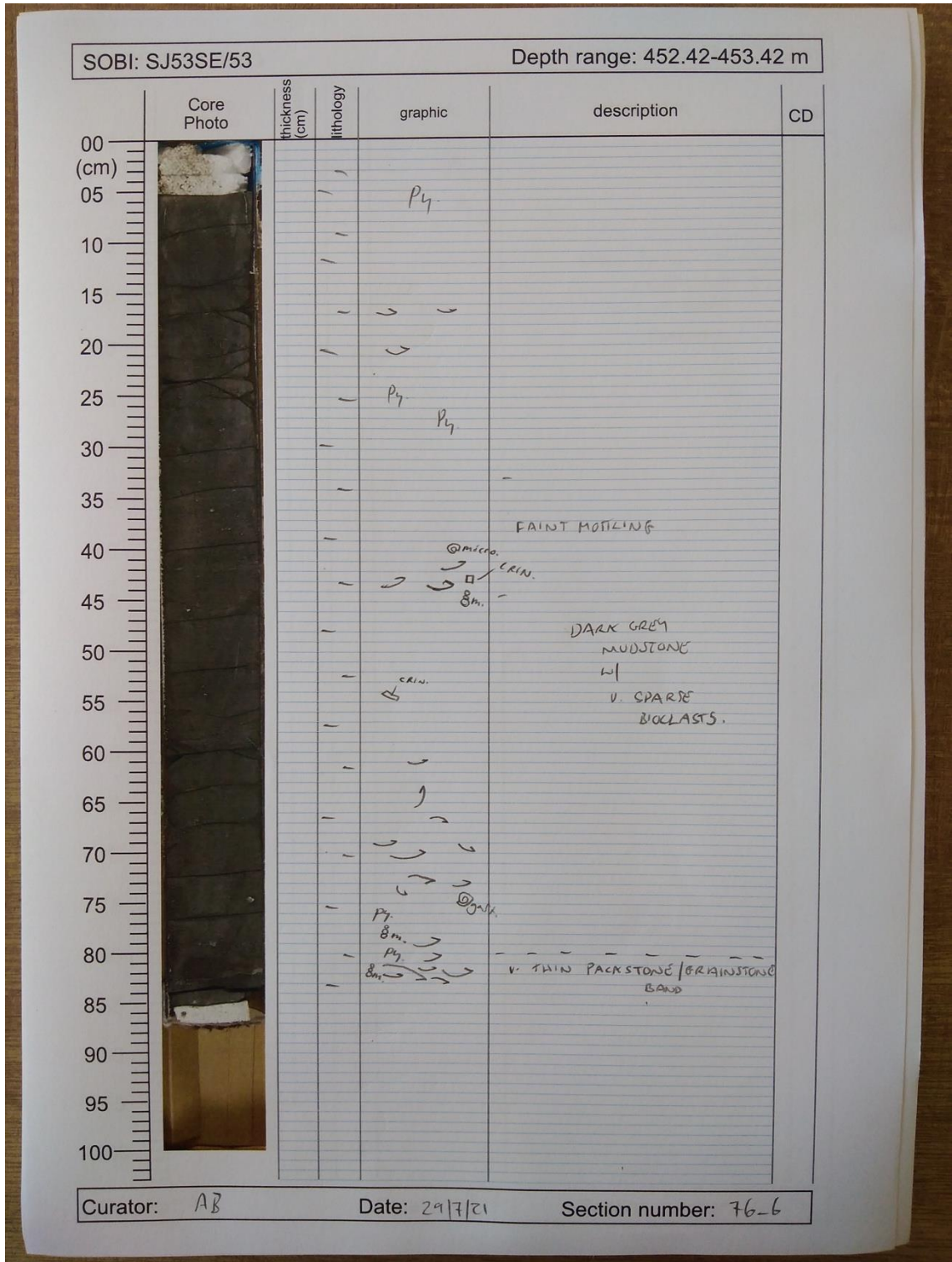
Appendices



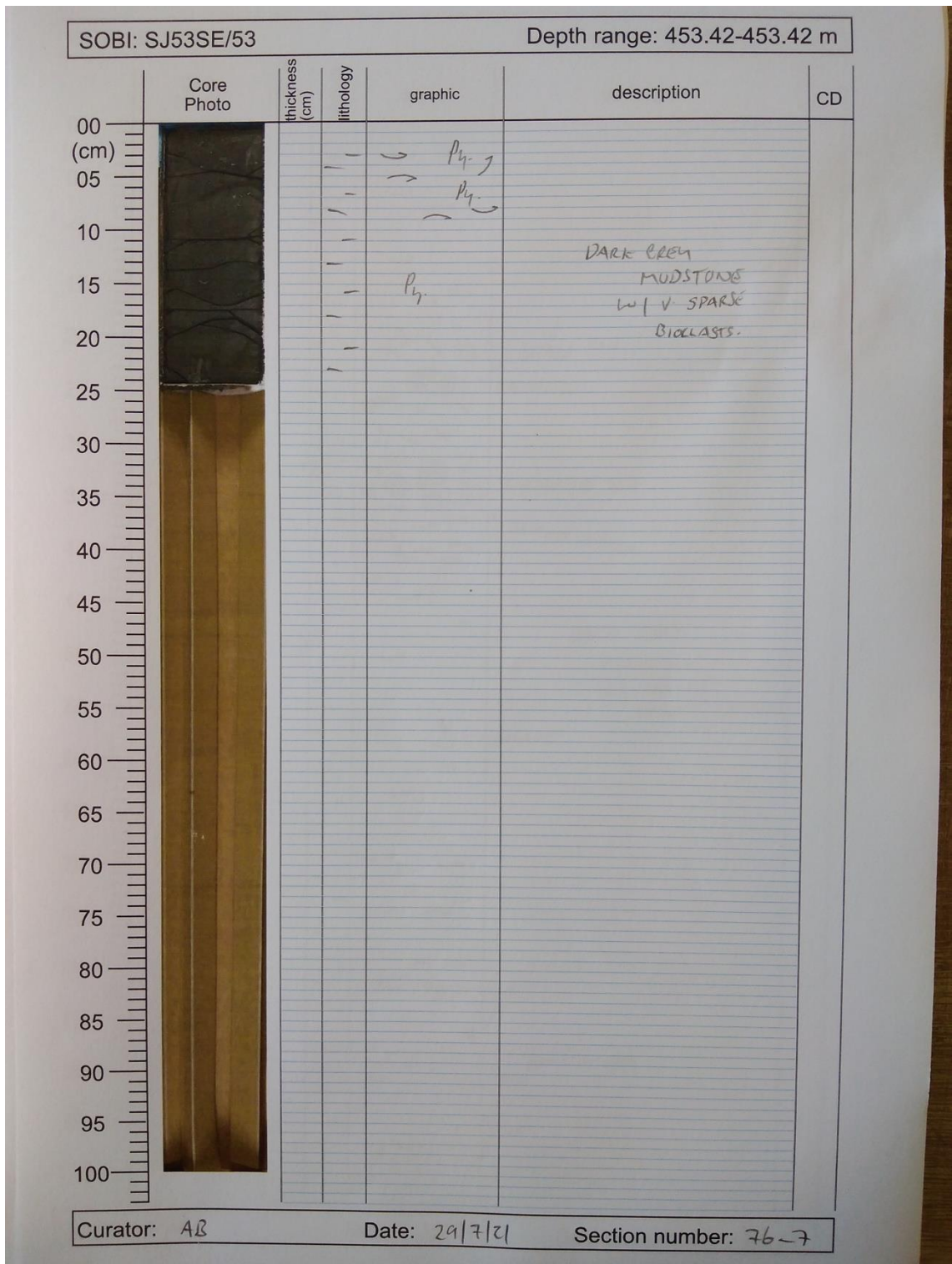
Quantifying marine redox across the Triassic–Jurassic mass extinction



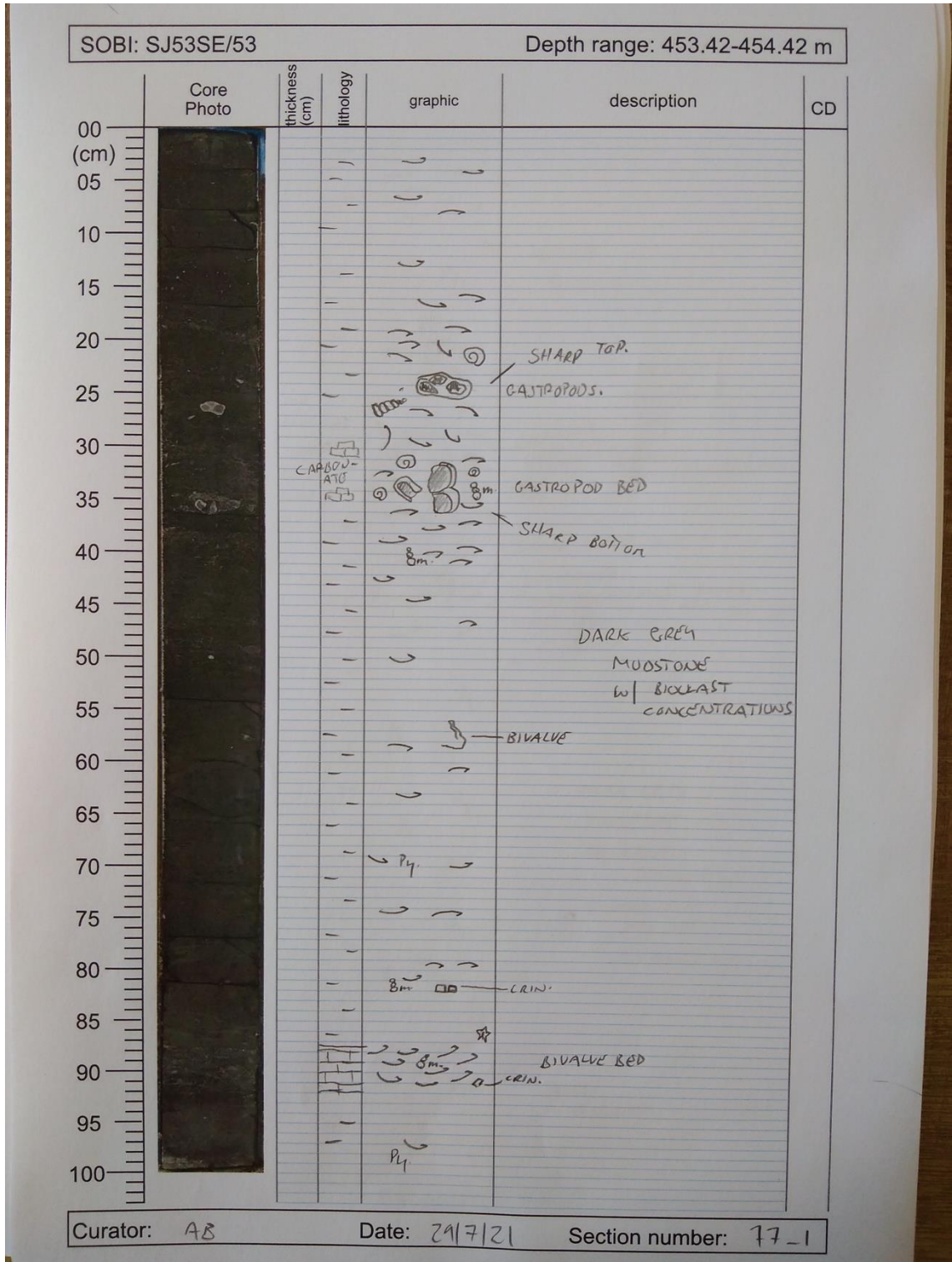
Appendices



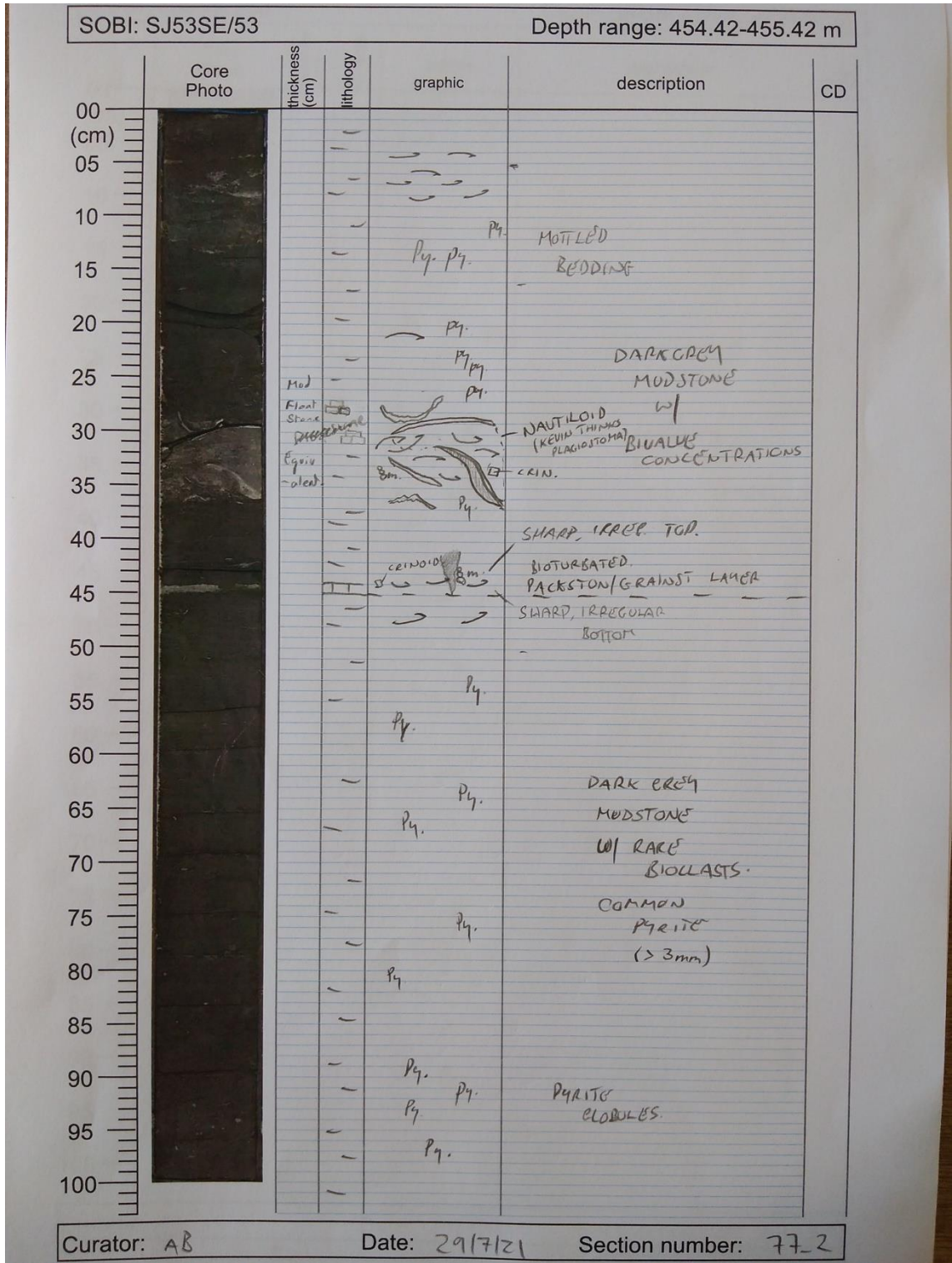
Quantifying marine redox across the Triassic–Jurassic mass extinction



Appendices



Quantifying marine redox across the Triassic–Jurassic mass extinction

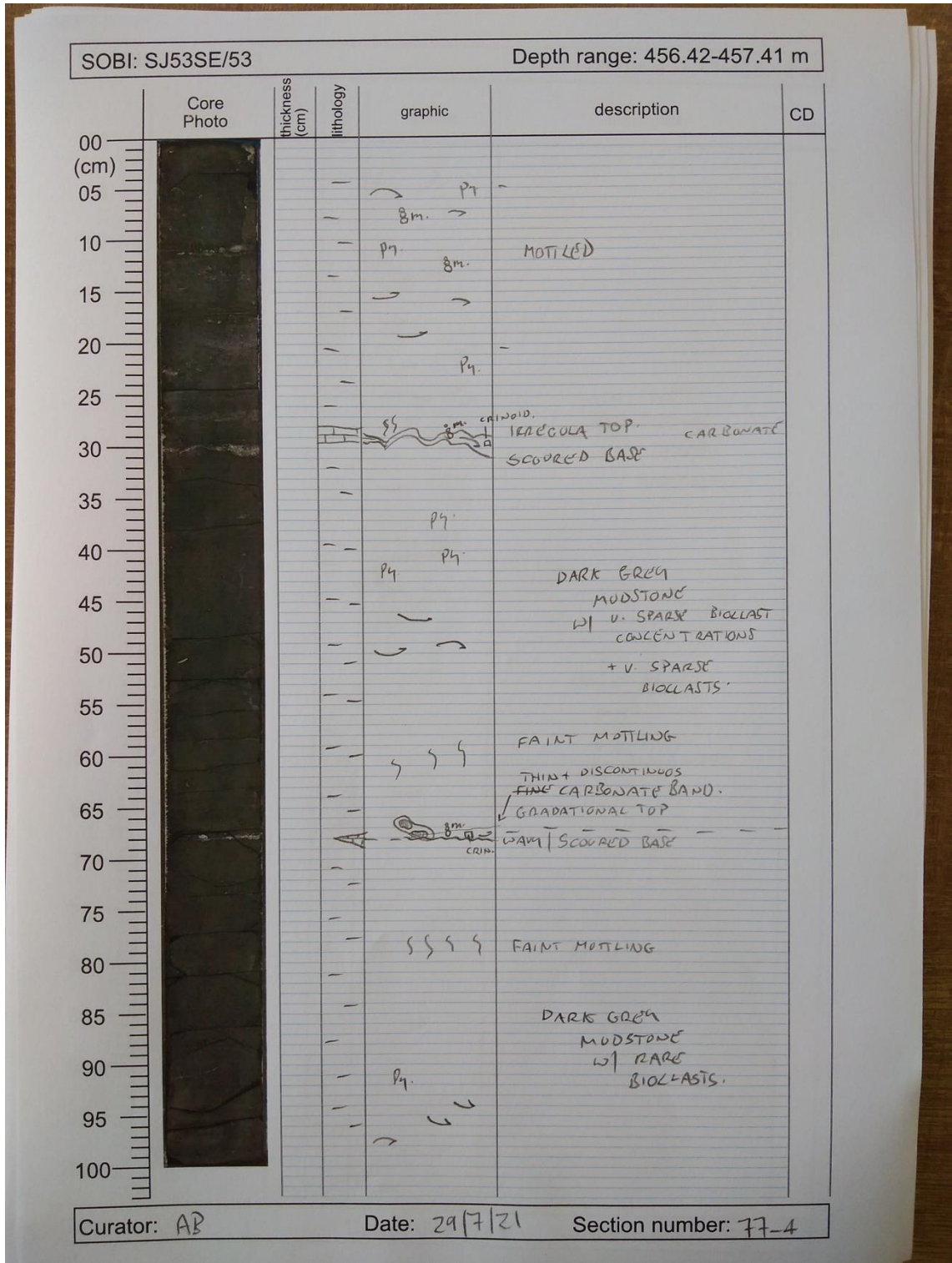


Appendices

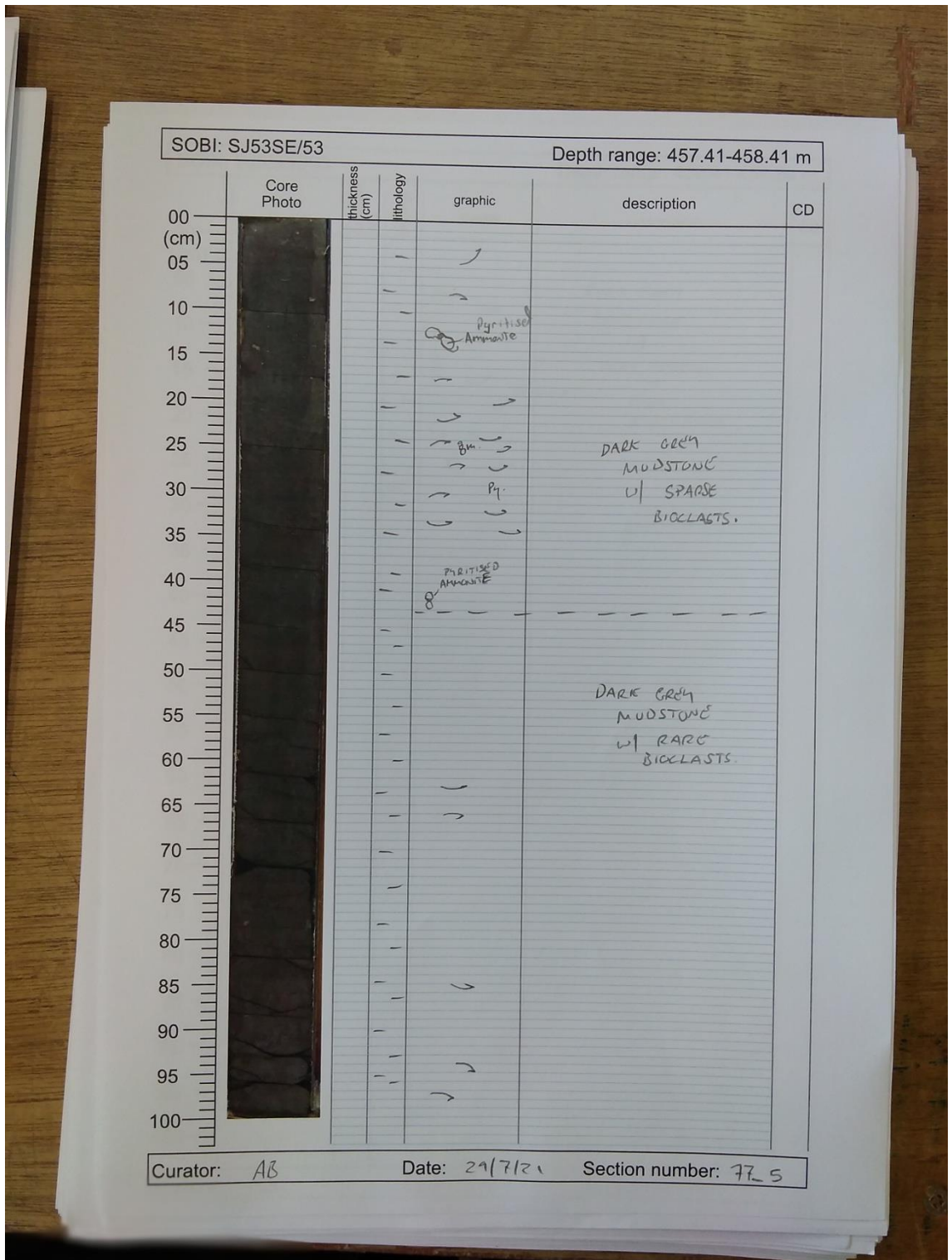
SOBI: SJ53SE/53		Depth range: 455.42-456.42 m			
Core Photo	thickness (cm)	lithology	graphic	description	CD
	00				
	05				
	10				
	15				
	20			P ₄	
	25			P ₄	
	30				
	35			Sm P ₄	DARK GREY MUDSTONE
	40			Sm	w/ v. SPARSE BIOCLASTS.
	45				MOTTLING
	50				
	55				
	60				
	65				
	70				
	75				
	80				
	85				
	90			P ₇	
95					
100					

Curator: AB Date: 29/7/21 Section number: 77-3

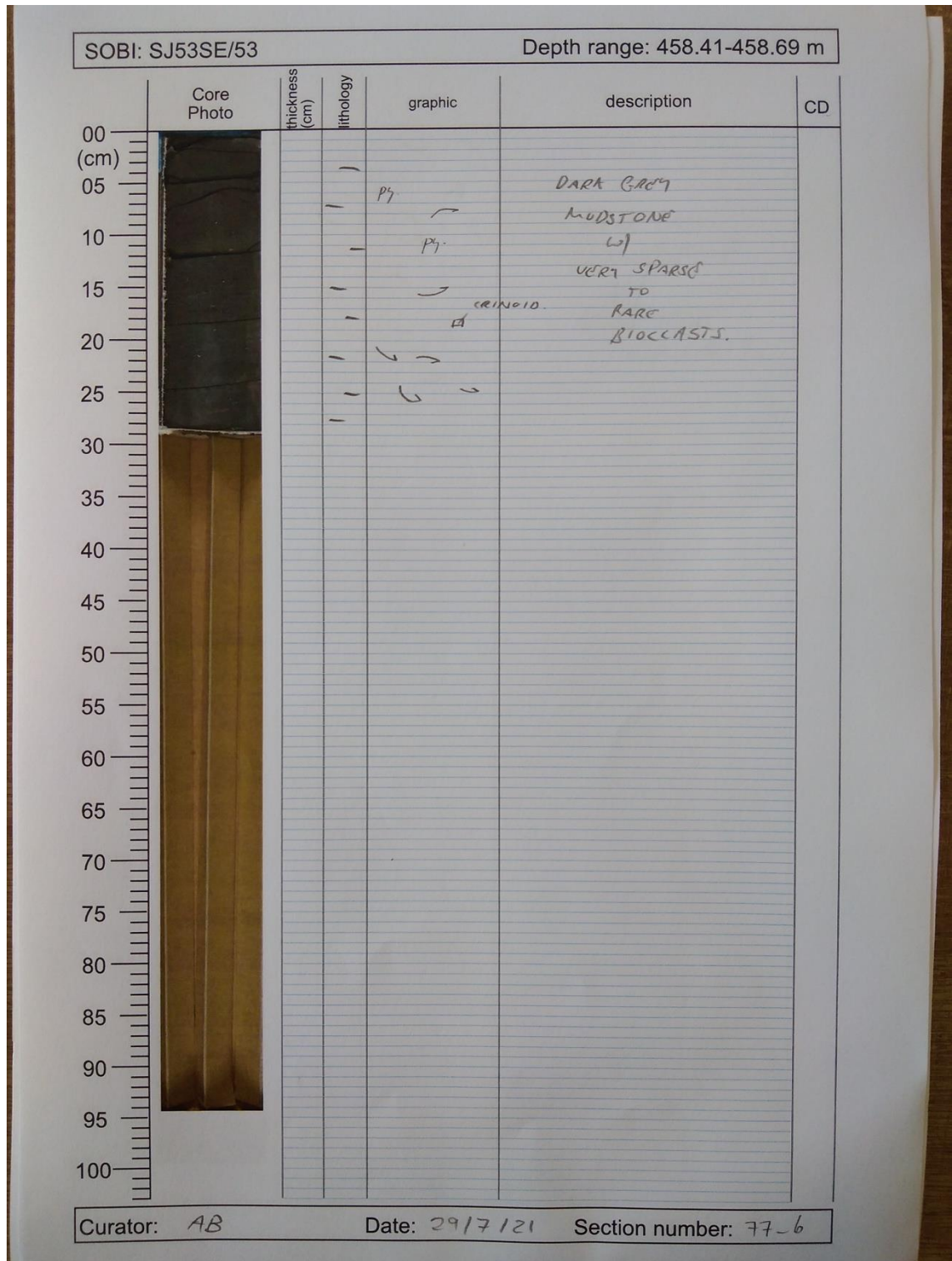
Quantifying marine redox across the Triassic–Jurassic mass extinction




Appendices



Quantifying marine redox across the Triassic–Jurassic mass extinction

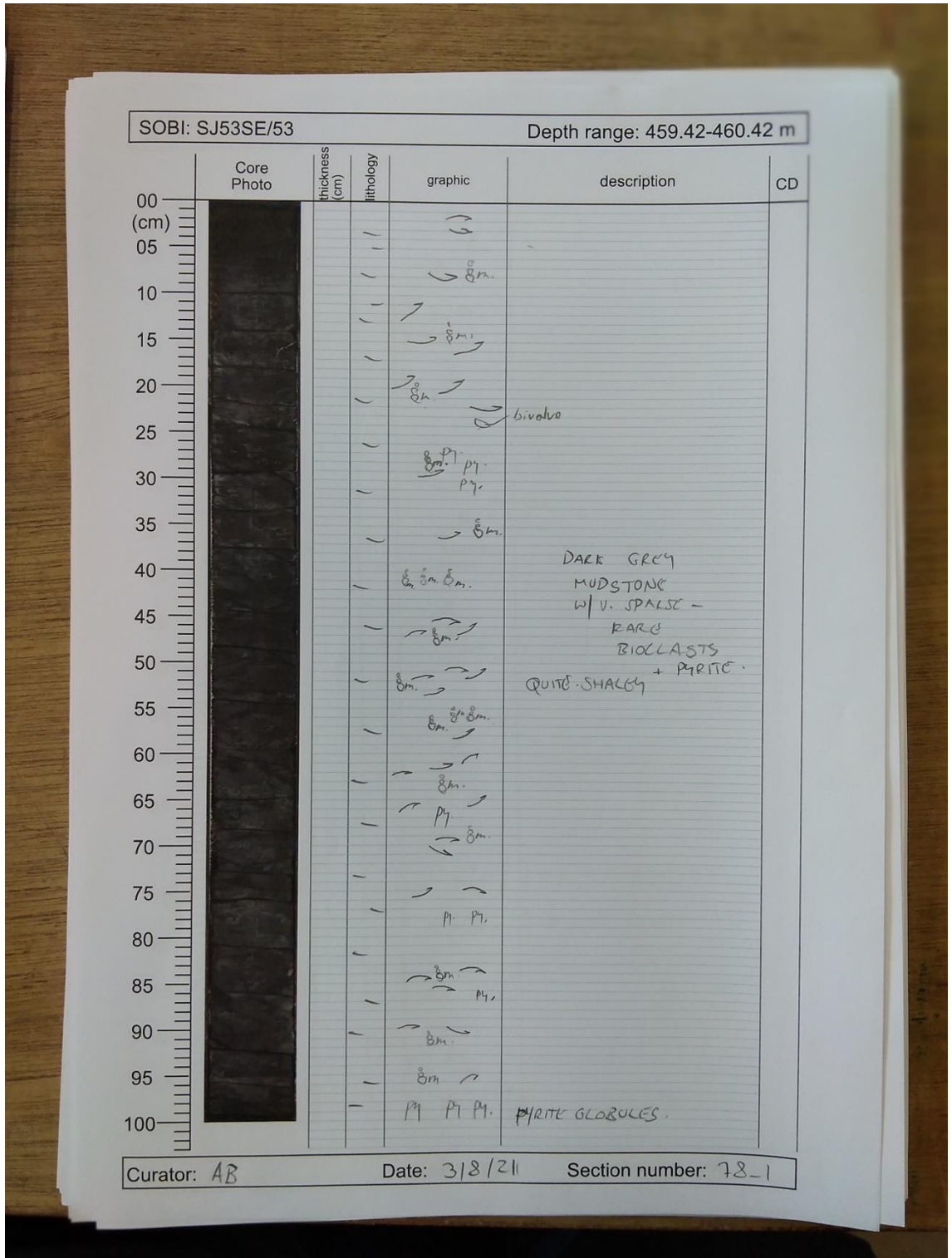


Appendices

SOBI: SJ53SE/53		Depth range: 458.69-458.98 m				
Core Photo	thickness (cm)	lithology	graphic	description	CD	
	00					
	05					
	10				DARK GRAY MUDSTONE	
	15				W/	
	20				V. SPARSE	
	25				BIOCLASTS.	
	30					
	35					
	40					
	45					
50						
55						
60						
65						
70						
75						
80						
85						
90						
95						
100						

Curator: AB Date: 29/7/21 Section number: 77-7

Quantifying marine redox across the Triassic–Jurassic mass extinction



Appendices

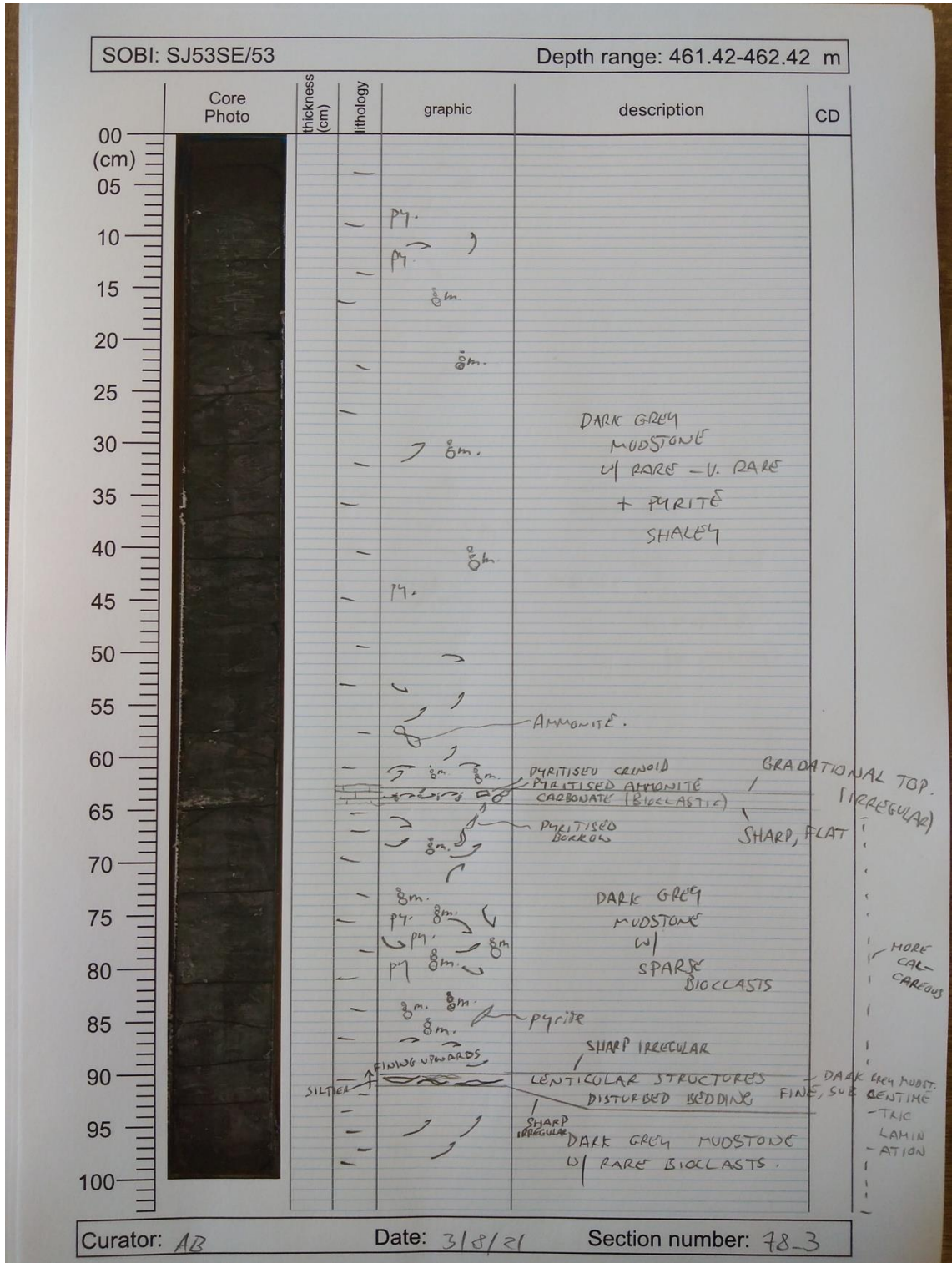
SOBI: SJ53SE/53		Depth range: 460.42-461.42 m				
	Core Photo	thickness (cm)	lithology	graphic	description	CD
00						
05				gm.		
10					P7.	
15					P7.	
20					gm.	
25						
30					gm.	
35					PYRITISED crinoid ossicle.	
40					PYRITISED bivalve	
45					gm.	DARK GREY
50						(SHALY) MUDSTONE
55						W/ RARE BIOCLASTS
60					gm.	+ PYRITE
65					gm.	
70						
75					PYRITE GLOBULES.	
80					PYRITE GLOBULES.	
85					gm. gm.	
90					P7.	
95					gm. P7. P7.	
100				gm. P7.		

Curator: AB

Date: 3/8/21

Section number: 78-2

Quantifying marine redox across the Triassic–Jurassic mass extinction

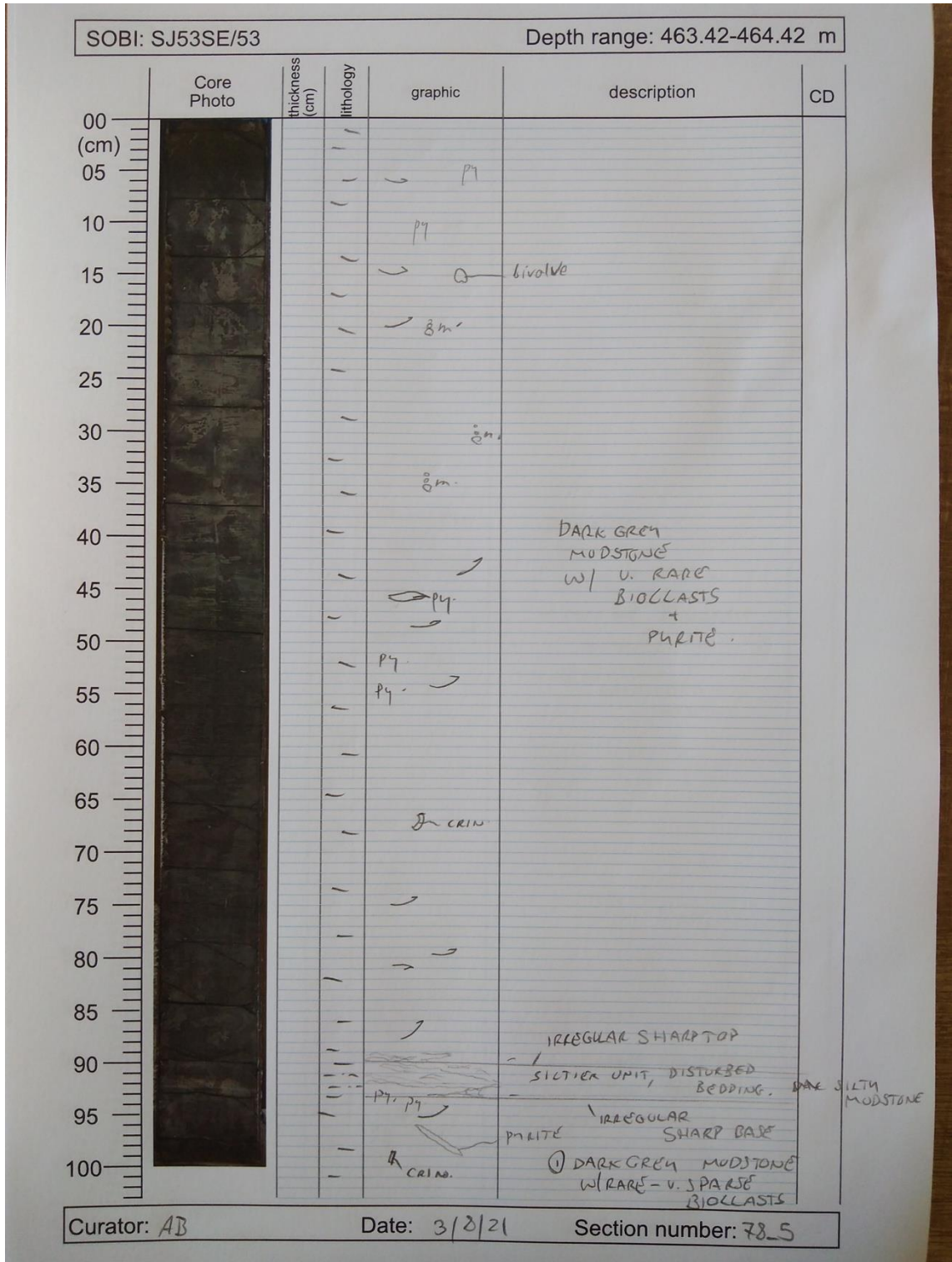


Appendices


SOBI: SJ53SE/53		Depth range: 462.42-463.42 m				
	Core Photo	thickness (cm)	lithology	graphic	description	CD
00						
(cm)						
05						
10						
15						
20						
25						
30						
35						
40						
45						
50						
55						
60						
65						
70						
75						
80						
85						
90						
95						
100						

Curator: AB	Date: 3/8/21	Section number: 78_4
-------------	--------------	----------------------

Quantifying marine redox across the Triassic–Jurassic mass extinction



Appendices

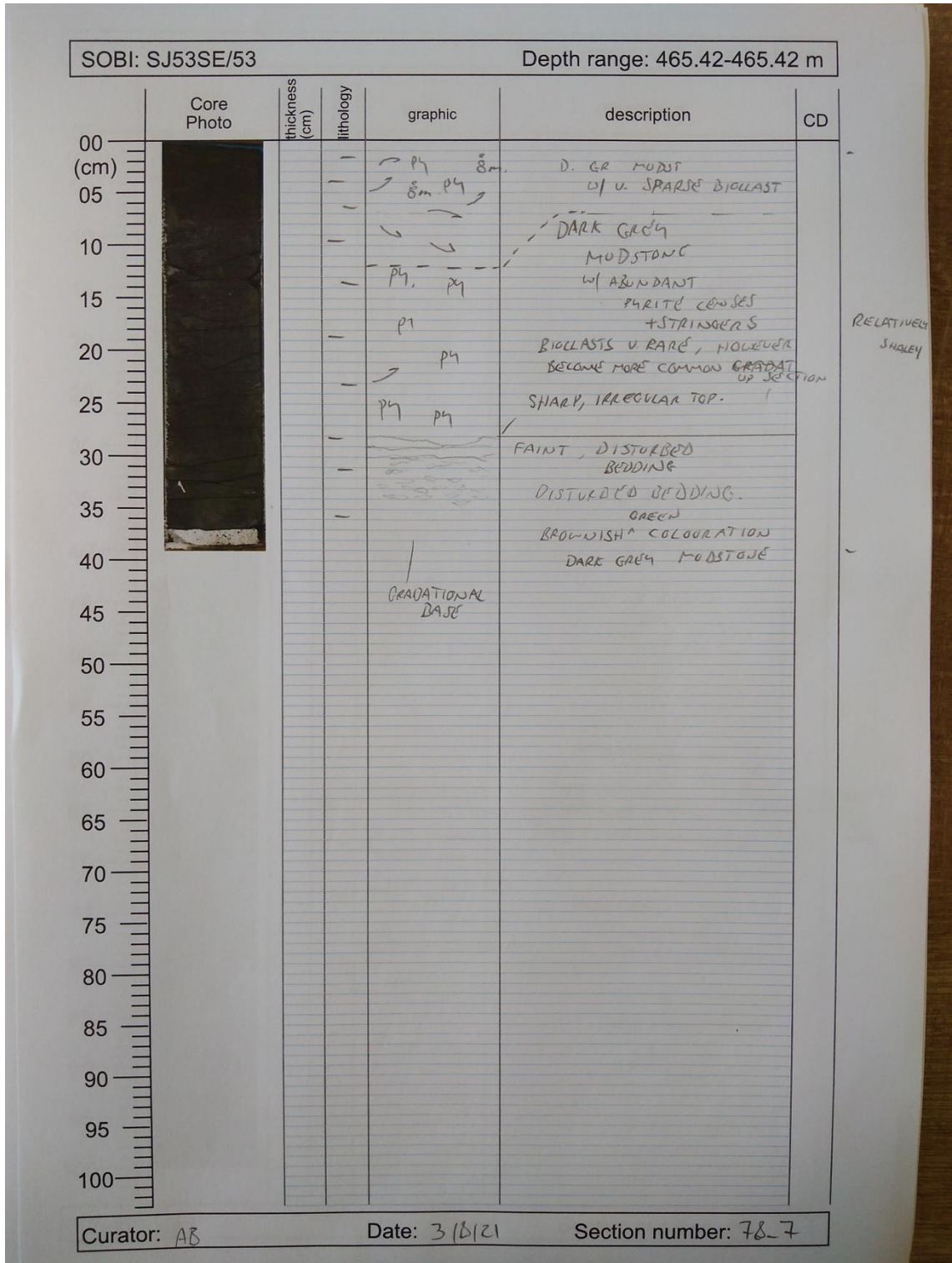
SOBI: SJ53SE/53		Depth range: 464.42-465.42 m				
	Core Photo	thickness (cm)	lithology	graphic	description	CD
00						
05						
10						
15						
20						
25						
30						
35						
40					P ₁ P ₄	DARK GREY MUDSTONE
45					P₁	W/ V. RARE
50				P₁ P ₁ pyritised	RARE VV RARE AND BIOCLASTS	
55				P ₁	+ PYRITE.	
60					WHOLE SECTION RELATIVELY SHALEY	
65						
70				∨		
75						
80						
85				P ₄ P ₄	DARK GREY MUDSTONE	
90				P ₄ ♂	ABUNDANT PYRITE GLOBULES + LENSES	
95				P ₄ ♂	+ STRINGERS	
100				P ₄ P ₄ P ₄	RARE - V RARE BIOCLASTS	
				P ₄ ♂		

Curator: AB

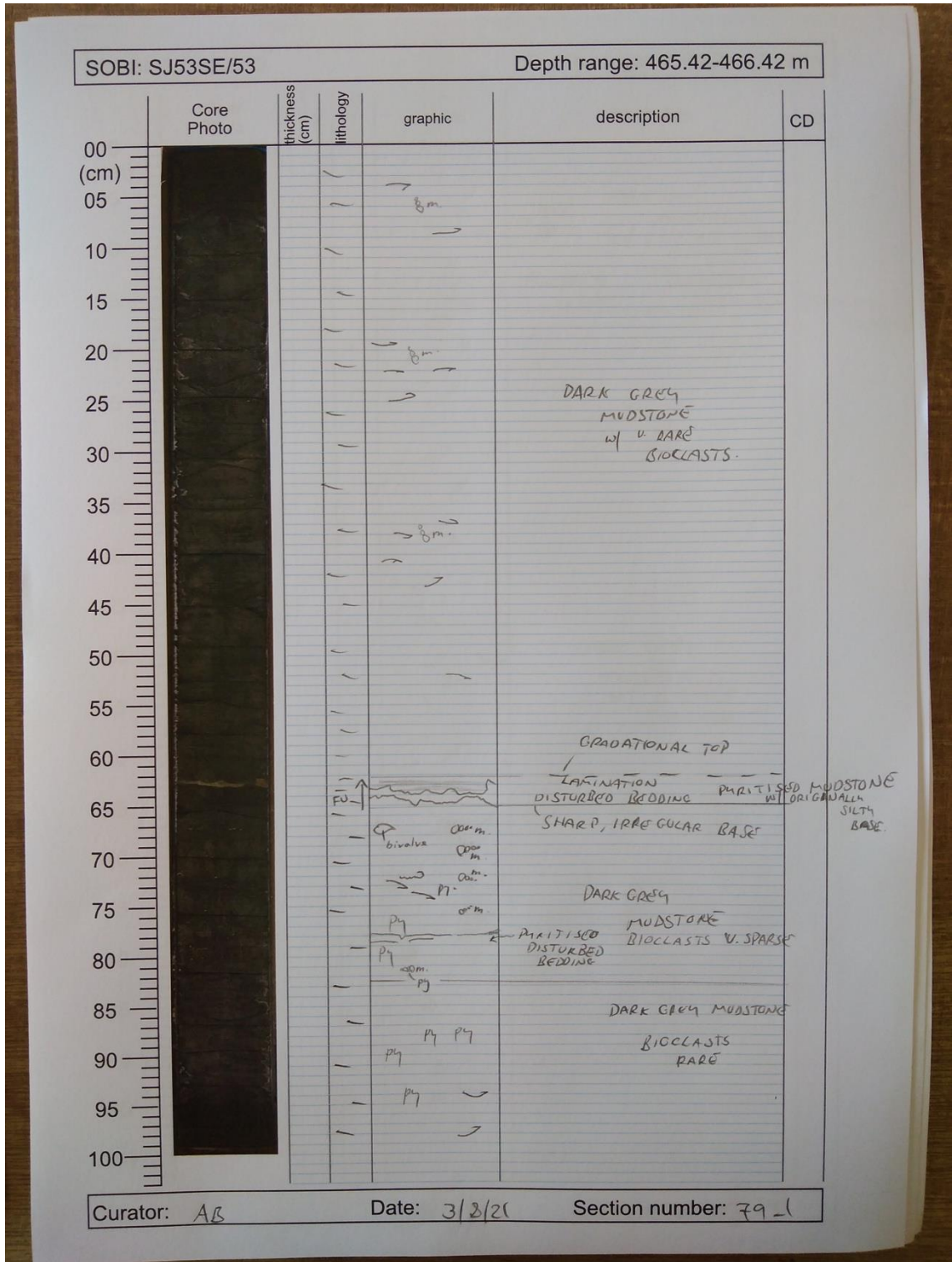
Date: 3/8/21

Section number: 78-6

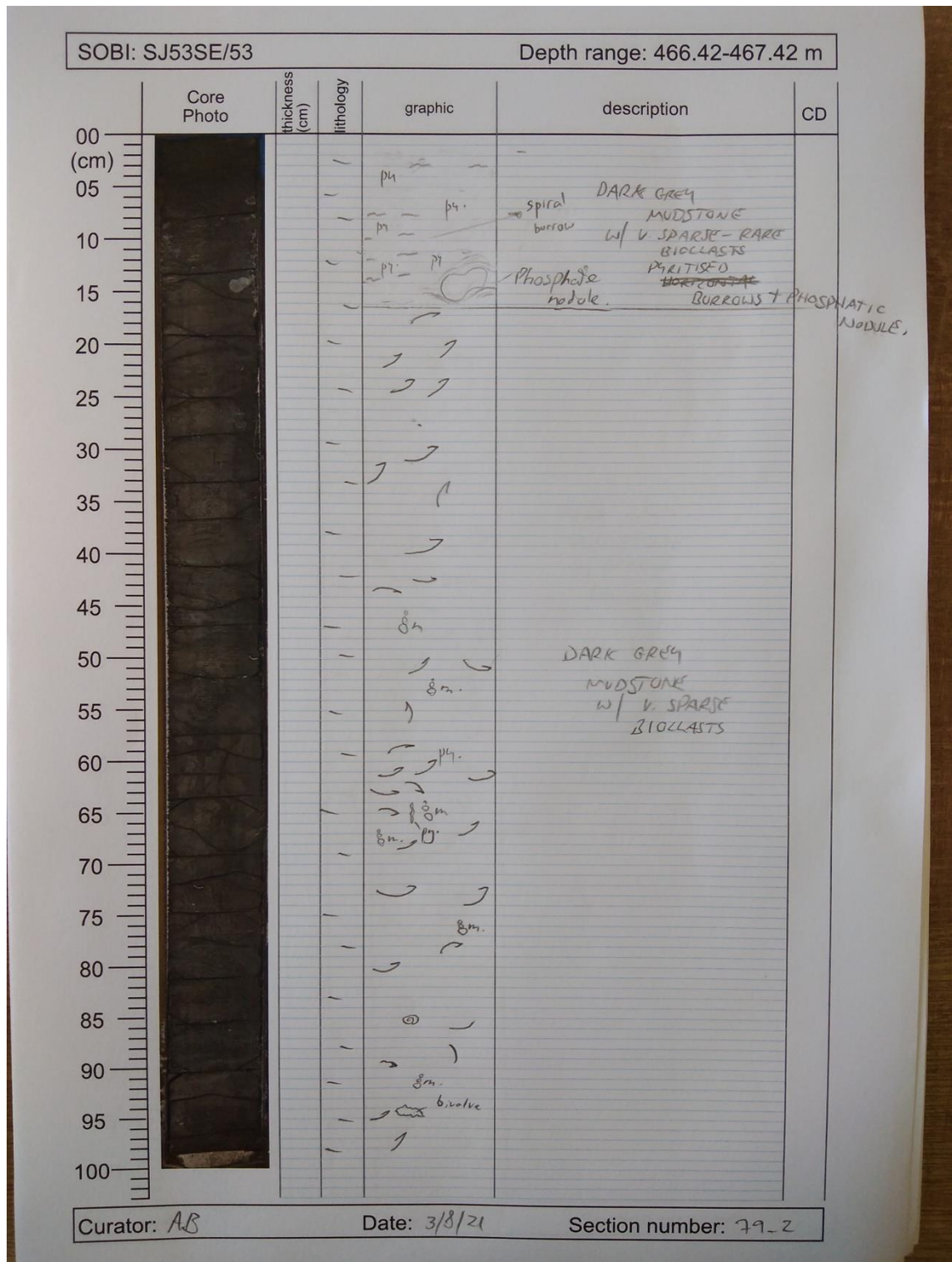
Quantifying marine redox across the Triassic–Jurassic mass extinction




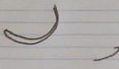
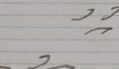
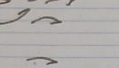
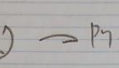
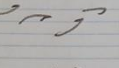
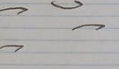
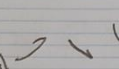
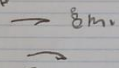
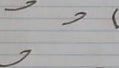
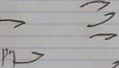
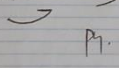
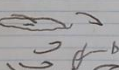
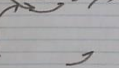
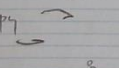
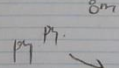
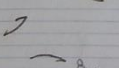
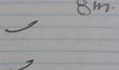
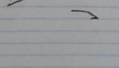
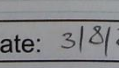
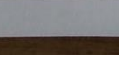
Appendices



Quantifying marine redox across the Triassic–Jurassic mass extinction



Appendices

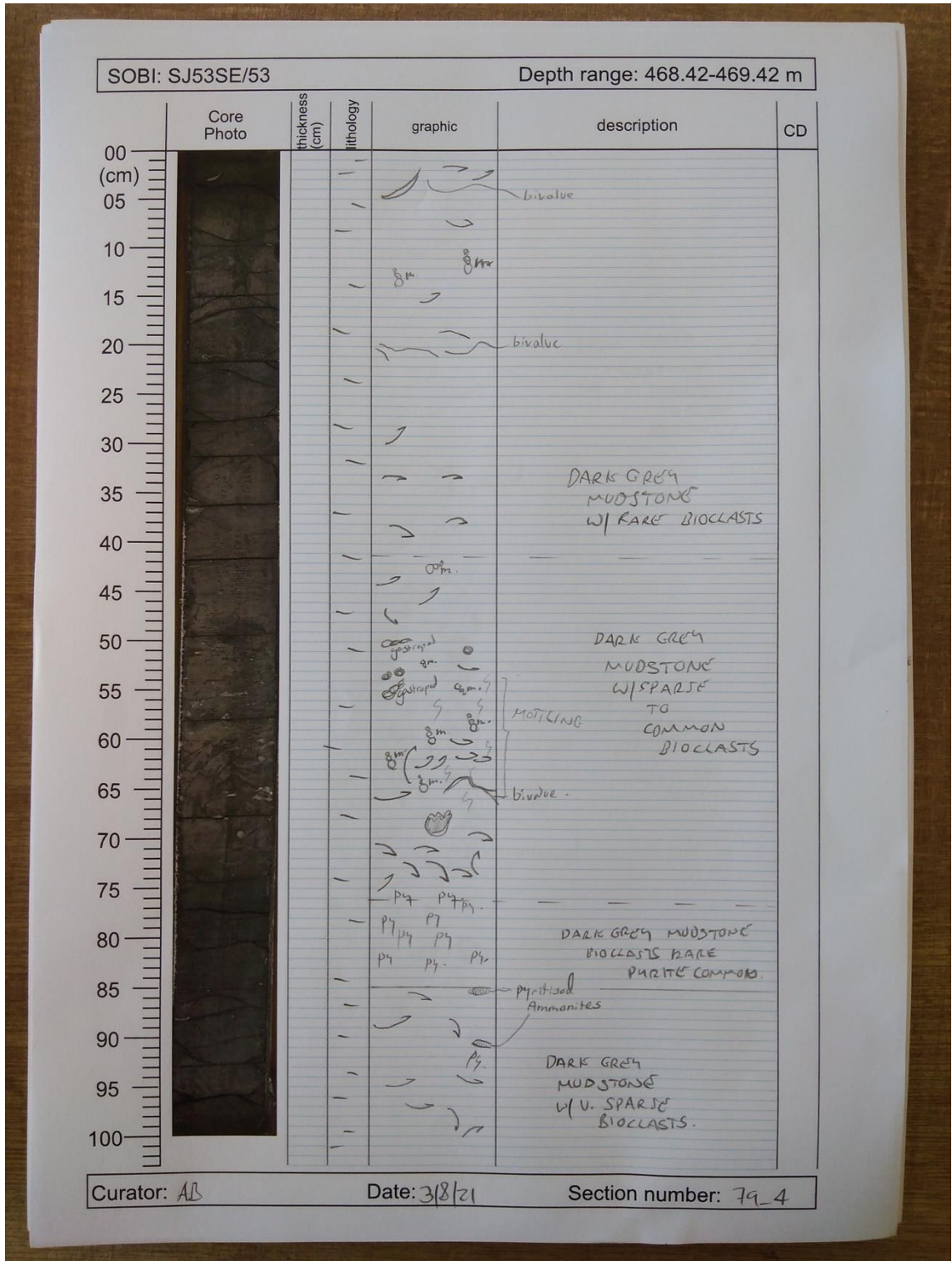
SOBI: SJ53SE/53		Depth range: 467.42-468.42 m				
	Core Photo	thickness (cm)	lithology	graphic	description	CD
00 (cm)						
05						
10						
15						
20						
25						
30						
35						
40						
45						DARK GREY MUDSTONE w/ SPARSE BIOLITE.
50						
55						
60						
65						
70						
75						
80						
85						
90						
95						
100						

Curator: AB

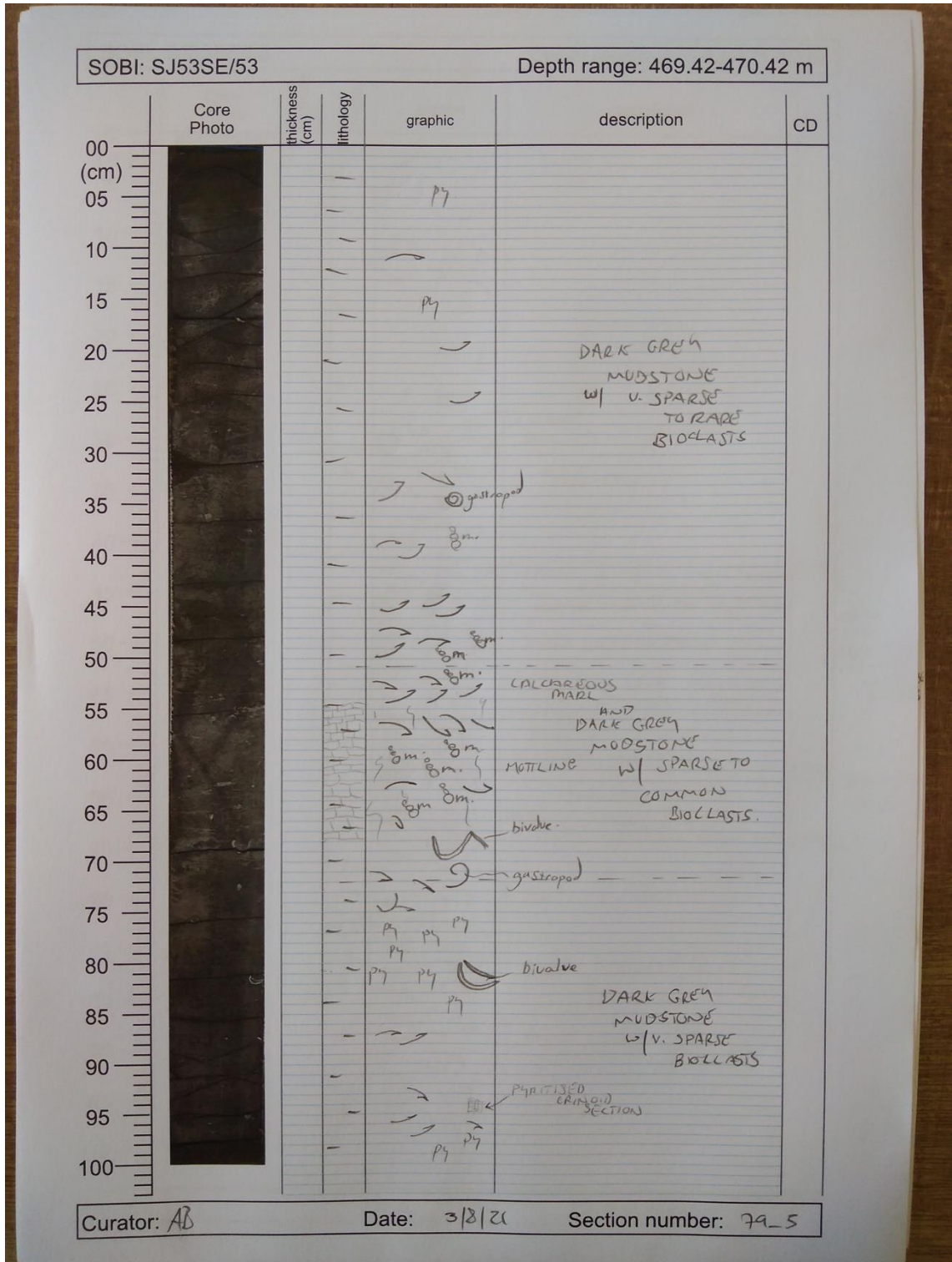
Date: 3/8/21

Section number: 79_3

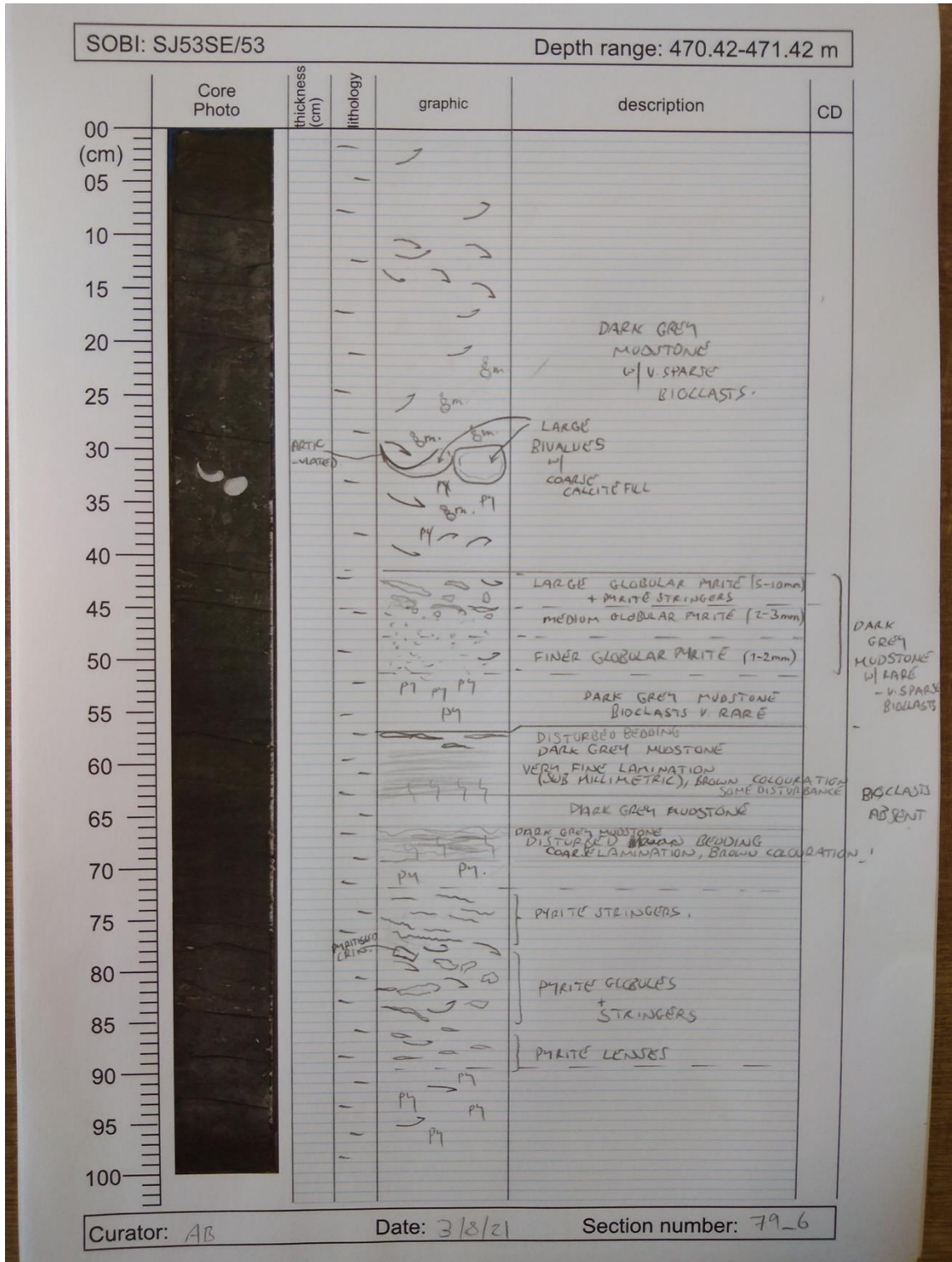
Quantifying marine redox across the Triassic–Jurassic mass extinction



Appendices



Quantifying marine redox across the Triassic–Jurassic mass extinction



Appendices

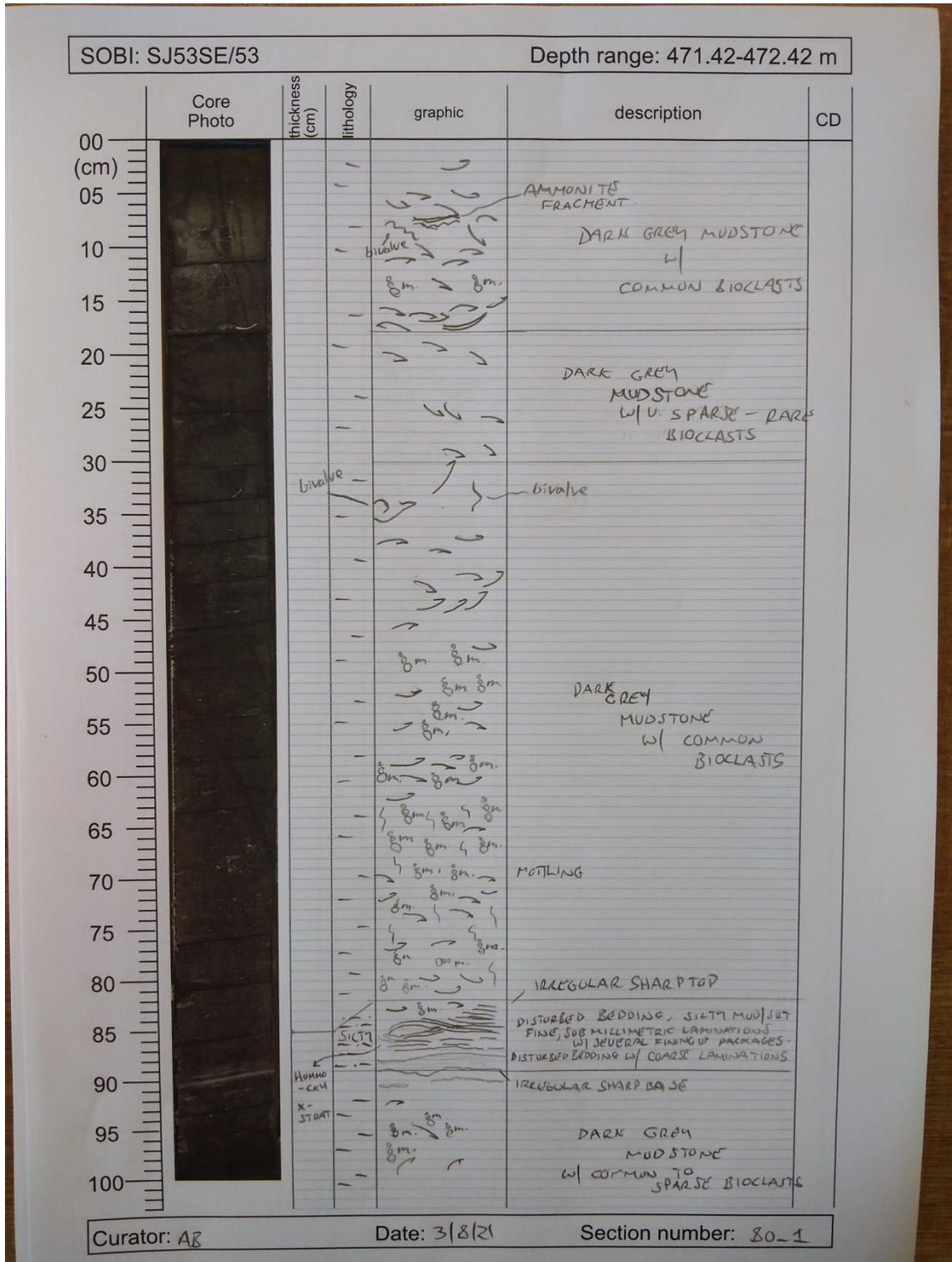
SOBI: SJ53SE/53		Depth range: 471.42-471.69 m				
Core Photo	thickness (cm)	lithology	graphic	description	CD	
	00 (cm)					
	05			→ P ₇		
	10				① RARE TO V. RARE BIOCLASTS	
	15			→ P ₇		
	20			→ S _m	① V. SPARSE TO RARE BIOCLASTS	
	25			→ S _m	① DARK GRAY MUDSTONE V. SPARSE BIOCLASTS	
	30					
	35					
	40					
	45					
50						
55						
60						
65						
70						
75						
80						
85						
90						
95						
100						

Curator: AS

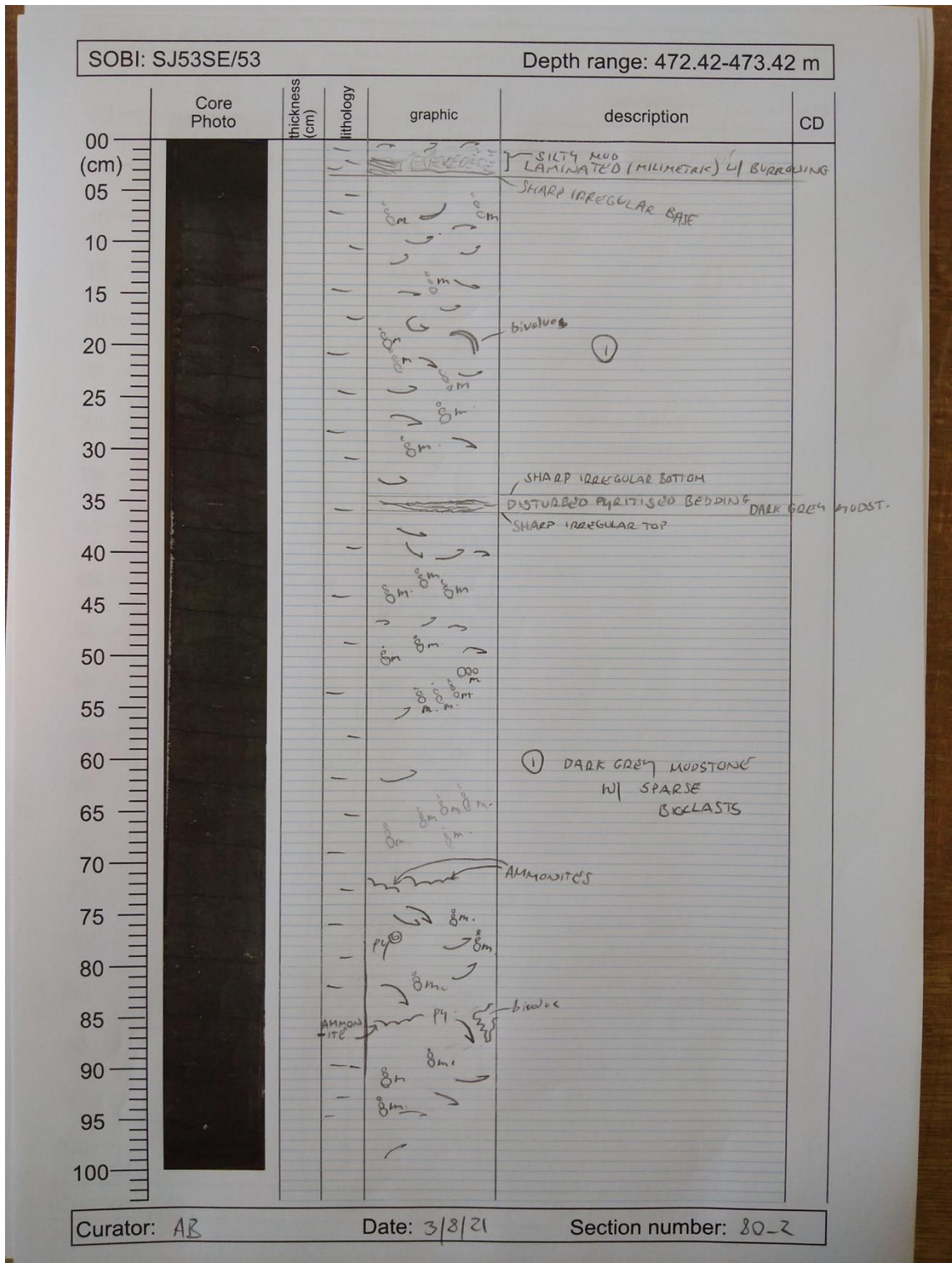
Date: 3/8/21

Section number: 79_7

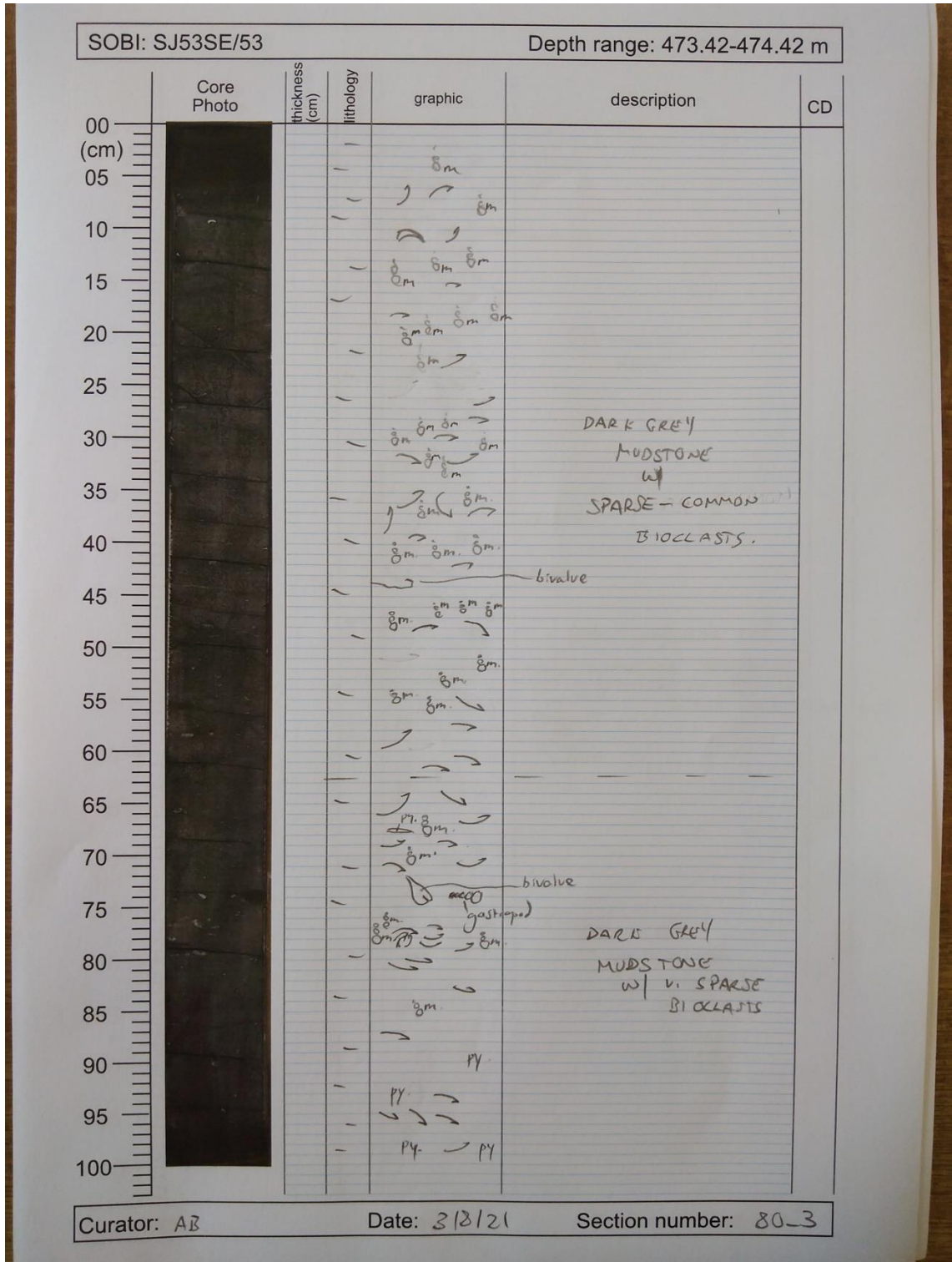
Quantifying marine redox across the Triassic–Jurassic mass extinction



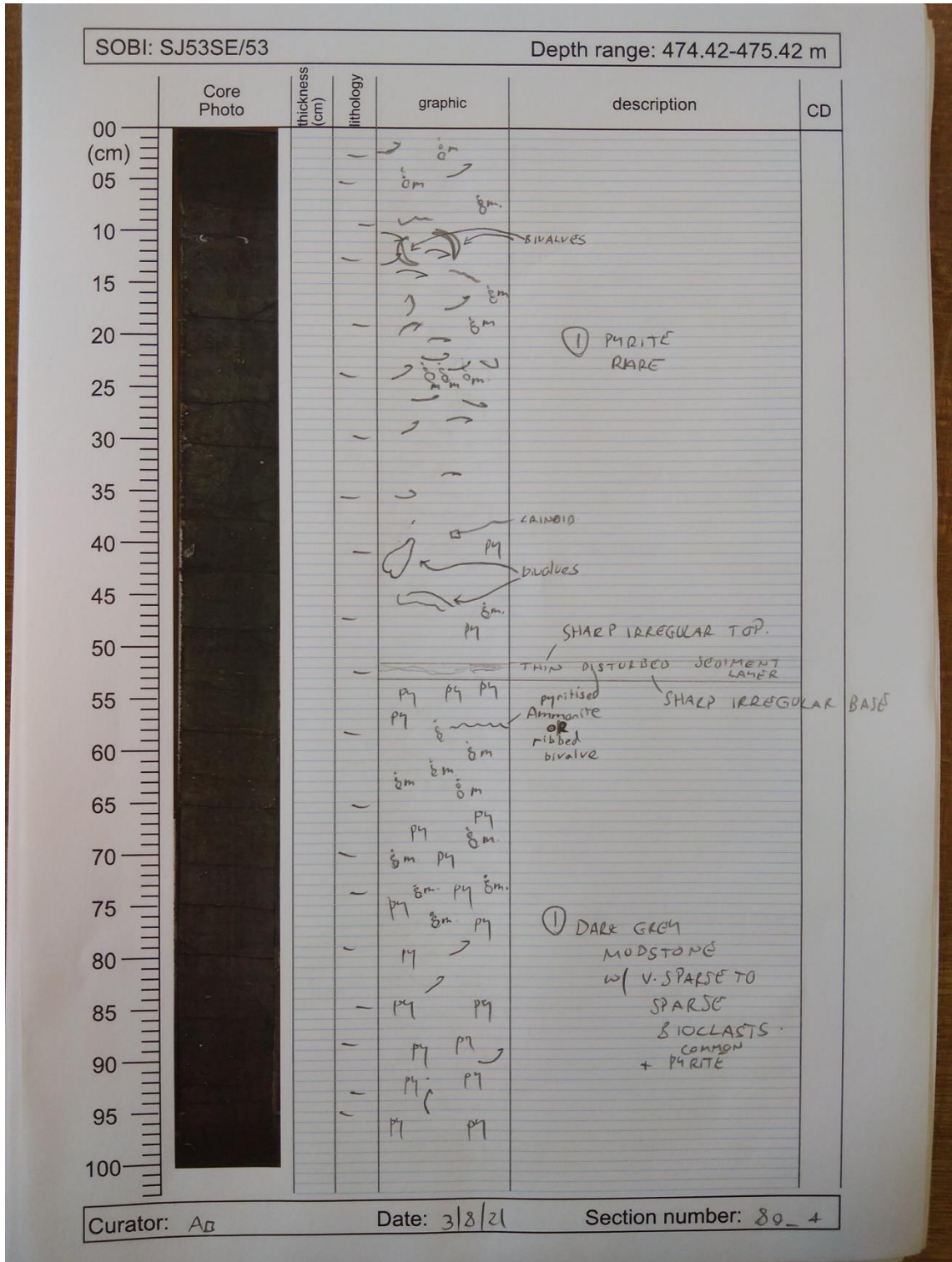
Appendices



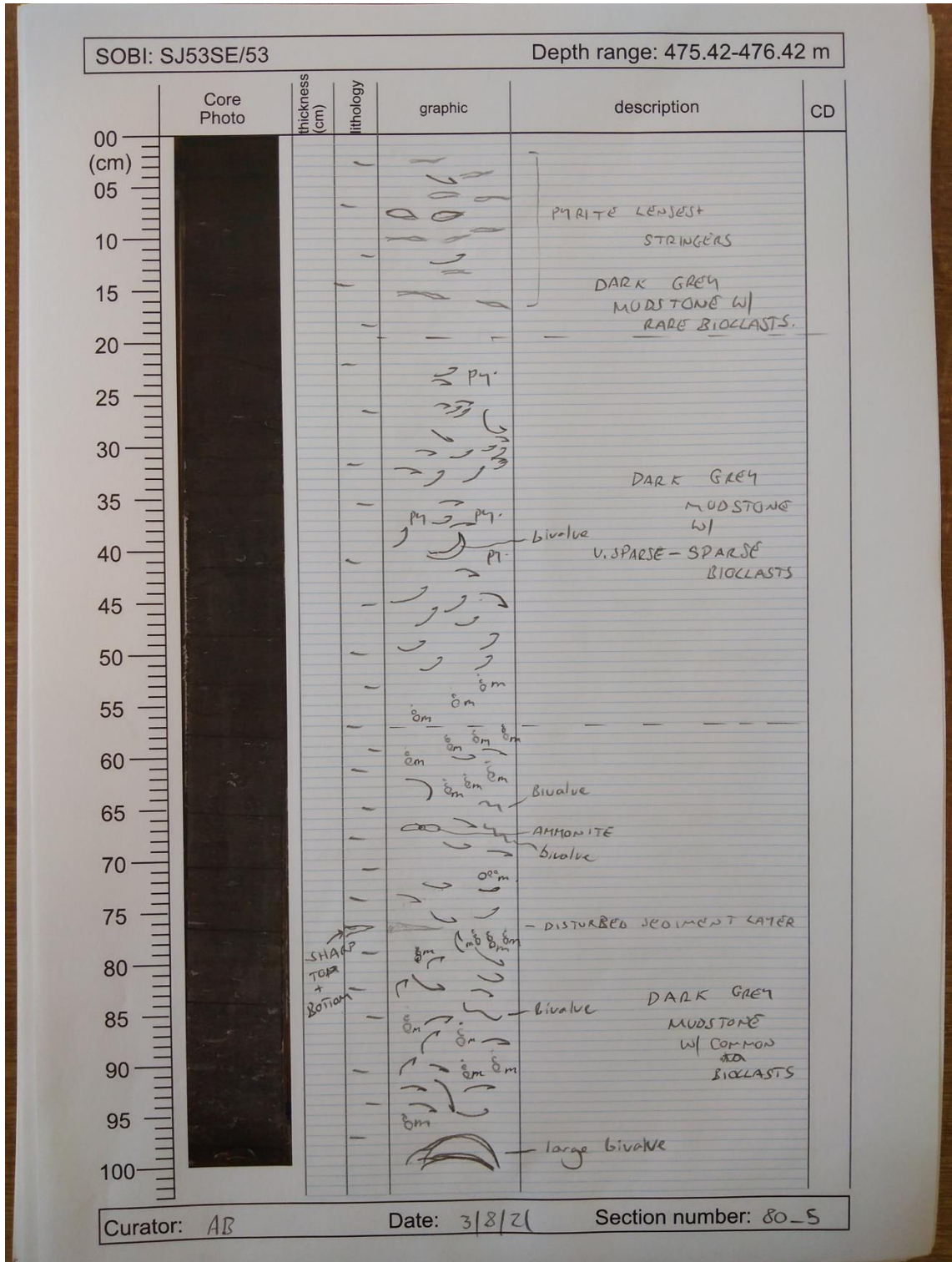
Quantifying marine redox across the Triassic–Jurassic mass extinction



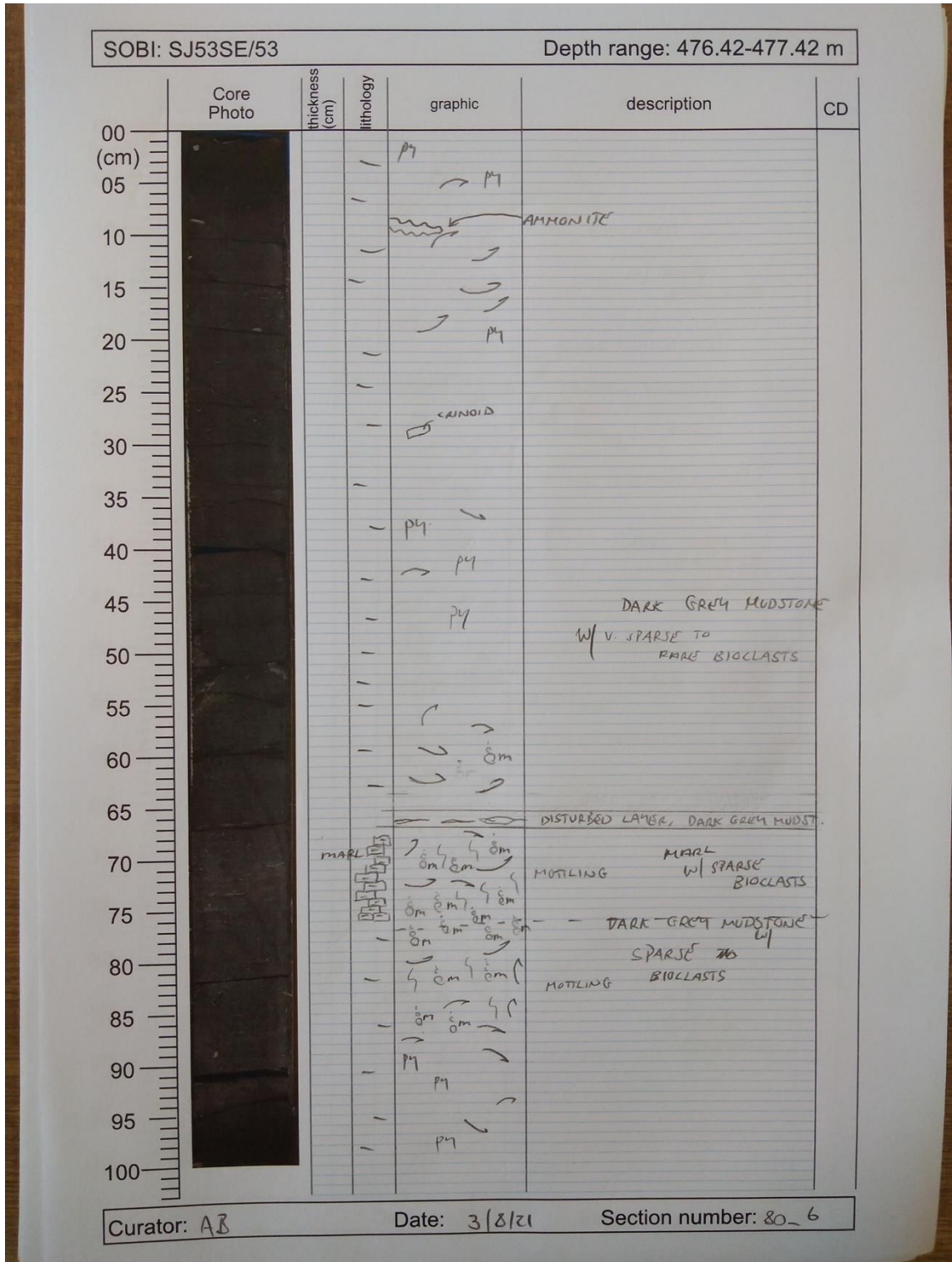
Appendices



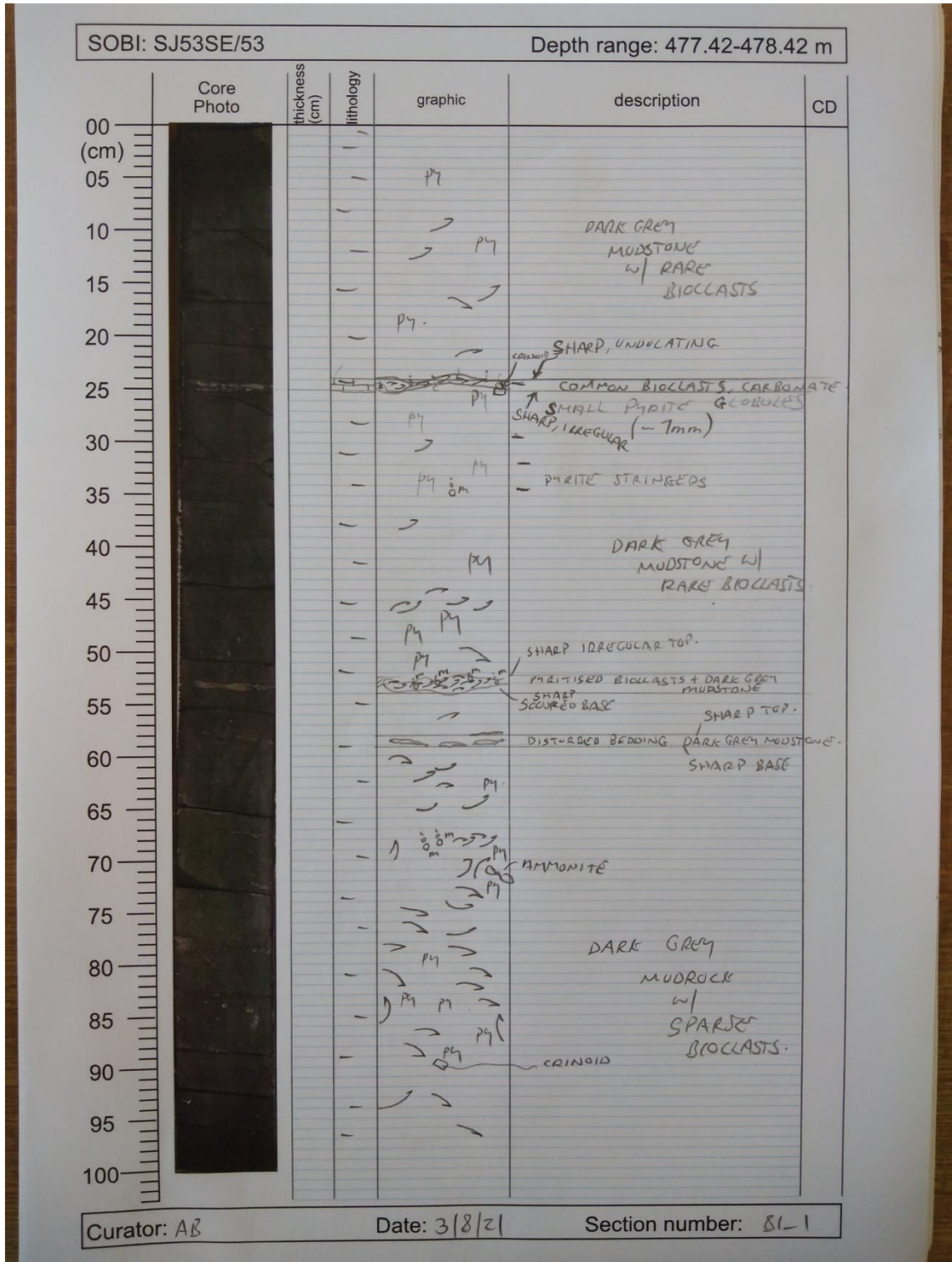
Quantifying marine redox across the Triassic–Jurassic mass extinction



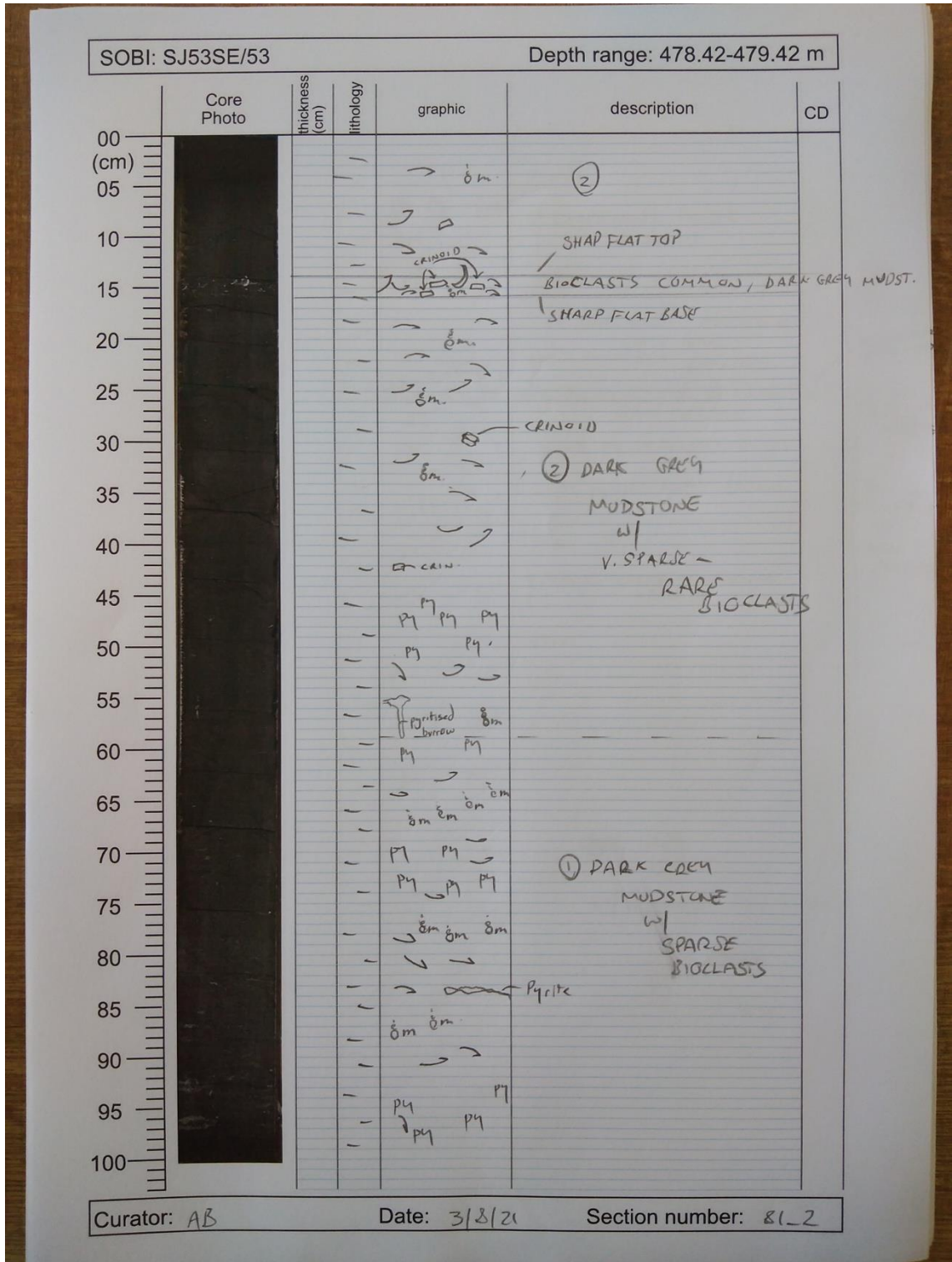
Appendices



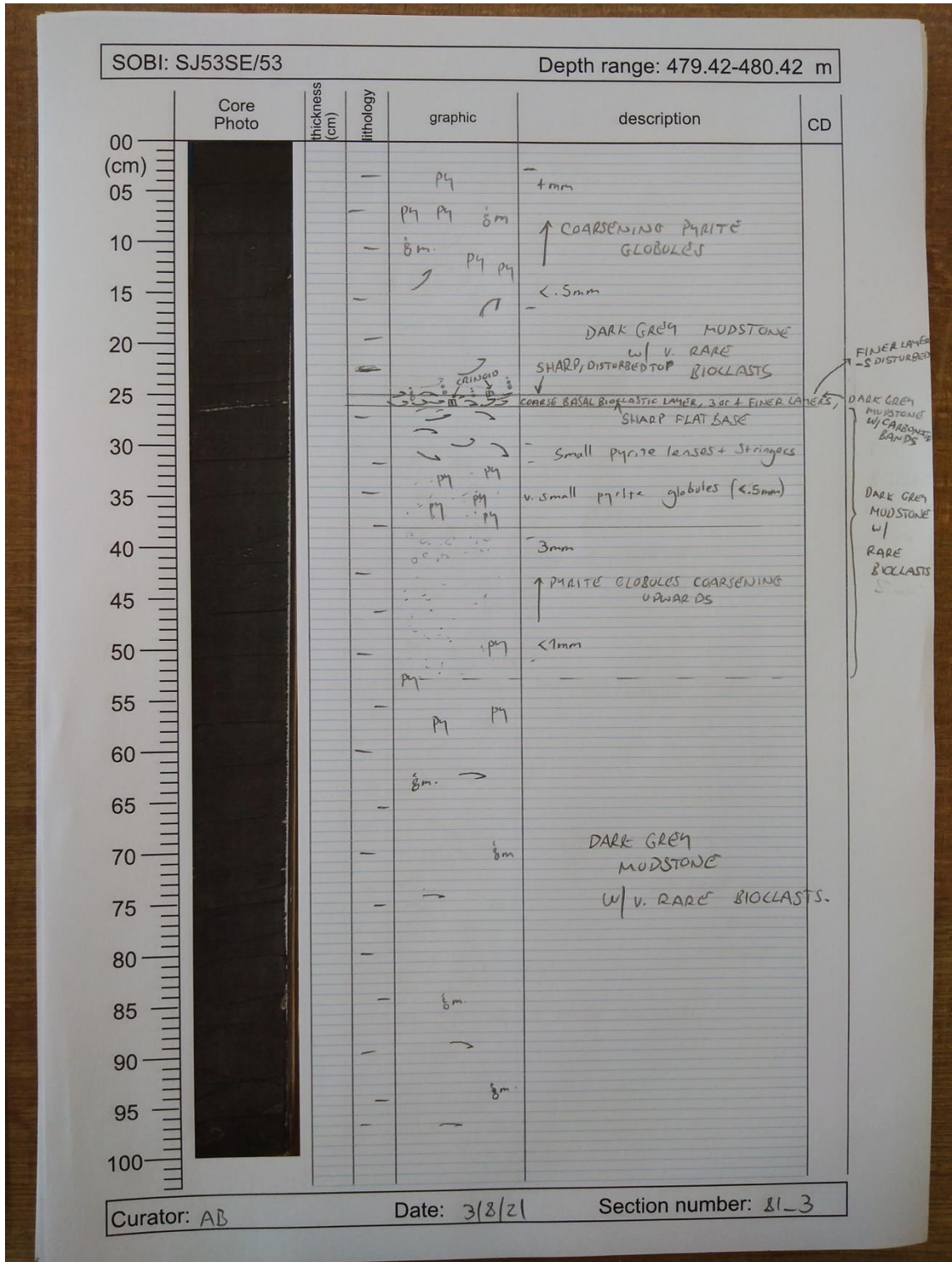
Quantifying marine redox across the Triassic–Jurassic mass extinction



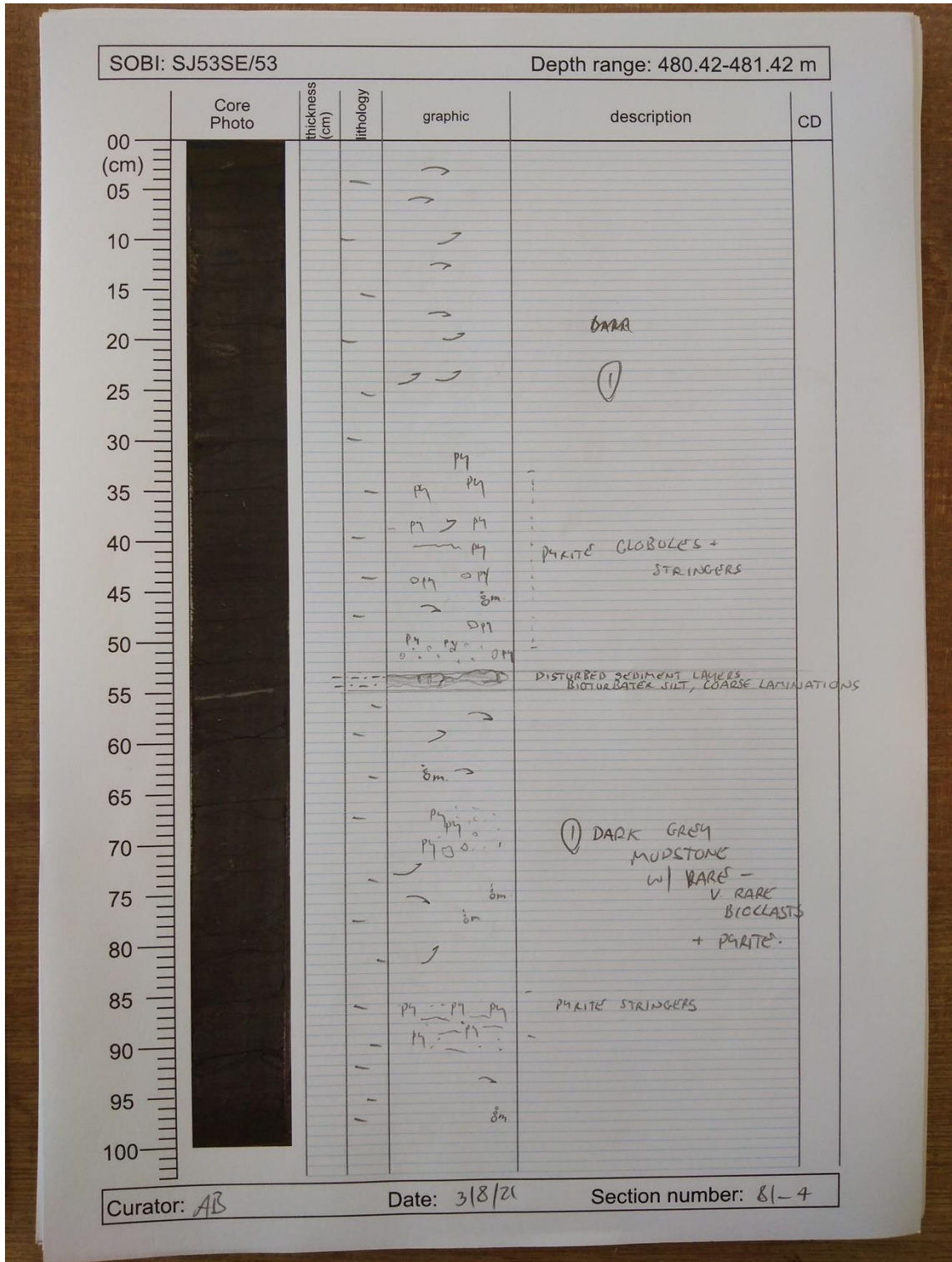
Appendices



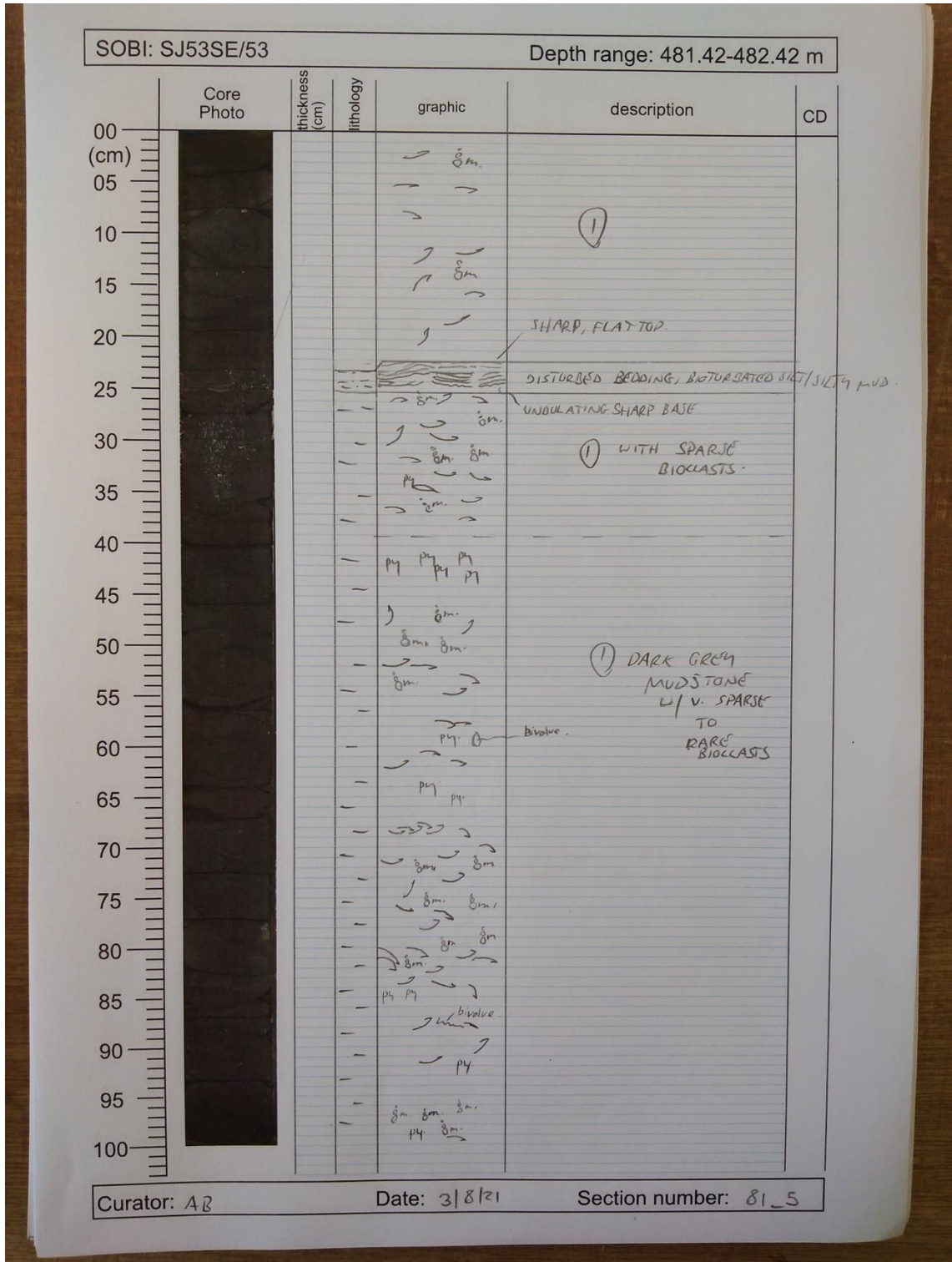
Quantifying marine redox across the Triassic–Jurassic mass extinction



Appendices



Quantifying marine redox across the Triassic–Jurassic mass extinction



Appendices

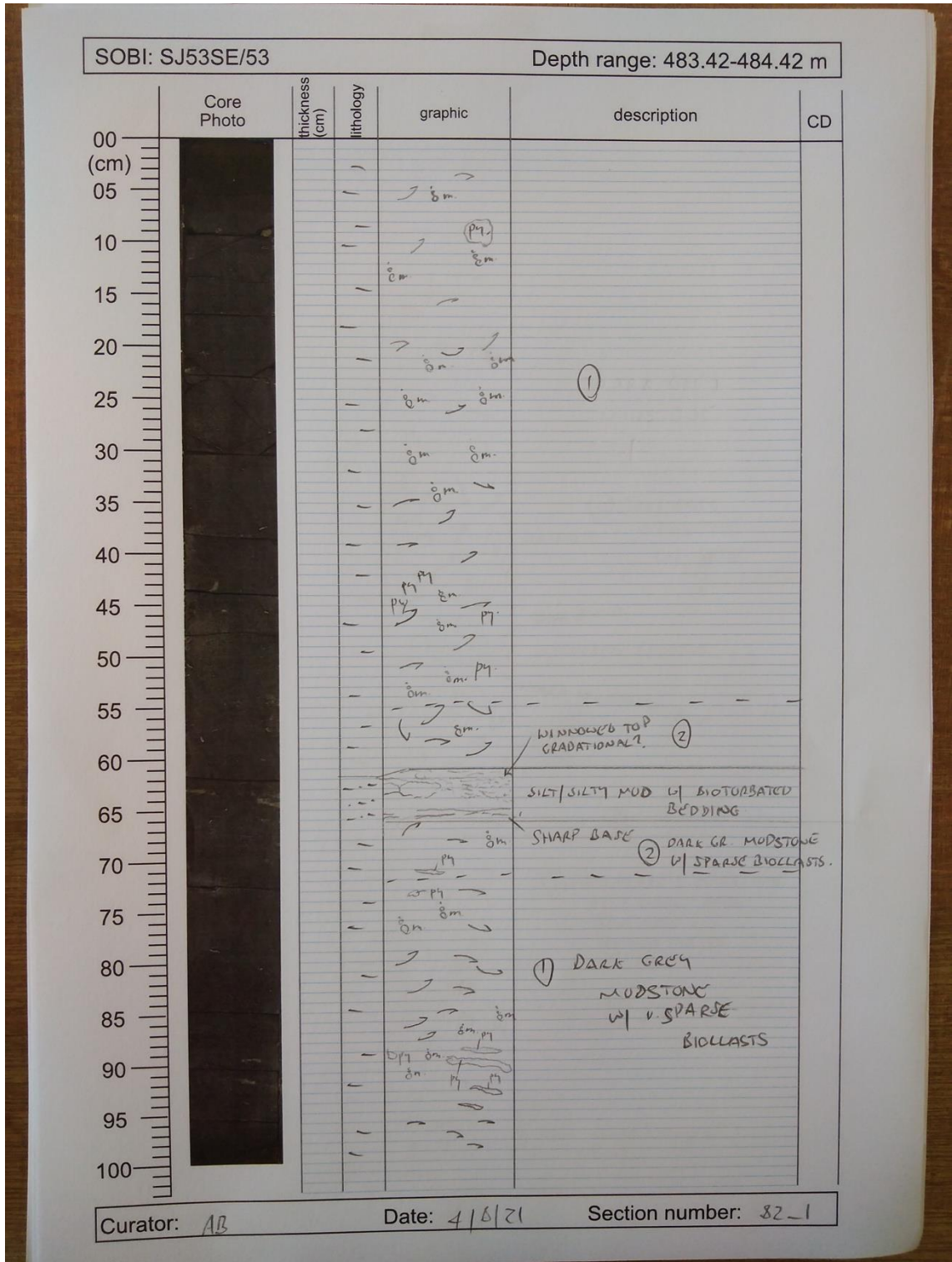
SOBI: SJ53SE/53		Depth range: 482.42-483.42 m				
Core Photo	thickness (cm)	lithology	graphic	description	CD	
	00					
	05			② DARK GREY MUDSTONE w/ SPARSE-V. SPARSE BIOCLASTS.		
	10			①		
	15					
	20					
	25					
	30				②	
	35				①	
	40					
	45				DARK GREY MUDSTONE w/ SPARSE BIOCLASTS.	
50						
55						
60						
65						
70				① DARK GREY MUDSTONE w/ V. SPARSE TO RARE BIOCLASTS		
75						
80						
85						
90						
95						
100						

Curator: AB

Date: 3/8/21

Section number: 81_6

Quantifying marine redox across the Triassic–Jurassic mass extinction



Curator: AB

Date: 4/6/21

Section number: 82-1

Appendices

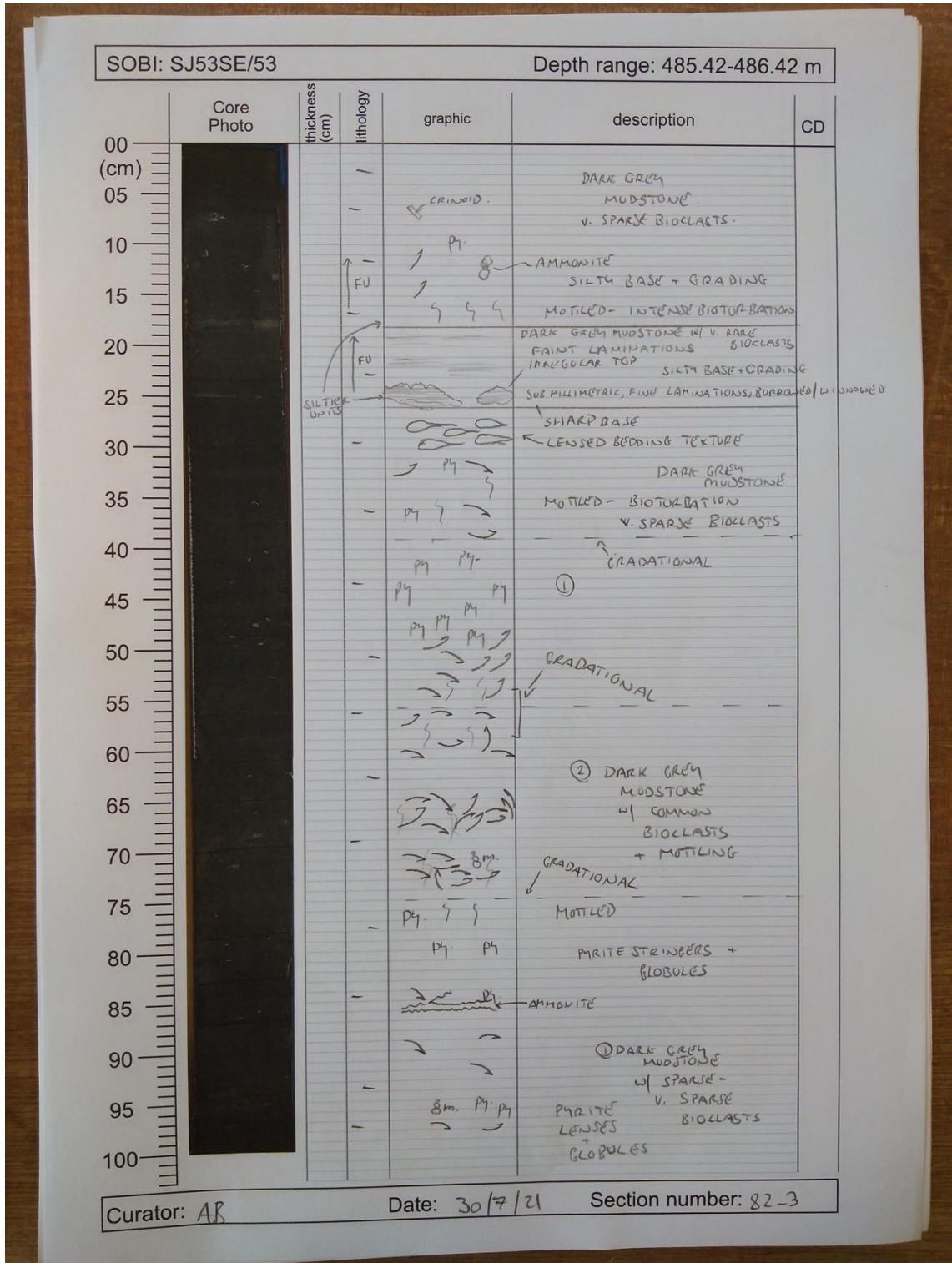
SOBI: SJ53SE/53		Depth range: 484.42-485.42 m				
	Core Photo	thickness (cm)	lithology	graphic	description	CD
00				P ₄ →		
05				→ P ₄		
10				→ P ₄ →		
15				P ₄ →	①	
20				→ P ₄		
25				→		
30				P ₄ P ₄		
35				P ₄ →	②	DARK GREY MUDSTONE
40				P ₄ →	MOTTLING	w/ SPARSE BIOCLASTS
45				P ₄ →	SHARP TOP	
50			P ₄ →	DISTURBED BEDDING		
55			P ₄ →	SHARP, IRREGULAR BASE		
60			P ₄ →	①		
65			P ₄ →	②		
70			P ₄ →	①	DARK GREY MUDSTONE	
75			P ₄ →	w/ V. RARE - RARE BIOCLASTS + COMMON PYRITE		
80			P ₄ →			
85			P ₄ →	Larger Pyrite globules + stringers	2mm+	
90			P ₄ →			
95			P ₄ →	Small globules + stringers	(< 1mm)	
100			P ₄ →			

Curator: AB

Date: 4/8/21

Section number: 82-2

Quantifying marine redox across the Triassic–Jurassic mass extinction



Appendices

SOBI: SJ53SE/53		Depth range: 486.42-487.42 m				
	Core Photo	thickness (cm)	lithology	graphic	description	CD
00	[Core Photo]					
05				p ₄		
10				p ₄		
15				p ₄		DARK GREY MUDSTONE w/ RARE BIOCLASTS
20				p ₄		
25				p ₄		
30				p ₄	p ₄	
35						
40					δ _m	② SPARSE BIOCLASTS
45						
50					δ _m δ _m	① MOTTLING
55					p ₄ p ₄ CRIN.	
60					AMMONITE CRIN.	②
65					δ _m δ _m	① MOTTLING
70					δ _m	② SPARSE BIOCLASTS
75						
80					δ _m δ _m	① MOTTLING
85						② DARK GREY MUDSTONE w/ V. SPARSE BIOCLASTS.
90						
95					py. δ _m	① DARK GREY MUDSTONE w/ COMMON BIOCLASTS
100				DISTURBED BEDDING		

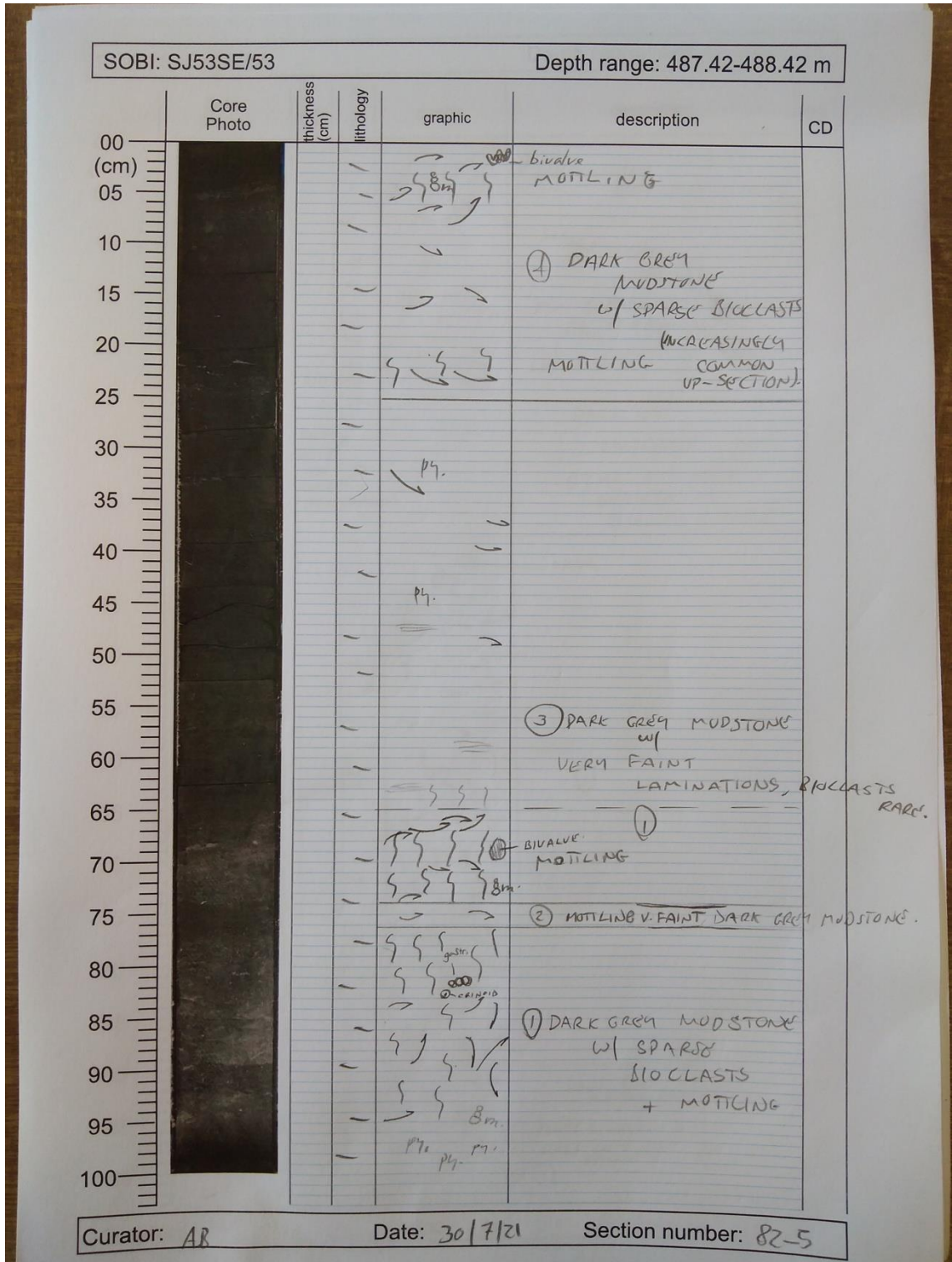
/ - GRADAT
 / - IONAL
 / - SHARP

Curator: AB

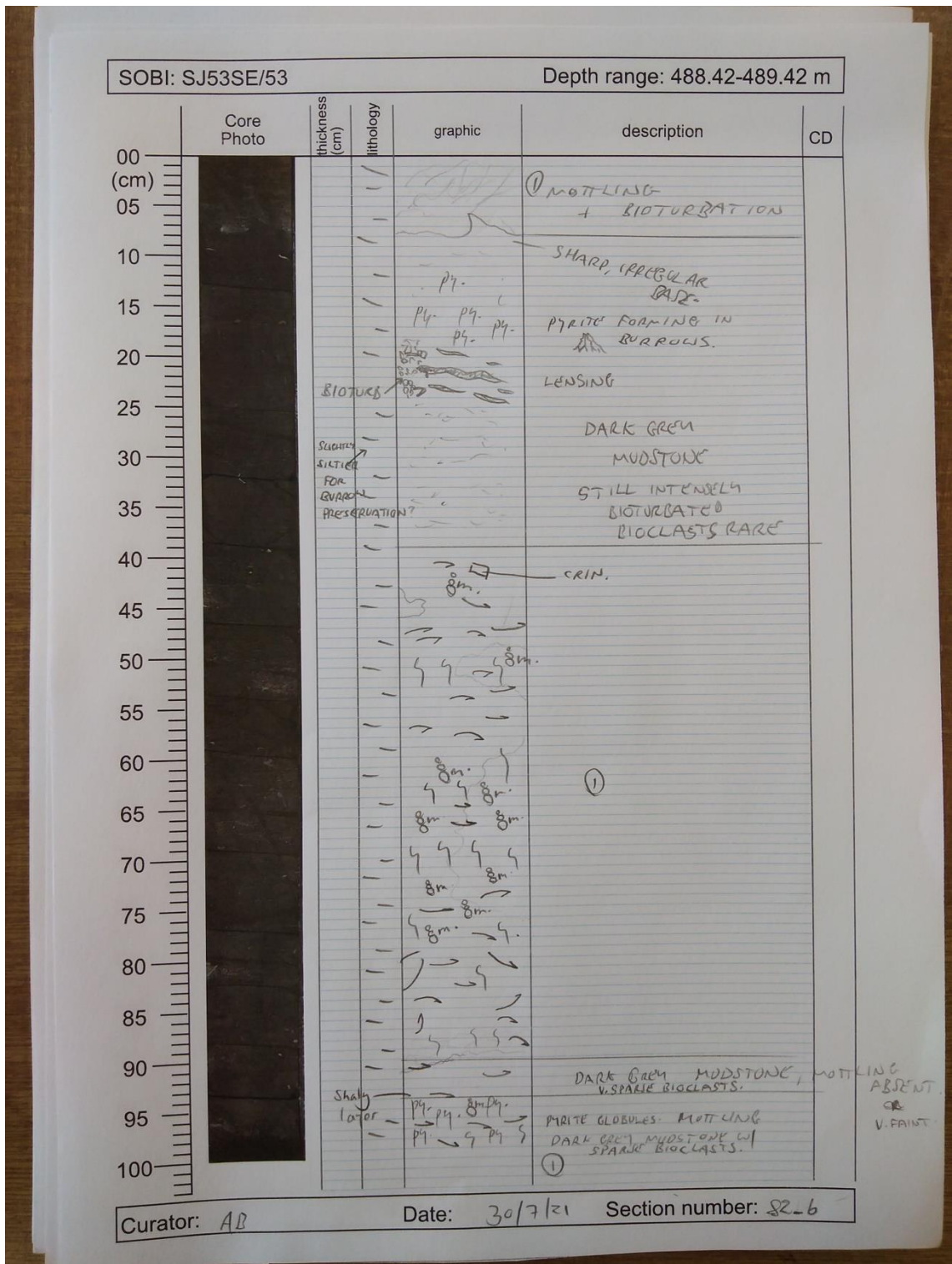
Date: 30/7/21

Section number: 82-4

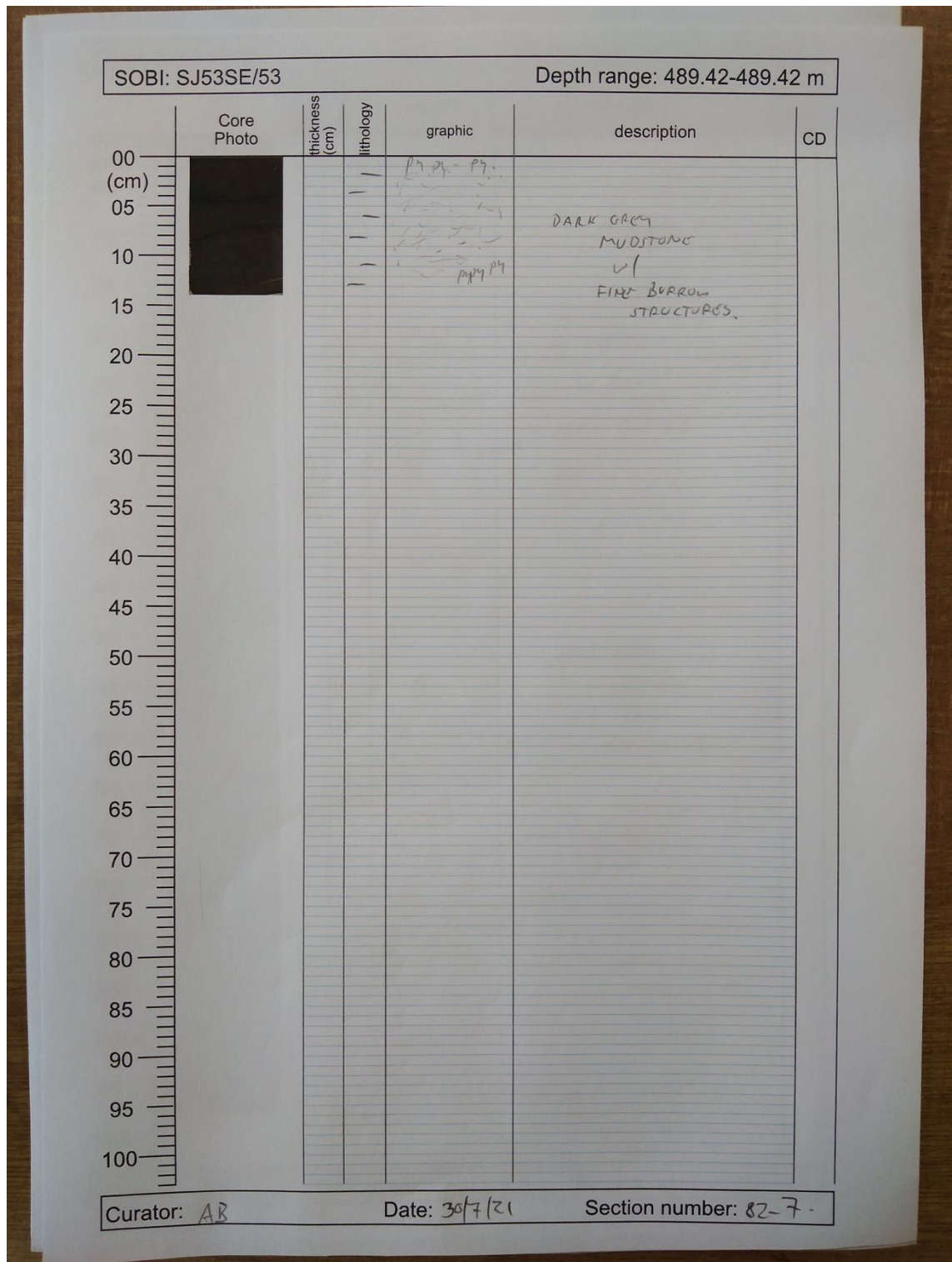
Quantifying marine redox across the Triassic–Jurassic mass extinction



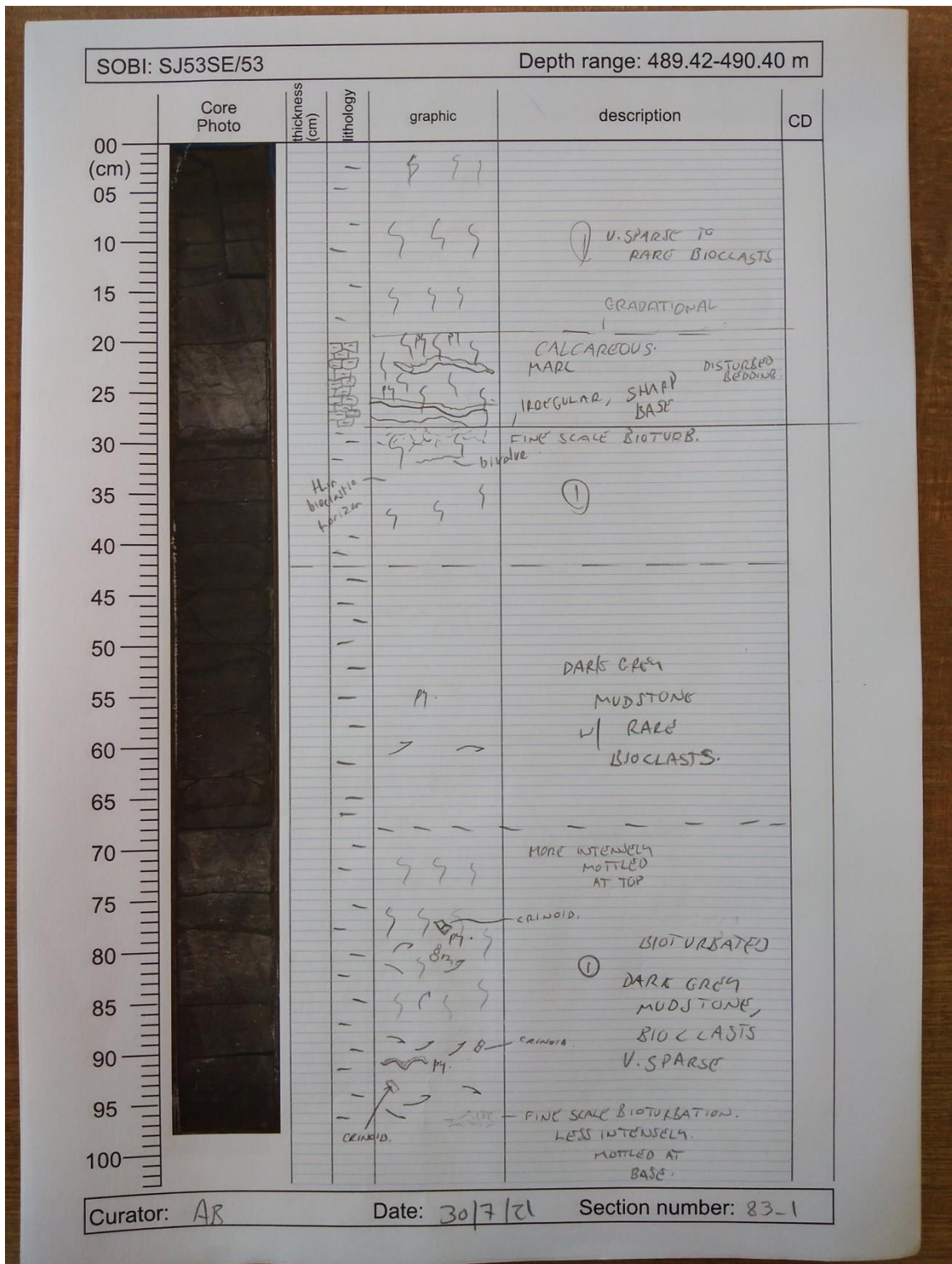
Appendices



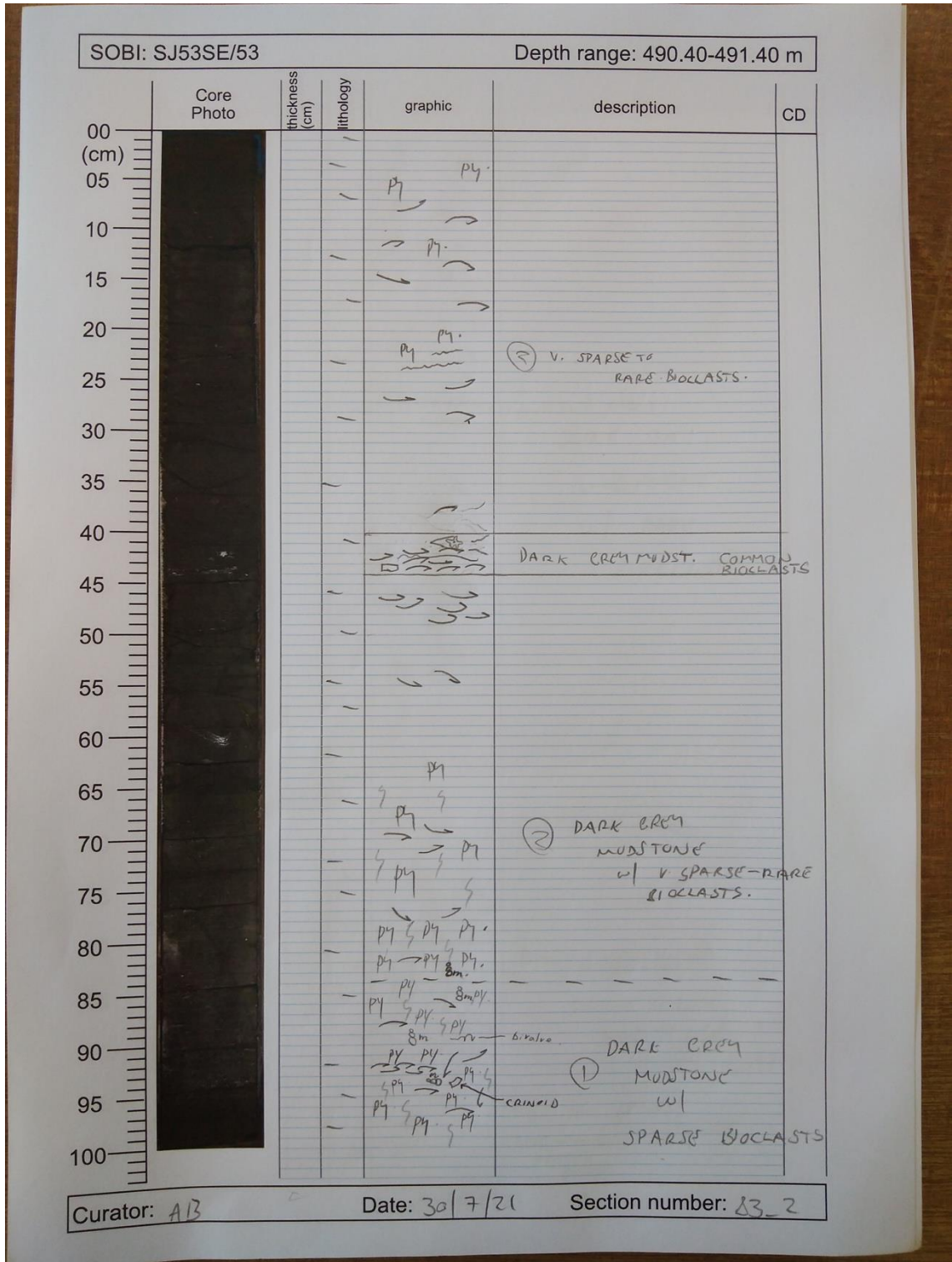
Quantifying marine redox across the Triassic–Jurassic mass extinction



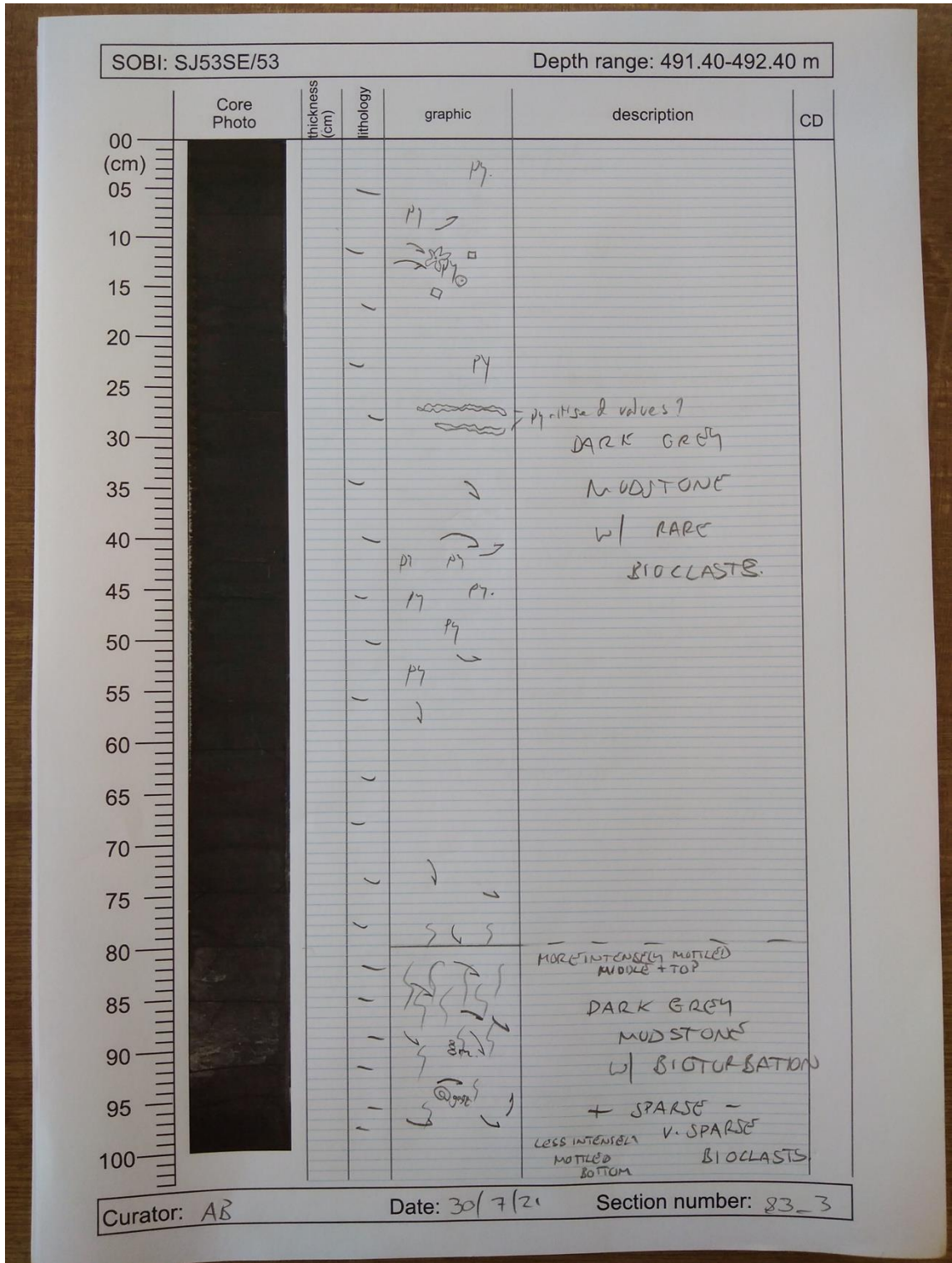
Appendices



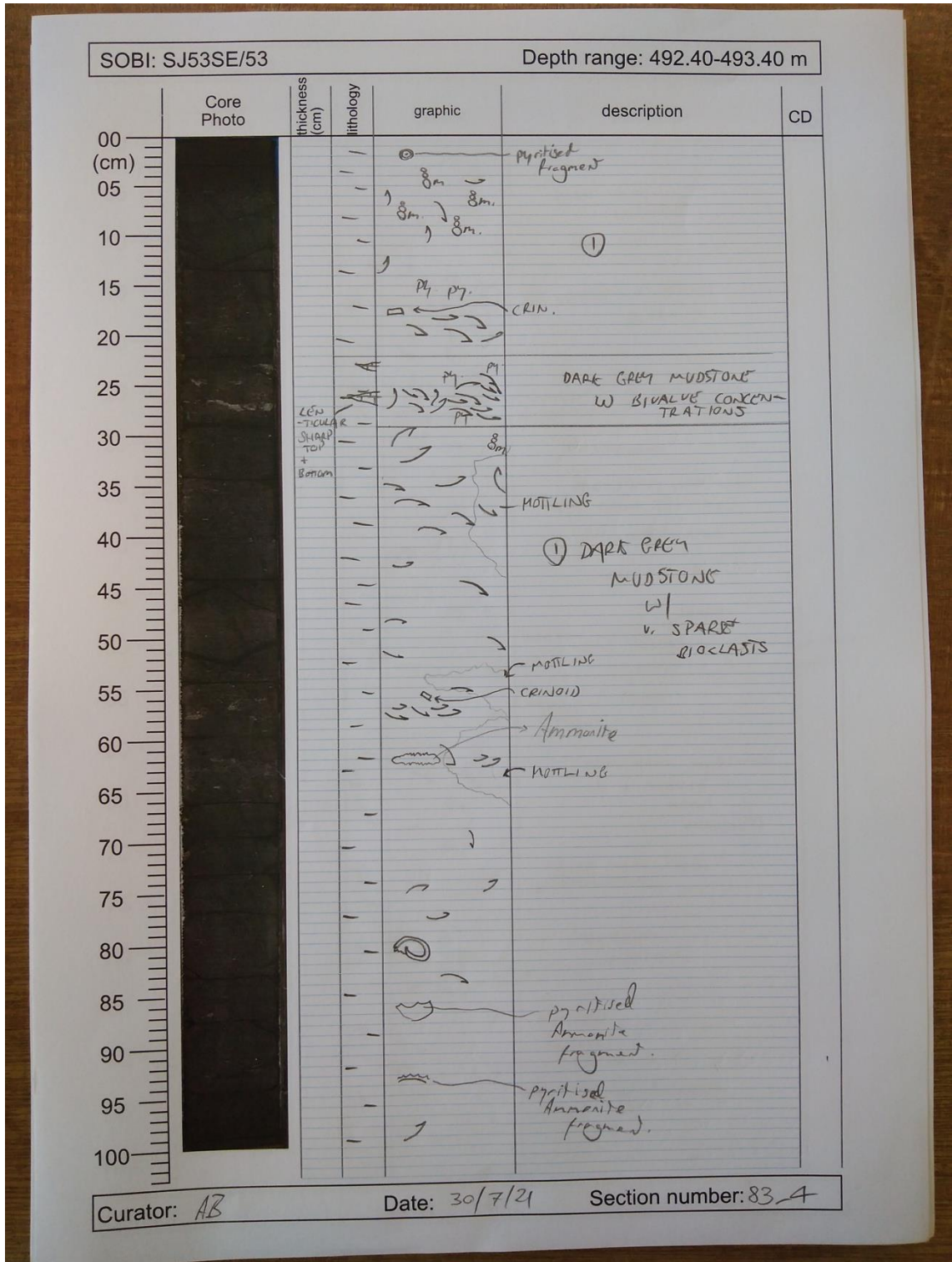
Quantifying marine redox across the Triassic–Jurassic mass extinction



Appendices



Quantifying marine redox across the Triassic–Jurassic mass extinction



Appendices

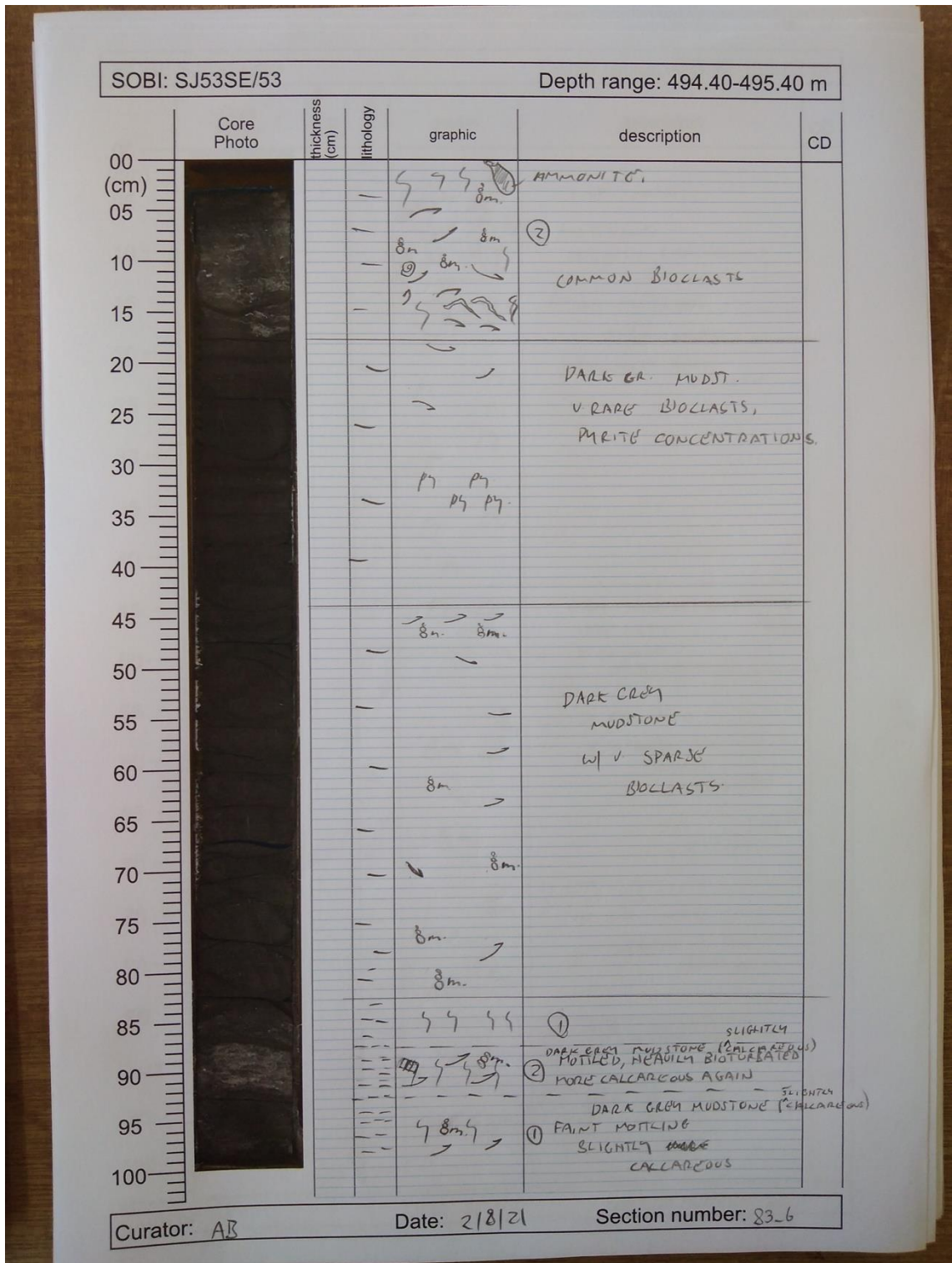
SOBI: SJ53SE/53		Depth range: 493.40-494.40 m				
Core Photo	thickness (cm)	lithology	graphic	description	CD	
	00					
	05			DARK GREY MUDSTONE		
	10			MOTTLED		
	15			SPARSE - V. SPARSE BIOLASTS		
	20					
	25			AMMONITE		
	30			AMMONITE		
	35			GRADATIONAL		
	40			DARK GREY MUDSTONE		
	45			VERY FAINT TEXTURES		
	50			(INDISCERNABLE)		
	55			RARE BIOLASTS		
	60			SHARP		
	65			DARK GREY MUDSTONE		
	70			FAINT LAMINATIONS V. RARE BIOLASTS		
75			SHARP			
80			CONOID ASSICLE.			
85			DARK GREY MUDSTONE			
90			V. SPARSE TO RARE BIOLASTS			
95			FAINT MOTTLED GRADATIONAL			
100			DARK GREY MUDSTONE			
			MOTTLED			
			HEAVILY BICTURBATED			
			SPARSE - V. SPARSE BIOLASTS			

Curator: AB

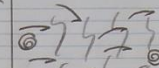
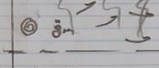
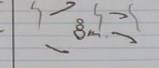
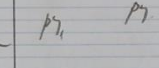
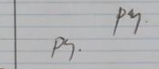
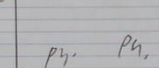
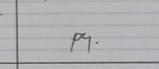
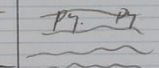
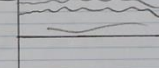
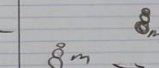
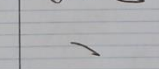
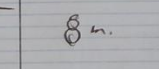
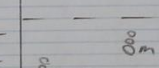
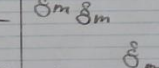
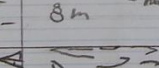
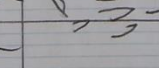
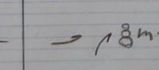
Date: 21/8/21

Section number: 83_5

Quantifying marine redox across the Triassic–Jurassic mass extinction



Appendices

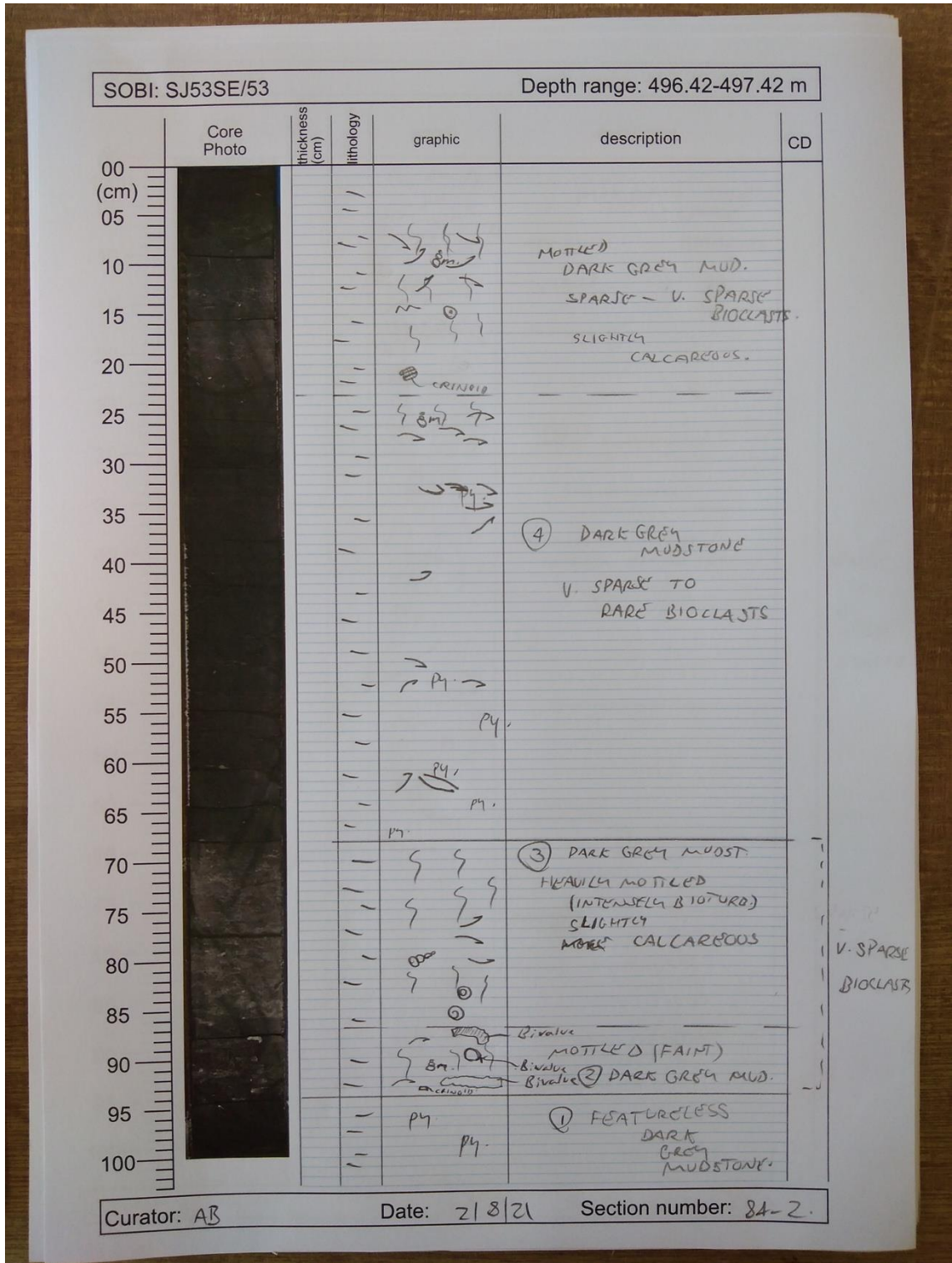
SOBI: SJ53SE/53		Depth range: 495.42-496.42 m				
	Core Photo	thickness (cm)	lithology	graphic	description	CD
00					D. GR. MUDST.	
05					MOTTLING SLIGHTLY CALCAREOUS	
10						
15					FAINT MOTTLING	
20					D. GR. MUDST.	
25					BIOLASTS RARE - V. RARE	
30						
35						
40						
45						
50					WAVE LAMINATIONS - SUB-CENTIMETRIC MORE SILTY	
55					D. GR. MUD	
60					V. SPARSE TO RARE BIOLASTS	
65						
70						
75					D. GR. MUD.	
80					SPARSE - V. SPARSE BIOLASTS	
85						
90					D. GR. MUDST. COMMON BIOLASTS	
95					SPARSE - V. SPARSE BIOLASTS - DARK GR. MUDST.	
100					FAINT MOTTLING	

Curator: AB

Date: 2/8/21

Section number: 84-1

Quantifying marine redox across the Triassic–Jurassic mass extinction



Appendices

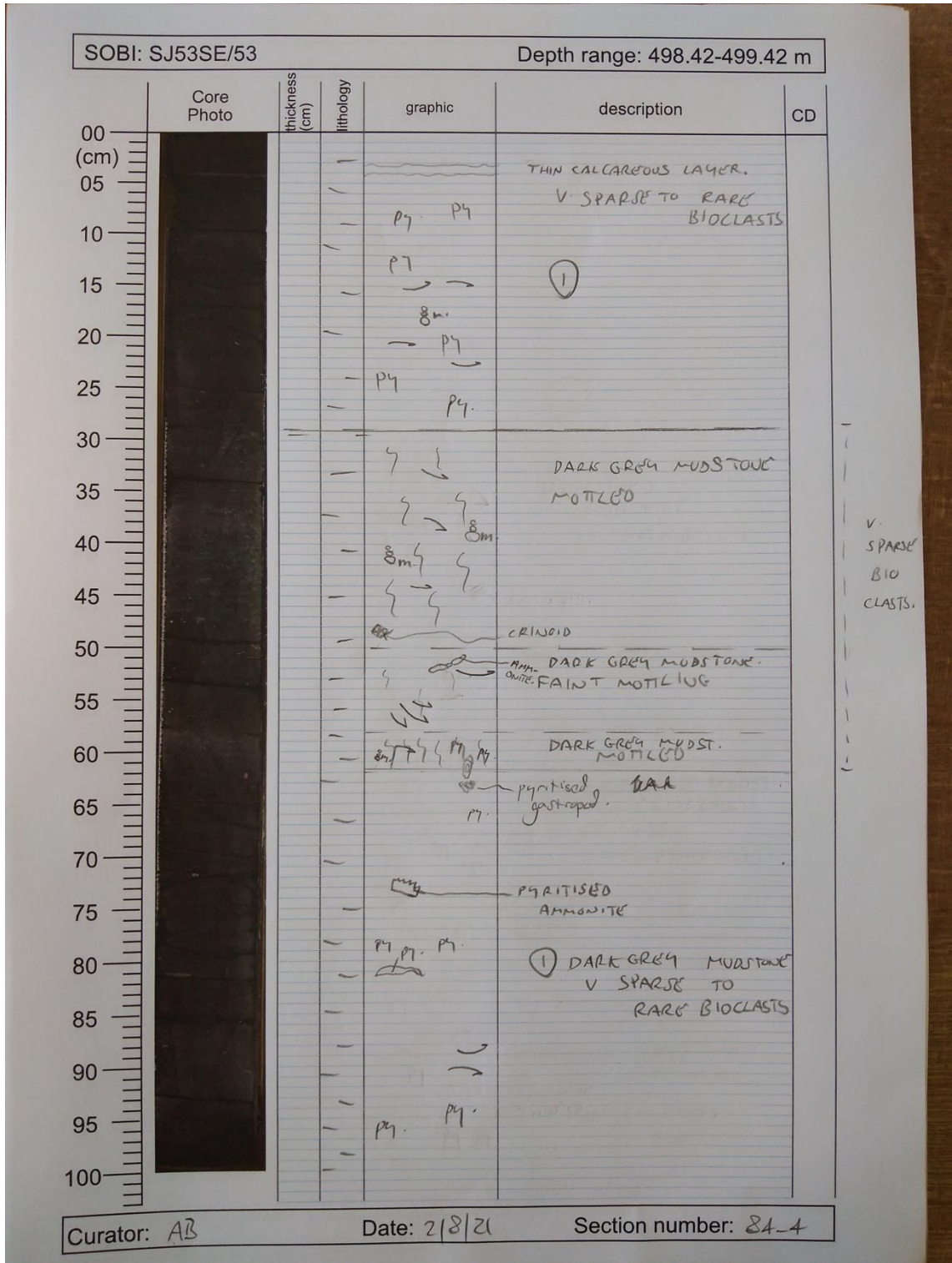
SOBI: SJ53SE/53		Depth range: 497.42-498.42 m					
	Core Photo	thickness (cm)	lithology	graphic	description	CD	
00	[Core Photo]			P4 P4 P4			
05					DARK GRAY MUDST. w/ SPARSE		
10					AMMONITE	BIOCLASTS.	
15					pyritised.		
20					AMMONITE.		
25							
30					MASSIVE LIMESTONE		
35					CRADATIONAL.		
40					8m	CALCAREOUS MUDST. HEAVILY BIOTURBATED.	SPARSE TO V. SPARSE BIOCLAST
45							
50							
55							
60					P4		
65					bivalve	pyritised AMMONITE.	①
70					bivalve		
75						pyritised BUREAU.	
80						V. FAINT MOTTLING.	
85							
90					P4 P4 P4	② DARK GRAY MUDSTONE. FAINT MOTTLING	
95					P4 P4	① DARK GR. MUDSTONE	
100					P4 P4		

Curator: AB

Date: 2/8/21

Section number: 84_3

Quantifying marine redox across the Triassic–Jurassic mass extinction



Appendices

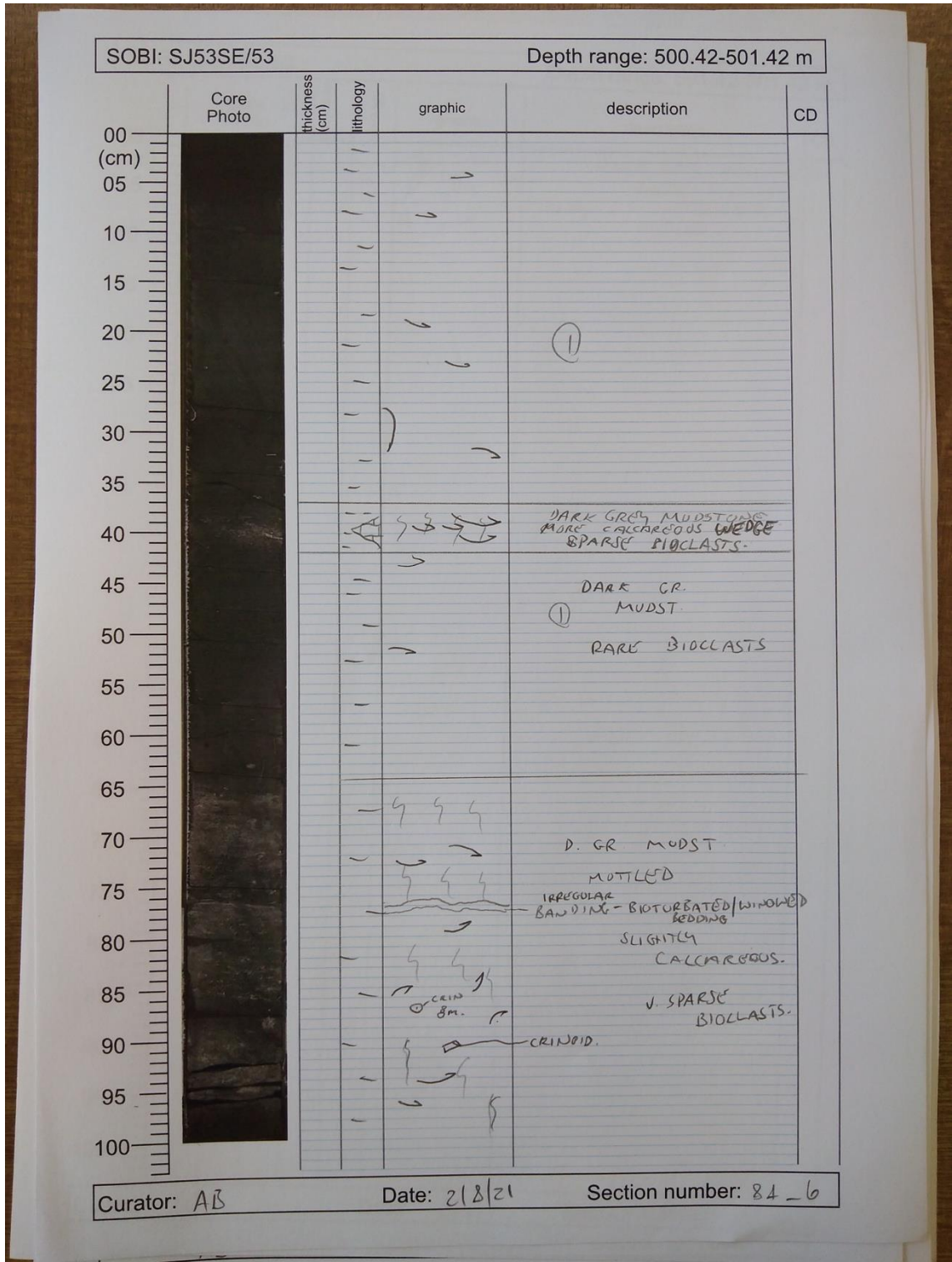
SOBI: SJ53SE/53		Depth range: 499.42-500.42 m			
Core Photo	thickness (cm)	lithology	graphic	description	CD
	00		p4 p4.		
	05				
	10				
	15				
	20			p4. p4.	
	25				③
	30				
	35			pyrite. p4.	
	40			p4.	
	45				
50			p4.	SLIGHTLY CALCAREOUS	
55					
60				② CALCAREOUS MARL MARLY LIMESTONE. V. RARE BIOCLASTS.	
65					
70			p4. p4. p4. p4.	③ D. GR. MUDST. RARE BIOCLASTS.	
75			p4. p4.	② CALCAREOUS PYRITISED MARL MUDDY AMMONITE. CARBONATE RARE BIOCLASTS.	
80					
85			p4.	① DARK GREY MUDSTONE V. SPARSE-RARE TO RARE BIOCLASTS.	
90					
95			p4. p4.	MOST BIOCLASTS PYRITISED	
100					

Curator: AB


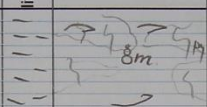
Date: 2/8/21

Section number: 84-5

Quantifying marine redox across the Triassic–Jurassic mass extinction

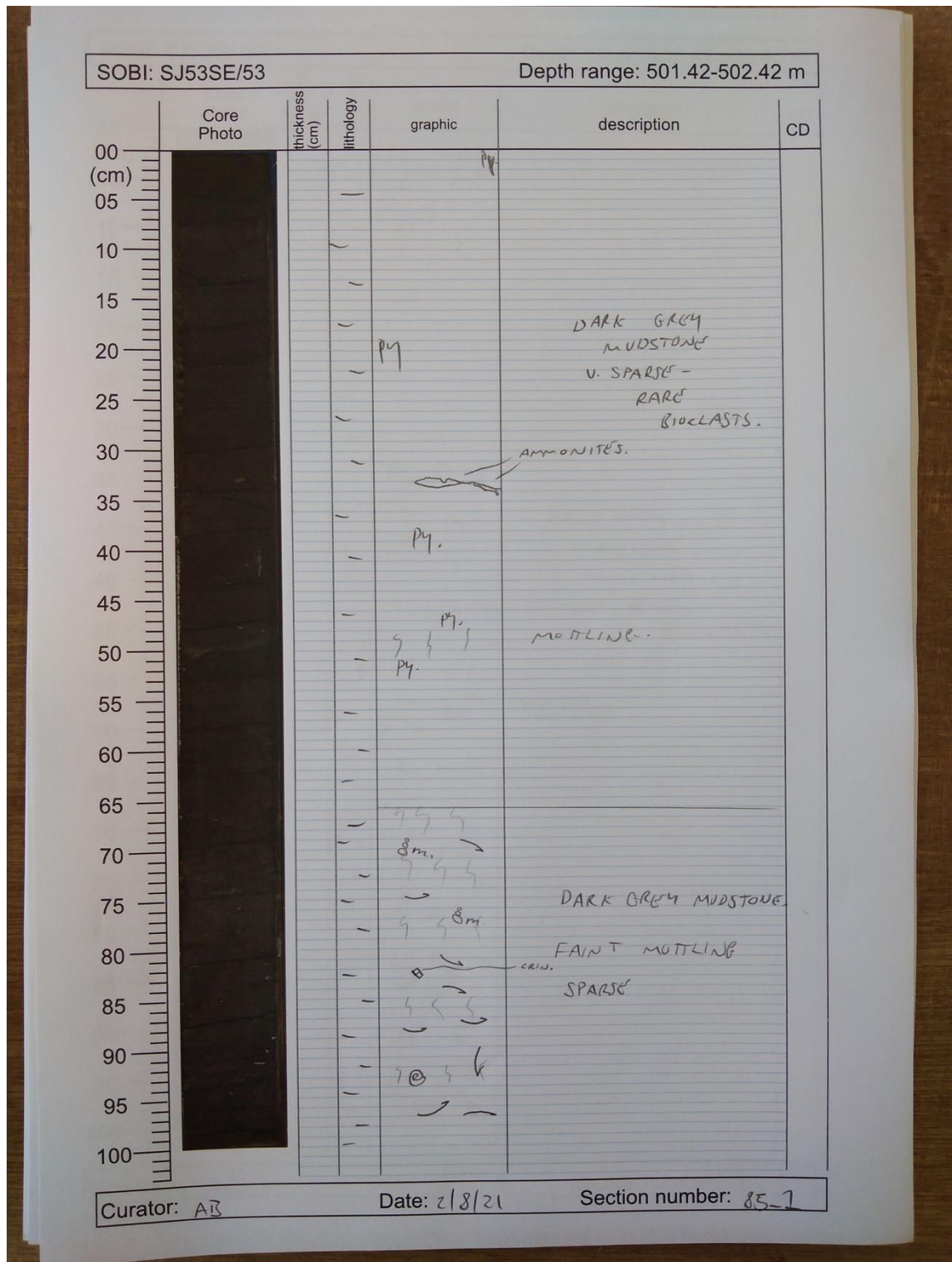


Appendices

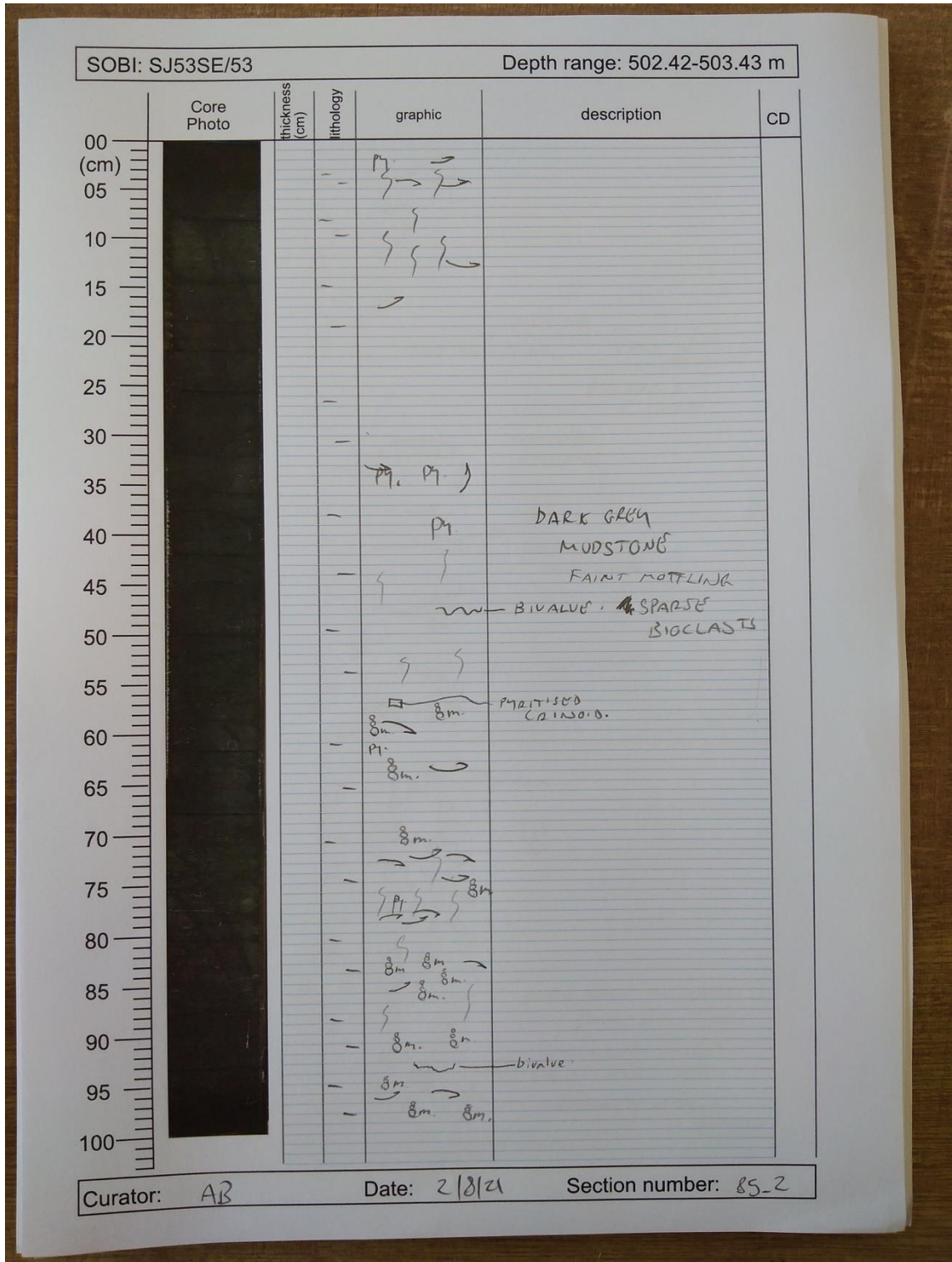
SOBI: SJ53SE/53		Depth range: 501.42-501.42 m				
Core Photo	thickness (cm)	lithology	graphic	description	CD	
	00					
	05				DARK GREY MUDSTONE. RARE - V. RARE BIOCLASTS. MOTTLING	
	10					
	15					
	20					
	25					
	30					
	35					
	40					
	45					
	50					
	55					
	60					
	65					
	70					
	75					
	80					
	85					
	90					
	95					
	100					

Curator: AB Date: 2/8/21 Section number: 847

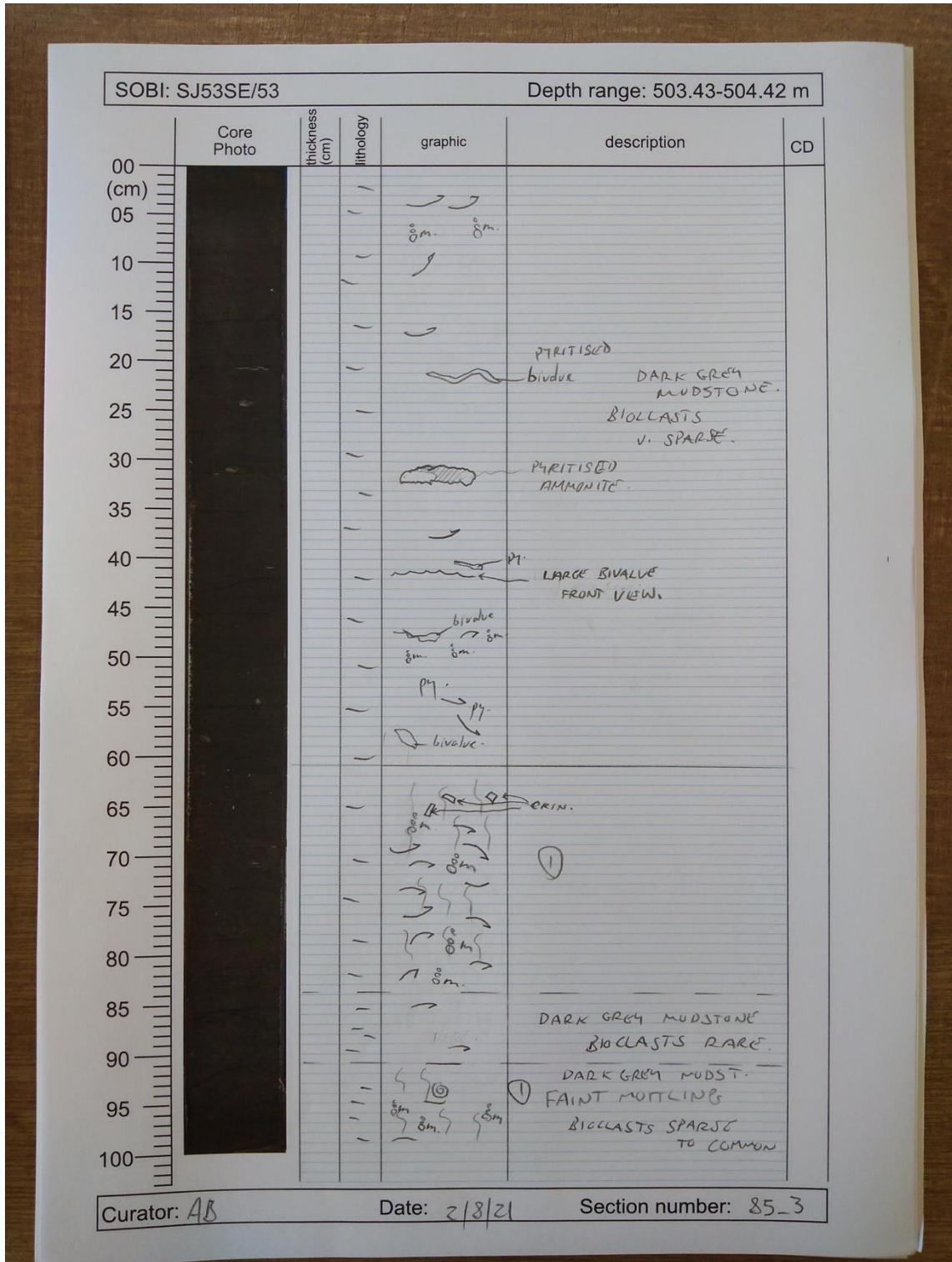
Quantifying marine redox across the Triassic–Jurassic mass extinction



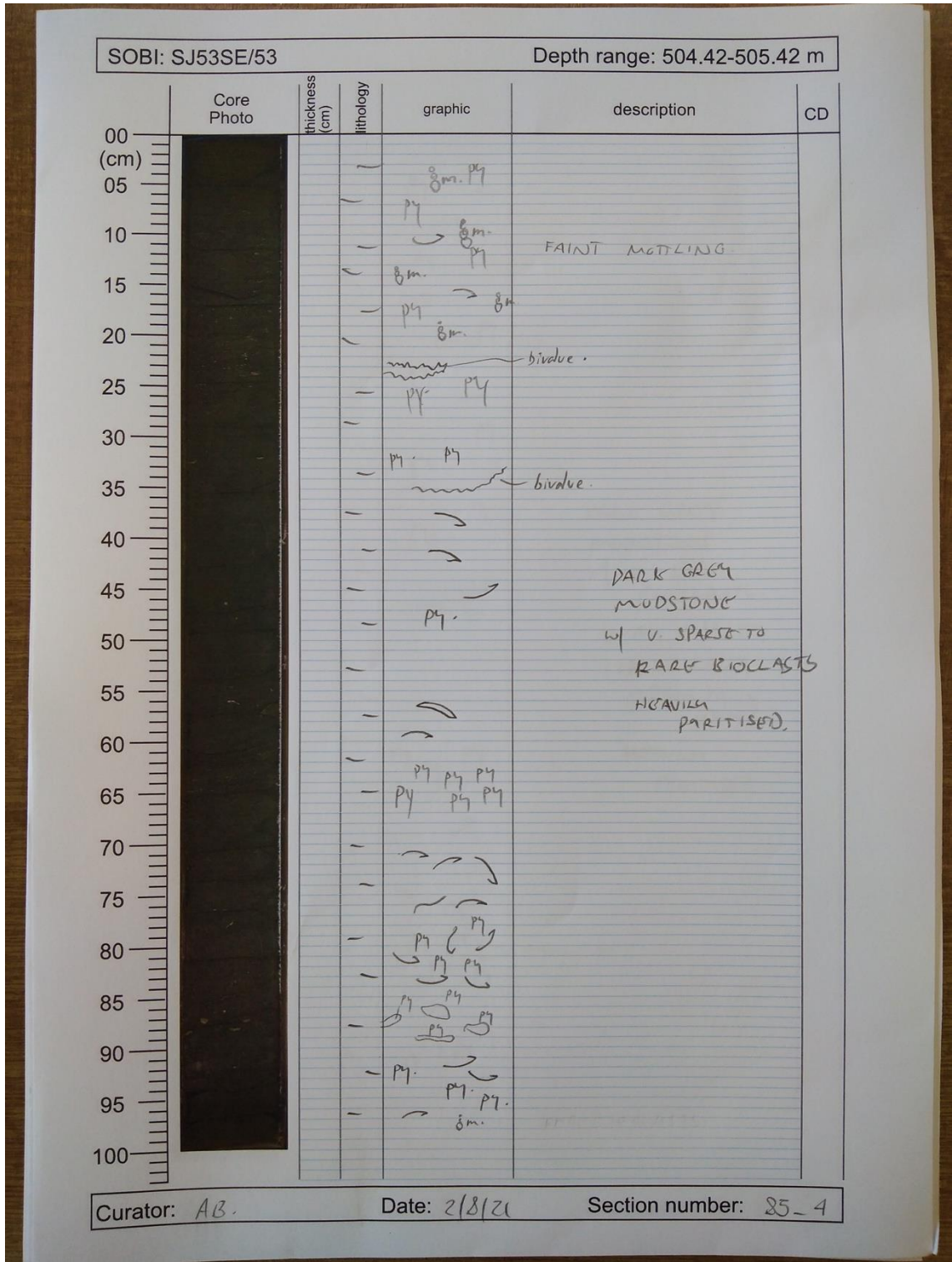
Appendices



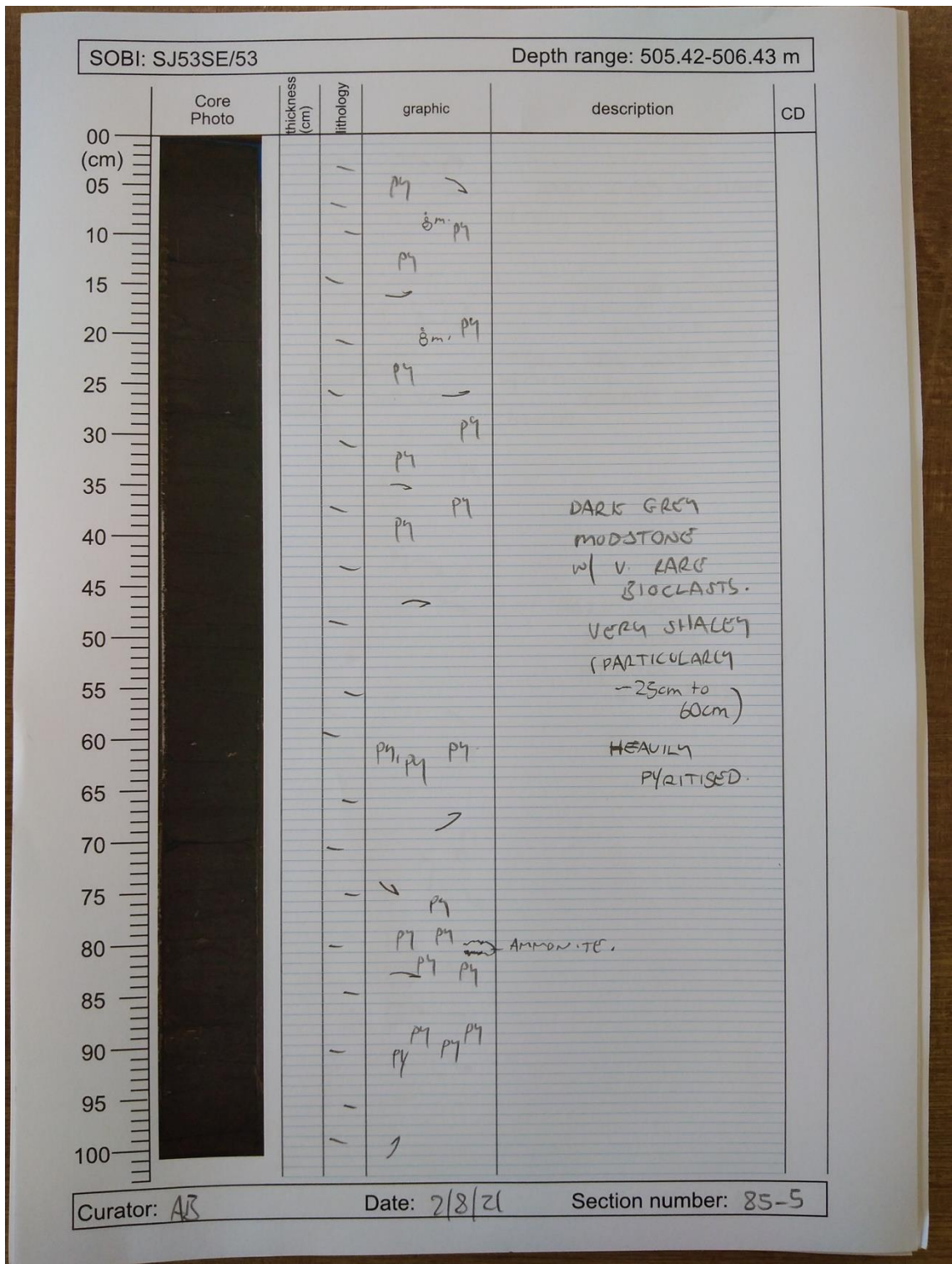
Quantifying marine redox across the Triassic–Jurassic mass extinction



Appendices



Quantifying marine redox across the Triassic–Jurassic mass extinction



Appendices

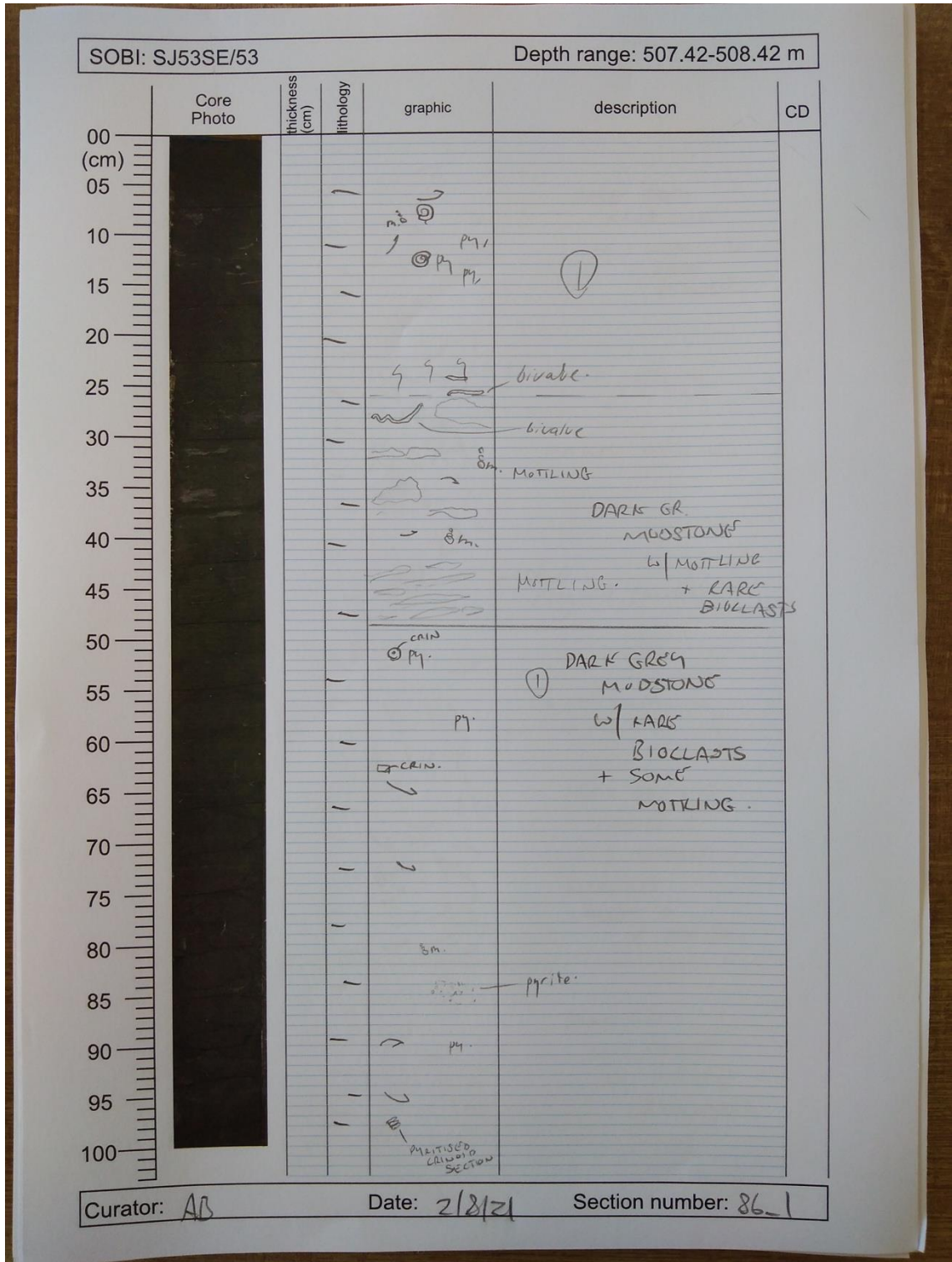
SOBI: SJ53SE/53		Depth range: 506.43-507.44 m				
Core Photo	thickness (cm)	lithology	graphic	description	CD	
	00					
	05		py.	DARK GREY MUDSTONE		
	10		py.	w/ FAINT MOTTLING		
	15		py.	DARK GREY MUDSTONE		
	20		py.	v. FAINT TO FAINT MOTTLING.		
	25		py.	DARK GREY MUDSTONE		
	30		py.	w/ MOTTLING		
	35		py.	BIOLLAISTS RARE		
	40		py.	bivalve.		
	45		py.			
	50		py.	DARK GREY MUDSTONE		
	55		py.	w/ RARE BIOLLAISTS		
	60		py.			
	65		py.			
	70		py.			
	75		py.			
80		py.				
85		py.				
90		py.				
95		py.				
100		py.				

Curator: AB

Date: 2/8/21

Section number: 85-6

Quantifying marine redox across the Triassic–Jurassic mass extinction



Appendices

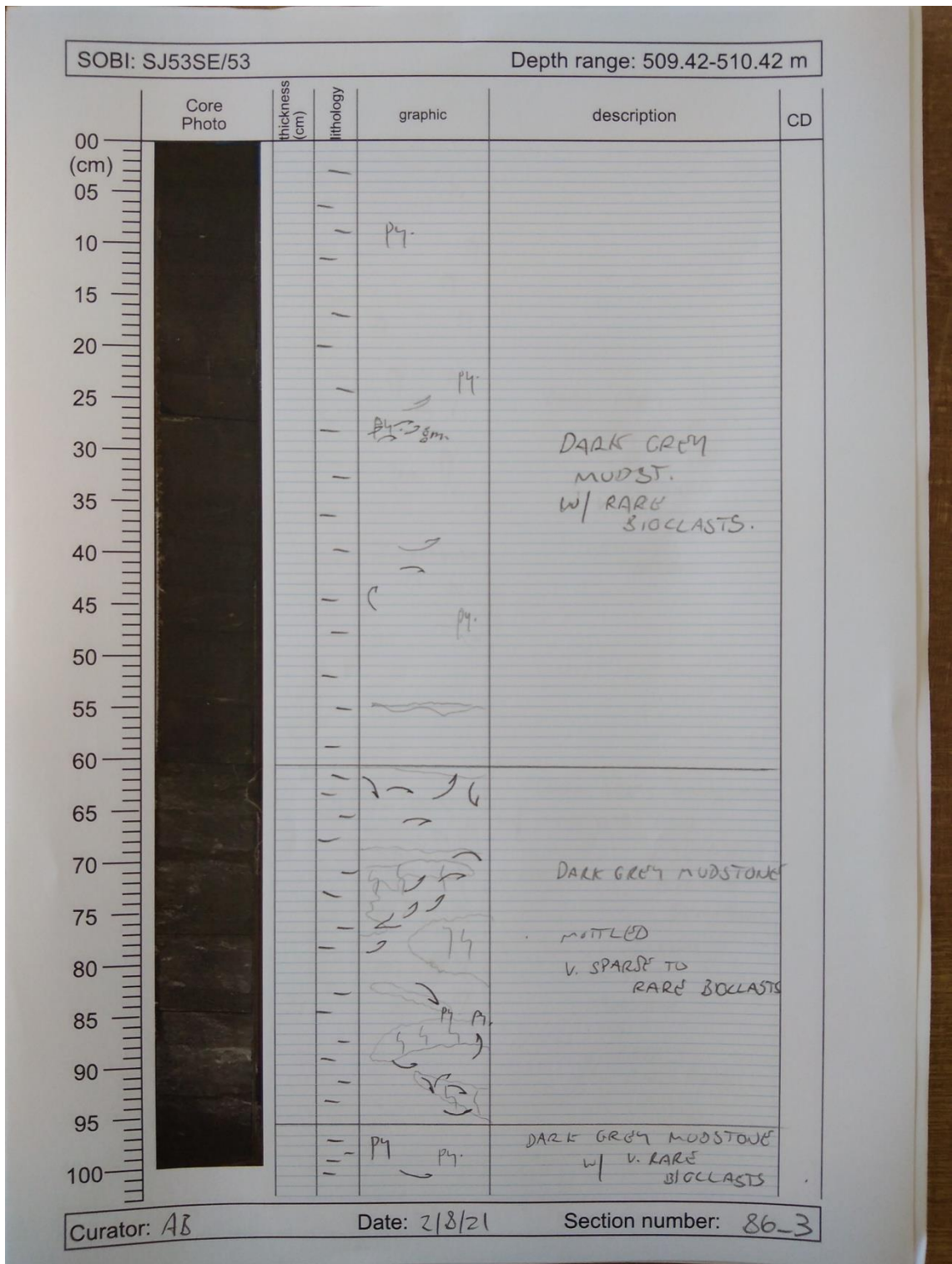
SOBI: SJ53SE/53		Depth range: 508.42-509.42 m				
Core Photo	thickness (cm)	lithology	graphic	description	CD	
	00	-	-	-	-	
	05	-	-	-	DARK GREY MUDSTONE	
	10	-	-	-	w/ v. SPARSE TO RARE BIOCLASTS	
	15	-	-	-		
	20	-	-	-		
	25	-	-	gm	FAINT MOTTLING	
	30	-	-	gm	FAINT MOTTLING.	
	35	-	-	gm		
	40	-	-	gm		
	45	-	-	Shell fragment (bivalve).		
50	-	-	-			
55	-	-	-	FAINT MOTTLING		
60	-	-	-			
65	-	-	gm	DARK GREY MUDSTONE		
70	-	-	gm	w/ MOTTLING.		
75	-	-	gm	BIOCLAST SPARSE TO		
80	-	-	gm	✓ SPARSE.		
85	-	-	-			
90	-	-	-	DARK GREY MUDSTONE		
95	-	-	gm	w/ v. RARE BIOCLASTS.		
100	-	-	pyc			

Curator: AB

Date: 2/18/21

Section number: 86-2

Quantifying marine redox across the Triassic–Jurassic mass extinction



Appendices

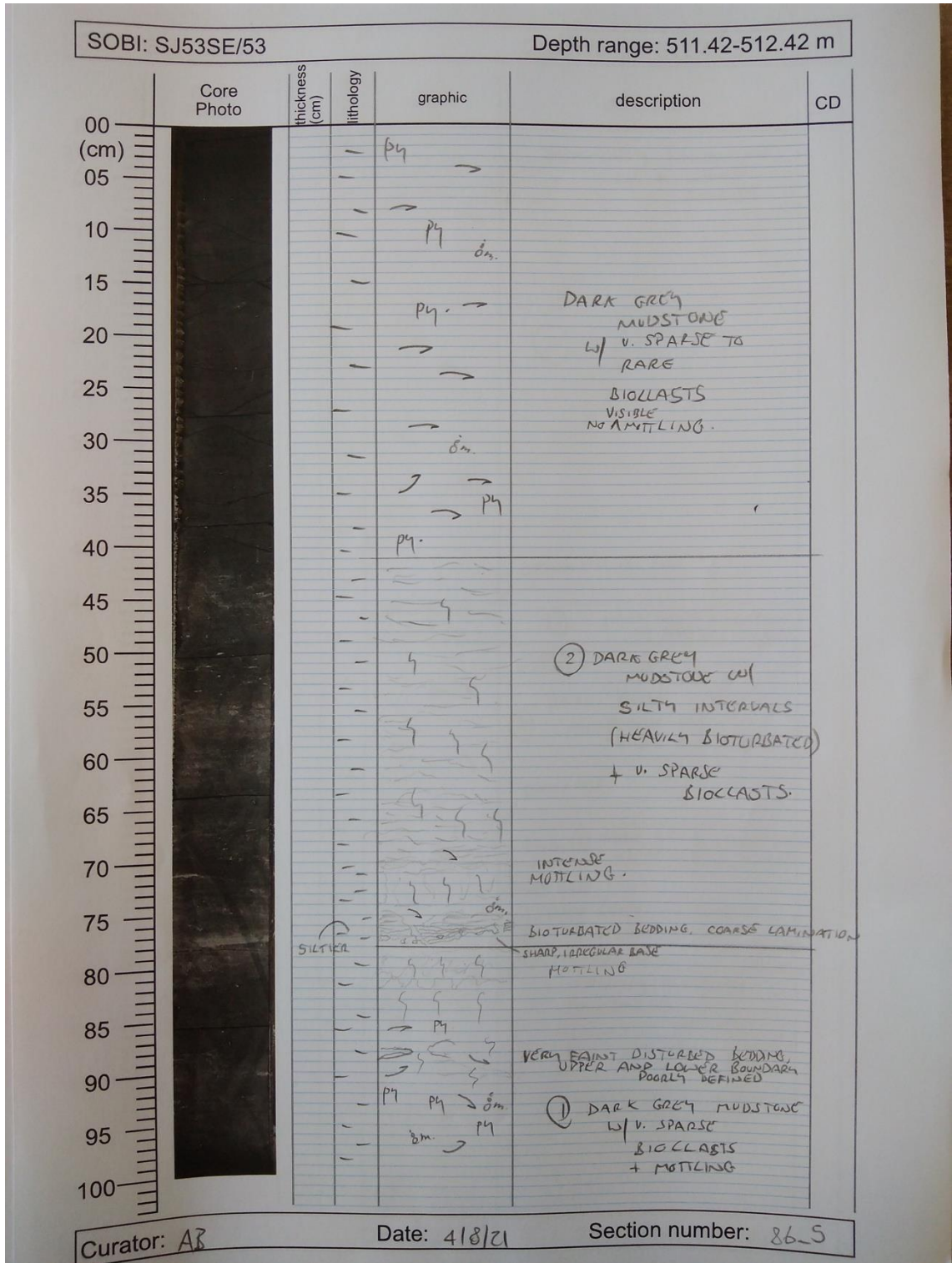
SOBI: SJ53SE/53		Depth range: 510.42-511.42 m				
Core Photo	thickness (cm)	lithology	graphic	description	CD	
	00 (cm)					
	05					
	10					
	15					
	20					
	25				DARK GREY MUDSTONE	
	30				w/ V. RARE BIOCLASTS	
	35				HEAVILY PARTISED.	
	40					
	45					
	50					
	55					
	60					
	65				DARK GREY MUDSTONE w/ MOTTLE AND V. SPARSE TO RARE BIOCLASTS	
	70					
	75					
	80				FAINT MOTTLE DARK GREY MUDSTONE w/ V. RARE BIOCLASTS.	
	85					
	90					
	95					
100						

Curator: AB

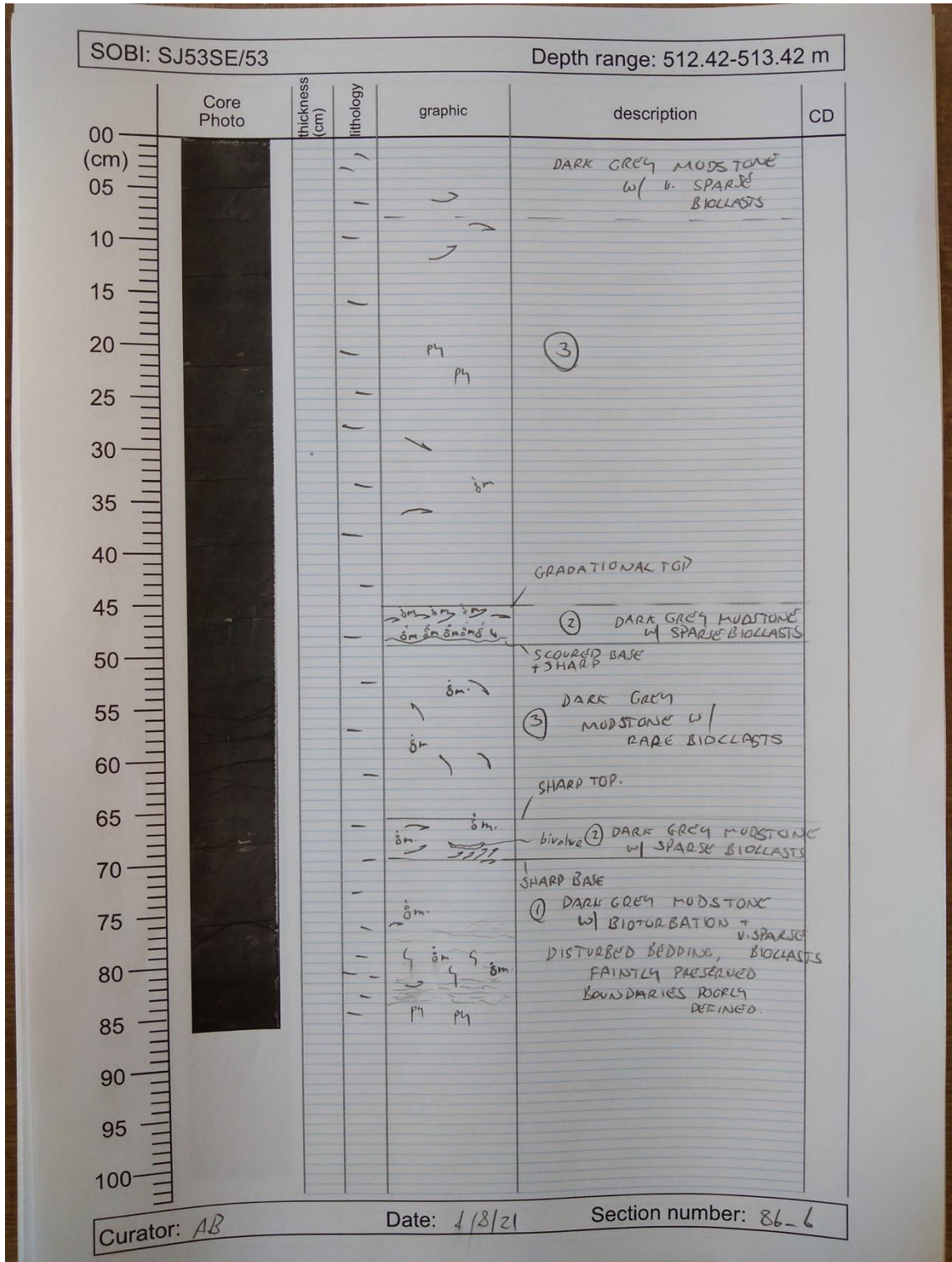
Date: 2/8/21

Section number: 86-4.

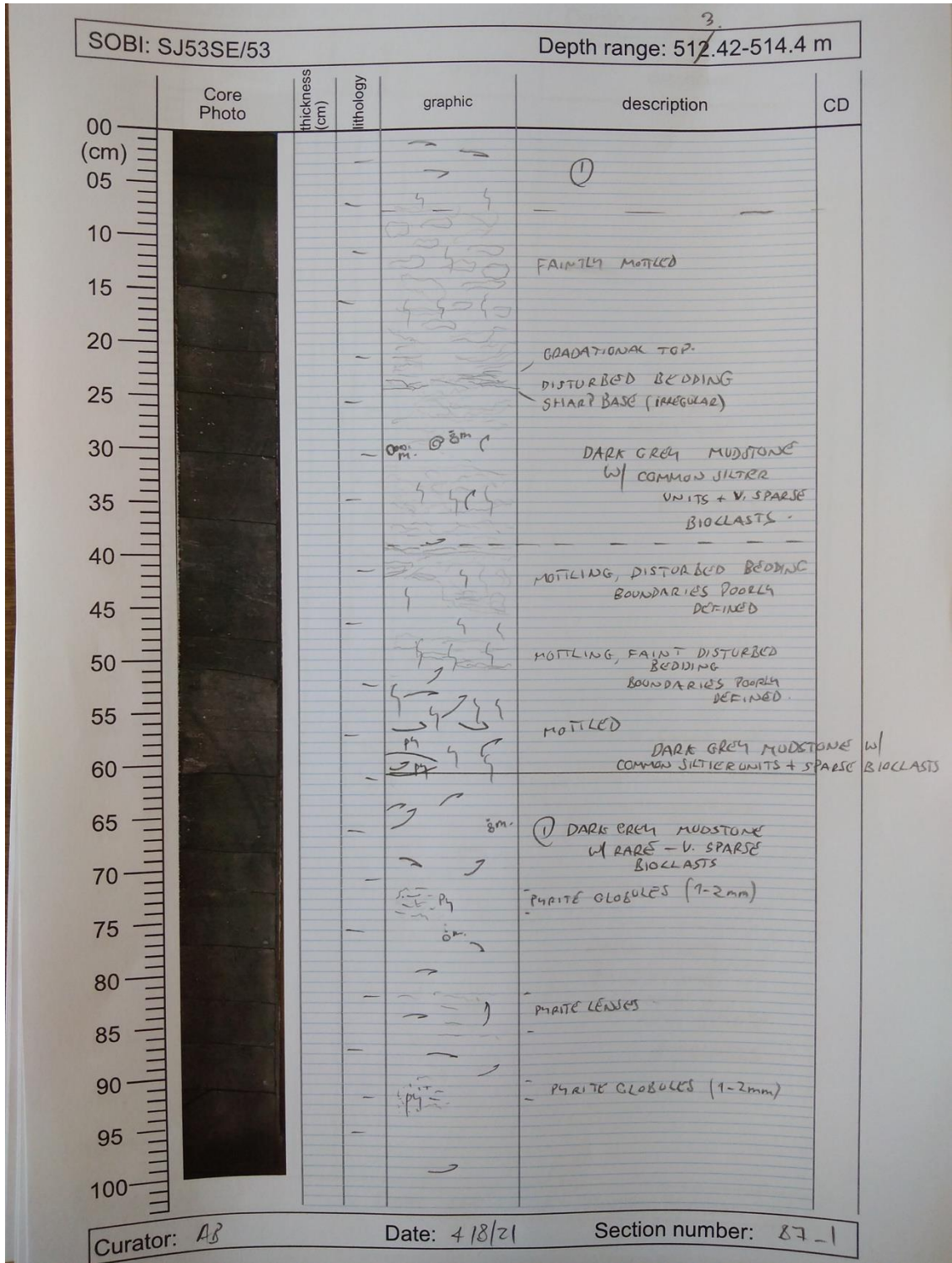
Quantifying marine redox across the Triassic–Jurassic mass extinction



Appendices



Quantifying marine redox across the Triassic–Jurassic mass extinction



Appendices

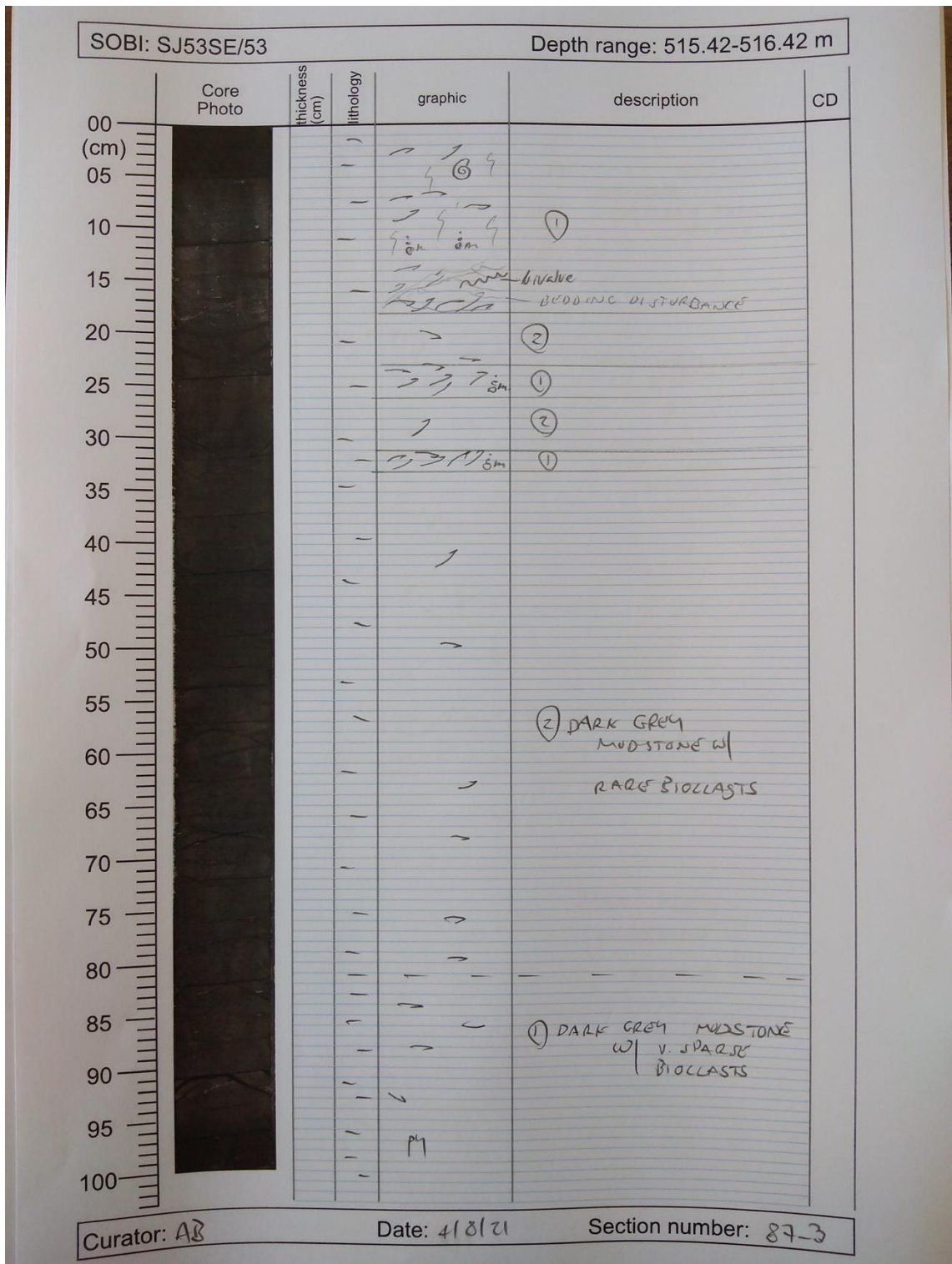
SOBI: SJ53SE/53		Depth range: 514.42-515.42 m				
Core Photo	thickness (cm)	lithology	graphic	description	CD	
	00					
	05			py		
	10			öm. py py		
	15			py		
	20					
	25			öm.		
	30				DARK GREY MUDSTONE w/ RARE BIOCLASTS.	
	35					
	40			öm.		
	45					
	50					
	55			py.		
	60				IRREGULAR, SHARP TOP.	
	65			bivalve	DARK GREY MUDSTONE w/ DISTURBED BEDS, SHARP, UNDULATING BASE	
	70			öm.		
75			öm.			
80			öm. öm. öm.	DARK GREY MUDSTONE w/ SPARSE - VERY SPARSE BIOCLASTS		
85			py py			
90			öm.			
95			öm.			
100						

Curator: AB

Date: 4/8/21

Section number: 87-2

Quantifying marine redox across the Triassic–Jurassic mass extinction



Appendices

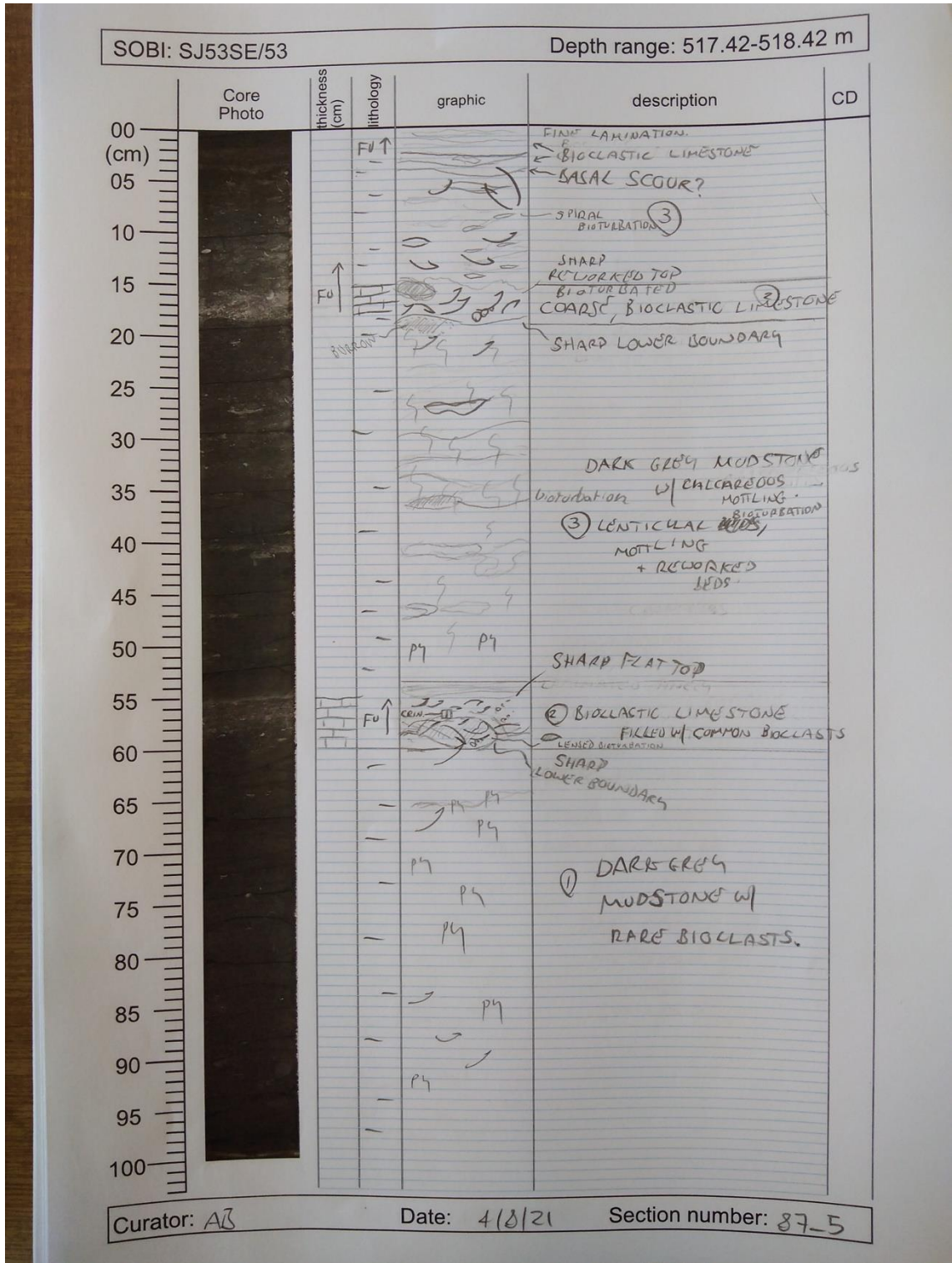
SOBI: SJ53SE/53		Depth range: 516.42-517.42 m				
Core Photo	thickness (cm)	lithology	graphic	description	CD	
	00					
	05			MOTTLED + DISTURBED BEDDING		
	10			TOP + BASE POORLY DEFINED.		
	15					
	20					
	25				DARK GREY MUDSTONE w/ SPARSE - & SPARSE BIOCASTS.	
	30				Faint mottling	
	35				UPPER + LOWER BOUNDARY POORLY DEFINED.	
	40					
	45					
50						
55						
60						
65						
70						
75				DARK GREY MUDSTONE w/ RARE BIOCASTS		
80						
85						
90						
95						
100						

Curator: AB

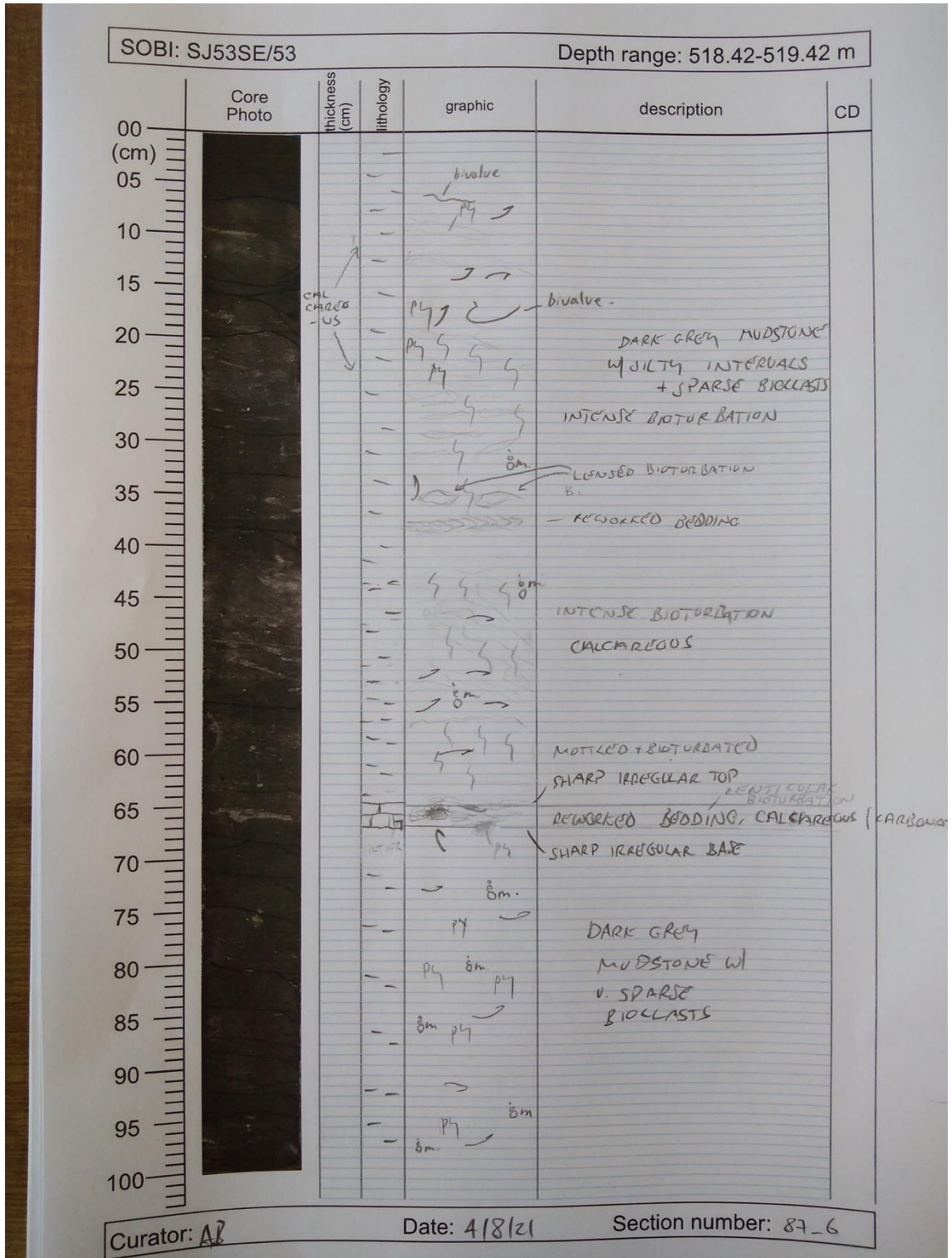
Date: 4/8/21

Section number: 87-4

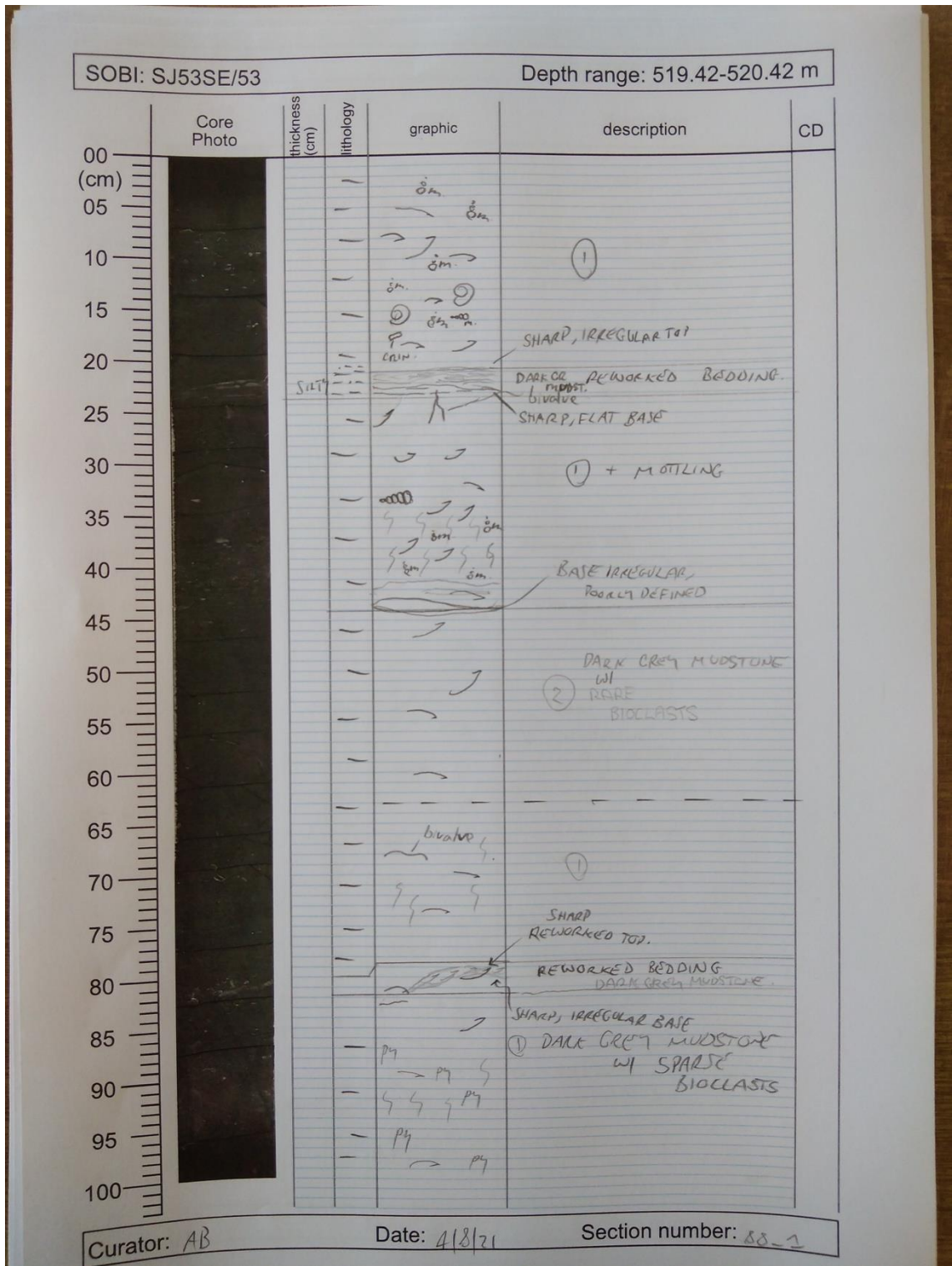
Quantifying marine redox across the Triassic–Jurassic mass extinction



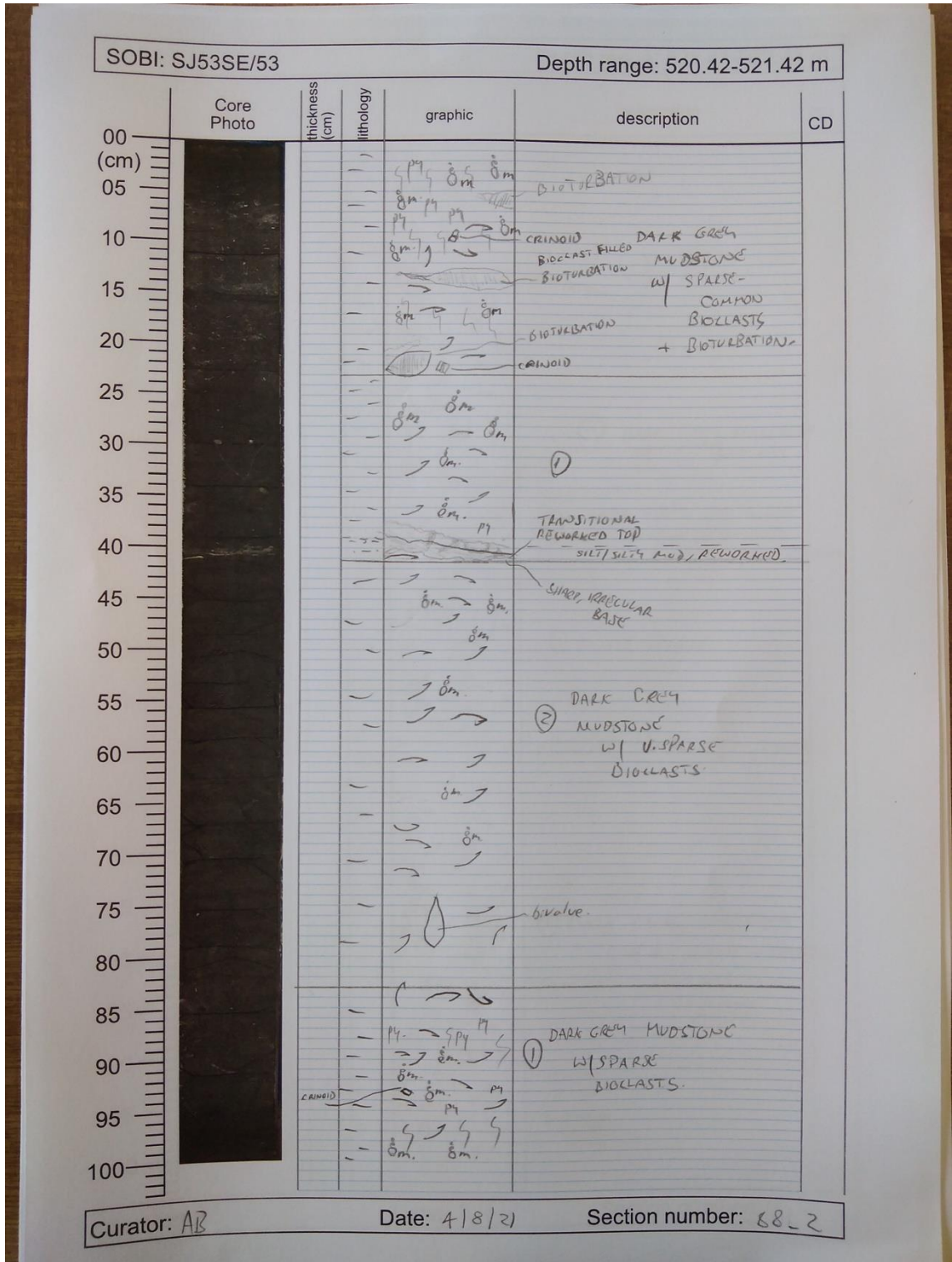
Appendices



Quantifying marine redox across the Triassic–Jurassic mass extinction

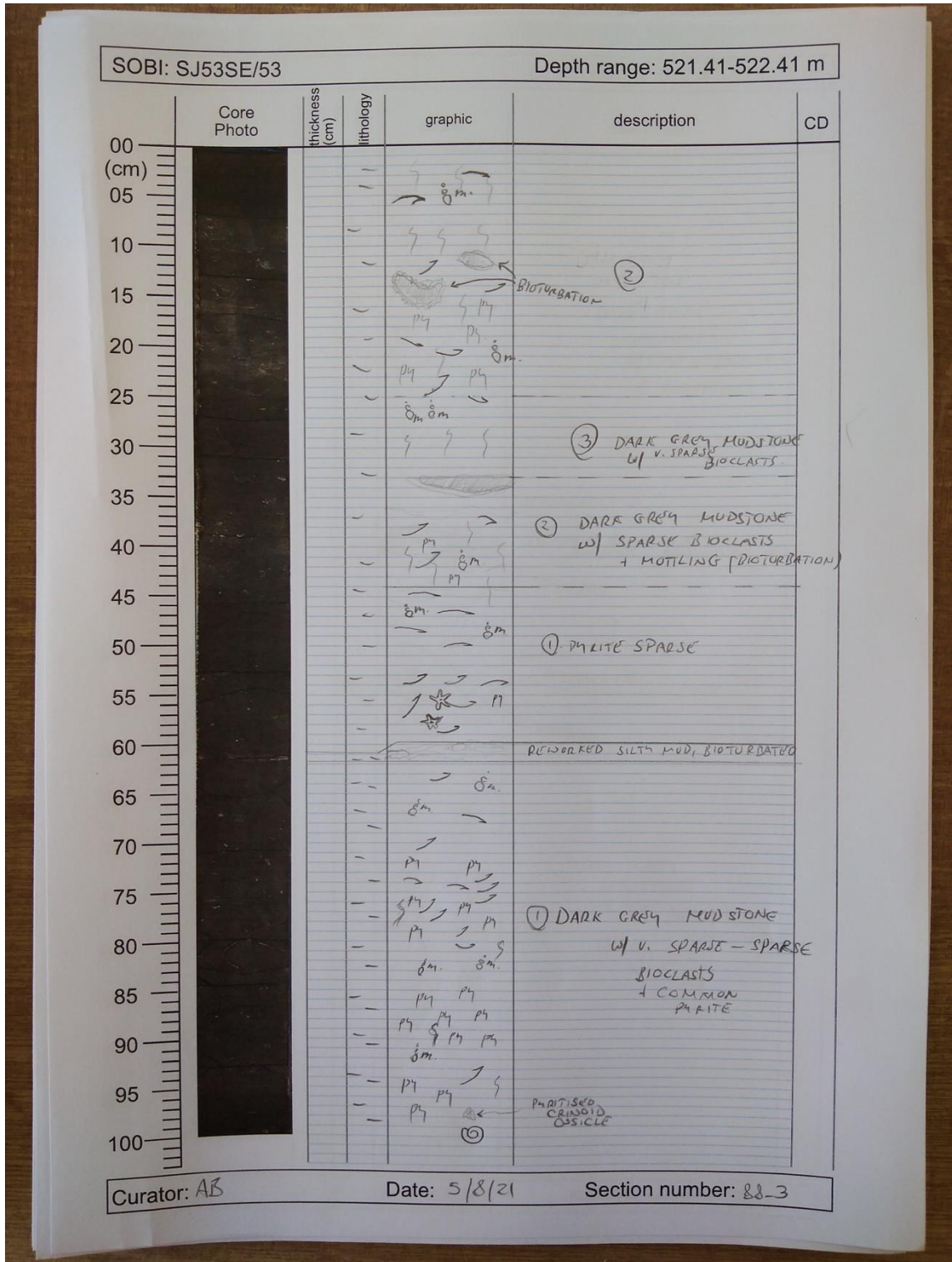


Appendices

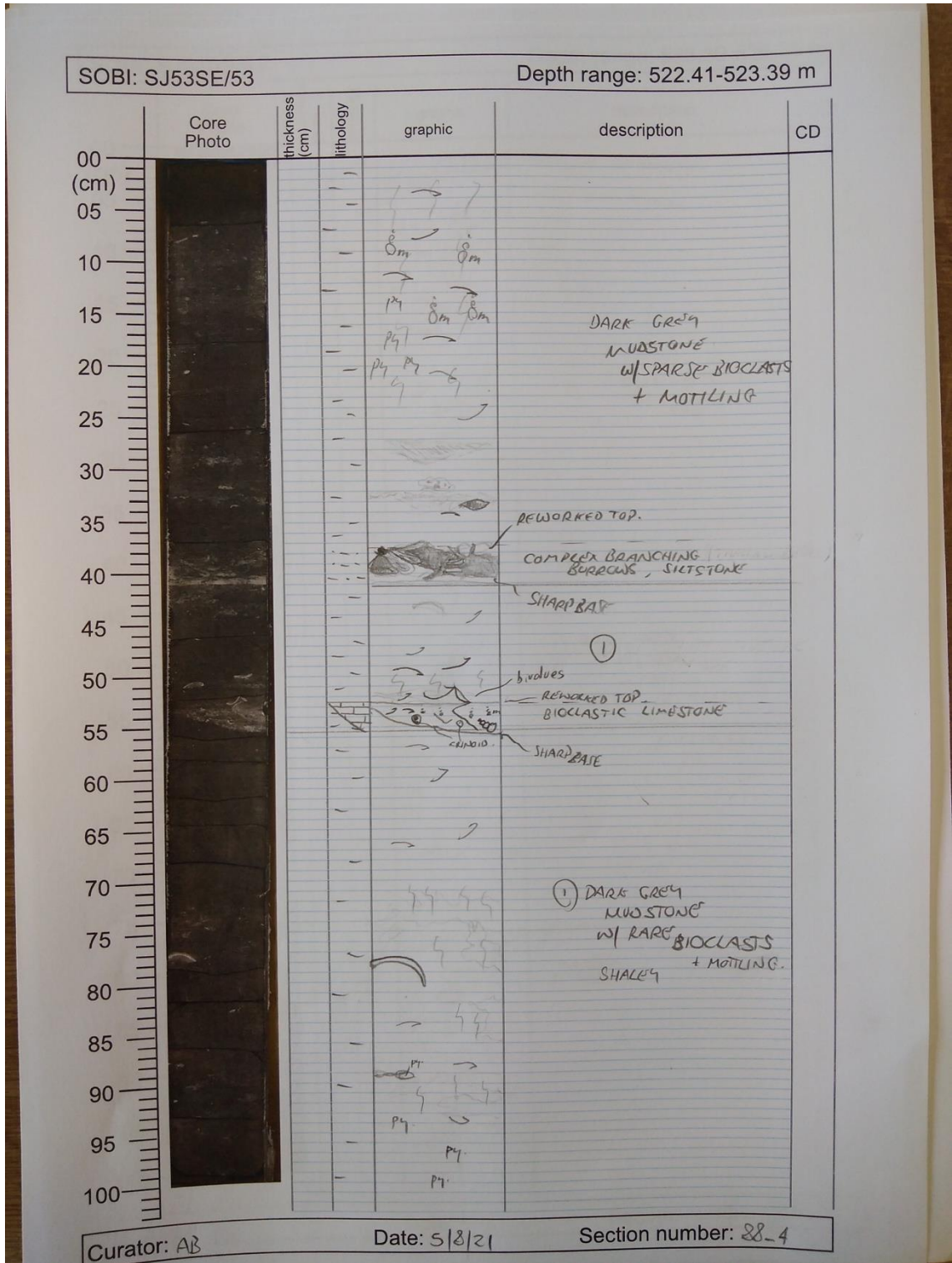


Curator: AR Date: 4/8/21 Section number: 68-2

Quantifying marine redox across the Triassic–Jurassic mass extinction



Appendices

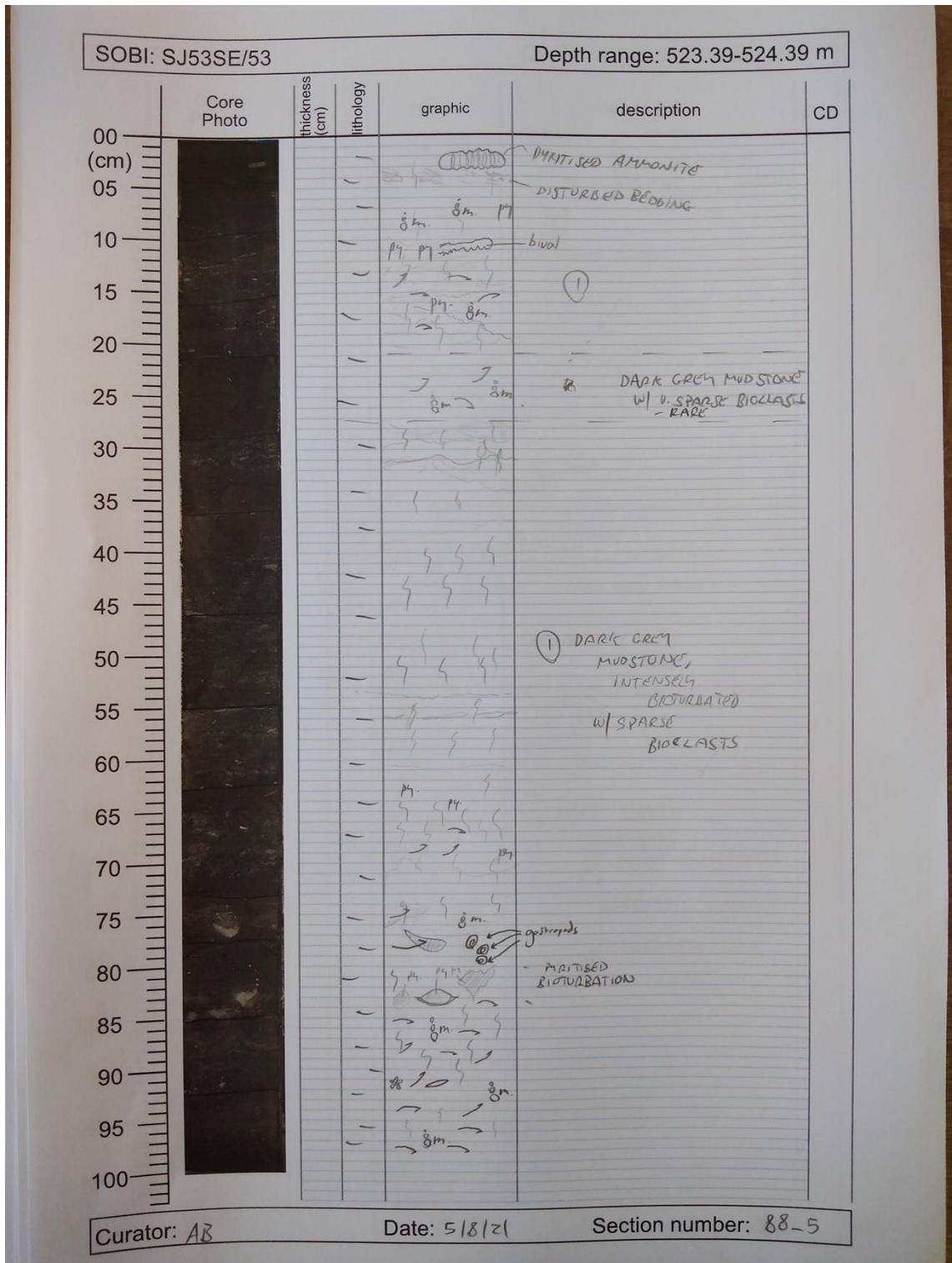


Curator: AB

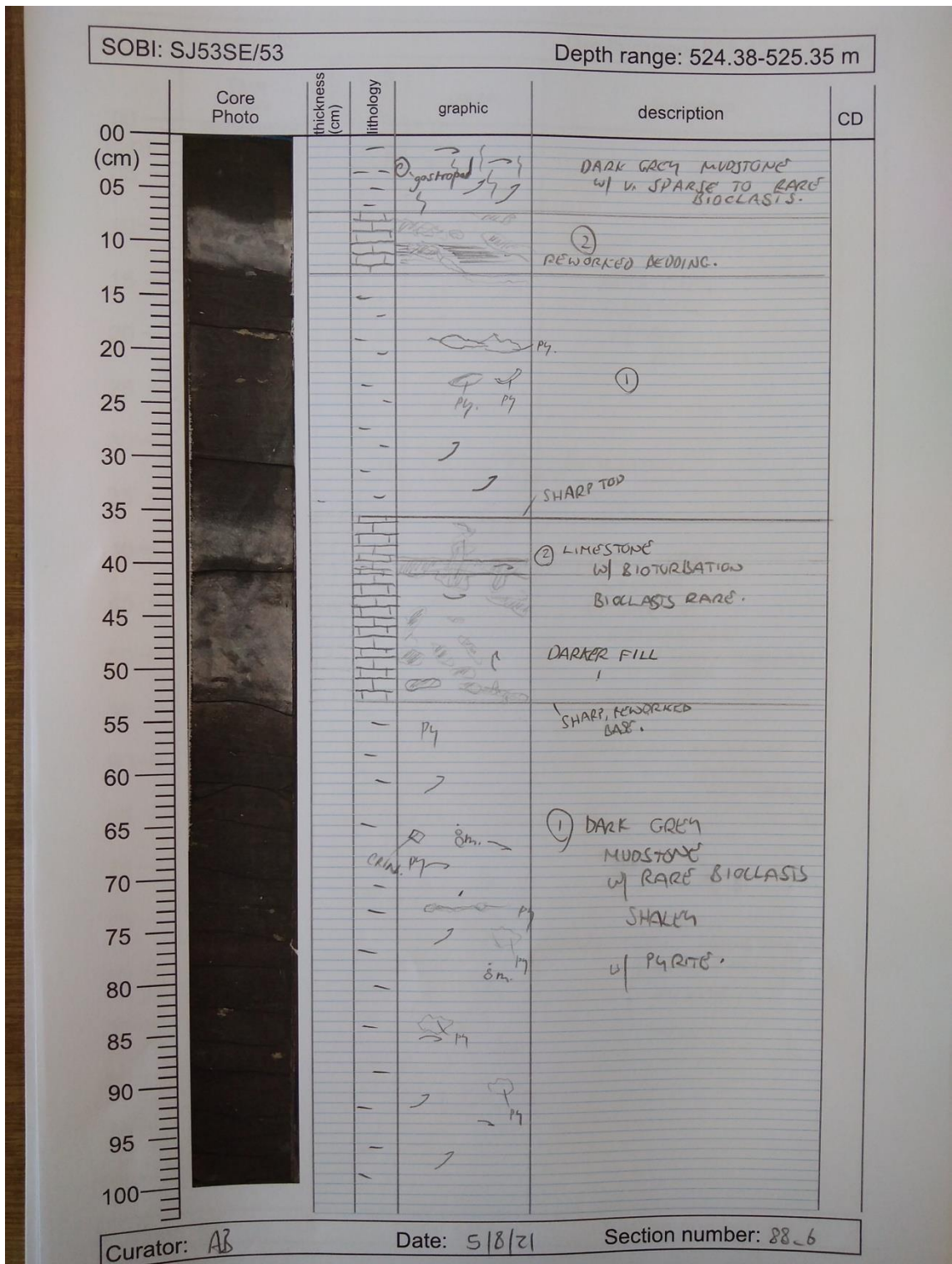
Date: 5/8/21

Section number: 88-4

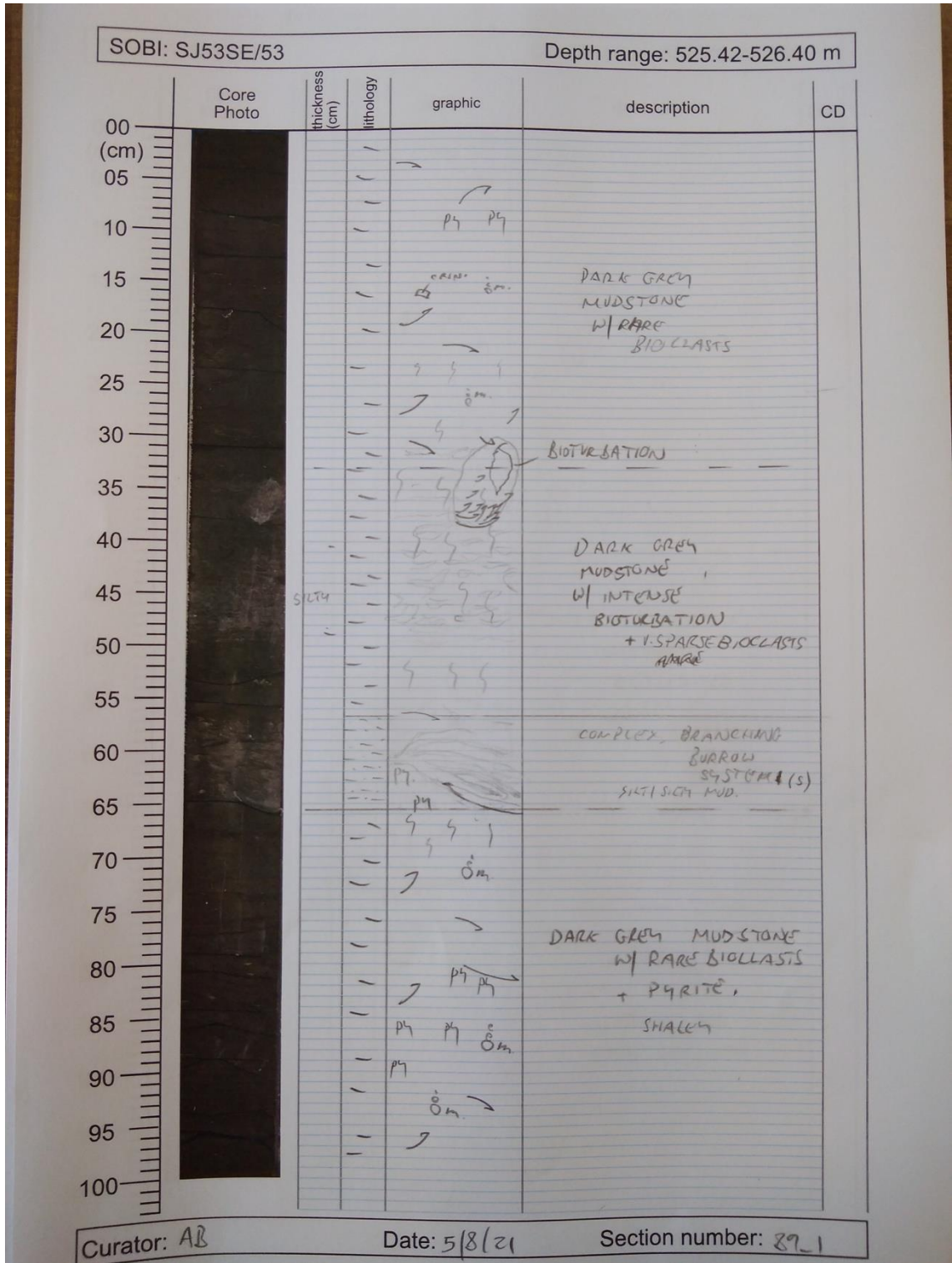
Quantifying marine redox across the Triassic–Jurassic mass extinction



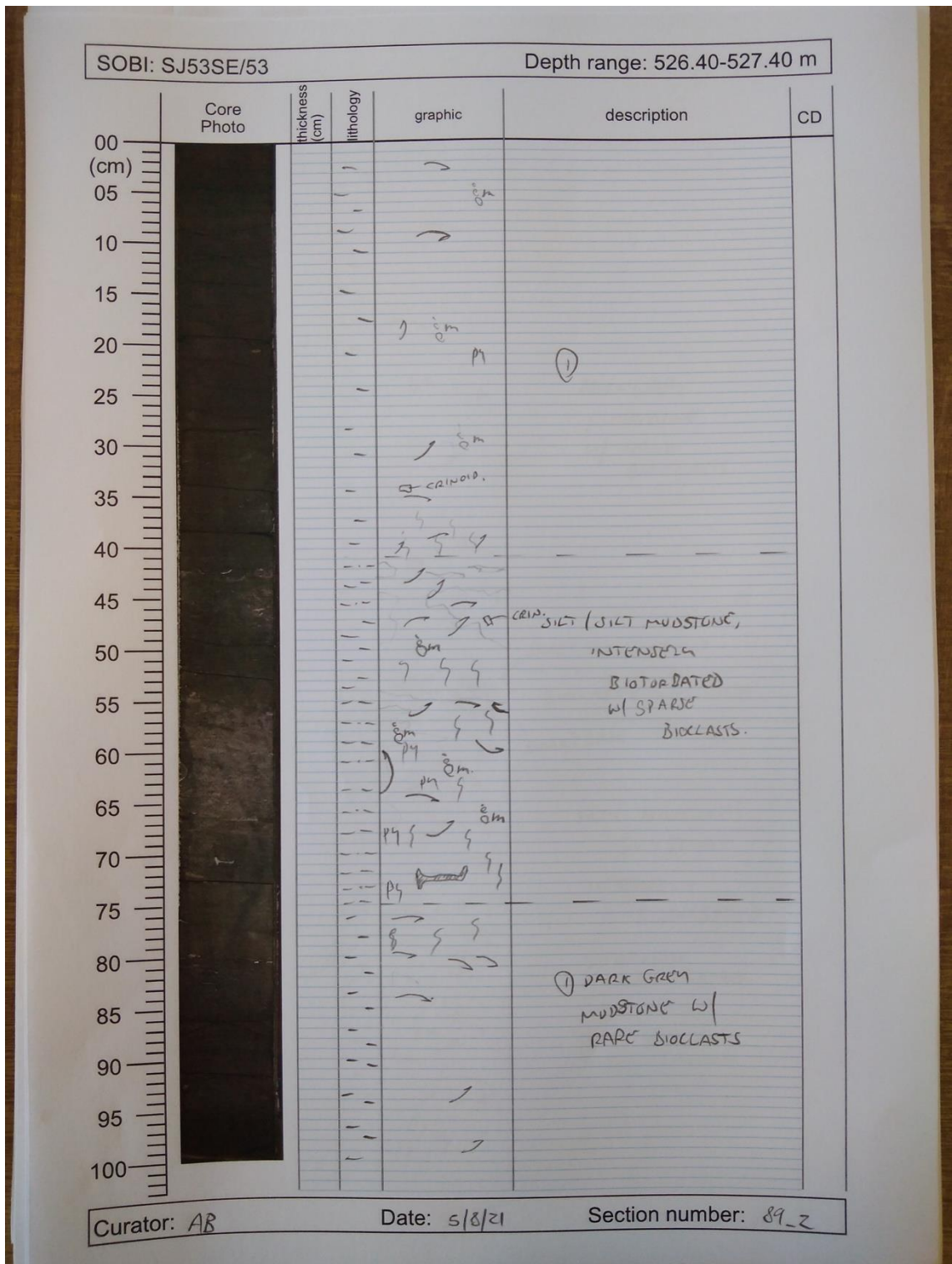
Appendices



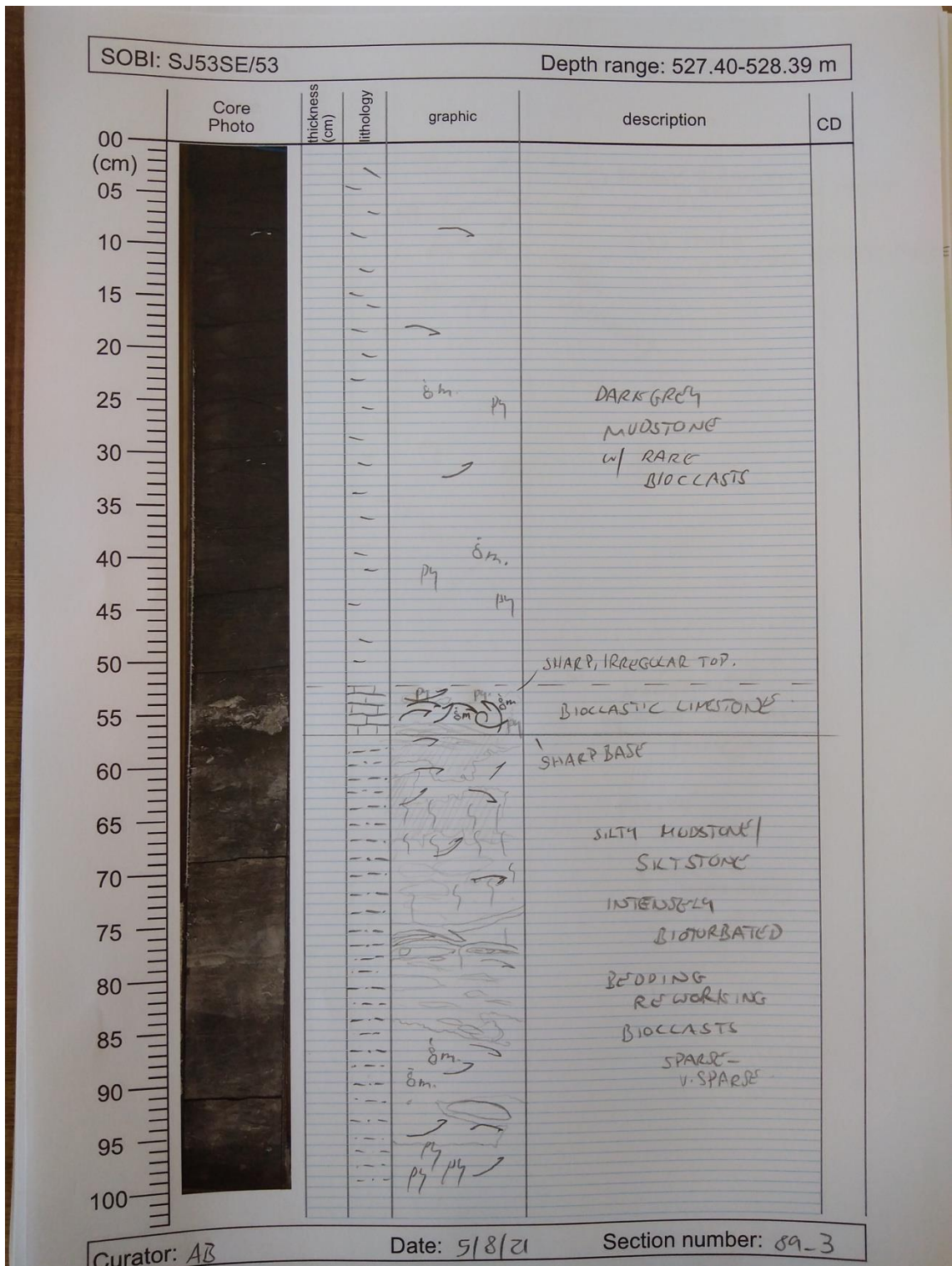
Quantifying marine redox across the Triassic–Jurassic mass extinction



Appendices



Quantifying marine redox across the Triassic–Jurassic mass extinction



Appendices

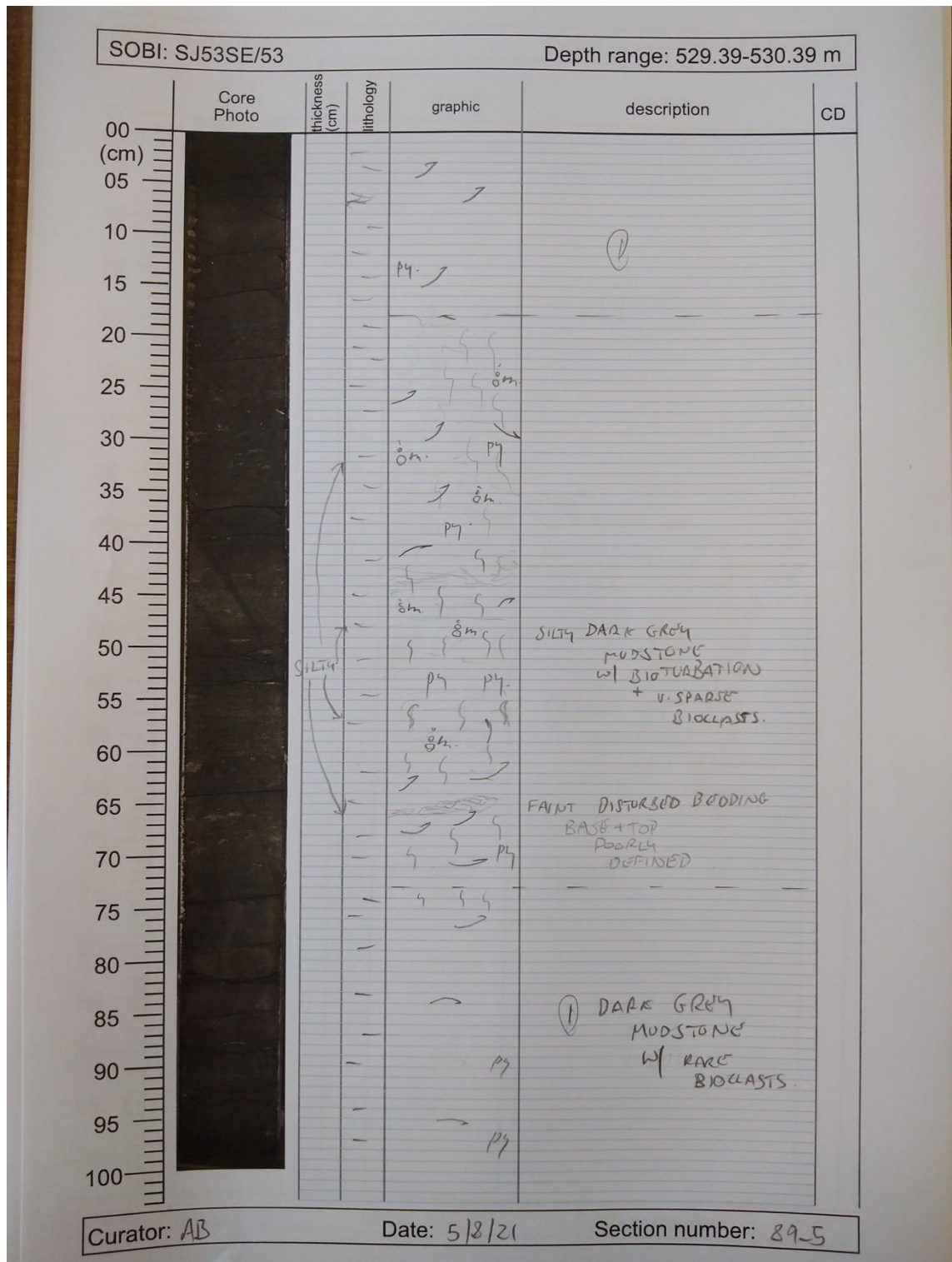
SOBI: SJ53SE/53		Depth range: 528.39-529.39 m				
Core Photo	thickness (cm)	lithology	graphic	description	CD	
	00					
	05			① SPARSE TO COMMON BIOCLASTS, NO PYRITE		
	10			① V. SPARSE BIOCLASTS, SPARSE PYRITE		
	15			CRINOID STEM (FOSSILS)		
	20					
	25					
	30					
	35					
	40					
	45					
50				① DARK GREY MUDSTONE W/ RARE BIOCLASTS (SHALEY)		
55						
60						
65				PYRITE COMMON		
70				(PARTICULARLY UPPER PART)		
75						
80						
85						
90						
95						
100						

Curator: AB

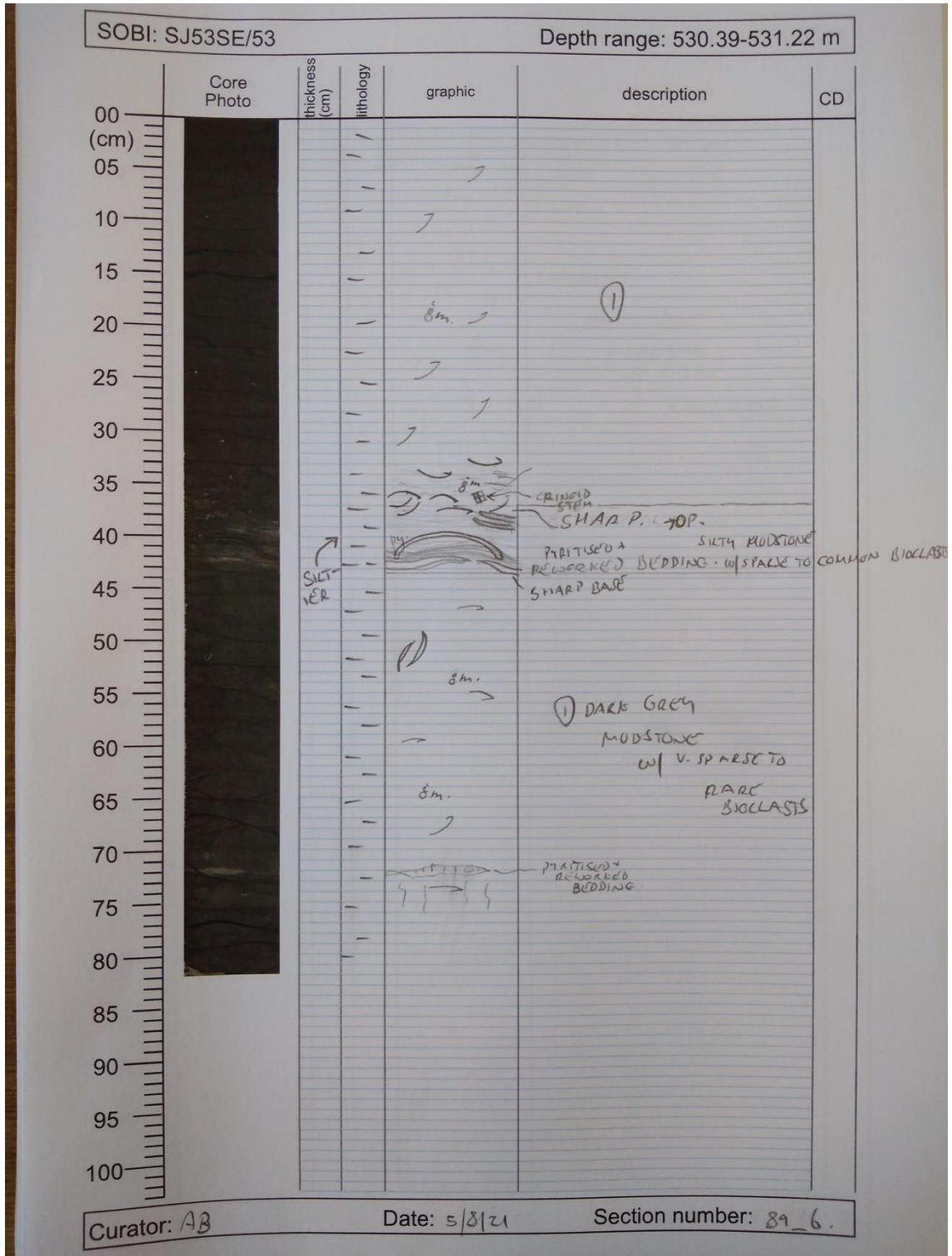
Date: 5/8/21

Section number: 89_4

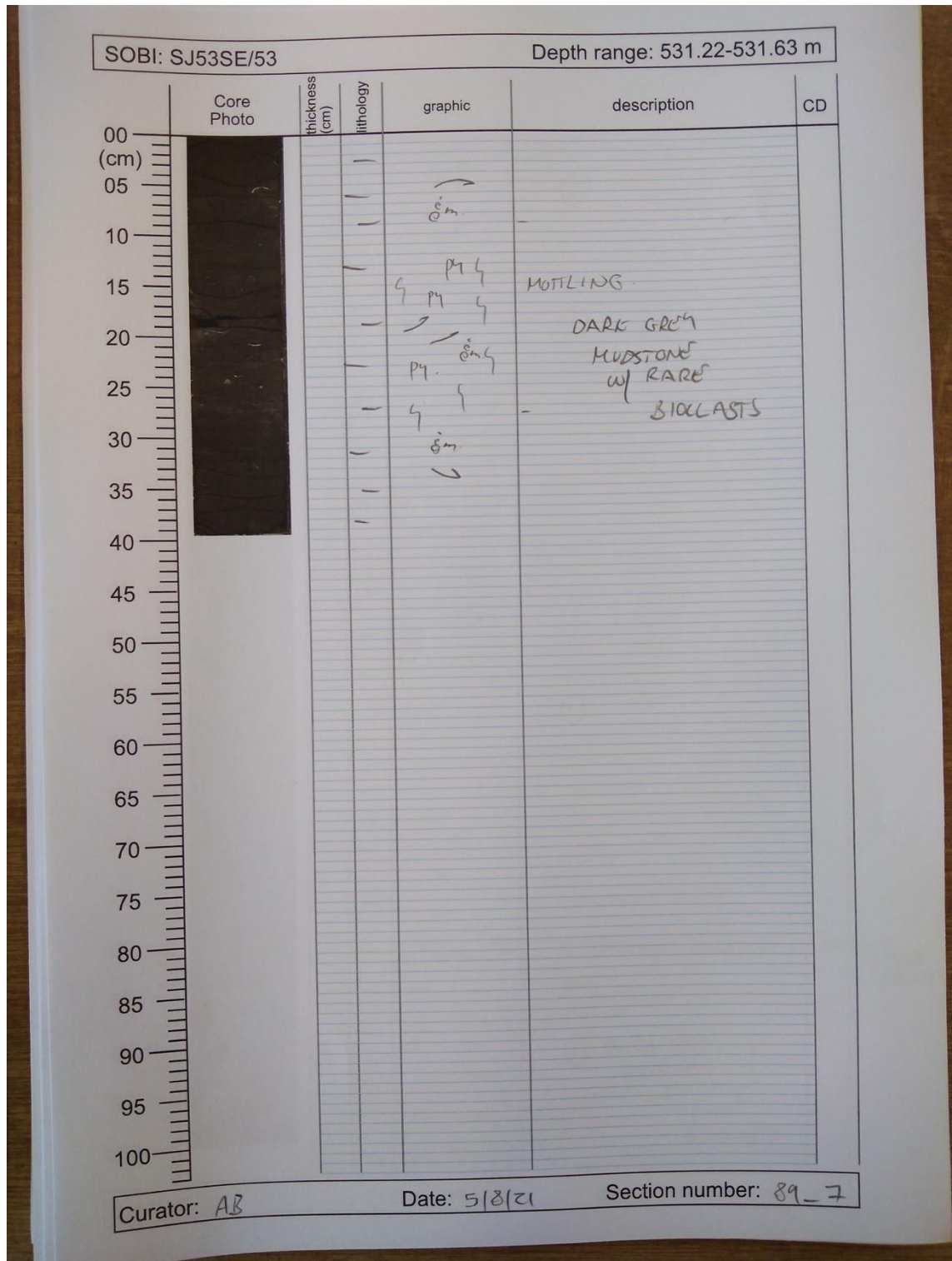
Quantifying marine redox across the Triassic–Jurassic mass extinction



Appendices



Quantifying marine redox across the Triassic–Jurassic mass extinction

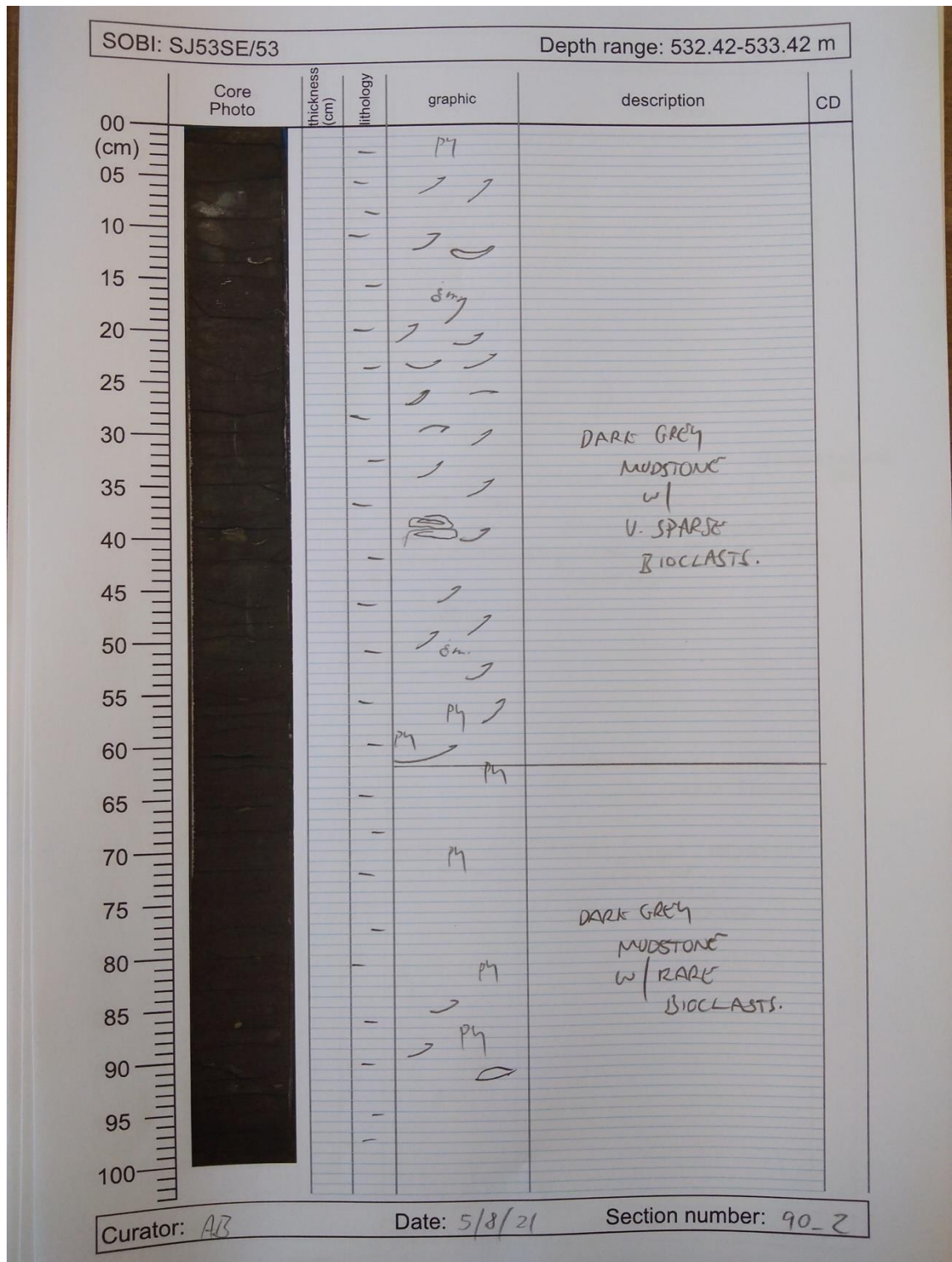


Appendices

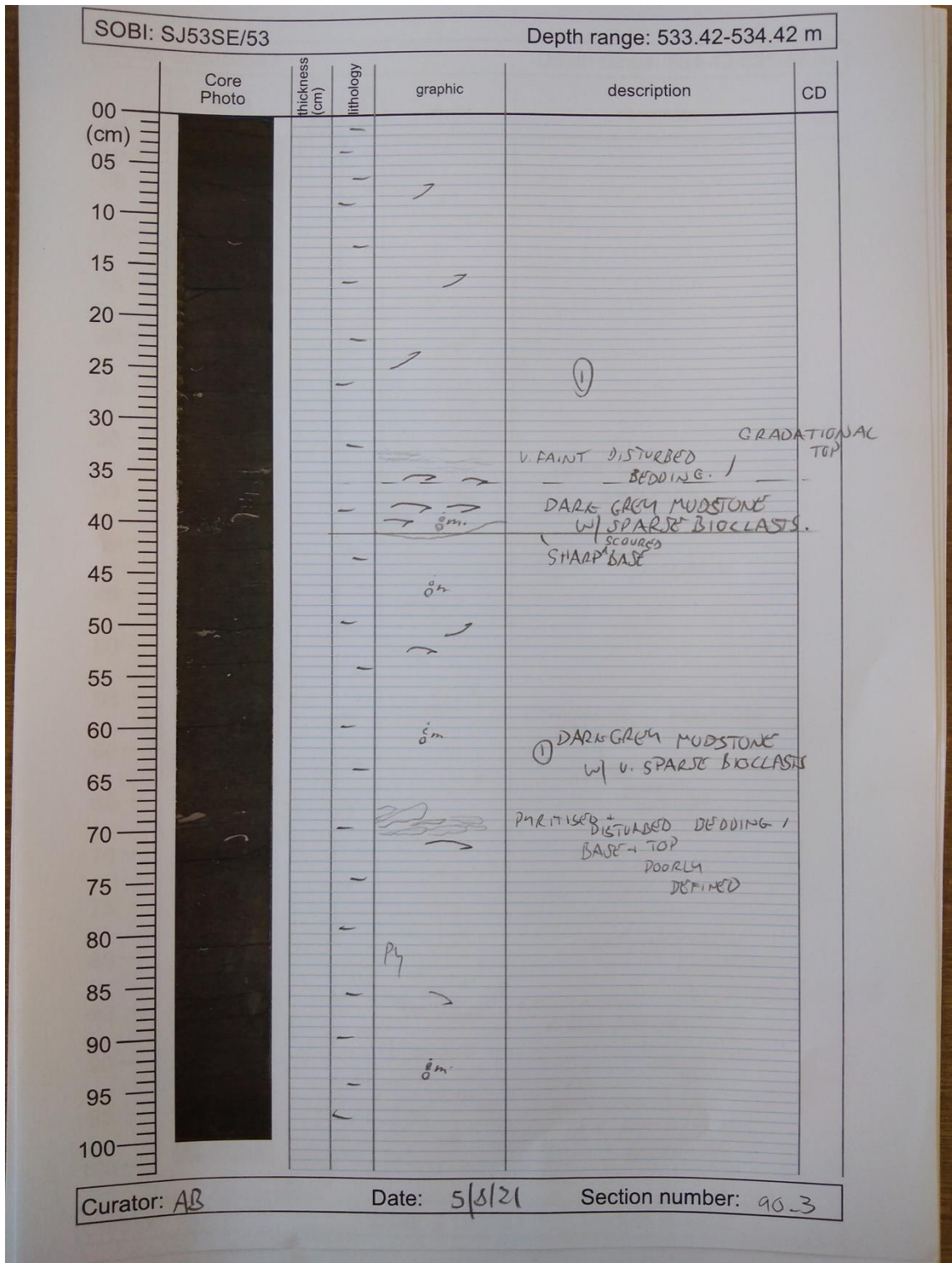
SOBI: SJ53SE/53		Depth range: 531.42-532.42 m			
Core Photo	thickness (cm)	lithology	graphic	description	CD
	00				
	05			(2)	
	10				
	15				
	20				
	25				
	30				
	35				
	40				
	45				
	50				
	55			(1)	
	60				
	65				
	70				
	75				
	80				(2) DARK GRN MUDSTONE w/ SPARSE - V. SPARSE BIOLLASTS
	85				
	90				(1) DARK GRN MUDSTONE w/ V. SPARSE - RARE BIOLLASTS
	100				

Curator: AB Date: 5/8/21 Section number: 90-1

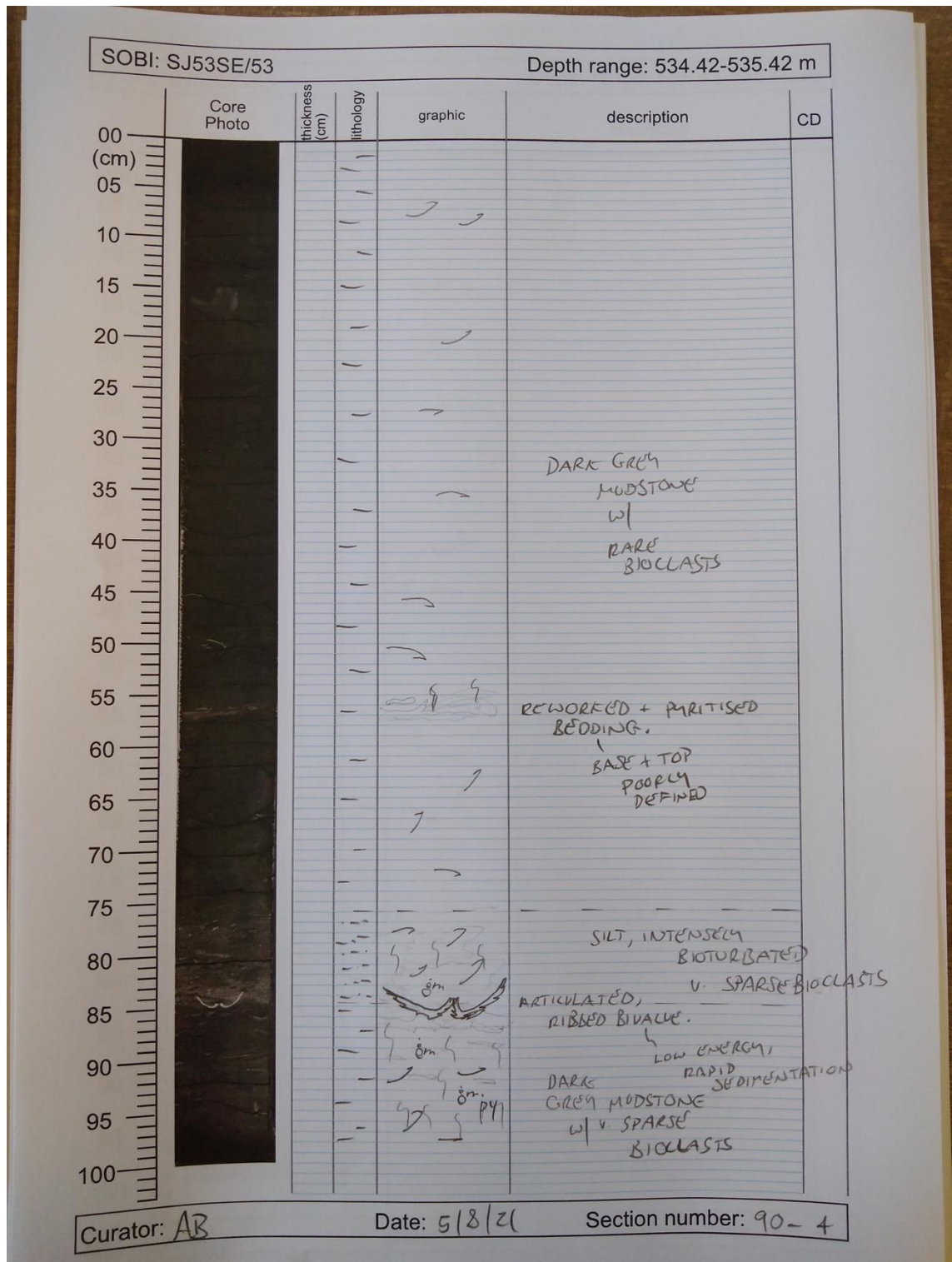
Quantifying marine redox across the Triassic–Jurassic mass extinction



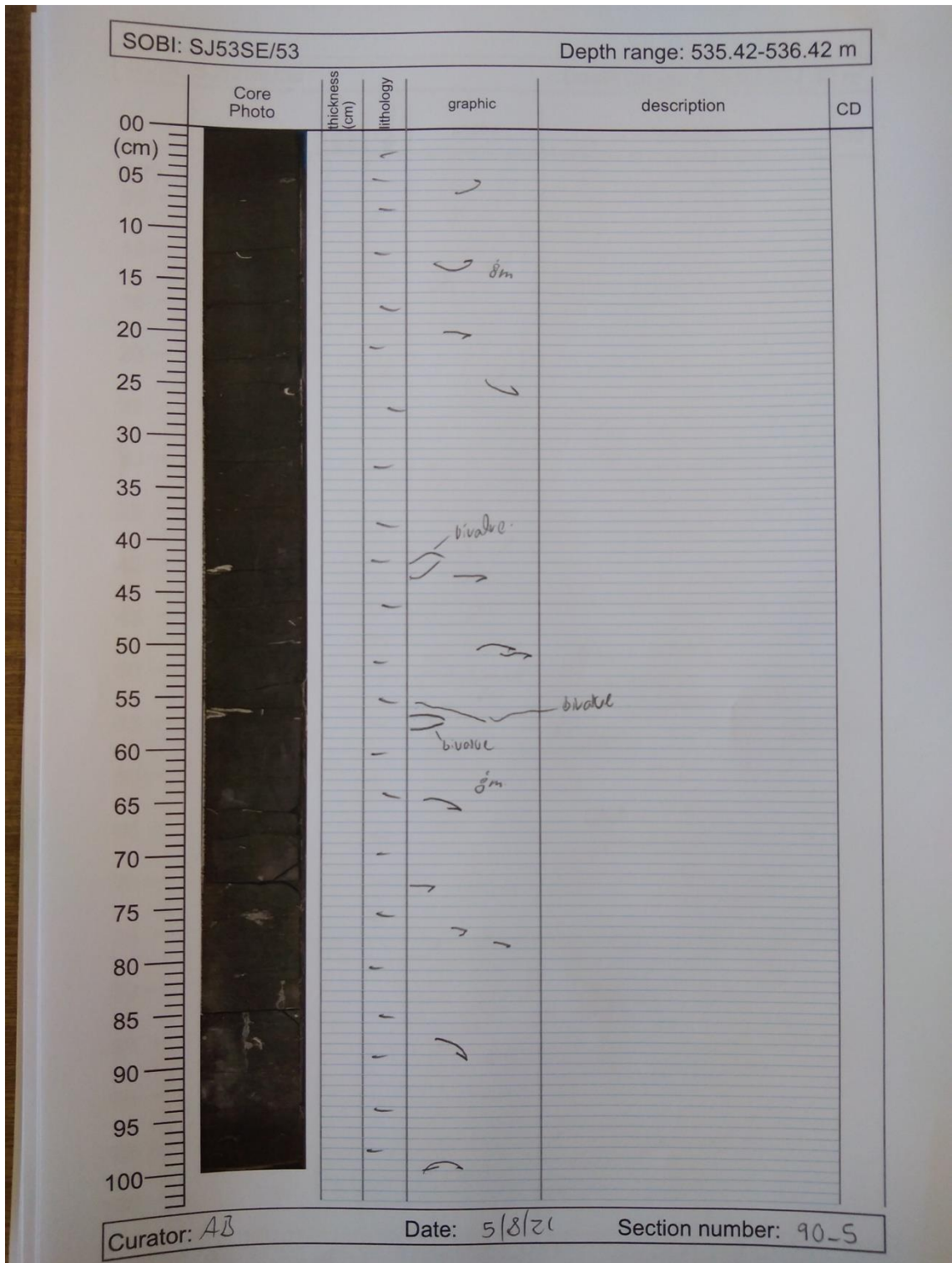
Appendices



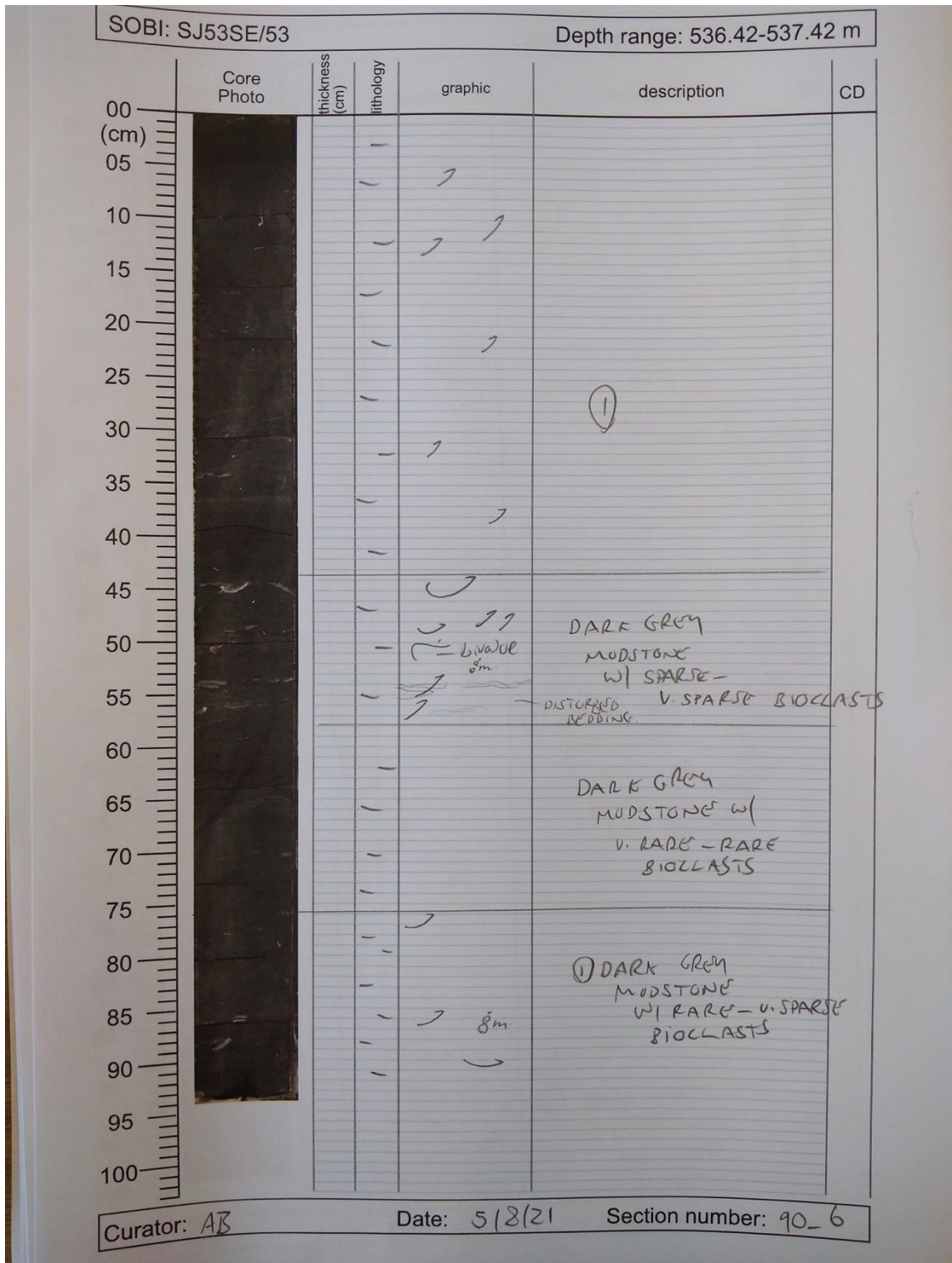
Quantifying marine redox across the Triassic–Jurassic mass extinction



Appendices



Quantifying marine redox across the Triassic–Jurassic mass extinction



Appendices

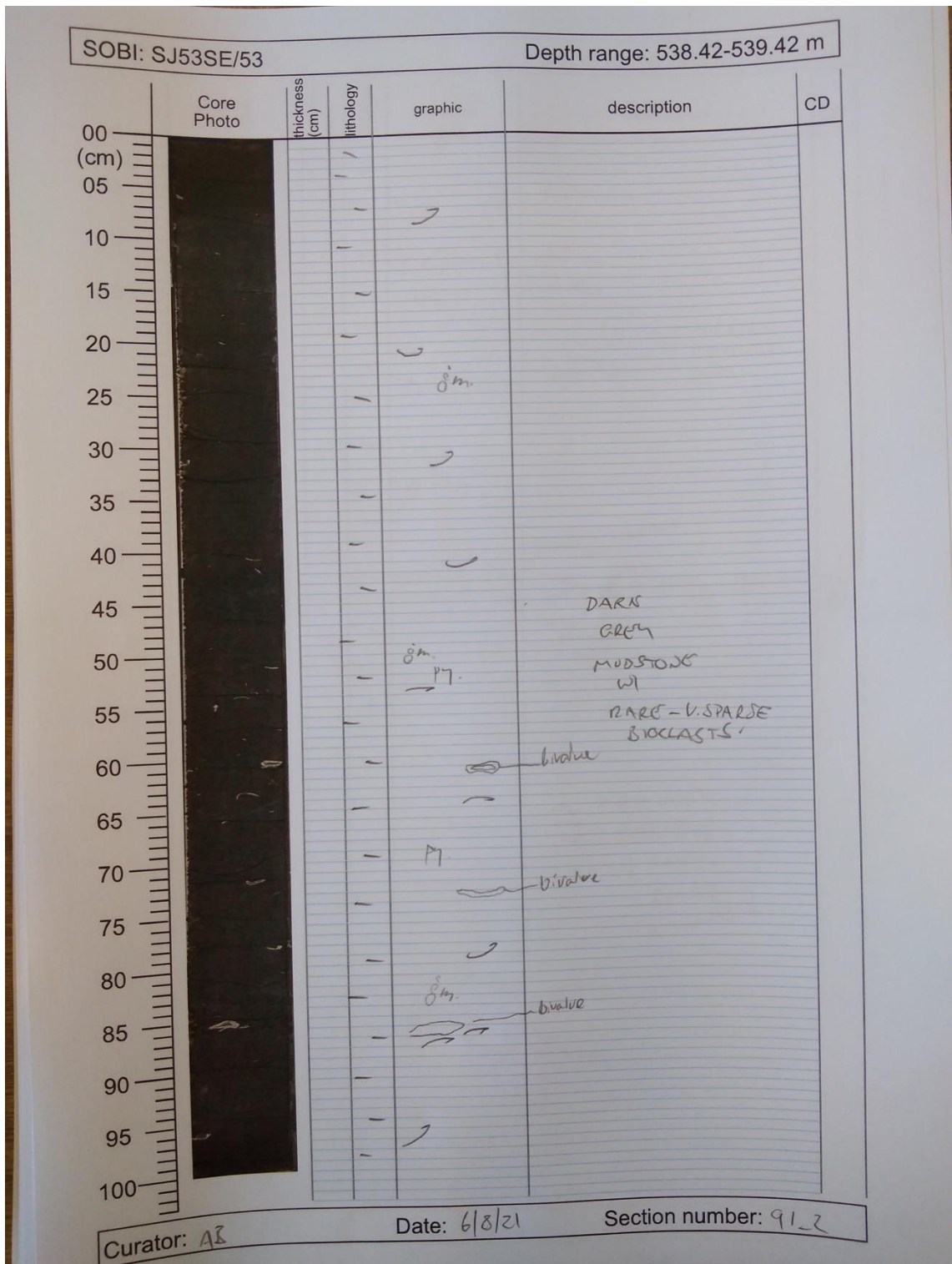
SOBI: SJ53SE/53		Depth range: 537.42-538.42 m				
Core Photo	thickness (cm)	lithology	graphic	description	CD	
	00					
	05					
	10				(2)	
	15					
	20					
	25				DARK GREY MUDSTONE w/ V. SPARSE BIOCLASTS	
	30					
	35					
	40					
	45					
50						
55				(2) DARK GREY MUDSTONE w/ RARE - V. RARE BIOCLASTS		
60						
65						
70						
75						
80						
85						
90				(1) DARK GREY MUDSTONE w/ SPARSE BIOCLASTS		
95						
100						

Curator: AB

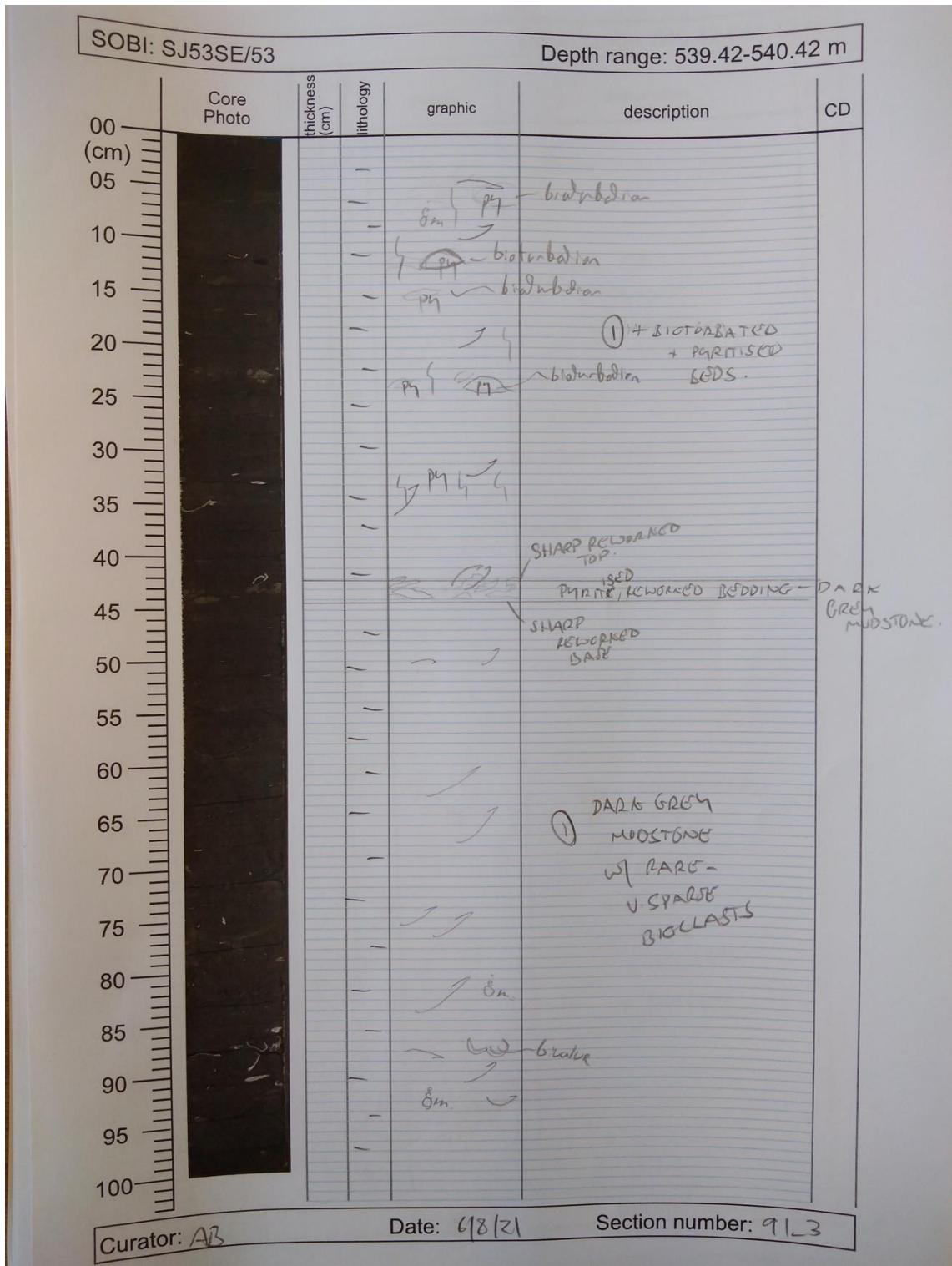
Date: 5/8/21

Section number: 9/1

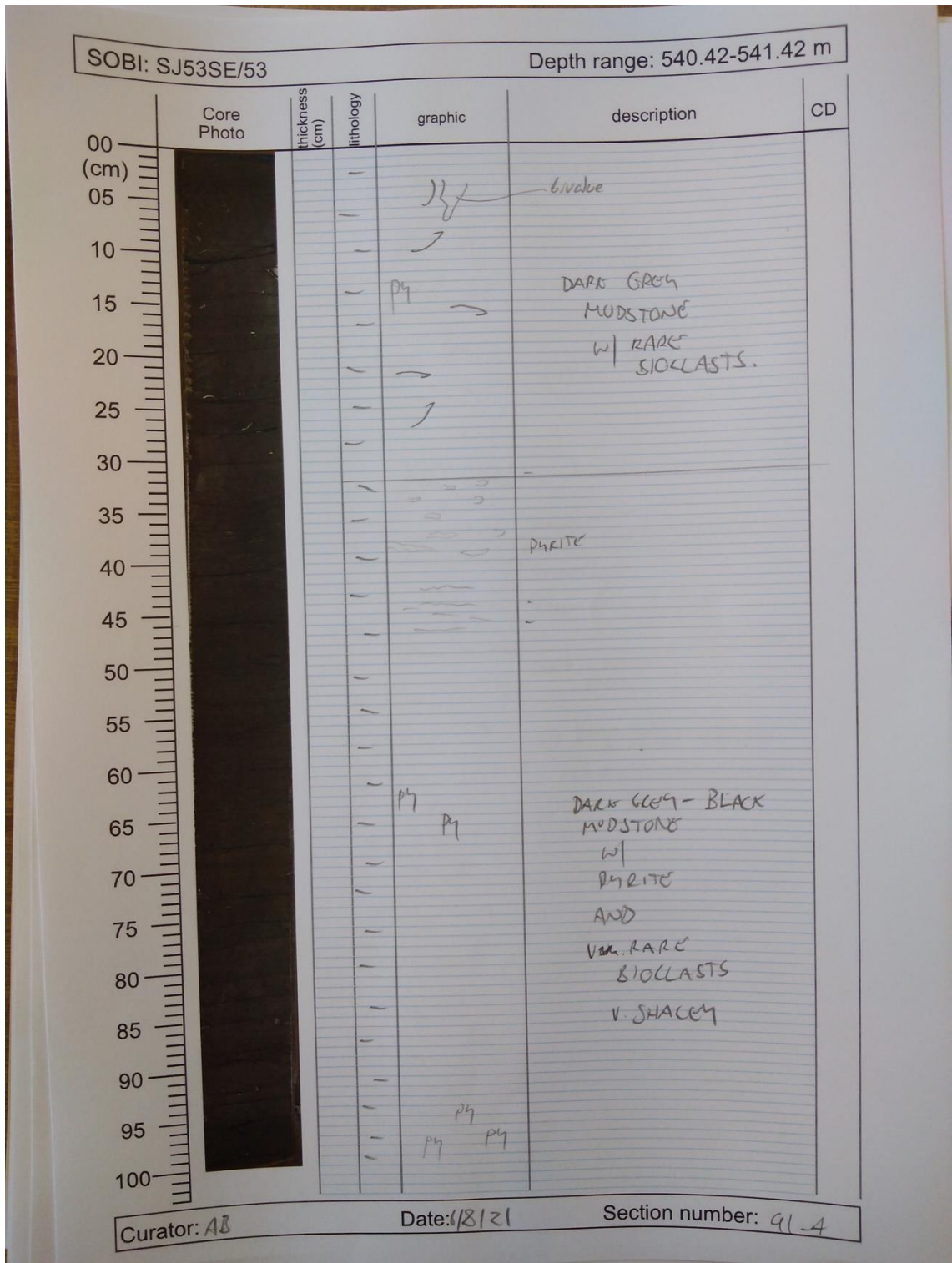
Quantifying marine redox across the Triassic–Jurassic mass extinction



Appendices



Quantifying marine redox across the Triassic–Jurassic mass extinction



Appendices

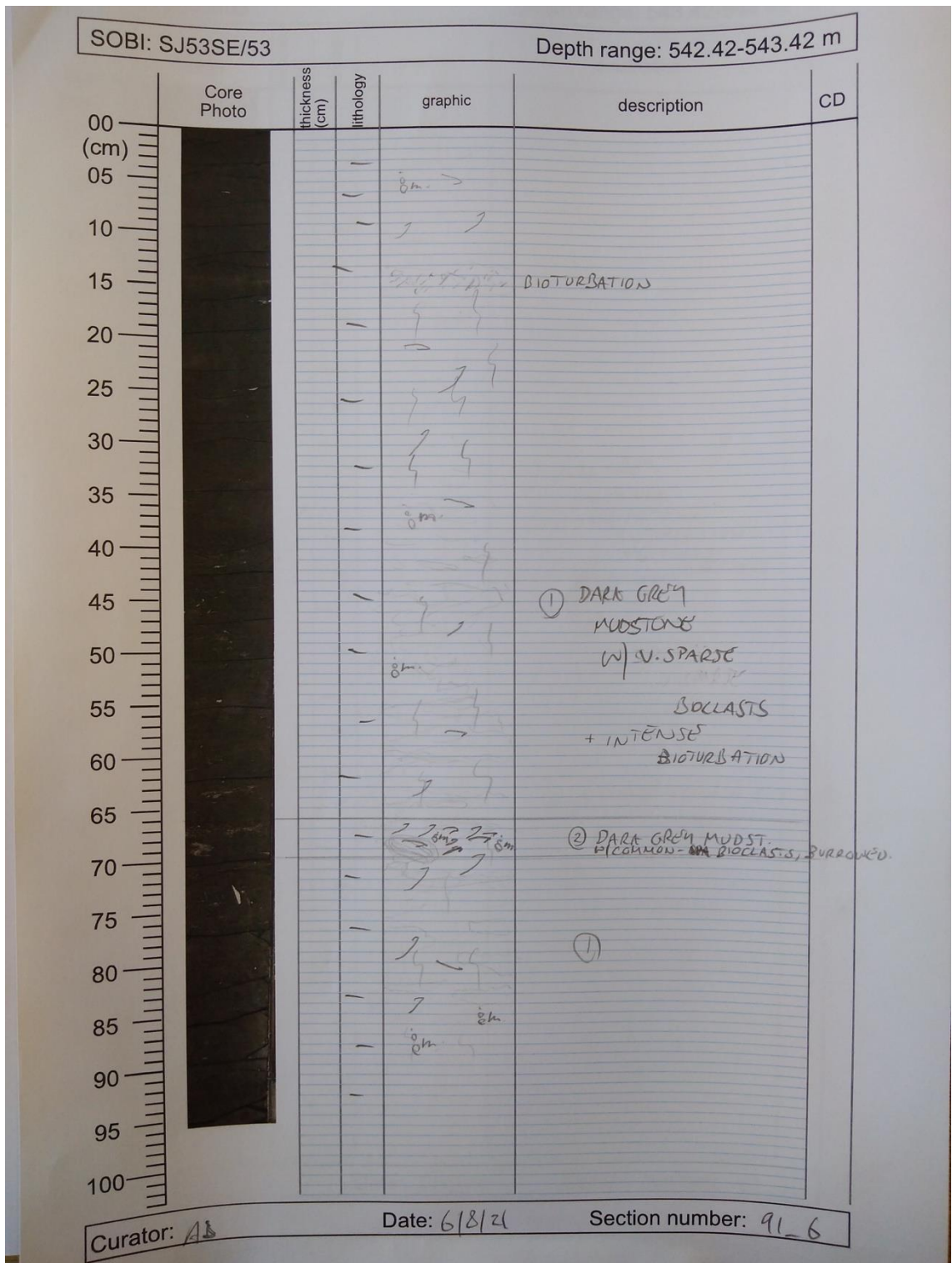
SOBI: SJ53SE/53		Depth range: 541.42-542.42 m				
Core Photo	thickness (cm)	lithology	graphic	description	CD	
	00					
	05					
	10					
	15					
	20					
	25				①	
	30					
	35					
	40				SHARP, RECORDED TO ? FINE, SUBMILLIMETRIC LAMINATION PARTIALLY MOTTLED MUDSTONE SHARP BASE	
	45				ORADATIONAL, RECORDED TOP DARK GREY MUDSTONE	
	50				SHARP, IRREGULAR BASE,	
	55				① DARK GREY MUDSTONE W/ SPARSE BIOTURBATED MOTTLED + BIOTURBATED BEDS.	
	60					
	65					
	70					
75						
80						
85						
90						
95						
100						

Curator: AB

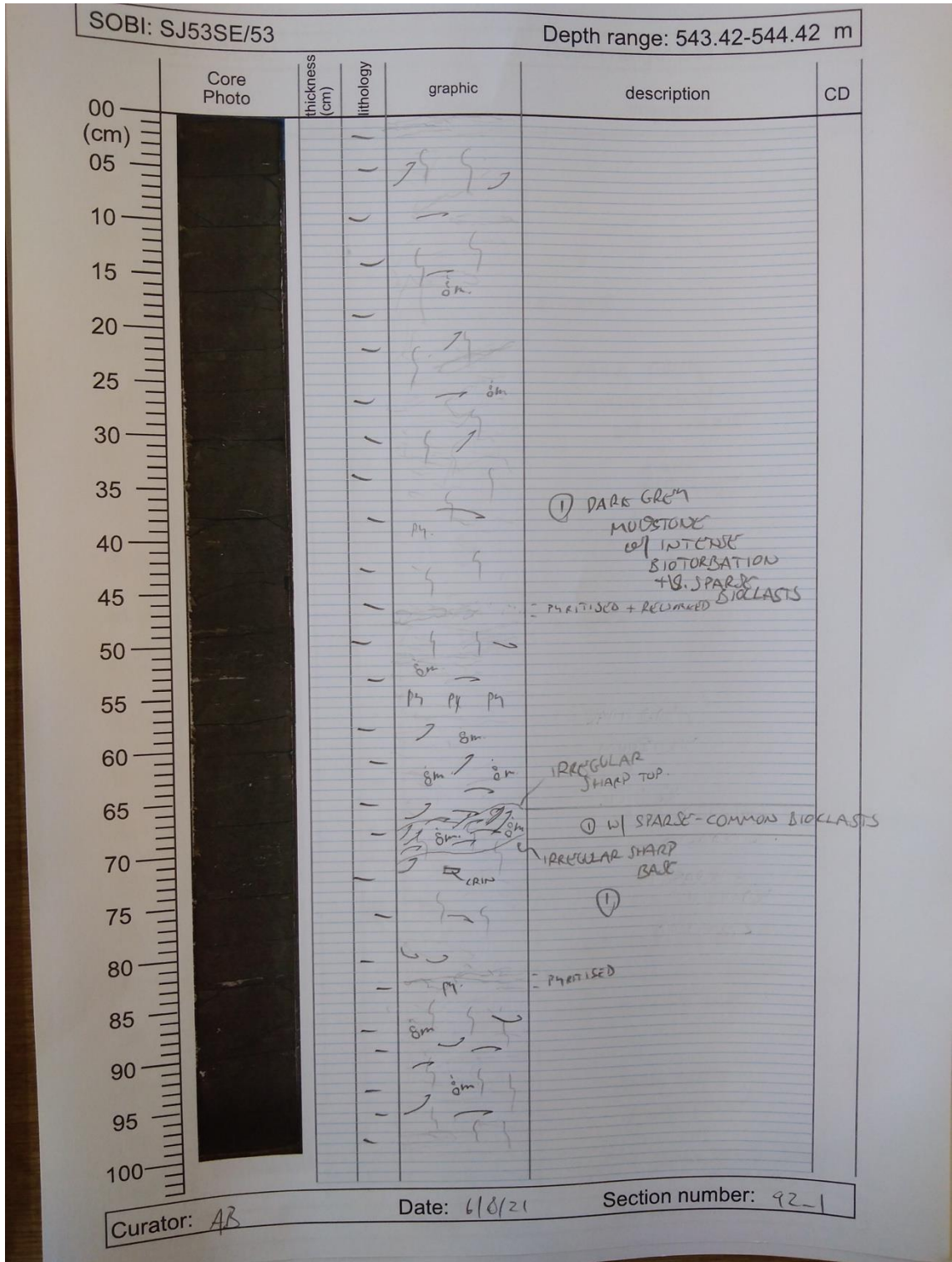
Date: 6/8/21

Section number: 91-5

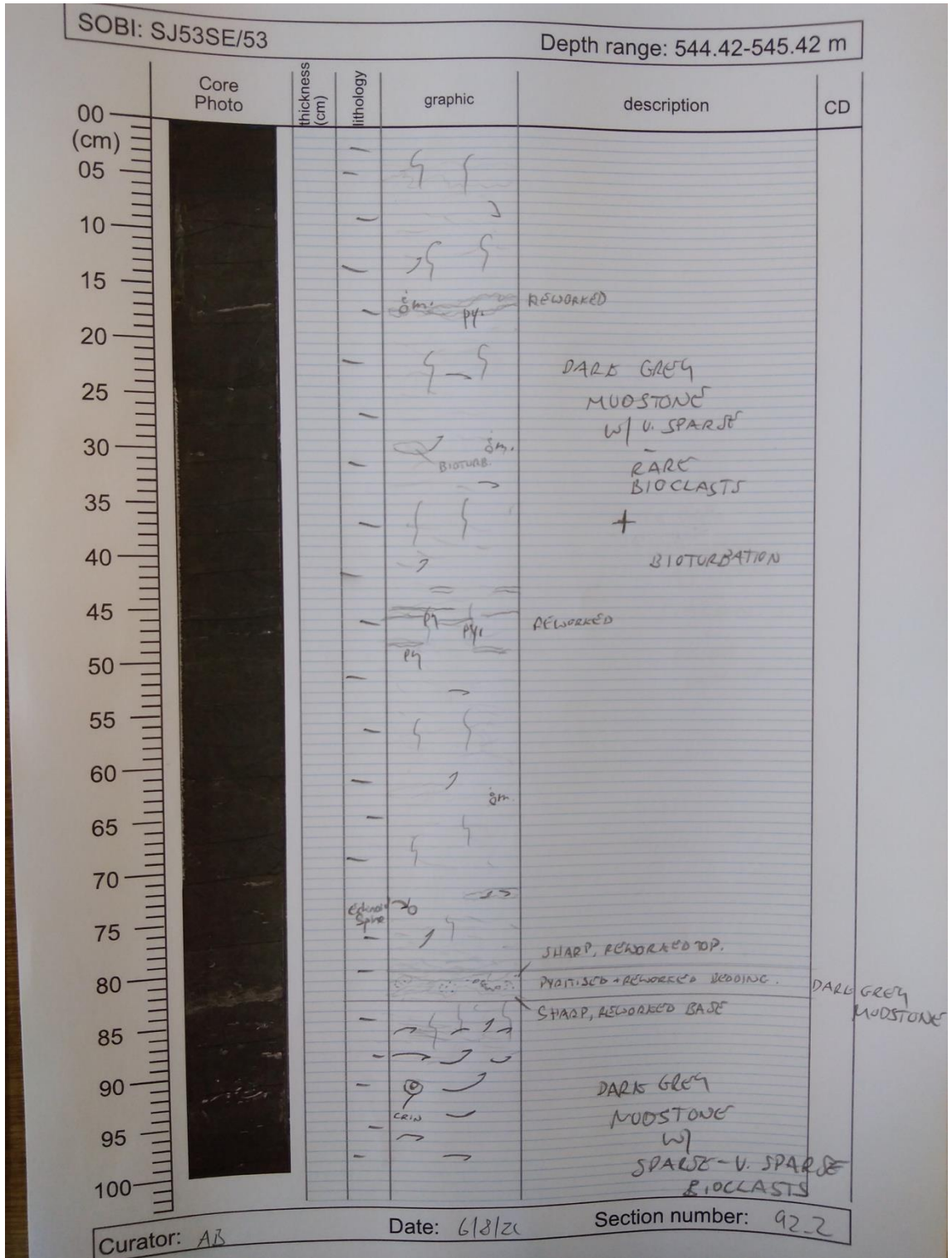
Quantifying marine redox across the Triassic–Jurassic mass extinction



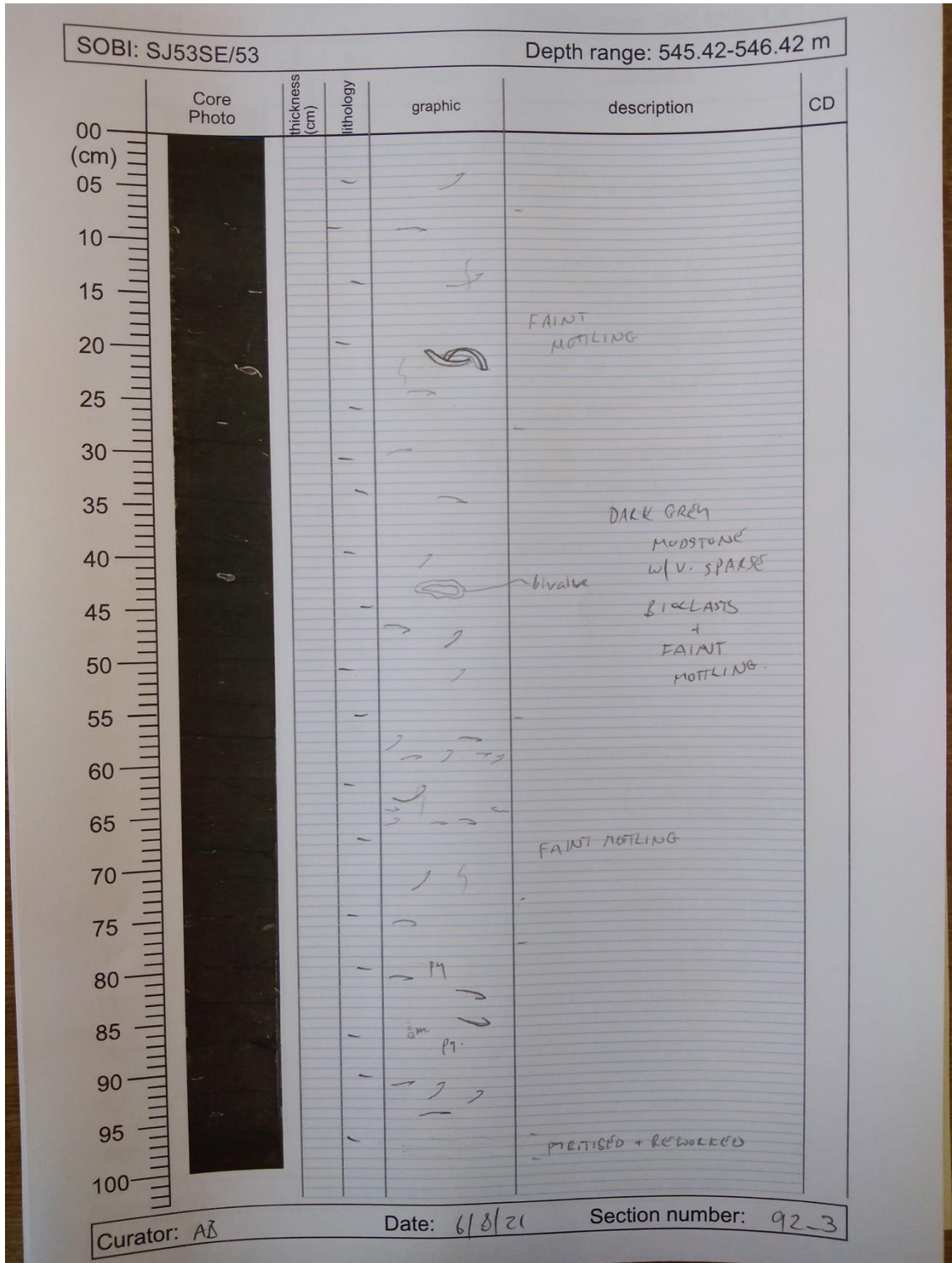
Appendices



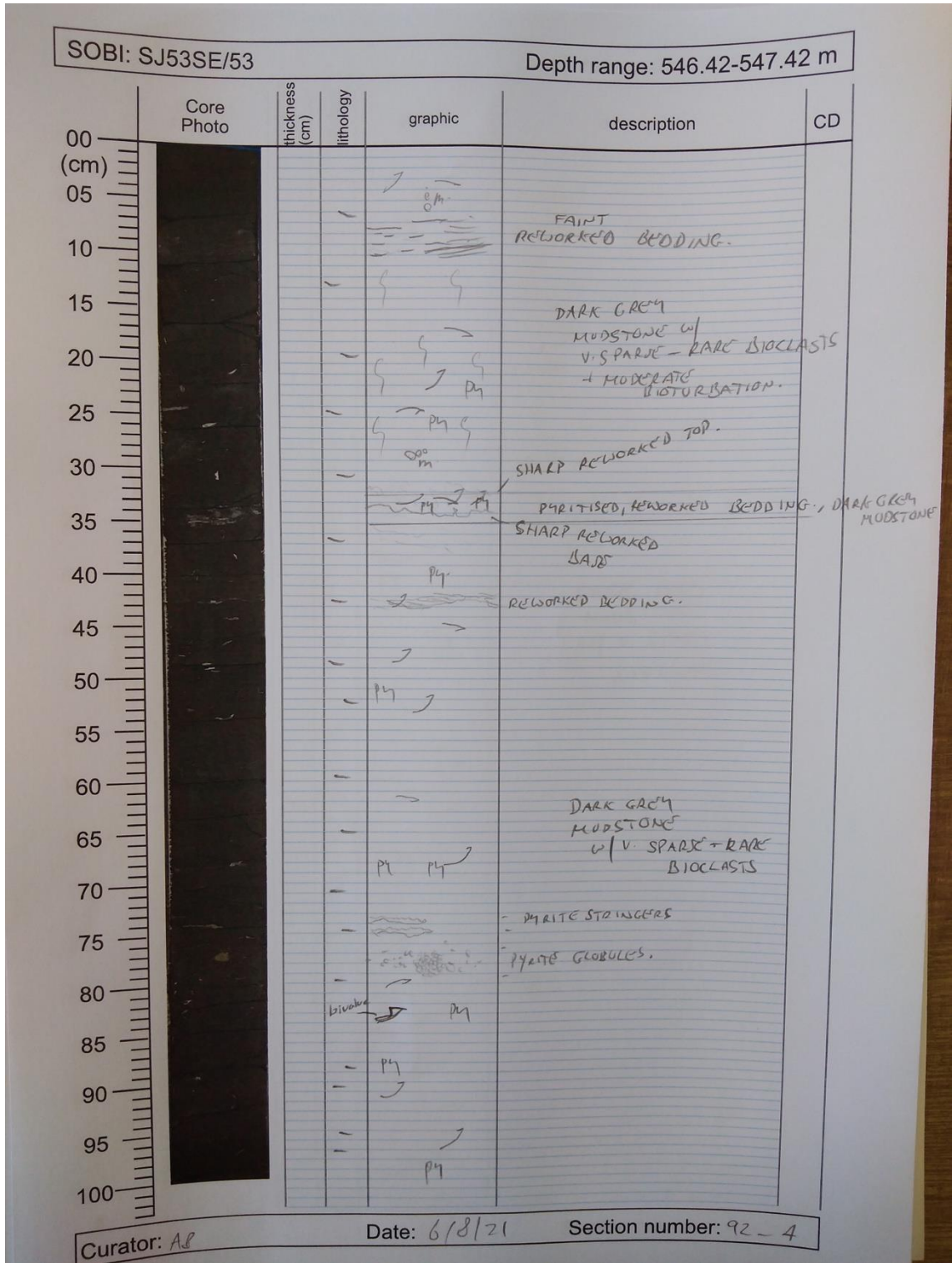
Quantifying marine redox across the Triassic–Jurassic mass extinction



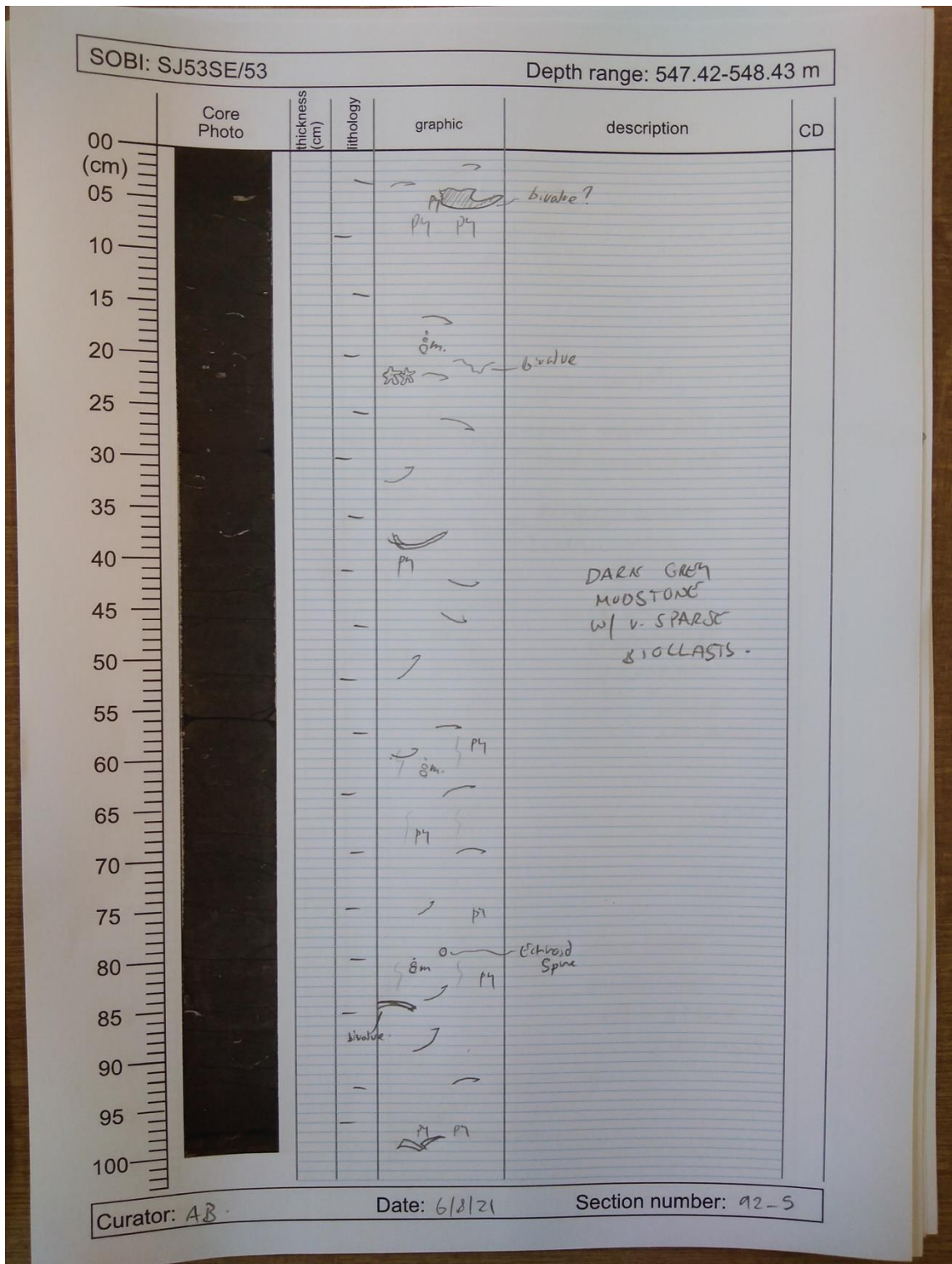
Appendices



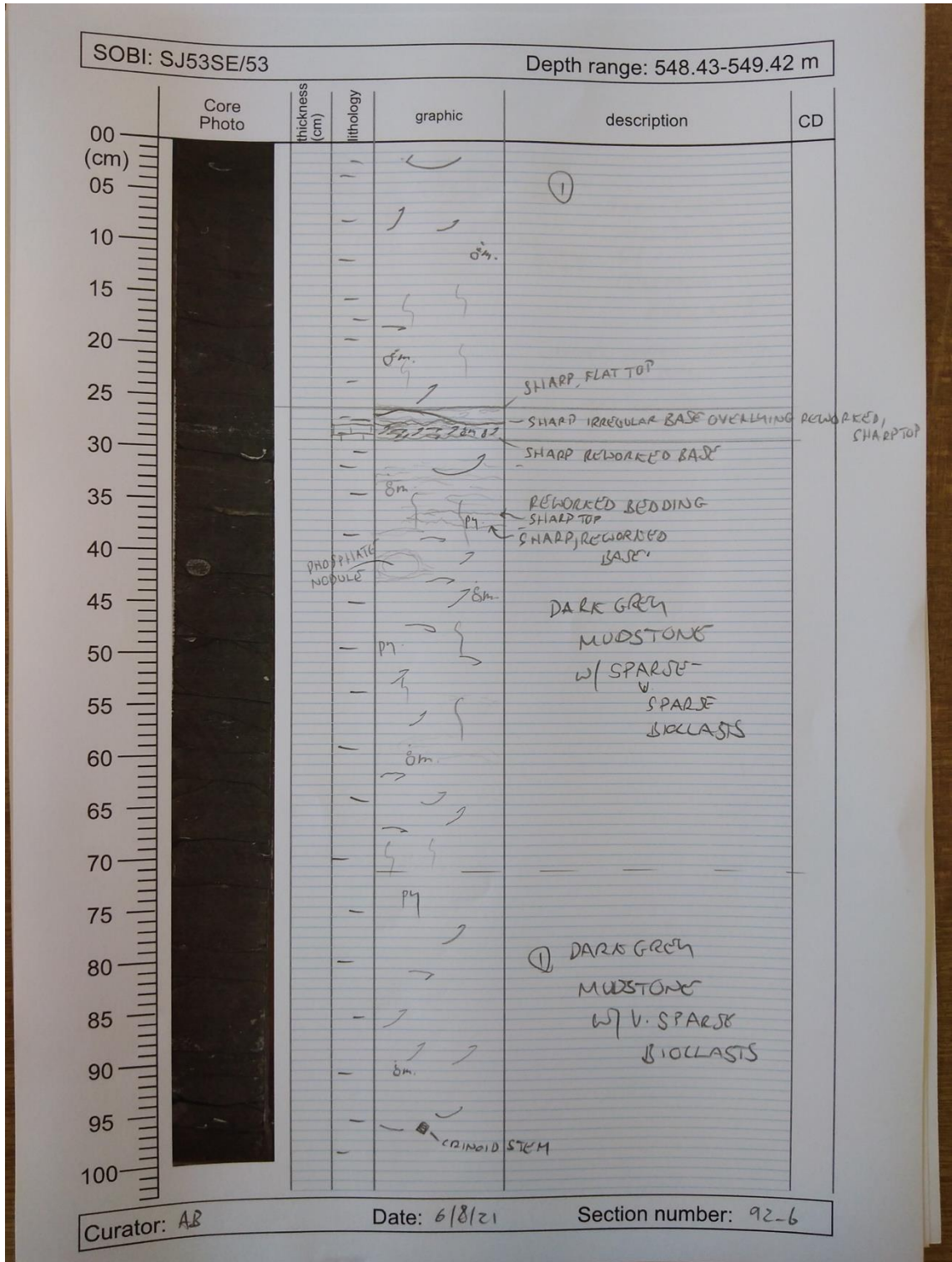
Quantifying marine redox across the Triassic–Jurassic mass extinction




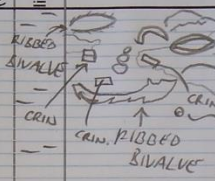
Appendices



Quantifying marine redox across the Triassic–Jurassic mass extinction

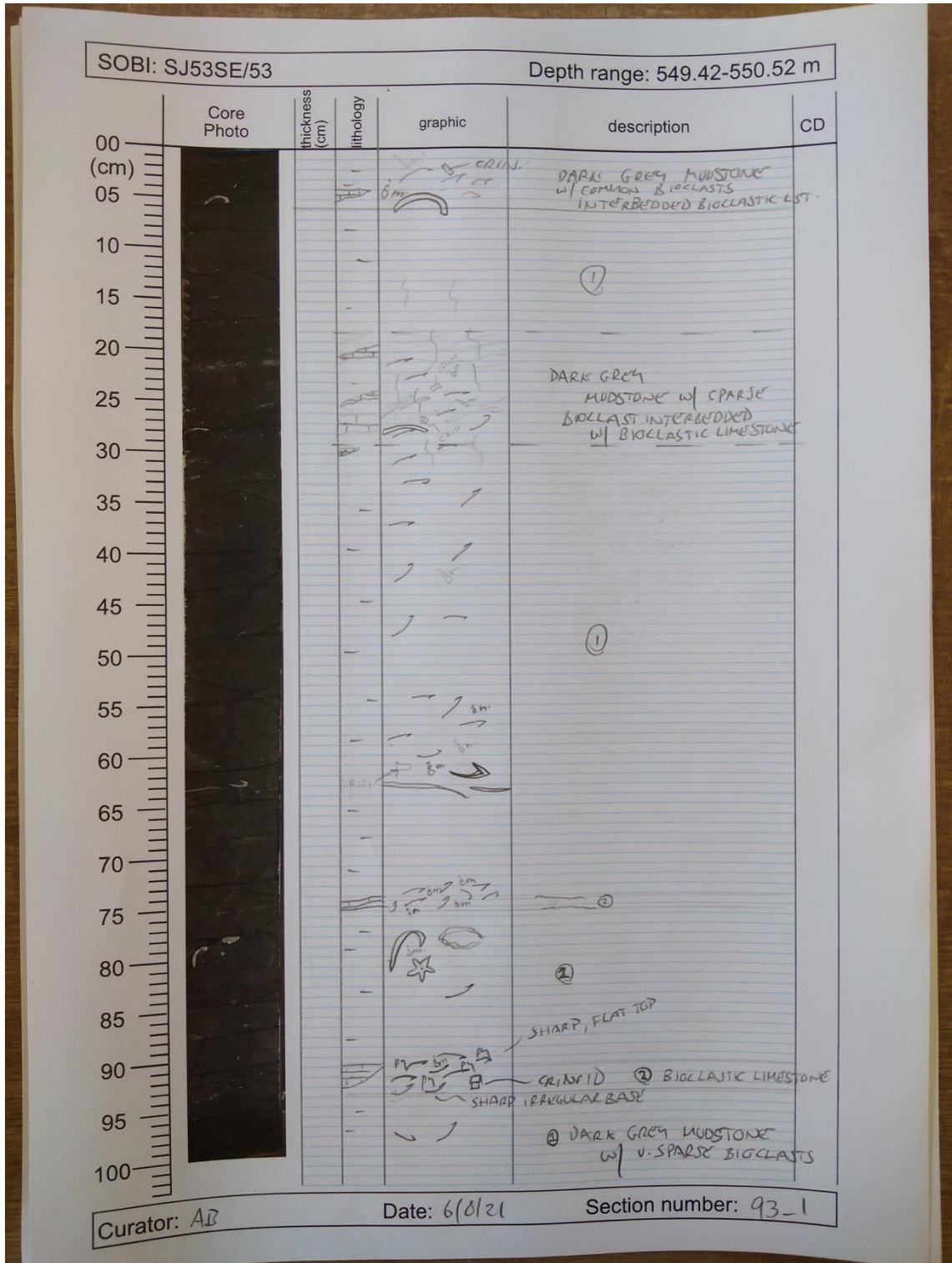


Appendices

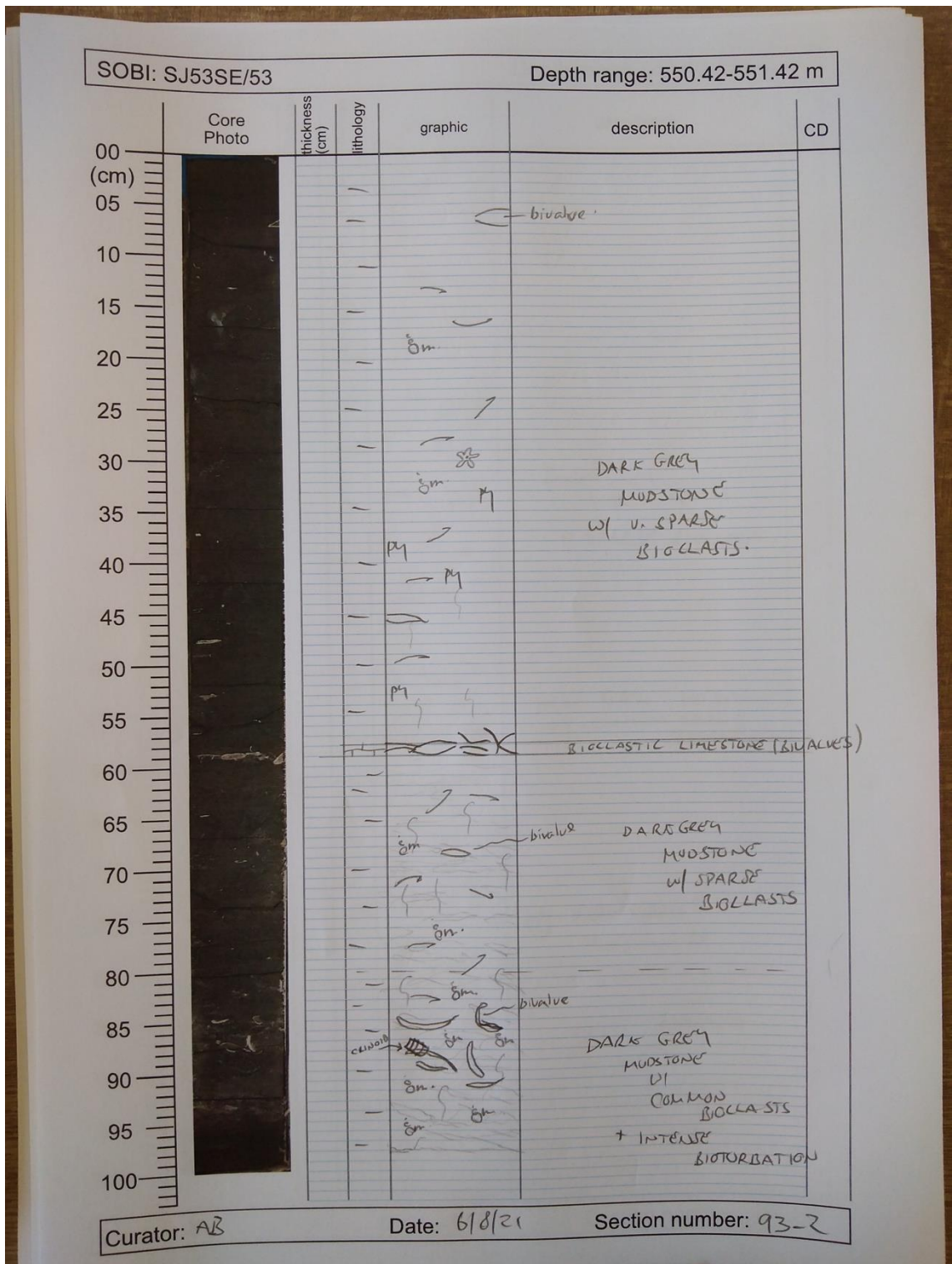
SOBI: SJ53SE/53		Depth range: 549.42-549.51 m				
Core Photo	thickness (cm)	lithology	graphic	description	CD	
	00					
	05					
	10				BIVALVE LIGHTER PATCHES. DARK GREY MUDSTONE W/ COMMON BIOCLASTS INTACT SHORT CRINOID STEM, ARTICULATED BIVALVES.	
	15					
	20					
	25					
	30					
	35					
	40					
	45					
50						
55						
60						
65						
70						
75						
80						
85						
90						
95						
100						

Curator: AB Date: 6/8/21 Section number: 92_7

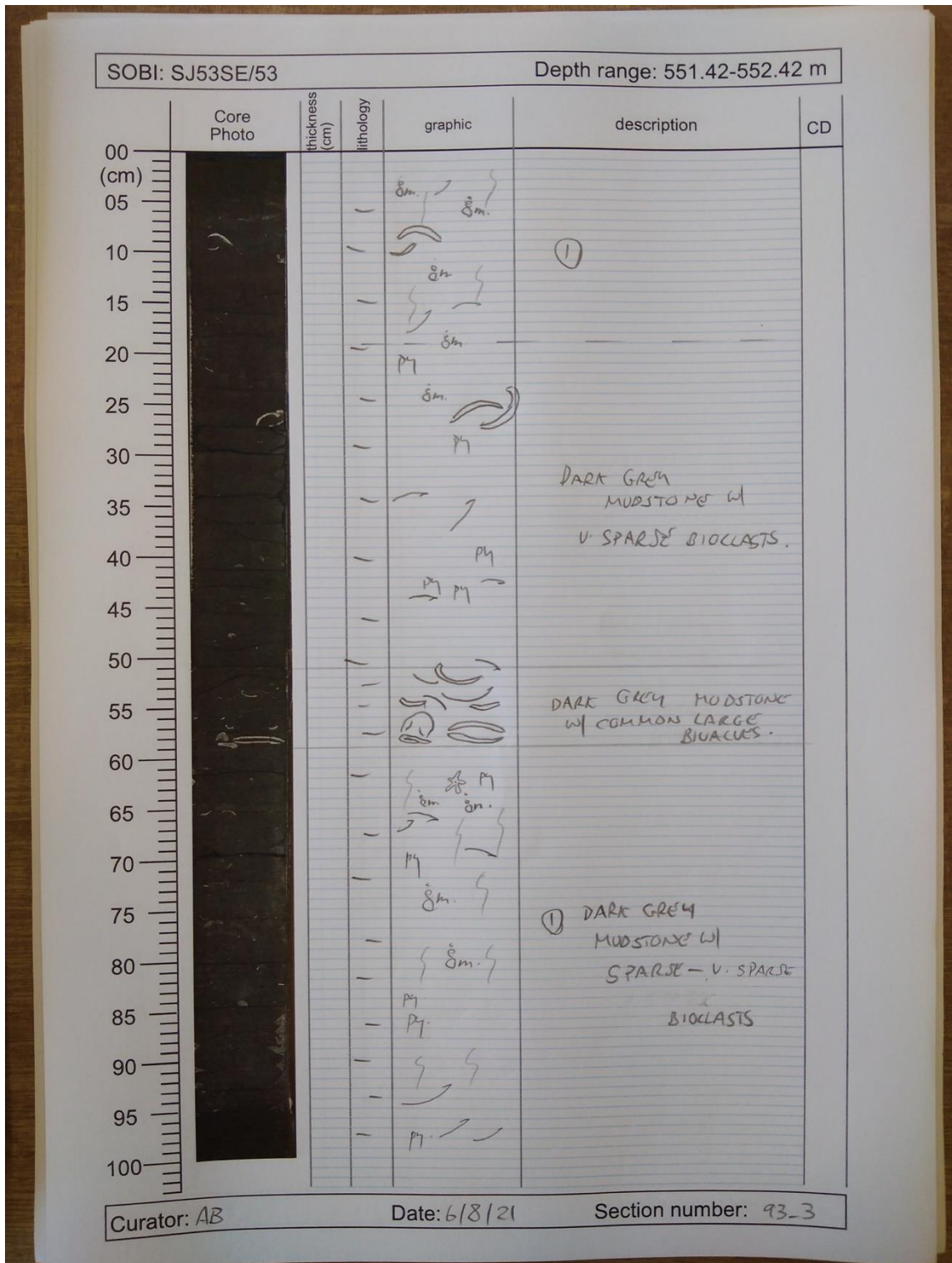
Quantifying marine redox across the Triassic–Jurassic mass extinction



Appendices



Quantifying marine redox across the Triassic–Jurassic mass extinction

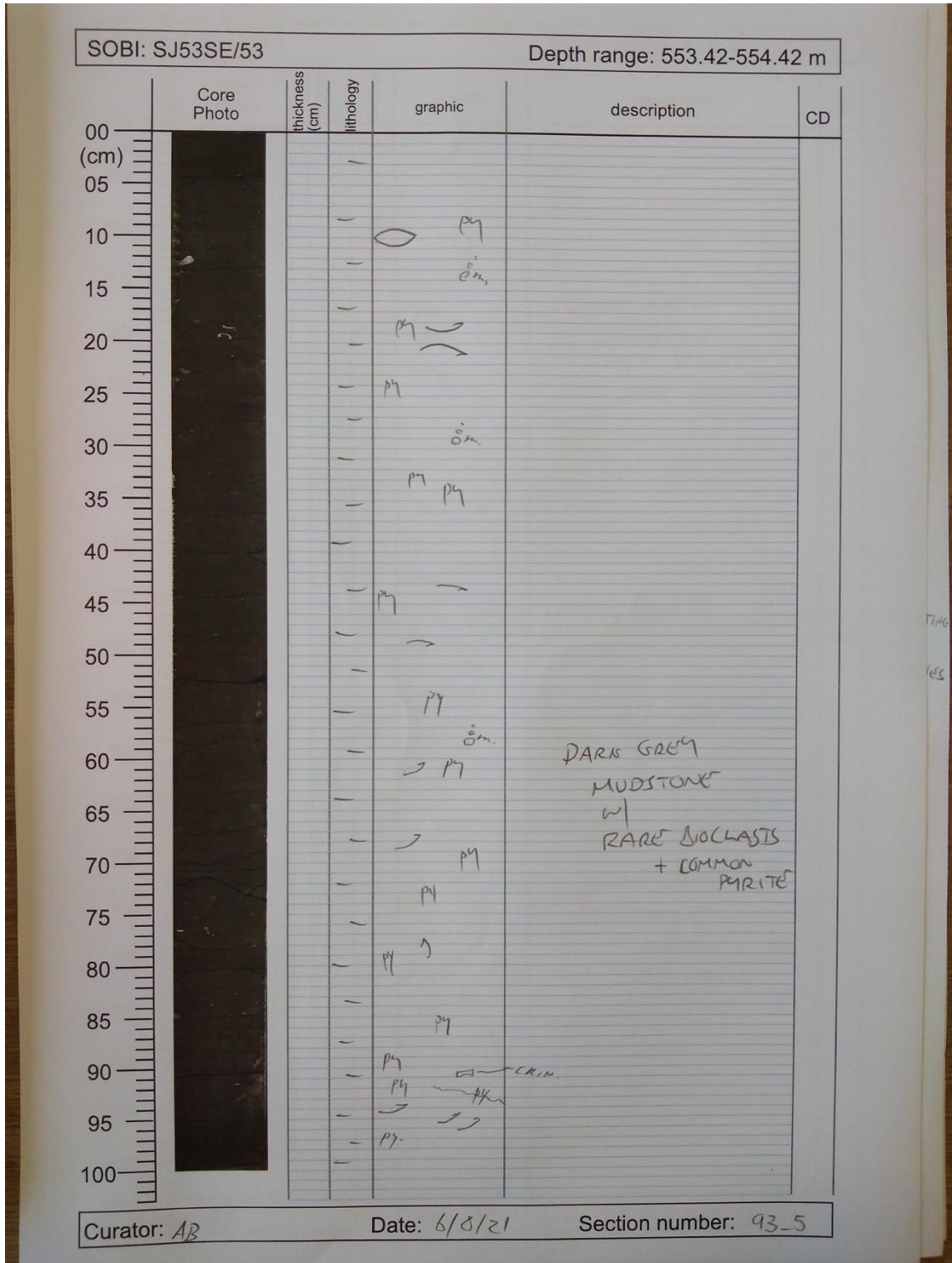


Appendices

SOBI: SJ53SE/53		Depth range: 552.42-553.42 m				
	Core Photo	thickness (cm)	lithology	graphic	description	CD
00	[Core Photo]					
(cm)						
05						
10					P4	
15					P4	
20					P4	
25					P4	
30					P4	
35					P4 P4	
40					P4	
45						
50						DARK GREY MUDSTONE
55					P4	w/ RARE - BIOLLAISTS.
60						
65						
70						
75						
80					P4 P4	
85						
90						
95				LITH.		
100						

Curator: AB Date: 6/8/21 Section number: 93-4

Quantifying marine redox across the Triassic–Jurassic mass extinction

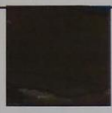


Appendices

SOBI: SJ53SE/53		Depth range: 554.42-555.42 m				
Core Photo	thickness (cm)	lithology	graphic	description	CD	
	00					
	05					
	10			py sm		
	15					
	20			py	DARK GREY MUDSTONE	
	25			py	W/ V. SPARSE RARE BIOCLASTS	
	30					
	35			py sm		
	40			py		
	45					
	50			py	BIOCLASTIC LST. CRINOIDAL LIMESTONE	SHARP + UNDULATING UNCONFORMABLE BOUNDARIES
	55					
	60					
	65			sm		
	70					
75				DARK GREY MUDSTONE		
80			py	W/ RARE BIOCLASTS		
85			py sm			
90			py			
95						
100			py			

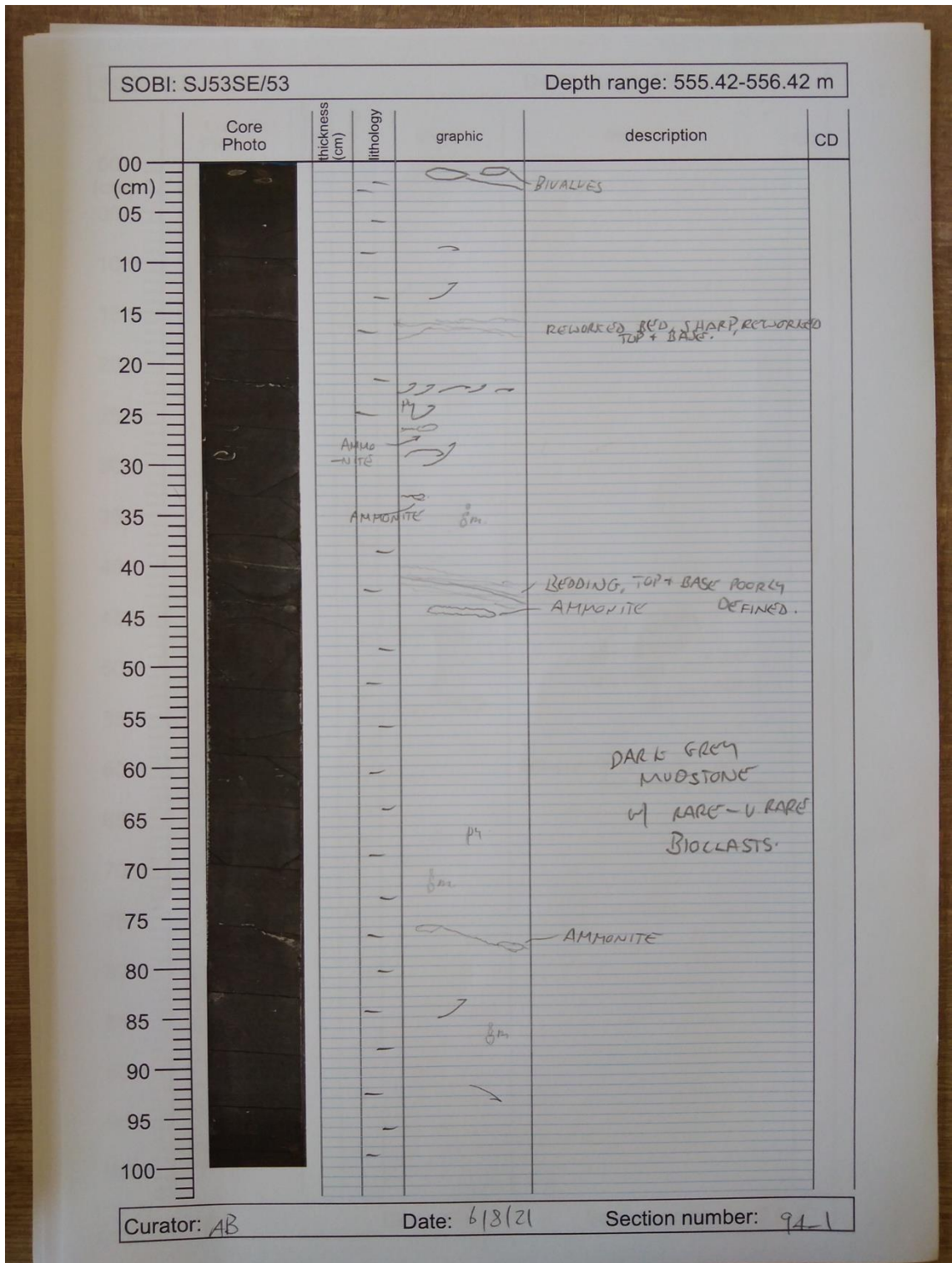
Curator: AB Date: 6/8/20 Section number: 93_6

Quantifying marine redox across the Triassic–Jurassic mass extinction

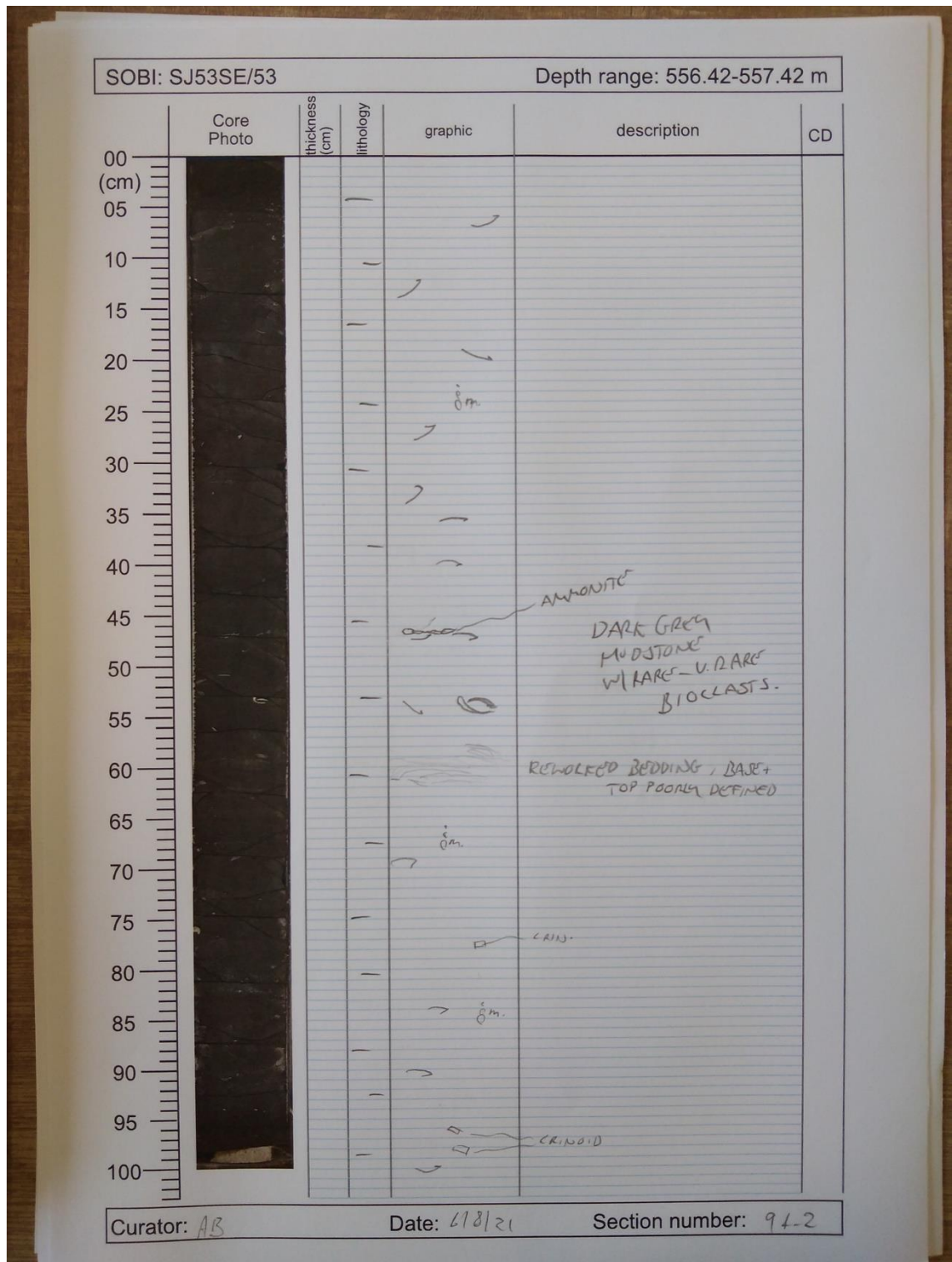
SOBI: SJ53SE/53		Depth range: 555.42-555.49 m				
	Core Photo	thickness (cm)	lithology	graphic	description	CD
00 (cm)				py →	DARK GR. MUDSTONE BIOCLASTS V. SPARSE - RARE.	
05				sm. py		
10						
15						
20						
25						
30						
35						
40						
45						
50						
55						
60						
65						
70						
75						
80						
85						
90						
95						
100						

Curator: AB Date: 6/8/21 Section number: 93_7

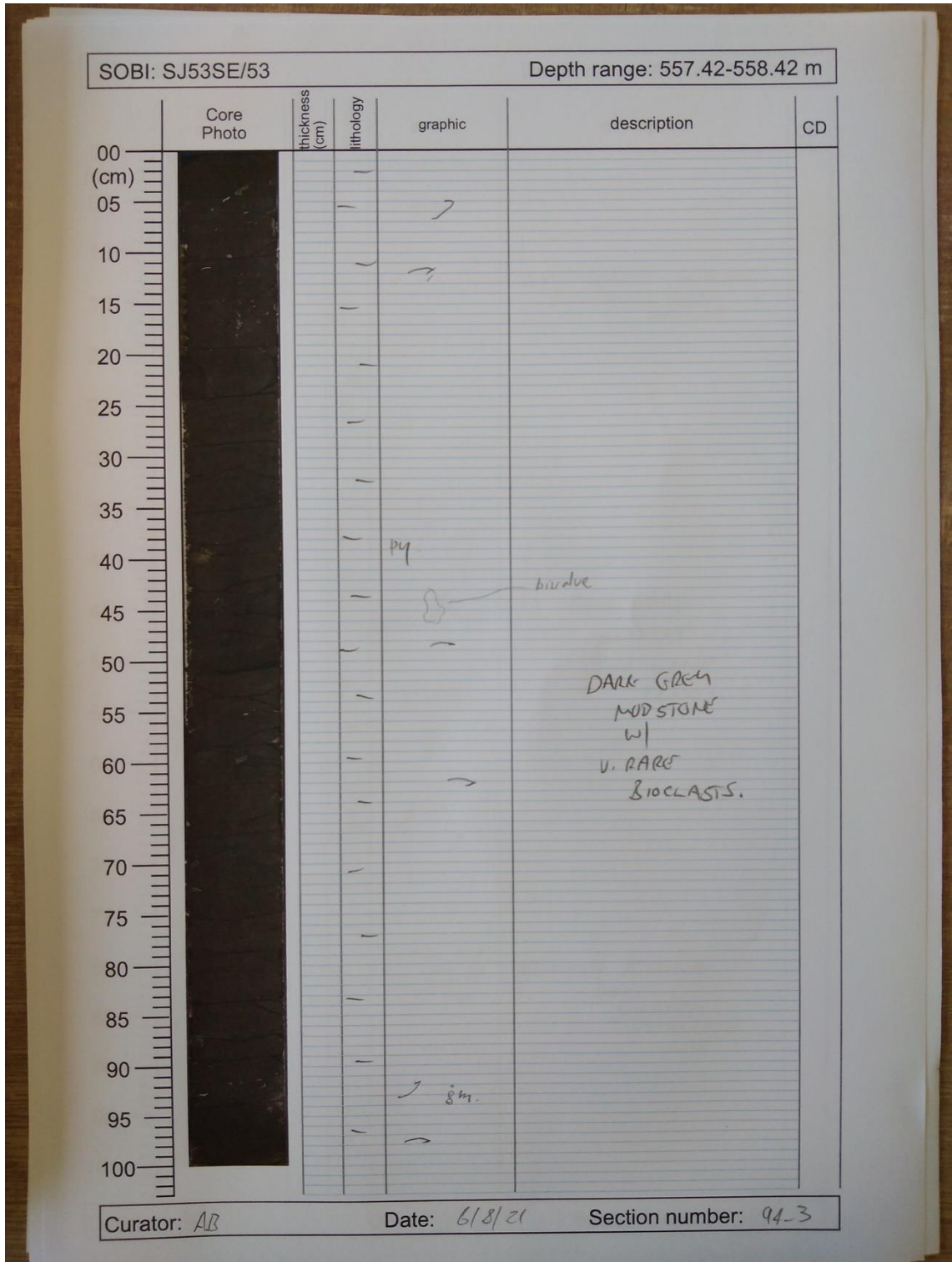
Appendices



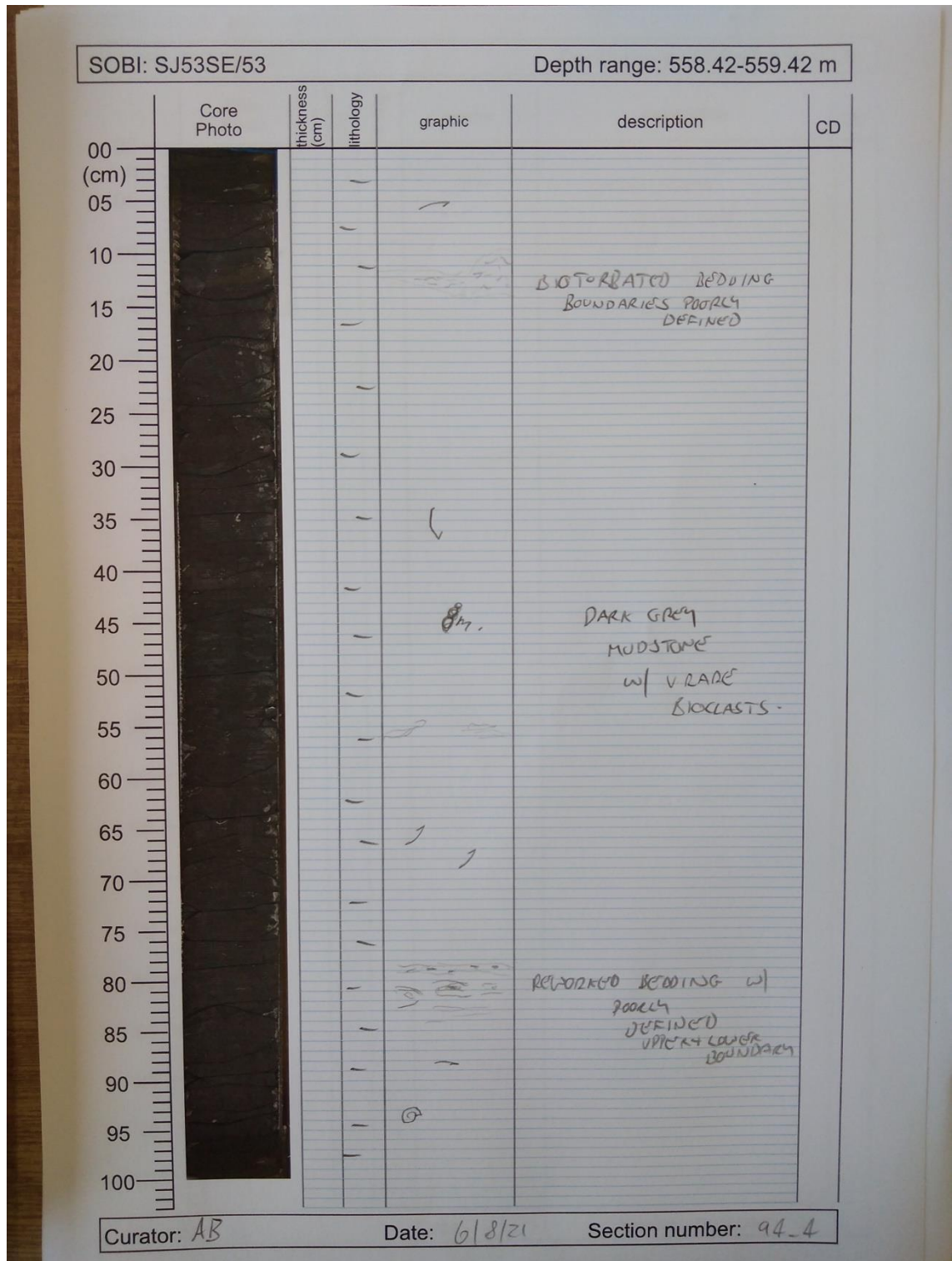
Quantifying marine redox across the Triassic–Jurassic mass extinction




Appendices



Quantifying marine redox across the Triassic–Jurassic mass extinction

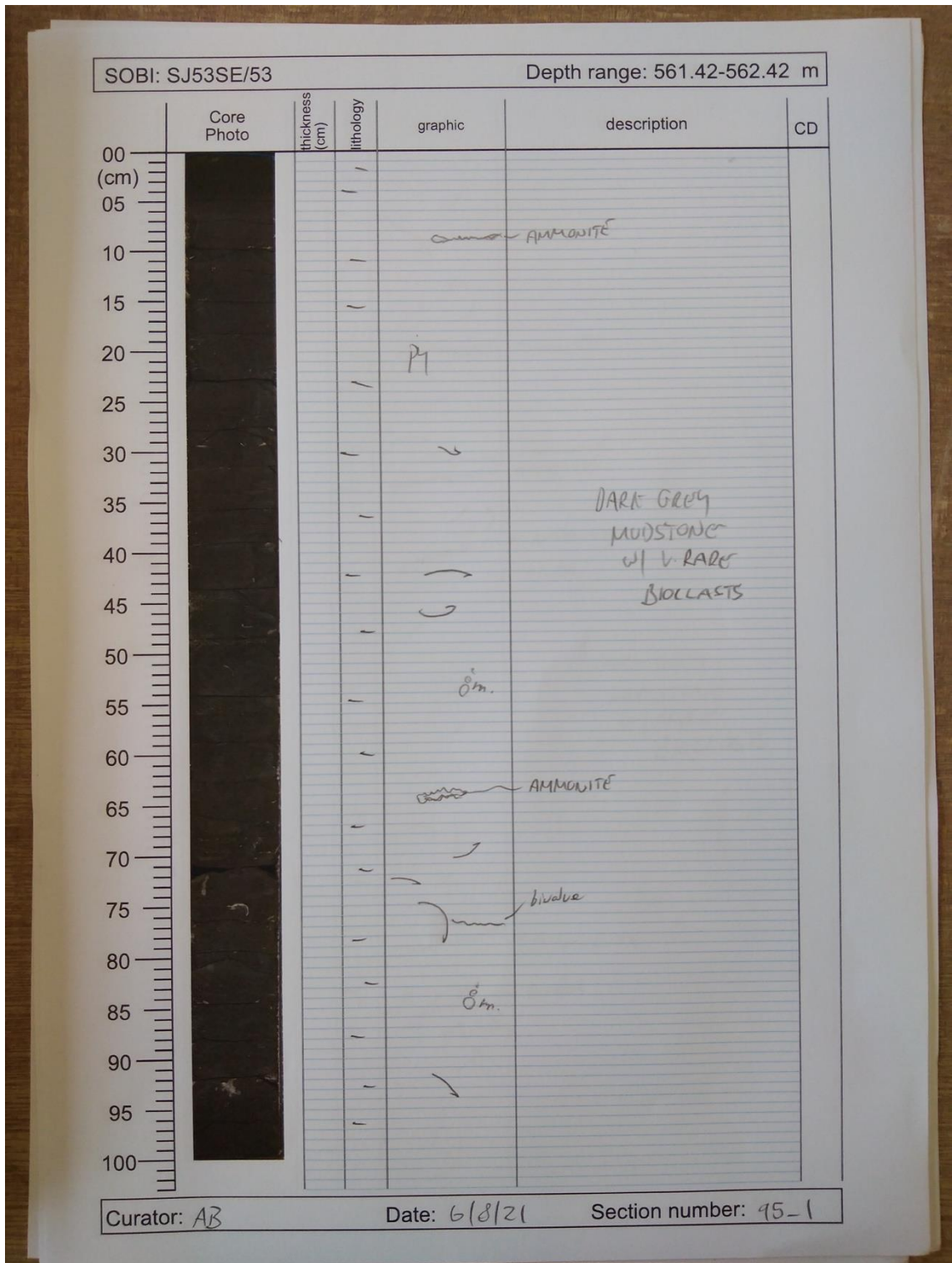


Appendices

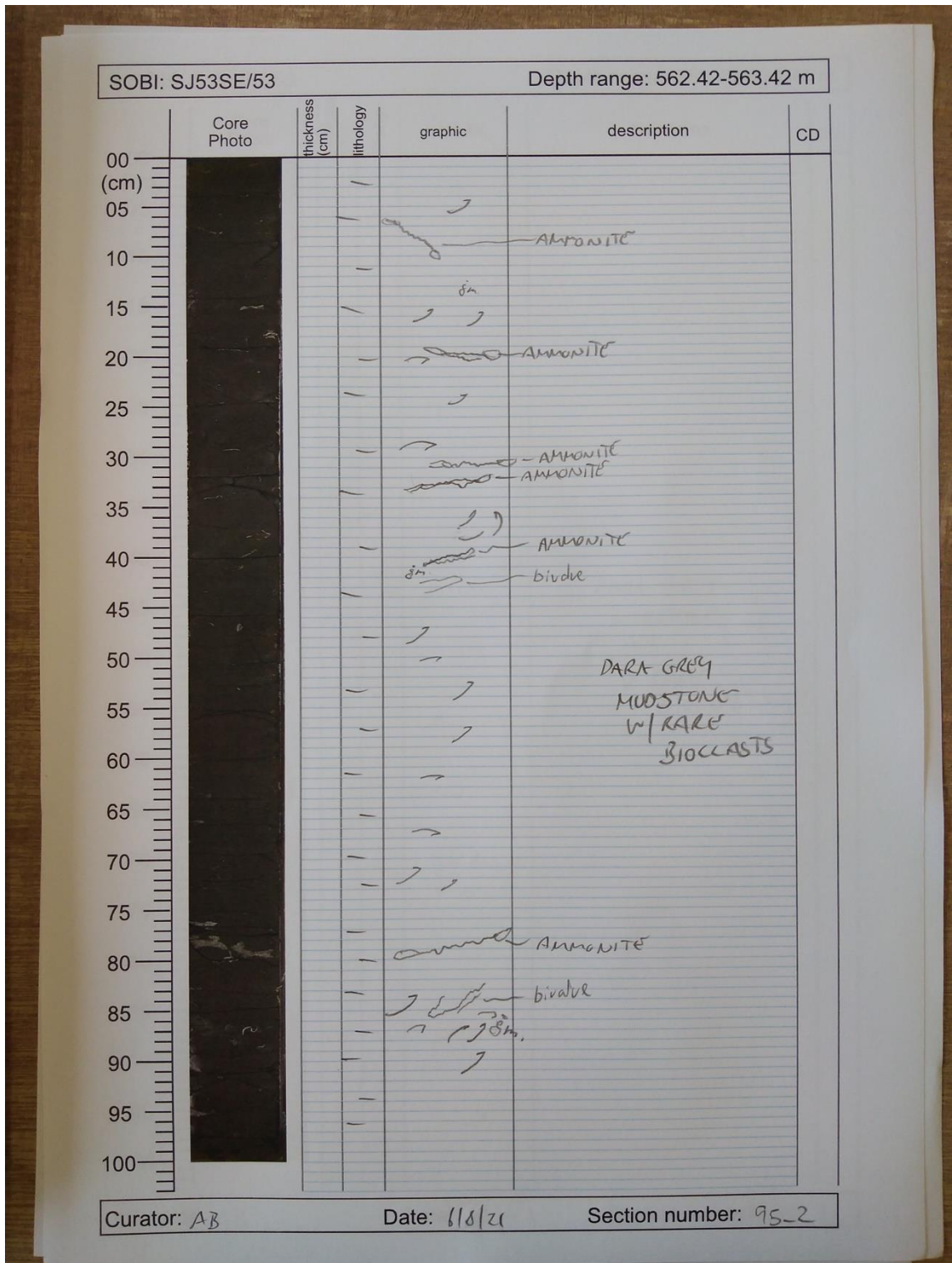
SOBI: SJ53SE/53		Depth range: 559.42-560.42 m				
Core Photo	thickness (cm)	lithology	graphic	description	CD	
	00					
	05			8a	DARK GREY MUDSTONE	
	10				w/	
	15			P7	V. RARE BIOCLASTS.	
	20					
	25					
	30					
	35					
	40					
	45					
50						
55						
60						
65						
70						
75						
80						
85						
90						
95						
100						

Curator: AB Date: 6/8/20 Section number: 94-5

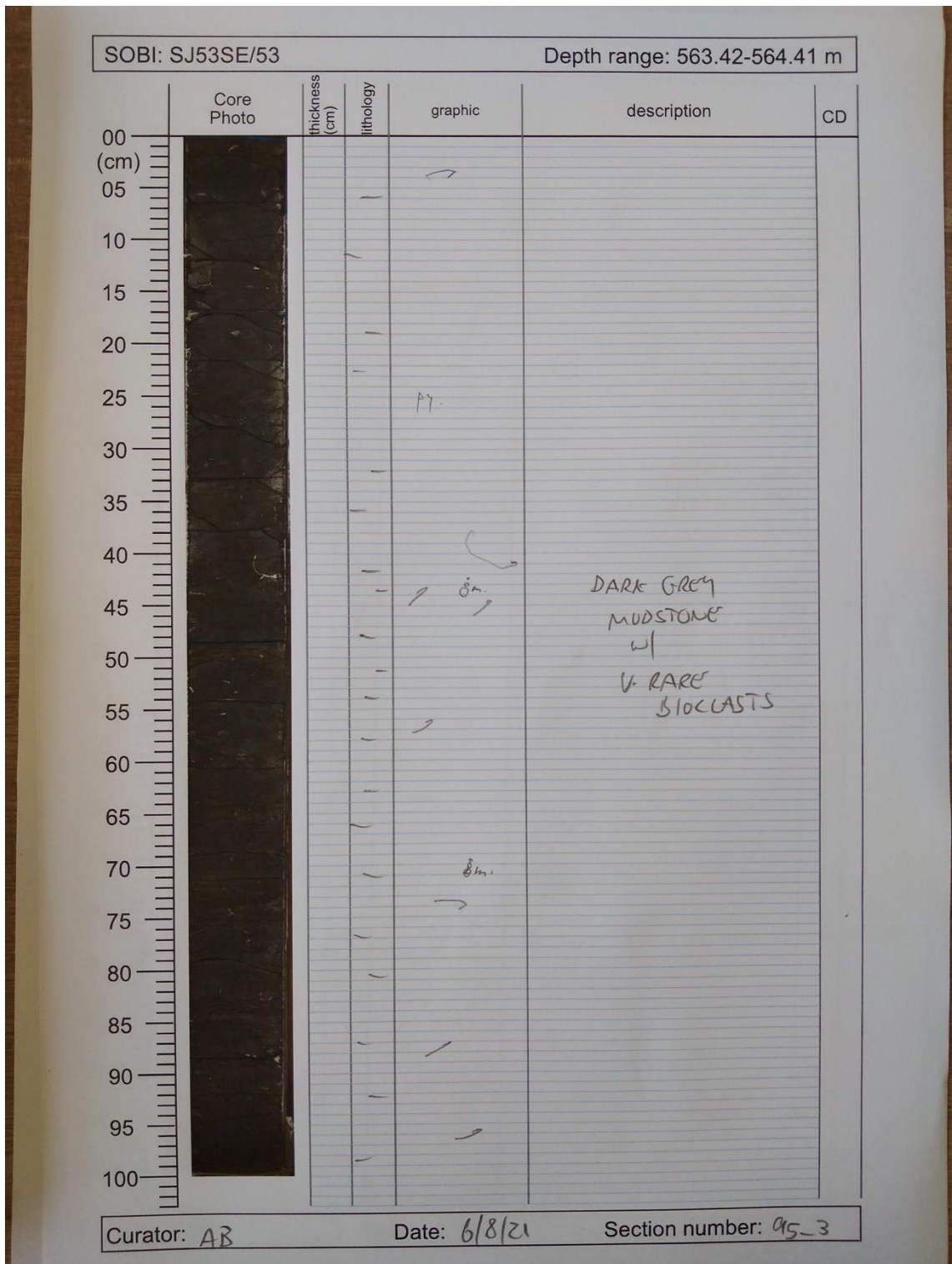
Quantifying marine redox across the Triassic–Jurassic mass extinction



Appendices



Quantifying marine redox across the Triassic–Jurassic mass extinction



Appendices

SOBI: SJ53SE/53		Depth range: 564.41-565.41 m				
Core Photo	thickness (cm)	lithology	graphic	description	CD	
	00					
	05				③	
	10					
	15				BIOCLASTIC LIMESTONE	
	20				② DARK GREY MUDSTONE - SPARSE W/ V. SPARSE BIOCLASTS	
	25					
	30				③ DARK GREY MUDSTONE W/ V. RARE BIOCLASTS	
	35					
	40					
	45					
	50					
	55					
	60					
	65					
	70				②	
	75				① DARK GREY MUDSTONE W/ V. SPARSE BIOCLASTS	
80				②		
85				①		
90						
95						
100						

Curator: AR

Date: 6/8/21

Section number: 95_4

APPENDIX 4: METHODS APPENDIX

APPENDIX 4.1: MILLING METHODOLOGY

Attached as a separate excel file online.

APPENDIX 4.2: SAMPLE MILLING PROCEDURAL GUIDE

The following section details the milling procedure used to powder core samples for this thesis. All samples were powdered within the Department of Earth Sciences at Royal Holloway University of London, Surrey, England.

Equipment used:

- Retsch RS 200 Vibratory Disc Mill
- 50ml Retsch Carbon Steel (Carbon Alloy) Mill (1.1740 & 01.462.0002)
- Paper towel
- Distilled water
- Acetone
- Air bench
- Rock oven
- Ceramic bowls
- Latex gloves
- Lab coat
- Glass sample vials
- Fine marker pen
- Hammer
- Anvil
- Plain A4 paper

Appendices

1. Place each sample in individual ceramic bowls and then leave in the oven at 40°C over the weekend. This step removes any moisture which could hinder milling whilst leaving any organic component of the sample unaffected.
2. After the samples have dried down, turn the oven off and turn the vibratory disc mill and air bench on. The air bench removes any dust, limiting sample contamination, and preventing fine sediment from being suspended in the air. Latex gloves and a lab coat should be worn to avoid sample contamination.
3. Remove the rubber seal from the lid of the disc mill capsule and clean using a paper towel and distilled water only. Clean the barrel, lid and puck of the capsule using paper towels, distilled water and acetone. Re-assemble the capsule ready for the first sample. This step ensures that mill is clean prior to the loading of any samples.
4. Label a glass sample vial with the sample ID using a fine marker pen.
5. If the sample is composed of small chips, <5mm across, load the sample into the barrel straight away. If the sample is composed of chips >5mm, wrap the sample in plain paper and break the sample up using a hammer and anvil, until no part of the sample is >5mm in diameter. This allows for the sample to be more easily processed by the vibratory disc mill.
6. Assuming the sample is now sufficiently fine, load the sample into the barrel of the mill, to one side of the barrel interior, and place the puck inside the barrel, to the side of the sample. The puck being placed to once side of the sample ensures that the puck can most efficiently powder the sample.
7. Place the lid on the barrel and place the capsule inside the vibratory disc mill. Lock the barrel into place and ensure that the capsule is fully secured.

Quantifying marine redox across the Triassic–Jurassic mass extinction

8. Set the vibratory disc mill to 1000rpm and programme the mill to run for 20 seconds. Press the ‘Start’ Button.
9. After the vibratory mill has run for 20 seconds, carefully remove the barrel. Study the sediment to determine if a homogenous consistency has been reached. This is determined by rubbing a small amount of the powdered sample between a gloved thumb and fore-finger. If the sample has a flour-like consistency with no larger fragments, then it is ready. A homogenous consistency for each sample is essential for producing representative geochemical results.
10. If the sample is homogeneous, tip the sample onto a plain piece of A4 paper and then funnel into the labelled sample vial. If the sample is not homogeneous then run the disc mill again at 1000rpm for 20 seconds until a homogeneous consistency has been reached. The approximate final grain size of these samples is 60µm.
11. After the sample has been transferred into the labelled sample vial, brush any remaining sediment away, onto the surface of the air bench. Also brush away any sediment adhering to the puck. Remove the rubber seal from the lid and clean with distilled water only. Then clean the barrel, puck and lid using distilled water and a paper towel, followed by acetone, until visually clean. Brush away any paper towel which has disintegrated inside the barrel. Re-assemble the capsule.
12. Repeat steps 4-11 for each sample, the exact methodology (i.e. timings and procedures) used for the samples milled as part of this PhD project can be found in Appendix 4.3.

APPENDIX 4.3: INDIVIDUAL SAMPLE MILLING PROCEDURE

Attached as a separate excel file online.

APPENDIX 4.4: CLEANING PROCEDURAL GUIDE

4.4.1 Cleaning Teflon (PTFE):

Teflon labware was initially cleaned using a damp tissue and a pen until visually clean. The containers were then filled with a small amount of concentrated HNO₃, the lids replaced, and refluxed on a hotplate at 120°C for 12–14 hours³. After this time the concentrated HNO₃ was removed, and the PTFE containers and lids were moved into a 5L Pyrex® container. The Pyrex® container was filled (submerging the PTFE) with 30–50% HNO₃, topped with a watch glass, and refluxed on a hotplate at 120°C for 12–24 hours.

Following the PTFE being refluxed in 30% HNO₃, the dilute HNO₃ was removed, and the PTFE was rinsed in milli-Q water to remove any remaining HNO₃. The PTFE was then submerged in 30% HCl, topped with a watch glass, and refluxed for 12–24 hours at 120°C. The dilute HCl was removed after the duration and the PTFE was rinsed in ultra-pure milli-Q water to remove any remaining HCl. The PTFE was then submerged and refluxed for 12–24 hours in ultra-pure milli-Q water at 120°C. This step was repeated three times with the old milli-Q water being removed between each wash. All four milli-Q washes were undertaken in a 5L Pyrex® container and topped with a watch glass. Following the fourth milli-Q wash, the milli-Q water was removed, and an empty fume cupboard was cleaned and lined with tissues. The PTFE was then left to air dry on the tissues for 24–48 hours or until the PTFE was completely dry.

³ The methodology evolved to later omit this stage of the cleaning

4.4.2 Cleaning Polypropylene (PP):

All pipette tips, micro-centrifuge tubes, centrifuge tubes and auto sampler vials were initially cleaned in dilute (~1%) HCl. The PP was moved into a Pyrex® container, submerged in weak (~1%) HCl, and topped with a watch glass before refluxing for 12–24 hours at 120°C. After the duration the ~1% HCl was removed, and the PP was rinsed with ultra-pure milli-Q water to remove any traces of HCl. The PP was then submerged in ultra-pure milli-Q water and refluxed at 120°C for 6–12 hours. This step was repeated three times with the old milli-Q water being removed between each wash. All four milli-Q washes were undertaken in a 5L Pyrex® container and topped with a watch glass. Following the fourth milli-Q wash, the milli-Q water was removed, and an empty fume cupboard was cleaned and lined with tissues. The PP was then left to air dry on the tissues for 24–48 hours.

APPENDIX 4.5: ELEMENTAL ANALYSIS PROCEDURAL GUIDE

Described below is the process adopted within this project for digesting powdered rock samples in order to obtain elemental concentration data. All samples were weighed in a clean (metal free) environmental where lab suits and surgical footwear were worn to limit sample contamination. Latex or nitrile gloves were also worn.

4.5.1 Whole rock digestion of non-carbonate samples

The following section details the procedure for the whole rock digestion of non-carbonate samples used within this thesis:

Equipment used: 1ml Eppendorf® pipette, 1ml Eppendorf® pipette tips (acid cleaned), 5ml Eppendorf® pipette, 5ml Eppendorf® pipette tips (acid cleaned), electronic precision scales, weighing paper, weighing table, ultra-pure milli-Q water (in a squeeze bottle), Tupperware® container, QMx 6ml PTFE digestion vessels (acid cleaned), 10ml ICP MS autosampler vials, Teflon coated spatula, concentrated hydrochloric acid (2 x triple distilled), concentrated nitric acid (2 x triple distilled), concentrated hydrofluoric acid, 1M nitric acid, waste beaker, tissues, fine-tipped permanent marker pen, hot plate, Ultem® socket caps, Ultem® spanners.

1. Wipe down the weighing table using ultra-pure Milli-Q water (in a squeeze bottle) and several tissues, then cover the bench with aluminium foil. Ensure the aluminium foil covers the entire surface of the weighing table and try to lay down the foil whilst the table is still damp, so the foil adheres to the bench surface. The

Quantifying marine redox across the Triassic–Jurassic mass extinction

- purpose of cleaning the weighing table and covering the table surface is to i) remove any fine sediment left by previous users, ii) further reduce sample contamination, and iii) limit contamination for subsequent users.
2. Position the scales in the middle of the table, on a flat and stable portion, and adjust the scale to ensure that they are level. Optimal positioning of the scales is achieved when the bubble on the spirit level of the scales is positioned centrally. Turn the scales on at the wall and then proceed to press the ‘on/ off’ button on the electronic scales. Zero the scales by pressing the button on the button assembly. Locate a small grey box, in which two check-weights are located (a 1mg and 100mg weight). Remove the 1mg weight using the accompanying tweezers and place the weight on the scales. Close the doors and wait for the scales to fall on a value, and rest at this value for at least 10 seconds. Record the value given by the scales. The value given by the scales should be close to 0.001g (within 0.0002g). If the check-weight is within the given range, proceed to step 4. If the check-weight is outside of this range, then re-weigh using the 100mg weight followed the 1mg weight a second time.
 3. Put the check-weights away and then take 0.6ml (600 μ l) of distilled concentrated HCl into a 1ml pipette tip using the 1ml pipette. Then carefully lay the pipette down horizontally.
 4. Next ensure the Teflon coated spatula is clean by washing with milli-Q water and wiping clean with a tissue.
 5. Label a Teflon digestion vessel (both the vessel and the lid) with the given sample number

Appendices

6. Take a sheet of the weighing paper and fold in half and then half again, tearing the paper into four, equal-sized squares (~30mm x ~30mm). Place one of these squares onto the scales, close the doors and zero the scales.
7. Open the first container of sediment powder on a bench behind, laid down with a tissue, and place the lid onto the bench. Turn to face the weighing table again and begin to load the sample slowly and carefully onto the square of weighing paper (on the scales) using the cleaned Teflon-coated spatula.
8. Continue to load the sediment onto the weighing paper until ~50 mg (0.05g) of sediment are on the paper
9. Close the doors and wait for the scales to rest on a figure and then record the exact weight of sediment in a workbook, next to the respective sample ID and given sample number. The exact weight is recorded in order for the ICP-MS and ICP-AES concentrations to be corrected for dilution factor.
10. Funnel the ~50mg of sediment powder into a clean 6ml Teflon digestion vessel by carefully pinching together two, opposite corners of the weighing paper. Ensure all of the sediment is funnelled into the digestion vessel and then dispose of the used weighing paper.
11. Immediately (slowly) add the 0.6 ml distilled concentrated HCl into the digestion vessel. The concentrated HCl removes any sediment that is lining the walls of the vessel, through electrostatic attraction, and also de-carbonates the sample⁴ so expect some fizzing. Do not let any sample 'creep' up the inside the vial and escape over the threads while fizzing.

⁴ $\text{CaCO}_3(\text{s}) + 2\text{HCl}(\text{aq}) \longrightarrow \text{CaCl}_2(\text{s}) + \text{H}_2\text{O}(\text{l}) + \text{CO}_2(\text{g})$

Quantifying marine redox across the Triassic–Jurassic mass extinction

12. Screw the lid loosely on top of the digestion vessel and place under an upturned Tupperware® container. The Tupperware® container reduces potential contamination.
13. Clean the Teflon-coated spatula, using the milli-Q water, and wipe clean using a tissue.
14. Repeat steps 6 through to 14 for all samples.
16. Once all of the samples have been weighed and added to concentrated HCl in a digestion vessel place the vessels under a fume cupboard.
17. Clean the workbench and put away all utensils from the weighing table. Dispose of any liquids down the sink, return the pipettes to the pipette rack, wash out any utensils/containers and bin the aluminium foil.
18. Locate a 5ml pipette and a clean 5ml pipette tip and take up 2ml (2000µl) of distilled concentrated nitric acid. Then remove the acid to the waste. This ‘pre-conditions’ the pipette tip.
19. Pipette into each digestion vessel, now filled with your de-carbonated sample, 1800µl (1.8ml) of (2x) triple distilled concentrated nitric acid. Then screw the lid back on to the digestion vessel until ‘hand tight’. Do this for each vessel. This produces a final ratio within each vessel of HNO₃ : HCl of 3:1 (inverse aqua regia). Inverse aqua regia preferentially dissolves authigenic minerals (e.g. organic compounds, pyrite and carbonate) and leaves most detrital minerals (e.g. quartz, phyllosilicates and feldspar)⁵ whilst leaching non-structurally bound metals from silicates (e.g. Molybdenum) [Xu *et al.*, 2012].

⁵ $\text{Mo(s)} + 3\text{NO}_3^- (\text{aq}) + 6\text{H}^+(\text{aq}) \rightleftharpoons \text{Mo}^{4+} (\text{aq}) + 3\text{NO}_2(\text{g}) + 3\text{H}_2\text{O}(\text{l})$
 $\text{Mo}^{4+} + 4\text{Cl}^- (\text{aq}) \rightleftharpoons \text{AuCl}_4^-(\text{aq})$

Appendices

20. Proceed to place an Ultem® socket cap on each digestion vessel and turn the cap between 45 and 90 degrees using the Ultem® spanners, until sufficiently sealed. Exercise judgement to avoid breaking the threads.
21. Place the vessels onto the hot plate at 150°C for 2–3 days or until the authigenic component of the sample has completely digested. Due to the process of inverse aqua regia digesting the sample at 150°C, the sample can build up large amounts of pressure very quickly. The use of Ultem® socket caps is therefore essential for holding the lids in place, preventing the threads from breaking and the lids being removed at high pressures.
22. After the authigenic component of the sample is completely digested, remove the Ultem® caps and lids from the vessels, placing the lids face down on a tissue, and dry-down the samples on the hotplate at 90–105°C.
23. Once dried down add 1ml (1000µl) of distilled concentrated nitric acid to each sample and then 0.5ml (500µl) of HF to each sample. Wear two pairs of gloves and eye protection when handling HF due to its high toxicity. HF acid digestion is a highly effective method for breaking down Si-O bonds⁶, HF forms SiF₆²⁻ ions in acidic solution with silicates being subsequently converted to volatile SiF₄ [Hu & Qi, 2014]. The combination of HF with HNO₃ ensures persistently uniform high oxidation states within final solutions [Hu & Qi, 2014].
24. Seal and place back on the hot plate at 120°C for 1–2 days or until the detrital component of the sample has completely digested.

⁶ $\text{MgSiO}_3(\text{s}) + 6\text{HF} \Rightarrow \text{SiF}_4(\text{g}) + \text{CaF}_2(\text{s}) + 3\text{H}_2\text{O}(\text{l})$

Quantifying marine redox across the Triassic–Jurassic mass extinction

25. After 1–2 days remove the lids, placing them face down on a tissue and allow the samples to dry out once again on the hot plate at 90–105 degrees for 1–2 days, until residue.
26. Once the samples have reduced to residue, add 100ul of distilled concentrated nitric acid to each vessel and wait for the acid to evaporate off. Repeat this once. This purpose of this process is to evaporate off any residual fluoride that could inhibit re-dissolution. Then place the lids back on the vessels.
27. Re-clean the weighing table with tissues and ultrapure milli-Q water. Re-level the scales and record the value of the check-weights. Place a sample on the scales and set the scales to zero. Fill the digestion vessel with 5ml of 1M HNO₃. Close the doors to the scales and note the exact volume (by mass) of 1M HNO₃ next to the sample ID and sample mass (see step 9.). Re-seal the vessel and place under a Tupperware® container. This step re-dissolves the residue to a final dilution of ~100 fold. Repeat this process for all samples. Place the samples back on the hotplate at 120°C overnight to equilibrate the residue with the 1M HNO₃.
29. The samples are now diluted to 100 fold (50mg is a 20th of 1g and the 5ml of acid multiplies (dilutes) this value by 5).
30. If the stock solution needs storing at this stage then the solution may be transferred into 15ml centrifuge tubes and stored in sealed ziplock bags to avoid contamination.

ICP AES: Take a pre-cleaned ICP autosampler vial (soak overnight in 3% HNO₃, rinse with MQ water, air dry) and add 4ml stock to 2ml ultra-pure milli-Q water, this produces a ~150-fold dilution. Place the lid on the vial. Repeat this step for all samples using a new pipette tip for every sample. Ensure all vials and lids are clearly numbered and upon completion of this step store vials to one side in a rack.

Appendices

1. Make up seven calibration standards (500ppm, 250ppm, 50ppm, 30ppm, 10ppm, 0.1ppm, 0ppm) for the ICP-AES:

500ppm: 10ml Fe Calibration Standard and 10ml Al Calibration Standard

250ppm: 10ml 3% HNO₃ and 10ml 500ppm solution

50ppm: 2ml of all 20 calibration standards (Al, Ba, Ca, Co, Cr, Cu, Fe, K, Li, Mg, Mn, Na, Ni, P, Pb, Sr, Ti, V, Zn, Zr)

30ppm: 12ml 50ppm solution and 8ml 3% HNO₃

10ppm: 4ml 50ppm solution and 16ml 3% HNO₃

0.1ppm: 40ul of 50ppm solution and 19.96ml 3% HNO₃

0ppm: 3% HNO₃ x 20ml

2. Take the aliquots and standards for ICP-AES analysis

3. Concentrations for each sample can be found by multiplying the measured concentrations of each element by the dilution factors.

ICP MS: Pipette 2090ul of ultra-pure milli-Q water into 25 numbered, safe lock micro centrifuge tubes. Using a new pipette tip for each sample, pipette 110ul of each numbered sample solution into its corresponding micro centrifuge tube (now filled with milli-Q water). Close the lids and shake each micro-centrifuge tube in turn. This produces a ~2000 fold dilution.

Quantifying marine redox across the Triassic–Jurassic mass extinction

Major elemental concentration data:

Major element concentration data was obtained through a Perkin Elmer Optima 3300RL ICP-AES (Inductively Coupled Plasma Aerial Emission Spectrometer). All ICP AES analyses for this thesis were processed within the Geochemistry Lab within the Department of Earth Sciences, Royal Holloway University of London. All analyses used the same standards where possible to remove unwanted bias. A series of in house standards ('M' and 50ppm standard) were used to measure instrumental drift after every 8 samples throughout the run. A 5-point calibration line constructed from certified standards (Table X) was used to convert elemental intensities to element concentrations. Data processing was undertaken in Microsoft Excel.

Minor elemental concentration data:

Minor and trace elemental concentration data was obtained through a Perkin Elmer NexION 350D ICP-MS (Inductively Coupled Plasma Mass Spectrometer). All ICP-MS analyses for this thesis were processed at the Department of Earth Sciences, University of Oxford. Each sample was also doped with 1ng/g Rh, In, Ir and Re to correct for instrumental drift. Calibrations were obtained for each element on the instrument using an external calibration constructed from a 10ppm custom-blend multi element standard produced by CPAchem Ltd. An external standard was also diluted and measured from a custom bought QMx multi element solution. The elemental data obtained for all samples can be found in Appendix 4.

Appendices

4.5.2 Digestion of carbonate samples

The following section describes the procedure for the digestion of carbonate samples used within this thesis. These steps are important to selectively dissolve Zn bound in the carbonate matrix and avoid liberating organic and oxyhydroxide bound Zn.

Equipment used: 10ml Eppendorf® pipette, 10ml Eppendorf® pipette tips, 5ml Eppendorf® pipette, 5ml Eppendorf® pipette tips (acid cleaned), electronic precision scales (2 d. p.), weighing table, ultra-pure milli-Q water (in a squeeze bottle), 0.15M citric acid + 12M ammonium solution, NaOH-buffered H₂O₂, 0.2M Acetic Acid, 15ml centrifuge tubes, Teflon coated spatula, waste beaker, tissues, fine-tipped permanent marker pen, hot plate, centrifuge, ultra-pure Milli-Q water.

1. Wipe down the weighing table using ultra-pure Milli-Q water (in a squeeze bottle) and several tissues, then cover the bench with aluminium foil. Ensure the aluminium foil covers the entire surface of the weighing table and try to lay down the foil whilst the table is still damp, so the foil adheres to the bench surface. The purpose of cleaning the weighing table and covering the table surface is to i) remove any fine sediment left by previous users, ii) further reduce sample contamination, and iii) limit contamination for subsequent users.
2. Next ensure the Teflon coated spatula is clean by washing with milli-Q water and wiping clean with a tissue.
3. Label a centrifuge tube with a sample number and place the centrifuge tube into a beaker, on top of the scales.
4. Unscrew the lid from the centrifuge tube but leave the lid on top of the tube.

Quantifying marine redox across the Triassic–Jurassic mass extinction

5. Open the first container of sediment powder on a bench behind, laid down with a tissue, and place the lid onto the bench. Turn to face the weighing table again. Remove the lid from the tube and place it onto a tissue and zero the scales.
6. Begin to load the sample slowly and carefully into the tube (on the scales) using the cleaned Teflon-coated spatula.
7. When the scales record ~0.3–0.5g, place the lid back onto the sample container, record the exact weight of the sample in a workbook, next to the respective sample ID, and given sample number.
8. Immediately add 10ml of ultra-pure milli-Q water to the sample, place the lid back onto the centrifuge tube and seal the tube. Shake the tube for one minute.
9. Repeat steps 2–9 for all samples.
10. Centrifuge all samples for 10 minutes at 4000 rpm and tip away the supernatant to the waste.
11. Repeat steps 8 and 10 once for all samples.

[If reductive cleaning is not required, skip to step 18]

12. Quickly pipette 5 ml of 0.15M citric acid + 12 M ammonium solution into each sample tube
13. Place the samples into a centrifuge tube rack and then place the rack onto a hotplate at 50°C for 15 minutes with the tubes sealed.
14. Centrifuge all samples for 5 minutes and tip the supernatant away, into a waste bottle (not the sink)
15. Immediately add 10ml ultra-pure milli-Q water and shake for 1 minute. Repeat for each sample.
16. Centrifuge samples from 5 minutes and tip away water to waste.

Appendices

17. Repeat steps 15 and 16 twice to ensure that all reducing solution has been removed.

[If oxidative cleaning is not required, skip to step 24]

18. Add 5ml NaOH-buffered H₂O₂ to each sample

19. Place samples onto a hotplate at 50°C for 30 minutes with the lids loosely on.

20. Centrifuge for 10 minutes and decant the buffered peroxide solution.

21. Immediately add 10ml ultra-pure milli-Q water and shake for 1 minute. Repeat for each sample.

22. Centrifuge samples from 5 minutes and tip away water to waste.

23. Repeat steps 21 and 22 twice to ensure that all oxidising solution has been removed.

24. Add 7ml of 0.2M acetic acid to each sample and shake for 1 minute.

25. Centrifuge all samples for 10 minutes at 4000 rpm and use the 5ml pipette and a cleaned 5ml pipette tip to carefully remove the supernatant into a clean 15ml PTFE vial.

26. Add a second 7ml aliquot to the powder, seal, shake for 1 minute, and leave overnight.

27. The next morning, centrifuge the samples for 10 minutes at 4000 rpm and using a 5ml pipette and clean pipette tip carefully remove the supernatant into the sample 15ml PTFE vial as the first leach.

28. Evaporate dry at 90°C over the weekend and then re-dissolve in 10 ml 3% HNO₃.

29. Aliquot 0.01ml of each leach solution into 9.99ml 3% HNO₃ to make ~20ppm Ca solutions. These can be run on the ICP-MS as concentration checks.

Quantifying marine redox across the Triassic–Jurassic mass extinction

30. Aliquot appropriate amount of stock leachate into 3% HNO₃ to make >5ml =20ppm Ca solution. These can be run on ICP-MS for element/Ca data.
31. Once Zn data are available, weigh appropriate amount of double spike into each vial and reflux overnight at 90°C.
32. Evaporate dry and re-dissolve in 1-2ml HF/HCl loading solution for mini-columns.

**APPENDIX 4.6: ORGANIC ELEMENTAL ANALYSIS PROCEDURAL
GUIDE**

Described below is the process adopted within this project for processing powdered rock samples in order to obtain organic elemental concentration data.

4.6.1 Weighing loss on ignition samples:

Required items:

- Sample powders
- 48 x 2 cm³ ceramic crucibles
- 1 x Aluminium crucible tray
- Tweezers
- Spatula
- Tissues
- Distilled Water
- Rock Standards

1. Arrange the ceramic crucibles in the aluminium tray and make note of which position corresponds to which sample.
2. Using the tweezers place one of the crucibles on the micro-balance and record its mass.
3. Remove the crucible from the micro-balance and fill ~1/3 of the way with sample powder (~30mg).
4. Using the tweezers, replace the crucible on the balance and record the total mass.
5. Repeat for the remaining samples and two standards.

4.6.2 Furnacing loss on ignition samples:

Required items:

- 48 x 2 cm³ ceramic crucibles
- 1 x Aluminium crucible tray
- Desiccator and/or Hot cupboard at 60°C
- Muffle Furnace
- Heat proof gloves
- Tongs

1. Place the weighed samples into the furnace keeping the tray in the same orientation (as to not lose track of sample order).
2. Loosely cover samples with aluminium foil to prevent contamination from muffle furnace.
3. Set the furnace to 200°C and leave at 200 for 5 minutes.
4. Set furnace to 450°C and leave at 450 overnight.
5. Turn the furnace off and remove the samples from the furnace using heat proof gloves and tongs.
6. Leave samples to cool for 5 minutes and then place samples in the desiccator
7. Leave door slightly open for ~60 minutes, allowing heat to dissipate, and then closely door and seal to prevent samples from taking on moisture.
8. Leave samples to cool overnight.

Appendices

4.6.3 Weight loss on ignition samples:

Required items:

- Furnaced samples in ceramic crucibles
 - Tweezers
1. Removed the cooled ceramic crucibles from the desiccator
 2. Using tweezers, place each crucible in turn on a zeroed balance and record the total mass.
 3. Calculate the loss on ignition (LOI) by dividing the final mass (total mass-crucible mass) by the initial mass (total mass-crucible mass).

4.6.4 Weigh loss on ignition samples into tin capsules

Required items:

- 8 x 5 mm tin capsules
 - Furnaced sample powders
 - Spatula
 - Tweezers x 2 (straight and curved)
 - Tissues
 - Distilled Water
1. Using tweezers placed a tin capsule onto the microbalance and zero the balance
 2. Add 8–10 mg powder to the capsule and record the mass in a notebook
 3. Using the straight tweezers, grasp the base of the capsule and pinch the top of the capsule using the curved tweezers. Compact the capsule until sufficiently small (until all air has been removed) without breaking the capsule.

Quantifying marine redox across the Triassic–Jurassic mass extinction

4. Place each capsule into a sample rack and note the sample order
5. Clean crucible using distilled water and a tissue and dry in an oven
6. Repeat for all samples

4.6.5 Weighing non loss on ignition samples:

Required items:

- 8 x 5 mm tin capsules
 - Sample powders (unfurnaced) from the same sample aliquot as LOI
 - Rock standards
 - Sulphanilamide chemical standard (10g)
 - Spatula
 - Tweezers x 2 (straight and curved)
 - Tissues
 - Distilled Water
1. Using tweezers, place a tin capsule in the microbalance and zero the balance
 2. Wight 8–10 mg of sample powder into the capsule
 3. Using the curved and straight tweezers pinch the top of the capsule and compact the capsule to remove all air
 4. Place each capsule into a sample rack and note the sample order
 5. Repeat for all samples (and standards)
 6. Weigh enough sulphanilamide for 1 standard every 10 samples and weigh enough rock standards for 1 standard every 20 samples. Also include 2 rock standards at the beginning and end of the batch.

APPENDIX 4.7: ISOTOPIC ANALYSIS PROCEDURAL GUIDE

Described below are the processes adopted within this project for digesting and processing powdered rock samples to obtain isotopic compositional data.

4.7.1 Spiking samples:

Prior to digestion the exact amount of both spike and sample that needed to be mixed (M) were calculated in Microsoft Excel⁷. The mass of spike and sample needed to fit within the optimal analyte amount but also the optimal spike to sample ratio, whilst using as little spike as possible. The optimal analyte amount for each sample was the natural analyte that needed to be weighed out to limit procedural blank contributions to <1% total. The optimal ratio was based on the amount of natural analyte that was being processed (see below).

Optimal analyte amount(s):

Molybdenum: 300 – 500 ng

Zinc: 500 – 600 ng

Cadmium: 50 - 100 ng

Spike concentration(s):

Molybdenum: 541 ppb

Zinc: 2650 ppb

Cadmium: 2700 ppb

Optimum Spike sample ratio(s):

Molybdenum: 0.3

Zinc: 1–2

Cadmium: 1–2

Once the target sample and spike weights were recorded the samples were weighed using the method in Appendix 4.5.

⁷ Analyte amount [ng] = Sample concentration (ppb) x sample weight (g)
Spike weight = analyte amount [ng] x spike: sample/ spike concentration

Quantifying marine redox across the Triassic–Jurassic mass extinction

After all samples were weighed out, decarbonated, sealed, and stored under Tupperware, the samples were transferred to a laminar flow hood (see the procedure for the digestion of powdered non-carbonate samples detailed in Appendix 4.5). The weighing table was then cleaned using ultra-pure milli-Q water and tissues, and the weighing table was set up once again. Each sample was then spiked using the calculated amount of double spike solution and the exact amount (mass) was noted.

4.7.2 Processing samples for anion exchange chromatography:

The samples were then digested in inverse aqua regia at 150°C for several days (Appendix 4.5). If the **elements** that were being measured **have a significant detrital component** (e.g. Zn) the samples were then dried down overnight at 90–105°C, and digested in HF and HNO₃ (1:2) at 120°C for 1–2 days. After the HF digestion the samples were dried down, 200µl of 4M HCl was added to each sample and allowed to evaporate twice. This step converts the residue into a chloride form which is essential for the loading solution to react with the column resin during the chromatography process of sample preparation. Once the 4M HCl had completely evaporated for the second time, 800µl of loading solution (1M HF + 0.5M HCl) was added to each sample, the digestion vessels were sealed, and the samples were refluxed at 90°C overnight on the hotplate.

If running for **elements** that are **do not have a significant detrital component** (e.g. Cd, Mo) then after the inverse aqua regia step (top of the previous paragraph) the samples were transferred into 15ml centrifuge tubes and centrifuged at 3500 rpm for 4 minutes. After the centrifuge step, the samples were transferred into 7ml round-bottomed FEP containers and were dried down at 90–105°C overnight. Once all of the samples had dried down, 200µl of 4M HCl was added to each sample and allowed to evaporate off.

Appendices

This step was repeated once. Once the HCl had evaporated the second time, 6ml of loading solution (1M HF + 0.5M HCl) was added to each sample, the PTFE containers were sealed, and the samples were refluxed at 90°C overnight on the hotplate.

4.7.3 Anion exchange chromatography

Column and resin cleaning- The samples were now ready to be chemically separated using anion exchange chromatography. This involves the dissolved sample being pipetted into a tapered tube or 'column' partly filled with a resin. When the sample is pipetted into the column, the resin adsorbs the ions from the sample. Then, depending on the acid which is filtered through the resin, different elements can be preferentially removed, or 'eluted', according to their chemical properties. This process is important as certain elements need to be removed from the solution prior to mass spectrometry. Iron (Fe) can form an argide interference on mass 96 which can affect ^{96}Mo measurements [Anbar, 2004; Kendall et al., 2017]. Zirconium (Zr) ($^{92,94,96}\text{Mo}$) and Ruthenium (Ru) ($^{92,96-100}\text{Mo}$) can also produce isobaric interferences for Mo [Anbar, 2004; Kendall et al., 2017]. Doubly charged Tungsten (W) ($^{92,96-100}\text{Mo}$) can also produce interference [Kendall et al., 2017]. Indium (In), (^{115}Cd), Palladium (Pd) ($^{105, 110}\text{Cd}$) and Tin (Sn) ($^{112, 114, 117}\text{Cd}$) can form isobaric interference for Cadmium (Cd) [Ripperger & Rehkämper, 2007; Bryan, 2018]. Gallium (^{111}Cd), Germanium ($^{112, 114}\text{Cd}$), Mo ($^{110, 111, 112, 114}\text{Cd}$), Ru ($^{110, 112, 114}\text{Cd}$), Zn (^{110}Cd) and Zr ($^{110, 112}\text{Cd}$) can produce molecular interferences across all of the most abundant Cd isotopes [Ripperger & Rehkämper, 2007]. It is therefore essential that the desired element is isolated from potential sources of interference prior to any isotopic measurement.

Prior to the samples being processed through the anion exchange columns both the columns and the resin were first cleaned. The following step-by-step process assumes

Quantifying marine redox across the Triassic–Jurassic mass extinction

that new resin is needed. What follows is a detailed explanation of column and resin cleaning in preparation of anion exchange chromatography (based on column methods detailed in Pearce et al., 2009 and Dickson et al., 2016).

Two sets of columns have been used for this research project; 3ml STFE shrink fit columns with a 200ul resin bed and 10ml BioRad polypropylene columns with a 2ml resin bed. Both sets of columns have been cleaned using a similar methodology.

Column cleaning procedure: Firstly, the columns were repeatedly rinsed with ultra-pure milli-Q water and left to air dry on a tissue. Two different resins have been used for this project; TRU SPEC resin for the 200µl columns only, herein referred to as TS, and AG 1-X8 resin for both the 200µl and 2ml columns, herein referred to as AG. The AG was stored in weak HCl and was therefore able to be loaded directly into both columns. The TS was stored dry and was therefore rinsed in ultra-pure milli-q water prior to loading i) as dry resin cannot be directly added to the column and ii) the milli-q rinse removes fine particulates to ensure an even grain size distribution. A small amount of TS was transferred into a sealable container with some ultra-pure milli-Q water, then shaken vigorously. After leaving the container to settle for five minutes, a thin layer of fine particulates had separated from the TS and formed at the top of the water. The fine particulate matter was poured into a waste beaker, and this step was then repeated several times until the water became noticeably clearer upon the settling of the TS.

Loading the resin(s)- The cleaned columns were placed into the column racks with waste beakers underneath each column. The column was filled with a small amount of ultra-pure milli-Q water and then, using a 200ul (200µl column) or 1ml (2ml column) pipette, a small amount of resin was taken up into the pipette tip. The resin was pipetted

Appendices

into the milli-Q water at the base of each column and allowed to settle. This process was repeated until the resin filled the resin bed (tapered portion at the base of the column). Any remaining milli-Q water was allowed to drain from the columns into the waste beakers, then the column method was followed as outlined in table below (Table 1). If eluting the first stage of Cd or Mo then method A1 was followed. If eluting Zn then method A2 was followed, and if eluting the second stage of Cd then method A3 was followed (Table 1). The column method was repeated once for Zn. After the elutes had been collected, the elute was dried down and redissolved in 1ml 3% HNO₃.

Resin used: Biorad AG 1 - X8 anion exchange resin

Phase	Quantity(mL)		Eluent	Purpose
	A1 10ml (Cd, Mo)	A2 2ml (Zn)		
Resin Cleaning	10	1.5	7.5M HNO ₃	Transition metal removal
	10	1	4M HCl	Converts resin to chloride form
	30	3	1M HCl	Removes major cations
Pre-conditioning	3	0.3	1M HF/ 0.5M HCl	Pre-conditioning
Load Sample	6	0.8	1M HF/ 0.5M HCl	Load Sample
Matrix Elution	8	1.5	1M HF/ 0.5M HCl	Elutes majors
Fe, Ba, Zr Elution	8	1	4m HCl	Isobars/Argides
Zn Elution	12**	2.2*	0.5M HF/0.1M HBr	CO.(Zn)*/ interf.**
Sn and Mo Elution	12*	n/a	3M HNO ₃ / 0.1M HBr	COLLECT (Mo)*
Cd Elution	6.5*	n/a	3M HNO ₃	COLLECT (Cd)*

Resin used: TrisKem TRU Spec resin

Phase	Quantity(mL)		Eluent	Purpose
	A3			
Resin Cleaning/ Pre-conditioning	2.5		3% HNO ₃	elutes Sn
	2.5		8M HCl	elutes Cd, conditions
Load Sample	0.5ml		8M HCl	Load Sample COLLECT (Cd)
Elution of Cd	1		8M HCl	COLLECT (Cd)

Table 1:- Column cleaning methodology adopted within this thesis amended from Byran (2018).

4.7.4 Measuring isotopic compositions

Multi-collector inductively coupled plasma mass spectrometry:

The samples were processed using a ThermoScientific Neptune Plus Multi-Collector Inductively Coupled Plasma Mass Spectrometer (MC-ICP-MS) within the department of Earth Sciences at Royal Holloway. Prior to any samples being run the Neptune Plus was turned on and tuned used the following procedure:

1. Both the argon and nitrogen tanks were opened, and all taps between the tanks and the Neptune were turned on (parallel with the gas lines).
2. The autosampler was turned on.
3. The Aridus III was turned on.
4. The nebuliser, in the autosampler, was placed in a centrifuge tube of milli-q water.
5. The nitrogen and argon were kept low/ICP ignition was selected.
6. The plasma was turned on within the Neptune software.
7. The peristaltic pumped was turned on within the Neptune software.
8. The Neptune was allowed to start up.
9. The chillers were checked and were confirmed to record temperatures of 20°C or less.
10. The air handling was checked within the ICP-MS lab.
11. The filters were checked.
12. The cup configuration was selected and set for the element being analysed.
13. The analyzer gate was opened (ICP ignition was turned off here if used).
14. A baseline calibration of 600 cycles was run.
15. The nebuliser was then washed in the rinse station.
16. The nebuliser was then placed in a 10ppb/20ppb tuning solution

Appendices

17. The mass was set to the isotope of the analyte set to the central faraday cup.
18. The relevant inlet system file was loaded.
19. The argon and nitrogen gas flows were increased until a maximum signal voltage was reached whilst being relatively stable.
20. The position of the ICP torch was moved to its optimal position by tweaking the X and Y position in the Inlet System tab.
21. The Focus, Shape, X and Y positions were amended in the Focus and Shape tab.
22. A mass scan was then initiated for the mass range of the central cup using the function 'mass scan'.
23. The focus was tweaked using the peak recorded a 'top hat shape' (steep sides and a flat top).
24. The focus was read and saved.
25. The peak was centred.
26. The nebuliser was moved to the rinse station to wash out and monitored to confirm and value of ~0.1% of the tuning solution was reached.

Sample Introduction- Mo and Cd was introduced as a dry plasma using a Teledyne Aridus III. Zn was introduced as a wet plasma using a glass spray chamber. Both sample introduction methods used a nebuliser with a 100 μ l/min flow rate.

Concentration checks- After the samples were redissolved in 3% HNO₃ and the instrument was tuned, the samples were now ready to be processed for concentration checks. Each sample was diluted 50-fold (20 μ l sample, 980 μ l 3%) in a 2.2ml microcentrifuge tube. These diluted samples were run to determine the concentration of ⁹⁶Mo within each sample so that the concentrations of the samples could be normalised

Quantifying marine redox across the Triassic–Jurassic mass extinction

to each other. The reason for normalising the samples was to confirm that the concentrations weren't too low and therefore that a sufficient signal was present for all samples to be run. But also, so that the concentrations weren't too high so that the detectors would be oversaturated. Measuring dilute sample solutions also allowed for spike/sample ratios to be determined which subsequently were used to make bracketing standards for Zn batches.

MC-ICP-MS run- After the samples has been diluted accordingly, a run list was set up within the Neptune software. Each sample proceeded a blank of 3% HNO₃ which was run for 5 cycles with each cycle having an integration time of 8.4 seconds. The blank prior to the sample was subtracted from the sample in order to remove background concentrations of the analyte. The sample itself was run for between 50 and 80 cycles with each cycle also having an 8.4 second integration time. A zero-delta reference standard was run every 4 samples to normalise the samples. Depending on the size of the batch, between 2 and 4 secondary standards were run during the batch. For Mo this was an open university molybdenum standard [*OU Mo; c.f. Goldberg et al., 2013*], for Cd an Alfa Aesar Specpure Cd concentration standard, Lot# 081192A [*OXCAD; c.f. Dickson et al., 2020*] and for Zn an Alfa Aesar Specpure Zn concentrations standard.

Isotopic data deconvolution and processing- Isotopic data was deconvolved offline using an Excel-based macros programme developed by Alex Dickson.

ANBAR, A. D. 2004. Molybdenum Stable Isotopes: Observations, Interpretations and Directions, *Reviews in Mineralogy and Geochemistry*, **55**, 429–454.

BRYAN, A. 2018. Investigation of the controls on cadmium isotope composition of modern marine sediments. PhD Thesis.

Appendices

DICKSON, A. J., Jenkyns, H. C., Porcelli, D., van den Boorn, S. & Idiz, E. 2016. Basin-scale controls on the molybdenum-isotope composition of seawater during the Oceanic Anoxic Event 2 (Late Cretaceous). *Geochimica et Cosmochimica Acta*, **178**, 291–306.

DICKSON, A. J., Idiz, E., Porcelli, D., & van den Boorn, S. H. J. M., 2020, The influence of thermal maturity on the stable isotope compositions and concentrations of molybdenum, zinc and cadmium in organic-rich marine mudrocks. *Geochimica et Cosmochimica Acta*, **287**, 205–220.

GOLDBERG, T., Gordon, G., Izon, G., Archer, C., Pearce, C. R., McManus, J., Anbar, A. D., & Rehkämper, M. 2013. Resolution of inter-laboratory discrepancies in Mo isotope data: an intercalibration. *Journal of Analytical Atomic Spectrometry*, **28** (5), 724–735.

HU, Z. & Qi, L. 2014. 15.5: Sample Digestion Methods in *K. Turekian & H. Holland (Eds.) Treatise on Geochemistry 2nd Edition*. p. 87–109.
<http://dx.doi.org/10.1016/B978-0-08-095975-7.01406-6> .

KENDALL, B., Dahl, T. W. & Anbar, A. D. 2017. The stable isotope geochemistry of molybdenum. *Reviews in Mineralogy and Geochemistry*, **82**, 683–732.

PEARCE, C. R., Cohen, A. S., & Parkinson, I. J. 2009. Quantitative separation of molybdenum and rhenium from geological materials for isotopic determination by MC-ICP-MS. *Geostandards and Geoanalytical Research*, **33** (2), 219–229.

RIPPERGER, S. & Rehkämper, M. 2007. Precise determination of cadmium isotope fractionation in seawater by double spike MC-ICPMS, *Geochimica et Cosmochimica Acta*, 71 (3), 631–642.

XU, G., Hannah, J. L., Bingen, B., Georgiev, S. & Stein, H. J. 2012. Digestion methods for trace element measurements in shales: Paleoredox proxies examined. *Chemical Geology*, **324–325**, 132–147.

APPENDIX 5: ELEMENTAL STANDARD COMPILATION

Attached as separate excel file online.

APPENDIX 6: ZINC ISOTOPE DATA

Attached as separate excel file online.

APPENDIX 7: EXTENDED THESIS DATASET

Attached as separate excel file online.